Design of Ships and Offshore Structures:
A Probabilistic Approach for Multi-Year Ice and Iceberg Impact Loads for Decision-making with Uncertainty

By

©Freeman E. Ralph P.Eng. M.Eng.

A Thesis
submitted to the School of Graduate Studies
in partial fulfillment of the requirements for the
degree of Doctor of Philosophy

Faculty of Engineering and Applied Science
Memorial University
St. John's, NL

October 2016

This page is intentionally left blank

Abstract

Ice is a complex material that exhibits different failure properties depending on the loading rate, temperature and salinity. Under fast loading rates such as a ship ramming a multi-year (MY) ice, it fails as a brittle fracturing material. Fracture and spalling processes non-simultaneously reshape the contact zone resulting in concentrated forces on localized contact areas. These localized High Pressure Zones (*HPZs*) are highly variable in time and space. The relationship between local and global processes is that the sum of *n HPZs* forces transferred into the structure at any point in time is the total global force transmitted to the structure. As with other fracturing materials, an inherent scale effect exists.

Global pressures result from the sum of *n HPZ* forces averaged over the nominal contact area (e.g. the imprint of a ship's bow into the ice without correction for spalling effects). The maximum global force will generally occur at the end of a ram at the maximum nominal contact area. Due to the random occurrence of natural flaws in the ice, pressures will vary as fractures occur, continually changing the contact face. A global scale effect exists such that pressures on larger contact areas, including zones of low and zero pressure, average out to be smaller.

Unlike global pressures, maximum local pressures may occur on any panel and at any point through the ram duration. Modeling exposure is important as design pressures will increase for increasing number of interaction events as well as increased penetration or duration. The scale effect for local pressures within the nominal contact area is more demanding than for global pressures such that pressures on smaller areas are considerably higher. While this is expected, given confinement can suppress damage and limit fracturing events, a force limit exists where microstructural damage occurs, softening the ice and causing *HPZs* to fail.

Local pressures on varying panel areas were studied based on spatial *HPZ* density and *HPZ* force. Building on earlier *HPZ* analysis using *Louis S. St. Laurent* data, in this thesis *HPZ*

density and forces were derived from analysis of four *Polar Sea* data sets. The occurrence and intensity of *HPZs* on panel areas were simulated using a Poisson Process and an exponential distribution for *HPZ* force. The influence of modeling *HPZ* cutoff force on *HPZ* density, *HPZ* force distribution as well as local pressure parameters were studied and appropriate combinations recommended.

Building on the *Polar Sea HPZ* analysis, a new model was developed for this thesis that considers *HPZ* occurrence in time through a ramming event, modeling *HPZ* rate. This was further enhanced by correlating *HPZ* rate with ship speed. Such a model allows the designer to determine baseline 'parent' local pressure design parameters based on vessel size and expected operational speed. The faster a ship operates through an ice regime, the greater the *HPZ* rate. Larger and faster ships will penetrate further, having longer interaction durations and hence a greater number of *HPZs* forming (unless, for example, the ship passes through a ridge). For design, we are interested in the maximum local pressure on a single panel area through the ram duration. Rates too will vary along the vessel being greater on the bow and least from mid-body to stern. For fixed structures designed for iceberg impacts, rate and duration based on iceberg size and drift can be used to model exposure in time. For floaters, modeling *HPZ* formation in time provides a means to estimate dynamic global forces and mooring loads illustrating benefit of compliance effects. Modeling of *HPZ* occurrence over a panel area is also very attractive for structure response analysis. The random placement of *n HPZs* over a structural panel gives a better basis to model stress localization, which is very important for limit states design.

A preliminary review of the IACS Polar Class rules was carried out in this thesis. Global impact forces are estimated using a kinetic energy collision model. Consideration for modeling ice crushing strength assumes a pressure-area relationship that is proportional to $A^{-0.1}$ which is not consistent with experimental results demonstrating a scale effect proportional to $A^{-0.4}$. The resultant design formulation models excessive semi-local pressures increasing with increasing semi-local contact area. While the intent is to model increasing pressures locally with increasing vessel displacement and subsequent penetration and contact area, justification for this trend suggests that there is no reason for traditional pressure area scale effects to exist and that with confinement, fracturing processes will be limited. But

fracturing processes exist at all scales. The occurrence and behavior of *HPZ*s either lead to very large stress localization that enhances fracture events or they undergo microstructure damage that softens the ice at the structure interface. While the design trend in the Polar Class rules may be okay, the background ice mechanics can be improved. An alternative collision model is developed in this thesis with an ice strength model based on data and an exposure algorithm to model pressures increasing locally with larger displacement vessels.

In the mid 1990s as part of the Arctic Shipping Pollution Prevention Regulations (ASPPR) proposal reviews, a probabilistic time-step ship ram model was developed to estimate impact forces. Consistent with the ASPPR work, exposure based on annual number of collisions was mapped to each Polar Class (e.g. PC1, PC2, PC3 can expect on the order of 10000, 1000, 100 rams per year respectively). Using the *MV Arctic* as a test case and exercising extremal analysis, impact forces were estimated for each Polar Class. Characteristic 10^{-2} global forces were compared with Polar Class rule estimates. Probabilistic local pressures were also compared with rule based estimates. Assuming impacts with MY ice, preliminary results show that plating design pressures may be reasonable, with recommendation for adjustment to the Polar Class 1 coefficients to reduce conservatism, and possible increases for lower classes. Analysis should be extended to other vessels and operating conditions.

A probabilistic methodology for design of ships based on the principles of safety and consequences is important and necessary both for design and safety validation. Such approaches can consider the class of the vessel on the basis of expected number of annual interactions with extreme ice features. An example illustration of a design based on an arctic shipping route, ice conditions, design strategy, risk mitigation via detection and avoidance and resultant local pressrues on the hull for structural design. .

Acknowledgements

I would like to express sincere gratitude to my supervisor, Dr. Ian Jordaan, for unwavering commitment and support through this research journey. Your passion for the subject made the journey enjoyable and rewarding. Your inspiration and guidance not only kept me focused, but has influenced my way of thinking. Thanks, too, to my supervisory committee members, Dr. Brian Veitch and Dr. Wei Qiu, for your support and commitment to the PhD process.

I would like to express gratitude to Dr. Charles Randell, President and CEO of C-CORE, for continued support and encouragement through this journey. Thanks also to many colleagues and friends, particularly Paul Stuckey and Mark Fuglem, who were always willing to assist and provide practical guidance when needed.

I would like to acknowledge HMDC, the Terra Nova Project and RDC who funded C-CORE's Centre for Arctic Resource Development (CARD), through which this work was possible.

Thank you to my parents, Bill and Dorothy Ralph and in-laws, Rod and Lavinia Jeans, for their constant support and encouragement.

Finally, I would like to thank my wife, Tina, and son, Corban, for their unwavering love, support, encouragement and patience, without which this would not have been possible.

To Tina and Corban

Table of Contents

LIST OF TABLES

List of Figures

List of Symbols

E	Elastic modulus.
σ	applied stress
σ_{11}	uniaxial applied stress
ε_e	elastic strain
ε_d	delayed elastic strain
ε_v	viscous creep strain
ε_{total}	elastic strain
C, A, q	constants
a_T	temperature dependent rate parameter
t	time
Qi	activation energy
R	gas constant
T	temperature
v	Poisson's ratio.
K, K_{Ic}	fracture toughness.
ℓ	crack length
$2c$	crack length
γ_S	surface energy per unit area
Cp	Coefficient of power law for mean Global pressure on $1m^2$ area.
Dp	Exponent of power law for mean global pressure.
W	Event that the weakest link fails.
V	Weibull volume of ice
V_0	Weibull reference volume
σ	Weibull applied stress
σ_0	Weibull reference stress

b	Weibull modulus.
R	Expected specimen strength.
σ_R	Standard deviation of strength.
HPZ	high pressure zone
ρ	*HPZ* density
γ	exponential distribution parameter for *HPZ* force
γ_0	exponential distribution plotting position for *HPZ* force
α	exponential distribution parameter for local pressure
x_0	exponential distribution plotting position for parent local pressure (and global measured force)
w_0	exponential distribution plotting position for annual maximum design distribution for global force
w_{100}	characteristic global force corresponding to 10^{-2} annual exceedance probability
μ	exposure parameter that represents the number of equivalent rams
n	number of impact events per unit period (e.g. a year)
$F_X(x)$	cumulative distribution for parent distribution
$Fz(z)$	cumulative distribution for design distribution
ELIE	extreme level ice load event
ALIE	abnormal level ice load event
ULS	ultimate limit state
L	vessel length
B	vessel beam
T	vessel draft
D	vessel displacement
P	vessel power
F_{MAX}	maximum ship ram force (also referenced as software name)
Cwp	waterplane coefficient
Amx	added mass for surge
Amy	added mass for sway
Amz	added mass for heave

$Amroll$	added mass for roll
$Ampit$	added mass for pitch
$Amyaw$	added mass for yaw
α	bow opening angle
γ	bow stem angle
β	buttock angle.
β'	buttock angle normal to hull
f_{ai}	bow geometry coefficient based on contact location
ϕ	opening angle defining geometry of ice edge in contact with vessel
KE	kinetic Energy
IE_C	ice crushing Energy
IE_R	kinetic energy rotation
M	mass of ship
Ma	added mass of ship
Co	equivalent mass reduction coefficient based on popov equations
V	impact speed
Vn	component of impact speed normal to hull
δ	distance crushed during impact event
Fn	crushing force normal to hull
F_{NMAX}	normal crushing force at maximum penetration
P_0	Power law pressure area constant for $1m^2$ area in polar class rules
P_{avg}	average global pressure
ex	power law exponent for pressure area in Polar Class rules
w_{ex}	coefficient for estimating semi local contact area dimension from global
ζ	unit penetration of ship crushing into ice
CF_C	Class factor for Crushing
CF_F	Class factor for flexure failure
CF_s	Class factor for Dimension
CF_{Dis}	Class factor for Displacement
σ_{flex}	ice flexural strength
h_{ice}	ice thickness

AR	aspect ratio
H_{NOM}	nominal contact area height in Polar Class rules
W_{NOM}	nominal contact area width in Polar Class rules
A_{NOM}	nominal contact area
b	semi-local contact area height in Polar Class rules after spalling event
w, w_{des}	semi-local contact area width in Polar Class rules after spalling event
AF	area factor
PPF	peak pressure factor for local ice pressure for shell plating design
PEF	peak exposure factor accounting for vessel mass
σy	yield strength of steel
s	spacing of frames supporting shell plating on ship
b	height of the ice local ice contact area for shell plating design

CHAPTER 1. Introduction

1.1 Background

Ice is a complex material that exhibits different failure properties depending on the loading rate. Under fast loading rates such as a ship ramming a multiyear (MY) floe, it fractures. Fracture and spalling occur across the whole interaction surface; both at the free edges (macro scale) and internally (micro and macro scale). As fracture and non-simultaneous failure reshape the contact face, the nominal contact area (i.e. imprint of bow into ice with no adjustment for spalls) will have zones or regions having very high pressures (*HPZ*s) and zones with no contact having zero or near zero pressure. The average pressure over this larger nominal area will be significantly less than the pressure on a single *HPZ* and reduces as the nominal area increases. Within the nominal contact area, the zones of actual contact also exhibit a scale effect such that pressures on the smallest contact areas are substantially higher than for larger contact areas.

One illustration of scale effect is illustrated in Figure 1, a compilation plot of pressure-area from various data sets. Limited data exist above 100m^2, and there is a considerable gap in measured data between areas 10 and ~200 m^2 which raises uncertainty and reluctance in modeling scale effects for larger interaction areas. An upper bound pressure is often specified modeling no scale effect. Recent research suggests that the few larger area *Molikpaq* data points are overly conservative (Frederking *et al.*, 2011; Jordaan *et al.*, 2005c). While larger scale measurements to fill the gap will add more confidence in modeling scale effects, the trend is intuitive considering the brittle, fracture prone nature of ice. Further, simulation modeling based on fundamental mechanics of ice failure proves very useful.

A common link between local and global processes is that at any instant during the interaction process, the sum of the contact forces transmitted into the hull through *n HPZ*s is the global force – recognizing too that extrusion will add to some small background pressure. A model for *HPZ* density within the nominal contact area would prove very valuable in

building confidence in the scale effects associated with both local and global ice failure. To date, this measure of global density has not been resolved.

Ship ram data account for a large volume of available ice crushing data, but unfortunately data that measure both global and local pressures simultaneously such that *HPZ* density can be directly estimated do not exist. Ship ram data consist either of global forces with some measure of the nominal contact area based on ice thickness and assumed ship imprint, or of local loads where a relatively small section of the hull was instrumented, typically one side of a bow. Figure 2 and Figure 3 illustrate the ram processes, the nominal contact area and the limited panel area for the measurements. Despite limited data, a main objective in this thesis is to model the occurrence of *HPZ*s both spatially across panel areas and in time through the ram duration. While the focus was modeling *HPZ* rate for local pressure design, it is recognized as noted above that global forces at any point in time result from the summation on *n HPZ* forces at that time.

Estimated design pressures in the IACS Polar Code (IACS 2011) seem conservative compared with other design codes such as CSA and API (Masterson and Kiring, 2008) particularly for higher class vessels above Polar Class 2. Based on results of this research, a review of the Polar Class rules was carried out, including the ship ice interaction model, as well as the basis for specifying "class coefficients." Validation using a probabilistic approach that models exposure in design pressure estimates based on the number of rams per year is carried out.

Modeling scale effect is important for design for ship-ice interaction. It is imperative that designs are safe, but it is not necessary to be excessively conservative beyond what is safe. Secondly, all codes should have a basis for assessing the safety of the system, quantitatively, not qualitatively. This can only be achieved using reliability based methods for design, despite the fact that single deterministic type solutions are easier to solve.

1.2 Thesis Outline

For ships interacting with multi-year ice, this thesis covers a range of design issues including probabilistic approach for design, ice mechanics and failure strength modeling, global impact forces, and local pressures within the global contact area for shell plate design. An example design illustration is presented with recommendation for future work. The outline below illustrates the content of the thesis, including a literature review of current knowledge and focus of original research (**bolded**). This thesis includes:

- A comprehensive literature review of probabilistic approach to design, ice structure interaction and ice mechanics including:
    - probabilistic methods showing the importance of exposure in modeling global design forces and local design pressures (i.e. annual number of events, duration of interaction events, probability of contact for panel areas);
    - ice structure interaction, including the occurrence of local high pressure zones within global interaction areas and corresponding pressures for design;
    - the mechanics of ice structure interaction relevant to ship design, including experimental data and relationships that model ice pressures on respective contact areas and corresponding scale effects;
    - a probabilistic methodology for modeling local design pressures based on maximum pressures on any subpanel area through the ram duration and the derivation of distribution parameters α and x_0 based on an exponential distribution fit to the tails of measured local pressure distributions;
- High Pressure Zone (*HPZ*) modeling for local pressure analysis and design:
    - an overview of probabilistic *HPZ* occurrence modelling to date that considers *HPZ* density and *HPZ* force and estimates design pressures on panel design areas;
    - **a new analysis of the sensitivity of local pressures to variability in *HPZ* force and density;**
    - **a new analysis of *HPZ* force and density based on *Polar Sea* data for rams with multiyear ice including Beaufort 1982, North Chukchi 1983, South Chukchi 1983, and Beaufort 1984 data sets**;

- **using *Polar Sea* data, development of a new probabilistic *HPZ* model that considers, in addition to the spatial occurrence of *HPZs* across a panel at any time instance, the rate of *HPZ* occurrence through the ram duration and correlates *HPZ* formation rate to vessel impact speed – larger, faster ships with greater kinetic energy will crush further into the ice thereby encountering a greater number of *HPZs*. A 'parent' local pressure distribution specific to a vessel's design requirements and operability can be readily obtained for extremal analysis and design. Also, as global force is based on the sum of *n HPZ* forces within a nominal contact area, this model marks a big step forward in modeling the formation of *HPZ*s in space and time, providing a basis for modeling global forces in time, which is particularly important for floater design and mooring loads**;

- Probabilistic modeling for ship design – methodology, verification of rules, and design:
  - an overview of extremal based probabilistic methodology for ship design including review of Arctic Shipping Pollution Prevention Regulations (ASPPR) proposals and consideration of annual exposure in estimating global design forces for different arctic class vessels;
  - an overview of a probabilistic time-step ship ram model developed during the ASPPR review (Carter *et al.*,1992) for simulating global impact forces **including a new analysis of conservatisms with extremal modeling, when ice strength (i.e. $P = Cp\ A^{-Dp}$) parameter *Cp* is modeled as a lognormal distribution and *Dp* is modeled as a normal distribution but raised to a power, thereby modeling a lognormal effect – consideration for alternative distributions (e.g. *Cp* modeled as a Weibull) is discussed**;
  - a review of Polar Class rules including deterministic global force estimates based on energy methods and interaction geometry to estimate local pressures for hull plating design. **Review highlighted the importance of modeling ice strength scale effects and exposure. An alternative model is developed that incorporates an improved ice strength model with consideration for scale effects, the occurrence of *HPZs* within the nominal contact area and**

a new relationship for exposure based on vessel displacement and impact speed;

- **applying extremal based probabilistic modeling, a preliminary verification of Polar Class coefficients (that govern design forces) was carried out, modeling annual exposure with each Polar Class (i.e. number of expected rams per year) and estimating global forces and local design pressures**; and

- **an example ship design illustration using a probabilistic methodology to estimate global impact forces, and local shell plating design pressures; a model that considers variability in the occurrence of extreme ice features, contact probability and influence of risk mitigation (i.e. tactical avoidance) on design loads**;
- **Recommendations for future work;**
  - **enhance modeling of *HPZ* rate and enhance structural analysis; and**
  - **full scale field experiments for further validation**.

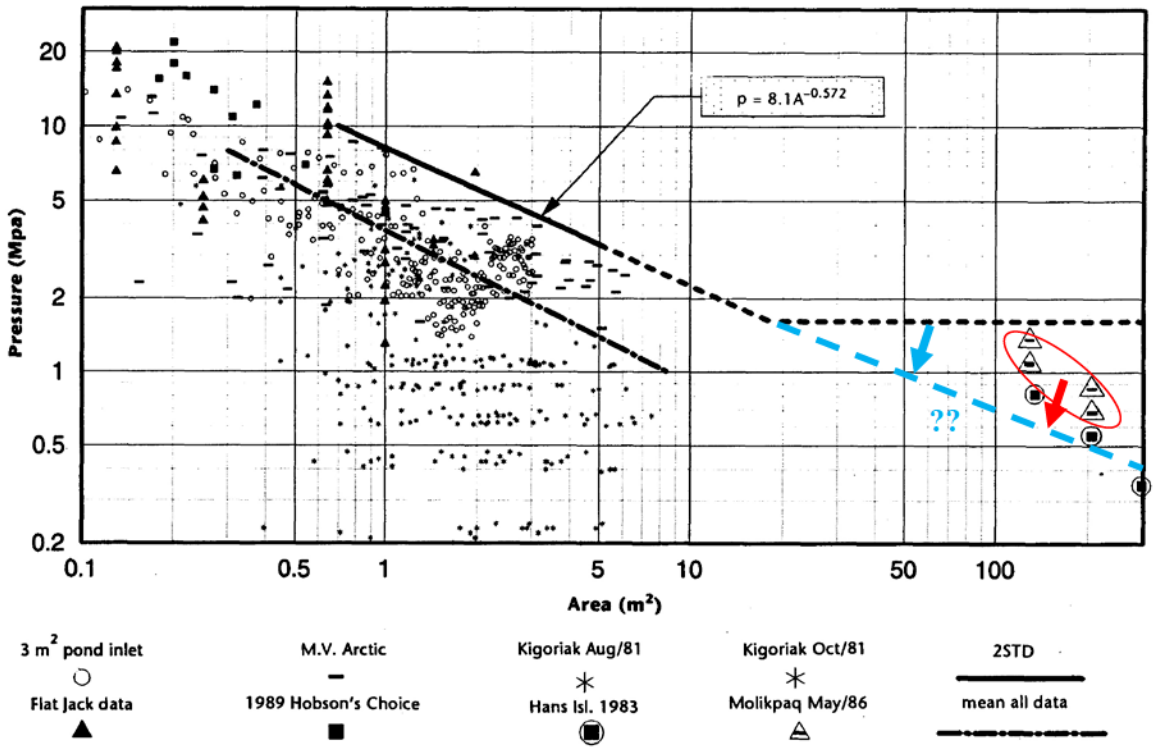

Figure 1 Pressure-area data and highlighted data gap (Masterson and Frederking, 1993)

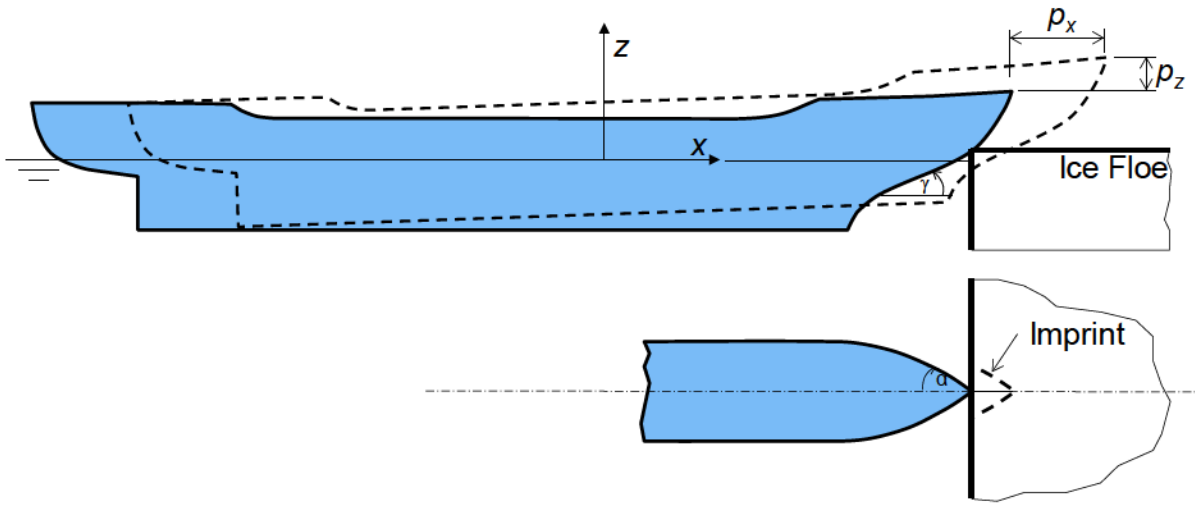

Figure 2 Illustration of contact geometry and coordinates for ship ramming into a floe

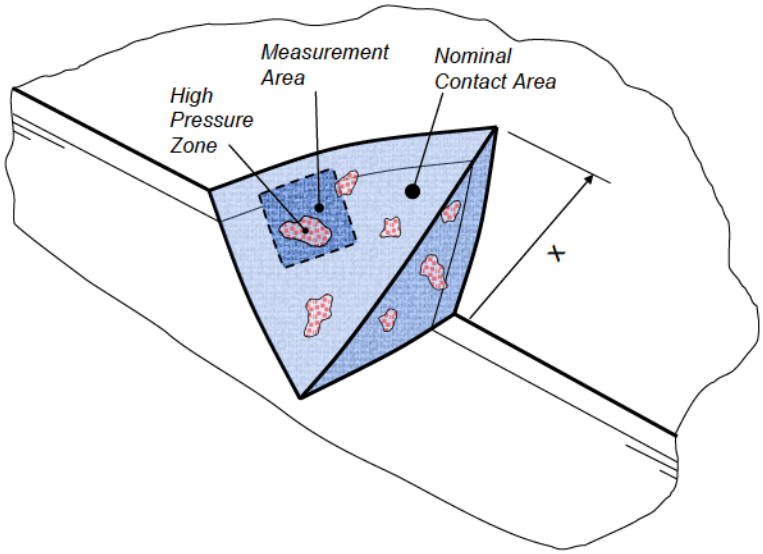

Figure 3 Imprint of ship bow into ice, illustrating the distribution of *HPZ*s relative to the nominal contact area and the measurement area at a specific point in time during a ship ram. (*Note that areas of spalling near the edge of the floe are included in the nominal area*.)

CHAPTER 2. Design for Ice Structure Interaction

2.1 Reliability Based Approach

2.1.1 Overview of Probabilistic Methodology

A probabilistic approach to design is appropriate where there is variability and uncertainty in environmental input parameters and corresponding design loads, for MY ice loads in the present case. Parameters that influence loads include: ice concentration and thickness, including seasonal variability; speed of the ice; mass and added mass of the ice feature and vessel (if floating); speed of the vessel; interaction geometry; and material properties including the density of random flaws that initiate fracture processes and the influence of scale effects on ice strength.

To estimate probabilistic design loads, the designer must first identify distributions for the input parameters for the ice loading scenarios. Ice forces for different interaction scenarios may depend on many parameters listed above. A general flow diagram outlining the approach for analysis and design is illustrated in Figure 4.

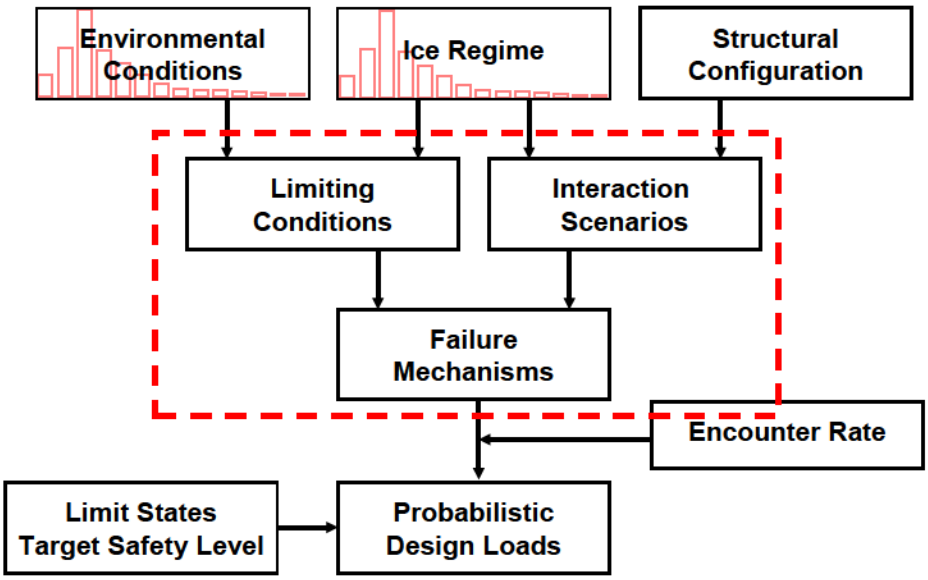

Figure 4 Example flow chart for probabilistic model development

2.1.2 Ice Load Distribution

Based on the input distributions, a distribution of loads can be determined for design. In some cases, it may be desirable to measure interaction forces directly. Figure 5 illustrates the distribution of measured maximum bow forces based on ship ramming trials with the MV *Arctic*.

Most likely or expected values correspond to the peak in the distribution. Unlikely loads are near the upper and lower tails. While this distribution provides some measure of variability and spread in loads, it is a single event distribution (sometimes called a "parent" distribution) and cannot be used directly for design load. The design load must consider the exposure of the vessel or facility, a key input in probabilistic extreme value analysis.

2.1.3 Extreme Value Design Loads

Exposure considers the expected number of interactions per specified period (or encounter frequency), which for design is typically referenced as a *year*. Other considerations include the region of the structure or hull under consideration and the proportion of hits on a particular panel relative to the overall interaction area, as well as duration through a ram.

With respect to annual interaction events, for design we are interested in the maximum load out of n expected interactions in any given year. The extreme value distribution Z for design will be given as

$$Z = \max(X_1, X_2, ..., X_N) \quad (1)$$

where there are N events for X_i, over the time interval (e.g. 1 year).

The influence of the number of interactions in a year (or period) on the extreme value design distribution, given a parent distribution, is illustrated in Figure 6. With many interactions per year the design distribution will shift to the right of the parent distribution; with multiple years between interactions, the design distribution shifts to the left with probability spike at zero load (Jordaan, 2005a).

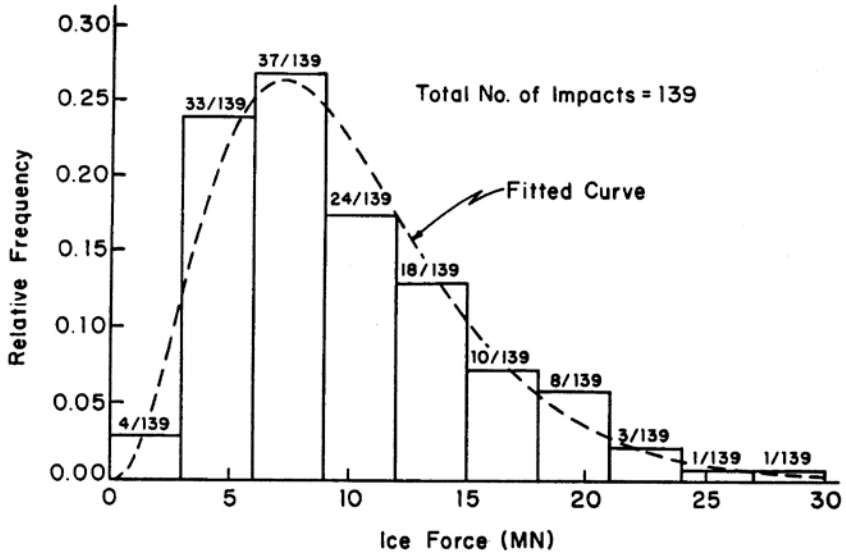

Figure 5 Histogram of ice ram forces measured during ram trials on board the MV *Arctic* off Colburg Island in May 1984 (Carter *et al.*, 1992)

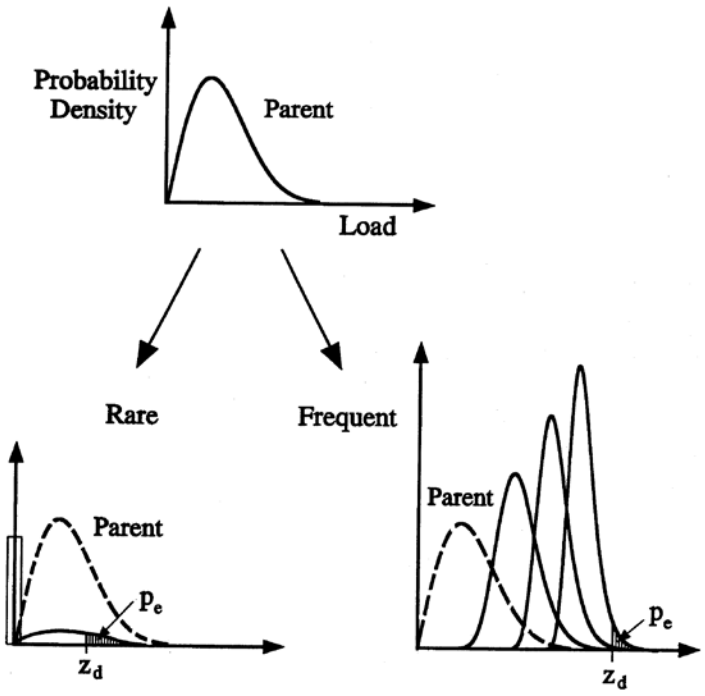

Figure 6 Illustration of the relationship between rare (i.e. years between interactions) and frequent (i.e. many interaction per year) distributions and the generic parent distribution for an environmental process (Jordaan, 2005a)

2.1.4 Design Strategy

For design, we are concerned for the safety of personnel, the structure and the environment, specifying design loads that have low probability. A design strategy references a specific load level from a distribution of annual maximums that corresponds to some target exceedence probability p_e. One strategy may reflect design for a 1 in 100 year *extreme level event* (1% annual exceedence probability), or 1 in 10,000 year *abnormal level event*, where the consequence of load exceedence may be loss of life and the platform. Another strategy may reflect frequent *serviceability* type conditions based on 1 in 10 year event (10% annual exceedence probability). Here the consequence of load exceedence may be minor localized damage to the structure or minor interruption of operations but no safety implications. The strategy may also reflect the integration of a risk mitigation system in the design (i.e. detection and avoidance).

Figure 7 illustrates how these are defined with respect to a design load distribution with the following notation:

$f_Z(z) = pdf$ = probability density function

$F_Z(z) = Pr(Z \leq z) = cdf$ = cumulative distribution function

$p_e = 1 - F_z(z)$ = probability of exceedence

Application of the design process based on routing options is illustrated in Figure 8, including the integration of risk mitigation where the number of interactions can be reduced through detection and avoidance.

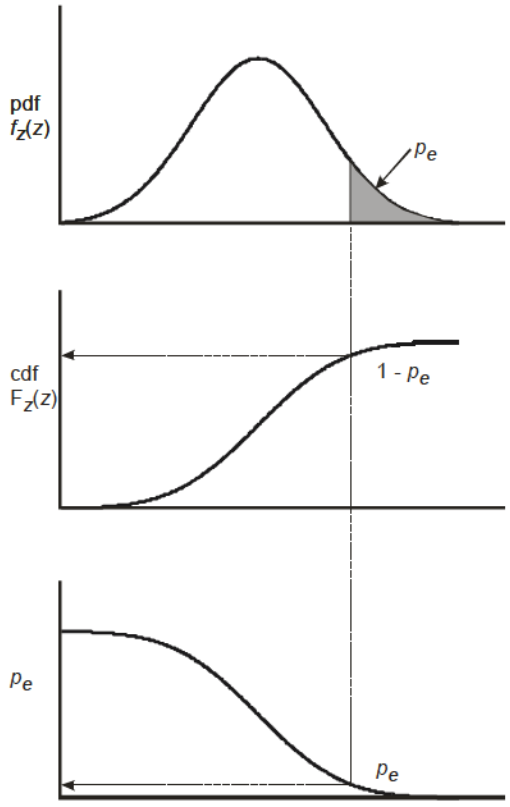

Figure 7 Definition of exceedence probability, p_e which defines a specific design strategy where the grey density represents the exceedence probability (e.g. 10%, 1%, 0.1% exceedence)

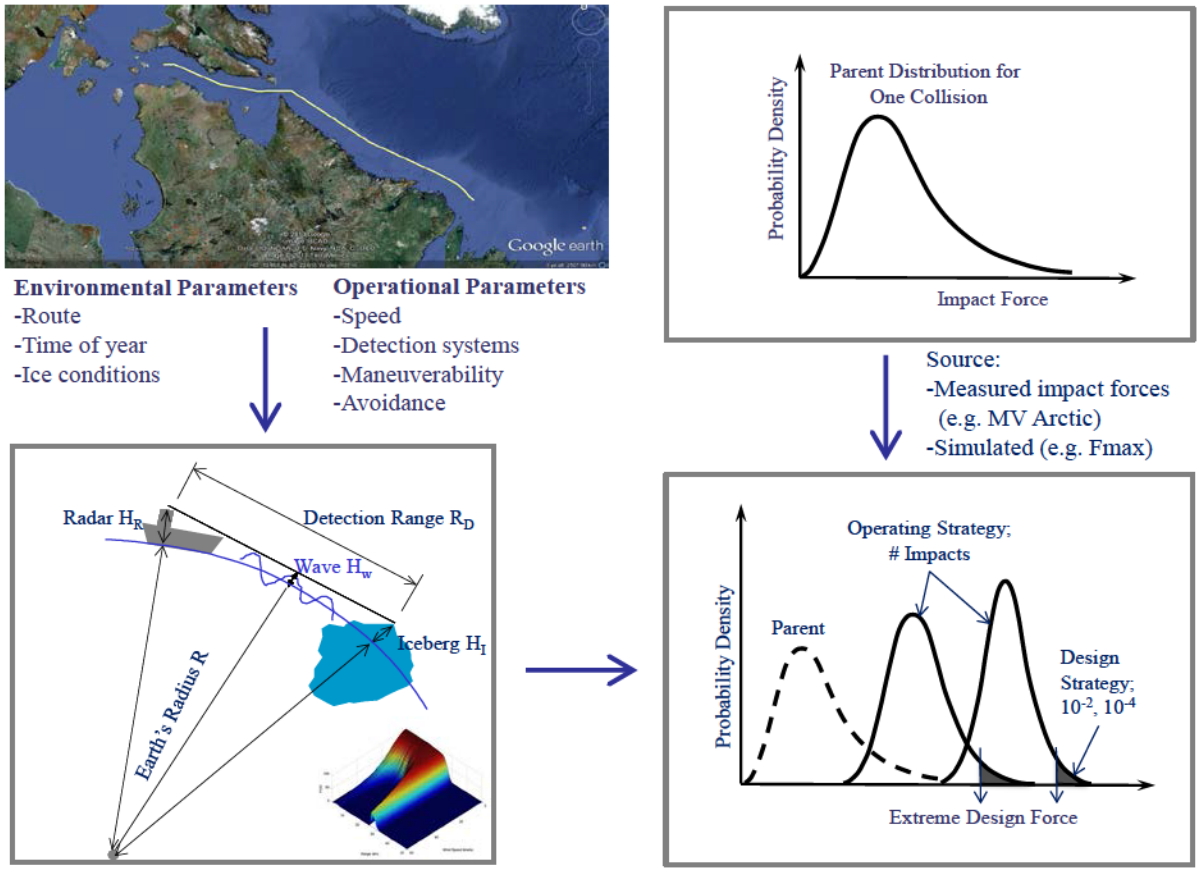

Figure 8 Illustration of the application of the probabilistic design approach from route selection through design loads based on design strategy

2.1.5 Structural Resistance

For an engineering system to be safe, the capacity of the system (i.e. its resistance to load), must exceed the extreme forces as illustrated in Figure 9. Often resistance is specified, but if distributions for load and resistance are provided, the probability of failure (i.e. the probability that the load exceeds the resistance) can be determined, represented by the region of overlap between both distributions. Since it is not economically feasible to remove *all* risk from a design, the designer must ensure that the failure probability is within some specified minimum safety target – or annual exceedence probability.

Referring to Figure 10, the distributions for load and resistance must be separated such that the required safety or failure probability (i.e. annual exceedence probability) is satisfied. The first priority for design is to ensure adequate safety of the system. But we also must consider

economy as part of the design. This is not to suggest that safety be compromised, but that with safety satisfied, we avoid over-conservatism and balance economy.

Depending on design strategy, the structure may be designed elastically (i.e. frequent events), have limited plasticity for Extreme-Level Ice Event (ELIE) and Ultimate Limit State (ULS) design or have considerable plasticity in the case of Abnormal-Level Ice Events (ALIE) and Abnormal Limit States (ALS) design. Mode of failure is also important since not all damage leads to collapse.

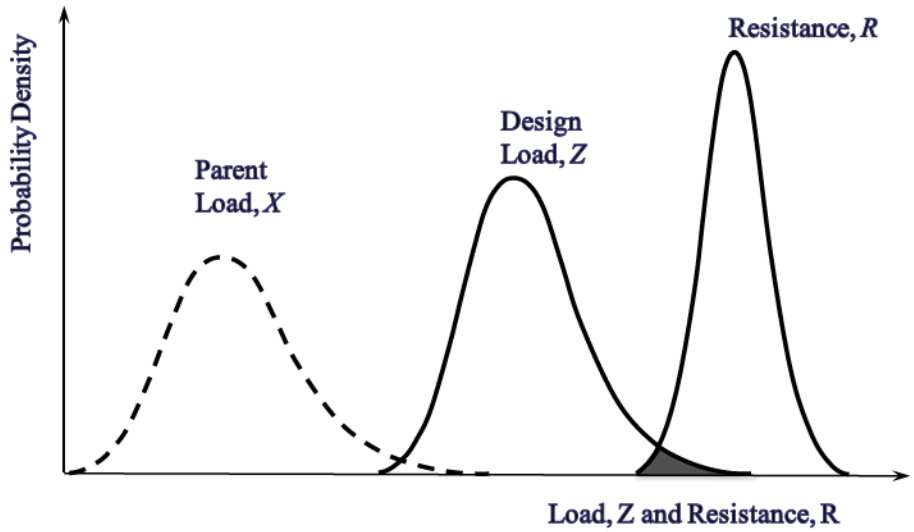

Figure 9 Probabilistic treatment of load and resistance (*Note that the probability of failure is not the area of the shaded region but a convolution*[1])

2.1.6 Specifying Safety Targets for Design

With the offshore oil and gas industry, International Standards set safety objectives for design based on the risk of loss of life as well as potential for environmental damage; see, for example, ISO 19906 – Arctic Offshore Structures (ISO, 2010). For design, safety is addressed by specifying "target failure probabilities" that cannot be exceeded. These

---

[1] Failure probability is the convolution of the two density plots (See Ebeling, 1997; Jordaan, 2005a)

$$p_f = \int_{-\infty}^{\infty} F_R(x) f_Z(x) dx = \int_{-\infty}^{\infty} f_R(x)[1 - F_Z(x)] dx$$

probabilities will be set sufficiently low to ensure the desired level of safety and consider society based risks that are unavoidable. The level of 1×10^{-4} is often given as the maximum risk per annum in industrial activities (Jordaan, 2005a).

Example annual target exceedence probabilities based on safety class and failure consequence are summarized in Table 1. These consider both load and resistance. Design targets are more stringent with increasing risk of loss of life and environmental damage. Load level event types, corresponding annual exceedence probability targets, and structural limit states for design are illustrated in Table 2.

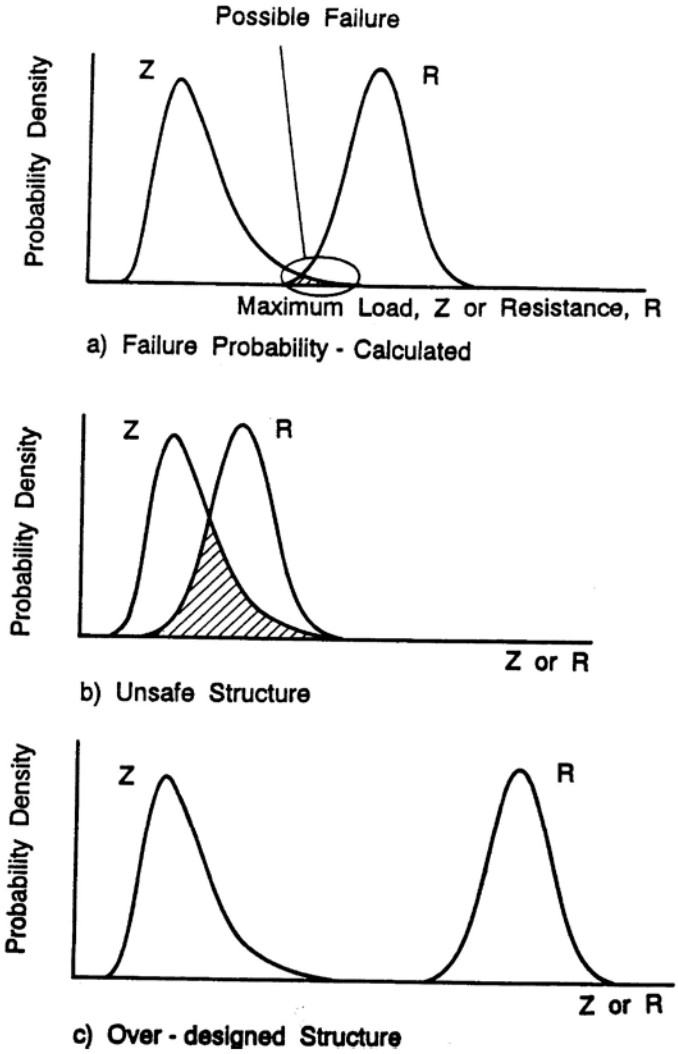

Figure 10 Illustration of safe, unsafe and overly safe design based on failure probability (*see note in Figure 9 and corresponding footnote regarding the estimation of failure probability*)

Table 1 Reliability targets based on risk to personnel and consequence of failure (ISO, 2010)

Safety Classes	Consequence of Failure	Target Annual Exceedence Probability
S1 Manned non-evacuated	C1 - High consequence	10^{-5}
	C2 - Medium consequence	10^{-5}
	C3 - Low consequence	10^{-5}
S2 Manned evacuated	C1 - High consequence	10^{-5}
	C2 - Medium consequence	10^{-4}
	C3 - Low consequence	10^{-4}
S3 Unmanned	C1 - High consequence	10^{-5}
	C2 - Medium consequence	10^{-4}
	C3 - Low consequence	10^{-3}

Table 2 Target safety level and load factors based on ice load event type (ISO 2010)

Ice Load Event Type	Annual Exceedence Probability P_E	Load Factor	Design Limit State for Structureal Design
Extreme-Level Ice Event (ELIE) frequent environmental events	10^{-2}	1.35	Ultimate Limit State (limited plasticity, eg. hinge failure)
Abnormal-Level Ice Event (ALIE) rare environmental events	10^{-4}	1.0	Abnormal Limit State (full membrane plasticity)

2.2 Principal Considerations for Global and Local Design

2.2.1 Ice Structure Interaction

Ice failure during interactions with a ship or marine structure (multi-year ridge, first year floe, or iceberg) will include fracture and damage processes. Figure 11 illustrates conceptually the contact face between a ship's hull and the ice (e.g. MY ridge) according to Riska (1987), although larger spalls near the free surface can be expected. Figure 12 provides a more detailed description of the failure process more representative of an iceberg or MY ice type impact (Jordaan *et al.*, 1996). The fracture process will result in a zone of spalling near the free surface (reducing actual contact area) as well as softening of the ice (i.e. damage) due to micro-fracturing and recrystallization at relatively low pressures, and softening due to recrystallization and pressure melting at higher pressures towards the middle of the interaction (Jordaan, 2001; Jordaan *et al.*, 2009). As the interaction progresses fracturing and spalling processes cause continual reshaping of the contact face with zones of high pressure or *HPZ*s forming and disappearing, contact progressively shifting from one location to another (relative to the structure), changing in size and intensity. Only a small portion of the ice face has actual contact with the structure. While extrusion will contribute to some background pressure, the total force exerted on the hull passes primarily through the local *HPZ*s. Adjacent to these may be regions of extruding crushed ice having low or near zero pressures.

The outside area, including spalling regions, represents the *nominal* contact area that is associated with average pressure and global loads. For large nominal areas greater than 100m^2, this pressure may be considerably less than 1.0 MPa. Within this nominal area away from edges and free surface effects, *HPZ* pressures on areas of the order of one cm^2 have been measured up to 70 MPa (Jordaan *et al.*, 2005b). Intermediate medium scale pressures of 2-4MPa have been measured on areas up to 3.0m^2. A scale effect exists such that average pressures on smaller areas are considerably larger.

A layer of water exists between the ice and the structure that will have some influence on ice crushing behavior. Since water is incompressible, there could be some cushioning effect, as well as enhanced fracture particularly for larger contact areas as water pressure is built up.

That said, for the ship ram data studied and analyzed in this thesis, we are inferring ice failure based on measured response of the hull. For design, we model the data directly, estimating hull response given expected impacts. In this way, hydrodynamics and any other effects are indirectly considered in the data, analysis and design.

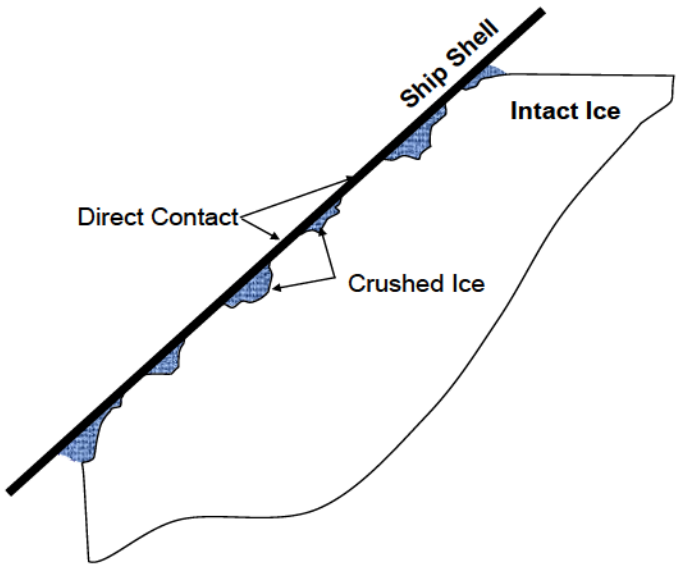

Figure 11 2-D Illustration of contact face between ship's hull according to Riska (1987)

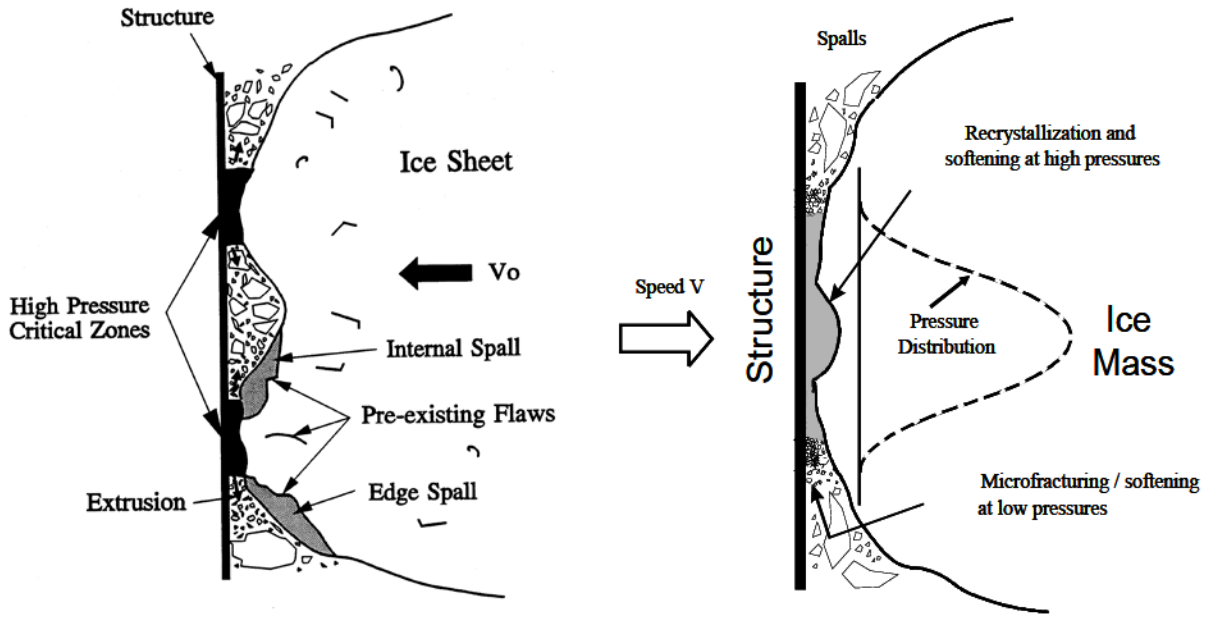

a) *moving ice, two critical zones shown* b) *moving structure, one critical zone shown*

Figure 12 Iceberg structure interaction illustrating regions of spalls (Jordaan, 1996)

2.2.2 Global Design

Global design is concerned with the maximum global force exerted onto the structure (i.e. bottom founded or moored offshore platform) or ship during a collision or ram event. In the case of a ship ram as illustrated in Figure 3, the global force will increase monotonically with bow penetration into the ice, with the maximum force occurring at the point of maximum penetration (or point where penetration stops and ride-up, then slide-down occurs). For continuous crushing, this is the maximum imprint. The imprint of the bow into the ice feature without any reduction for spalls that may come off is termed the *global* or *nominal contact area*. The *nominal design pressure* is the total maximum force averaged over the *nominal contact area* and includes zones of low and zero pressures.

To estimate the maximum global force for design, we need only the nominal area and corresponding nominal pressure (Varsta, 1983; Riska, 1987; Frederking, 1998). Consistent with Figure 3, Figure 13 shows a section through a plane of interaction with an iceberg (or MY ice) illustrating the nominal contact area and distribution of local *HPZ*s.

In terms of reference, global design is closest associated with the ice feature itself with forces governed by the development of nominal contact area as penetration increases. For design and modeling the interaction of ice with the structure, the nominal contact area, the imprint of the structure onto the ice, is the only geometry that can be readily and accurately determined.

2.2.3 Local Design

For local design, we are interested in the maximum pressure and force that can develop on a single panel within the nominal contact area throughout the full interaction duration (Jordaan *et al.*, 1996). For a ship, as illustrated in Figure 14, we are concerned for the highest pressures on the smallest panels on the hull - a section of plating supported on the perimeter by main frames and stringers. Unlike global forces that occur at the end of the interaction,

*HPZ*s can occur at any point through the interaction duration and vary spatially across the interaction face and nominal contact zone (although more likely nearer the center).

In terms of reference, local design is referenced to a specific part of the structure and considers the extreme pressures that develop as ice passes over it, particularly the probable occurrence of an *HPZ*.

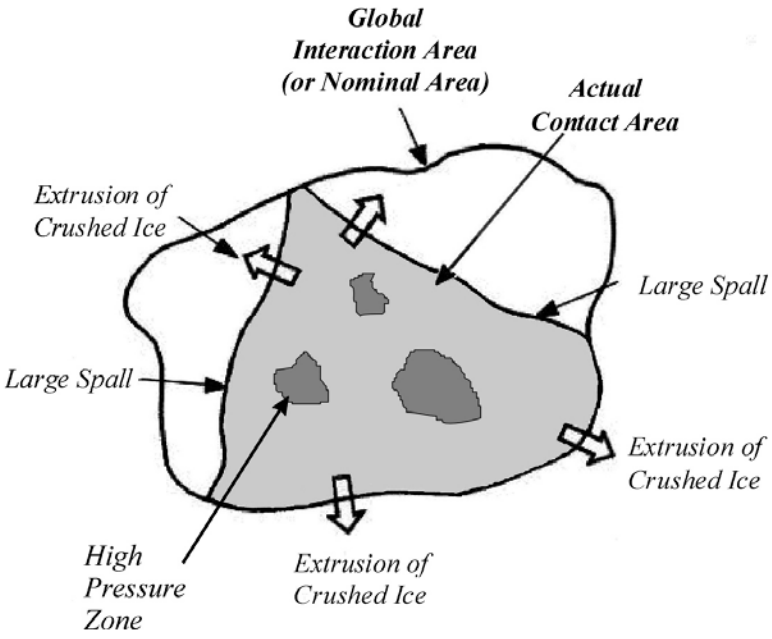

Figure 13 Illustration of nominal contact area (Jordaan *et al.*, 2005b)

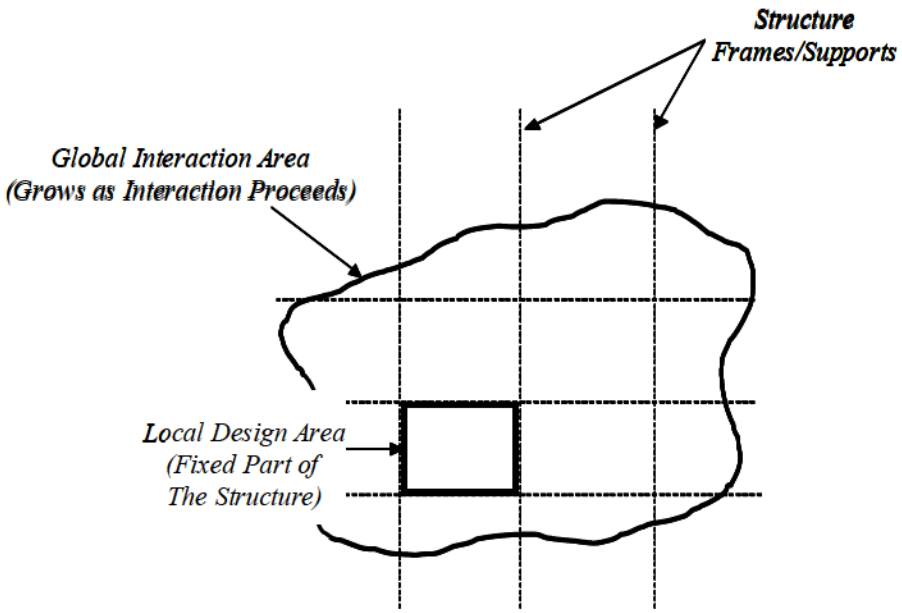

Figure 14 Illustration of local pressure design area (Jordaan *et al.*, 2005b)

2.3 Global and Local Pressure-Area Relationships for Design

2.3.1 Data Sources

Typically, data sets for analysis of ice failure and corresponding design pressures fall into two main categories:

- *Global* data represented by total force measured over the whole structure; and
- *Local* data measured on a specific part of a structure.

Data sets most applicable for this research initiative include high loading rate interactions with glacial and MY ice. Types of data include medium scale, full scale and ship ram data with MY and iceberg ice.

Medium-scale data include measurements of ice forces on indentors penetrating into an ice feature. Two test programs, the Pond Inlet Indentation Experiment (1984-85) and Hobson's Choice Indentation Experiment (1989-90) are illustrated in

Figure 15 and Figure 16 (See Frederking *et al.*, 1990; Jordaan and McKenna, 1991; Muhonen, 1991; Sandwell, 1990, 1992, 1993; and Daley, 1994 for detailed review of these tests). Penetration was controlled by the extension of hydraulic rams. The two types of tests conducted included: 1) penetration of indentors with different sizes and geometry, and 2)

indentation of a flat surface onto prepared ice surfaces (e.g. spherical shape, wedge, pyramid, and block). These data are useful in the study of ice failure and formation of *HPZ*s. Other medium scale data includes JOIA MSFIT data (Takeuchi *et al.*, 2000) where a vertical indenter with independent sensors capable of measuring both local and global forces was pushed against level ice. Example pressure area data from the Pond Inlet tests are illustrated in Figure 19.

Full-scale ice-structure interaction data include measurements made on several caisson structures in the Beaufort Sea, particularly on the *Molikpaq* structure at Amauligak I-65 1985-86 (See Figure 17), measurements of MY floe impacts with Hans Island 1980-81, and iceberg impacts with an instrumented rock face at Grappling Island 1995 (Crocker *et al.*, 1995; and Ralph *et al.*, 2004).

Ship ram trials typically included the measurement of hull response using strain and pressure gauges on the frames and shell plating for rams with ice floes. An array of gauges formed a panel area. The measurement panels typically covered only a specific portion of the full bow area, and thus local ice pressures were obtained. For other voyages, global loads were measured using strain gauges and accelerometers.

Ship based trials include:

- *SS Manhattan* Voyages, 1969-70;
- *CCGS Louis S. St. Laurent* Voyage, 1980 and 1994;
- *Canmar Kigoriak* Voyages, 1981 and 1983;
- *Polar Sea* Voyages 1982, 1983, 1984, 1985 and 1986;
- *MV Arctic* Voyage, 1984;
- Swedish Icebreaker *Oden* Arctic Ocean Expedition, 1991;
- *USCGC Healy* Trials, 2000; and
- *CCGS Terry Fox* Bergy Bit Impact Study, 2001.

An example of data from the *Polar Sea* ram illustrating panel location and distribution of single panel forces over the measurement area and through the ram duration is given in Figure 18. Figure 20 illustrates a compilation of pressure area data from many iceberg and

MY iceberg impact trials. While these data clearly illustrate a local pressure area scale effect and some upper bound envelop to measurements, the range of pressures for a given area is not specifically considered. Further analysis needs to consider exposure such that a bench mark 'parent' pressure distribution can be identified. A design curve then considers interaction time, ram duration and the number of annual interactions per year. Otherwise some upper bound curve to the bulk of data only considers some standard deviation of the data measured to date. If an order of magnitude more data were available, such reference lines would be higher. Figure 21 illustrates alternative reference curves to local pressure data as well as an illustration of exposure curve using local pressure design curve (See Section 2.3.3).

For further study, additional datasets for first year ice and fresh water ice include, flat jack flaking tests in first year ice in 1993 and 1997 and fresh water ice in 1994 (See Croasdale *et al.*, 2001) as well as the five year (1996-2000) JOIA first year ice trials (See Sodhi *et al.*, 1998, 2001; Takeuchi *et al.*, 1997; Matsushita *et al.*, 1997; Kamio *et al.*, 2000; Taylor *et al.*, 2008).

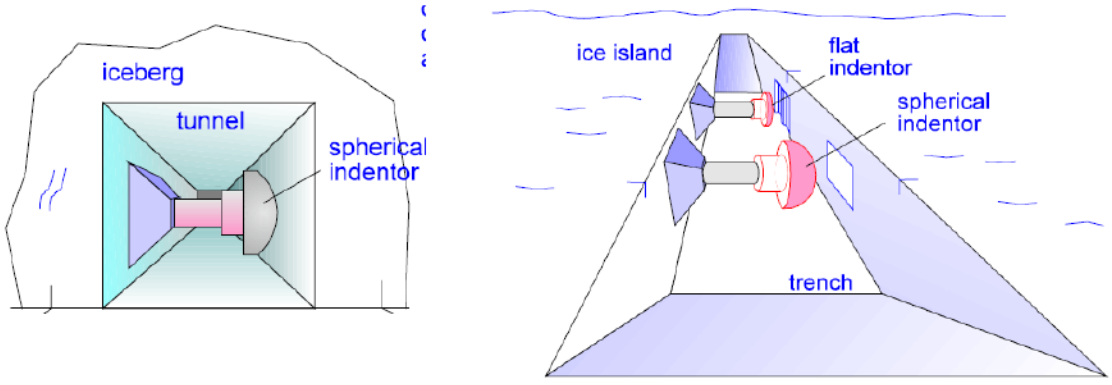

a) Pond Inlet 1984 Iceberg Tests

b) Hobson's Choice 1989-1990 Ice Island Tests

Figure 15 Concept illustration for Pond Inlet and Hobson's Choice medium scale indentation tests (Daley, 1994)

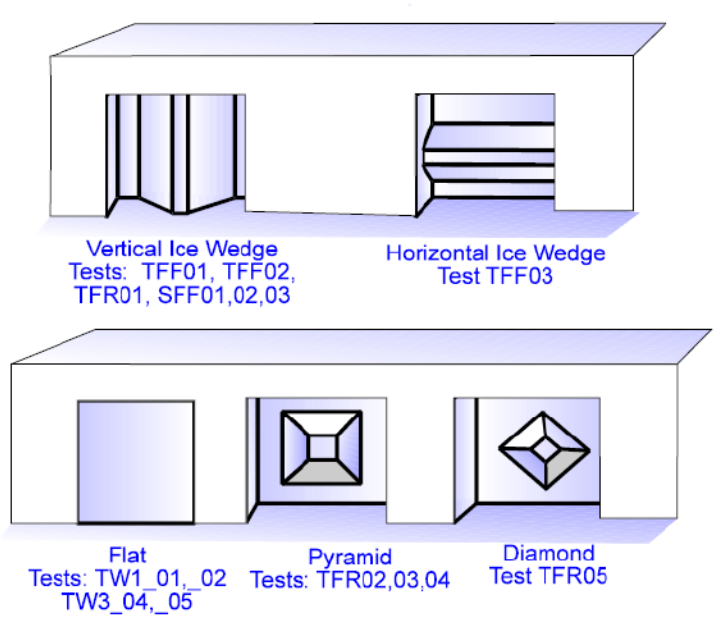

Figure 16 Prepared faces for the 1990 Hobson's Choice flat indentor faces (Daley, 1994)

Figure 17 MY ice crushing against the *Molikpaq*

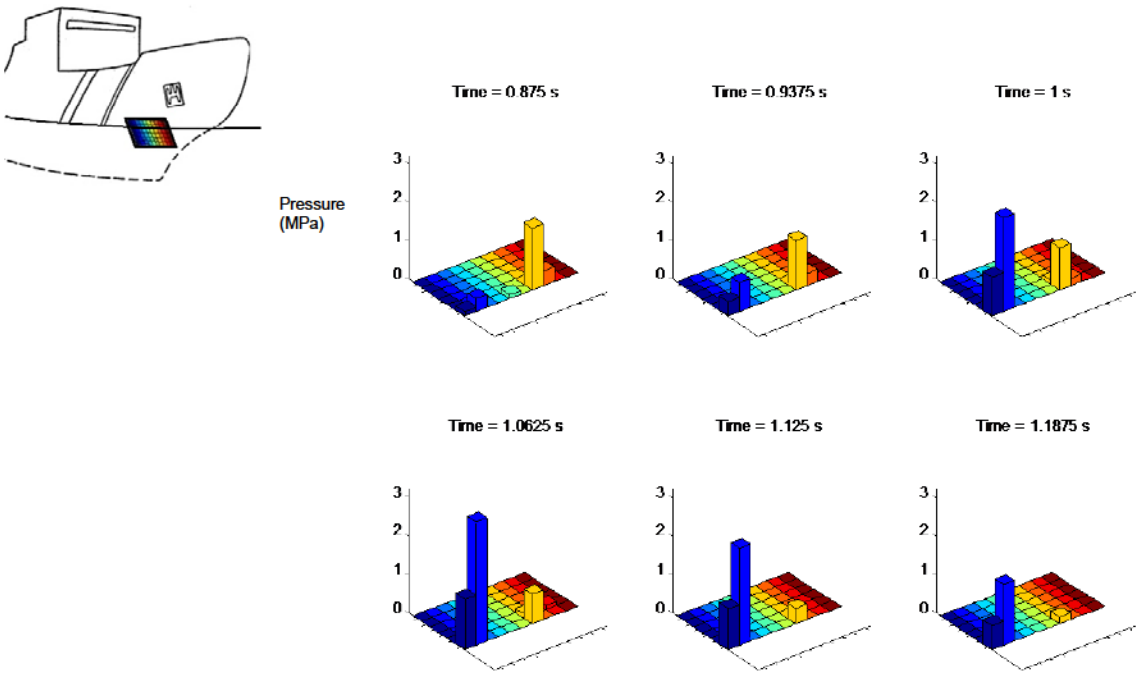

Figure 18 Distribution of pressures for a MY ice impact on the *Polar Sea* 1982

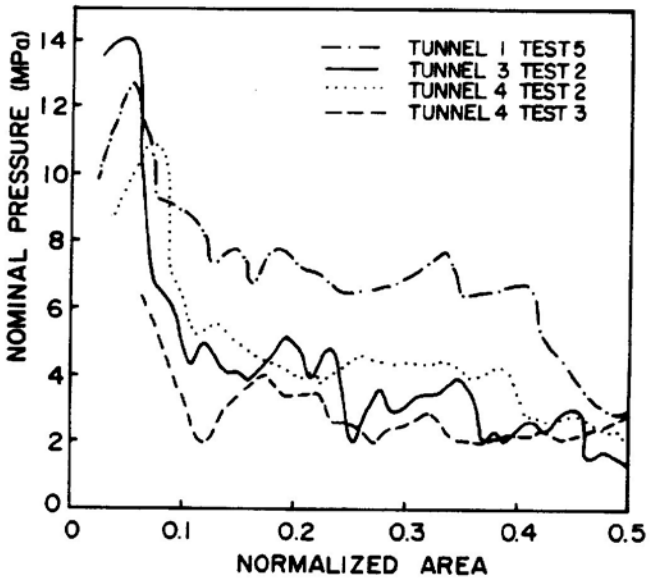

Figure 19 Measured nominal pressure area relationship from ice island indentor tests (Masterson *et al.*, 1992)

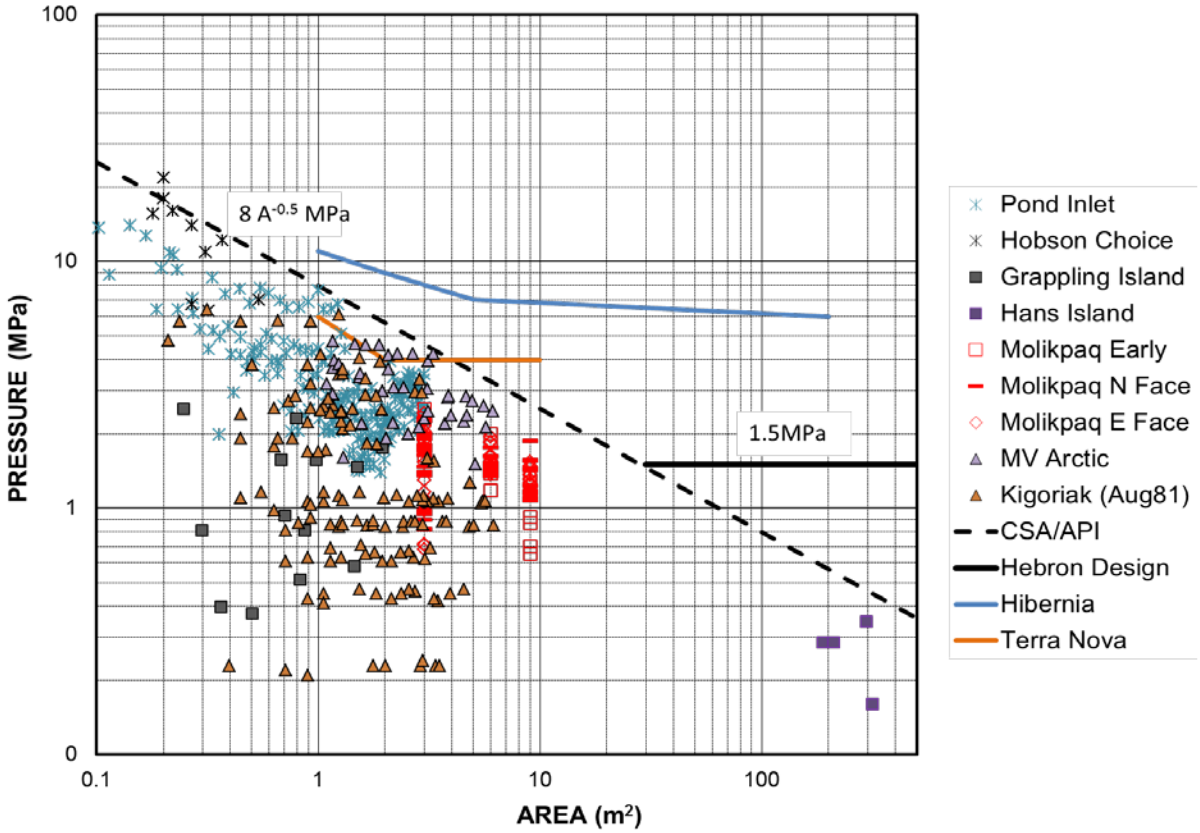

Figure 20 Compilation of pressure area data including example design curves (Note that plot includes local and global pressures)

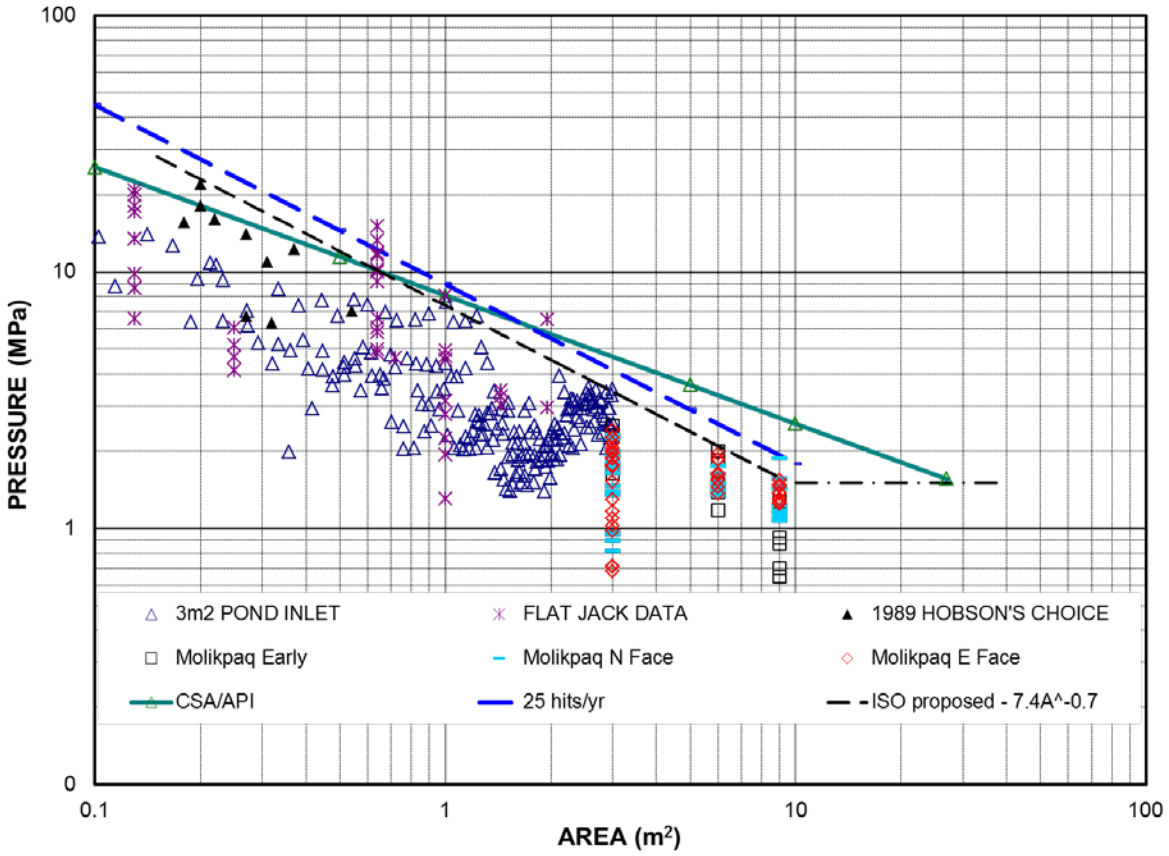

Figure 21 Illustration of local pressure data including CSA/API design curve (i.e. $8.5A^{-0.5}$), ISO design curve as well as comparison with an exposure based local pressure curve and 25 impacts per year as described in Section 2.3.3.

2.3.2 Global Forces and Pressure-area Relationship

Among the first researchers to introduce the concept of nominal interaction area and nominal pressure were Varsta (1983) and Riska (1987). Riska's idealized bow imprint is illustrated in Figure 22. The relationship between average pressure and nominal contact area for both the ship ram and inclined plane trials is given in Figure 23. The power law expression for average pressure for the ship collision data was

$$p_{av} = \begin{cases} p_{nom} & A \le A_0 \\ C_1 A^{C_2} p_{nom} & A > A_0 \end{cases} \qquad (2)$$

where $A_0 = 0.6$, p_{nom} which depends on indentation geometry was 11.3MPa, $C_1 = 0.3$, $C_2 = -0.40$.

A combination of all available pressure-area data from laboratory tests, medium scale field tests, full scale arctic structure loads, and mesoscale predictions are given in Figure 24 (Sanderson, 1988 and Blanchet, 1990). Palmer and Croasdale (2013) give a description of these tests. Frederking and Masterson (1992) compiled a pressure-area data set for MY and glacial ice including medium scale Pond Inlet, Hobson's Choice, Hans Island, *Molikpaq* MY ice interaction, and ship ram trials including *Kigoriak* and MV *Arctic*. These are plotted in Figure 21 and Figure 25. The global scale effect is clearly evident; that pressures decrease with increasing contact area.

As part of the development of a ship ram software for modeling global bow forces (Carter *et al.*, 1996; Jordaan *et al.*, 1996; see also section 4.2), a random pressure-area relationship was calibrated by comparing the distribution of measured forces with simulated forces using data from *Kigorak* (1983), MV *Arctic* (1984), SS *Manhattan* (1969), *Oden* (1991), and *Polar Sea* (1984). An example comparison for the MV *Arctic* (1984) is given inFigure 27. The resultant global pressure-area relationship was

$$P(a) = CpA^{Dp} \qquad (3)$$

with parameters

Cp lognormal distribution: $\mu = 3\ MPa$ $\sigma = \pm 1.5\ MPa$
Dp normal distribution: $\mu = -0.4$ $\sigma = \pm 0.2$

This relationship is consistent with Riska's Eq. (2). For illustration, the influence of Cp and Dp on estimates of nominal pressures for nominal contact areas is given in Figure 26.

The maximum force is then the product of nominal pressure and nominal area given as

$$F_{MAX}(a) = CpA^{Dp+1}. \qquad (4)$$

Using extremal type analysis (maximum of n events), simulated pressure-area data were compared with measured data derived from the MV *Arctic* trials as shown in Figure 28 (Frederking, 1998 and Jordaan, 2005a). Note that while a good comparison is modelled, almost all data points fall well below the curve created using the Jordaan *et al.*, (1993). As will be discussed further in Section 4.2.7, simulated results may be conservative.

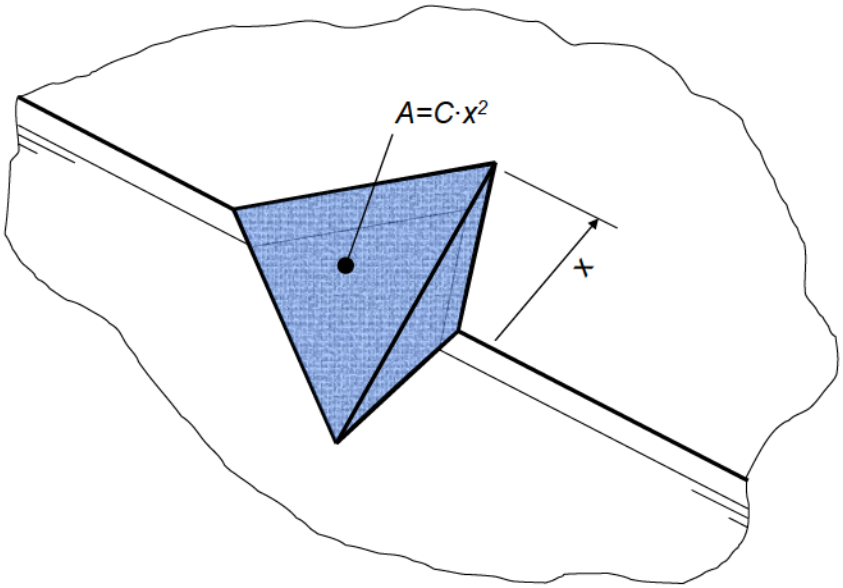

Figure 22 Nominal area for ship penetration into an ice floe used to determine average or nominal ice pressure (Riska, 1987) - area extent is basically the imprint of bow into ice. (*Note that areas of spalling near the edge of the floe are included in the nominal area.*)

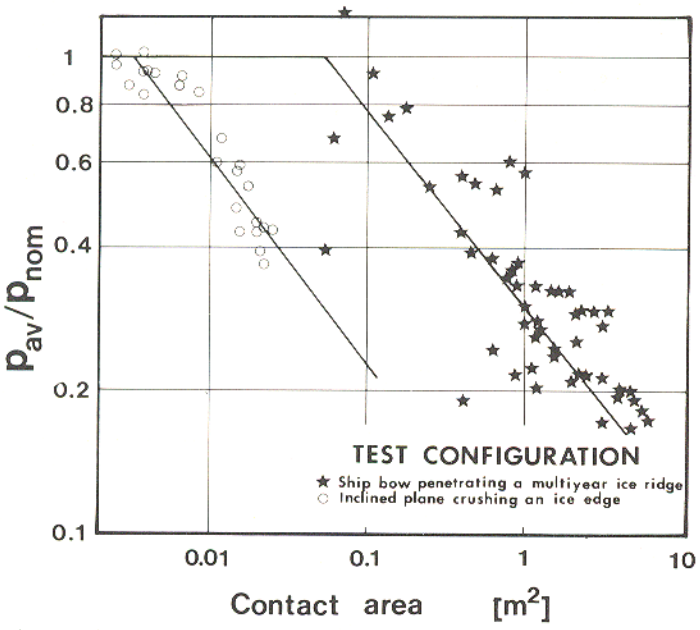

Figure 23 Average pressure-area data and least squares regression (Riska, 1987)

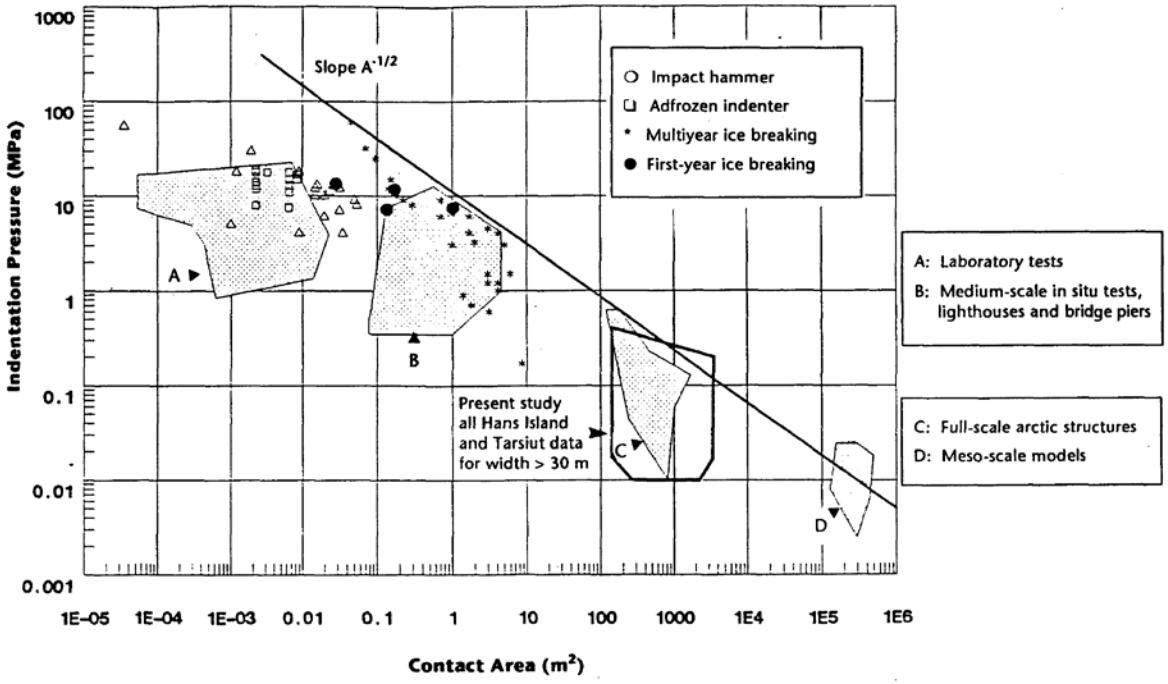

Figure 24 Measured ice failure pressure versus contact area for a wide range of interaction and loading situations for various ice types, temperatures and strain rates (Blanchet, 1990 after Sanderson, 1988).

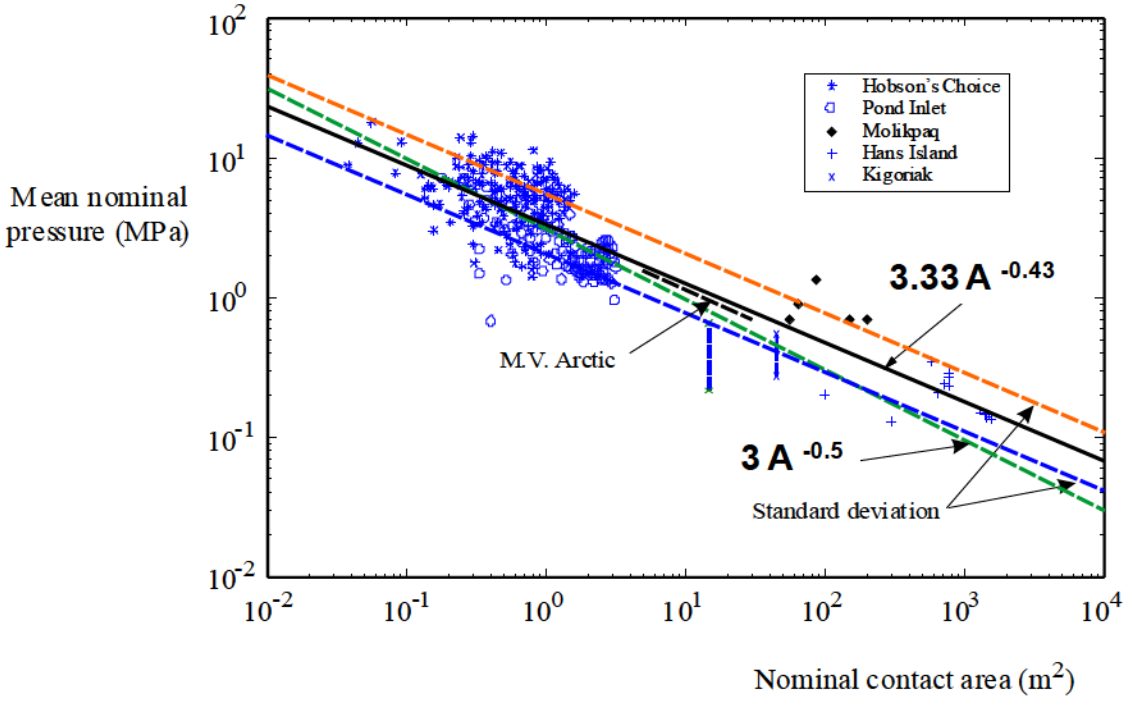

Figure 25 Nominal pressure area relationship from field data (Jordaan *et al.* 2005b)

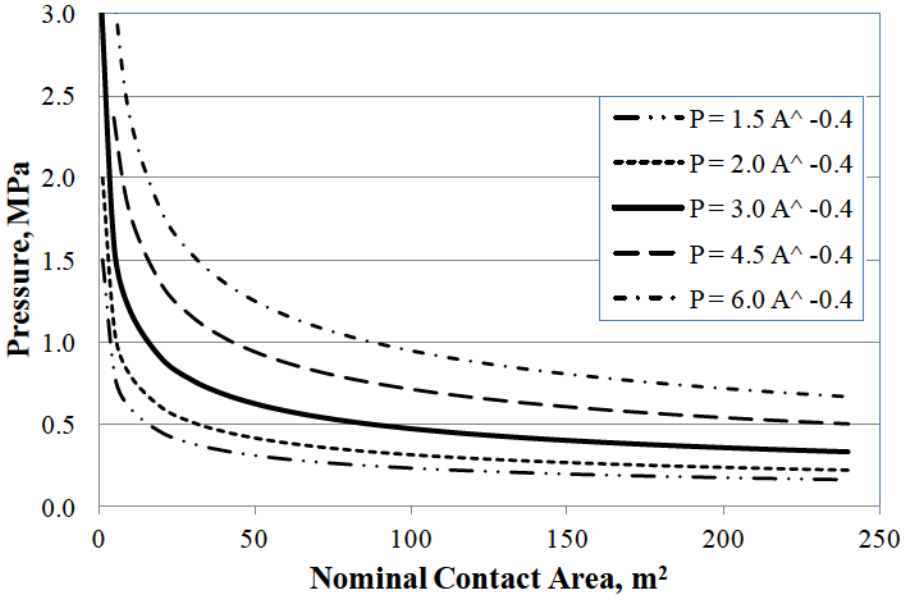

a)

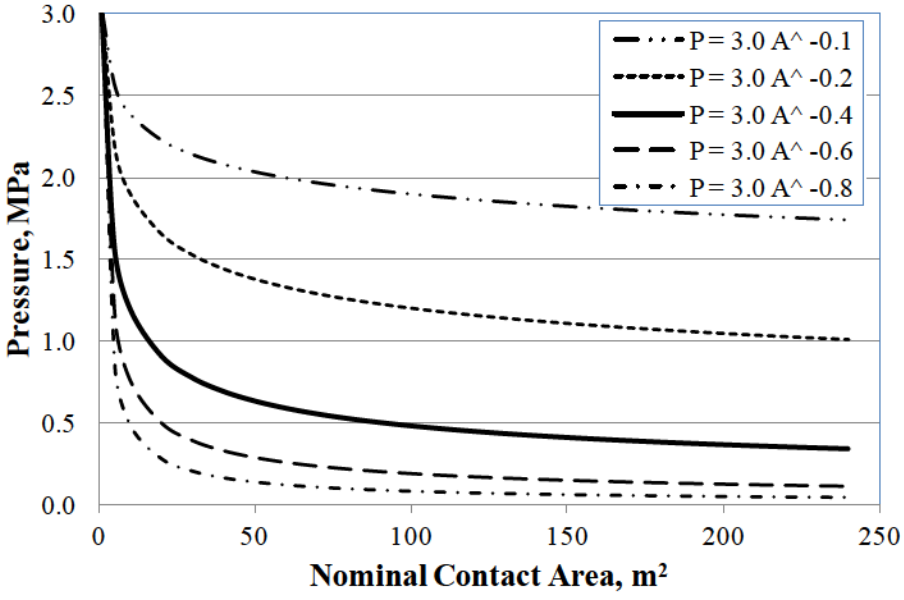

b)

Figure 26 Illustration of the sensitivity of Nominal Pressure to a) *Cp* and b) *Dp*

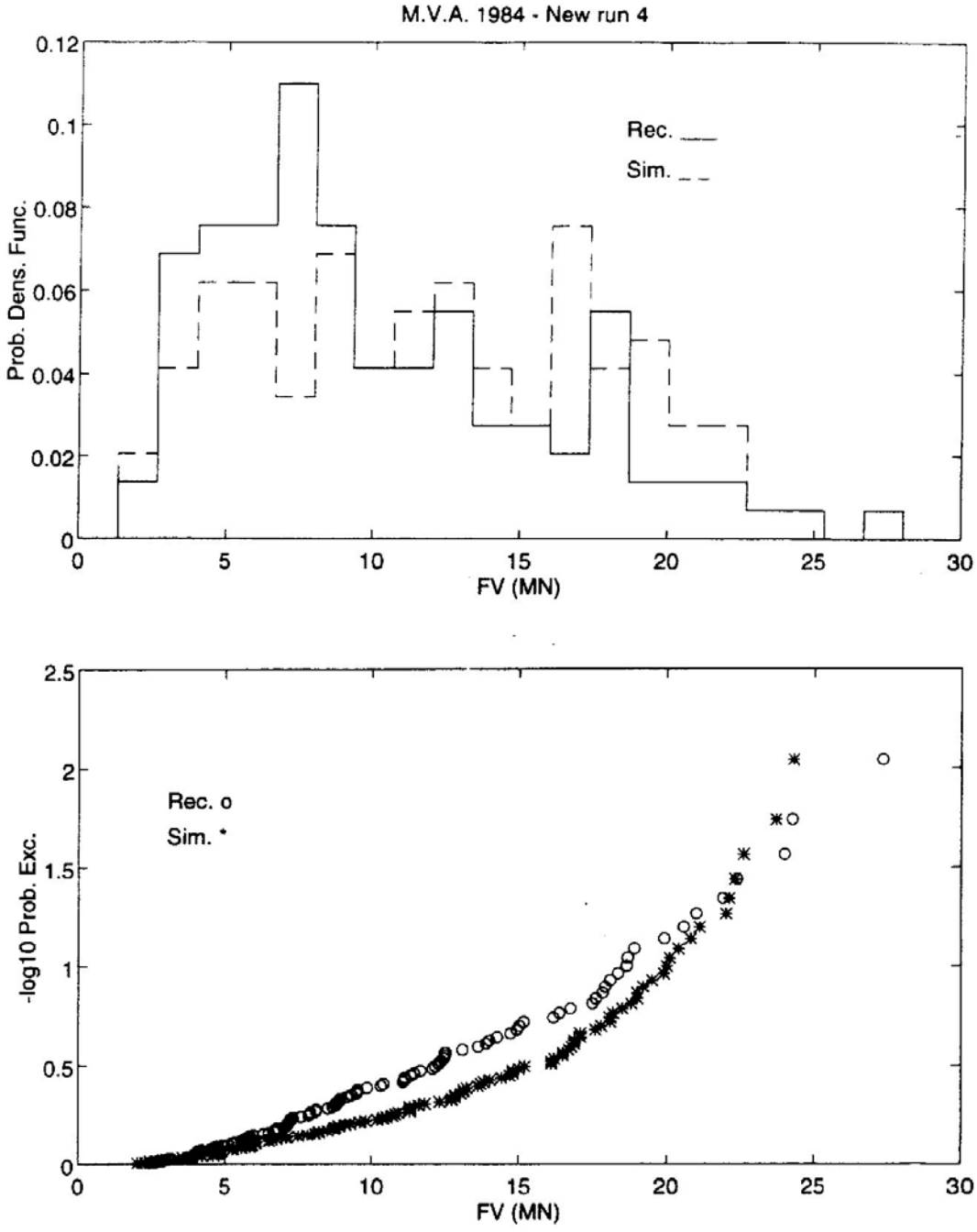

Figure 27 Histogram and exceedence probabilities of simulated and observed individual (parent) rams for MV *Arctic* 1984, for $P = 3.0\ A^{-0.4}$,$\sigma_C = 1.5$MPa; $\sigma_D = 0.2$ (Carter *et al.*, 1996).

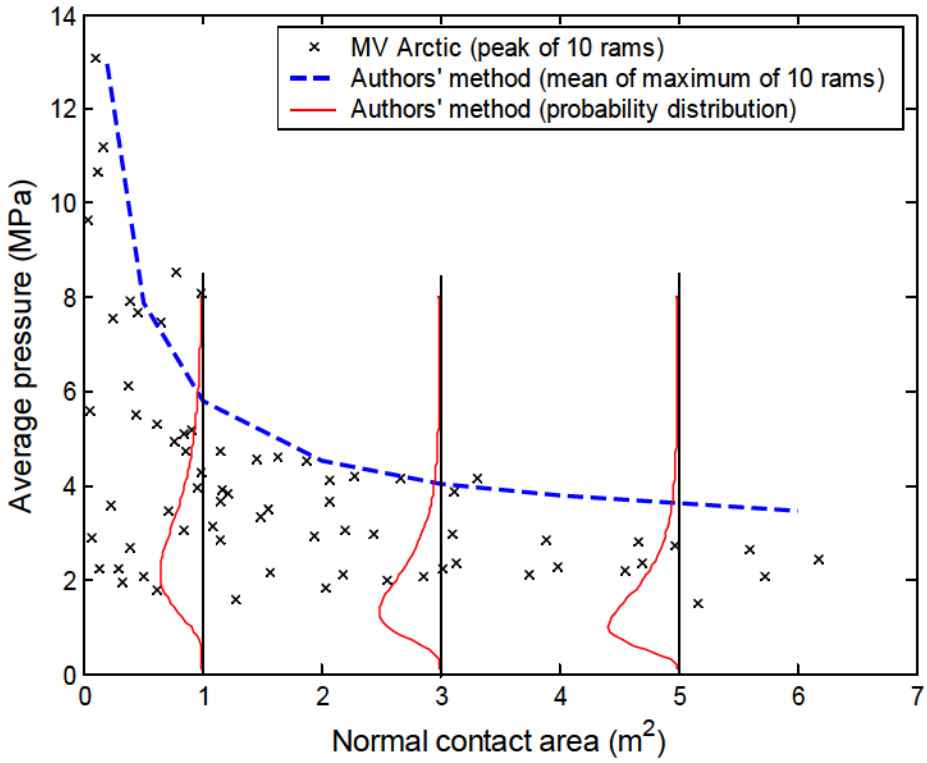

Figure 28 MV *Arctic* measurements, peak of ten events (Frederking, 1998, Jordaan *et al.*, 2005b)

2.3.3 Local Design Pressures

2.3.3.1 Methodology

The scale effect for global design is not adequate for local design – areas less than $10m^2$ representative of localized panels between primarily levels of framing on a ship hull. For local areas within the larger global interaction area, pressures on the hull or structure originate from actual high pressure contact zones (*HPZ*s); excluding zones of low or zero pressure. Confinement within the nominal contact area could very well lead to suppression of damage thereby increasing pressures. A relationship and scale effect that predicts a greater demand for ice failure strength is needed.

The compilation of data given in **Error! Reference source not found.** does not consider adjustment for exposure, including the selection of a design curve. It is possible for certain extreme design conditions, for the local pressure coefficient to exceed 7.4 or 8.1 MPa. In

Figure 21, the expression for 25 impacts per year at a 10^{-2} annual exceedance probability is $11A^{-0.7}$. Analysis of impact pressures on single panels resulting from ship rams is given in Figure 29 and Figure 30. It is observed that no direct correlation exists between pressure and vessel impact speed for speeds above 2 knots (~1 m/s). For lower speeds, a trend may be approximated since forces should approach zero for zero speeds. But for higher impact speeds, the process is random. One could attempt to fit some upper bound curve, but such a fit is arbitrary. With more measurements the upper bound would most likely increase consistent with the nature of probabilistic processes. Stochastic effects and exposure is important.

As illustrated in Figure 31, a reasonable approach is to rank the data for a specific panel or subpanel area and plot against the logarithm of the Weibull plotting position[2] $[i/(j+1)]$ for the i^{th} data point of a set of j pressure measurements (or number of data points). Ranked pressures in the tail can be represented by an exponential distribution given as

$$F_X(x) = 1 - \exp\left[-\frac{(x - x_0)}{\alpha}\right] \qquad (5)$$

where X is the random quantity for pressure on a given area (or panel/subpanel) plotted against the log of probability of exceedence p_e. For a specific area, the constant α represents the inverse slope of the best fit line to the tail of the distribution and x_0 is the plotting position of the exponential distribution, the intercept of the best fit line through the x axis (or x abscissa).

[2] See Jordaan (2005a) for discussion on alternative plotting positions

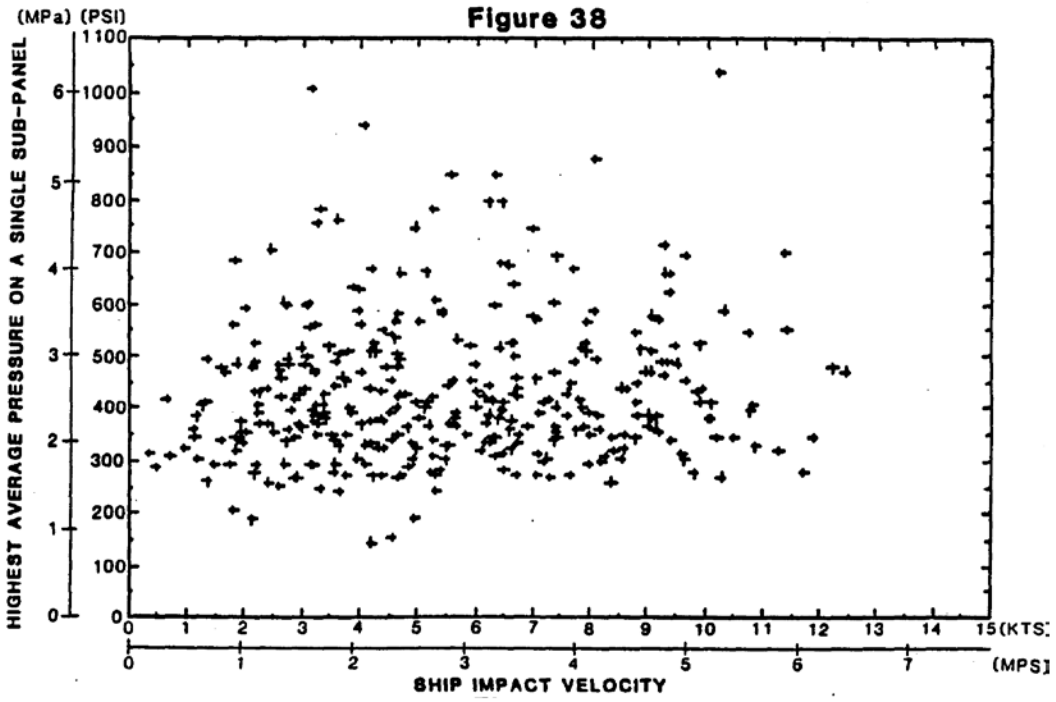

Figure 29 Average peak pressure vs. impact speed for *Polar Sea* trials (St. John, 1984)

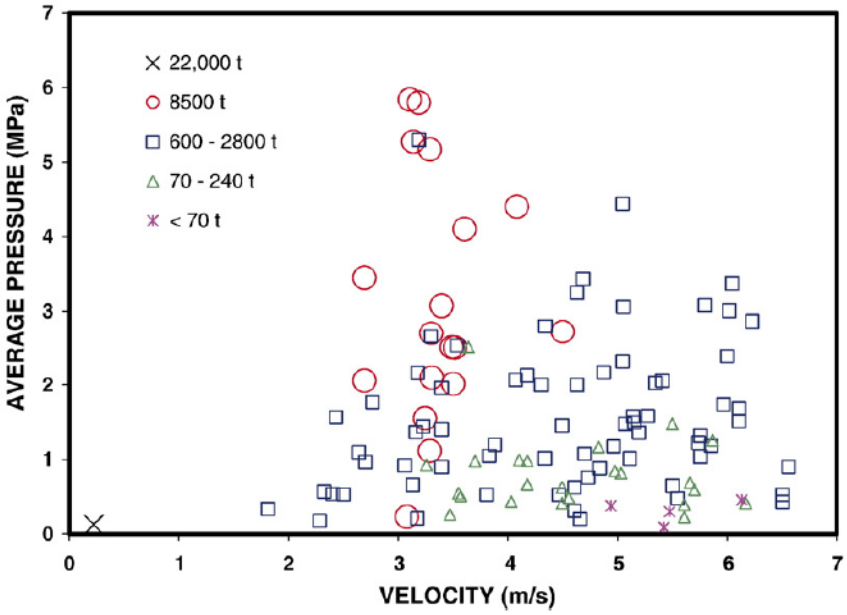

Figure 30 Average pressure on a 0.33 m^2 subpanel area as a function of velocity and bergy bit mass from bergy bit impact trials (Ritch *et al.*, 2008)

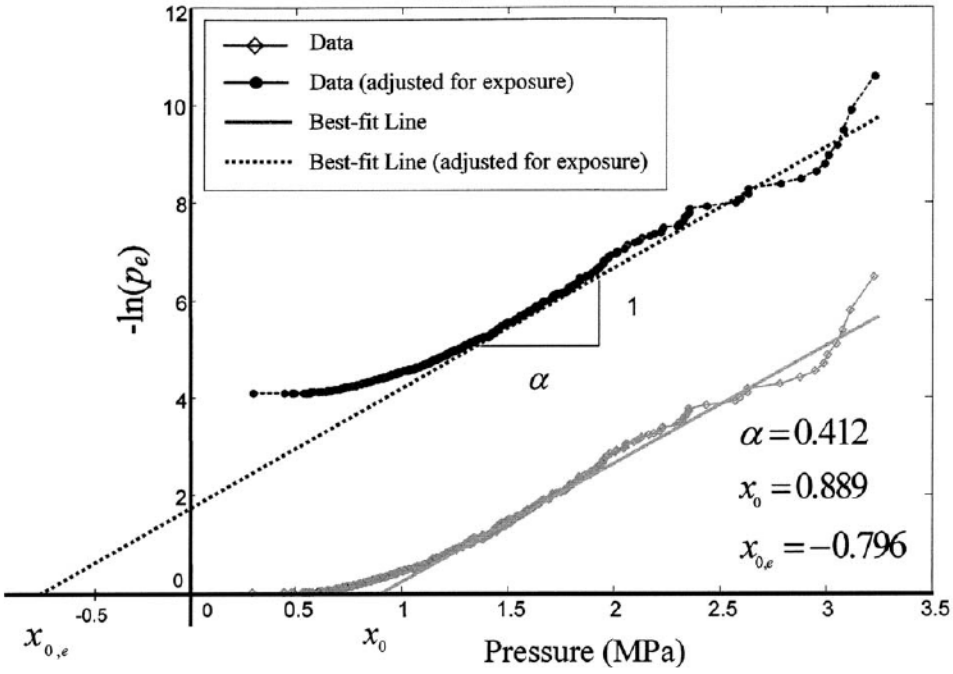

Figure 31 Example of local pressure measurements on a single panel for a *Polar Sea* 1983 interaction event – 1 subpanel area = 0.1516m^2 (Jordaan *et al.*, 2007 and Taylor *et al.*, 2009)

2.3.3.2 Derivation of Local Pressure Parameter α

For design, it is the peak pressures throughout the full interaction duration that are needed, not just the peak pressures at the point of maximum force (see Figure 32 for example). For each subpanel area, peak pressures through the full ram duration are identified for all ram events in a data set and plotted as in Figure 31. The distribution parameter α is then determined for each incremental subpanel area up to maximum design area. In the case of the *Polar Sea* data from 1986, there were 512 impacts recorded on the sixty smallest 0.15m^2 subpanels within the 9.1m^2 total instrumented area. The second smallest area would be 2 × 0.15 = 0.30 m^2 and 30 subpanels. This approach has been used to process all local ship ram and Molikpaq data (See also Frederking, 2005; Ritch *et al.*, 2008; Jordaan *et al.*, 2010).

Figure 33 illustrates the first derivation of α vs. contact area based on ship ram data from the *Polar Sea* and *Kigoriak*. Figure 34 illustrates distribution of alpha for different panel areas from the bergy bit trials. Figure 35 illustrates α vs. contact area *Oden*, *Polar Sea*, *Louis S. St-Laurent* and *Terry Fox*. The α curves from all data sets show a consistent scale effect being reasonably bound using the design curve $\alpha = 1.25A^{-0.7}$

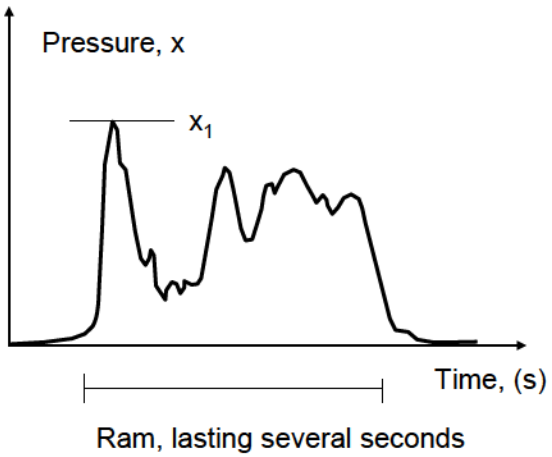

Figure 32 Illustration of a ramming event lasting a few seconds

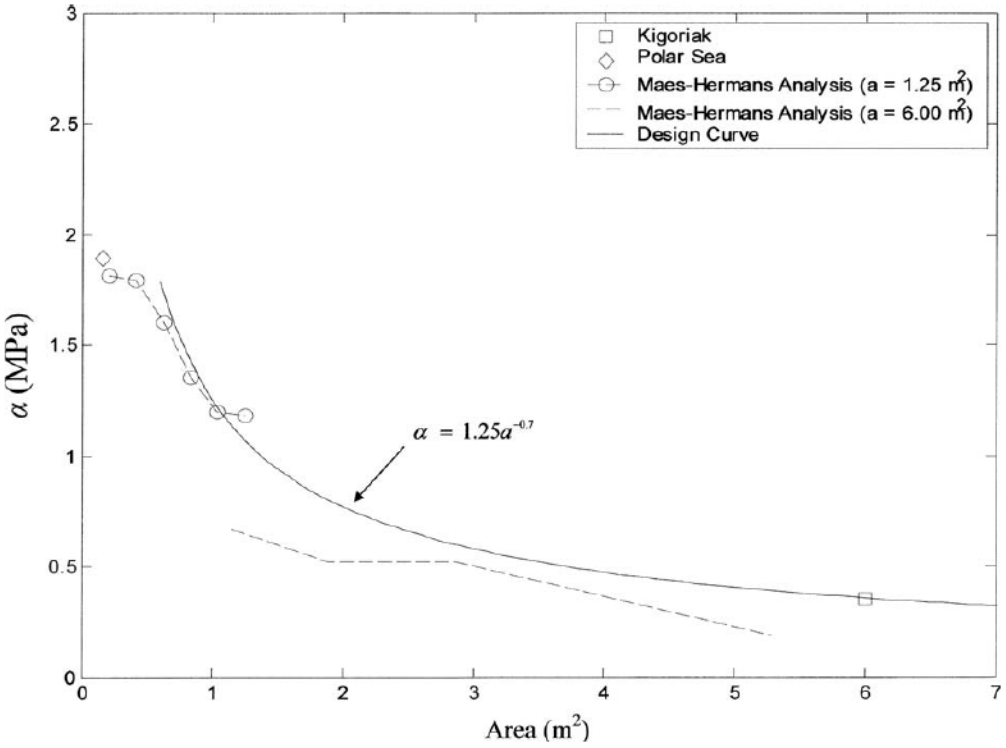

Figure 33 Local pressure parameter α vs. local contact area (Jordaan *et al.*, 1993).

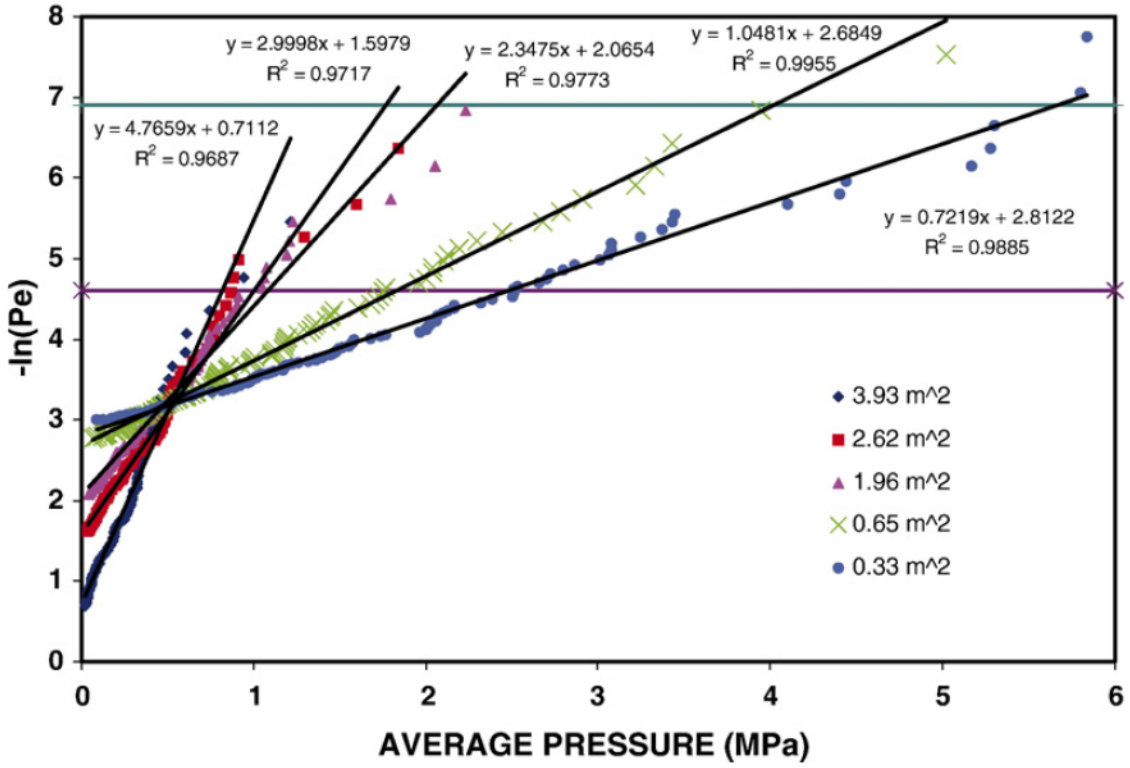

Figure 34 Distributions of local pressures for different panel areas, local pressure parameter α the exponential fit to the distribution tail for the Bergy Bit impact trials (Ritch *et al.*, 2008)

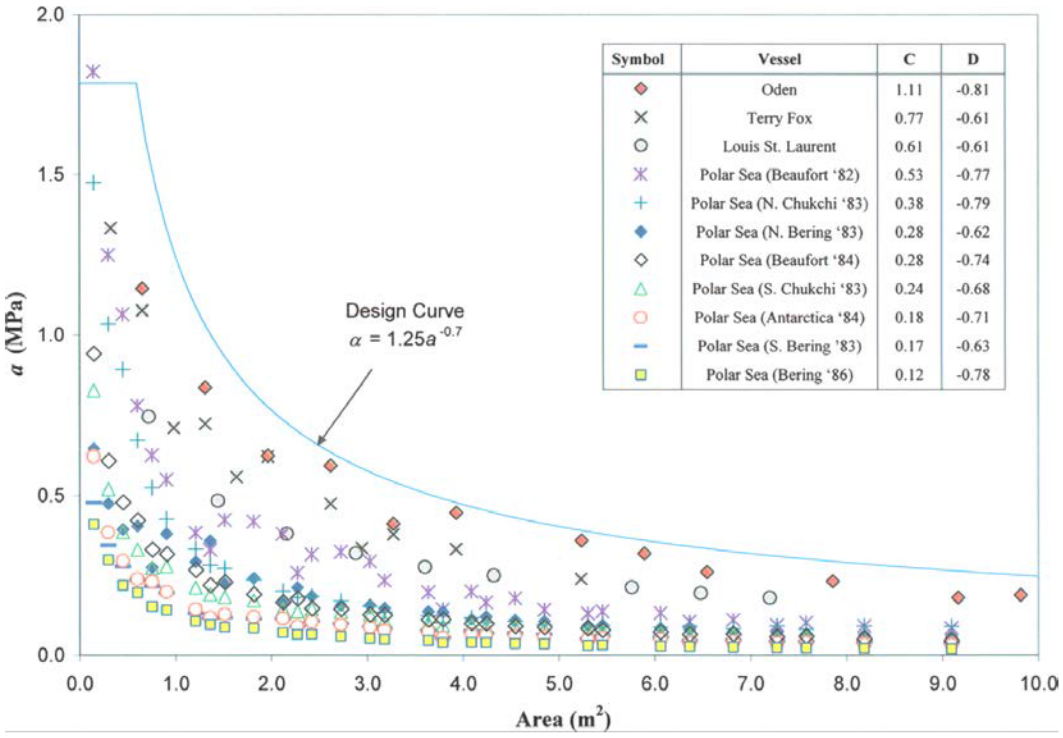

Figure 35 Local pressure parameter α vs local contact area for *Oden*, *Terry Fox* and *Polar Sea* ship ram trials (Jordaan *et al.*, 2007 and Taylor *et al.*, 2009)

2.3.3.3 Exposure

Exposure models the extent to which the whole ship or part of the ship's hull is likely to encounter hits; the higher the exposure the greater the design requirements. The upper line in Figure 31 represents the measured pressure data adjusted for *panel* exposure. If one just looks at the peak force during a local event and determines an average peak pressure over some contact area, then exposure becomes arbitrary. The objective, however, is to identify local pressures and exposure on a ***single panel*** and not just the maximum for an arbitrary number of panels. Therefore, considering the number of panels exposed (i.e. m panels), the plotting position is adjusted using $[i/(mj+1)]$which results in a vertical shift of the measured data and best fit line in Figure 31. To illustrate, the exposure for the smallest single panel out of 30 panels in a measurement area of $1a$ is 1/30; for three of the smallest adjacent panels having area 3a it is 1/10, etc. This does not change α, but shifts the distribution plotting position x_0 to represent a per panel 'parent' distribution. Figure 36 gives the x_0 values for all the ship ram data given in Figure 34. Based on observations by Frederking (2000), x_0 values can reasonably be capped based on a minimal contact (design) area of $0.6m^2$ with an upper limit at $10m^2$. A mored detailed discussion is provided in Section 4.3.8.

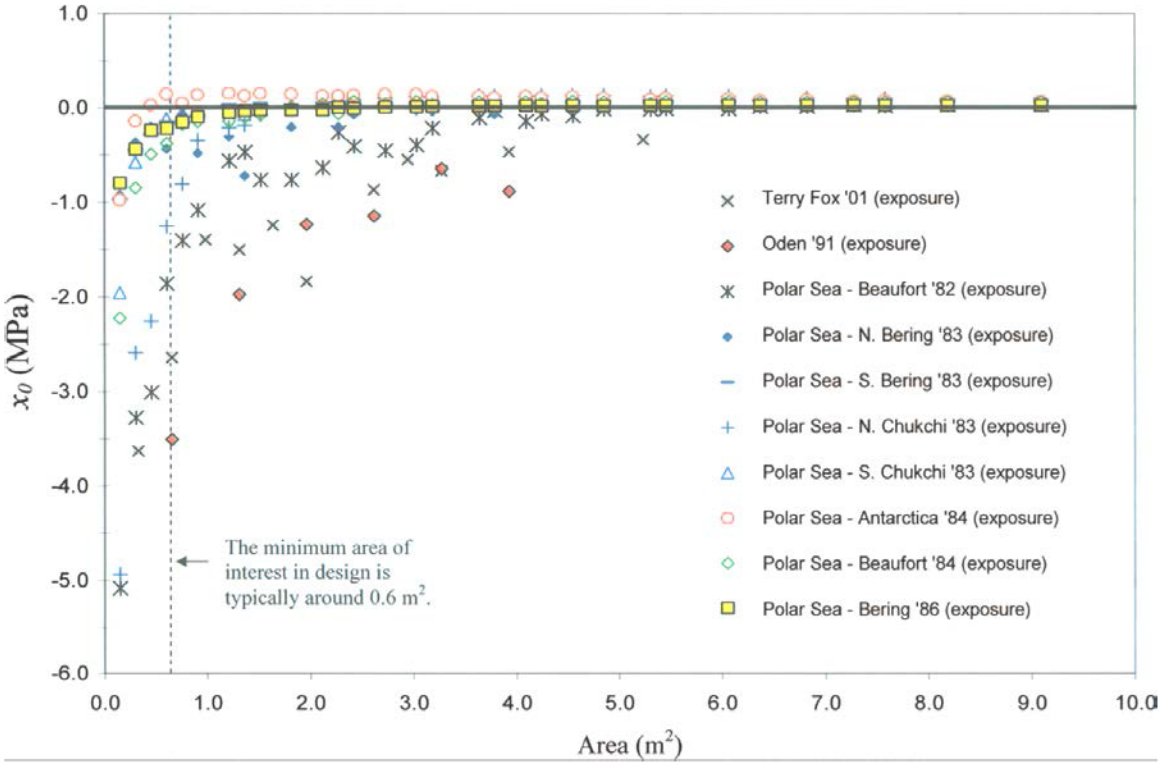

Figure 36 Plot of x_0 vs. area for ship ram and bergy bit impact data including exposure effects (Jordaan *et al.*, 2007 and Taylor *et al.*, 2009)

2.3.3.4 Application for Design

As noted in Section 2.1.1, considering the number of events *Xi* in an interval of time, of interest is the distribution of maximum pressure on a single panel over a given time interval (ram duration) which can be represented as $Z = \max(X_1, X_2, ..., X_N)$ where there are N events for pressures X_i, over the time interval. The number of hits on a specific panel can be modeled using a "Poisson" process such that

$$F_Z(z) = \exp[-\mu(1 - F_X(z))] \qquad (6)$$

Applying extremal analysis to Eq. (5), which is equivalent to substituting Eq. (5) into Eq. (6), results in a double exponential expression for a peak local pressure distribution for a given area as

$$F_Z(z) = \exp\left[-\exp\left(-\frac{(z - x_0 - x_1)}{\alpha}\right)\right] \qquad (7)$$

where $x_1 = \alpha(\ln \mu)$, μ is the design exposure and x_0 is the panel exposure constant. The exposure is given as the proportion of events that represent actual hits (i.e. adjusting for misses) given as

$$\mu = v \cdot r \cdot \frac{t}{t_K} \qquad (8)$$

where v is the expected number of events in a time period (typically a year. Example calculation in Eq. (87)), r is the proportion of events giving "direct hits" on a specific panel (e.g. 0.48 for *Kigoriak* data), t is the design event duration, and t_K is a reference duration associated the with the α design curve (e.g. t_K = 0.7s for *Kigoriak* rams). Figure 37 illustrates the influence of increased number of events v on design pressures. Reference is made to *Kigoriak* as it represents the bounding design curve for α, but in theory, region specific designs could use a specific data set and corresponding α and t_K values.

For design, to determine the impact duration t for a new build, a global impact analysis would be carried out to estimate the impact penetration based on vessel displacement, bow geometry and impact speed. Measured data from a similar vessel can be used if available. Probabilistic modeling is attractive from which the average penetration and duration can be estimated. Global ship ram type models similar to F_{MAX} introduced in Section 2.3.2 and discussed in Section 4.2 are useful. It is noted that reference to time in Eq. (8) can converted to penetration using average impact speed. Exposure will be the same.

2.3.3.5 Illustrative Example

Consider a 10^{-2} local design pressure on a $2m^2$ panel of bow plating between two main frame stiffeners on a bulk carrier. Using global ram analysis based on vessel displacement, design operational speed, bow shape, the average impact duration based on average penetration is t ~5s. The expected number of ramming events ν is 1000 per year. The proportion of true hits r on the design area is assumed to be 0.7 (i.e. r = 0.7).

From Eq. (5), $\mu = 1000 \cdot 0.7 \cdot \frac{5}{0.7} = 4900$

Eq. (7) can be rewritten to determine the pressure corresponding to a specified target exceedence probability, α, μ, and x_0 and is given as

$$\begin{aligned} z_{0.01} &= x_0 + \alpha\left[-\ln\left(-\ln F_Z(z_e)\right) + \ln\mu\right] \\ &= x_0 + \alpha\left[4.6 + \ln 4900\right] \\ &= x_0 + \alpha\left[13.1\right] \end{aligned}$$

Using $\alpha = 1.25A^{-0.7}$ and assuming $x_0 = 0$ (reasonable assumption given x_0 in Figure 36), the design pressure-area curve is $P = 16.37A^{-0.7}$. The pressure on the 2 m^2 panel is estimated to be 10.1 MPa. Note that this illustrative design pressure curve exceeds the curves given in **Error! Reference source not found.**. Figure 38 illustrates local pressure design curves for both 10^{-2} and 10^{-4} annual exceedence probabilities.

The influence of the number of rams per annum on design pressures is illustrated in Figure 37. A practical basis for classification of arctic vessel classes is discussed in Section 4.2.6 (i.e. the highest Polar Class vessel PC1 can be calibrated to coincide with on the order of 10,000 rams per annum).

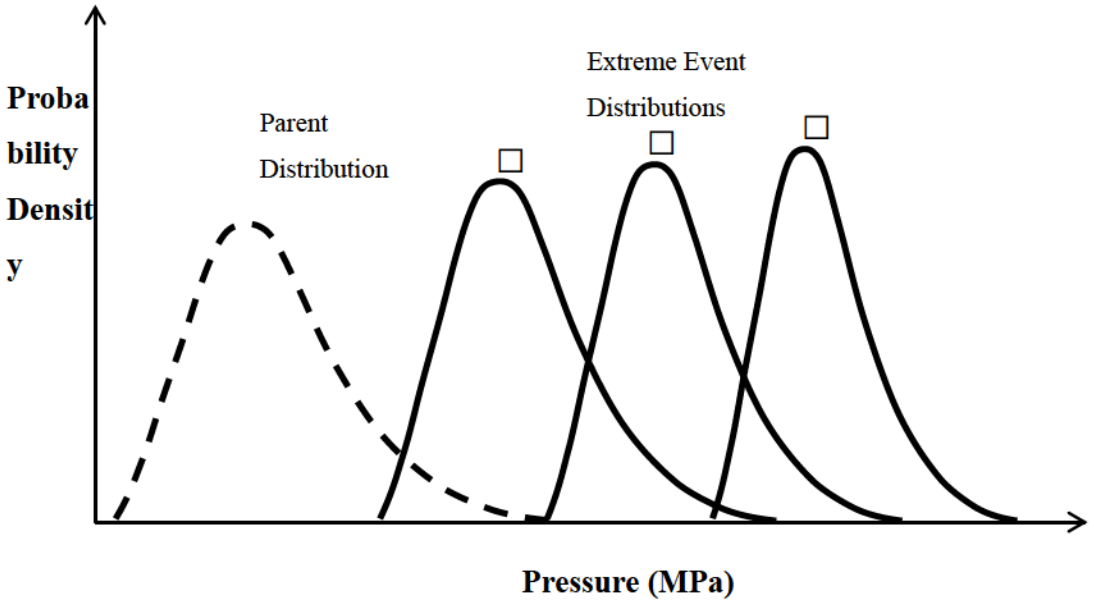

Figure 37 Illustration of influence of exposure (i.e. number of annual events) in determining design distributions for annual maximum pressures for design

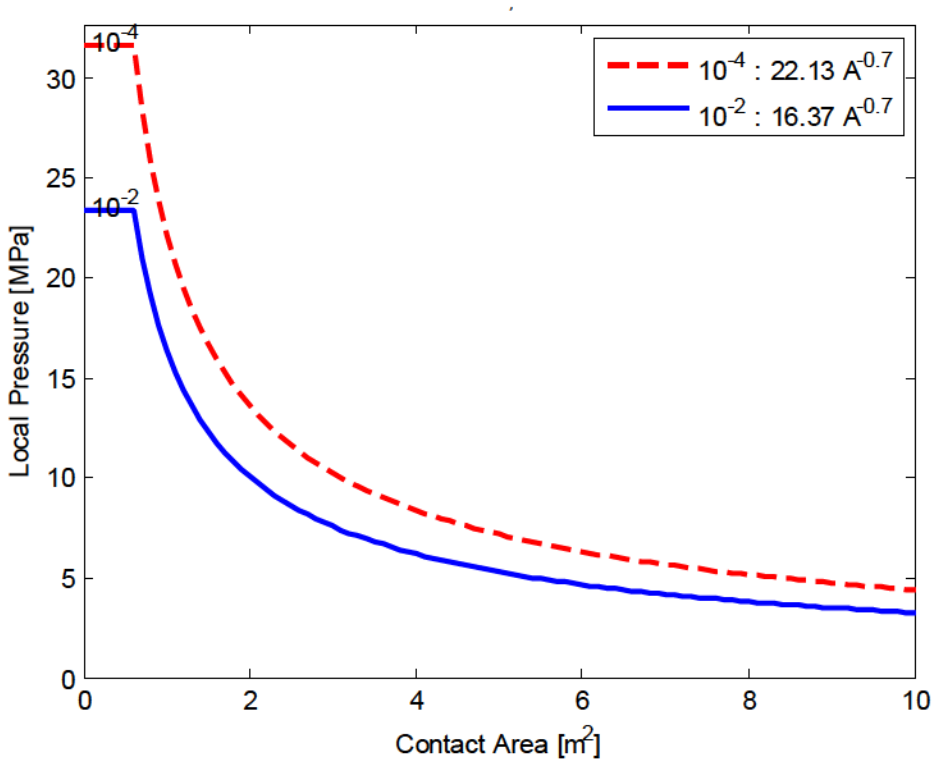

Figure 38 Local pressure curves for 10^{-2} and 10^{-4} annual exceedence probabilities for 1000, 5 second rams.

2.3.4 Other Pressure-area Considerations

2.4.3.1 Spatial Pressure-area

The term *spatial* pressure-area relationship was introduced by Frederking (1998, 1999) and defines the distribution of pressure on particular subpanels within a contact zone (or measurement area) at a (any) particular point in time during an interaction event. Pressures on individual and adjacent subpanels can be grouped and the individual subpanel pressures averaged to obtain average pressures on areas of increasing size. The process is illustrated in Figure 39. A spatial curve essentially represents the distribution of pressure across an *HPZ*. The resultant distribution of pressure with increasing area shows a decreasing trend and hence a local scale effect. A typical spatial pressure-area curve is shown in Figure 40. The progression of spatial pressure-area curves during a ship ram up to an arbitrary point of global force (as measured on a panel) is illustrated in Figure 46. With continued interaction, the *HPZ* would eventually fail and the spatial curves progressively disappear.

For local design, spatial curves have limited value since consideration must be given to peak pressures on specific panel areas through the ram duration and not just a distribution of pressure at some arbitrary point. Otherwise peaks may be missed.

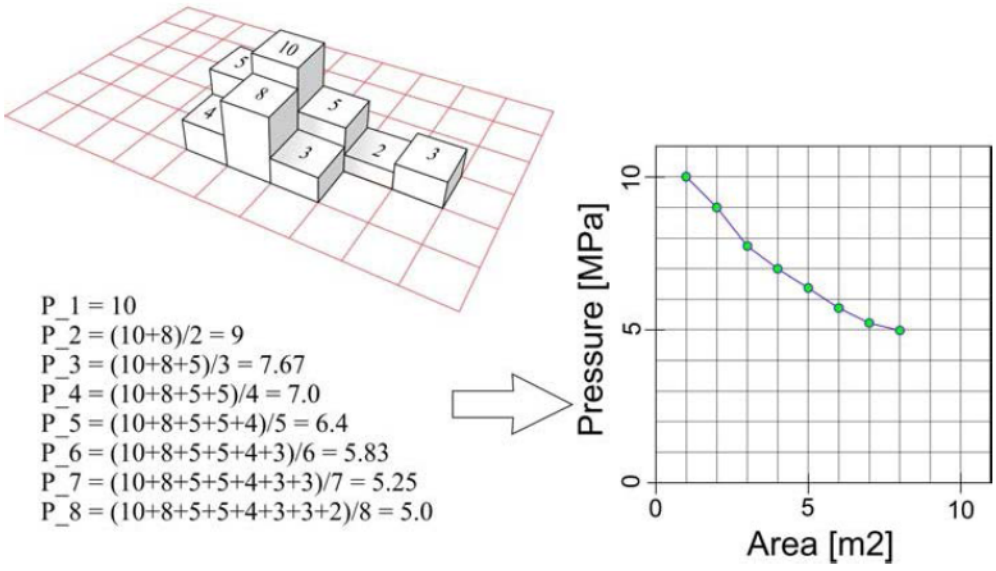

Figure 39 Illustration of spatial pressure-area relation (Daley, 2004)

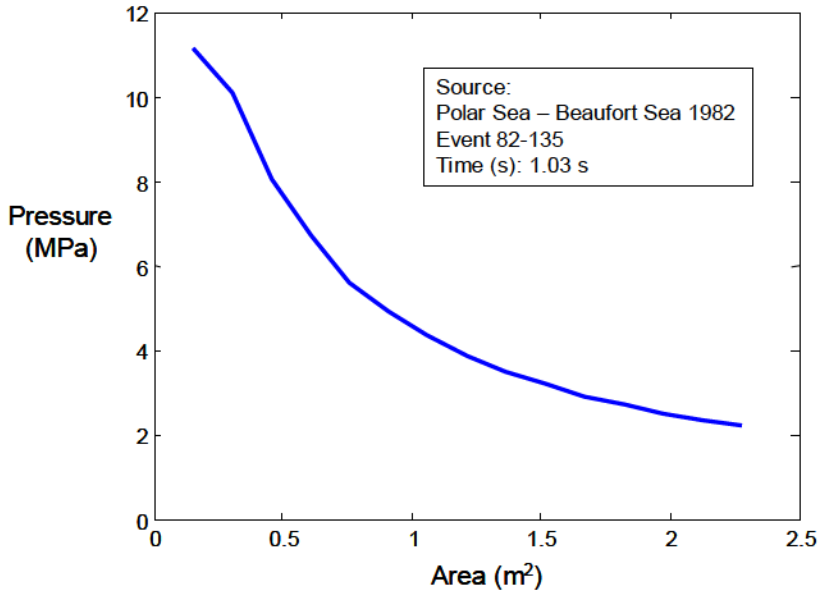

Figure 40 Typical spatial pressure-area relationship from *Polar Sea* 1982 event (Frederking 1999)

2.4.3.2 Process Pressure-area

Frederking (1998) a first introduced the concept of *process* pressure-area. Frederking (1999 and 2005) describes the changes in average global pressure with nominal contact area during an interaction event as *process* pressure-area effects, making reference to Riska's (1987) analysis. The key point here is that *process* relates to changes in average global pressures over nominal contact areas including regions of zero pressures through the ram duration. Attempts to model process pressure-area curves for different ship impact trials as well as iceberg impact trials are given in Figure 41 through Figure 44. While pressures may increase for short time increments, generally, pressures decrease with increasing nominal area, although for many of these tests, true nominal contact areas were not measured. Randomness consistent with non-simultaneous failure is noted. Frederking (1999) conducted an analysis of process pressure-area for the *Oden* 1991 trials and observed no *process* trend.

Based on observations from Medium Scale Indentation and Figure 45, Daley (1994) and Daley *et al.*, 1998), describes *process* pressure-area as a repeating series of events where pressures steadily rise during a sequence of minor failure events until a major failure occurs.

He concludes that the local trend is one of rising pressures, but the larger trend, due to the limits imposed by the major failure is one of falling pressures. He notes that the sharp drops in pressure result from a major crack and if additional confinement was present to suppress crack formation and growth, a major failure event may be temporally suspended leading to a rise in pressures. This is a most important observation that can get easily misapplied if one imposes an artificial and unrealistic notion of infinite confinement. Practical application here is most important. Consider a scenario of a ship ramming 5 m thick ice. Free surfaces exist all around the interaction area where a crack can propagate thereby limiting any build-up of confinement. With this in mind, the idealistic medium scale tests must be considered upper bound and used with caution.

Polar Sea 1982 and 1983 trial data were analyzed by Daley (2004) to study process effects. Observations from *Polar Sea* 1982 events are illustrated in Figure 46. Spatial pressure-area curves progress in an upward fashion as the penetration progresses. A critical assumption is that the end of the ram corresponds with the peak force after which the vessel slides off. Only the rising part is considered important thus ignoring progressive drop in the spatial curves. A trend is suggested with each progressing spatial pressure-area curve (average pressure associated with the largest area), one of increasing average pressure with increasing contact area. Daley (2004) suggests that with increased force (larger ships; higher speeds), *process* pressure-area could increase. He notes that unlike the *spatial* pressure-area relationship (see previous section), there is no a-priori reason for the pressure to fall with increasing area and that factors such as increasing confinement could well lead to increasing average pressures as the interaction proceeds.

The first observation with this analysis concerns the use of area. By isolating only zones of actual contact (i.e. panels with measured forces), the areas used in the Daley (2004) analysis are not global or nominal areas. Global contact areas are based on the projection of the structure onto the ice without reduction for spalling as discussed in Section 2.2.2. The averaging of *HPZ* forces over the nominal contact area leads to global scale effect.

In the context of *HPZ* behavior from other observations, the observation of progressive spatial curves in Daley (2004) captures the occurrence of a *HPZ* (i.e. he isolates only zones

of actual contact with structure - ignoring zero pressure zones). By assuming the peak force from a *HPZ* represents the end point of a ram and then assuming the corresponding peak spatial pressure-area curve (or peak pressures on specific local areas) would continue to rise if increased force were available to increase penetration, Daley idealizes the formation of a force dependent on a *HPZ* that never fails. But physical observations show otherwise, that *HPZ*s will appear and fail, moving from place to place as illustrated in Figure 3 and Figure 18. Corresponding spatial pressure-area curves will rise and fall. Longer duration events (e.g. continuous MY ice crushing against the *Molikpaq*) illustrates this process.

It is correct that with confinement, local pressures on smallest panels will increase with increased penetration. But modeling only the formation of a *HPZ* (i.e. ignoring failure) that apparently produces an inverse global scale effect seems misleading and not consistent with the material properties of ice and mechanics of fracturing materials. Increased global penetration and global contact area will lead to increased force as more *HPZ*s develop to transfer load into the hull, but this does not reflect nor change the scale effect. Consideration for exposure is needed; increased penetration and impact duration from larger, faster impacting vessels will result in increased pressures locally.

With respect to confinement, it must be kept in mind that ice fractures at all scales. If a free surface is present (which is in the case for practical application of ship rams where irregular ice geometry is present), fracture will occur and confinement is lost. This occurred in the most confined idealized medium scale experiments (compared to ship rams) the Hobson Choice ice island tests as illustrated in Figure 47 (Frederking *et al.*, 1990). Further the very high and complex stress states associated with the occurrence of *HPZ*s enhance crack growth and fracture events. Should confinement persist, an *HPZ* force limit exists where microstructural damage occurs at the ice structure interface that softens the ice and fails the *HPZ*.

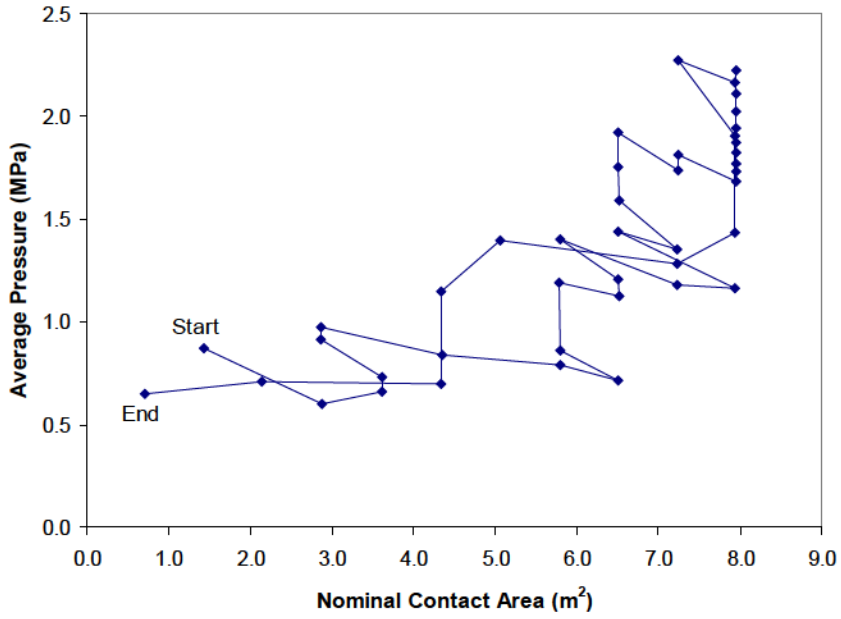

Figure 41 Process pressure-area for 5.4m/s glancing collision with 4-5m thick ice on *Louis S. St-Laurent* (Frederking, 1998)

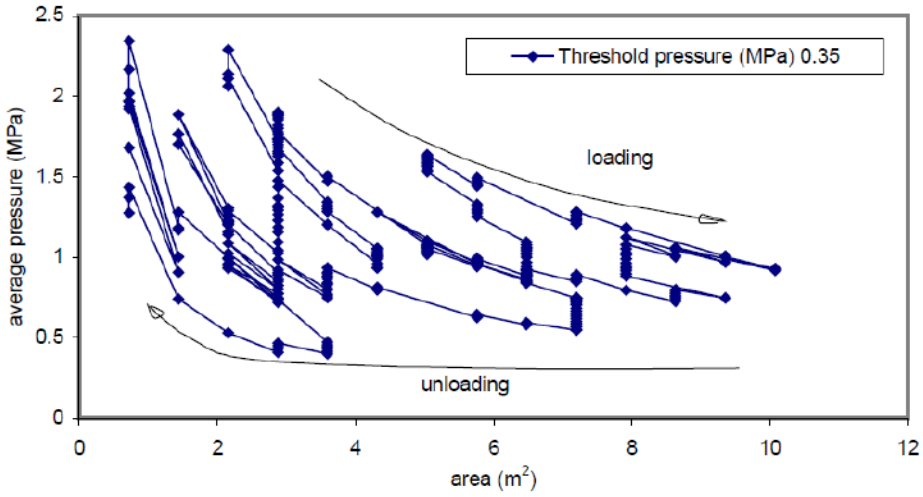

Figure 42 Process PA for *Louis S. St-Laurent* – 4m/s against 1-2 m thick floe (Frederking, 1999)

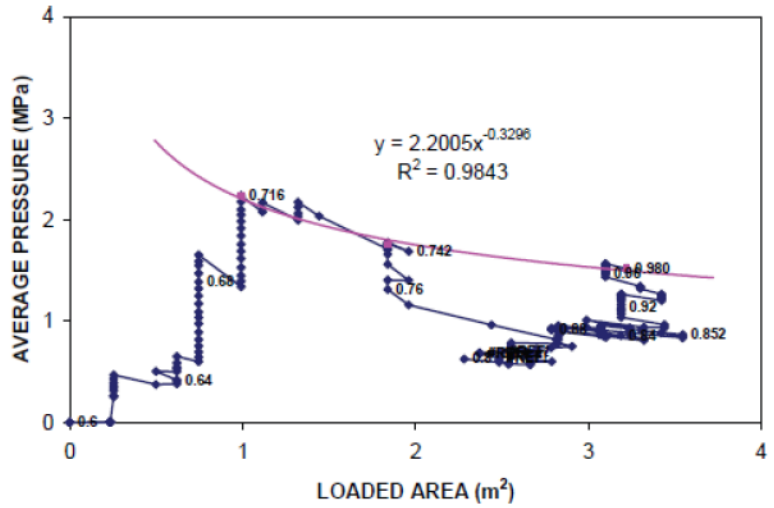

Figure 43 Upper-bound process pressure-area curve fit to bergy bit impact E23_B17_162 (Frederking and Ritch, 2009)

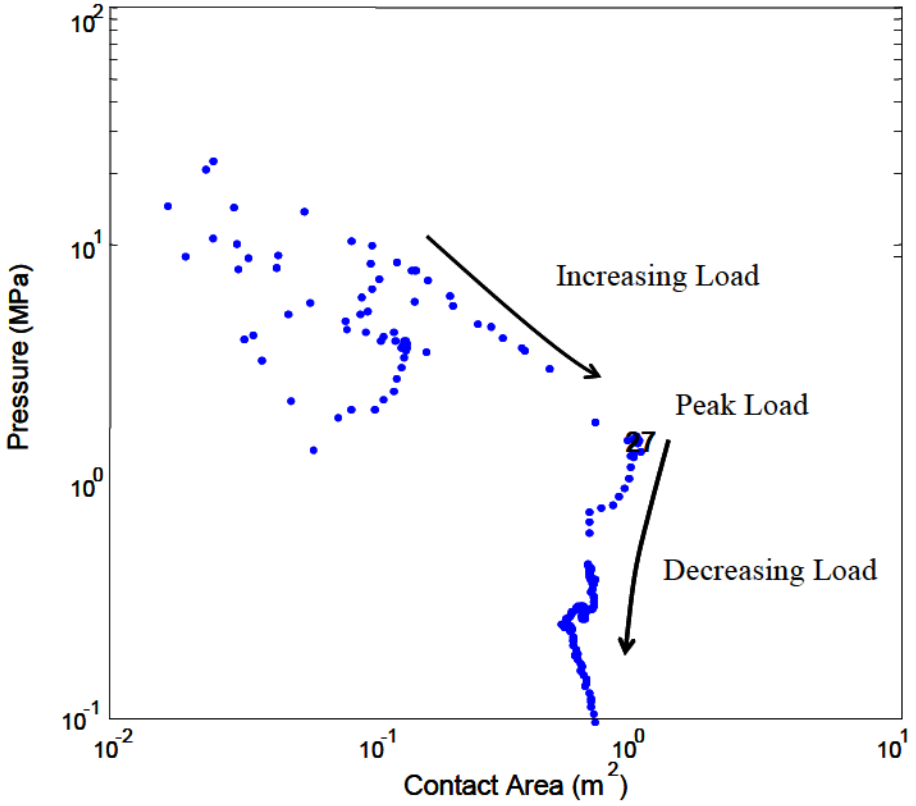

Figure 44 Process pressure-area curve for Grappling Island growler tests (IMP 27)

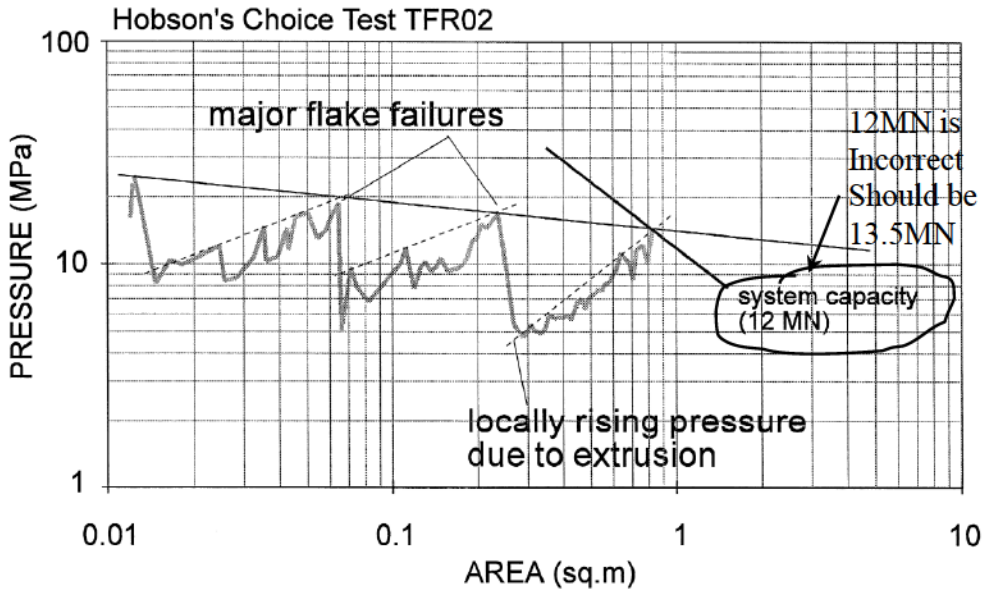

Figure 45 Hobson's choice data showing discrete failures (Daley *et al.*, 1998) – Note that reference to 12 MN system capacity is incorrect. System capacity was 13.5 MN, and displacement controlled and set to stop at less than 150mm (Masterson and Frederking, 2010)

Trials: USCGC POLAR SEA - Beaufort Sea
Event Number: 83-410
Date: 24-Apr 1983
Time: 16h 11m 59s
Force [MN] : 4.9
max Pressure [MPa] : 7.9

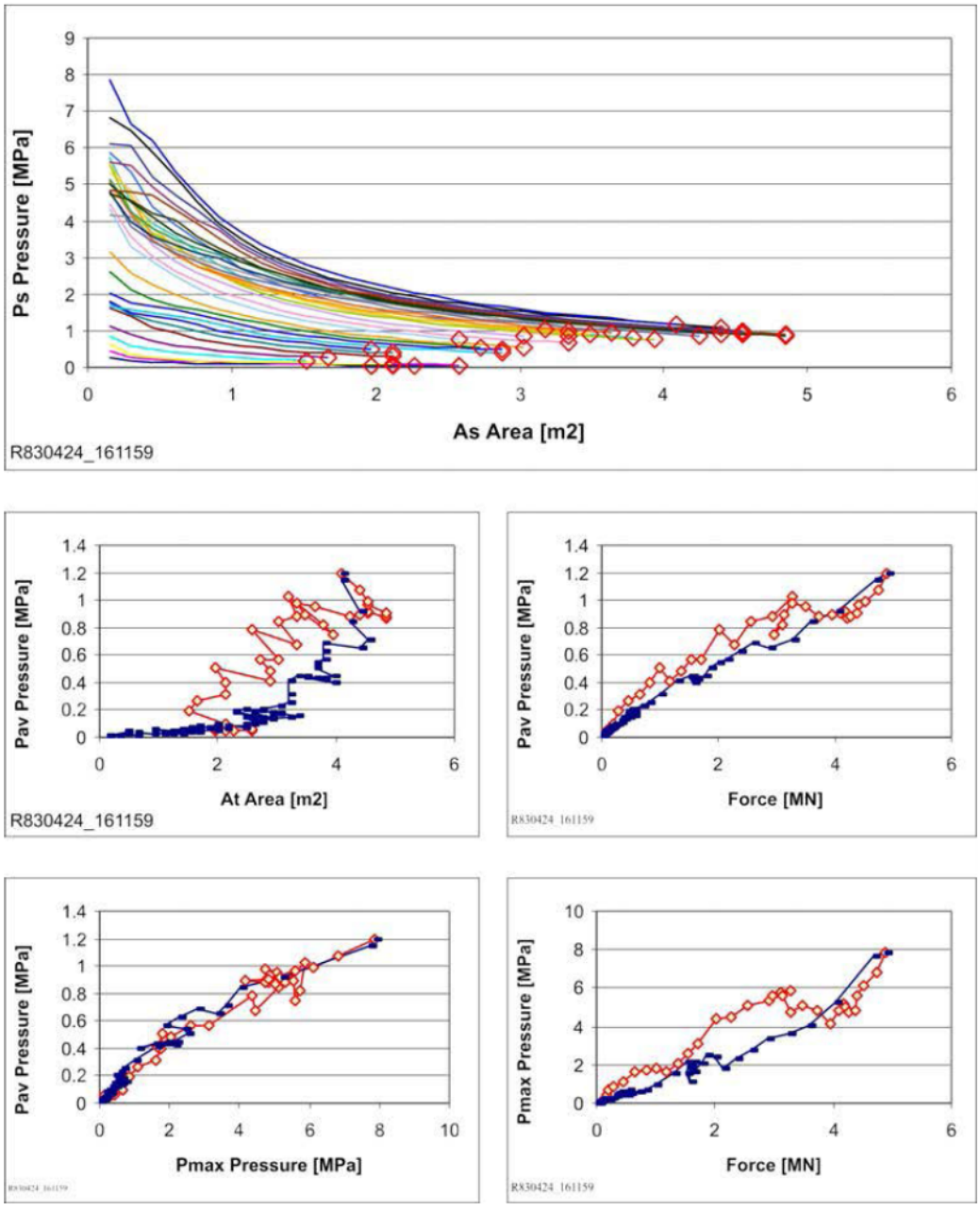

Figure 46 Progression of spatial pressure-area curves from *Polar Sea* 1983 event #410 (Daley, 2004).

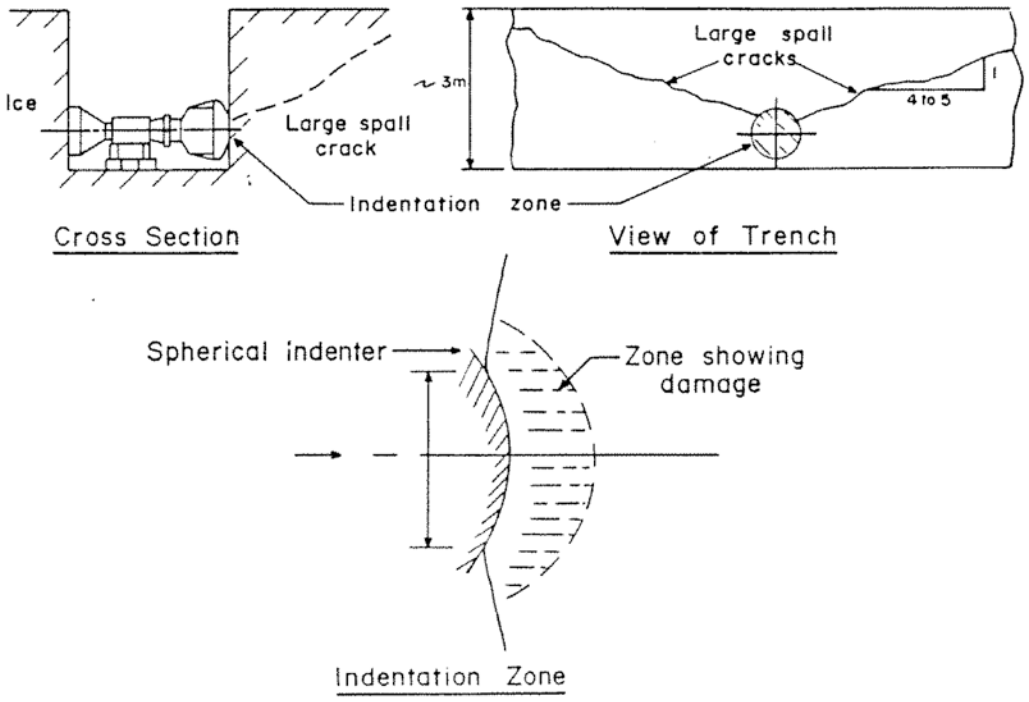

Figure 47 Schematic of global fracture event during medium scale Hobson's Choice ice indentation test NRC 01 a slow loading test (Frederking *et al.* 1990)

CHAPTER 3. Compressive Ice Failure and Scale Effects

3.1 Mechanics of Compressive Ice Failure

Ice failure is a dynamic process that is rate dependent. At slow loading rates below 10^{-5} s^{-1} creep dominates with a small elastic component, at intermediate rates viscous flow with irrecoverable creep, and at fast loading rates, continuous brittle crushing. An illustration of the response of ice to both slow and fast loading rates is illustrated in Figure 48 based on medium scale indentation tests (Masterson *et al.,* 1999) and a 1 m^2 indentation area. A permanent depression is observed at slow rates, whereas fracture and spalling is evident at the faster loading rate.

The response of ice to applied load is illustrated in Figure 49 which includes an immediate elastic strain ε_e, a transient time dependent delayed elastic ε_d, and a transient time dependent nonlinear viscous creep ε_v. Delayed elastic strain is often referred to as primary strain and is largely recoverable. Viscous strain is often referenced as secondary creep and is permanent.

Total strain is given as $\varepsilon_{total} = \varepsilon_e + \varepsilon_d + \varepsilon_v$ where

$$\varepsilon_e = \sigma / E \qquad (9)$$

$$\varepsilon_d = \frac{C\sigma}{Ed}\left\{(1 - \exp[-(a_T t)^q]\right\}$$

$$\dot{\varepsilon}_v = A\sigma_{11}{}^n \exp\left(-\frac{Qi}{RT}\right); \quad \varepsilon_v = \dot{\varepsilon}_v \bullet t$$

and where C and A are constants, a_T is a temperature dependent rate parameter, σ is a constant applied stress at $t = 0$, E is the Modulus, t is time, q is a constant, σ_{11} is a uniaxial applied stress, Qi is the activation energy dependent on ice type i, R is a gas constant, and T is the temperature (K). The viscous creep strain rate is observed to be proportional to n^{th} power of the stress, where n is about 3 according to Glen (1955).

The transition to brittle failure occurs with a strain rate above 10^{-4} s^{-1}. For faster loading rates above 10^{-3} s^{-1}, brittle fracture occurs particularly where cracks can nucleate and propagate to the free surface. This results in substantial loss of strength.

The enhanced strain rates above 10^{-5} illustrated in Figure 50 are not only influence by brittle fracture, but by microstructural damage accumulation at both low and high confining pressures which substantially enhances creep rate. Microstructural modifications are active over a range of stress conditions, though the relative importance of each is a function of confinement, deviatoric stress level and total accumulated strain and temperature (Meglis *et al.*, 1999; Melanson *et al.*, 1999)

Hydrostatic confinement would naturally lead to suppression of both nucleation and propagation of cracks thereby increasing failure stress as is illustrated in Figure 51 for different strain rates. But this is limited by microstructural changes as noted above.

Figure 52 and Figure 53 illustrate the process for interaction with a level ice sheet. Pressure distribution varies from low nearer the free surface to very high pressures near the middle. At lower confining pressures, softening occurs near the free edge adjacent to an *HPZ* including nucleation of microcracks along with extensive recrystallization and microfracturing. Nearer the center of the contact zone, high pressures cause damage in the form of pressure melting and recrystallization. A very soft absorbing layer of fine grained crystals is produced. Kheisin and Cherepanov (1973) and Kurdyumov and Kheisin (1976) observed similar behavior. The growth of the two damage zones continues in a layer until both zones meet resulting in rapid extrusion of crushed ice particles. The strain rate is highly enhanced (many orders of magnitude up to 10^6) and contributes to the loss of strength (Melanson et al, 1999; Meglis *et al.*, 1999). In this case, elastic and delayed elastic properties are lost and the "burgers model" shown in Figure 49 reduces to a single dashpot modeling viscous flow as illustrated in Figure 54. Once pressure drops and material is extruded, the material hardens and sinters together. While *HPZs* are conceptually illustrated in Figure 52 through Figure 54 to occur towards the middle, *HPZs* can randomly occur across the interaction face, although more likely towards the middle.

The influence of confining pressures on damage is illustrated in Figure 55 based on a series of triaxial tests (Meglis *et al.*, 1999). Damage at lower confining pressures (i.e. brittle fracture, microcracking and recrystallization) is suppressed as hydrostatic pressure is increased, increasing material strength. But for higher confining pressures damage rate (characterized by pressure melting and recrystallization) increases resulting in loss of strength. It is suggested that loss of strength for higher confining pressures was not observed in the Figure 51 because tests only modeled low damage levels.

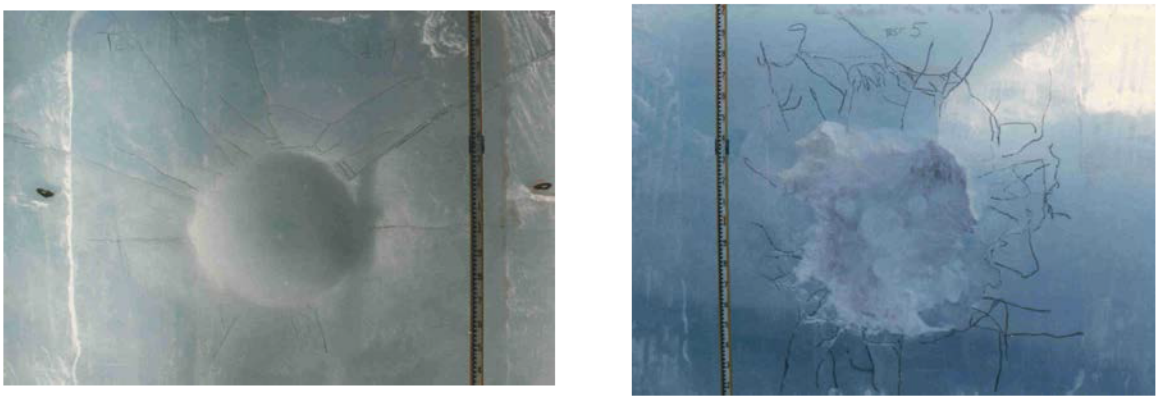

(a) (b)

Figure 48 Medium scale insitu testing (Masterson *et al.*, 1999) with interaction area of 1.0 m2: (a) 0.3 mm s—1, ductile failure; (b) 10 mm s—1, brittle failure. Courtesy Dan Masterson. Damaged ice at lower rates is evidenced by the permanent depression without spalls (left). Damaged ice at faster rates show fracture around the high-pressure region (right).

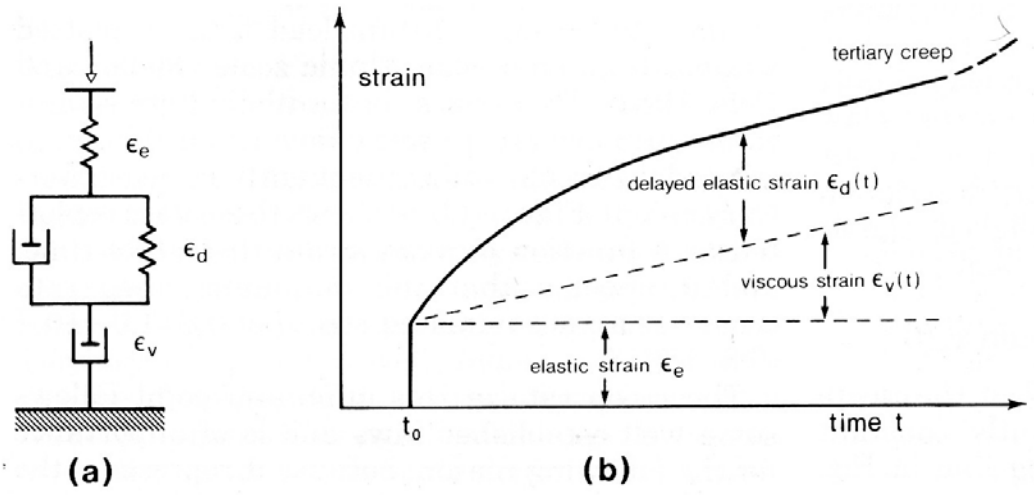

Figure 49 Illustration of strain development with time for an applied stress as a function of time including Burgers model approximation in (a) (Sanderson, 1988).

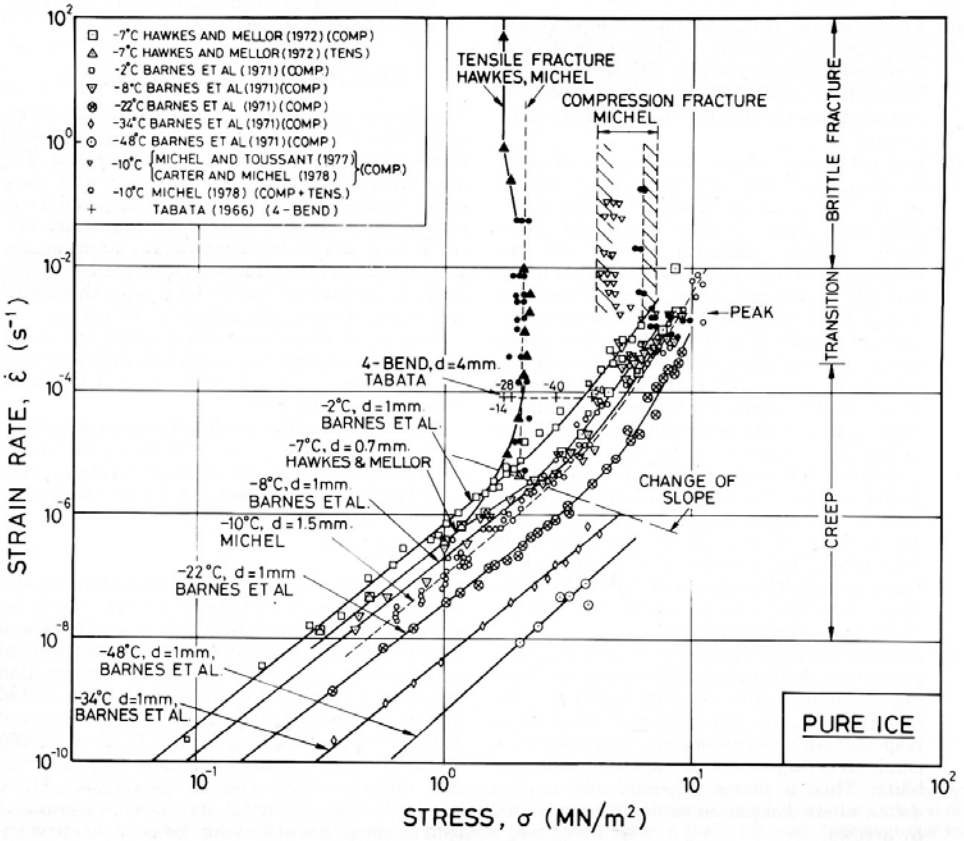

Figure 50 Uniaxial loading of pure polycrystalline ice and influence of strain rate and temperature (Sanderson 1988 after Hallam, 1986)

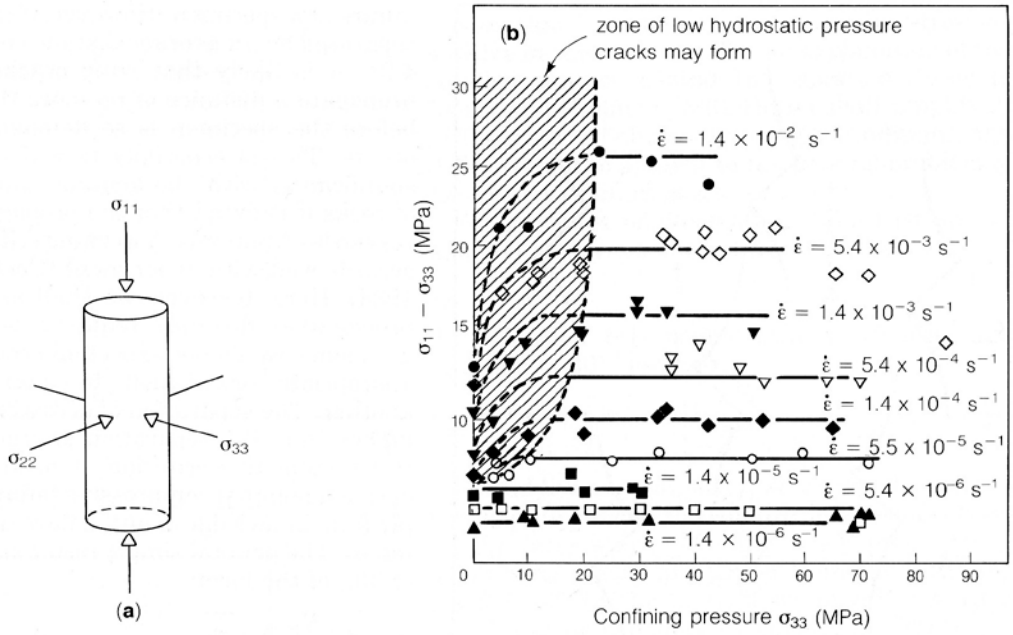

Figure 51 Influence of confining pressure on maximum stress difference (deviatoric stress) for multiple strain rates (figure from Sanderson 1988).

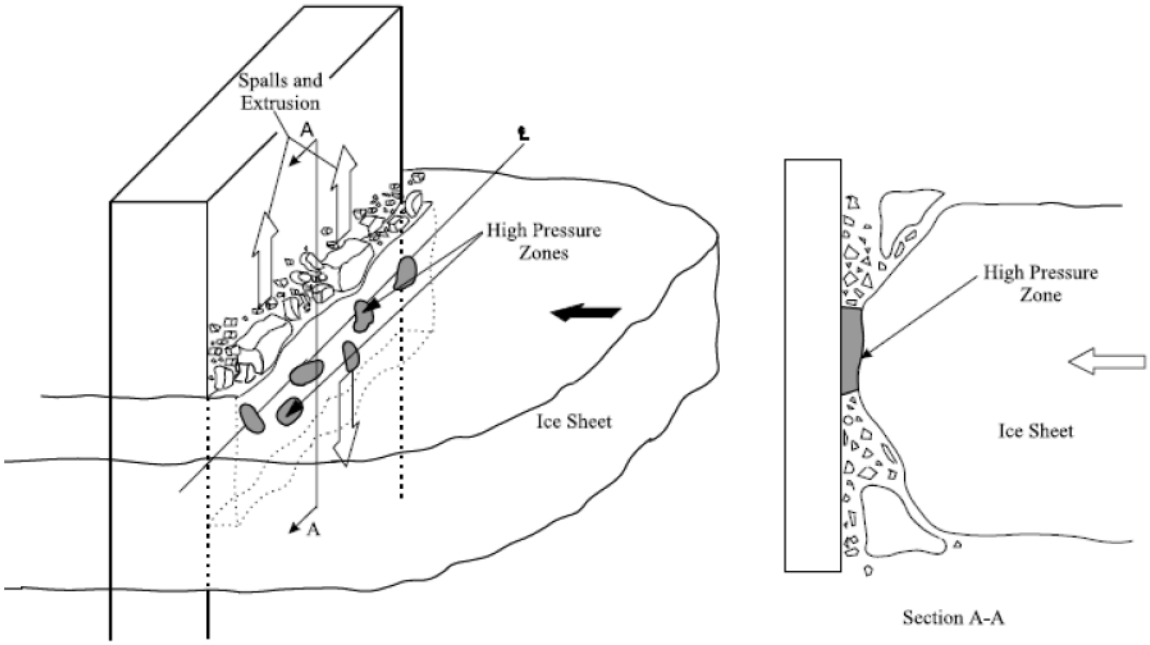

a)

b)

Figure 52 Illustration of ice failure process including localized contact near the center of the ice sheet as a result of non-simultaneous failure.

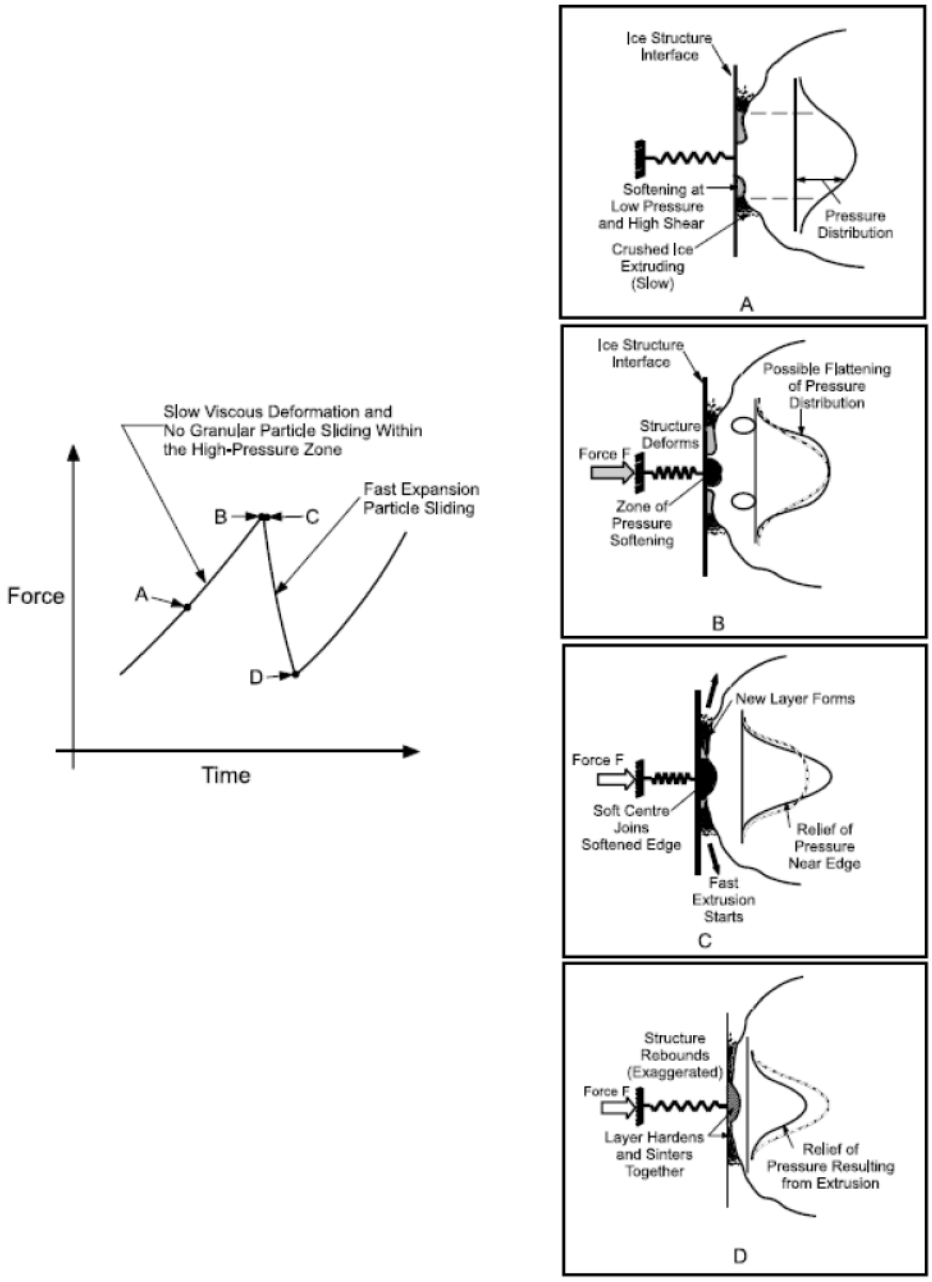

Figure 53 Illustration of compressive ice failure associated with *HPZ*s and the corresponding fluctuations in forces (Jordaan, 2001).

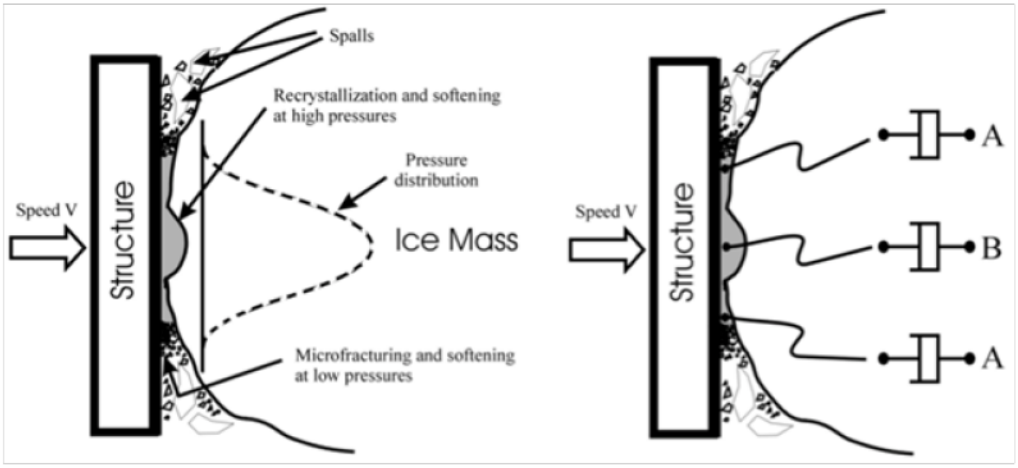

a) b)

Figure 54 Processes that characterize ice failure at high loading rates including (b) final state of viscous flow (i.e. Burgers model in Figure 49 reduced to single dashpot) once damage has occurred across the full layer and even before crushed material is extruded.

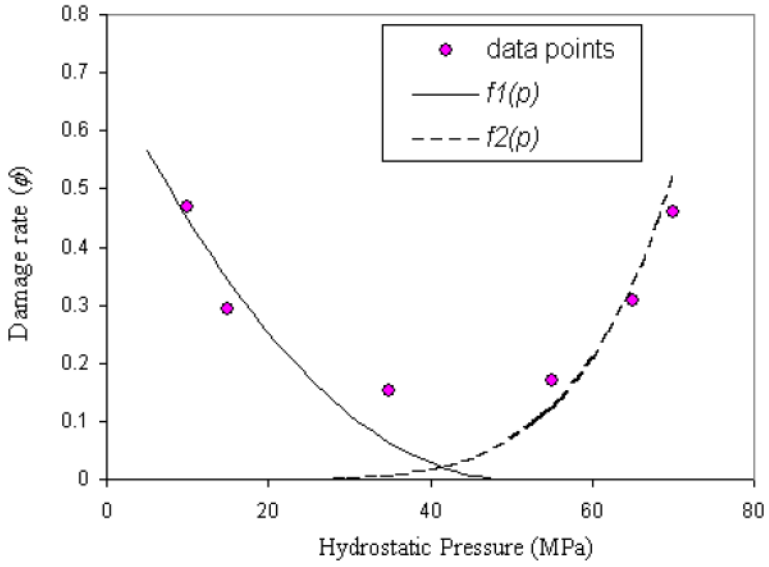

Figure 55 Influence of confining pressure on damage rate and resultant failure pressure (Meglis *et al.*, 1999, Jordaan, 2001)

3.2 Size and Scale Effects

The significance of scale effect in ice mechanics was largely realized when Sanderson (1988) first compiled all available pressure-area data into a single plot in Figure 56. The additional of ship ram data as well as Hans Island MY impact data and observed power law curve fit is illustrated in Figure 24. While the effects of exposure, confinement, salinity, aspect ratio, and temperature effects, were not accounted for in the data presentation, the influence of scale with interaction area was evident. But the extent of scale was uncertain and an objective of further research.

Controversy still exists, from those who argue that size effect is obvious, to those who deny its existence (Schulson and Duval, 2009). Skeptics fear that the scale effect may be used to justify economics of an offshore structure or ship that in the end may not withstand the ice forces. The following sections attempt to demonstrate that scale effect is an inherent property of ice for fast loading rates of interest, but that uncertainty exists and considerable research is required before a complete understanding is achieved.

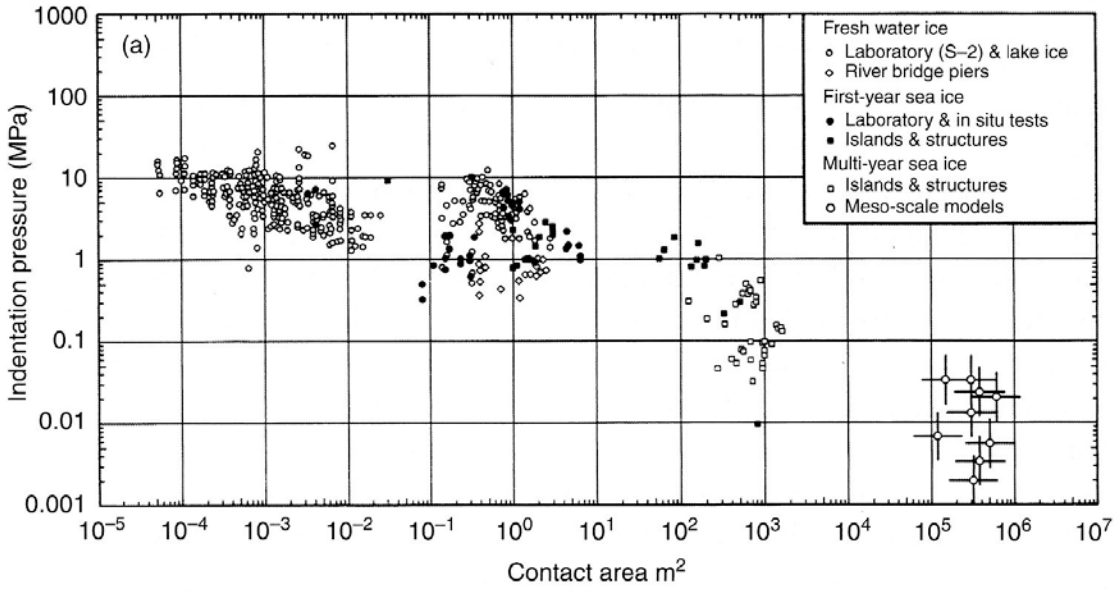

Figure 56 Compilation of pressure-area data illustrating scale effect (Sanderson, 1988)

3.2.1 Non-Simultaneous Failure

At slow loading rates as ice creeps, contact across the face of the structure will be uniform and simultaneous. At high loading rates, brittle fracture and spalling (local and global) will continually reshape the contact face resulting in non-simultaneous failure. Actual points of contact with the structure shift from place to place varying spatially and temporally as ice crushes. The majority of the load transmitted into the structure is through a much reduced contact area relative to the nominal area namely *HPZs* (Johnston et al., 1998; Taylor 2010).

Kry (1978) was among the first to observe irregular contact across the face of the structure as ice continuously pushed past noting macroscopic cracking and cleavage cracks. Ashby *et al.*, (1986) was among the first to provide convincing evidence of non-simultaneous failure and influence on scale effect using indentation tests with brittle wax (See Figure 57). Fractures and spalls resulted in the continual change in the number and position of contact points as the interaction progresses. He also noticed the significance of high local pressures as well as the averaging of pressures across the entire nominal contact face. Ashby's idealized mechanical and probabilistic failure model is illustrated in Figure 58 and comparison with physical data in Figure 59.

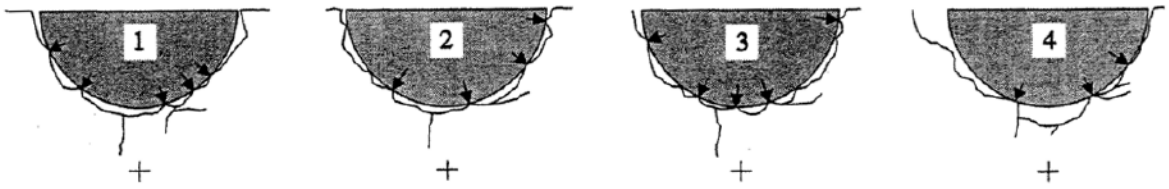

Figure 57 Illustration of non-simultaneous failure using brittle wax indentation tests (Ashby *et al.*, 1986)

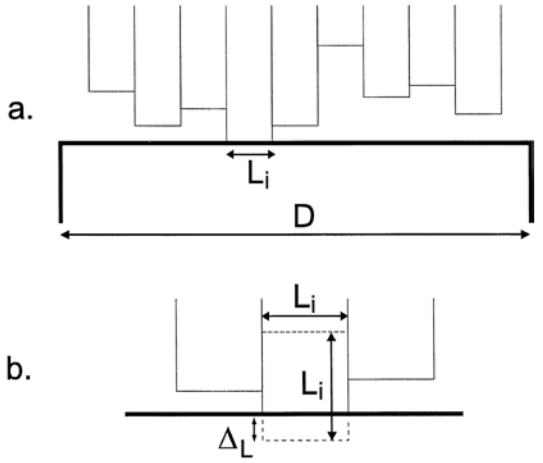

Figure 58 Geometric non-simultaneous failure model and assumptions (Sanderson, 1988 after Ashby *et al.*, 1986)

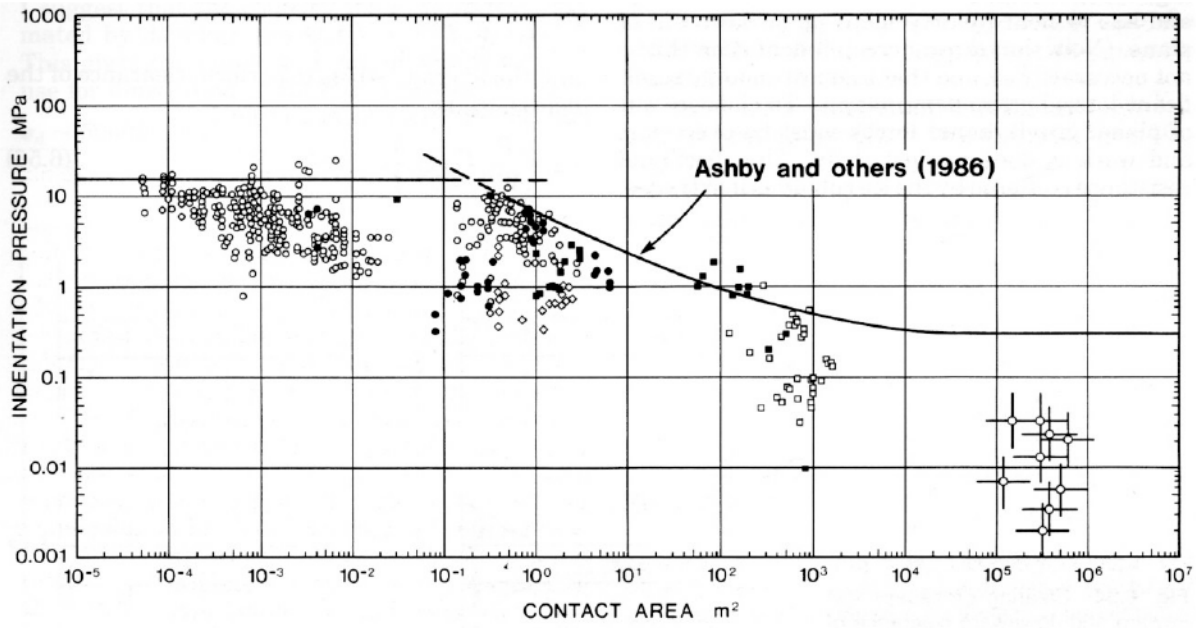

Figure 59 Theoretical curve of Ashby *et al.*, 1986 with Li =1, P_L = 15MN and ΔL = 0.02 m bounded by experimental data (Sanderson, 1988)

Riska (1987, 1991) and Riska *et al.*, (1990) illustrated the concept of non-simultaneous failure for a ship hull interacting with a MY ice ridge as illustrated earlier in Figure 11. Glen and Blount (1984) observed non-simultaneous failure using ship ice interaction trials onboard the *CCGS Louis S. St. Laurent* (see Figure 103). Contact forces and pressures vary in space and time across the instrumentation area. Similar results were observed by St. John

et al., (1984) from the *USCS Polar Sea* trials (see Figure 18) and Kujala (1994) from the icebreaker *Sampo* trials. Kujala (1996) using full scale nominal pressure-area data modeled non-simultaneous failure as a random compound Poisson process. Pressure-area scale effect was observed. Consistent behavior and scale effect was observed in the Hobson's Choice medium scale ice island tests (See
Figure 15 and Figure 16) from variations of local pressures across the face of the indenter and with increased penetration. (See Frederking *et al.*, 1990; Jordaan and McKenna, 1991; Muhonen, 1991; Sandwell, 1990, 1992, 1993.)

Similar non-simultaneous behavior was observed with lab scale indentor tests (see Joensuu and Riska 1989; Fransson *et al.*, 1991; and Tuhkuri 1995 and 1996). With the Tuhkuri tests (See Figure 60), the ice was pushed out of a confinement cylinder. Reducing the gap and increasing confinement resulted in increasing pressure since cracks were restricted from running to the free surface. Other lab scale and model testing was carried out by Kamesaki *et al.*, (1997), Sodhi (1992, 1998) and more recently Huang (2010). Sodhi observed both simultaneous and non-simultaneous failure for both slow and fast interaction rates respectively. He argues that scale effect is dependent on interaction rates and not an area effect (the Sodhi tests used a constant ice thickness and structure width, keeping the contact area constant). Observations from the ship ram trails (St. John *et al.*, 1984 and Ritch *et al.*, 2008) indicate that forces and pressures are independent of interaction speed (see Figure 29 and Figure 30). With more data, the random nature of loads may be more apparent in the Huang tests.

3.2.2 Line-Like Contact and HPZ Locations

As a result of brittle fracture and spalling nearer the edges, contact is most likely nearer the center of the ice sheet. Joensuu and Riska (1989), Fransson *et al.*, (1991), Tuhkuri (1993, 1995) observed wavering *line-like* patterns of brittle flaking introducing the concept of *line-like* contact as illustrated in Figure 60. Riska *et al.*, (1990) and Riska (1991), using a transparent window and pressure transducers installed in an icebreaker hull observed similar *line-like* patterns with high pressures along a wavering line, and low pressures elsewhere. Sodhi *et al.*, (1998) notes similar interaction geometry from medium scale JOIA tests. Jordaan (2001) illustrates in Figure 61 the spatial distribution of high pressures zones

(*HPZ*s), regions of contact remaining after spalls and crushed ice is extruded. As a result of non-simultaneous failure, *HPZ*s appear and disappear and represent the actual contact locations where the majority of force is transmitted into the structure.

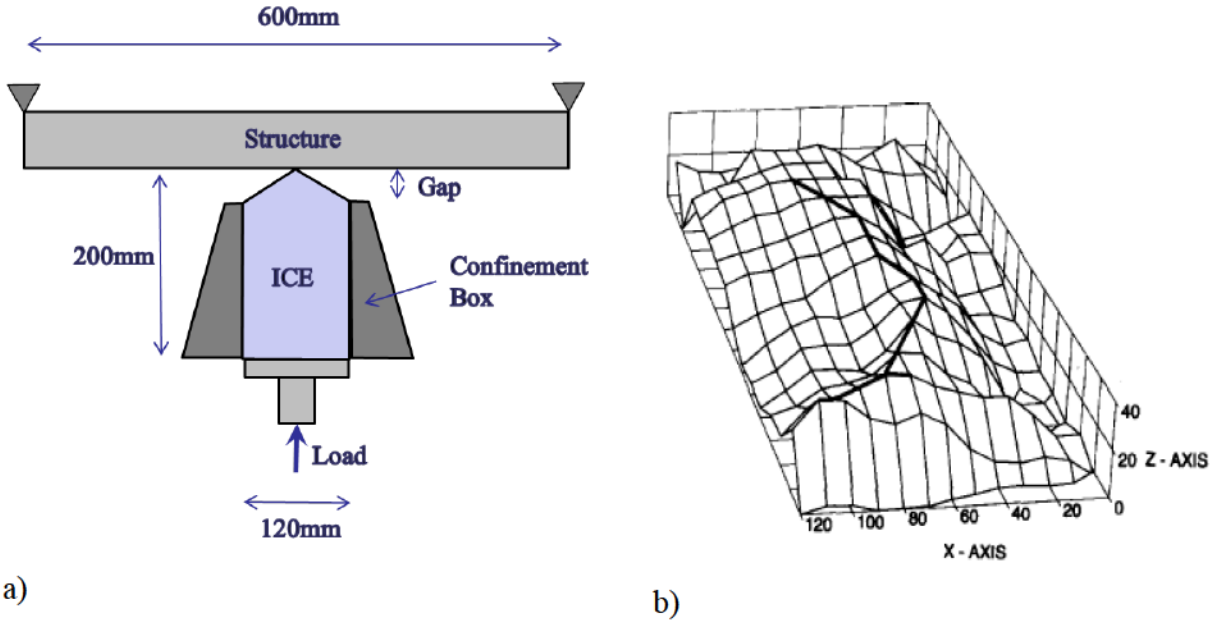

a) b)

Figure 60 a) Experimental test setup by Tuhkuri (1995) with ice block being pushed out of a confinement box; b) line-like surface profile following test with 40mm gap

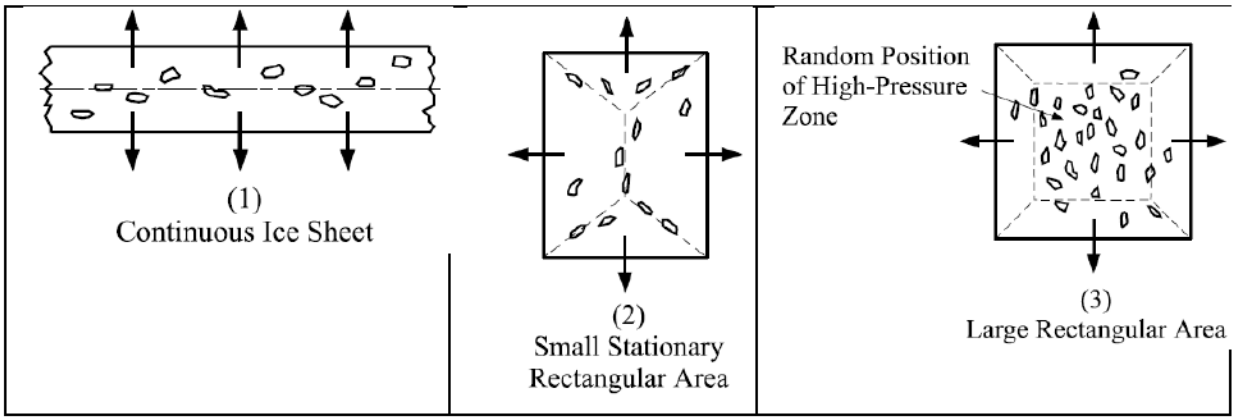

Figure 61 Conceptual distribution of *HPZ*s for different interaction geometries: *HPZ*s tend to be concentrated along or in the case of (3) within the dotted lines (Jordaan and Xiao, 1999)

3.2.3 Pressure-Averaging Effects

Kry (1978) following observations of non-simultaneous failure across the structure width; developed a statistical model of independent failure zones to analyze design stresses based on interaction duration and probability of stress exceedence. He observed that peak stresses averaged across the contact face (i.e. multi-zone area across wider structures) will be lower than the area of a single zone (i.e. narrower structures). Further, the more ice that passes the structure, the greater the chance of higher stresses being observed consistent with laws of probability.

Dunwoody (1991) developed a model of non-simultaneous failure linking global loads to loads on a local panel. He presented a formulation to express the average and the standard deviation of global force on a structure in terms of the average and standard deviation of local ice force per unit length and a correlation length parameter. Jordaan *et al.* (2006), Taylor *et al.* (2007), Taylor (2010) and Taylor and Jordaan (2011), studied the probabilistic aspects of random spalling resulting from non-simultaneous failure during fast interactions observed in the JOIA MSFIT data (Takeuchi *et al.*, 2000) and Molikpaq data (force measurements using localized instrumented panels across the width of the structure). Fracture and spalling across the interaction face will result in zones of zero pressure within the global interaction area. "Simple" averaging however, of individual localized panels across the structure face assumes a uniform pressure distribution. Subsequent extrapolation of global pressures across an interaction face will be highly conservative. Global pressures that consider statistical averaging of *HPZ*s across the interaction face will have the same mean as the localized panel pressures but have a reduced standard deviation as illustrated in Figure 62.

A similar pressure averaging, variance reduction method was used by Spencer and Morrison (2012) to analyze wide aspect ratio ice crushing pressure trends reported in the ISO 19906. Model parameters were consistent with *line-like HPZ* formation for both Arctic and Baltic ice conditions, and horizontal and vertical correlations between panels were modeled. Predictions were within 2% of ISO recommendations as illustrated in Figure 63. The influence of averaging increases with increased structure width and contributes to the pressure-area scale effect.

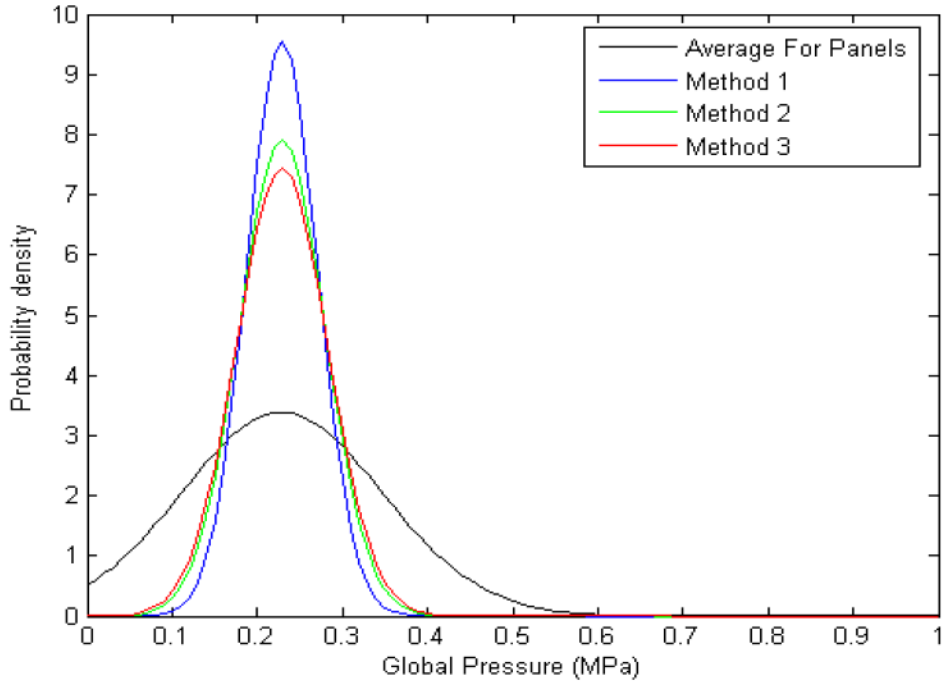

Figure 62 Illustration of pressure averaging across a structure face having nonsimultaneous failure

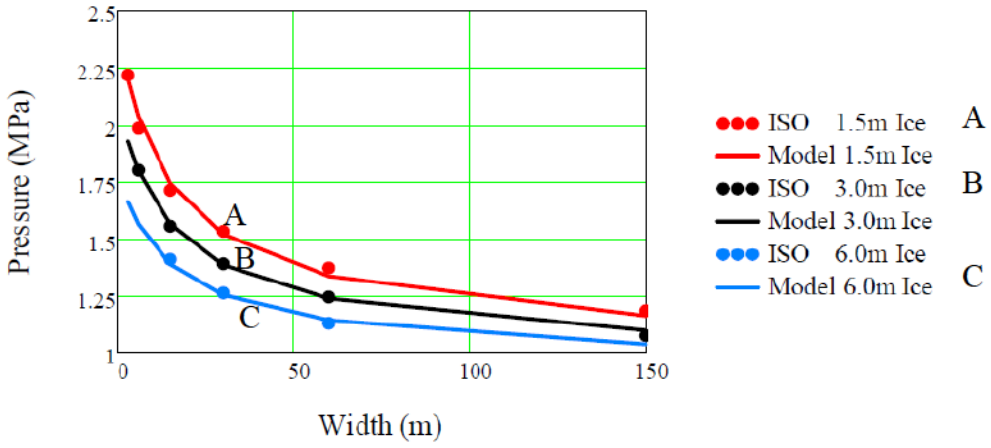

Figure 63 Comparison of pressure averaging model results with ISO predictions for arctic conditions (Spencer and Morrison, 2012)

3.2.4 Importance of Fracture

3.4.2.1 Classical Materials

The failure strength of "classical" materials (e.g., elastic, plastic, or viscoelastic) in continuum mechanics does not exhibit any scale effect. As illustrated in Figure 64, there is no change in the failure pressure (strength of the material) with change of scale. The stress strain relationship does not contain a length parameter compared with the strength of fracturing materials where failure stress can be represented as

$$\sigma = K / \sqrt{\pi \ell}, \qquad (10)$$

where K = fracture toughness and ℓ = crack length (Griffith, 1921).

Numerous studies exist studying the material properties of classical materials. Li *et al.*, (2005) studied the material properties of ice using a series of small-scale indentation tests. Four different sizes of spherical indentors (10mm, 20mm, 40mm and 100mm in diameter) and three different order of magnitude loading rates (e.g. 0.1, 1, and 10) were tested to examine the relationship between stress and contact area (See Figure 65). Results were compared with field results from the medium scale indentation tests (Frederking *et al.*, 1990; Masterson *et al.*, 1999). While scale effects for intermediate and fast displacement rates are evident, very little or no scale effect was observed for the slow displacement tests. At slow displacement rates, ice behaves as a viscoelastic (classic) material, which as discussed above, exhibits no scale effect. Sodhi (1998) and Huang (2010) observed similar behavior but suggest that scale effect is rate dependent only and not dependent on contact area. Jordaan *et al.*, (2009) notes that the observed scale effect from the faster displacement rate tests are a result of fracture and spalling which localizes actual contact into zones of high pressure or *HPZ*s. Materials that fracture are inherently scale dependent, and specimens containing larger flaws will have a lower failure stress.

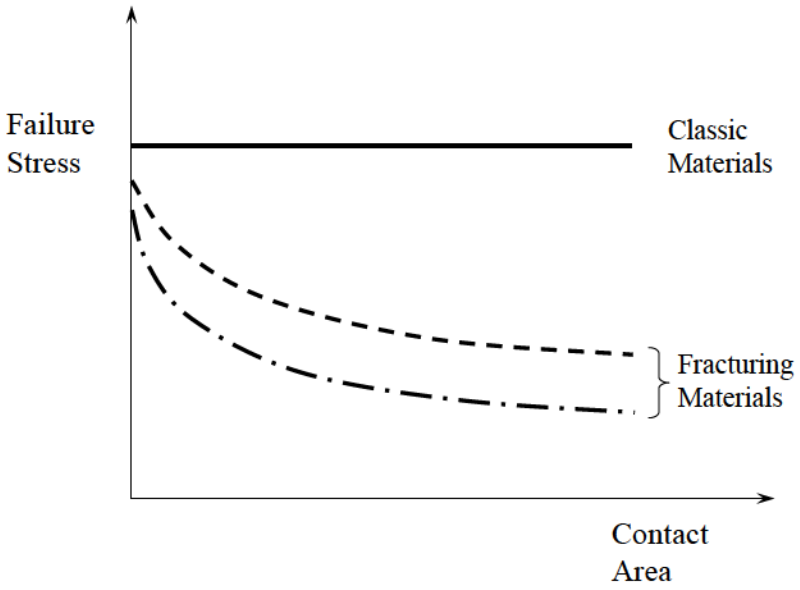

Figure 64 Illustration of scale effect in materials

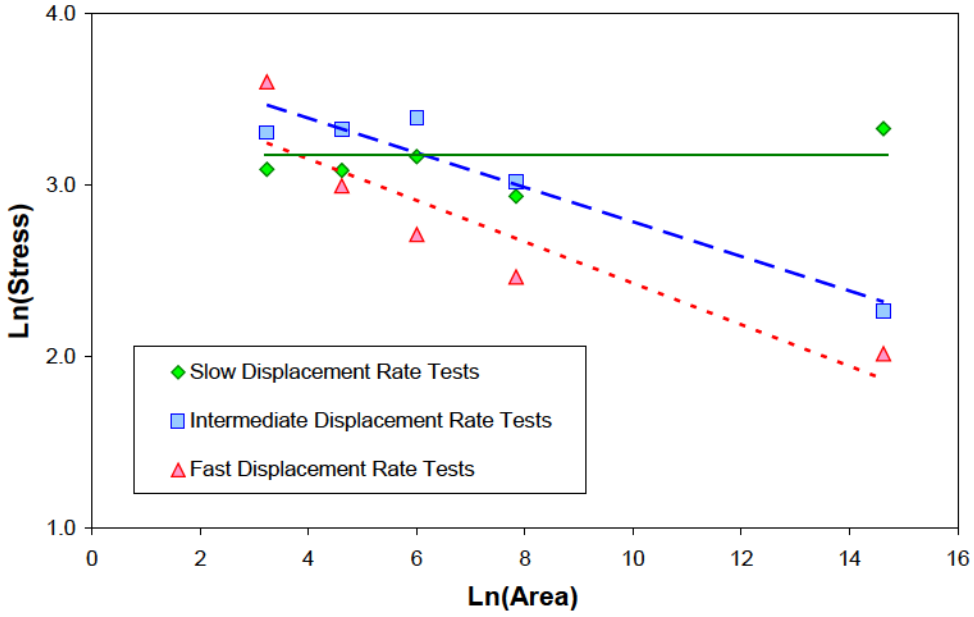

Figure 65 Scale effects from laboratory and field indentor tests for different sizes and indentation rates (after Li *et al.*, 2005)

3.4.2.2 Importance of Flaws and Cracks

Consistent with the probabilistic nature for spall and *HPZ* occurrence, flaws, too, have probabilistic characteristics. Following the review of Bazant (1999), the earliest references to statistical size effects came with Leonardo Da Vinci (1500s) and observations that longer cords, having equal thickness to shorter cords, had lower strengths. While Galileo (1638) with the invention of stress contended that this could not be true, Mariotte (1740) following extensive experiments concluded that long and short ropes of equal thickness will have similar strength unless the long cord happened to have some limiting flaw. Marriott proposed the principle of "the inequality of matter whose absolute resistance is less in one place than another." This principle is consistent with the statistical theory of size effect which simply states that the larger the structure, the greater the probability of encountering a material flaw or element of low strength. Griffith (1921) the founder of fracture mechanics showed that the theoretical molecular strength of a material is of the order of 100 times its practical strength (e.g. 14,000 MPa vs 170 MPa for glass (Gordon, 1968)). Griffith experimentally tested the strength of glass fibres with diameters down to 2.5mμ noting the increase nominal strength with decreasing diameter (and vise versa). He concluded that the presence of microscopic discontinuities and flaws in isotropic materials contribute to the reduced strength. Statistical theories of size effect started with Pierce (1926) who formulated a weakest-link chain model and extreme value statistics building on work by Tippett (1925). Work continued with Fischer and Tippett (1928), Frèchet (1927) and refined by von Mises (1936). Weibull (1939) introduced the Weibull distribution to adequately capture the extremely low probability of low strength values in the tail of the distribution (see also Section 3.4.2.7). The probability of a small material element is modeled as a power law of the strength difference from a finite or zero threshold. Sanderson (1988) following work by Weibull (1951) assumed that a population of cracks will be randomly distributed through a body of ice having a size distribution. A probabilistic model by Maes (1992) modeled the random dispersion of cracks throughout the volume as a Poisson process.

Kendall (1978) suggested that a probabilistic approach is a "dubious statistical argument involving invisible flaws" and developed a deterministic "double cantilever beam" model. Zou, (1996) found that the double cantilever beam model, with an assumption that two struts can be treated as elastic is only valid for large crack length. Such large cracks are rarely

found in nature. While large cracks have been observed, (Kärnä and Muhonen, 1990), they are likely the result of propagated cracks that were once initiated by internal flaws (Zou, 1996). Such internal flaws are likely a derivative of weak grain boundaries in natural ice (Taylor, 2010). Precursor cracks may propagate in a tensile mode, a shear mode or a mixed mode and will likely lead to the formation of spalls. In addition to modeling the conditions under which cracks nucleate and propagate, it is important to understand the trajectory of propagating cracks. Mixed model fracture as well as crack trajectory have been studied extensively by researchers including Sih (1973); Palaniswamy and Knauss (1978); Conrad (1976); Cotterell and Rice (1980); Sih and Tzou (1983); Hutchinson and Suo (1992); Zou (1996).

Zou (1996) conducted some initial analysis of small closed cracks positioned at three different locations within an ice sheet (see Figure 66) and showed that shear cracks and mixed mode cracks are the likely candidates for spall development. The location and orientation of a crack are indicative of the propagation trajectory which will dictate the size and location of critical zones.

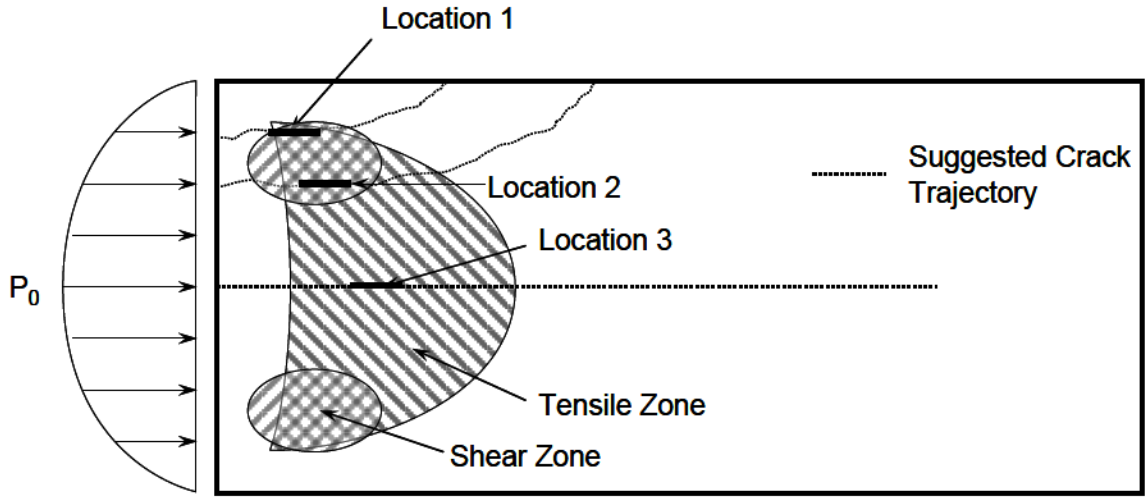

Figure 66 Location of cracks for investigation of propagation and formation of cracks illustrating tensile and shear stress zones (Zou, 1996)

3.4.2.3 Spalling Fracture

To further study local pressure and scale effect, Taylor (2010) conducted an analysis of fracture using a simplified probabilistic model of spalling fracture processes. JOIA MSFIT data were used as a benchmark for model calibration. Variations in crushing force were modeled using a monotonic increasing pressure with failure modeled as an idealized sequence of spalling fracture events.

An elastic finite element stress analysis was carried out to model the distribution of stress within an ice block. A parabolic distribution of force was applied at various locations relative to the centroid and edge of the ice block. A matrix of elemental stresses and volume changes for each loading condition were obtained for input in a probabilistic model. Shear and tensile crack effects were analyzed based on a distribution of flaws in the ice, grain size and the distribution of preprocessed elastic element stresses (see Figure 67). Failure was characterized by unstable crack growth in any element that would result in a spall (spalling fracture).

The power law expression relating failure pressure to ice thickness was determined to be

$$P = 0.15h^{-0.5} \qquad (11)$$

following calibration with benchmark JOIA data.

Taylor further used the PFM to study the influence of ice edge geometry and taper angle on failure pressures. Observations showed that for blunt faces (zero degree taper angle), there is a significant reduction in the pressure coefficient and an increased scale effect (higher absolute exponent) suggesting that blunt faces are more prone to scale effects. The higher the density of flaws, the greater the effect. With increased bluntness, the zone of shear is larger, resulting in more crack propagation and spalling fractures, and the distance a crack needs to extend to reach the free edge is reduced.

For level ice interaction, Taylor's results provide further evidence in support of the scale effects based on the probabilistic nature of crack or flaw density, size and orientation within a specimen and crack instability associated with fracturing materials. The influence of contact geometry and effect on failure stress is also modeled.

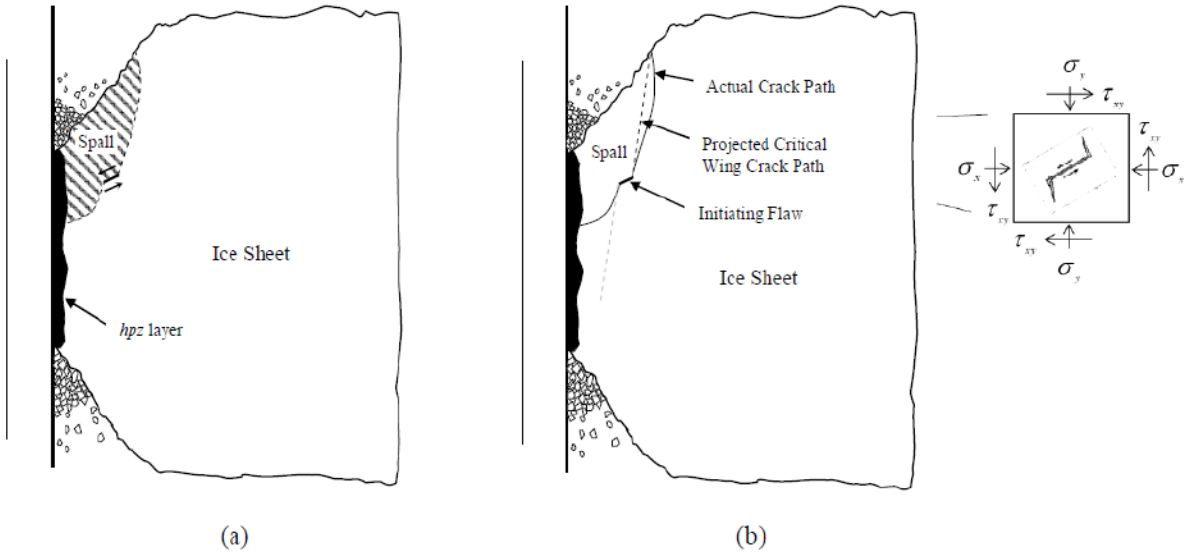

Figure 67 Spalling fracture idealization, showing: (a) shear crack spalling mechanism (; (b) wing crack elemental stress analysis and growth model used to estimate probability of spalling (Xiao, 1997 and Taylor, 2010).

3.4.2.4 Additional Review of Ice Edge Failure Models

Although not directly relevant for this work, for further study on ice edge failure models see:

- Peyton (1966) Matlock *et al.*, (1969, 1971) Eranti (1992) and Withalm and Holfman (2010) for development of a discrete brittle fracture models based on a series of independent cantilever failures;
- Riska and Varsta (1977) for a qualitative description of ship induced shear fracture and flexure failure (or bending fracture);
- Croasdale *et al.*, (1975) and Croasdale (1980) for development of a wedge failure and through-body slip plane failure model based on Tresca failure criteria theorizing the cyclic force time history and illustrating the pressure scale effect;
- Daley (1992) for development of a discrete flaking model where through-body shear failures (i.e. flaking) are based on a Mohr Coulomb failure criterion;
- Timco (1986), Timco and Jordaan (1987) and Sanderson (1988) for a conceptualized model of ice crushing based on the accumulation of damage, pulverization and extrusion of crushed particles;

- Kärnä (1993) who, following level ice indentation tests (Muhonen *et al.*, 1992), developed a hybrid pulverization model that included large shear cracks cleavage cracks following work initially introduced by Saeki and Ozaki (1979).
- Daley *et al.*, (1998) who conceptualized pulverization using four mechanisms: 1) microcracking; 2) flake explosion upon failure and stress release; 3) comminution of flakes created by macrocracks; 4) rapid cascade and coalescence of macrocracks.

Regarding the use of Mohr-Coulomb or similar criteria for ice flaking type failure, Singh *et al.*, (1995) suggested that within the interface layer of crushed ice under high pressures, the friction angle approaches zero, which is not consistent with the Mohr-Coulomb assumptions where higher friction angles drive highest forces. Sammonds and Rist (2000) state that under triaxial stress states, a Mohr-Coulomb criterion does not apply. Further the complex state of stresses across the interaction zone makes it difficult to imagine the formation of thin flakes (Jordaan 2001). While these models may give good approximations for certain conditions, the mechanics of ice failure is idealized.

3.4.2.5 Dimensional Analysis

Palmer and Sanderson (1991) and Palmer and Dempsey, (2007) noted that simple dimensional analysis can account for some of the scale effect independent of any other mechanism. Ice being a brittle fracture material at the high impacts, they suggest that fracture toughness, K_{IC} is the key parameter and assume that it is scale independent.

Assuming interaction of a structure with an ice sheet, the parameters that influence ice force include thickness h, width w, and some material property X, and possible aspect ratio. Force can expressed as $F = w^A h^B X f(w/h)$ from which the laws of similitude define the dimensionless group $\frac{F}{w^A h^B X} = f(w/h)$. Thus X must follow $\left[\frac{ML}{L^A L^B T^2}\right] = \left[\frac{ML^{1-(A+B)}}{T^2}\right]$ using the fundamental dimensions of Mass, Length and Time.

If $A + B = 2$ then X follows $\left[\frac{M}{LT^2}\right]$ which is the dimensional description for strength.

If $A + B = 1.5$ then X follows $\left[\frac{F}{L^{3/2}}\right]=\left[\frac{M}{L^{1/2}T^2}\right]$ with describes fracturing materials and fracture toughness K.

Observations from STRICE data (Kärnä *et al.*, 2006) model ice pressure empirically as $Pc = \gamma C_R h^{-0.5}\left(\frac{w}{h}\right)^{-0.16}$ where γ is a constant, C_R is a regional material constant (ISO 2011). Following this model, the dimensional description of C_R is $\left[\frac{M}{L^{1/2}T^2}\right]$ which is the dimensional form for fracture toughness.

If we assume that force on a structure is a function of contact area A and fracture toughness K, we can define a dimensionless group

$$\frac{F}{A^{3/4}K_{IC}} = c \qquad (12)$$

Schulson and Duval (2009) note that assuming this group to have a constant value c and assuming geometrically similar scenarios, it follows that F is proportional to $A^{3/4}$ and force/unit area (F/A) is proportional to $A^{-1/4}$. Comparing with data in Figure 24 and **Error! Reference source not found.**, this would represent the maximum value of a scaling exponent (or minimum absolute value) more applicable to larger contact areas. Palmer *et al.*, (2009) notes that dimensional analysis does not explain the full scale effect but that simple models of indentation cracking and spalling in brittle materials also contribute, referencing the work of (Evans, 1978; Thouless *et al.*,1987; Chai and Lawn, 2006).

3.4.2.6 Geometric Analysis

Schulson and Duval (2009) point to a simple geometric analysis based on Griffith's (1921) theory of brittle failure where the critical stress for crack propagation under constant loading is

$$\sigma_P = \left(\frac{2E\gamma_S}{\pi c}\right)^{1/2} \qquad (13)$$

where E is the modulus, γ_S is the surface energy per unit area and $2c$ is the crack length. It follows that critical stress is inversely proportional to the square root of the largest size flaw within a contact zone and decreases with increasing crack length. If then the crack length c is proportional to the width W of the contact zone ($c \propto W$) and contact area $A = Wh$ (h being thickness) from which $W = A/h$, then it follows that $P \propto A^{-1/2}$.

While a scale effect is illustrated, as Sanderson 1988 discusses, it is rather artificial to assume that an ice field against a 100 m diameter structure necessarily contains a flaw 1 m long if a 1 m specimen contains a flaw 1 cm in length. The random occurrence of flaws having random lengths within a reference volume of ice is more reasonable as the Weibull theory illustrates below.

3.4.2.7 Weibull Theory

Weibull (1951) theory for brittle failure assumes that within a volume of ice exists a population of cracks distributed throughout the body having a distribution of sizes (Sanderson, 1988). The statistical occurrence of cracks was also modeled by Maes (1984). The overall strength of the material is then governed by the strength of the element containing the most dangerous largest flaw. The larger the body, the greater the probability for a larger flaw to exist that reduces the strength of the material.

The probability of failure is modeled as

$$P_f = 1 - \exp\left\{\left(-\frac{V}{V_0}\right)\left(\frac{\sigma}{\sigma_0}\right)^b\right\} \qquad (14)$$

where V is the volume, V_0 is a reference volume, σ and σ_0 represent the applied stress and reference stress respectively, and b is the Weibull modulus. If strength scales according to $\sigma \sim V^{-1/b}$ and since $V \sim A^{3/2,}$ then indentation pressure can be assumed to be $P \sim A^{-3/2b}$. Sanderson (1988) assumes that a reasonable value for the Weibull modulus is $b = 3$ resulting in $P \sim A^{-1/2}$. Schulson and Duval (2009) question the references for $b = 3$ and recommend a modulus value by Kuehn *et al.*, (1993) derived directly from brittle compressive strength tests on unconfined ice cubes having different sizes ($10^3 \text{mm}^3 \leq V \leq 10^6 \text{mm}^3$). In this case, b was estimated to be 5.5 ± 0.8 resulting in $P \sim A^{-0.27 \pm 0.04}$. Again, given the natural processes

in the formation of ice including deformation processes (i.e. MY ice), it is reasonable that cracks of varying sizes are randomly distributed throughout a body and that scale effect exists.

3.4.2.8 Statistical LEFM Hot Spot Analysis

Palmer *et al.*, (2009) using Linear Elastic Fracture Mechanics (LEFM) model the occurrence of *HPZ* and the corresponding scale effect in an attempt to explain the scale effect of $P \propto A^{-0.7}$ for contact areas less than 10 m^2 (as observed in the data shown in **Error! Reference source not found.**). They assume that the *HPZ* force is governed by the location of the *HPZ* relative to the edge of the zonal contact area, and critical forces limited by this limiting crack length, and the area corresponding to the *HPZ* (area *D* or *M*) is different and smaller than the area *S* in Figure 68.

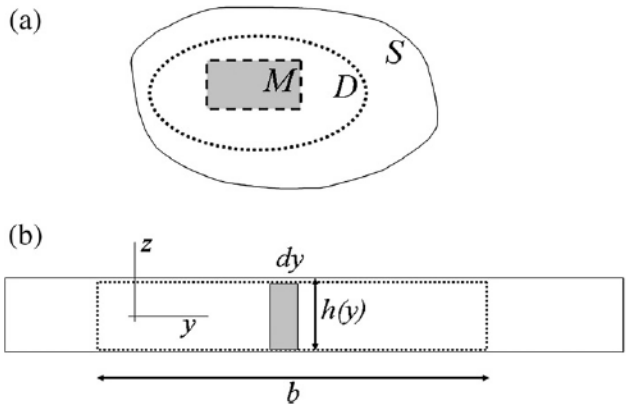

Figure 68 Contact between vertical sided structure and broad ice sheet.

Referencing Figure 69, the model randomly positions the center of the *HPZ* within a particular area noted *S* according to $x/l = -1/2 + R_1$ and $y/l = -1/2 + R_2$, where R_1 and R_2 are random numbers on the interval [0,1]. The limiting critical crack length (minimum) from the center of the *HPZ* to the nearest edge of the area *S* that causes a spall to occur is given as $l \min(R_1, 1 - R_1, R_2, 1 - R_2)$.

Therefore the limiting force using LEFM and assuming fracture toughness is a constant based on $F/l^{3/2}$ (Chai and Lawn, 2006) is

$$F = \alpha K_Q \left[l \min(R_1, 1 - R_1, R_2, 1 - R_2) \right]^{3/2} \quad (15)$$

where α is a dimensionless multiplier.

To determine an associated *HPZ* pressure, a contact area is required. Palmer *et al.*, (2009) suggest that this area too is random but limited by the distance from the *HPZ* center to the edge of the reference area *S*. Based on a new random number R_3, between [0,1], the *HPZ* area can be defined as

$$A = R_3 \left[l \min(R_1, 1 - R_1, R_2, 1 - R_2) \right]^2 \quad (16)$$

and corresponding force/unit area (i.e. pressure) is given as

$$\begin{aligned} F / A &= \frac{\alpha K_Q \left[l \min(R_1, 1 - R_1, R_2, 1 - R_2) \right]^{3/2}}{R_3 \left[l \min(R_1, 1 - R_1, R_2, 1 - R_2) \right]^2} \\ &= \alpha K_Q \frac{1}{R_3 \left[l \min(R_1, 1 - R_1, R_2, 1 - R_2) \right]^{1/2}} \end{aligned} \quad (17)$$

Normalizing F/A with αK_Q and $l^{-1/2}$ gives

$$\frac{F / A}{\alpha K_Q l^{-1/2}} = \frac{1}{R_3 \left[\min(R_1, 1 - R_1, R_2, 1 - R_2) \right]^{1/2}} \quad (18)$$

which when plotted against normalized area A/l^2 for a simulation of *n* values for R_1, R_2, R_3 gives the density plot shown in Figure 70. Palmer *et al.*, (2009) note that the scale effect represented by $(A/l^2)^{-0.8}$ has a striking resemblance to the observed scale effect in the data (see Figure 21.). Expected scatter in predicted pressure-area results is bounded by two limits. Firstly, the maximum force per unit area (i.e. pressure) corresponds to a simulated *HPZ* in the center of the square of dimension *l* (greatest distance *d* to the edge), having the smallest simulated *HPZ* area. The minimum pressure is represented by an *HPZ* having smallest distance *d* to the edge of area *S* with the maximum *HPZ* area that fits within the zonal area *S*. For the later case, area is given as d^2 which results in pressure scaled according to $A^{-1/4}$. This represents the lower boundary scale effect in Figure 70.

Predictions show some agreement with measured data in particular the observed scale effect illustrating the importance of random processes in modeling ice failure mechanics. While

the model is highly idealized (e.g. The random position of an *HPZ* within a large square is not consistent with field observation of *HPZ*s nearer the center), assumptions regarding a single *HPZ* dominating each event and use of edge spalling work by Chai and Lawn (2006) where force is proportional to the distance to an edge (i.e. $F \propto l^{3/2}$) is reasonable.

The work doesn't to consider other mechanical and probabilistic failure theories. The mechanical and material processes associated with the birth and death of *HPZ*s and microstructural influences are not discussed. Also, the random occurrence of flaws within an ice lattice is consistent with other geophysical materials which dictate that probabilistic failure theories such the Weibull theory discussed above be considered. With regard to local pressure design, Palmer *et al.*, (2009) recommend a revised equation that doesn't include influence of exposure (i.e. number of annual interaction events) on design pressure, suggesting that a constant reference pressure (i.e. 7.4 MPa in the equation $P = 7.4A^{-0.7}$) be used. For certain applications with a large number of interactions (e.g. ice management icebreaker in MY conditions), this reference pressure could be considerably higher.

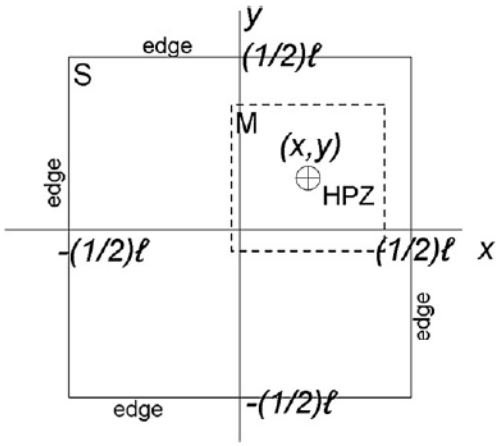

Figure 69 Square block of elastic brittle material with one *HPZ* (Palmer *et al.*, 2009).

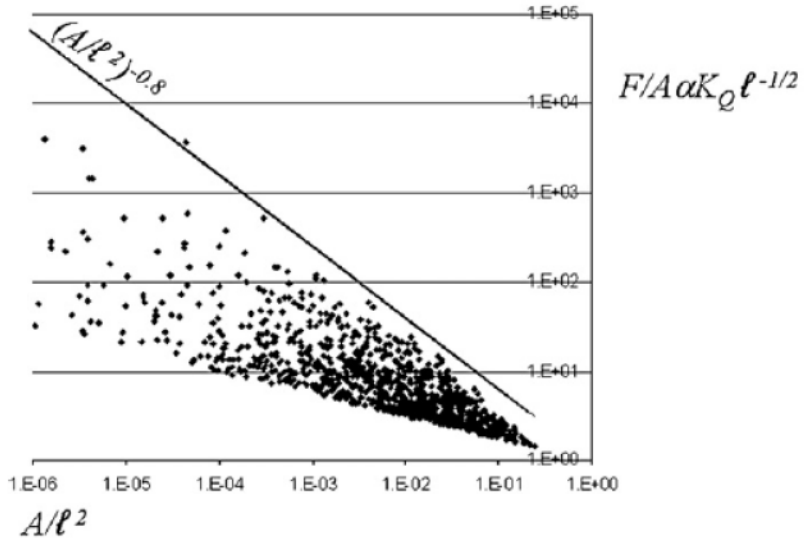

Figure 70 Estimated pressure-area relationship from simple hot spot model (Palmer *et al.*, 2009).

3.4.2.9 Fractals

Fractal models have been proposed to explain the scale effect in ice strength starting with modeling the distribution of ice fragments that occur as ice is broken or crushed (Palmer and Sanderson, 1991, Parsons, 1991a,b, Weiss, 2001, Xu *et al.*, 2004). Fractals are typically referenced as self-similar patterns being the same or nearly the same at different scales. This means that the number of fragments having dimensions greater that say L, is proportional to L^{-D} (Turcotte, 1986). Fractal dimensions D vary from 1.7 to 2.8 with 2.5 being a reasonable value for many applications: For ice floe sizes from aerial photographs and satellite imagery, see Rothrock and Thorndike (1984), Kergomard (1989), Lensu (1990), Dowdeswell and Forsberg, (1992), Crocker (1993), Løset and Carstens (1996); for ice fragments from experiments, see Timco and Jordaan (1987), Savage *et al.*, (2000), Frederking *et al.*, (1990), Cammaert and Crocker (1991), Tuhkuri (1994), Weiss and Gay (1998).

In fractal modeling, a fragment breaks from a parent ice and may then fracture into two or three second generation fragments; of which one of the second generation fragments further fractures into two or three third generation fragments (Turcotte, 1986; Palmer and Sanderson, 1991). The number of next generation fragments is modeled as a probability of next generation fragment forming. The process may continue for n generations until some

order r of the fractal process is reached resulting in a fragment size distribution that is ultimately cleared away from the crushed zone (Palmer and Sanderson, 1991).

Bhat (1990) initially proposed a 2D surface effects model that was later extended by Palmer and Sanderson (1991) to a 3D model as illustrated in Figure 71. Palmer and Sanderson (1991) model forces as a hierarchy of splitting events where the force required to split a fragment is related to the fragment size d and fracture toughness given $\alpha K_{IC} \times d^{-1/2}$ where α is a constant.

Referencing ice failure, force/unit area scale effects in the literature range from $A^{-1/4}$ (Palmer and Sanderson, 1991; Xu *et al.*, 2004) to $A^{-0.8}$ (Parsons, 1991a, 1991b), which Weiss (2001) suggests is too high. Comparison of models with full scale data is illustrated in Figure 72.

While fractal modeling demonstrates a size and scale effect for brittle materials, it is an idealized mathematical model which does not consider mechanics of the interaction. There is also considerably variability on the extent of scale that is not yet justified. Also, the influence of confinement and distribution of pressures from the center of the contact zone to the free surface is not considered.

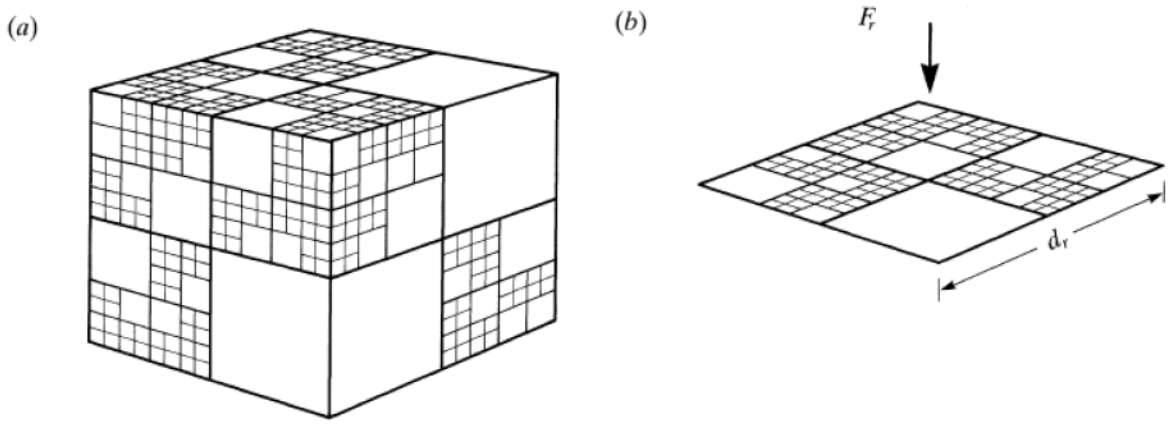

Figure 71 Illustration of fractal crushing of a brittle solid having an order r =4 and where each cubic element fragment has a probability p of being crushed into n sub elements (here p = 0.75 and n = 8). Total force F_r is carried by a fractal hierarchy of elements of dimension d_r or less (Palmer and Sanderson, 1991 after Turcotte, 1986))

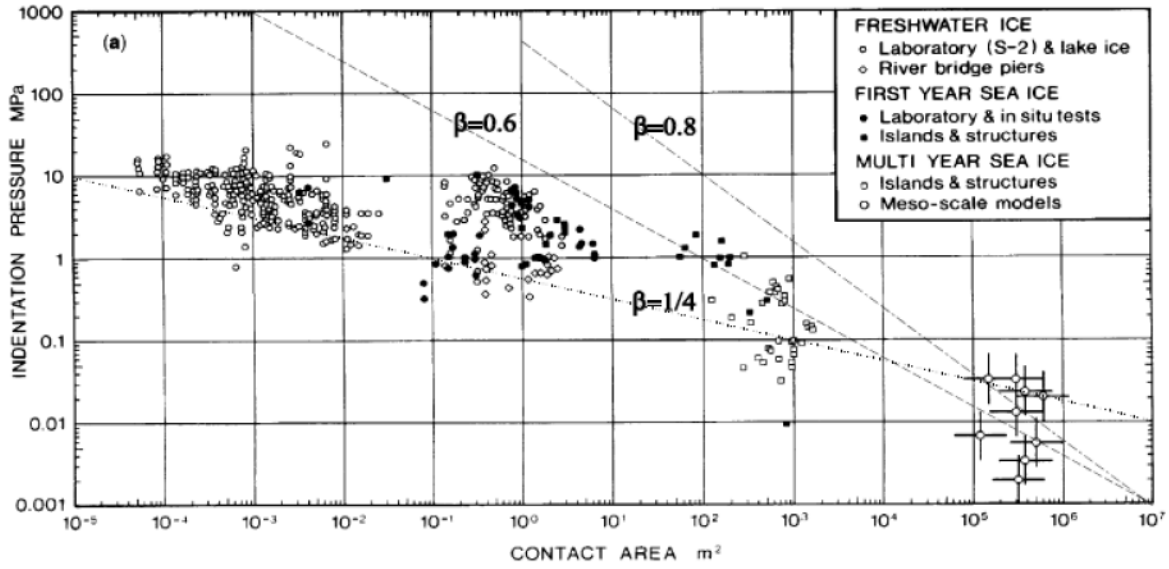

Figure 72 Comparison of ice strength data (Sanderson, 1988) with fractal models by Palmer and Sanderson, 1991 ($\beta = 0.25$), Parsons, 1991 ($\beta = 0.8$) and Weiss, 2001 ($\beta = 0.6$) – figure from Weiss (2001).

3.3 Summary

Ice under the loading rates of interests behaves a brittle fracturing material which theoretically exhibits scale effect. The compilation of pressure-area data by Sanderson (1988) and Masterson *et al.*, (2007), as well as many additional small scale experiments and theoretical applications provide strong evidence. Both data and numerical models demonstrate scale effect, although uncertainty exists. The scale effect on local pressures has been modeled to be as high as $P \propto A^{-0.8}$ with strong evidence that $P \propto A^{-0.7}$. For global processes, the scale effect has been suggested to be as low as $P \propto A^{-0.25}$ but $P \propto A^{-0.4}$ seems most reasonable. What has not been quantified is the linkage between local and global failure processes and scale effect. It is intuitive that stronger scale effect exists for local pressures within global interaction areas since confinement could well suppress damage and increase failure strength, but microstructural changes limit *HPZ* force and confinement.

Since one link between both scales is that the sum of *n HPZ* forces equates to the total global force on the structure, understanding the global *HPZ* density will prove very useful in further understanding scale effects at both scales.

CHAPTER 4. Global Ship Ram Simulation and Local *HPZ* Model – Baseline Models for Present Research

4.1 Background

Whether an icebreaking vessel transects a region having some occurrence of multi-year ice, or whether an icebreaker is required to repeatedly ram ice to transect a challenging region, design requires two considerations: 1) Peak global force and contact area for hull girder design – typically corresponds to the end of a ram, 2) peak local pressures on small local panels of hull plating between frames for plating design – may occur at any location across the interaction face and at any point through the ram process, although more likely near the center of the global contact area near the end of the ram.

As first illustrated in Section 2.2, Section 3.1 and Section 3.2.2, the failure process results in localization of contact points within the global area having very high pressures called *HPZ*s. The large majority of force transmitted into the hull occurs through the localized *HPZ*s, on the order of 95% according to Johnston *et al.*, (1998). The remaining background pressure results from extrusion of crushed ice pieces.

The following sections review two numerical models for ice forces during ship rams. The first is a global ship ram model where global forces are associated with the nominal contact area, the imprint of the bow into the ice feature without consideration for spalling. Extremal design using a 'parent' distribution of modeled impact forces is discussed. The second is local pressure modeling, the simulation of local *HPZ* occurrence, forces, density and force/unit area (pressure) on specific local parts of the hull or design panels. Both models have been calibrated with full scale data and form the fundamental basis for modeling the larger interaction and intermediate zones of contact. A fundamental principle is that with

increased impact energy, greater penetrations will coincide with the development of larger global contact areas. The greater the contact area, the greater the number of local contact *HPZ*s through which the impact force is transferred into the hull. The greater the number of *HPZ*s, the greater the probability that an *HPZ* with an even greater local pressure will form.

4.2 Modeling Global Forces, Hull Response and Nominal Contact Area from Ship Rams

4.2.1 Overview

A number of ship ramming trials were carried out in an attempt to understand the development of ice forces on the bow as a function of vessel displacement and collision speed. The interaction geometry and response of the vessel to impact force at the bow is illustrated in Figure 73. Several stages of progression of a ship ram based on field observations are illustrated in Figure 74 (Dome, 1982). The stages are characterized according to ship speed (plotted as absolute values), global interaction area and global bow force. The key stages include approach, impact phase, penetration and slide-up, ice skeg impact and penetration, and slide-off.

Ice crushing is most significant during the impact phase until the vessel starts to slide up (slide-up may be limited by an ice skeg). The impact phase may last from slightly less than a second for small vessels to a few seconds for larger vessels.

An example of measured bow force against ship speed for full scale *Oden* and *Polar Sea* trials is illustrated in Figure 75 (see also Figure 29). It is evident that there is significant variability in impact forces for any ship speed making the derivation of a deterministic relationship uncertain. A reasonable approach is to model explicitly the variability by ranking the data and modeling a distribution as illustrated in Figure 75. While a good relationship is illustrated, this is based on *measured* data for a *specific* vessel and has limited usage for design of new vessels unless they are similar designs.

Traditional methods in design codes often use deterministic empirical equations to estimate maximum bow force. The recommended relationship for maximum bow force in the former ASPPR (1995) rules based on power P and displacement D is given as

$$F_{MAX} = a_{new} \cdot D^{b_{new}} \left(1 + \left(\frac{P}{D^{2/3}} \right)^{1/3} \right) \qquad (19)$$

where a_{new} = 4.4 and b_{new} = 0.7. Note that the original equation before the Carter et al., (1996) reviews was based on a_{old} = 2.6 and b_{old} = 0.9 (i.e. F_{MAX} is proportional to 2.6 $D^{0.9}$ (See Figure 91))

Some traditional design methods calculate the maximum bow force for the most extreme ice loading condition (the highest class vessel, capable of unrestricted year round operations) and then scale for lower classes according to the following factors (ASPPR 1995).

CAC1	1.0
CAC2	0.8
CAC3	0.6
CAC4	0.4

The more recent IACS Polar Class (IACS, 2011) rules specify class factors (e.g. PC 1 through PC7) based on limiting ice pressure, ship speed, ice thickness and ice type (MY vs. different stages of first year). Maximum bow force is then calculated as

$$F_{MAX} = fa \cdot CF_C \cdot D^{0.64} \qquad (20)$$

where fa is a coefficient based on bow shape, and CF_C is a Class Factor for crushing based on some representative ice strength P_0 and impact speed Vs.

Traditional approaches being deterministic do not consider variability as noted in Figure 29 and Figure 75. A distribution for maximum force as in Figure 5 is desirable whether measured or simulated.

Carter *et al.*, (1996) developed a time based probabilistic simulation model of a vessel ramming large MY ice floes as shown in Figure 73 (See also Fuglem *et al.* 1999). The resultant software termed "F_{MAX} "was designed to:

- estimate bow forces for ship rams based on impact conditions (i.e. vessel mass and speed), ice characteristics (i.e. floe thickness and strength) and ice failure modes (i.e. crushing and flexure);
- develop a single event 'parent' distribution of maximum bow force F_{MAX} for any vessel design based on impact speed, ice conditions and ice failure strength; and
- Estimate extremal design forces based on the maximum of n rams per year

Details of the Fmax software, including a description of interaction geometry, area given in Appendix A.

Based on the extremal force distribution and design strategy as discussed in Section 2.1, reliability based design forces could be estimated. Global forces are needed for hull bending calculations and girder design. Also, penetration and impact duration could be estimated to model exposure which is needed for local pressure and plating design.

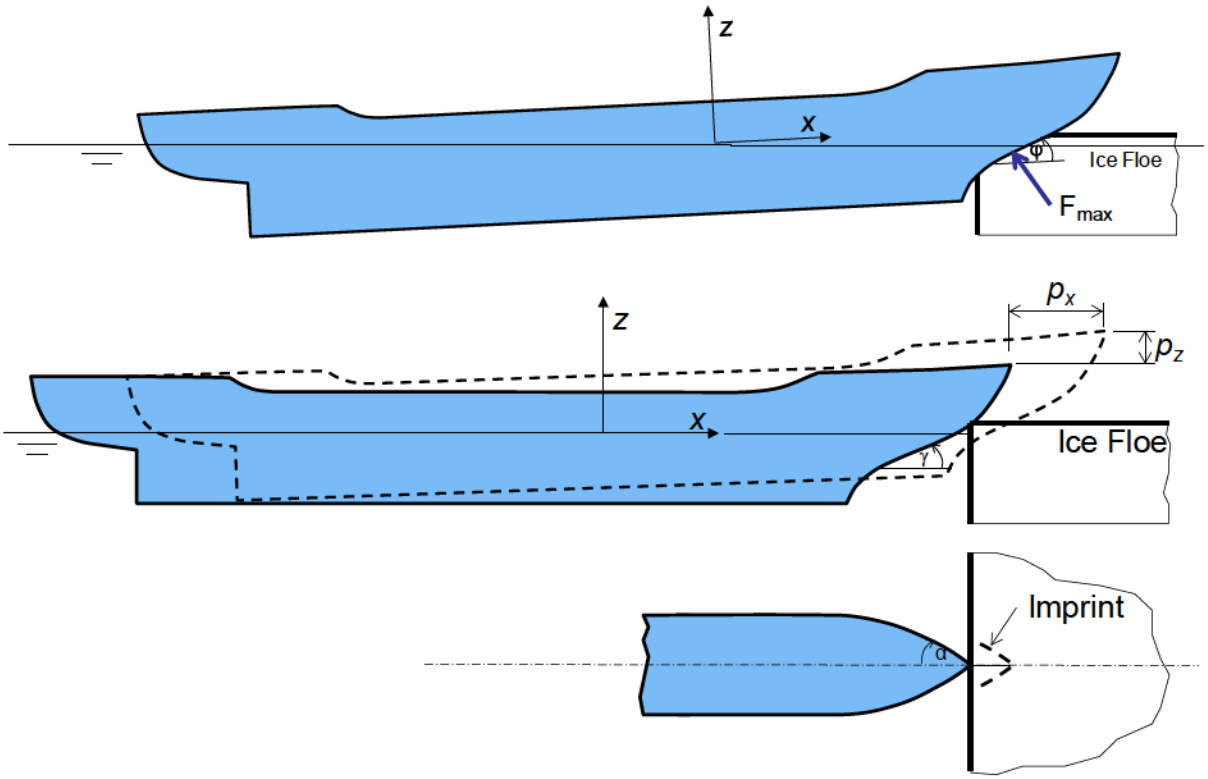

Figure 73 Illustration of global interaction force, F_{MAX} during a ram event and response of vessel

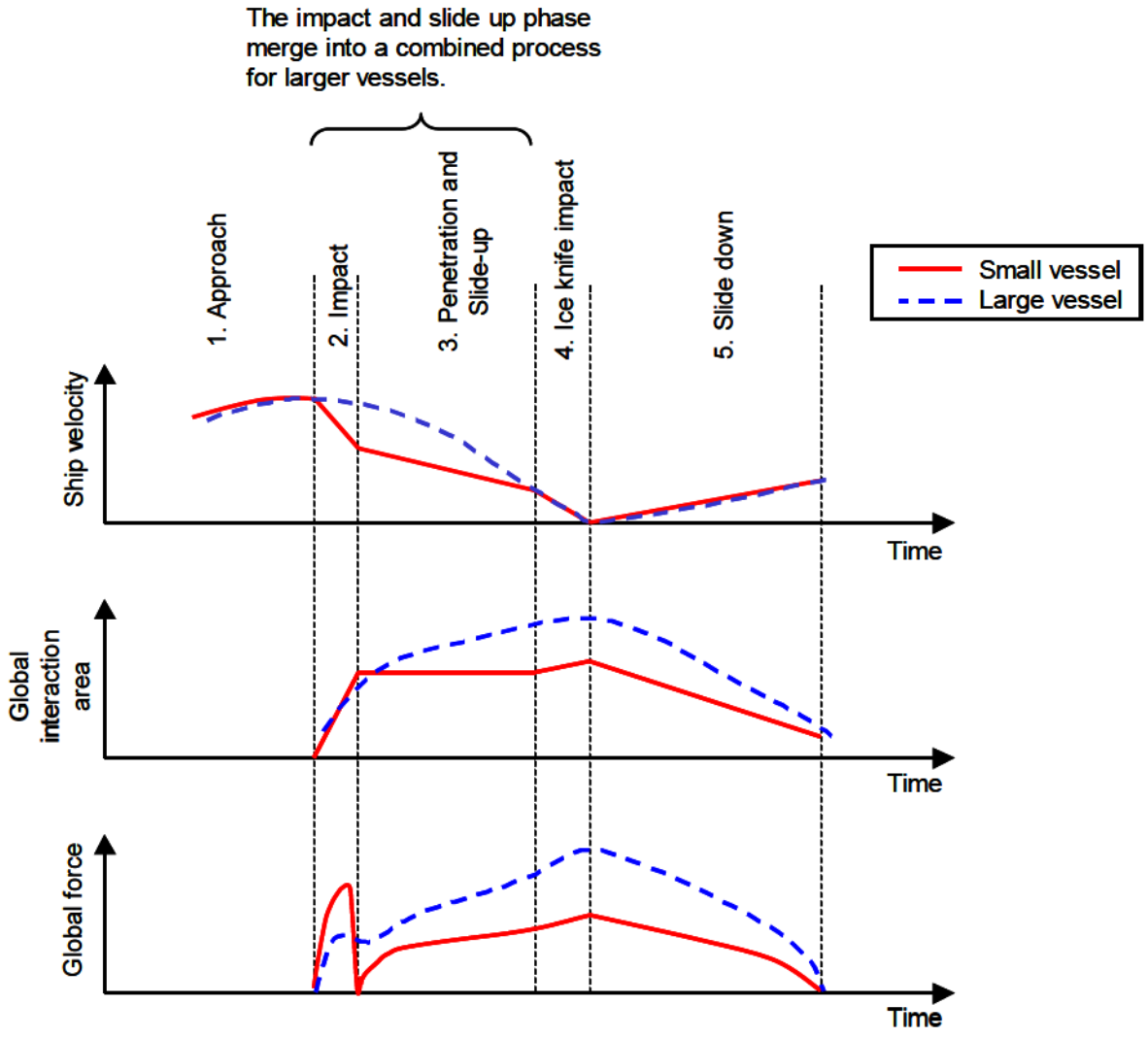

Figure 74 Illustration of different interaction stages as a ship rams progresses (Jordaan *et al.*, 2007)

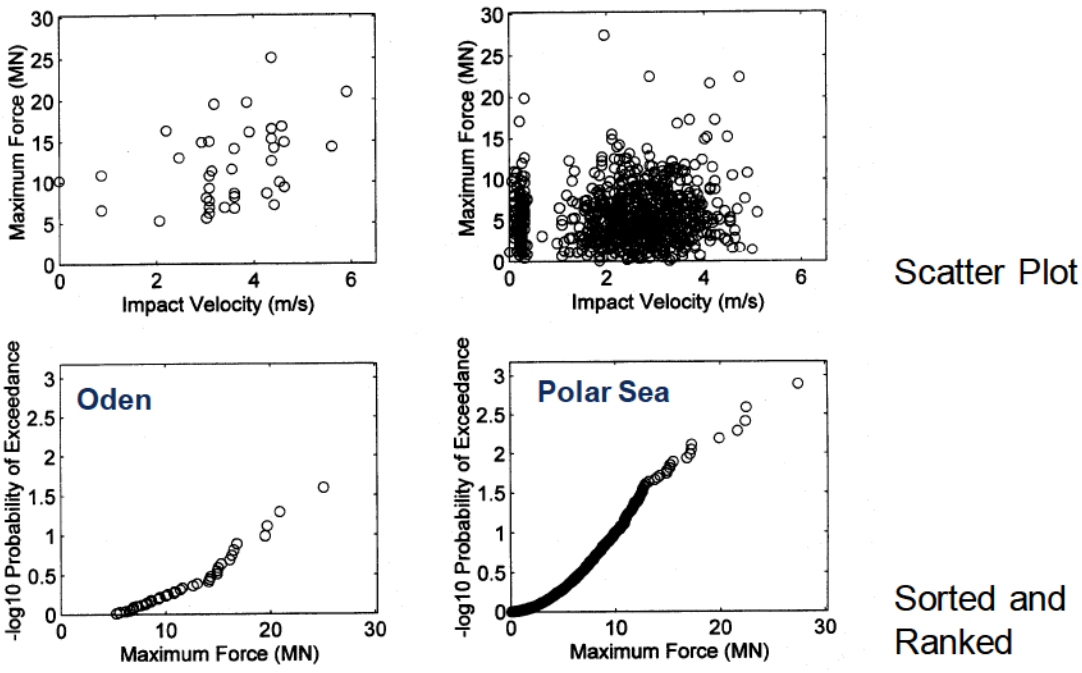

Figure 75 Scatter plots vs. sorted and ranked force data for *Oden* and *Polar Sea* trials (Fuglem *et al.* 1999)

4.2.2 Vessel - Ice Interaction

The program F_{MAX} was used to model vessel response to developing bow forces using an idealized bow geometry as illustrated in Figure 22 and considered friction forces, ice skeg interaction, modal hull response and damping, as well as limits on contact area development. Limiting loads based on flexural failure and floe tipping was also incorporated. A damaged soft layer of ice was modeled during the beach phase to prevent the simulation of unrealistic vessel motions and loads. A detailed description of the model is included in Appendix A.

Ice failure strength was modeled using a random pressure-area relationship given as

$$P = CpA^{-Dp}$$

where the random parameters *Cp* and *Dp* are discussed in Section 2.3.2.

The final equations of motion for both surge and heave/pitch motion (assuming concentric head-on hits) for individual rams are:

$$\ddot{x} = \frac{\left(-k_x x - c_x \dot{x}\right) - F_H}{M_x}$$
$$\ddot{y} = \frac{\left(-k_y y - c_y \dot{y}\right) + F_V}{M_y} \quad (21)$$

where F_H and F_V are the horizontal and vertical components of ice crushing force (See Figure 73) , k_x and k_y are the horizontal and vertical spring constants, and c_x and c_y are the horizontal and vertical damping coefficients. Time is set as zero at first contact. As the interaction progresses, the bow accelerates upward due to heave and pitch, while the horizontal motion decelerates as crushing and inertial forces erode the initial kinetic energy, slowing the vessel to a stop at some point in time. As the vertical velocity increases, the rate of penetration decreases. When the direction of motion approaches the stem angle, penetration approaches zero and the force approaches the static beach load.

4.2.3 Model Validation and Simulation Results

The F_{MAX} model was validated by comparing simulations with full scale measurements. Figure 76 and Figure 77 illustrates time traces of measured vertical bow forces during *Kigoriak* October 1981 impacts and the *MV Arctic* 1984 impact trials (Carter *el al.*, 1996). The *Kigoriak* is a 6400 tonne icebreaker while the *MV Arctic* is a 39,000 tonne OBO carrier. One observation with *Kigoriak* measurements is the unique initial impact phase followed by loss of contact, rebound, multiple impacts (in some cases), slide-up and slide-down (Dome 1984). Multiple impacts are less likely with larger vessels which have a longer initial impact duration.

Figure 78 and Figure 87 shows the results of a time based simulation of *Kigoriak* and *MV Arctic* ramming with a MY floe having a thickness of 10 m, using the random pressure model $P = 3.0 \pm 1.5\ A^{-0.4 \pm 0.2}$. Simulation results are consistent with measured data, capturing the initial impact phase before slide-up. Multiple impacts are also noted. The F_{MAX} software was shown to satisfactorily model ship ram processes, particularly maximum bow forces.

A second validation exercise by (Carter *el al.*, 1996) compared disributions of simulated global impact forces with measured forces. Figure 80, Figure 81, and Figure 82 illustrate comparisons for *Kigoriak* (1981), *MV Arctic* (1984) and *Oden* (1991) trials demonstrating again the reasonable performance of the F_{MAX} simulation model.

4.2.4 Simulation Results

To illustrate a design scenario, the MV *Arctic*, a CAC 4 type vessel was selected for analysis. Experience suggests exposure capability consistent with approximately 10 - 15 rams per year (Carter et al, 1996). Global forces have been measured from *MV Arctic* trials as illustrated in Figure 5. Modeling parameters including vessel size, speed ice thickness and strength are listed in Table 3 below.

Of particular interest are the initial crushing phase and corresponding force, area and duration. As illustrated in Figure 74 this phase is clearly defined for small vessels but less pronounced for larger vessels. As illustrated Figure 83, Figure 84, and Figure 85 (select rams for the MV *Arctic* CAC4 for different vessel speeds, ice thickness and strength), this initial phase can be identified by: 1) a sudden drop in vertical bow force (i.e. lift off); and/or 2) where vertical bow acceleration is zero.

An estimated distribution of vertical bow force for the MV *Arctic* ramming events is illustrated in Figure 86 based on 200,000 ram realizations. Corresponding distributions for contact area and duration are illustrated in Figure 87 and Figure 88. The first hump in ram duration plots in Figure 88 represents scenarios where the initial impact crushing phase of the ship ram is clearly defined before ride-up occurs as illustrated in Figure 74 – first peak clearly defined in Figure 83 and Figure 84. The duration on average is less than 4 seconds for MV *Arctic*, CAC 4 type vessel impact conditions. The second hump in the duration plot captures ~10% of impact scenarios (except for several extremes) having only a single force hump for the entire duration (i.e. no subsequent peak forces). For these scenarios the simulated conditions represent soft ice allowing continuous crushing for the entire duration.

The mean vertical contact area and duration is 26 m^2 and 3.8 seconds respectively. Based on the idealized bow shape modeled, the nominal contact area based on geometry of bow is

given as $Av/cos\gamma$, γ being the stem angle of = 30°. The corresponding exposed nominal contact area is 30m^2. These are the parameters used to determine exposure for modeling local pressures.

It is noted that distributions for vertical force, contact area and duration in Figure 86, Figure 87 and Figure 88 contain extreme realizations; some possibly unrealistic. A detailed examination of practical limits imposed on input distributions has not been carried out for this work, but should be considered as a follow-on to this research.

Table 3 Input parameters for global force simulation

Parameter	**Value**
Vessel & type	MV Arctic - OBO (Ore, bulk, Oil)
Displacement, Length, Breadth, Draft	39,000 tonnes, 196.6 m, 22.9 m, 11 m
Vessel Class, Number of rams/year	CAC4, 10
Operating speed parameters (mean, stddev, Distribution)	5 knots (2.57 m/s), 1 knot (0.51 m/s), Beta
Ice thickness parameters (mean, stddev, Distribution)	3.89m, 1.58m, Gamma
Ice crushing pressure	$P = CpA^{-Dp}$
*C*p ice crushing parameter (mean, stddev, Distribution)	(3.0 ±1.5, Lognormal)
Dp ice crushing parameter (mean, stddev, Distribution)	(0.4, ±0.2, Normal)

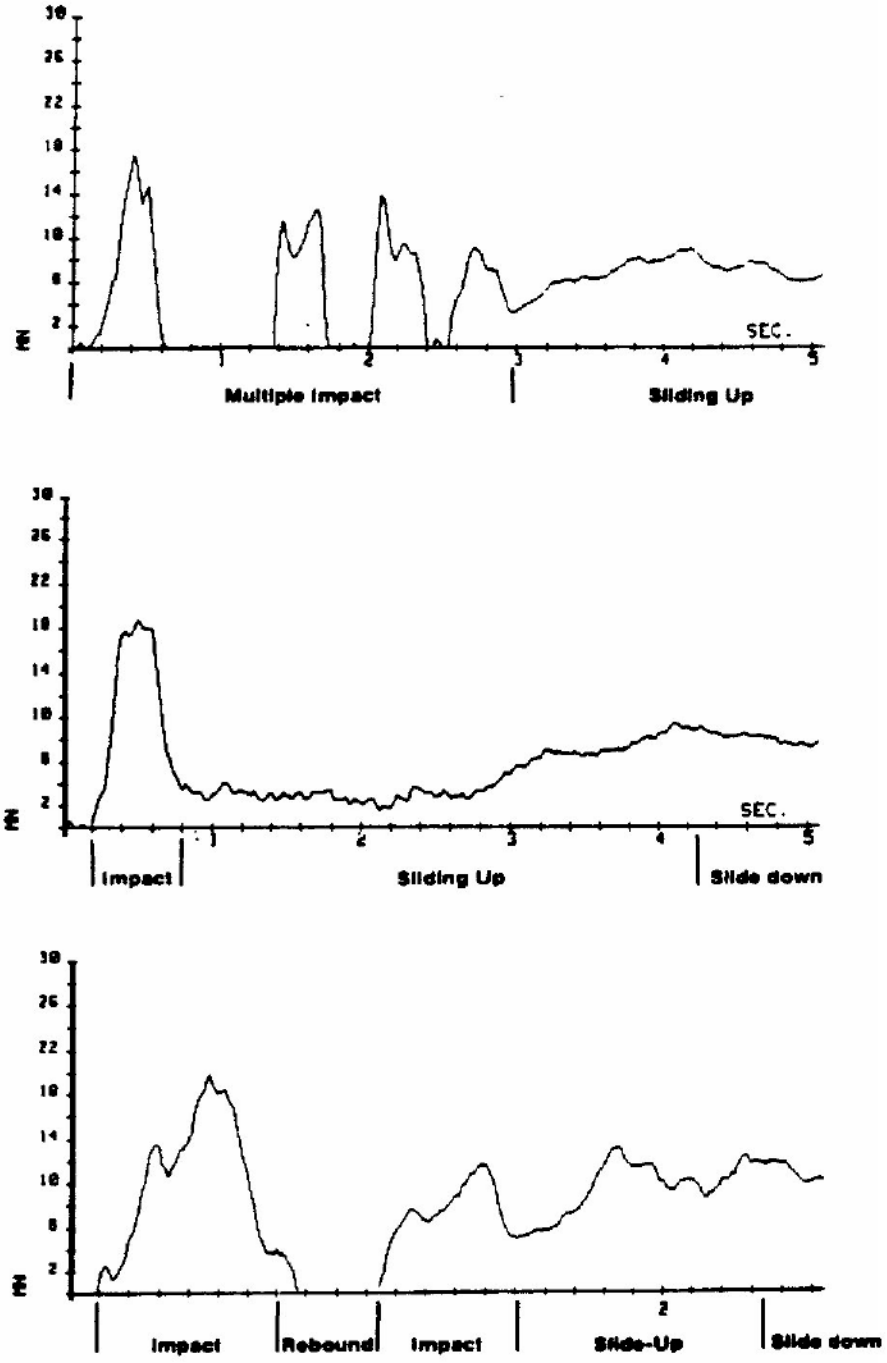

Figure 76 Example time trace for vertical bow force from *Kigoriak,* October 1981 trials (Carter *et al.*, 1996) – note force is in MN.

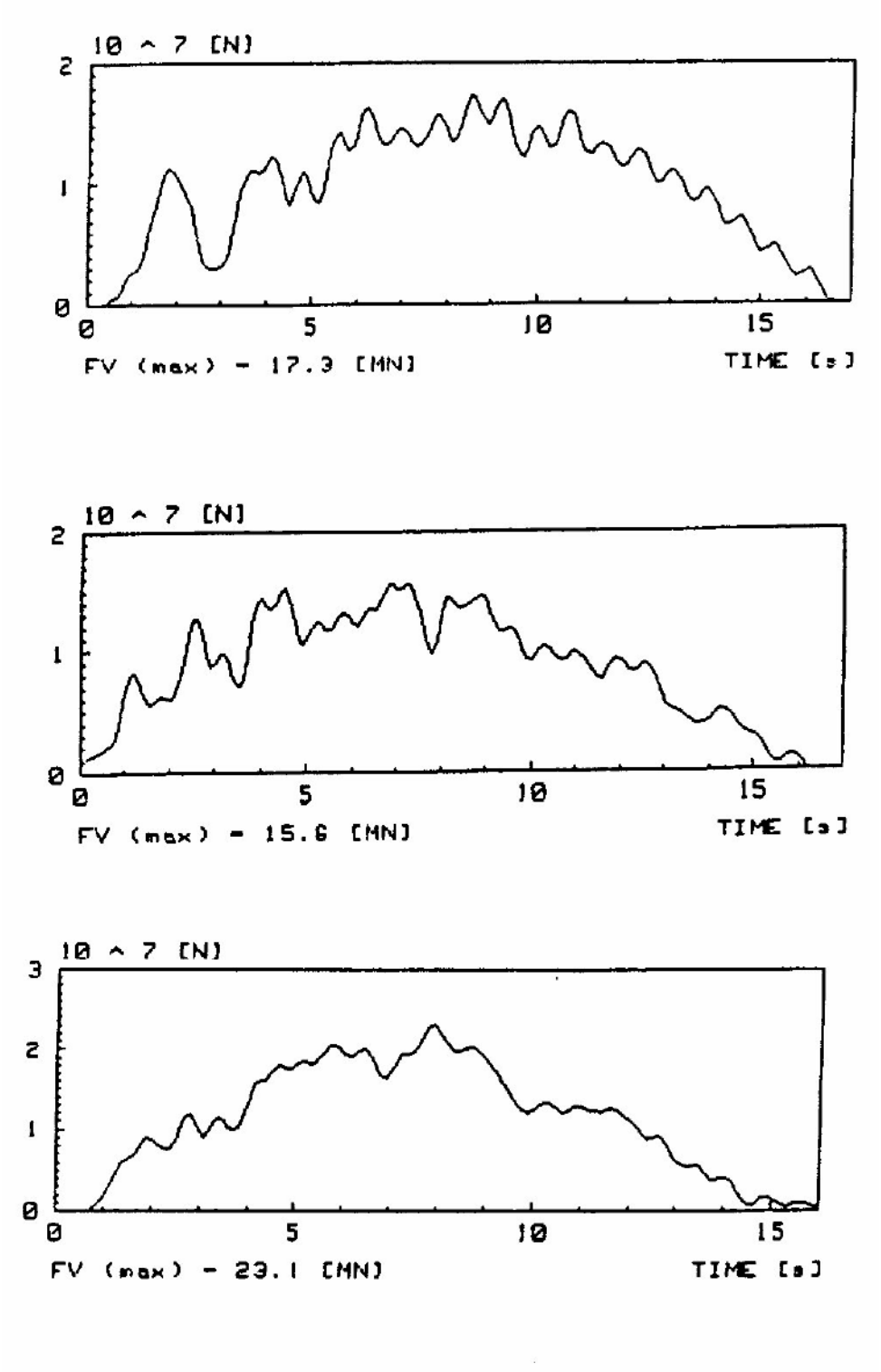

Figure 77 Example time trace for vertical bow force from *MV Arctic* 1984 trials (Carter et al., 1996)

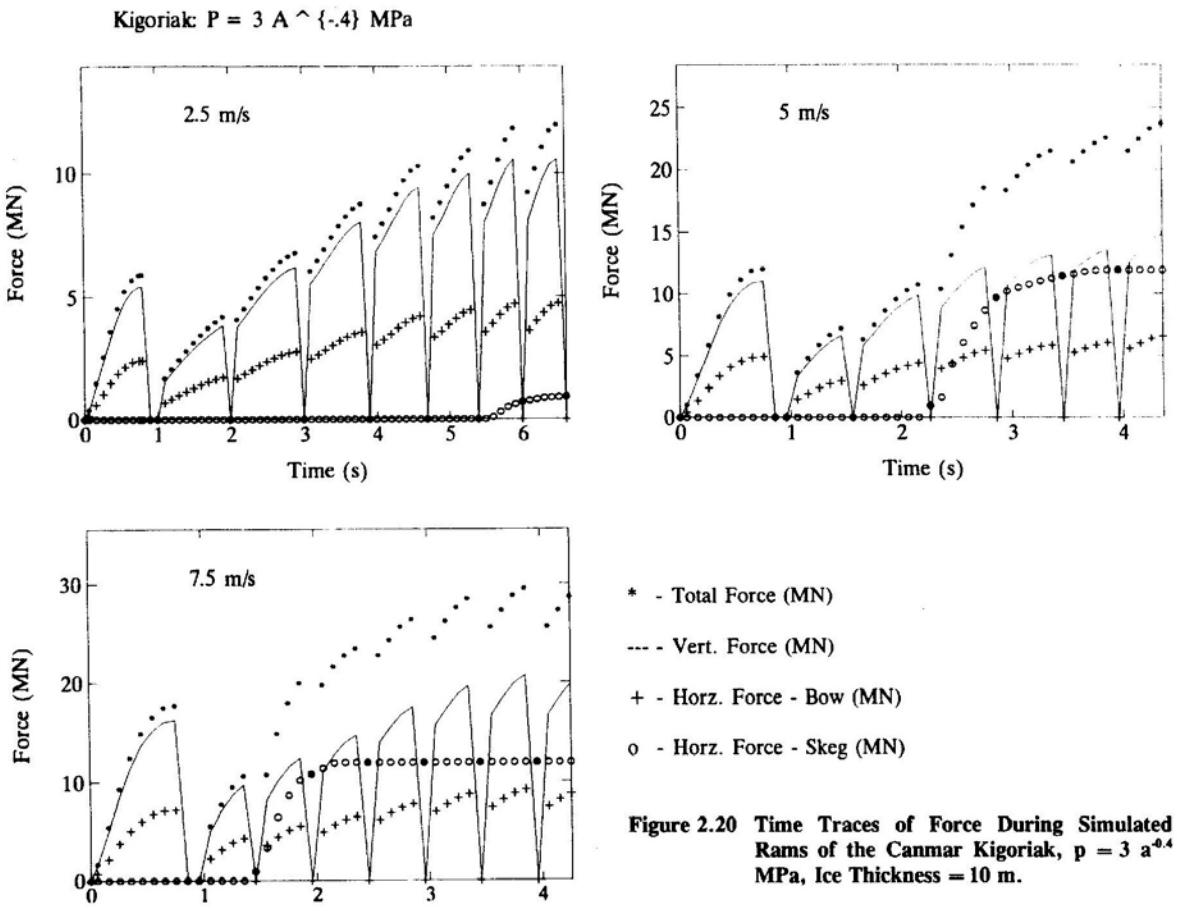

Figure 2.20 Time Traces of Force During Simulated Rams of the Canmar Kigoriak, p = 3 a$^{-0.4}$ MPa, Ice Thickness = 10 m.

Figure 78 Simulation of time dependent force from *Kigoriak* ram with 10m thick MY ice having pressure-area relationship $P = 3.0\ A^{-0.4}$ (Carter *et al.*, 1996)

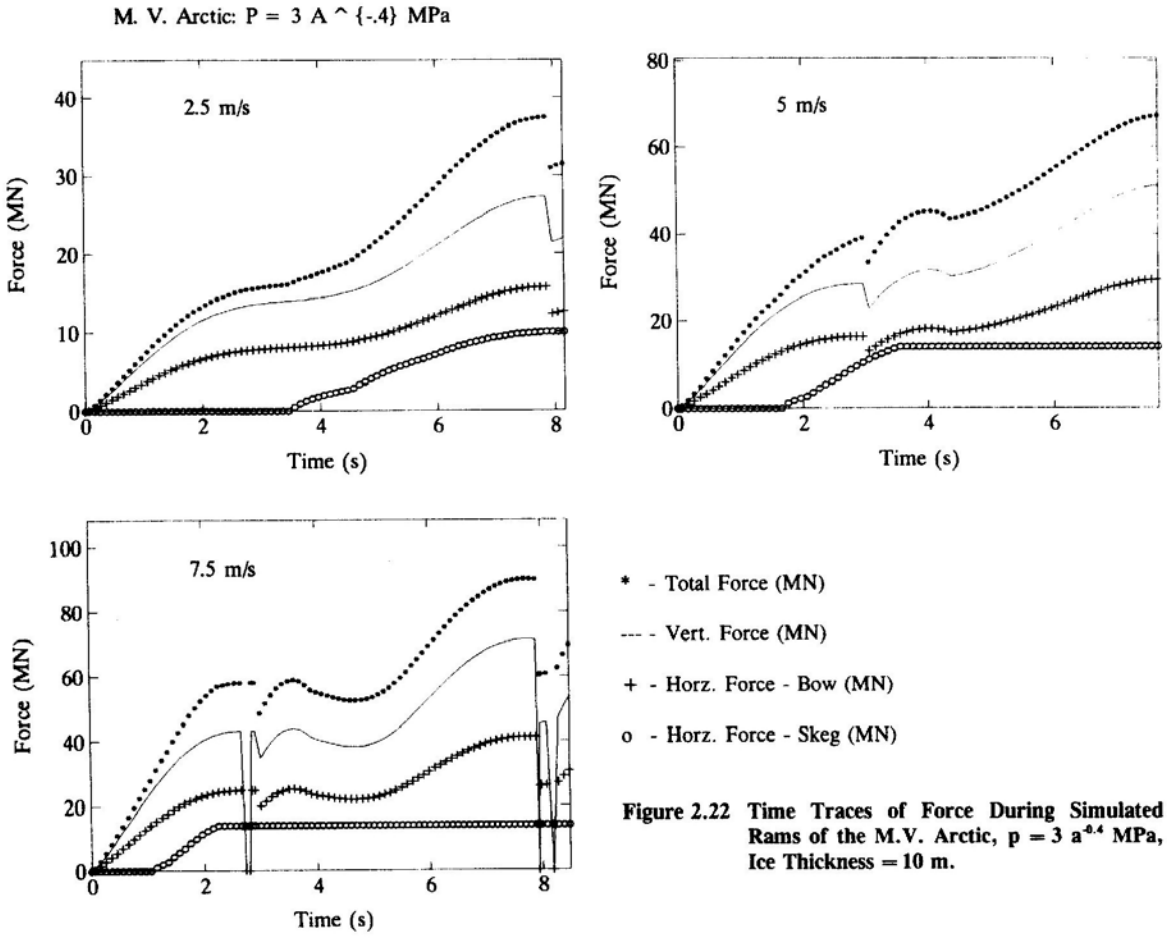

Figure 2.22 Time Traces of Force During Simulated Rams of the M.V. Arctic, p = 3 $a^{-0.4}$ MPa, Ice Thickness = 10 m.

Figure 79 Simulation of time dependent force from *MV Arctic* ram with 10m thick multiyear ice having pressure area relationship P = 3.0 $A^{-0.4}$ (Carter et al., 1996)

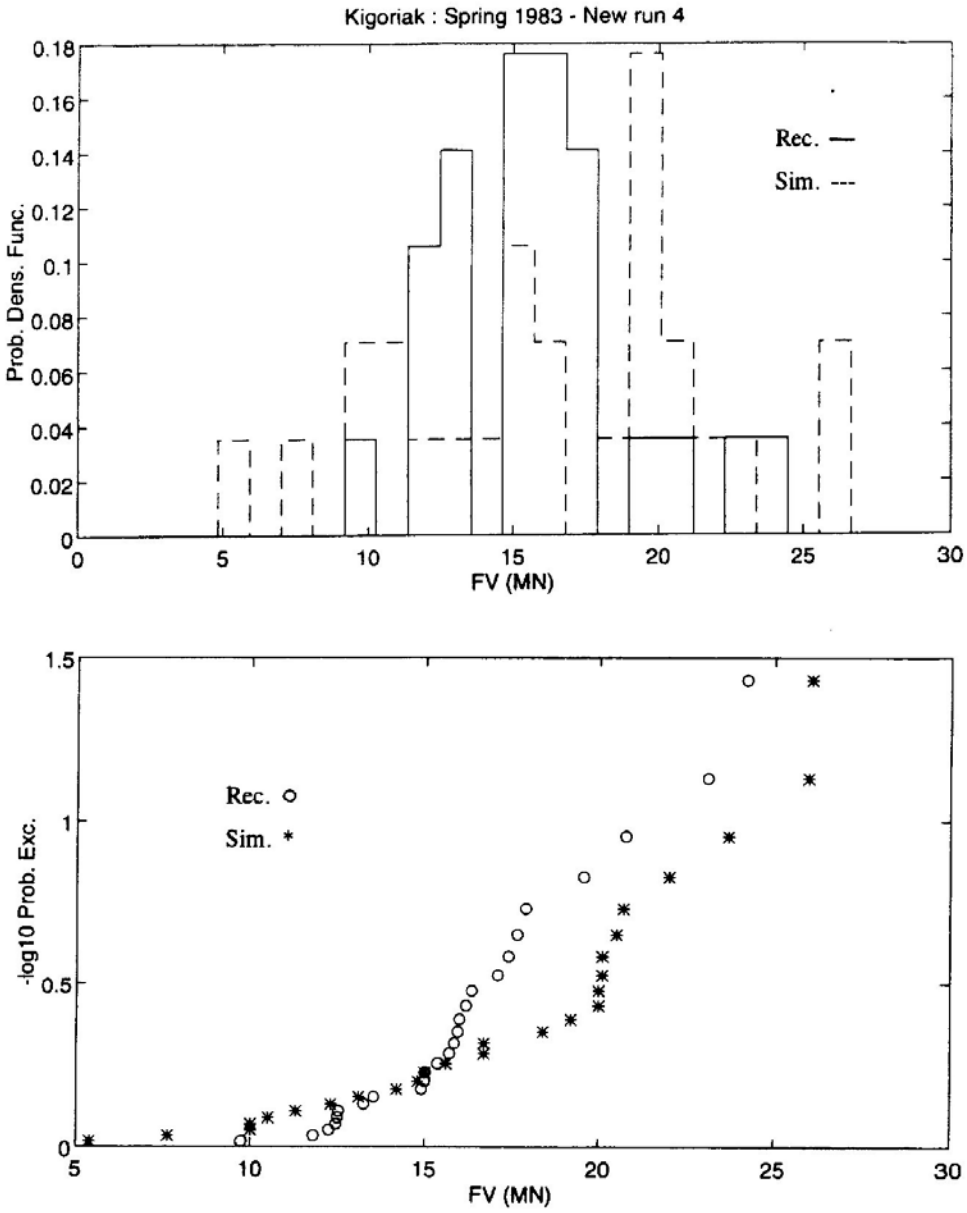

Figure 80 Histogram and exceedence probabilities of simulated and observed individual (parent) rams for *Kigoriak,* October 1983 for $P = 3.0\ A^{-0.4}$,$\sigma_C = 1.5$MPa; $\sigma_D = 0.2$ (Carter et al., 1996).

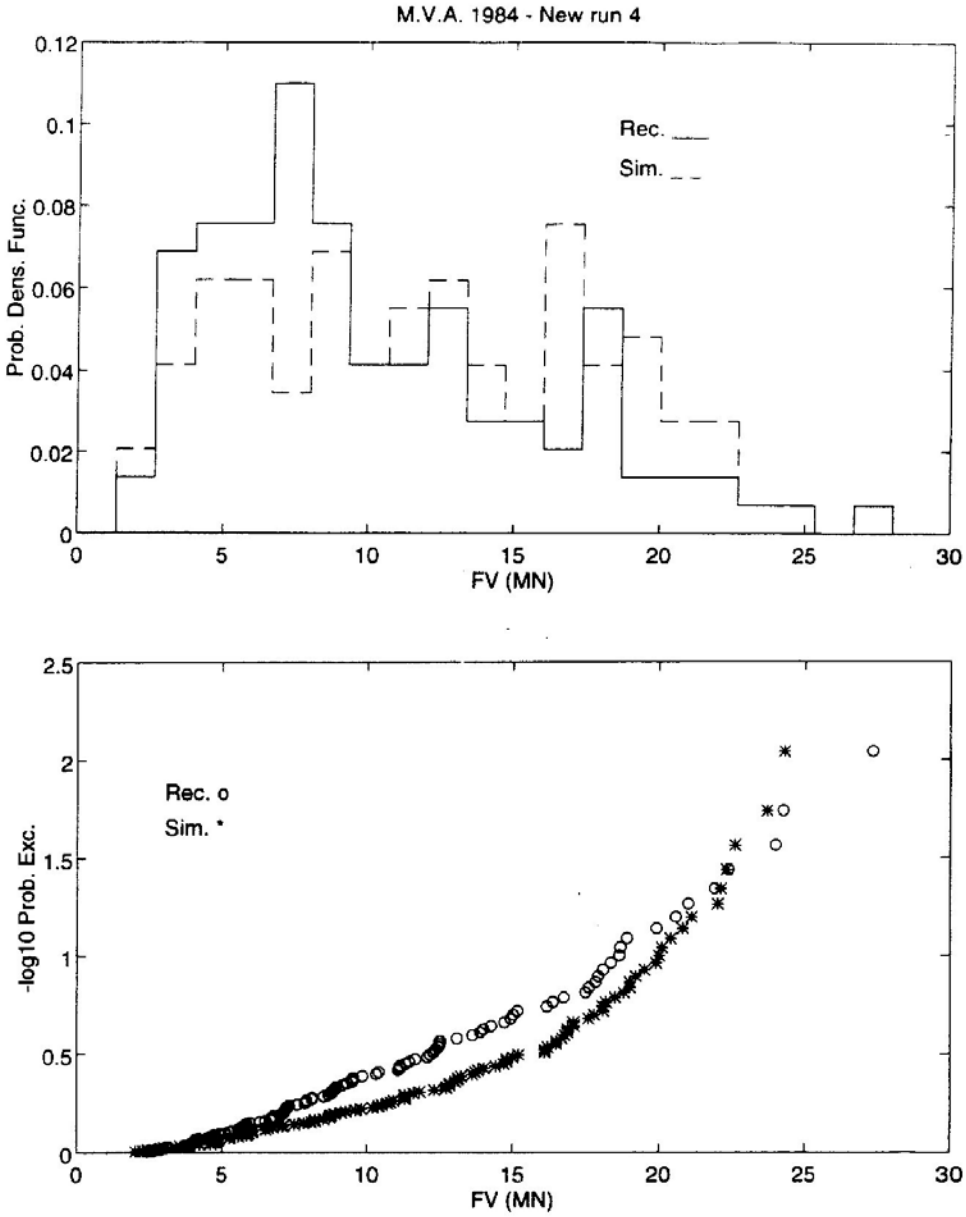

Figure 81 Histogram and exceedence probabilities of simulated and observed individual (parent) rams for *MV Arctic* 1984, for $P = 3.0\ A^{-0.4}$,σ_C = 1.5MPa; σ_D = 0.2 (Carter et al., 1996).

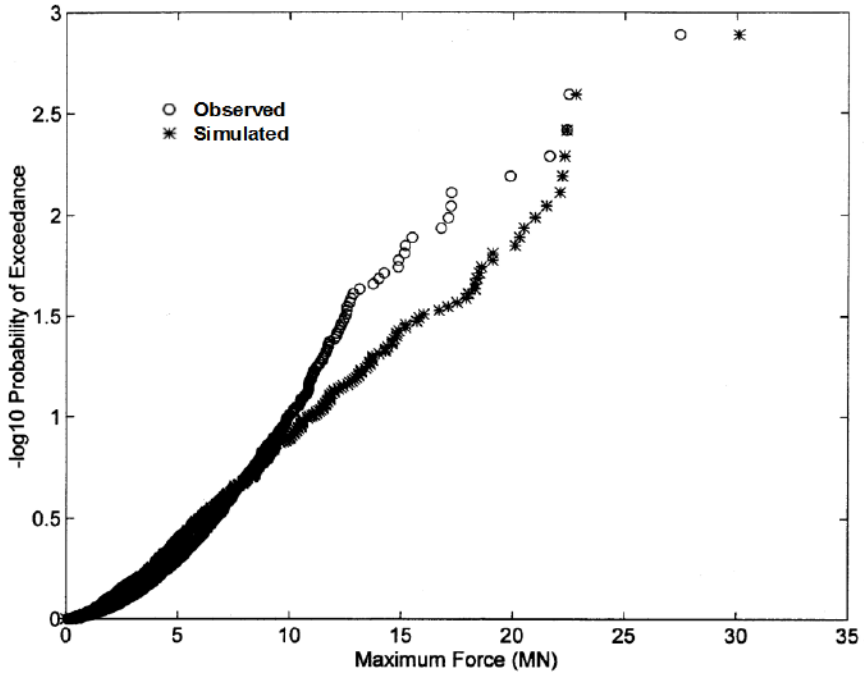

Figure 82 Comparison between observed and simulated peak forces for ice interaction events with the icebreaker *Oden*, 1991. Results include flexural failure (Carter et al., 1996).

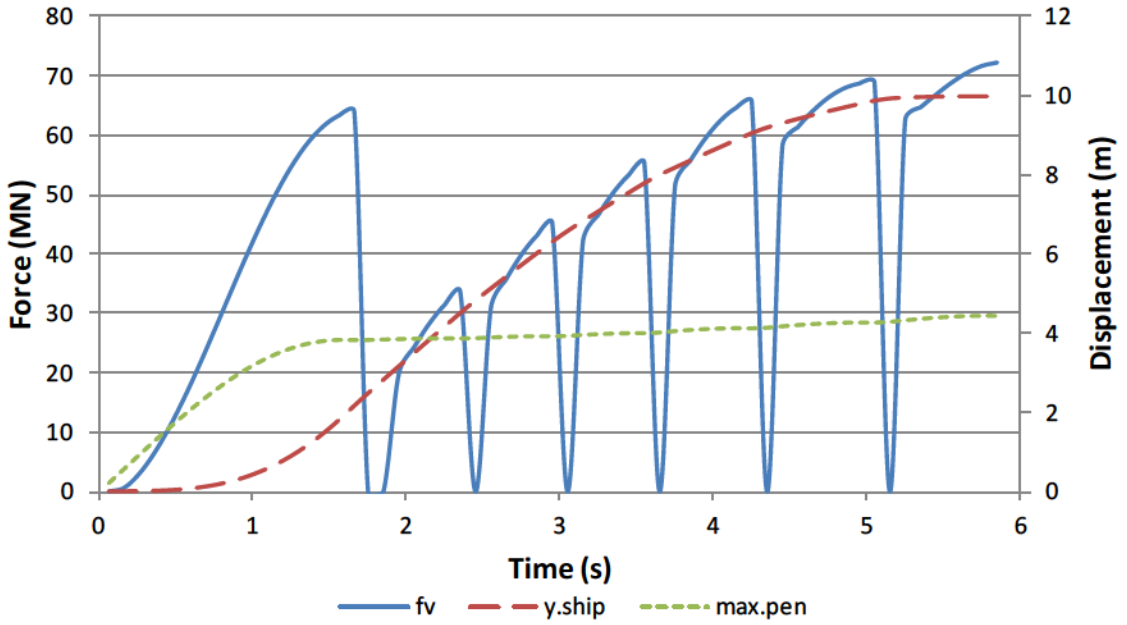

Figure 83 MV *Arctic* CAC4 ship ram simulation including vertical bow force, vertical bow displacement (ice thickness 19.9m, ship speed 7.24 knots, *Cp* = 3.7 MPa, *Dp* = -0.19). Note that impact phase clearly defined.

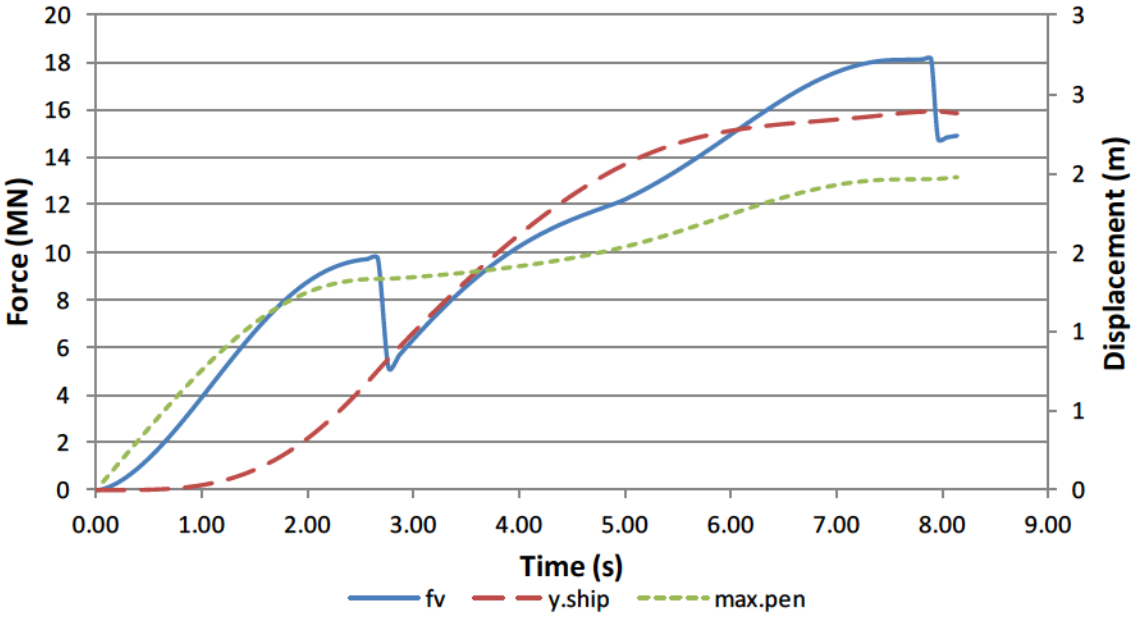

Figure 84 MV *Arctic* CAC4 ship ram simulation including vertical bow force, vertical bow displacement (ice thickness 23.4 m, ship speed 1.58 knots, *Cp* = 3.13 MPa, *Dp* = -0.2).

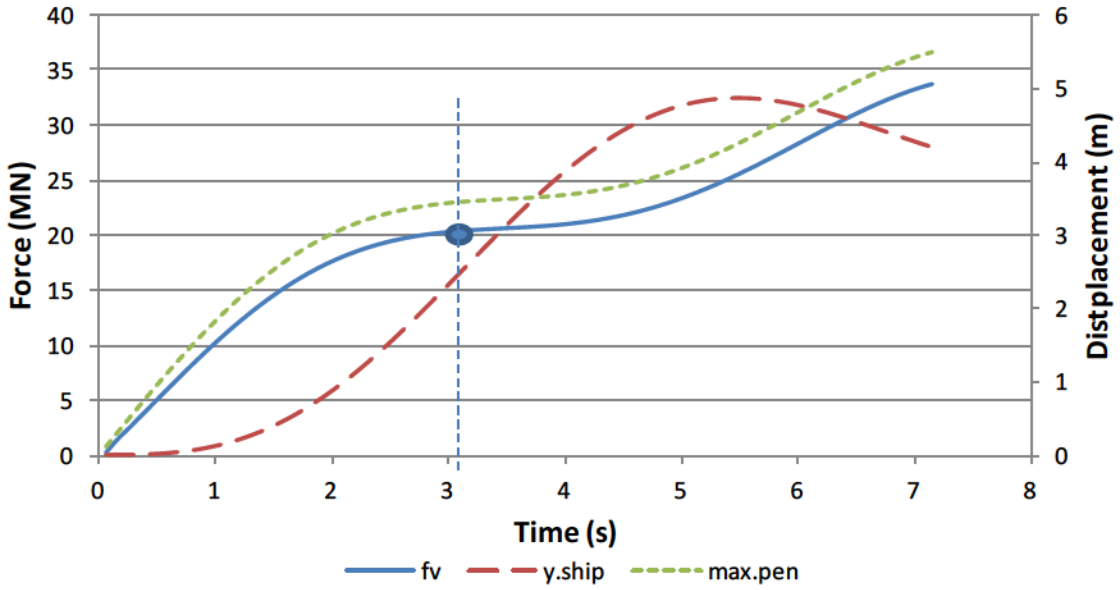

Figure 85 MV *Arctic* CAC4 ship ram simulation including vertical bow force, vertical bow displacement and penetration (ice thickness 16.6 m, ship speed 3.9 knots, *Cp* = 3.63 MPa, Dp = -0.46). Impact phase end identified as point where vertical acceleration is zero (i.e. second derivative of ship.y = 0.

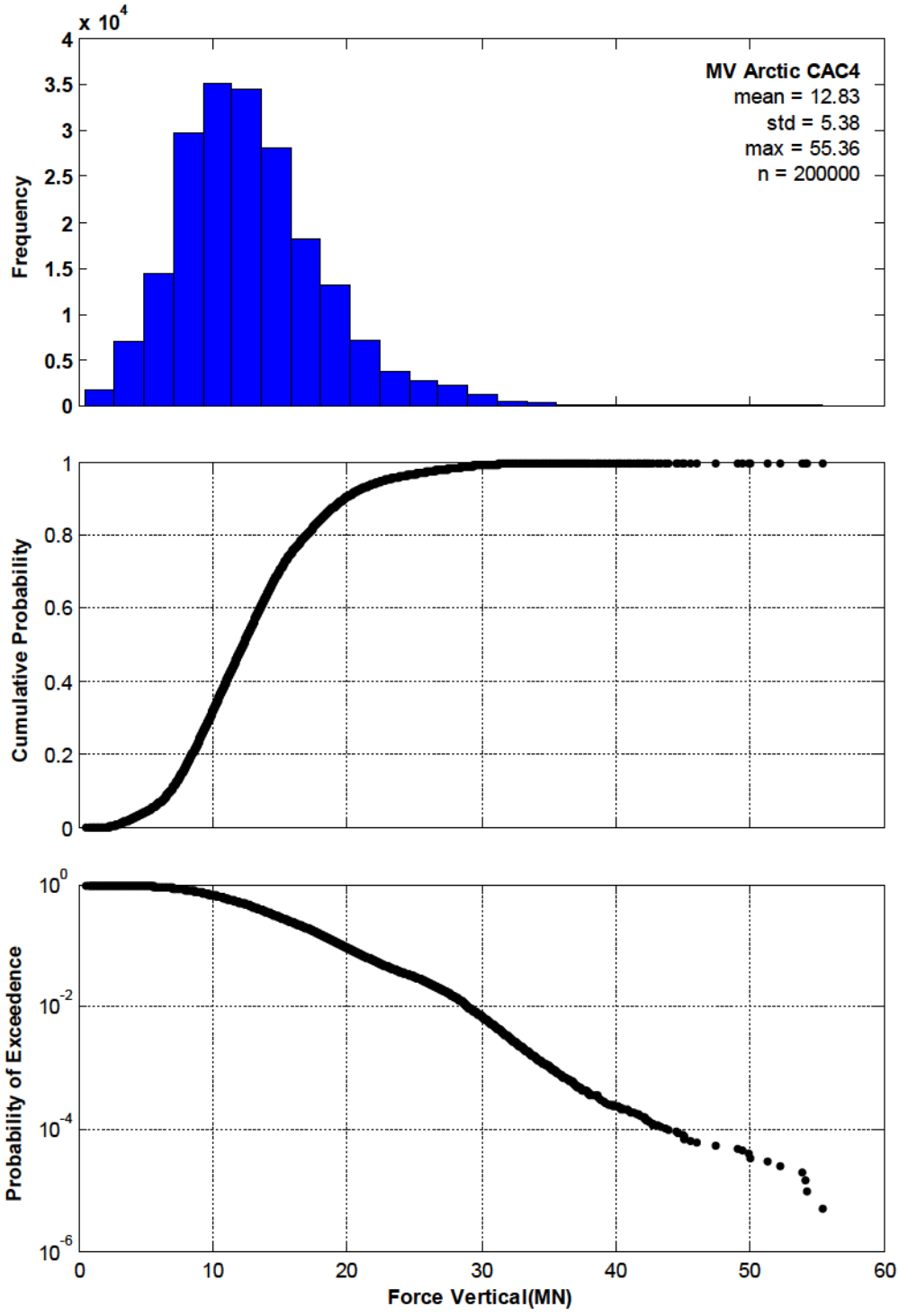

Figure 86 Parent distribution for maximum vertical bow force corresponding to initial impact phase for MV *Arctic* CAC4 type vessel.

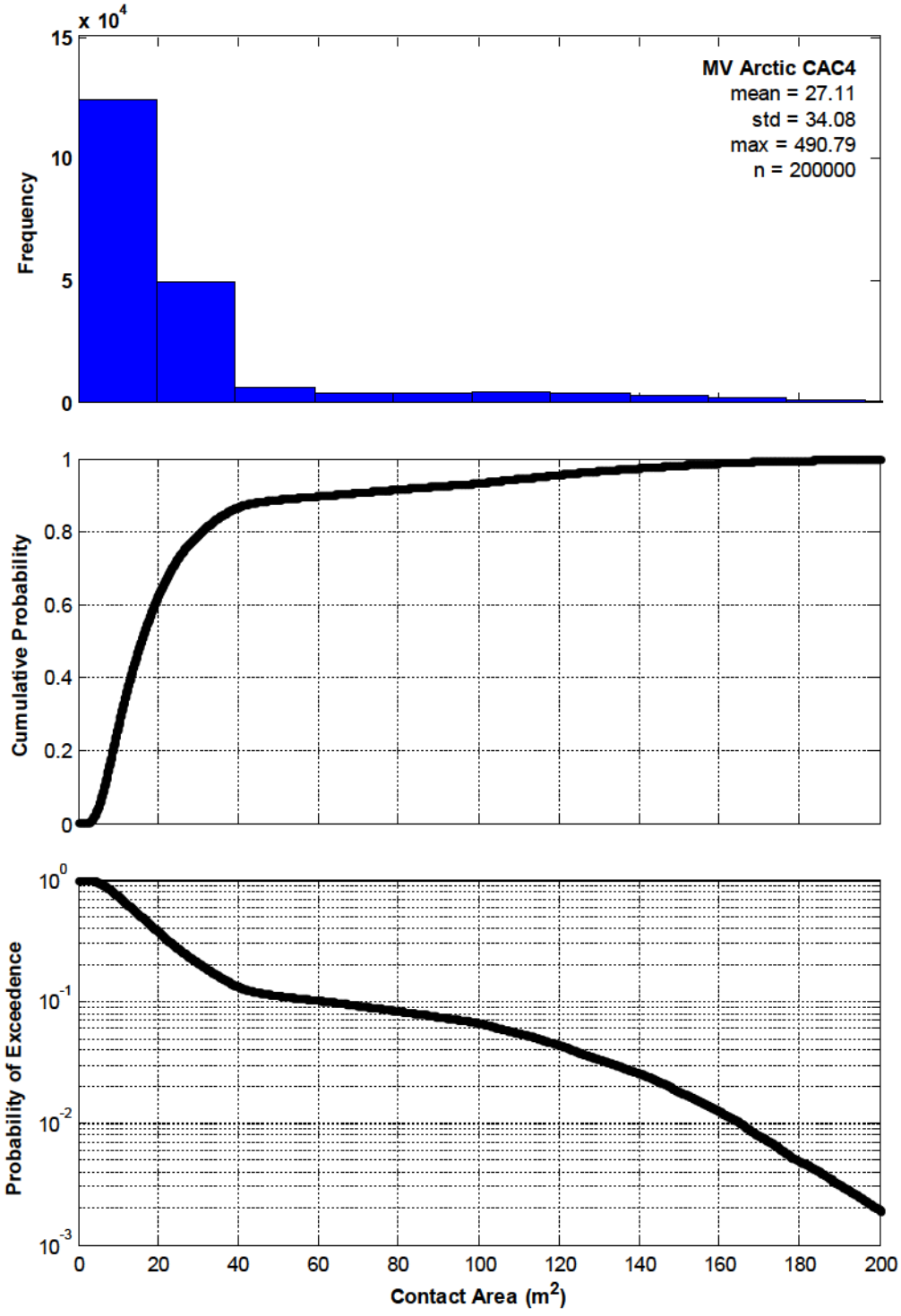

Figure 87 Contact area for initial impact phase for *MV Arctic* CAC4 type vessel

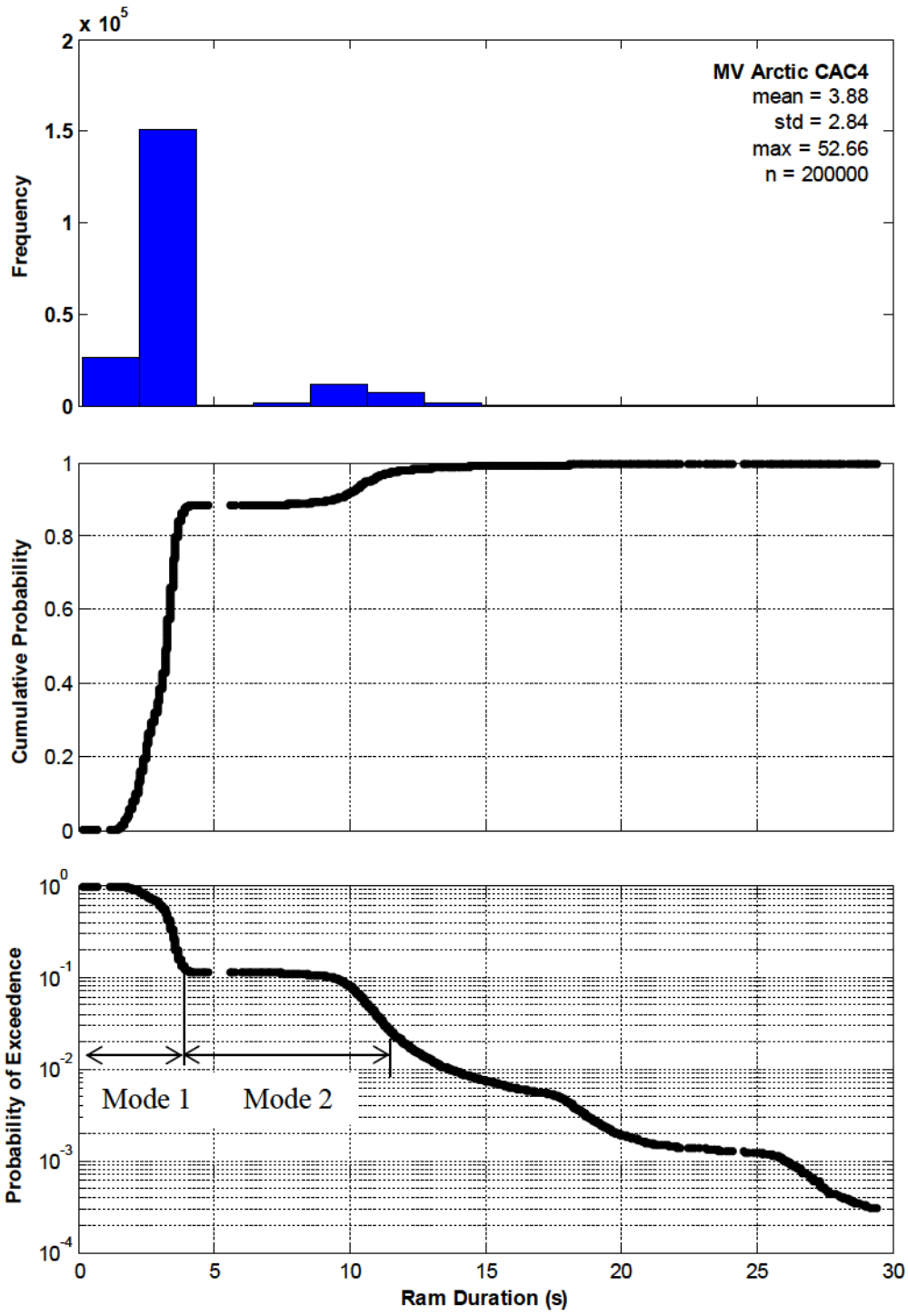

Figure 88 Maximum time corresponding to initial impact phase for *MV Arctic* CAC 4 type vessel. Mode 1 corresponds to the majority of simulated impacts with initial impact crushing phase with duration less than 4 seconds followed by beaching phase. Mode 2 relates to impact scenarios (except for several extremes) with softer ice such that crushing occurs through full duration.

4.2.5 Application for Design - Probabilistic Methodology

A probabilistic methodology for extremal analysis is rather useful for design. An exponential distribution (or distribution that provides the best fit) was fitted to the tail of the 'parent' distribution for impact forces. The fit is to the tail since we are only concerned with maximums for design.

Considering the number of expected interactions within a period of time as random, a Poisson process was used. The maximum load W based on the expected number of encounters v per given time period (e.g. one year) is given as

$$F_W(w) = e^{-v\exp(-\lambda w)}. \qquad (22)$$

where v is the exposure parameter based on number of interactions in a year and λ is the exponential distribution parameter.

The design load for 100 year return period is given as

$$0.99 = e^{-v\exp(-\lambda w_{100})} \qquad (23)$$

from which

$$w_{100} = \frac{4.60 + \ln v}{\lambda}. \qquad (24)$$

This expression can be used to estimate design loads based on a 'parent' distribution of *measured* data from specific vessels (e.g. MV *Arctic* in Figure 5) or as this chapter further outlines, the simulation of a 'parent' distribution for any specific vessel. Then, depending on the requirements for use of the vessel and expected number of interactions per annum, the appropriate design load distribution maximum forces can be produced.

4.2.6 Extremal Analysis

Extending from the previous section, as first introduced in Section 2.1, for design we are concerned for the maximum force of n ramming events in a year based on the expected or 'parent' distribution of force for any ram. An example 'parent' distribution for a vessel size equivalent to the *Kigoriak* is illustrated in Figure 89 (see also Figure 5 for MV *Arctic*). An

extremal design distribution based on the max of n impacts in a year (e.g. 100) based on an exponential fit to the tail of the 'parent' force distribution is illustrated in Figure 90.

To verify the Arctic Shipping Pollution Prevention Regulation (ASPPR) proposals (Carter *et al.*, 1996), an extremal modeling approach was used. Firstly, following discussion with Arctic captains, the estimated number of annual rams with MY ice with each vessel class was estimated as illustrated in Table 4. To verify, the MV *Arctic*, a CAC4 vessel, was expected to ram an average of 10-15 rams per year. Experience on the ODEN during delivery of supplies to an ice port resulted in repeated ramming for 20 days, 24 hours per day. Assuming approximately 10 rams per hour equates to 4800 rams. It is reasonable to model a linear change in loads with a step change in arctic class corresponding to an exponential change in exposure (e.g. 10,000, 1000, 100, 10 impacts per year for vessel classes ranging from CAC1 through CAC4 respectively (see Carter *et al.*, 1996).

Using 'parent' distribution of measured force on MV *Arctic* from Figure 86, and exercising equations in Section 4.2.5, corresponding forces for 10^{-2} annual exceedance probability is illustrated in Table 4. The forces normalized to the CAC1 force are also illustrated. While the coefficients in the rules are somewhat lower than the estimated factors based on normalize extremal based forces, the linear trend is illustrated. Later in Section 5.7 these are discussed for each of the Polar Classes.

Table 4 Illustration of ASPPR class factors, estimate for annual number of rams, estimated and normalized force for MV *Arctic* type vessel and 10^{-2} annual exceedance probability.

Canadian Arctic Class	Class Factor	Number of rams per year	Force at 10^{-2} annual exceedence probability	Force normalized to CAC1
CAC1	1.0	10,000	54.3	1
CAC2	0.8	1,000	46.0	0.85
CAC3	0.6	100	38.8	0.71
CAC4	0.4	10	31.5	0.58

To exercise the Fmax software and simulation of a parent load distribution, as well as design forces for different exposure levels and characteristic design values, the simulation matrix of different load cases is given in Table 5. For illustration, a selection of the results is given in Table 6. Additional detail can be found in the detailed report (Carter *et al.*, 1996). Figure 91 compares F_{MAX} simulation results for different arctic class vessels to the traditional ASPPR F_{MAX} equation including a recommended best fit adjustment to the design curve coefficients (i.e. updating a_{old} and b_{old} in Eq. (19) with a_{fit} and b_{fit}). As shown in Table 7, the adjusted analytical expression in Eq. (19) for estimating maximum bow forces compares reasonably well to the measured data, demonstrating the validity of the extremal verification approach used.

The normalized forces relative to the Canadian Arctic Class 1 (CAC1) force show good agreement with the originally proposed class factor from CAC1 to CAC4 or 1.0, 0.8, 0.6, 0.4. This verifies that a quantified approach to selection of vessel class based on exposure (expected number of rams) is reasonable and appropriate.

Considerable detail is given here to illustrate the utility of the F_{MAX} tool to model the global interaction and forces as well as application of a risk based approach to design and verification. This approach is used as a base for review of the Polar Code in CHAPTER 5. Incorporating this approach in the Polar Code would substantially enhance the design methodology.

Table 5 Analysis matrix for calibrating F_{MAX} design equation (after Carter *et al.*, 1996)

Vessel	Displacement (tones)	Powering (MW)	Canadian Arctic Class	Expected number of rams	Exceedence probabilities
Kigoriak	6615	12.2	1	10000	1%
			2	1000	5%
			3	100	10%
			4	10	
MV Arctic	38940	10.86	1	10000	1%
			2	1000	5%
			3	100	10%
			4	10	
New Large Displacement (NLD)	140,000	20.5	1	10000	1%
			2	1000	5%
			3	100	10%
			4	10	

Table 6 Probabilistic design loads based on Cp = 3 ±1.5 and Dp = -0.4 ±0.2 for design strategy corresponding to 1% probability of exceedence (after Carter *et al.*, 1996)

Probability of exceedence	CAC	*Kigoriak*	*MV Arctic*	NLD
Forces	1	40.00	107.00	273.00
	2	32.10	90.40	231.00
	3	23.20	64.30	176.00
	4	15.20	42.30	119.51
Normalized forces to CAC1	1	1.00	1.00	1.00
	2	0.80	0.84	0.85
	3	0.58	0.60	0.64
	4	0.38	0.40	0.44

Table 7 Comparison of maximum vertical bow force *Fv* for select vessels using Eq. (19) following the ASPPR revision analysis (after Carter *et al.*, 1996)

Vessel	CAC	Original *Fv* (MN)	Proposed *Fv* (MN)	Measured *Fv* (MN)
Kigoriak	1	31.2	37.6	35
Louis St.Laurent	3	58.1	36.4	
MV Arctic	4	121.4	41.2	35-45
NLD	4	370.8	97.3	

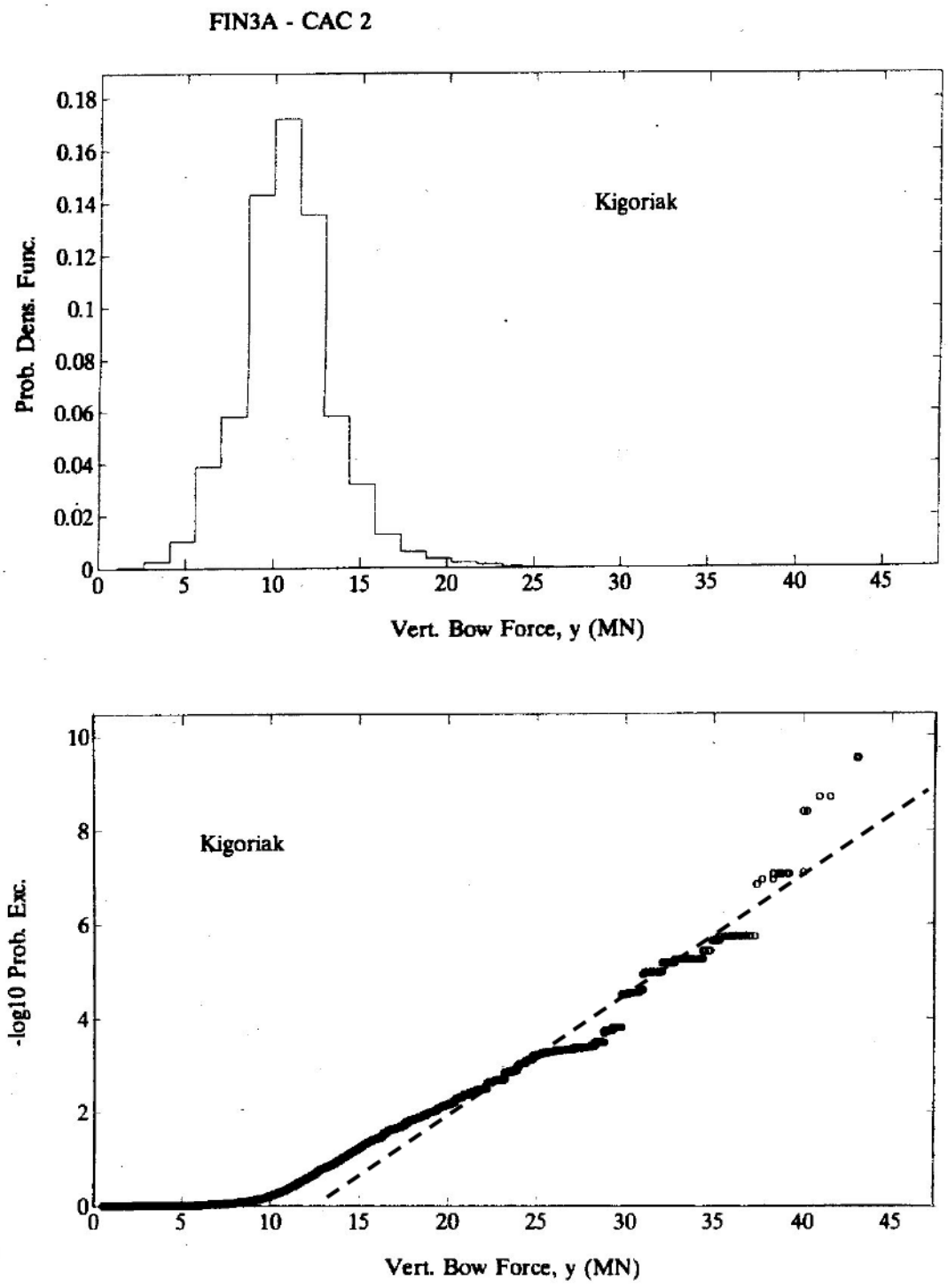

Figure 89 Histogram and exceedence probabilities of simulated individual 'parent' rams for *Kigoriak* size vessel using $P = 3.0\ A^{-0.4}$, $\sigma_C = 1.5$MPa, $\sigma_D = 0.2$ and illustrated exponential fit to the tail of the 'parent' distribution (Carter *et al.*, 1996)

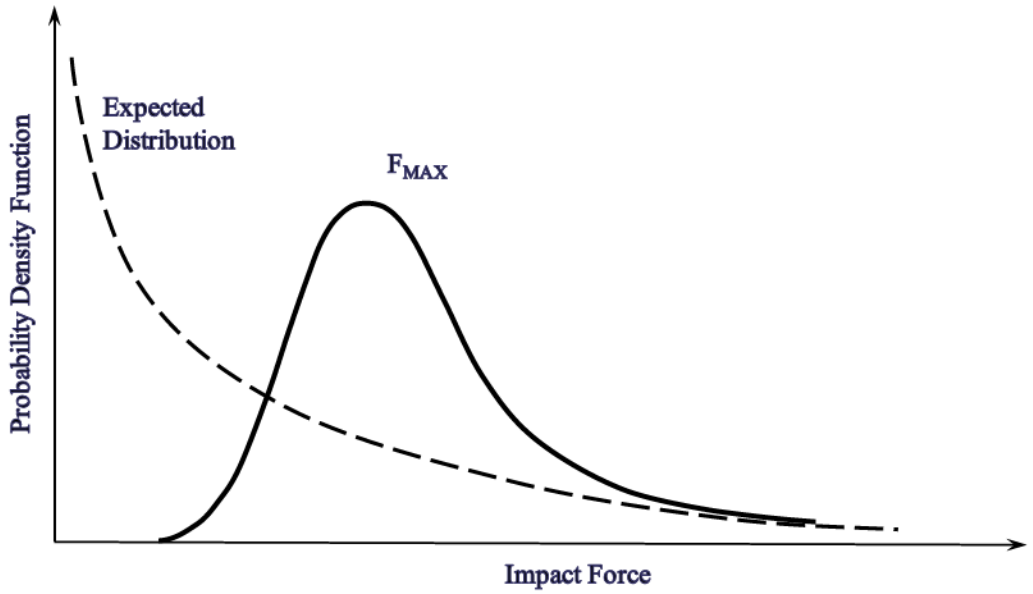

Figure 90 Illustration of extremal F_{MAX} distribution based on the number of impacts using the exponential distribution as a best fit to the tail of the 'parent' distribution (after Carter *et al.*, 1996)

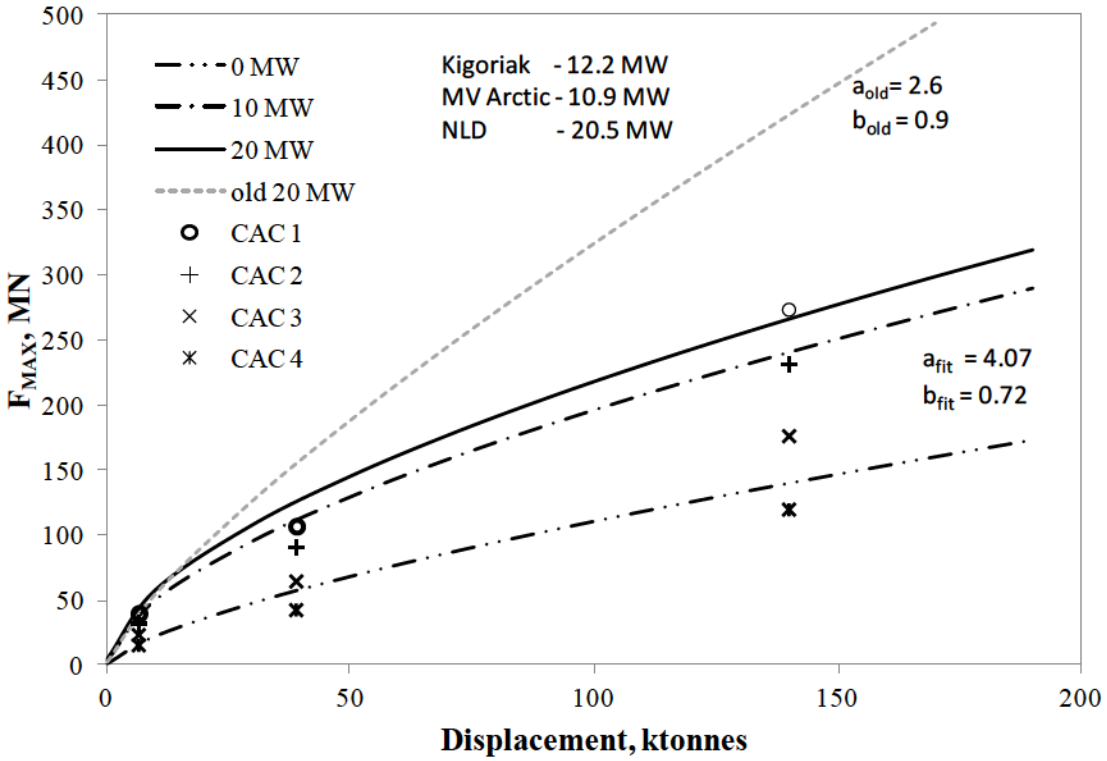

Figure 91 Probabilistic design loads based on Cp = 3 ±1.5 and Dp = -0.4 ±0.2 for design strategy corresponding to 1% probability of exceedence as well as the old and best fit F_{MAX} design curve (after Carter *et al.*, 1996). See Eq (19) for discussion on a_{old}, b_{old}, a_{fit}, b_{fit}

4.2.7 Sensitivity to Pressure Area Constant, Cp and Modeled Distribution

The global pressure-area used for ship rams with MY ice, $P = Cp\ A^{-Dp}$, models *Cp* using a lognormal distribution. While simulated pressures using this relationship compared with pressures derived from measured forces on the MV *Arctic* are in good agreement, as illustrated in Figure 92, the use of a lognormal distribution results in a fat tail (i.e. inherently picks up increased probability that may lead to over conservatism, particularly with many interaction or events per year). An alternative distribution such as a Weibull should be considered.

Comparing Weibull distribution with the lognormal distribution in Figure 93 for the same mean and standard deviation (i.e. $Cp = 3.0 \pm 1.5$) the significance of the added probability in the tail of the lognormal distribution is illustrated. Further, comparing different classes of extremal distributions as illustrated in Figure 94, the lognormal 'parent' distribution tends toward substantially increased spread in the extremal design distributions (i.e. maximum of *n* events) for increased numbers of events within a period (e.g. one year). The design point based on some characteristic design target probability (i.e. 1 in 100 years or 10^{-2} exceedence probability) will tend to be overly conservative. It is noted in Figure 93, there is a range of *Cp* values, 2 MPa < *Cp* < 6 MPa where the probability of *Cp*(Weib) is greater than the probability of *Cp*(LogN).

To test the influence of Weibull vs. lognormal distributions for *Cp*, the Fmax software was exercised for 1,000,000 Monte Carlo ship ram simulations. The example design scenario is 100 impacts per year with a 1/100 year return period design condition or 10^{-2} annual exceedance probability.

Figure 95 and Figure 97 illustrate the estimated design impact force distributions for both the lognormal and Weibull *Cp* models respectively. Figure 96 and Figure 98 compare the contributing *Cp* and *Dp* values to the characteristic design point (i.e. 100 rams/yr and 10^{-2} annual exceedance probability or 10^{-4} exceedence probability in Figure 95 and Figure 97).

These simulation results estimate that for this design scenario, the *Cp*(LogN) simulated crushing forces are less than the *Cp*(Weib). At the 10^{-5} exceedance probability level, the

forces are approximately the same. This is unexpected since theoretically *Cp* values should create an opposite effect. Comparing the contributing *Cp* and *Dp* values in Figure 96 and Figure 98, the *Cp* values are just within range where theoretically Weibull estimates of *Cp* are expected to be greater than lognormal estimates (See Figure 93).

A further observation is that contributing *Dp* values for both extremal simulations are rather high (above 0). Since scale effect exists even at extreme levels, and while the spirit of *Dp* modeling was to incorporate some extra conservatism in the selection of pressure area parameters (i.e. for some duration in a ram, stronger ice may be encountered and pressures may increase), *Dp* may be too conservative.

Since theoretically, a Weibull based *Cp* model is most reasonable, and there is no experimental justification for *Cp* being lognormal, it is recommended that the pressure area model be changed. Since *Dp* is presently raised to a power, meaning that the effect on area is lognormal, then this parameter should be investigated further.

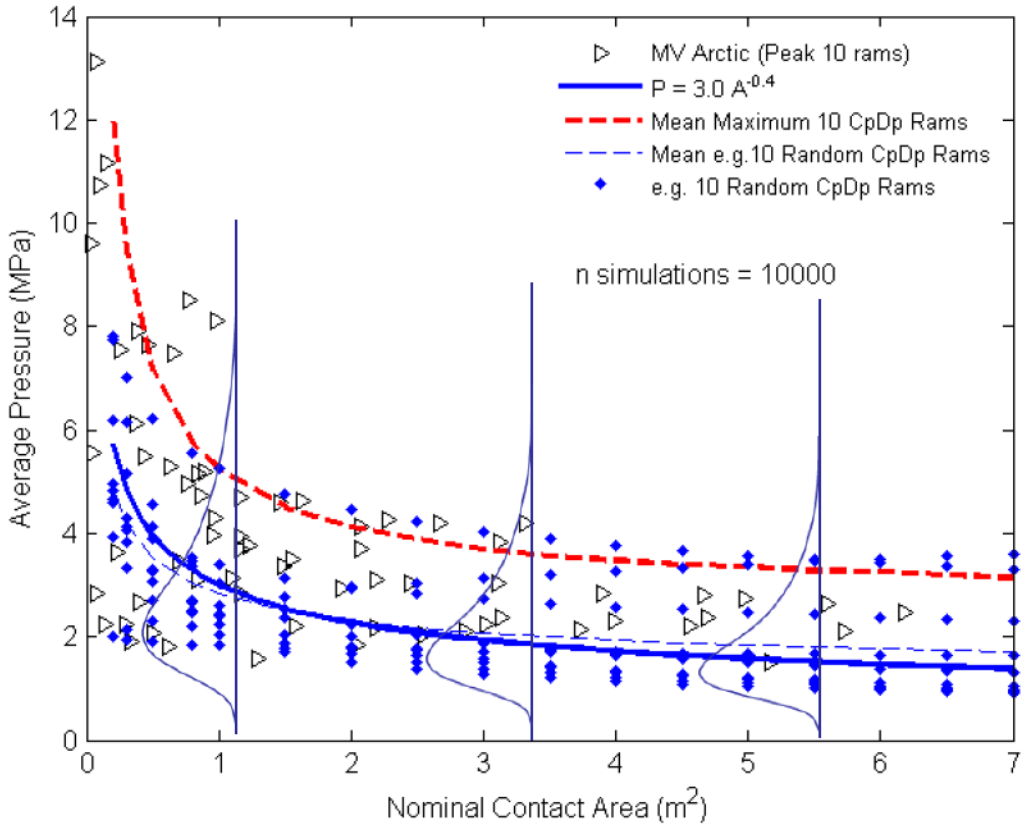

Figure 92 MV *Arctic* measured vs. simulated pressure-area data where *Cp* is modeled as lognormal distribution and *Dp* a normal distribution (after Frederking 1998)

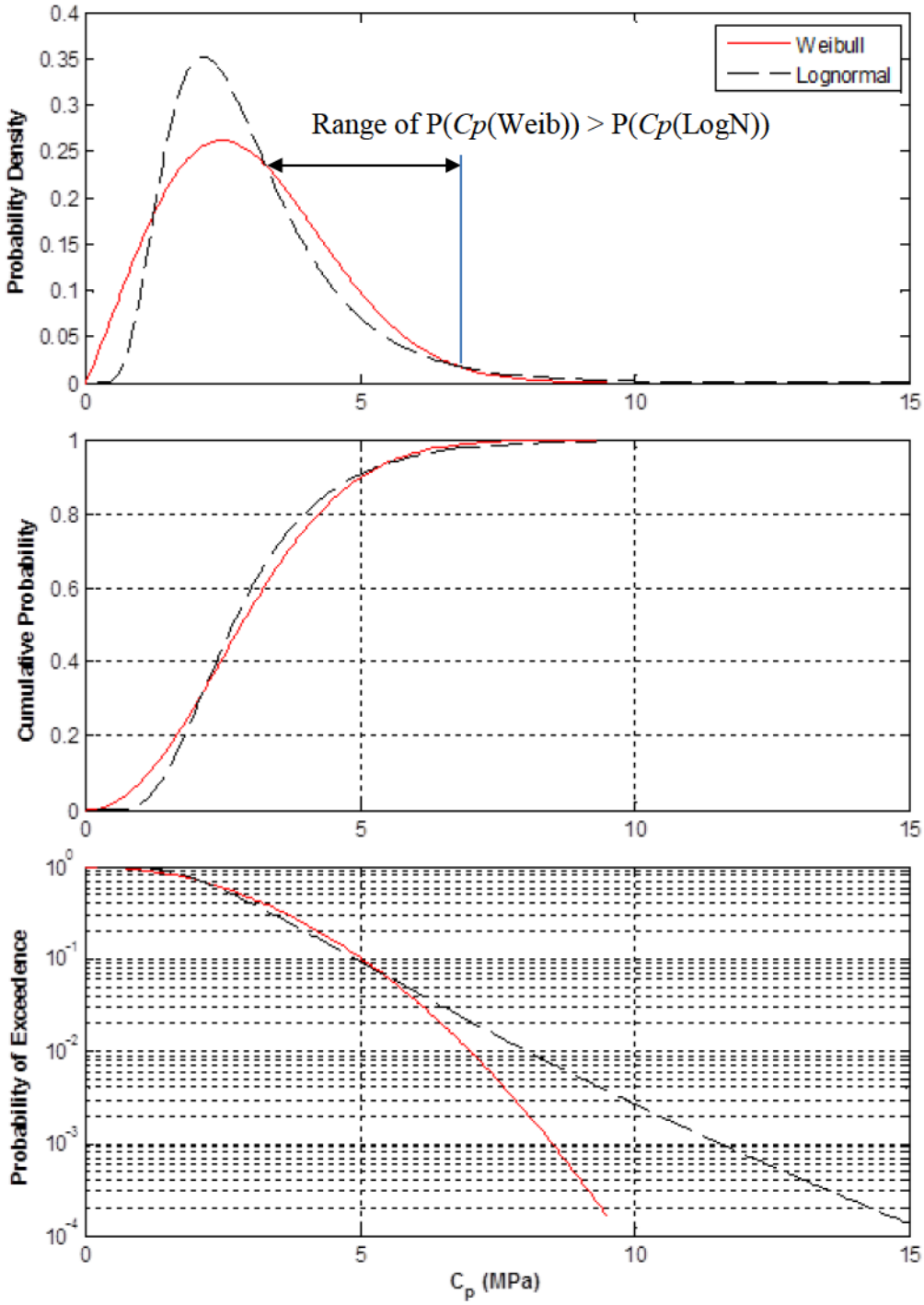

Figure 93 Influence of distribution type, lognormal or Weibull on sampling of global pressure parameter *Cp*

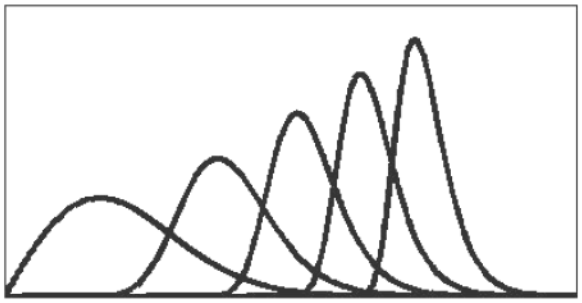

E1
Rayleigh
Distribution

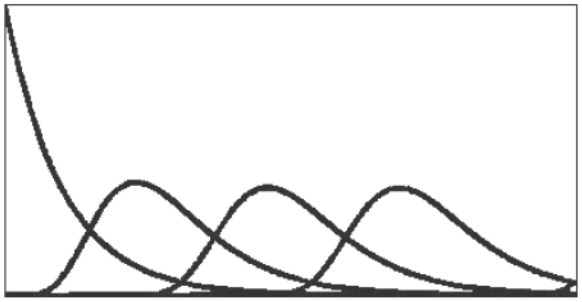

E2
Exponential
Distribution

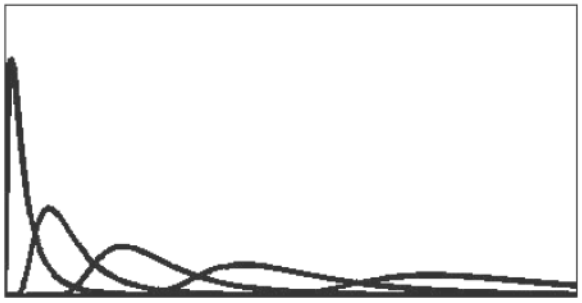

E3
Lognormal
Distribution

Figure 94 Classes of extreme distributions (Jordaan, 2005a)

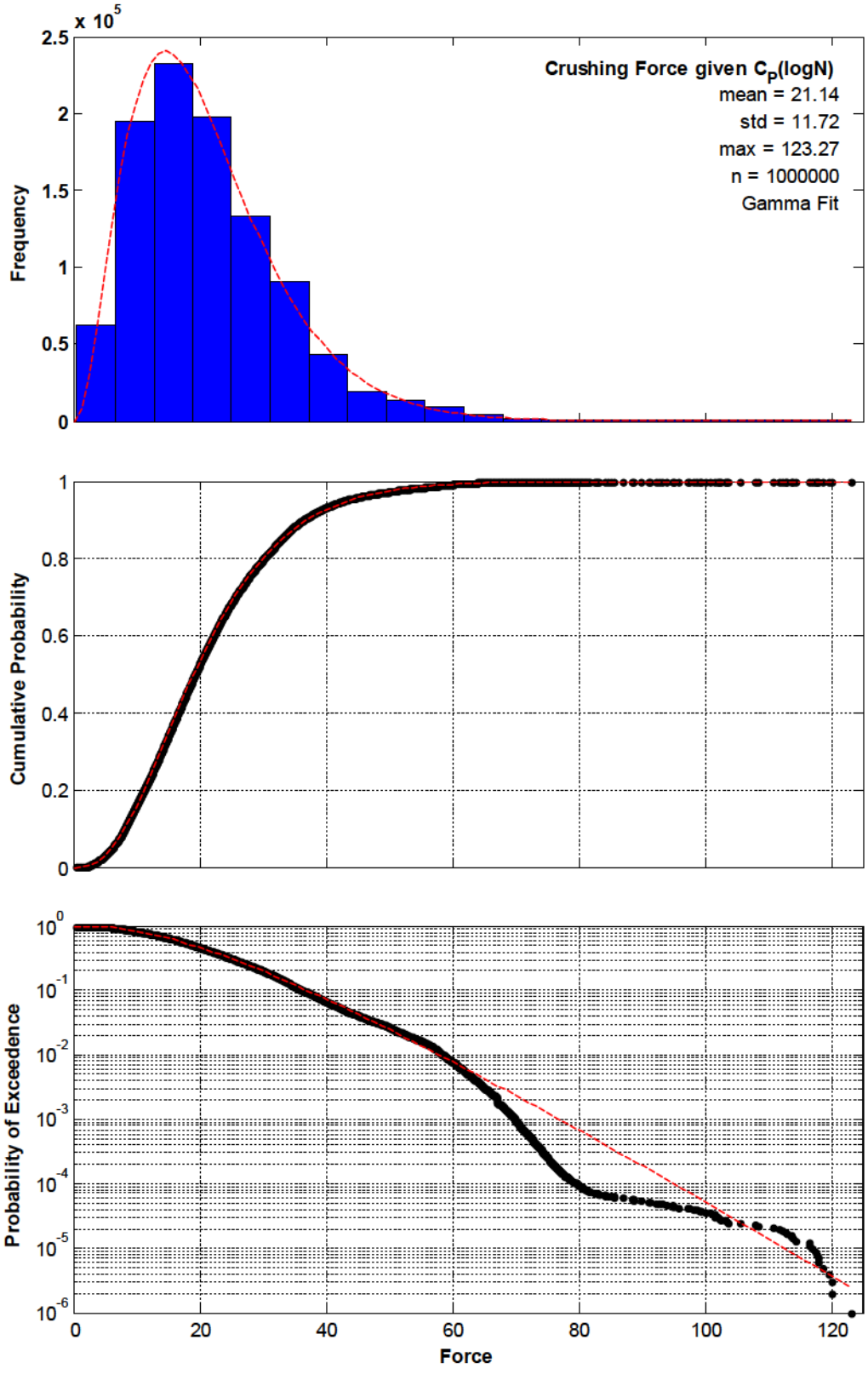

Figure 95 Extremal analysis exercising Fmax software for MV *Arctic* CAC1 type vessel modeling pressure area parameter *Cp* as lognormal distribution

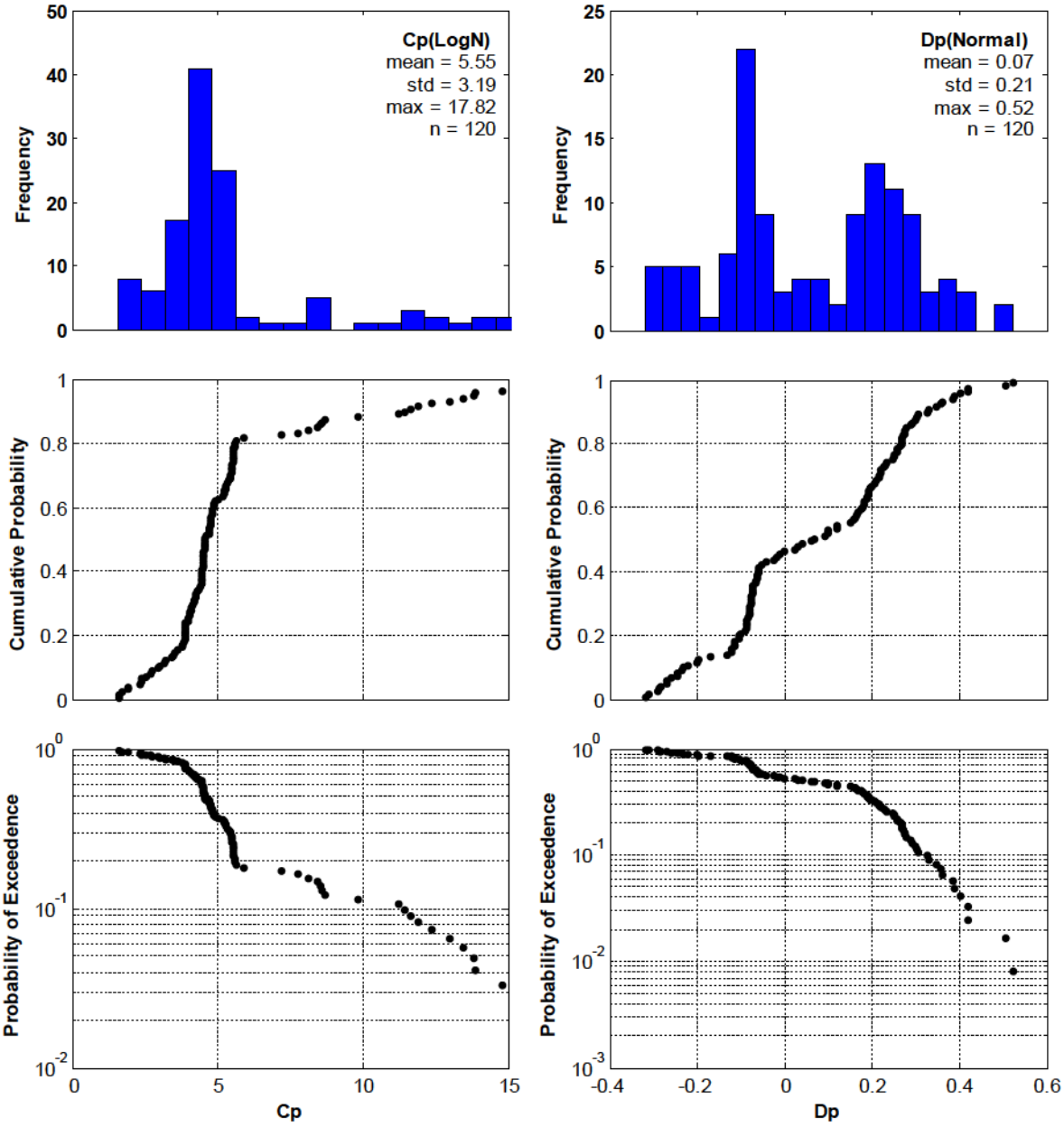

Figure 96 Contributing *Cp* and *Dp* for design condition based on the maximum of 100 rams per year and a 10^{-2} annual exceedence criteria (i.e. 10^{-4} exceedence probability) for MV *Arctic* CAC1 simulation modeling *Cp* as lognormal distribution

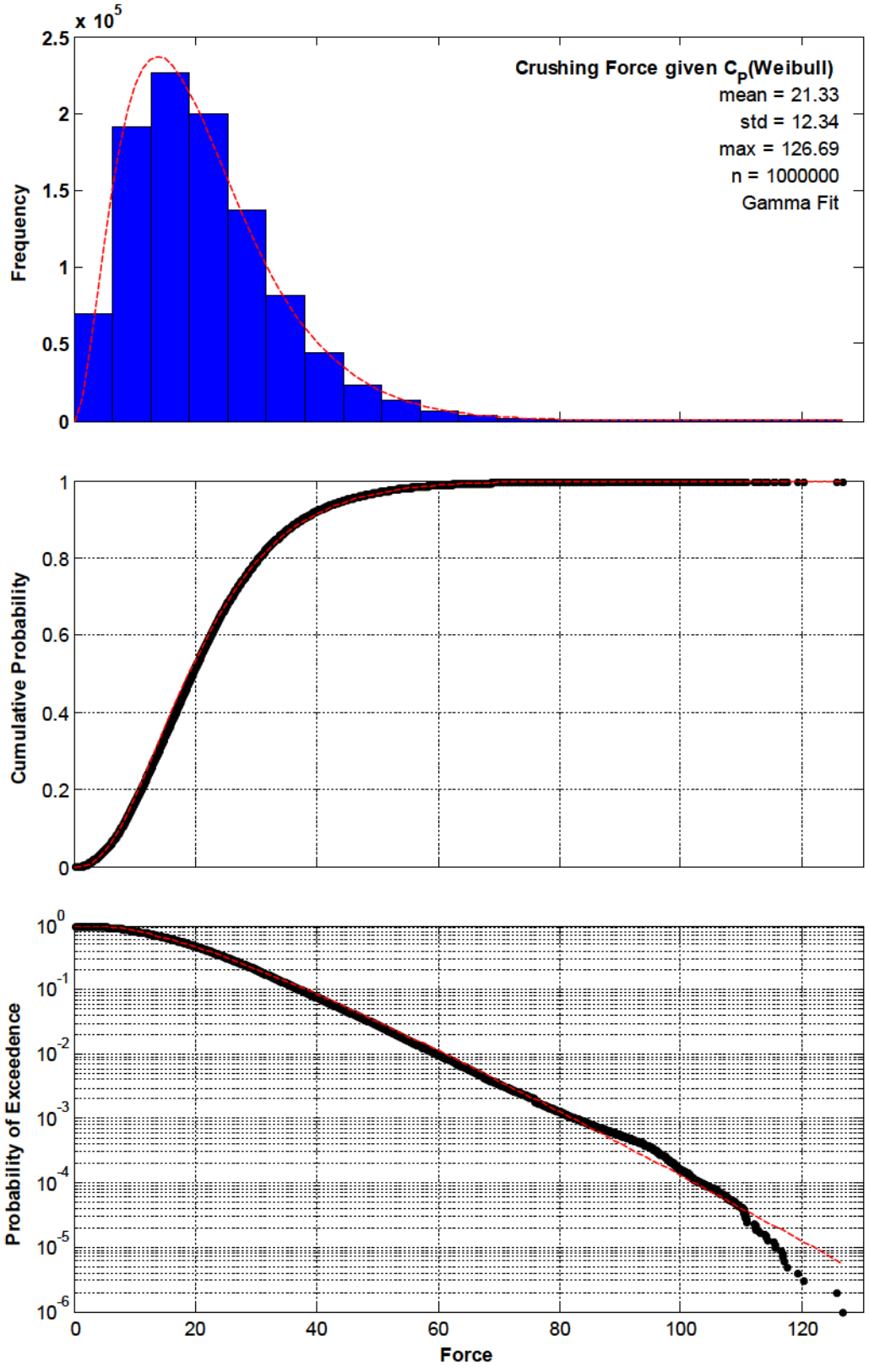

Figure 97 Extremal analysis exercising Fmax software for MV *Arctic* CAC1 type vessel modeling pressure area parameter *Cp* as Weibull distribution.

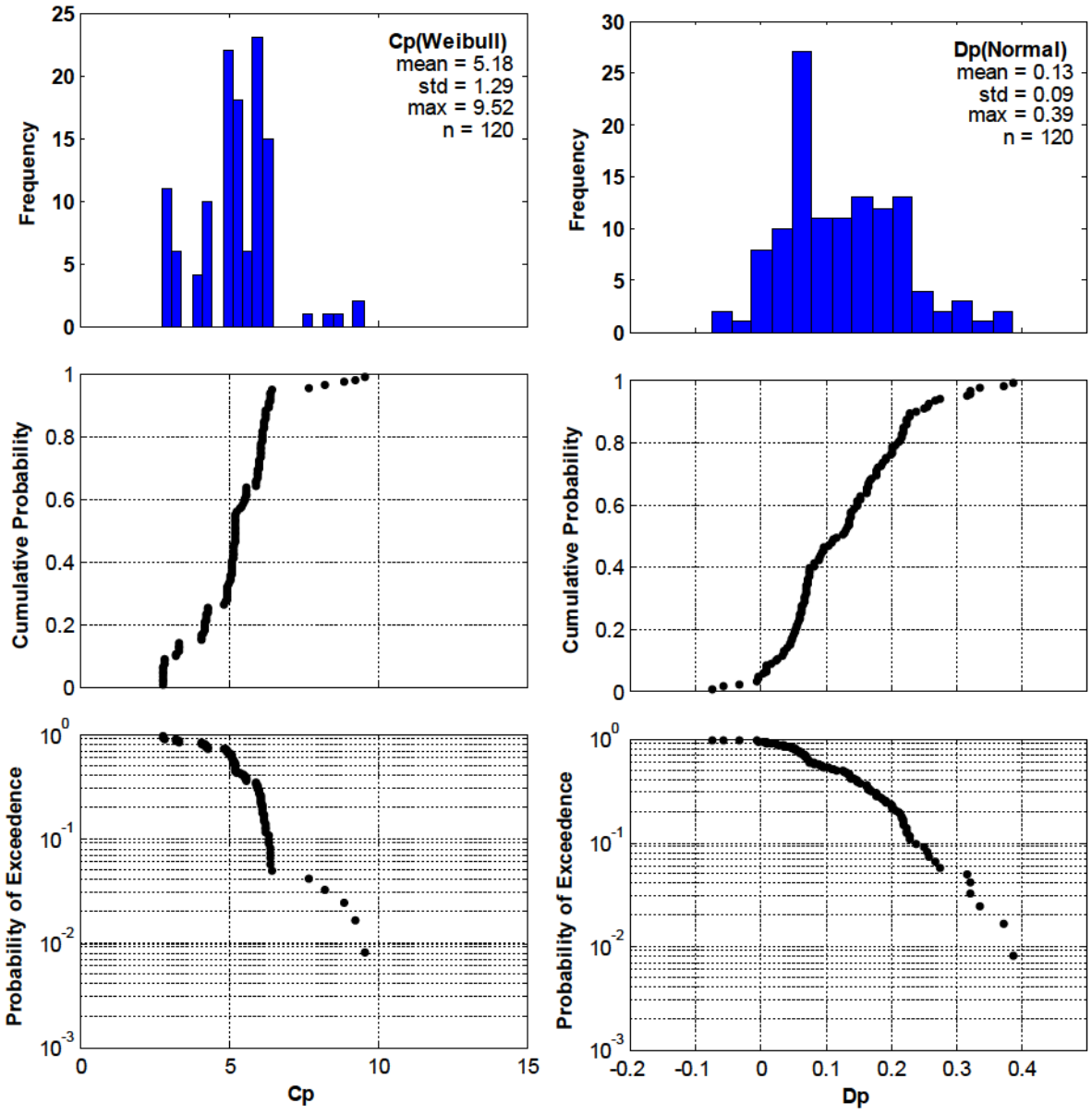

Figure 98 Contributing *Cp* & *Dp* for design condition based on the maximum of 100 rams per year and a 10^{-2} annual exceedence criteria (i.e. 10^{-4} exceedence probability) for MV *Arctic* CAC1 simulation modeling Cp as Weibull distribution.

4.2.8 Sensitivity to Pressure Area Constant, Dp and Modeled Distribution

While a new model for pressure area is outside the scope of this thesis, a discussion on the influence of *Dp* on simulation of pressures for nominal contact area is provided. The current

random pressure area relationship models *Dp* as a normal distribution (μ = -0.4, σ = 0.2) but since *Dp* is raised to a power, the influence on nominal contact area is lognormal. The influence as illustrated in Figure 99 is that the standard deviation on pressure increases with increasing contact area. There is no theoretical or practical justification for this effect and the influence for extremal analysis will result in considerable conservatism in high energy impacts with larger numbers of impacts per year. As a comparison, a simulation with *Dp* modeled as a constant (μ = -0.4) is illustrated Figure 100. While variability is pressures in modeled with a random *Cp*, it may be desirable to have some randomness in *Dp* more control over the scatter is needed. Since a refined model for *Dp* was not an objective of this research, no further analysis was carried out for this thesis.

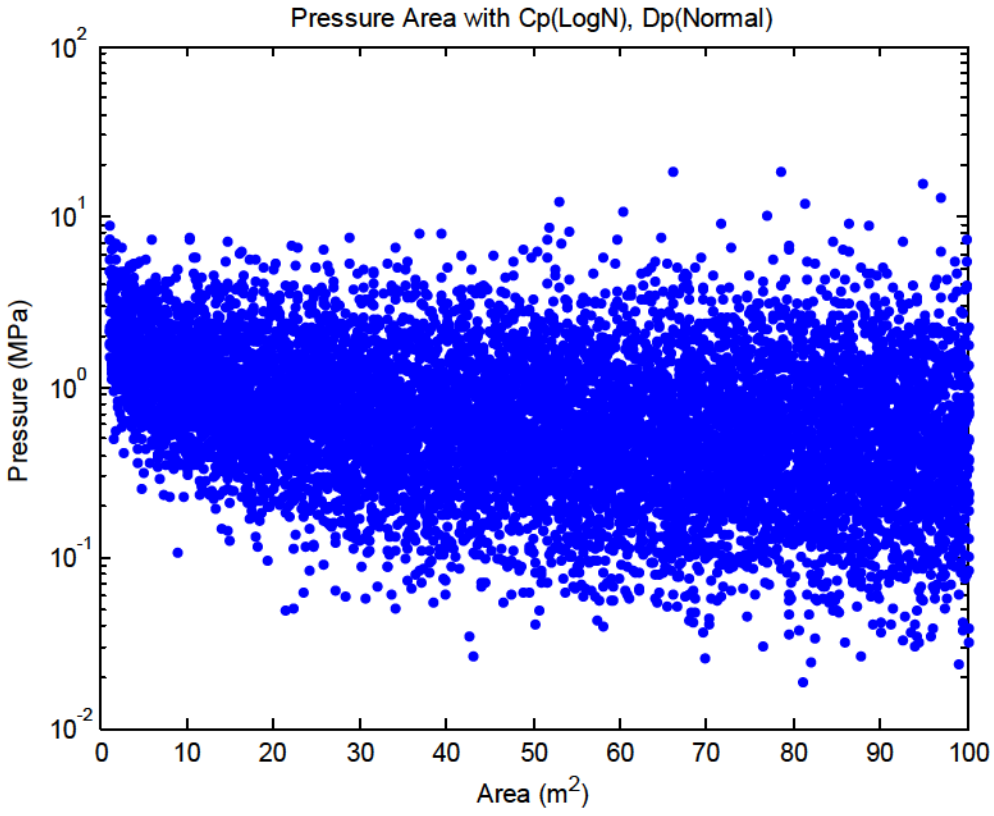

Figure 99 Pressure area base on $P = Cp\ A^{-Dp}$ with *Cp* model as Lognormal distribution (μ = 3.0, σ = 1.5) and *Dp* modeled as normal distribution (μ = -0.4, σ = 0.2)

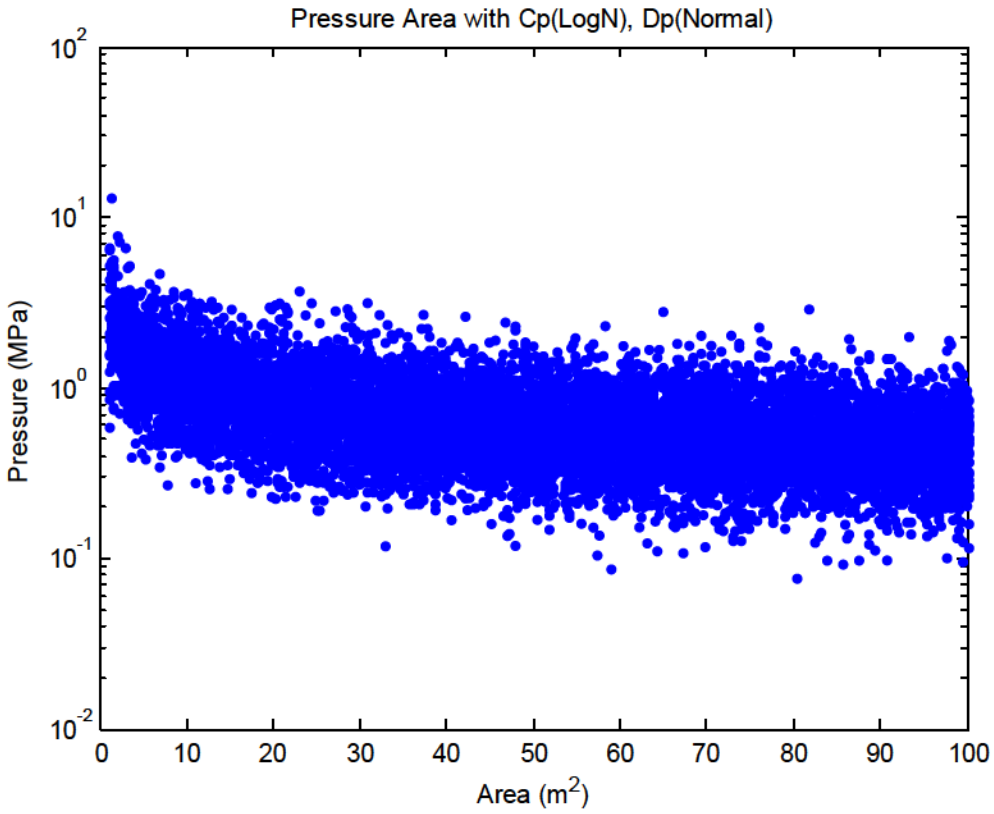

Figure 100 Pressure area base on $P = Cp\ A^{-Dp}$ with Cp model as Lognormal distribution (μ = 3.0, σ = 1.5) and Dp modeled as fixed valued (μ = -0.4)

4.3 Probabilistic Modeling and Simulation of *HPZ*s

As introduced several times in this thesis, for design, one is interested in the total force expected on a design area. The failure process results in localization of contact points within the global area having very high pressures called *HPZ*s. The occurrence of *HPZ*s through the interaction process is the key to modeling forces transmitted into the hull both locally through peak pressures on a single *HPZ* and globally through the summation of *n HPZ* forces across the interaction area. Background pressure through crushed ice can be included but as Johnston (1998) and Taylor (2010) report, these are very small noting that greater than 90% - even on the order of 95% - of total force is transmitted to the hull through local *HPZ*s. The average local pressure for the design area is the total *HPZ* force divide by the design area.

This section analyses the spatial occurrence and density of *HPZ*s as well as *HPZ* force to model peak pressures on local structural elements (i.e. shell plating between supporting main frames, stringers and web frames) and global forces on the hull.

Zou (1996) carried out an analysis of *HPZs* using *Louis S. St. Laurent* 1980 dataset to firstly establish parameters for *HPZ* density and failure force, and secondly to model and simulate local pressure parameters. His simulations compared well with the local pressure design curve developed by Jordaan, 1993 (See Figure 33). But the local pressure design curve represents very aggressive impact conditions with the strongest MY ice. The local pressure parameters for different ice conditions vary considerably, as illustrated in Figure 34 (Jordaan *et al.*, 2007). Ice strengths further south, as well as interactions with thinner first year (FY) ice are considerably lower. The full *Polar Sea* dataset is rich in this regard where measurements were made on the same panel across a wide range of conditions. Corresponding local pressure parameters illustrate the effect. Understanding *HPZ* parameters based on *Polar Sea* measurements is important and is addressed further in this chapter.

This section initially reviews the work of Zou (1996) and then studies the sensitivity of local pressures to variability in *HPZ* density and force using *Louis S. St. Laurent* 1980 data. A comprehensive analysis and modeling of *HPZs* is then carried out using the *Polar Sea* data

focusing on MY ice interactions. Comparing different datasets, the importance of sensor resolution and system thresholds are studied. A revised estimate for *HPZ* density is presented as well as recommendations on *HPZ* force parameter based on correlation with measured local pressure data.

4.3.1 Review of Zonal Force Analysis

Kujala (1994) and later Kujala and Arughadhoss (2012), following the work of Joensuu and Riska, (1989), Fransson *et al.*, (1991), Tuhkuri, (1995) who studied the brittle failure process of ice and line- like contact during ship ice interaction, developed a statistical model to describe the crushing process for Baltic Sea ship ice interaction conditions. Field trial measurements onboard the MT *Uikku*, IB *Sampo*, MS *Arcturus* and the IB *Sisu* as well as lab scale trials were studied. The crushing of ice under the nominal contact area was assumed to occur at random contact spots as illustrated in Figure 11. The force for each contact spot was modeled as an exponential distribution. The occurrence of contact spots were assumed to follow a Poisson process, such that the force can be described as a compound Poisson process. The nominal pressure was estimated as the sum of n contact forces over the nominal contact area. Similar modeling was followed by Zou (1996) as discussed in detail below.

Johnston (1993, 1998) conducted an analysis of *HPZ* force and density using MY impact data from *Louis S. St-Laurent* trials from November, 1980 (Blount *et al.* 1981 and Glen and Blount, 1984). The pressure sensor arrangement relative to the local structural arrangement in the bow thruster compartment is illustrated in Figure 101. The representative area corresponding to each pressure sensor was estimated to be 0.047 m^2. Sensors only recorded pressures above 1.37 MPa. Johnston assumed in her analysis that *HPZs* occur where measured pressures exceeded 2 MPa. She illustrated variability in *HPZ* occurrence through the ram duration as shown in Figure 102. Based on nine examined cases from her analysis, the mean *HPZ* area was estimated to be 0.112 m^2 and HPZ force 1.09 MN. The average spatial density was 0.76 zones/m^2 (based on an average of 1.28 zones over an instrumented area of 1.69m^2.

Johnston *et al.*, (1998) extended the analysis to include Hobson's Choice Indentation (HCI) tests (Frederking *et al.*, 1990), as well as *Kigoriak* (CanMar, 1992) and *Molikpaq* (Jefferies, 1988) measurements. Density measurements from the HCI tests were considerably higher at 8.3 zones/m^2. This was believed to result from confining stresses, given location of indentation tests relative to free surface. The mean zonal force and area was estimated to be 1.93 MN and 0.104 m^2 respectively.

Ram forces from the *Kigoriak* trials were based on strain gauge measurements of structural response over an instrumented area of 1.25m^2. The sensor resolution was 0.208 m^2 compared with 0.047 m^2 on the *Louis S St. Laurent*. Mean *HPZ* force and area was estimated to be 1.31 MN and 0.352 m^2 respectively. It was noted that the reduced resolution could result in averaging a few *HPZ*s on a single panel sensor, contributing additional background pressure. Assuming the density of 0.76 zones/m^2 to be correct, 0.27 zones would be expected on 0.352 m^2 area. Following statistical modeling of *HPZ*s occurrence using a Poisson process, it was noted that one or more *HPZ*s could have a force of 1.25 MN, which could well contribute to an average background force on the order of 0.3MN on any active panel indicating similar results from both trials (Johnston *et al.*, 1998).

Johnston *et al.*, (1998) also studied *HPZ* density using *Molikpaq* trials and particularly the loading event of May 12, 1986 (Jeffries, 1988), where a force of 130 MN was estimated to have occurred over a global contact area of 126 m^2 (average ice thickness of 2.7m across 60m face length). The analysis illustrated that a zonal density of 0.74 zones/m^2 and mean zonal force of 1.09 MN, would lead to 119 zones giving a total force of 130 MN consistent with observations from *Louis S St. Laurent* measurements. Given the focus of this work is ship rams, no further consideration for fixed platform interactions and loads will be considered.

Zou (1996) extended the work of Johnston (1994) to include 19 ram events and 266 time slices from the *Louis S St. Laurent* 1980 trials by relaxing the 2 MPa cutoff pressure. He also examined the influence of an effective measurement area being 1.25 m^2 vs. the total sensor area of 1.67 m^2 (see Figure 101). Zou also noted that limited spatial resolution could influence the possible occurrence of *HPZs* along the border of the active window (though not

measured directly). Consistent with the work by Johnston (1994) assuming *HPZ*s to be within the instrumented window, estimated density was 0.89 zones/m^2. The mean *HPZ* area was estimated to be 0.08 m^2. Densities greater than 1 zone/m^2 likely include very small *HPZ*s. The result of Zou lowering the *HPZ* cutoff pressure from 2 MPa resulted in a higher density of 0.89 zones/m^2 but lower mean force of 0.78 MN compared with the work of Johnston. Relative to *HPZ*s most relevant to design, he too may have picked up some very small *HPZ*s. This will be discussed further in the *Polar Sea* analysis in Section 4.4.

4.3.2 Zonal Force Modeling

The work by Zou (1996), being a foundation for improved local pressure modeling presented in Section 4.5, is considered in more detail. The analysis by Zou (1996) included 19 ram events and a combined total of 266 time slices. The occurrence of *HPZ* at different time slices is illustrated in Figure 102. At each time slice, the number of *HPZ*s can be identified and the *HPZ* force approximated as

$$F_{HPZ} = \sum_{i=1}^{n} p_i A_i \qquad (25)$$

where n is the number of active pressure sensors, p_i is the pressure on the i^{th} sensor, and A_i is the area represented by the i^{th} sensor.

Measured *HPZ* forces corresponding to the 266 time slices were ranked and plotted against exceedence probability. The Weibull plotting position

$$p_e = \frac{i}{(n+1)}, \qquad (26)$$

was used where i is the rank, and n is the number of the time slices. Depending on number of data points, other plotting positions could be considered as discussed by Jordaan (2005a) and Fuglem *et al.*, (2013).

As noted earlier, Zou (1996) studied two assumptions regarding the occurrence of *HPZ*s relative to the instrumented area. Assumption A assumed that all *HPZ*s were within the instrumented area. As a sensitivity, Assumption B considered that some *HPZ*s may have been present on the boundary. Resultant densities are illustrated in Table 8. *HPZ* forces

plotted against exceedence probability for both Assumption A and B as illustrated in Figure 104. *HPZ* forces consistent with Assumption A are reproduced in Figure 105.

The *HPZ* forces were fitted with an exponential distribution where probability is given as

$$p = \frac{1}{\gamma}\exp\left(\frac{-(x - x_1)}{\gamma}\right) \qquad (27)$$

and the parameters γ and x_1 estimated as 0.78 MN and 0.035 MN respectively.

The following sections discuss the sensitivity of cutoff force on the parameters γ and x_1 as well as *HPZ* density.

Table 8 Spatial density and mean *HPZ* area from *Louis S. St. Laurent* data (Zou, 1996)

	Assumption A assuming *HPZ*s fully within the design area	Assumption B Assuming *HPZ*s within and along boundary edge	
Spatial Density ρ	0.8927 zones/m^2	Within window 0.6183 zones/m^2	On border 0.1674 zones/m
Spatial Density ρ*	1.16 zones/m^2	0.80 zones/m^2	
Mean Zonal Area	0.0809 m^2	0.136	
Mean number of time slices for each ram: 9			

ρ* corresponds to the effective instrumented area of 1.25 m^2

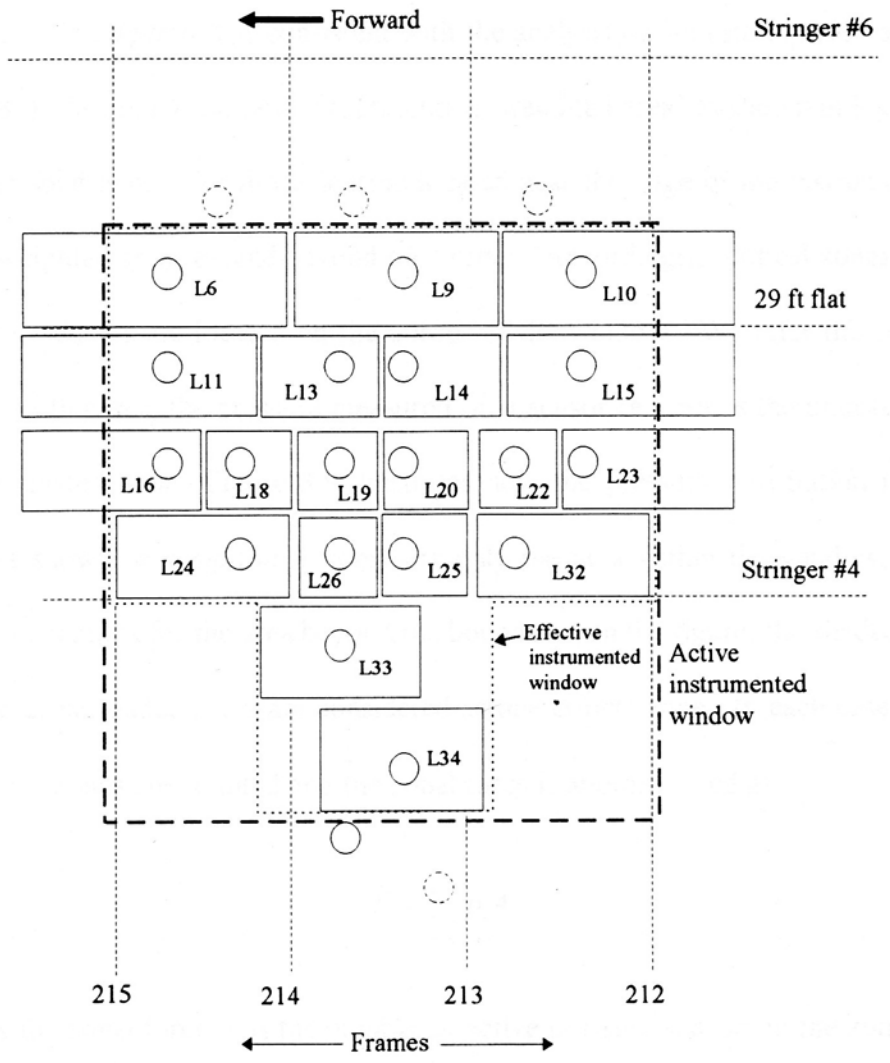

Figure 101 *Louis S. St-Laurent* measurement panel including location of pressure sensors, as well as assumed sensor region – dashed line encompassing active regions, dotted lines effective instrumented window, solid line rectangles sensor area (Zou, 1996)

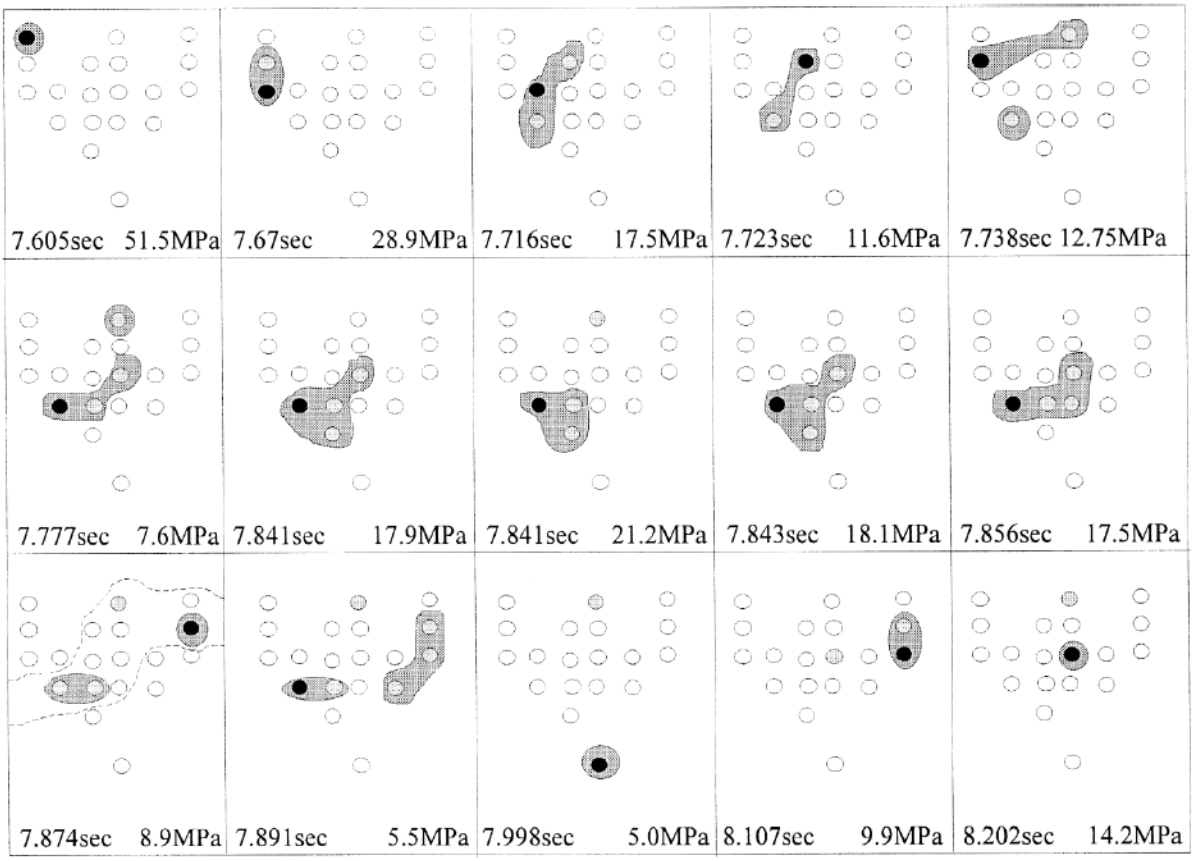

● Indicates transducer of maximum pressure
Instantaneous peak pressure is noted in lower right corner

Figure 102 Distribution of *HPZ* occurrence and pressure during a *Louis S St. Laurent* ram (Johnston *et al.*, 1998)

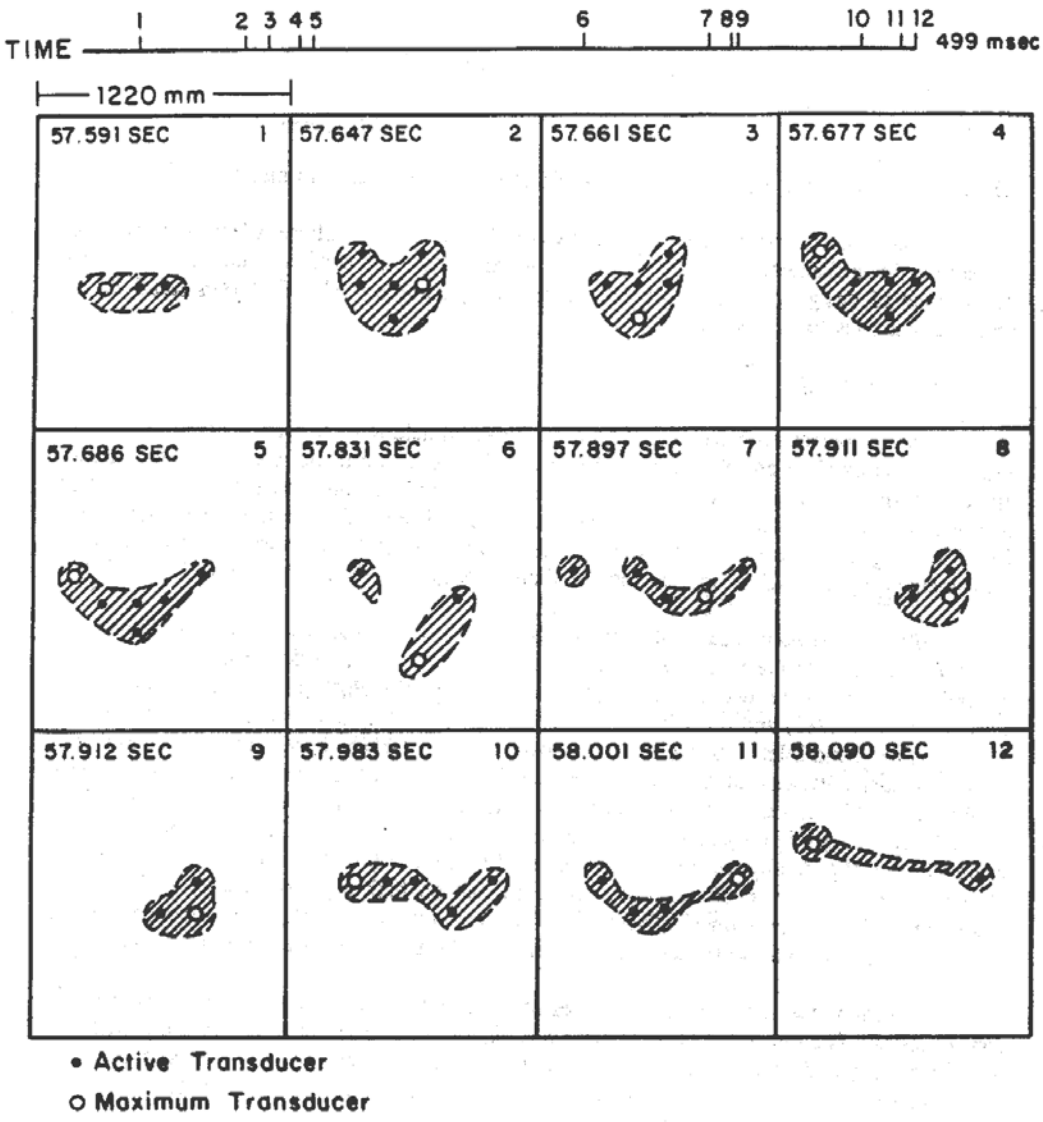

Figure 103 Distribution of *HPZ*s occurrence during a ram (Glen and Blount, 1984)

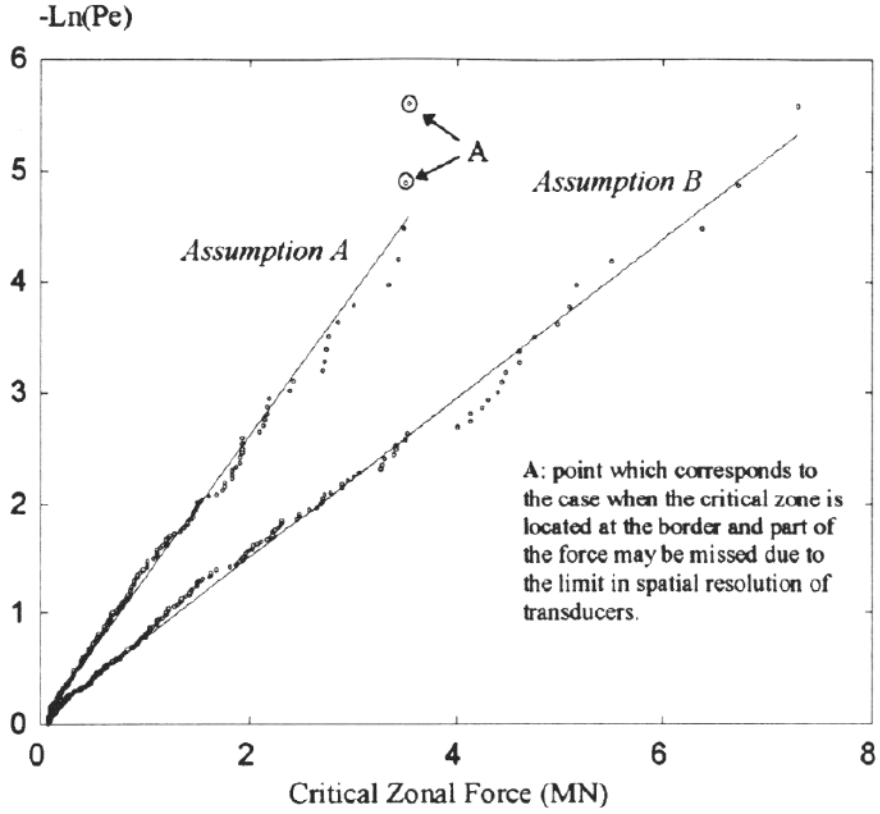

Figure 104 Distribution of measured *HPZ* forces considering Approach A, *HPZ*s fully within measurement window and Approach B, possibility of *HPZs* on perimeter of measurement window (Zou, 1996)

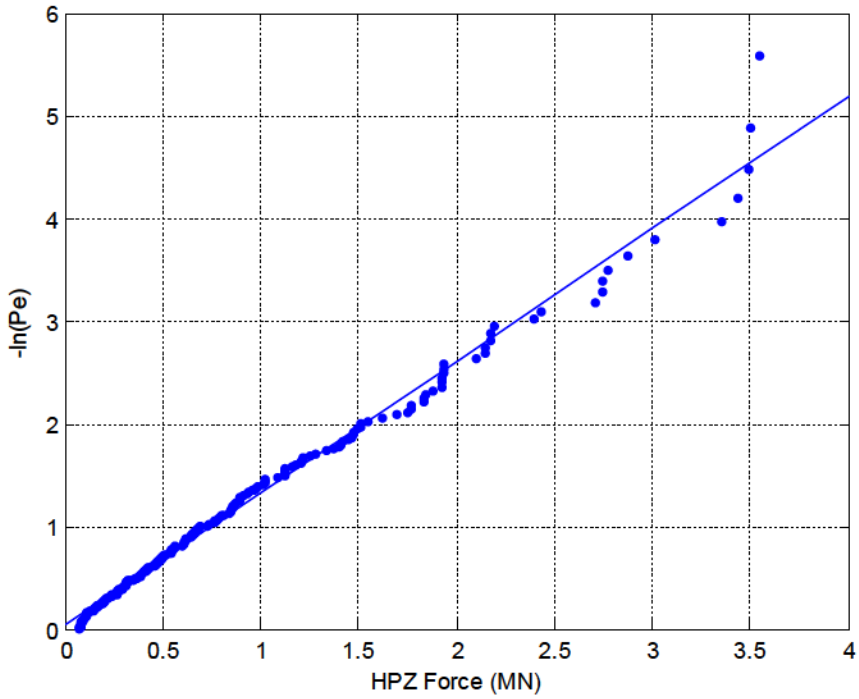

Figure 105 Distribution of measured *HPZ* forces from 1980 *Louis S. St. Laurent* trials using Assuming all *HPZ*s are within the instrumented area.

4.3.3 Monte Carlo Simulation of HPZ Occurrence

HPZ occurrence during interaction events can be simulated using a Monte Carlo process. In general, the *HPZ* force X can be approximated by a Gamma distribution

$$f_X(x) = \frac{1}{\Gamma(v)} \beta^v x^{v-1} e^{-\beta x} \qquad (28)$$

where the scale parameter β and the shape parameter v are given as

$$\beta = \frac{E(X)}{Var(X)} \qquad (29)$$
$$v = E(X)\beta$$

respectively and where $E(X)$ and $Var(X)$ are the mean and variance of the zonal force distribution.

The total force Y on a design area is the sum of n *HPZ* forces $\left(Y = \sum_{i=1}^{n} X_i \right)$

If the *HPZ* force follows an exponential distribution (i.e. the shape parameter v in Eq. (28) is 1), the distribution mean and variance are given as

$$f_X(x) = \beta e^{-\beta x} \qquad (30)$$

$$E(X) = \frac{1}{\beta}$$

$$Var(X) = \frac{1}{\beta^2}$$

The force distribution can be written in terms of the force parameter γ and shift parameter x_1 as given in Eq. 3, as

$$f_X(x) = \frac{1}{\gamma} \exp\left(\frac{-(x - x_1)}{\gamma} \right)$$

The cumulative distribution is given as

$$F_X(x) = 1 - \exp\left(\frac{-(x - x_1)}{\gamma} \right) \qquad (31)$$

Following a Monte Carlo simulation process, by randomly sampling $F_X(x)$ between 0 and 1, we can simulate random values of *HPZ* force for given parameters γ and x_1.

The expected number of *HPZ* within a specified area can be suitably modeled as a Poisson process as

$$P_N(n) = \frac{1}{n!} (\rho A)^n e^{-\rho A} \qquad (32)$$

where n is the number of individual *HPZs*, ρ is the *HPZ* density and A is the design area. Assuming *HPZ* forces follow an exponential distribution, the force for each simulated *HPZ* is randomly sampled using Eq. (31). The total force on a given design area is then the sum of the individual *HPZ* forces $\left(Y = \sum_{i=1}^{n} X_i \right)$. The average pressure on a design area is the total force divided by the design area, Y/A. An assumption with this analysis is that all *HPZs* are within the design area. An example distribution of simulated *HPZ* forces for a design

area of 5 m^2 is illustrated in Figure 106. For illustration, a gamma fit is presented but it is noted that for design, an exponential fit to the tail with appropriate cutoff may better represent the extreme forces.

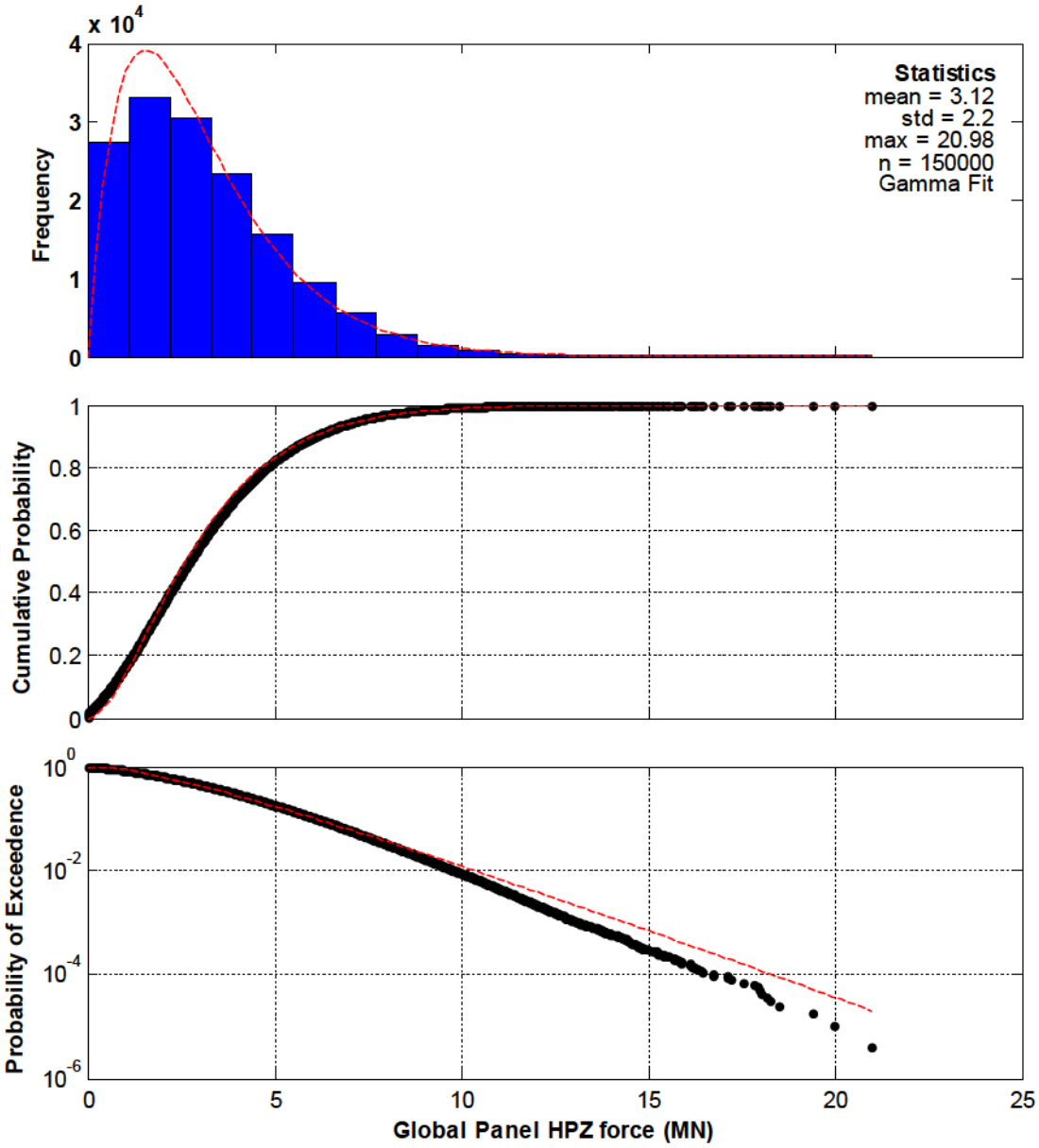

Figure 106 *HPZ* forces (ΣF_{HPZi}, where i is the number of *HPZ*s) on a 5 m^2 local panel area

4.3.4 Simulation of Local Pressure

Simulations of local *HPZ* forces and corresponding distribution of ranked pressures plotted as $-ln(p)$ on design areas ranging from 0.6 to 10 m^2 are illustrated in Figure 107. The number of *HPZ*s within a given area was modeled as a Poisson process as given in Eq. (32) assuming an *HPZ* density of 0.89/m^2. *HPZ* forces were modeled using an exponential distribution as in Eq. (31) with force parameter γ of 0.78 MN. Consistent with local pressure analysis of Jordaan *et al.*, (1993), an exponential fit was obtained to the tail of each local pressure distribution the parameter α and x_0 determined. Recall that the parameters α and x_0 represent the parameters that give a best fit for an exponential distribution to the tail of the local pressure data; x_0 being the plotting position. A plot of α and x_0 for design areas up to 10 m^2 and comparison to the ISO 19906 design curve is illustrated in Figure 108 and Figure 109.

The following sections discuss sensitivity of the force parameters γ, x_1, and *HPZ* density ρ on simulated local pressure design parameters α and x_0. In processing measured data from the LSSL 1980 trials, the sensitivity of *HPZ* cutoff force and influence on force parameters γ, x_1 and density ρ is studied including subsequent influence on local design parameters α and x_0.

The parameters for *HPZ* force and density, 0.78 MN and 0.89 zones/m^2 respectively, reasonably model the local pressure design curve. But as illustrated in Figure 34 and *Polar Sea* measurements, local pressure parameters vary across a wide range of ice conditions. It is important to understand how force and density vary also which is the focus of Section 4.4.

Note that the illustration of *HPZ* forces and comparison to ISO 19906 local design models, represent per impact scenarios on any panel. Exposure (i.e. number of expected impacts per year, number of panels, ram duration or penetration distance) is needed for design.

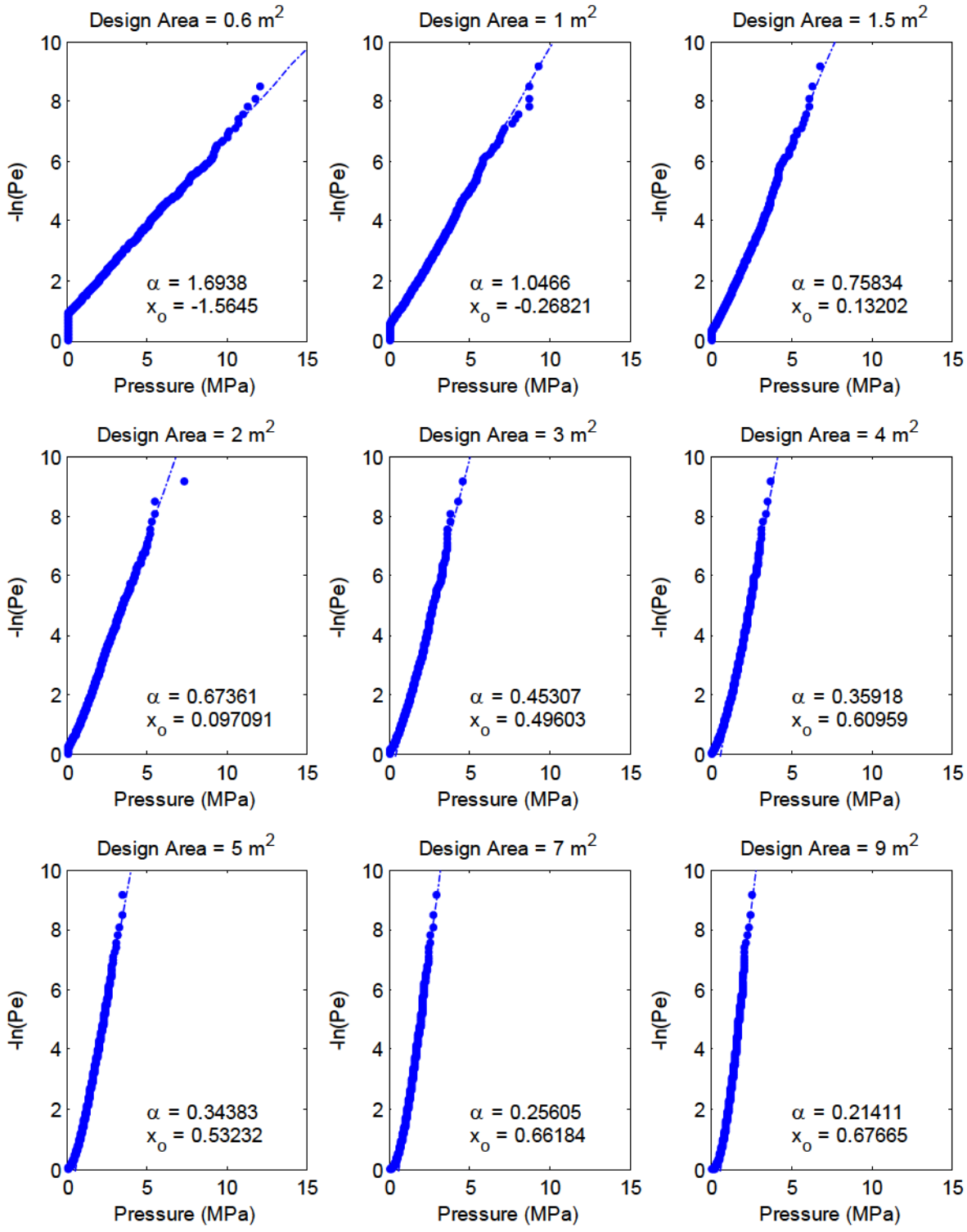

Figure 107 Probability plots for average local pressure on local design areas and estimation of local pressure parameters α and x_0 corresponding to an exponential fit to the tail of each simulated local pressure distribution based on *HPZ* density, $\rho = 0.89$ zones/m^2, and force parameter $\gamma = 0.78$ MN

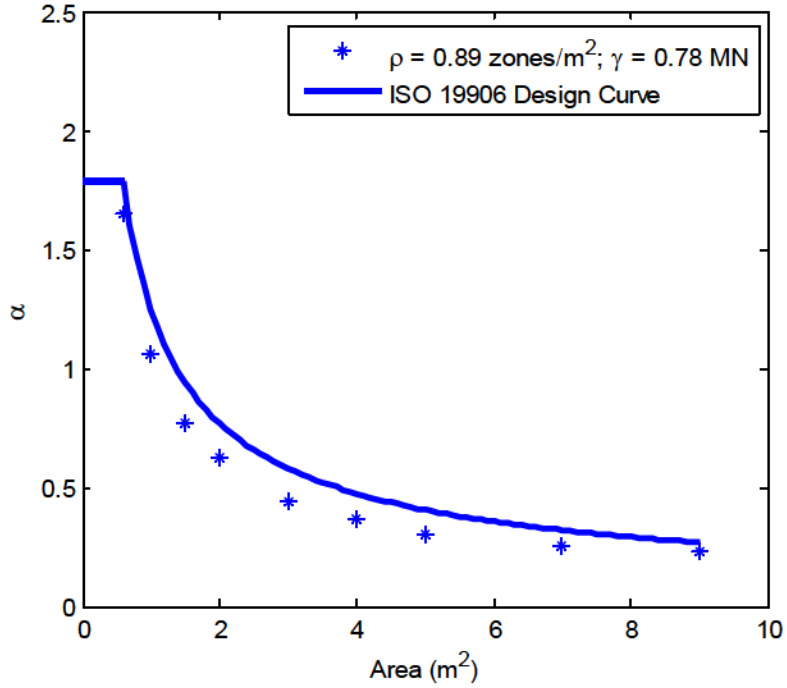

Figure 108 Comparison of ISO 19906 α design curve with simulation based α vs. contact area using *HPZ* density and force simulation model derived from analysis by Zou (1996) and *Louis S. St. Laurent* local pressure data.

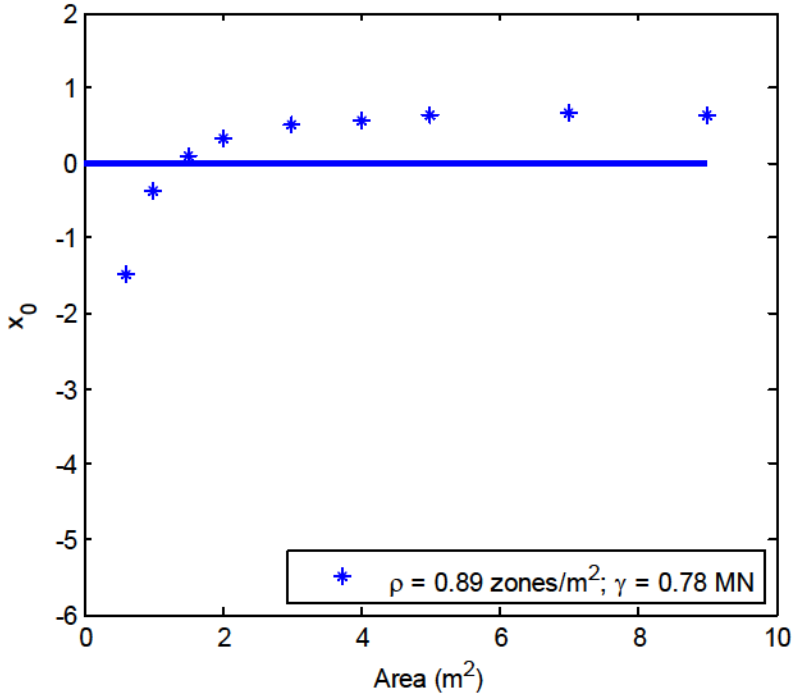

Figure 109 Illustration of x_0 vs. Area using *HPZ* density and force simulation model derived from *Louis S. St. Laurent* local pressure data.

4.3.5 Sensitivity of Local Pressure to HPZ Density and Force Parameter γ

The sensitivity of local pressure parameters α and x_0 vs. design area to *HPZ* density and force parameter γ is illustrated in Figure 110. With *HPZ* force parameter γ fixed at 0.78MN, *HPZ* densities were varied from 0.4 to 1.2 zones/m^2. With density fixed at 0.89 zones/m^2, the force parameter γ was varied from 0.4 to 1.2 MN. Comparing the top two subplots, we see that the local design parameter α is quite sensitive to *HPZ* force parameter but relatively insensitive to density. Looking at the bottom two subplots, we observe neither force nor density have great influence on x_0.

Looking at the two left most subplots, the observed influence of density is to shift the whole pressure distribution: the lower the density, the lower x_0; the higher the density the greater x_0. Also, the smaller the density, the greater the number of probable misses on a single panel. Hence density can be correlated to individual panel exposure. Looking at the two right most subplots, the influence of force on x_0 is very small compared with α. While only marginally sensitive however, we observe an interesting trend. As the force parameter gets smaller, x_0 approaches zero. With density modeled at 0.89 zones/m^2, the crossover (i.e. x_0 = 0) occurs between 1.5 and 2m^2. With increasing force, x_0 values are more negative for areas less than the crossover, and greater for areas larger than the crossover area. Stronger ice having the greatest *HPZ* failure forces will have increased number of misses (i.e. no *HPZ* occurrence) on smallest single panels; hence lower x_0. While the notion of a 'total' miss may not be correct, pressures may be very small relative to higher *HPZ* design pressures. Yet on larger areas, greater *HPZ* force leads to increased average panel pressure and hence increased x_0.

The area corresponding to the crossover will increase with reduced density. It is noted that for design of extremes with many impacts, x_0 will have less significance.

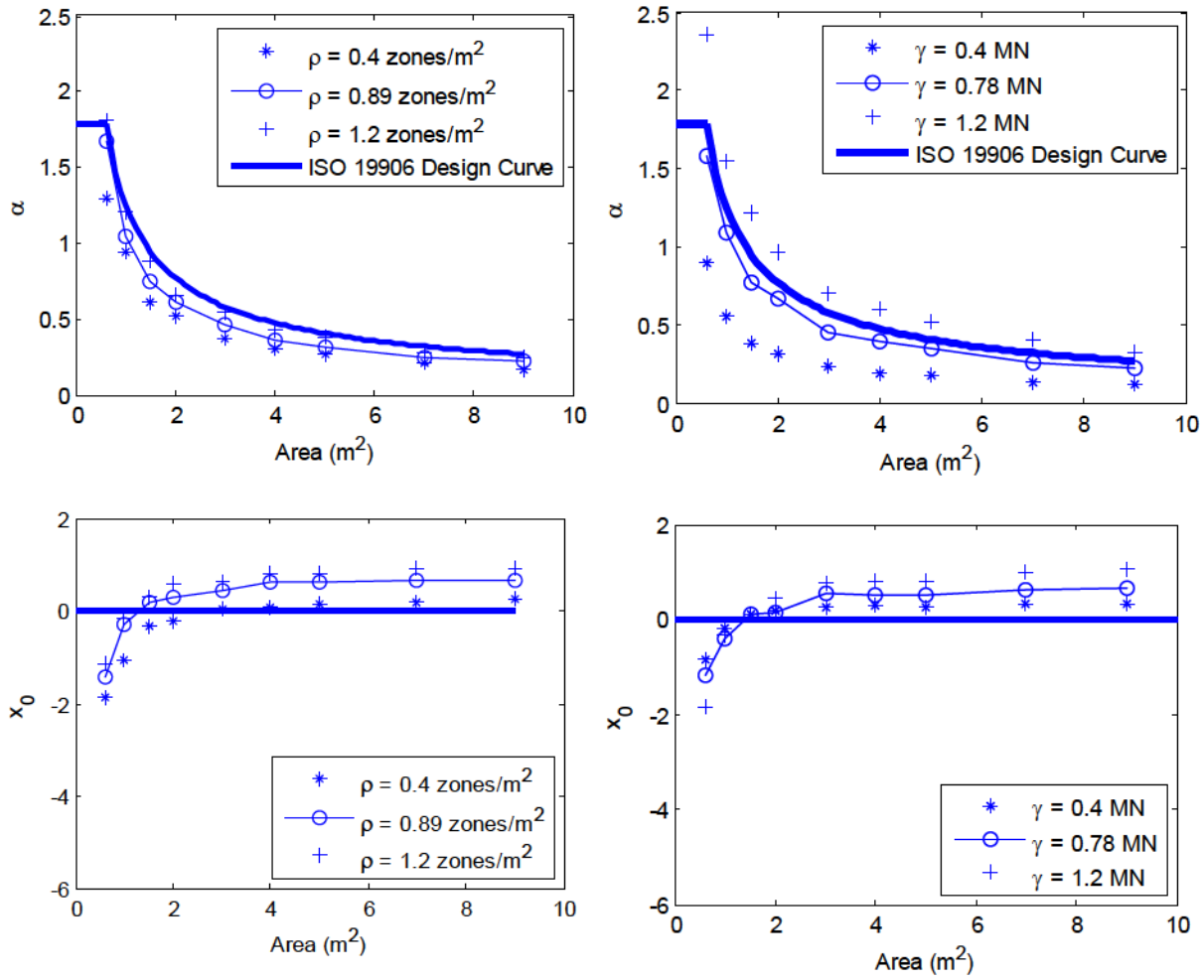

Figure 110 Sensitivity of local pressure parameters α and x_0 vs. Area to *HPZ* density ρ and force parameter γ.

4.3.6 Influence of HPZ Force Cutoff

The influence of *HPZ* force cutoffs ranging from 0.25 MN up to 2 MN were analyzed. A force cutoff of 1 MN and the resultant γ and x_1 is illustrated in Figure 111. The influence of force cutoffs on *HPZ* density, *HPZ* area as well as for the exponential force parameter γ and γ_0 are given in Table 9 and illustrated Figure 112. Increasing force cutoff is equivalent to removing *HPZs* from the dataset. Reduction in *HPZ* density with cutoff force can be approximated as

$$\rho_{CO} = \rho_0\left(1 - \frac{n(X < x_{CO})}{n(X)}\right) \qquad (33)$$

where ρ_0 is the original density for no cutoff (i.e. 0.89 *HPZs*/m^2) and X represents *HPZ* forces from the distribution relative to x_{CO}, the cutoff force.

As Table 9 and Figure 112 illustrate, x_1 increases with increased force cutoff and *HPZ* density drops as smaller *HPZs* are removed. The force parameter γ remains relatively unchanged since it is weighted towards the tail of the force distribution. The mean *HPZ* area increases with increased cutoff force as smaller *HPZs* are removed. For modeling purposes application of a cutoff force may be used but only with the correct density adjustment. The same applies for applying *HPZ* forces over a structural area. If higher cutoff forces are modeled which reduce density, the corresponding increase in *HPZ* effective area should be considered.

Local pressure simulations were carried out to further model the influence of cutoff force and corresponding γ_0 and decrease in *HPZ* density. For these simulations, the force parameter γ was modeled as 0.78MN consistent with Zou (1996). Distributions of simulated *HPZ* pressures on design areas for cutoff forces 0.75MN and 1.5MN and corresponding densities 0.314 zones/m^2 and 0.124 zones/m^2 respectively are illustrated in Figure 113 and Figure 114. The influence of cutoff force and density on the simulated local pressure parameters α and x_0 are illustrated in Figure 115. Cutoff force has a negligible influence on the local pressure parameter α assuming the correct density and cutoff force are properly selected. To choose a cutoff force without modeling the correct change in density will lead to conservatism in the simulation results as illustrated in Figure 116. Similarly for x_0, while the influence of cutoff

force and density is not as significant as with α, modeling the correct combination of both is needed to avoid over conservatism in simulation.

The conclusion is that local pressure parameters α and x_0 are influenced primarily by *HPZ* force and corresponding exponential parameter γ. Establishing the correct *HPZ* force from data is imperative. The influence of density is considerably less having greatest influence on the position of local pressure distribution, x_0. Modeling cutoff forces must consider a corresponding change in *HPZ* density.

It is also important to note that a measurement system and programmed thresholds may influence estimates of force and density that may not necessarily reflect material properties. The same applies to the application of cutoff forces to artificially introduce conservatism in results. Estimates of density may be biased and for simulation must be accounted for.

As illustrated in Figure 113 and Figure 114 another influence of density in simulating local pressures, particularly for smaller areas, is the sampling of Poisson based zeros (i.e. zero *HPZ* occurrence or panel misses). Depending on density, for smaller areas there is an increased probability of having no *HPZ* simulated on a single panel. The zero pressures result in a probability spike at zero which is directly correlated with x_0. (i.e. the lower the density, the greater the number of zeros and the lesser x_0. As will be discussed further in the following section, density can be related to panel exposure. With regard to position on the ship, increased exposure and increased density may be expected nearer the bow compared with shoulder and outer bow.

Table 9 Influence of *HPZ* force cutoff on *HPZ* density, area, and force model parameters

		***HPZ* Force Cutoff (MN)**						
		0	**0.25**	**0.5**	**0.75**	**1**	**1.5**	**2**
HPZ Density		0.89	0.629	0.435	0.314	0.218	0.124	0.064
HPZ Area		0.081	0.095	0.109	0.117	0.129	0.151	0.159
Force Parameter Exponential Fit	γ	0.78	0.79	0.80	0.80	0.79	0.73	0.70
	x_1	0	0.25	0.5	1.0	1.0	1.5	2.0

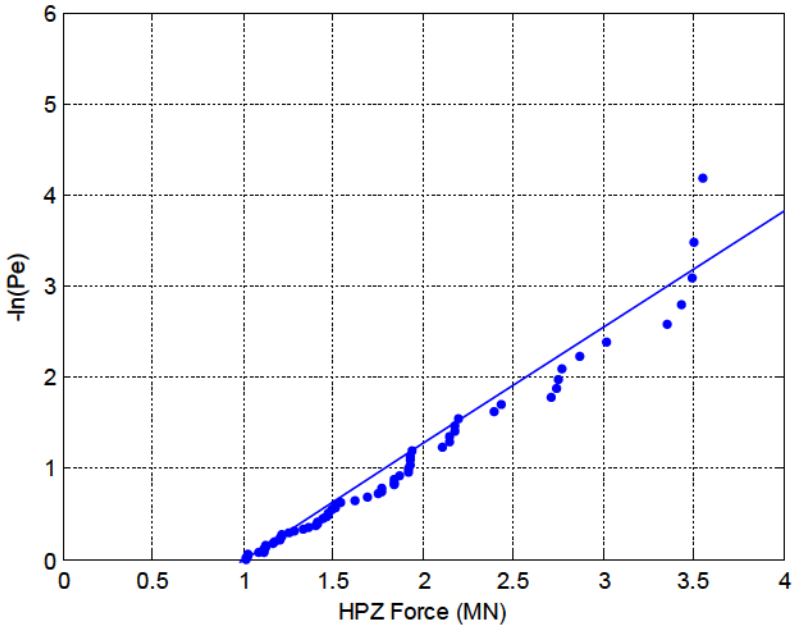

Figure 111 Illustration of *HPZ* Force cutoff of 1 MN giving γ = 0.78 MN and x_0 = 1.0 MN. Corresponding density is 0.218 zones/m^2 (see Table 9)

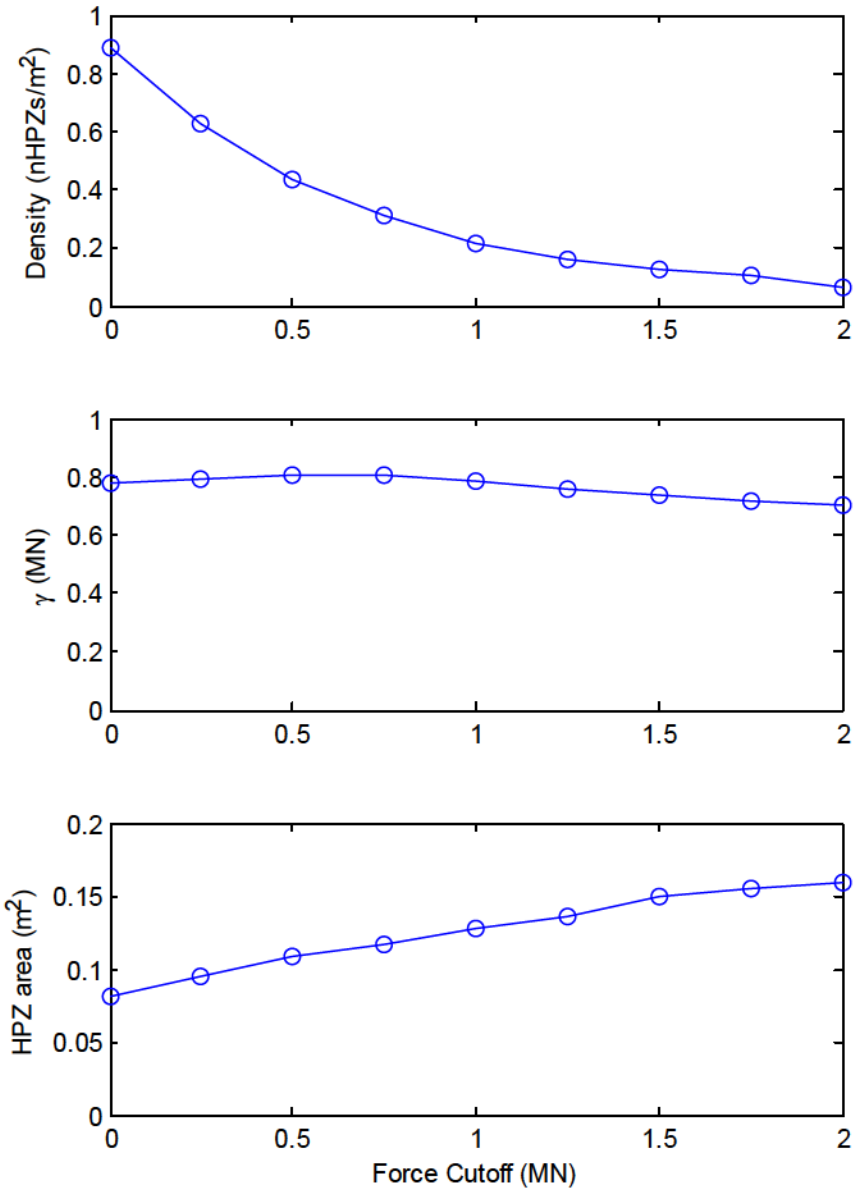

Figure 112 Influence of *HPZ* Force cutoff on *HPZ* density, force parameter γ and area.

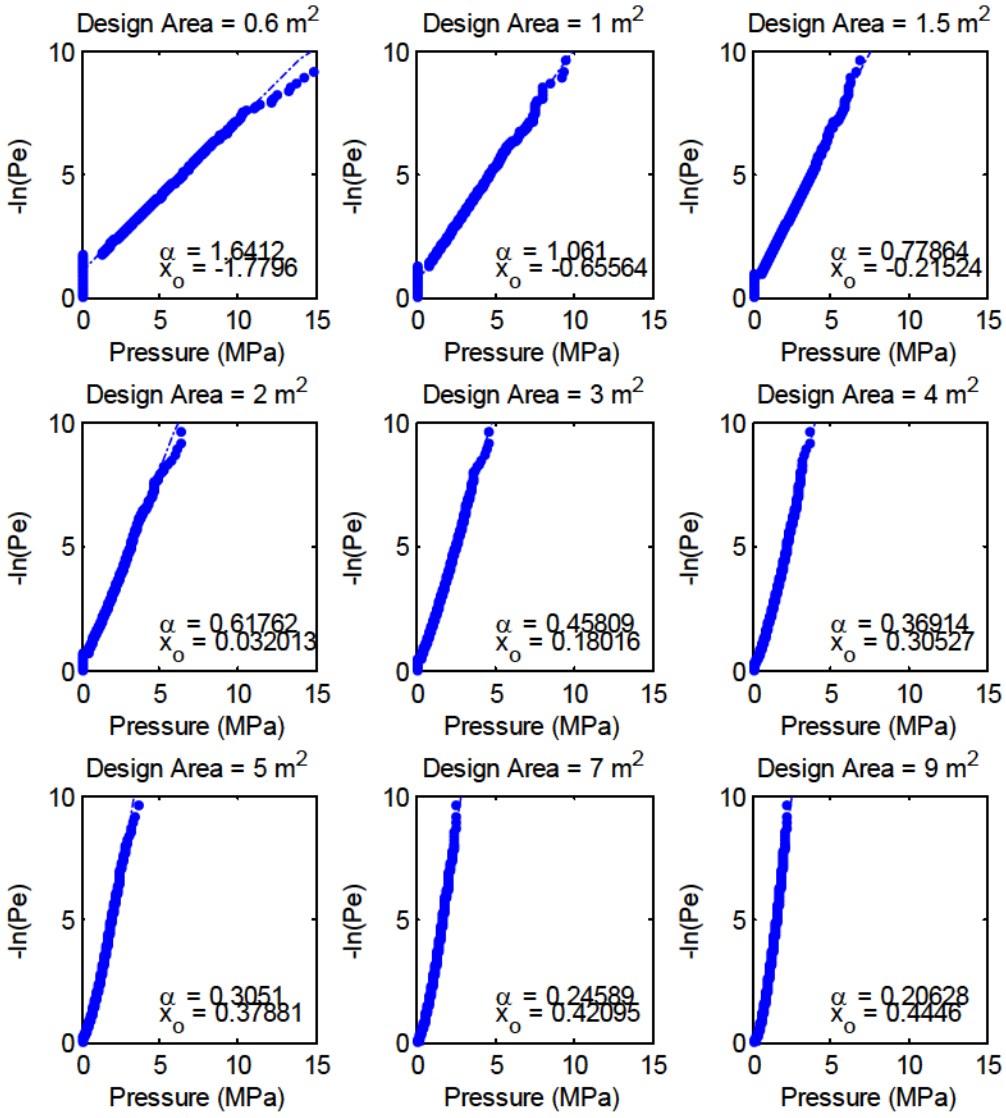

Figure 113 Probability plots for average local pressure on design areas and corresponding parameter α corresponding to an exponential fit to the tail of each distribution based on *HPZ* Cutoff force of 0.75MN and corresponding density, $\rho = 0.314$ zones/m^2, and $\gamma = 0.78$ MN

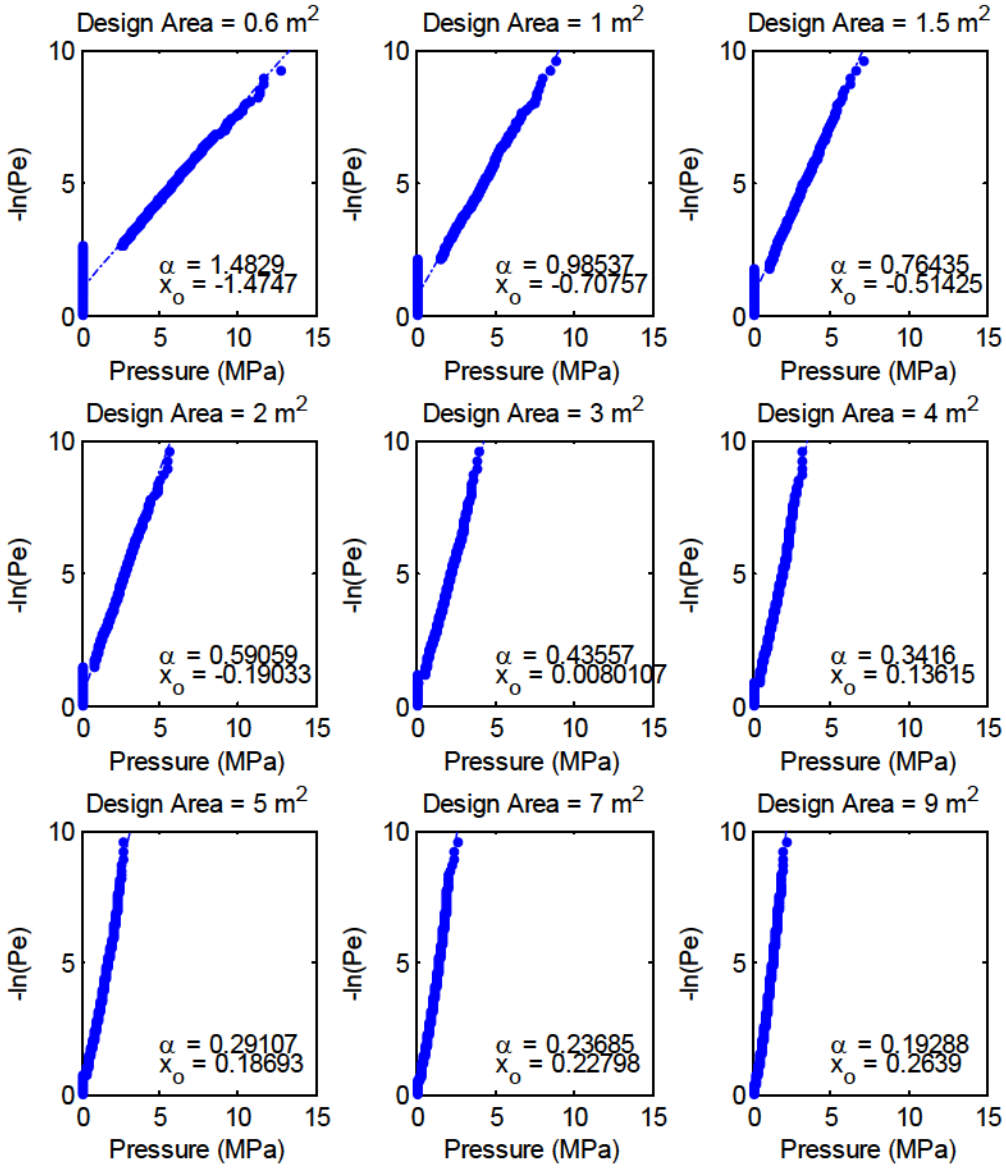

Figure 114 Probability plots for average local pressure on design areas and corresponding parameter α corresponding to an exponential fit to the tail of each distribution based on *HPZ* Cutoff force of 1.5MN and corresponding density, $\rho = 0.12$ zones/m^2, and $\gamma = 0.78$ MN

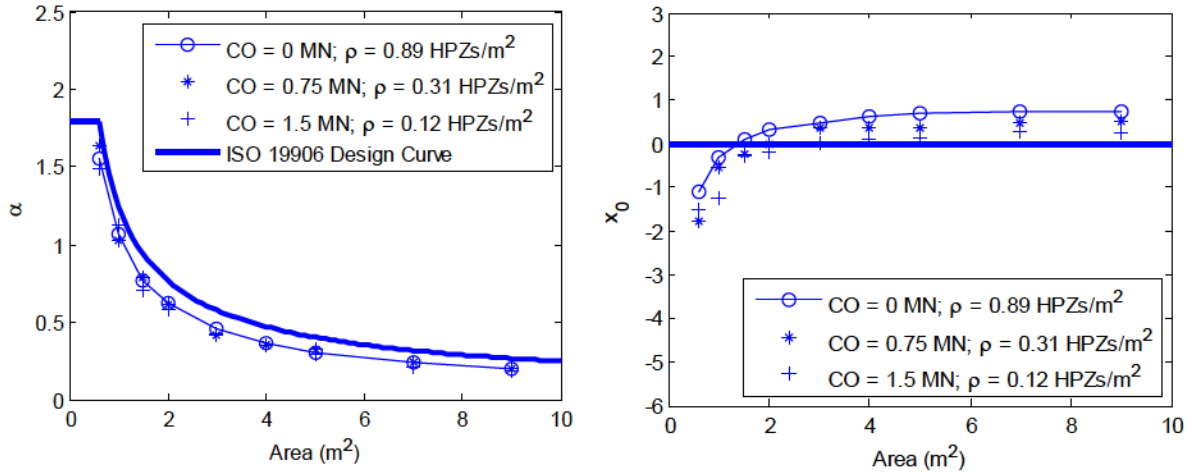

Figure 115 Sensitivity of *HPZ* force cutoff (CO) and parameters density ρ and x_0 on local pressure parameters α and x_0 vs Area in Table 9.

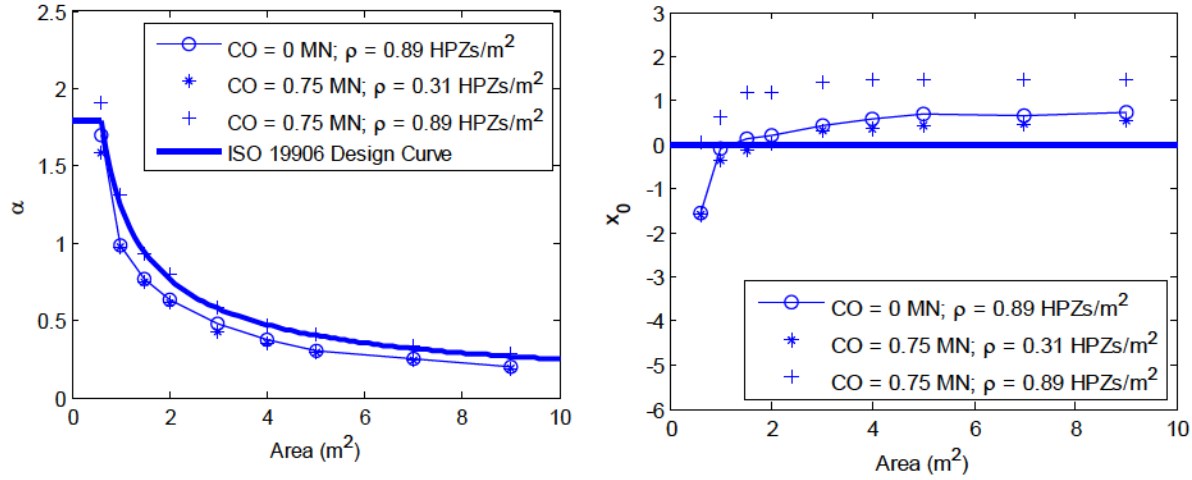

Figure 116 The influence of cutoff force CO = 0.75MN with and without corresponding density drop on local pressure parameters

4.3.7 Poisson Simulated Panel Misses

Depending on *HPZ* density and panel area, the Poisson simulation process will result in misses or zero *HPZ*s as illustrated in Figure 107, Figure 113 and Figure 114. These result in a probability spike at zero pressure which is directly proportional to x_0. The lower the density the greater the probability of no *HPZ* occurring and the lower (i.e. more negative) the

x_0 parameter. The parameter γ is unchanged. The proportion of misses as a function of design area based on *HPZ* simulation parameters γ = 0.78 MN, ρ = 0.89 zones/m^2 is illustrated in Table 10 – note that panel misses are equal to 1 minus the panel hits (i.e. 1 – hits).

Figure 117, Figure 118 and Figure 119 illustrate the influence of *HPZ* cutoff force γ_0, plus the removal of simulated zero *HPZ*s; removal of the probability spike at zero and positive shift of the local pressure plotting position parameter x_0. Figure 120 illustrates the influence on simulated local pressure parameter α and x_0. The parameter α is unaffected since it is weighted toward the tail of the distribution. The parameter x_0 is shifted considerably in the positive direction. The areas greater than 3 m^2 have negligible influence since the probability of simulating a miss (or Poisson zero) is very small. Note however that misses are a direct function of *HPZ* density.

Two options are considered to account for simulated *HPZ* zeros or misses: 1) direct simulation based on density and force parameters; or 2) or modeled separately based on the proportion of misses as a function of area as illustrated in Table 10. These misses would be accounted for by adjusting the plotting position for the distribution of simulated *HPZ* forces.

Table 10 Proportion of simulated *HPZ* occurrences (i.e. [1 – misses]) based on Poisson sampling – γ = 0.78 MN, ρ = 0.89zones/m^2.

Area	Proportion hits
0.6	0.51
0.8	0.61
1.0	0.69
2.0	0.91
3.0	0.97
4.0	0.99
5.0	0.99
7.0	1.0
9.0	1.0

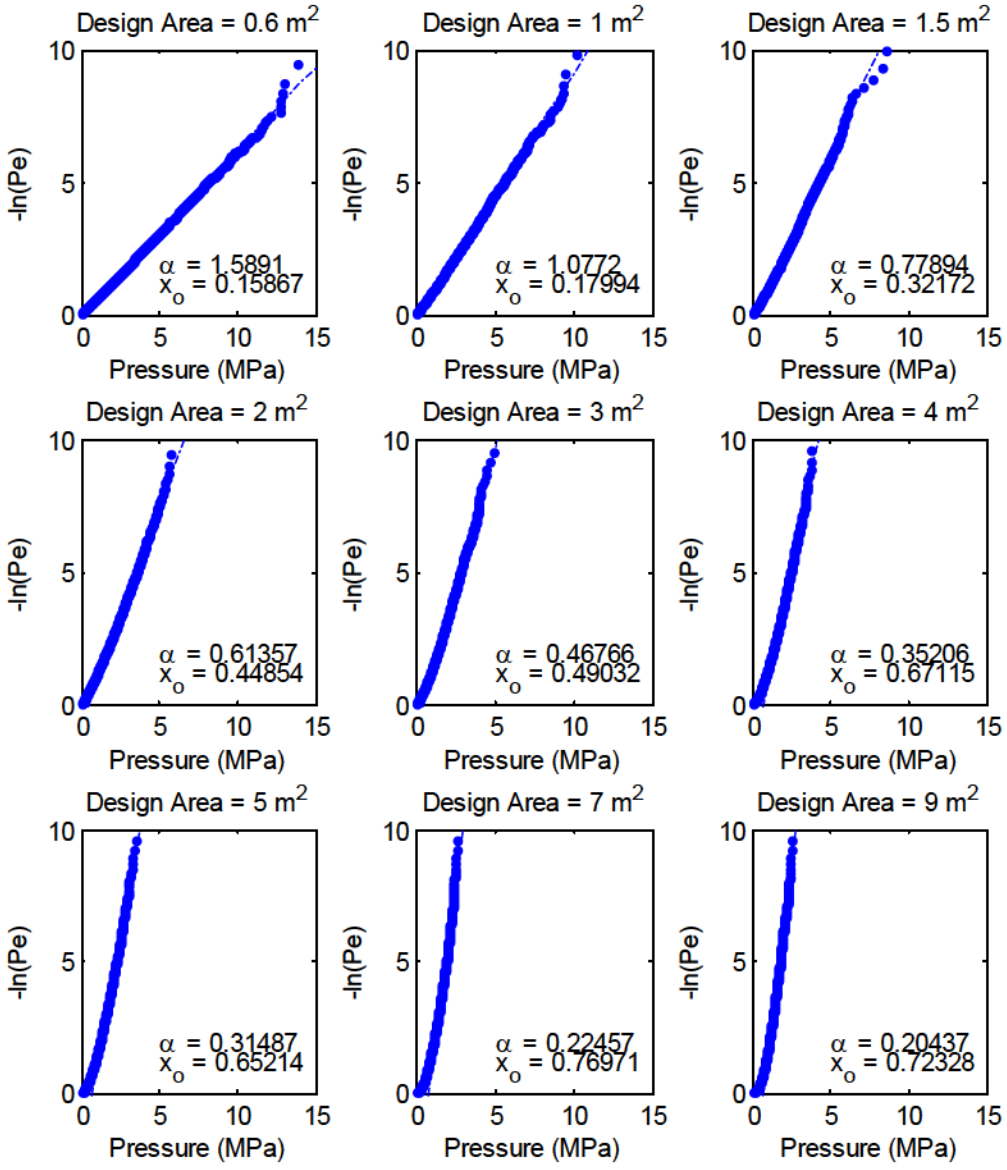

Figure 117 Probability plots for average local pressure on design areas and corresponding parameter α corresponding to a exponential fit to the tail of each distribution based on *HPZ* density, $\rho = 0.89$ zones/m^2, and $\gamma = 0.78$ MN – Simulated zeros removed compared with Figure 107

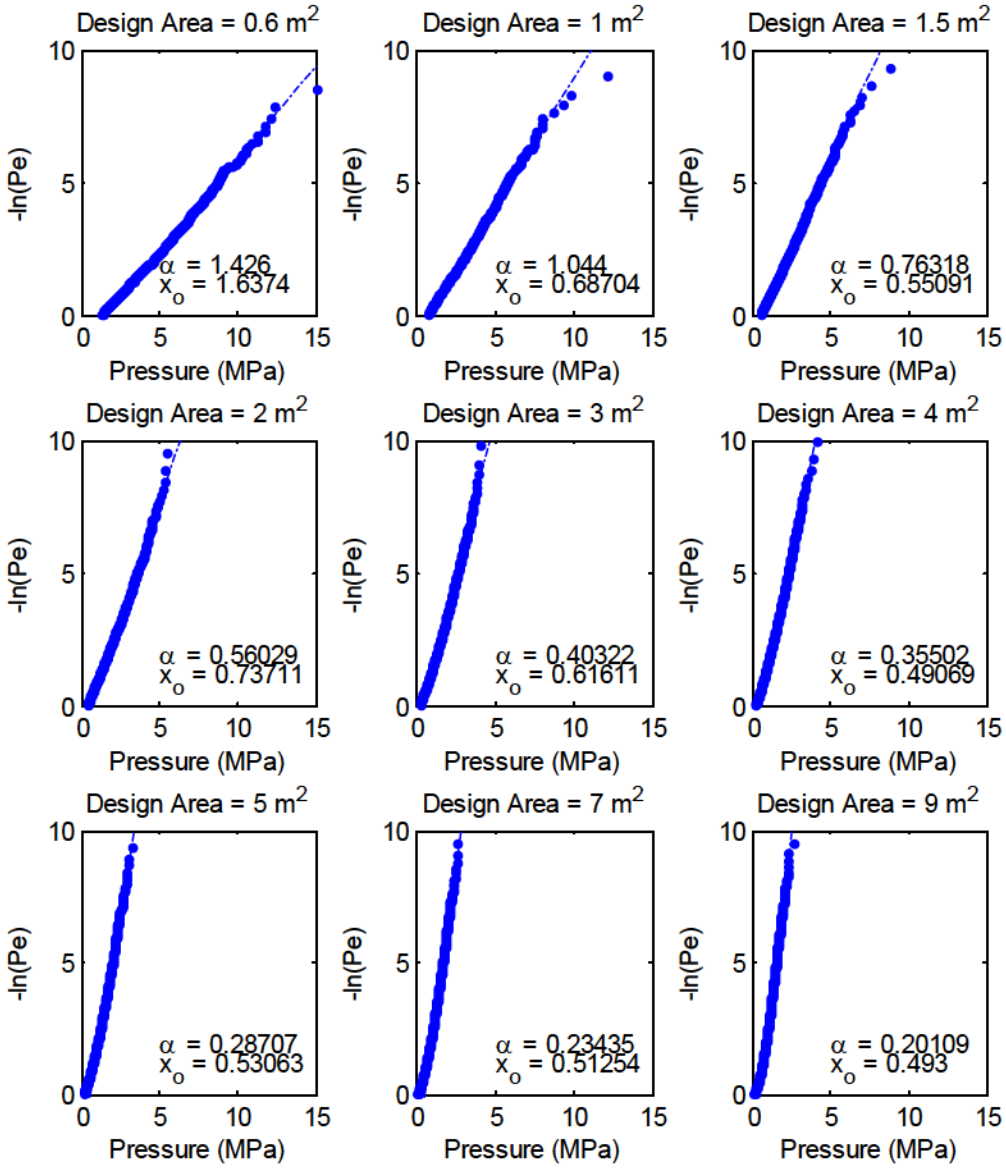

Figure 118 Probability plots for average local pressure on design areas and corresponding parameter α corresponding to a exponential fit to the tail of each distribution based on *HPZ* Cutoff force of 0.75MN and corresponding density, $\rho = 0.314$ zones/m^2, and $\gamma = 0.78$ MN – Simulated zeros removed

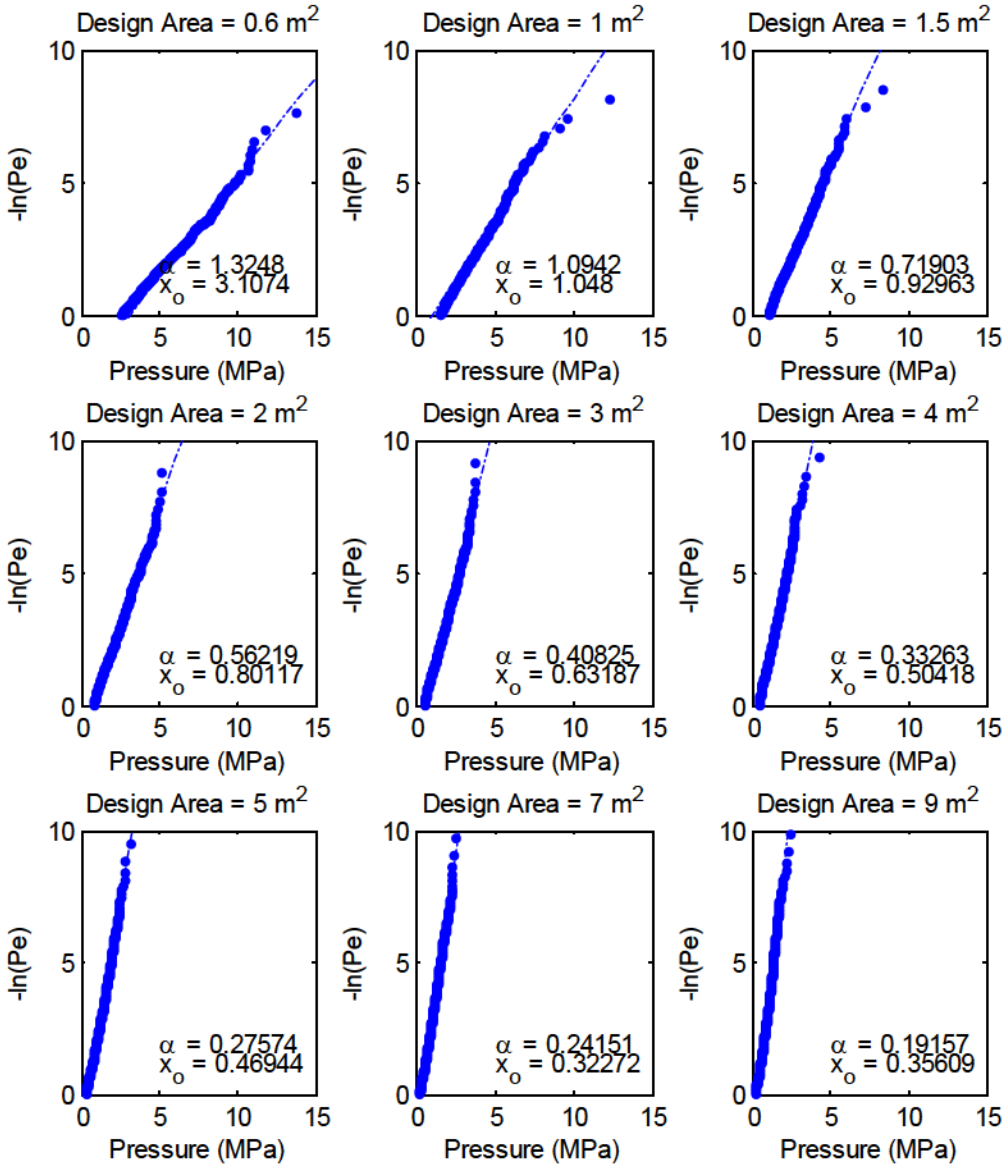

Figure 119 Probability plots for average local pressure on design areas and corresponding parameter α corresponding to a exponential fit to the tail of each distribution based on *HPZ* Cutoff force of 1.5MN and corresponding density, $\rho = 0.12$ zones/m^2, and $\gamma = 0.78$ MN – Simulated zeros removed

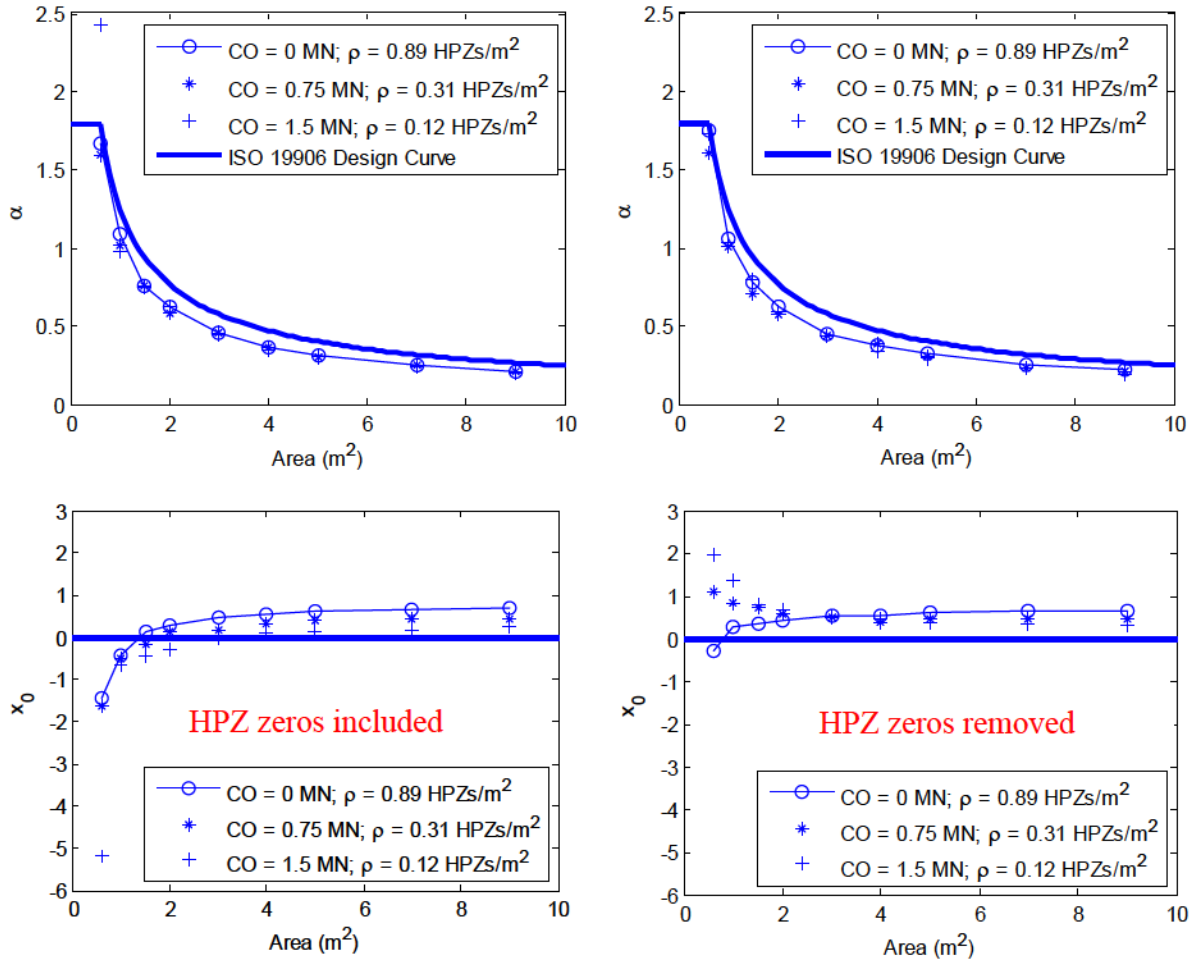

Figure 120 Sensitivity of *HPZ* force cutoff on local pressure parameters α and x_0 vs Area based on *HPZ* force parameters density ρ and x_0 in Table 9 but with Poisson simulated misses on small areas removed. The greater the cutoff force, the greater the x_0 for small areas. Larger areas are unchanged.

4.3.8 Exposure

Exposure models the extent to which the whole ship or part of the ship's hull is likely to encounter hits. The higher the exposure the greater the design requirements. Application of exposure for local pressure was first discussed in this thesis in Section 2.3.3.3. Exposure in general considers:

- the number of expected ramming events with extreme features per unit time (e.g. a year) and includes for example contact with MY ice and icebergs along shipping routes and/or breaking ridges using an ice management;

- the duration of interaction events;
- number of panels exposed within the interaction zone; and
- location on the hull (i.e. bow has more contacts than side or stern and some rams are on one side of the bow).

Event Based Exposure (e.g. Annual Exposure) considers the number of rams or interactions within a given time period (e.g. a year). For extremal design, it is the maximum pressure Z of n expected rams and corresponding pressures X_n within a specific time frame given as

$$Z = \max(X_1, X_2, X_3, ..., X_n,) \quad (34)$$

If the number of ram events is fixed in time and events are independently identically distributed (*iid*), the resultant distribution of extremal forces can be modeled as

$$F_Z(z) = [F_X(x)]^n \quad (35)$$

F_X being the 'parent' cumulative distribution for any ram event. This is also equivalent is to sampling n ram pressures (e.g. 100 rams per year) from the 'parent' 'per impact' distribution $F_X(x)$, choosing the largest and throwing out the others. The process is repeated until a new distribution $F_Z(z)$ of extreme pressures is obtained having sufficient data points to accurately determine characteristic design values based on target return periods or annual exceedence probabilities (e.g. 1/100 year or 10^{-2} annual exceedence probability; 1/10,000 year or 10^{-4} annual exceedence probability).

The occurrence of events will likely be random in nature and modeling events using a Poisson process is appropriate. The extremal distribution will follow

$$F_Z(z) = \exp\{-\mu[1 - F_X(x)]\} \quad (36)$$

where μ is the average equivalent number of rams in a year.

If pressures follow an exponential distribution,

$$F_X(x) = 1 - \exp\left[\frac{x - x_0}{\alpha}\right] \quad (37)$$

where α and x_0 are the distribution parameters, extremal design pressures will follow

$$F_Z(z) = \exp\left\{-\mu \exp\left[\frac{x - x_0}{\alpha}\right]\right\}. \quad (38)$$

This approach is conceptually consistent with design for extreme waves where the cumulative distribution for single wave height follows the Raleigh distribution

$$F_H(h) = 1 - \exp\left[-2\left(\frac{h}{H_S}\right)^2\right], \quad (39)$$

H_S being the significant wave height. Using Eq. (35), the extreme wave height distribution based on n waves per storm is then modeled as

$$F_Z(z) = \left\{1 - \exp\left[-2\left(\frac{z}{H_S}\right)^2\right]\right\}^n \quad (40)$$

Depending on location, the number waves n per storm can be 10, 100, 1000 ...etc.

Event Duration Exposure considers the interaction time associated with individual ram events. Events may be short in duration lasting seconds, or continuous interaction lasting minutes or days (See Figure 32 for illustration of a ram lasting several seconds and Figure 121 for events lasting several minutes). In this work, focus is MY ice or iceberg interactions having relatively short durations. The maximum pressure through the ram duration is

$$Z = \max(X_1, X_2, X_3, ..., X_i), \quad (41)$$

with i representing the number of time slices through the ram.

Larger and faster ships having greater kinetic energy will penetrate further into an ice floe. Duration may also relate to the length of transect through an ice feature. For any given ram event, the duration would be the lesser of time to crush a distance x before the vessel stops or time to transect though the flow. For design we are concerned with peak pressures through the full ram duration. The longer the duration, the greater the probability of encountering stronger ice and larger pressures or *HPZ*s.

Duration can be considered using a couple of approaches. Jordaan (2001) suggests scaling equivalent exposure (i.e. equivalent number of rams) based on the ratio of expected ram duration for new ship design t_{new} to average *Kigoriak* ram duration t_{Kig} = 0.7s (i.e. $t_{new}/t_{Kig} = t_{new}/0.7$). *Kigoriak* measurements are considered very aggressive ramming conditions

representing a reasonable upper bound on local pressures for equivalent *Kigoriak* ram conditions (i.e. similar ship). The local pressure design parameter α (fit to exponential fit to tail of peak ram pressures on panel areas) is modeled as a function of area and given as $\alpha = 1.25A^{-0.7}$. Intuitively, a larger faster ship would have a longer ram duration which ultimately increases the exposure μ, and the equivalent number of rams.

An alternative approach to modeling duration is to estimate the rate at which *HPZ*s occur for any given ram. Rate multiplied by ram duration is a measure of *HPZ* occurrence through the ram. A Poisson process can model *n HPZ* occurrences through the ram based on *HPZ* formation rate and duration as

$$F_Z(z) = \exp\{-\mu_r[1 - F_X(x)]\} \quad (42)$$

where $\mu_r = Rate \times Duration$. Consistent with modeling of extremes, the maximum of *n HPZ* pressures through the ram duration is needed for design. This is consistent with the approach to analyzing local pressures, determining the maximum pressure on any panel through the full ram duration. The challenge is determining the *HPZ* rate and possible correlation with ship ram speed.

Derivation of *HPZ* rate is discussed in Section 4.5 based on local pressure simulations and measurements. A suggested relationship between *HPZ* rate and average ram speed is presented.

Panel Exposure considers the maximum pressure on any panel within an array of *m* subpanels within the contact area. Extreme panel pressures are modeled as

$$Z = \max(X_1, X_2, X_3, ..., X_m,) \quad (43)$$

For design, one is interested in the maximum pressure on a single panel of *m* subpanels given as

$$F_Z(z) = [F_X(x)]^m \quad (44)$$

$F_X(x)$ represents the cumulative 'parent' distribution of pressures on 'any' panel. In extremal modeling, we may be concerned for the maximum pressure on a single panel out of *m* subpanels within a nominal contact area. The larger the contact area, and increased number

of subpanels, the greater the probability of a larger pressure on a single panel. If looking at measured data, it is appropriate to determine the peak pressure among m subpanels through a ram duration. Without adjustment for exposure, this distribution is intuitively an extreme distribution. To determine parameters for the 'parent' panel distribution (i.e. pressures on any panel), exposure is considered by adjusting or scaling the plotting position according to

$$p_e = \frac{i}{m \times j + 1} \qquad (45)$$

where i is the rank of data point, j is the number rams in the distribution and m is the number of subpanels. For *Polar Sea* measurements, m for a 0.6m^2 panel area (4 × 0.15m^2 subpanels) is 9.1 m^2 / 0.6 m^2 (or 60 subpanels / 4 subpanels) = 15. The required probability shift to model the correct parent distribution is ~1/15. For a 1.8m^2 panel m represents 12 × 0.15 subpanels and the exposure is 60 / 12 = 9.1 / 1.8 = 5.

For *Polar Sea* measurements, it is assumed that the whole measurement panel at 9.1m^2 (60 sensors) is exposed. It could be argued that the full 60 panel exposure may be too high and often only part of the panel was contacted. However it is reasonable to assume that missed panels were part of the randomness associated with ice structure interaction. There may be cases in the data where thinner first year ice was encountered, but for the MY data of interest in this work, it is reasonable that a full 60 sensor area is considered. One could look at sensitivity to x_0 assuming an exposure based on 50 panels (5 rows vs. 6). However, it is noted that the actual sensor on the *Polar Sea* was 10 columns by 8 rows or 80 subpanels. For each set of trials, depending on the expected exposure for the whole sensor area, only 6 of the 8 rows of subpanels were activated. While choice of sensor rows would be in part influenced by the vessel draft, the active sensor was selected based ice conditions and expected contact. It seems reasonable that exposure adjustment for *Polar Sea* trials be based on 60 subpanels.

Local Hull Exposure considers the region or position of impacts on the hull. For a ship or ship form offshore production facility, the bow will have more impacts than a side or stern panel, particularly if the system is naturally weathervaning. Figure 122 and Table 11 illustrate hull exposure using area factors; proportioning of the whole hull relative to the bow

(IACS, 2011). Extremal analysis and equivalent exposure can be factored based on these factors.

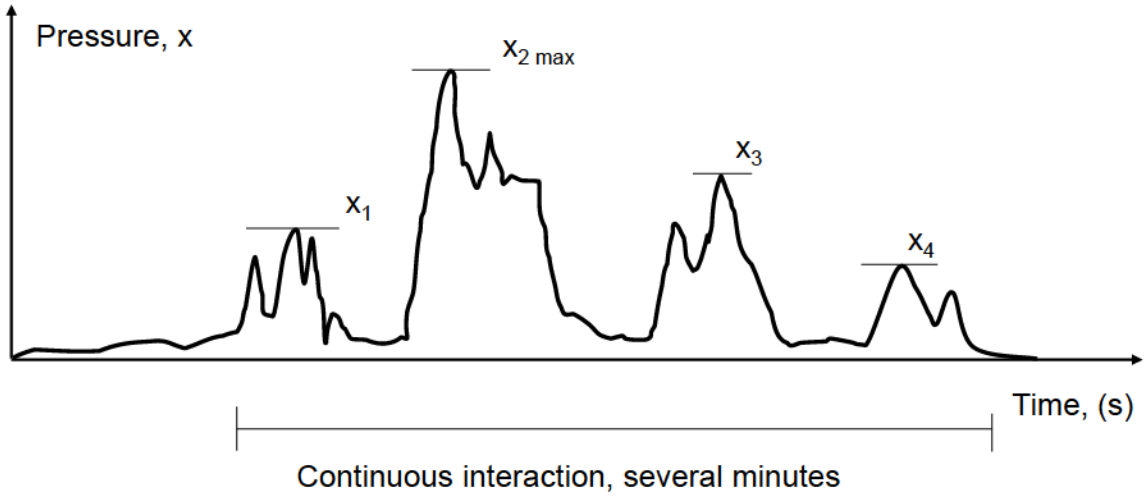

Figure 121 Illustration of continuous interaction events lasting several minutes

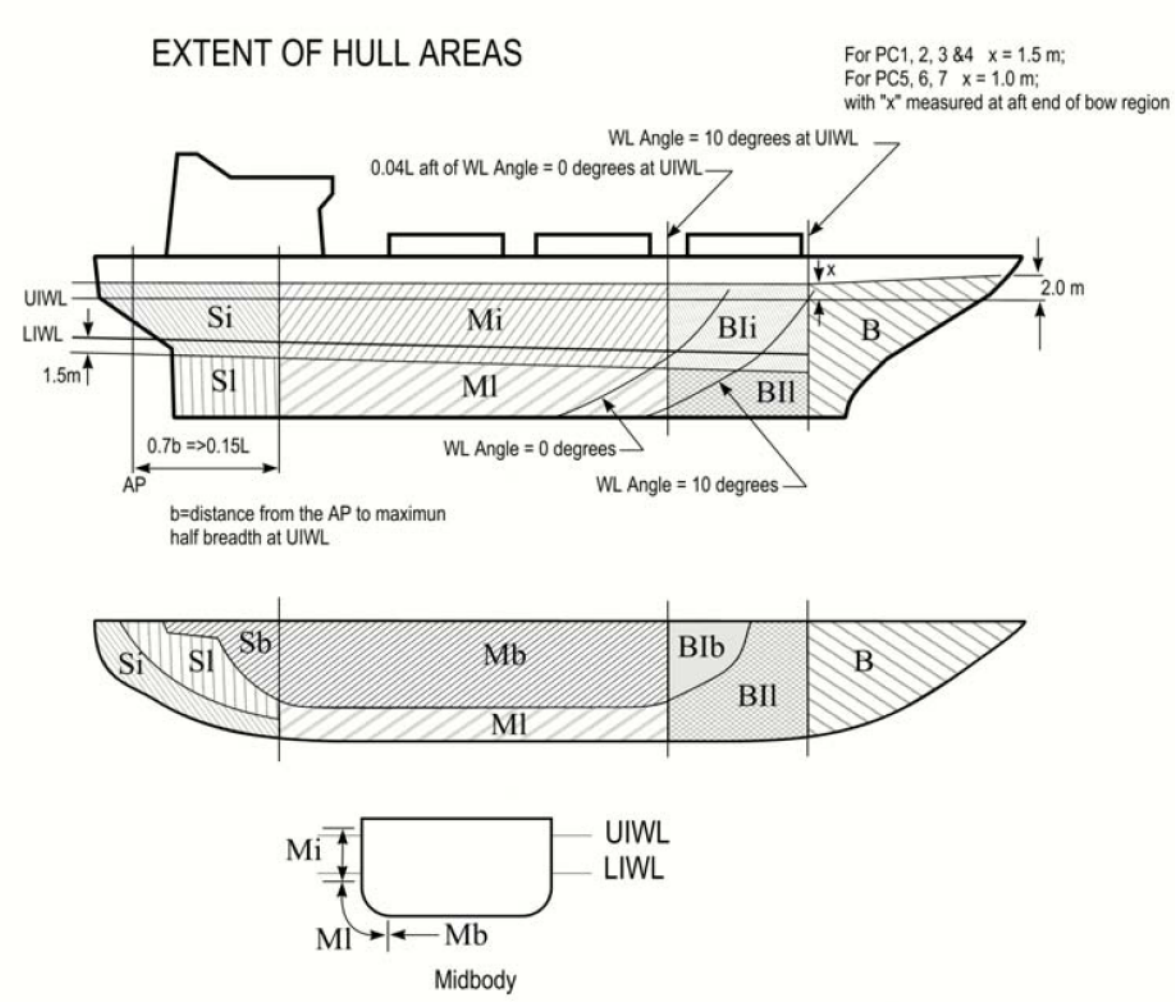

Figure 122 Hull Area Extents (IACS, 2010)

Table 11 Hull Areas and corresponding Hull Area Factors in Figure 122 (IACS, 2010)

Hull Areas		Area	Polar Class						
			PC1	PC2	PC3	PC4	PC5	PC6	PC7
Bow(B)	ALL	B	1.00	1.00	1.00	1.00	1.00	1.00	1.00
Bow Intermediate (BI)	Icebelt	BI_i	0.90	0.85	0.850	0.8	0.8	1.00	1.00*
	Lower	BI_L	0.70	0.65	0.65	0.60	0.55	0.55	0.50
	Bottom	BI_B	0.55	0.50	0.45	0.40	0.35	0.30	0.25
Midbody (M)	Icebelt	M_i	0.70	0.65	0.55	0.55	0.50	0.45	0.45
	Lower	M_L	0.50	0.45	0.40	0.35	0.30		0.25
	Bottom	M_B	0.30	0.30	0.25	**	**	**	**
Stern (S)	Icebelt	S_i	0.75	0.70	0.65	0.60	0.50	0.40	0.35
	Lower	S_L	0.45	0.40	0.35	0.30	0.25	0.25	0.25
	Bottom	S_B	0.35	0.30	0.30	0.25	0.15	**	**

* See I2.3.2(iii) in Polar Code

* Indicates that strengthing for ice loads is not necessary.

4.4 *HPZ* Analysis based on *Polar Sea* Data

High Pressure Zone (*HPZ*), also referenced as zonal force, analysis was introduced in Section 4.3.2 and a model for local pressure based on *HPZ* force and density was discussed. This analysis by Zou (1996) was based on *Louis S. St. Laurent* ramming trials. While the resolution of the sensor was rather high at 0.0472 m^2, the sensor area was relatively small on the order of 1.25 m^2. It is anticipated that the *HPZ* density analysis by Zou (1996) included very small *HPZ* forces, which would result in considerably higher estimates of density.

In this section, the *Polar Sea* data are analyzed to estimate *HPZ* density and force. Within the *Polar Sea* data set, there are a large number rams in different ice conditions, in different regions, and with a relatively large instrumented area at ~9 m^2. Compared with the *Louis S. St. Laurent* data, the resolution of the *Polar Sea* data is lower, with the smallest subpanel area being 0.15 m^2; this needs to be taken into account when estimating *HPZ* area and force. Of the *Polar Sea* data sets available as listed in Section 2.3.1, only four having MY ice were considered, namely Beaufort 1982, North Chukchi 1983, South Chukchi 1983 and Beaufort 1984.

Illustration of local pressure and *HPZ* occurrence over a section of hull girder for three ramming events during the *Polar Sea* Beaufort 1982 trials is illustrated in Figure 18, Figure 123 and Figure 124. The random occurrence and disappearance of local *HPZ*s across the sensor is illustrated. The sampling frequency is 32 Hz.

Comparison of local pressure parameter alpha (α) vs. area for the various *Polar Sea* trials and other local pressure measurements was illustrated in Figure 34. Of the four sets of *Polar Sea* ram data, the Beaufort 82 dataset represents the highest pressures likely attributed to stronger ice further north.

4.4.1 Polar Sea Measurement System

With the *Polar Sea* measurements, different thresholds were used for different trials to limit data storage, focusing on collection of the highest pressures having the most influence for design. The system was activated when any 0.15 m^2 panel within the 60 subpanel array

recorded a threshold pressures above 1.41 MPa to 3.4 MPa (i.e. threshold strains ranged from 100 to 250με corresponding to 200-500 psi). Six seconds of hull strains and corresponding local panel pressures were recorded on all subpanels for the ram duration. For comparison, sensors on the *Louis S. St. Laurent* trials referenced in Section 4.3 recorded pressures exceeding 1.37 MPa on the thru hull pressure sensors corresponding to a force of 0.065 MN on a 0.0472m^2 area. Regarding system thresholds related to both the *Louis S. St. Laurent* and *Polar Sea* trials, two observations are noted:

- The *Louis S. St. Laurent* system recorded events that would have been missed on the *Polar Sea* system;
- While *Polar Sea* data may reflect a higher event threshold on a single subpanel, the subsequent recorded pressures on all subpanels through each event may be considerably lower than the Louis St Laurent threshold of 1.37 MPa. Since pressure scales proportionally with area, and assuming the local pressure scale effect, $A^{-0.7}$, a consistent lower bound pressure for *Polar Sea* measurements based on a 0.15 m^2 panel area would be estimated at 1.37 MPa $\times$ (0.15 m^2)$^{-0.7}$ / (0.0472 m^2)$^{-0.7}$ = 0.60 MPa. This would correspond to a threshold force of 0.09 MN.

Consistency with the lower bound pressures in the data analysis is important when processing *HPZ* force and density. A lower threshold will result in a higher density and lower forces.

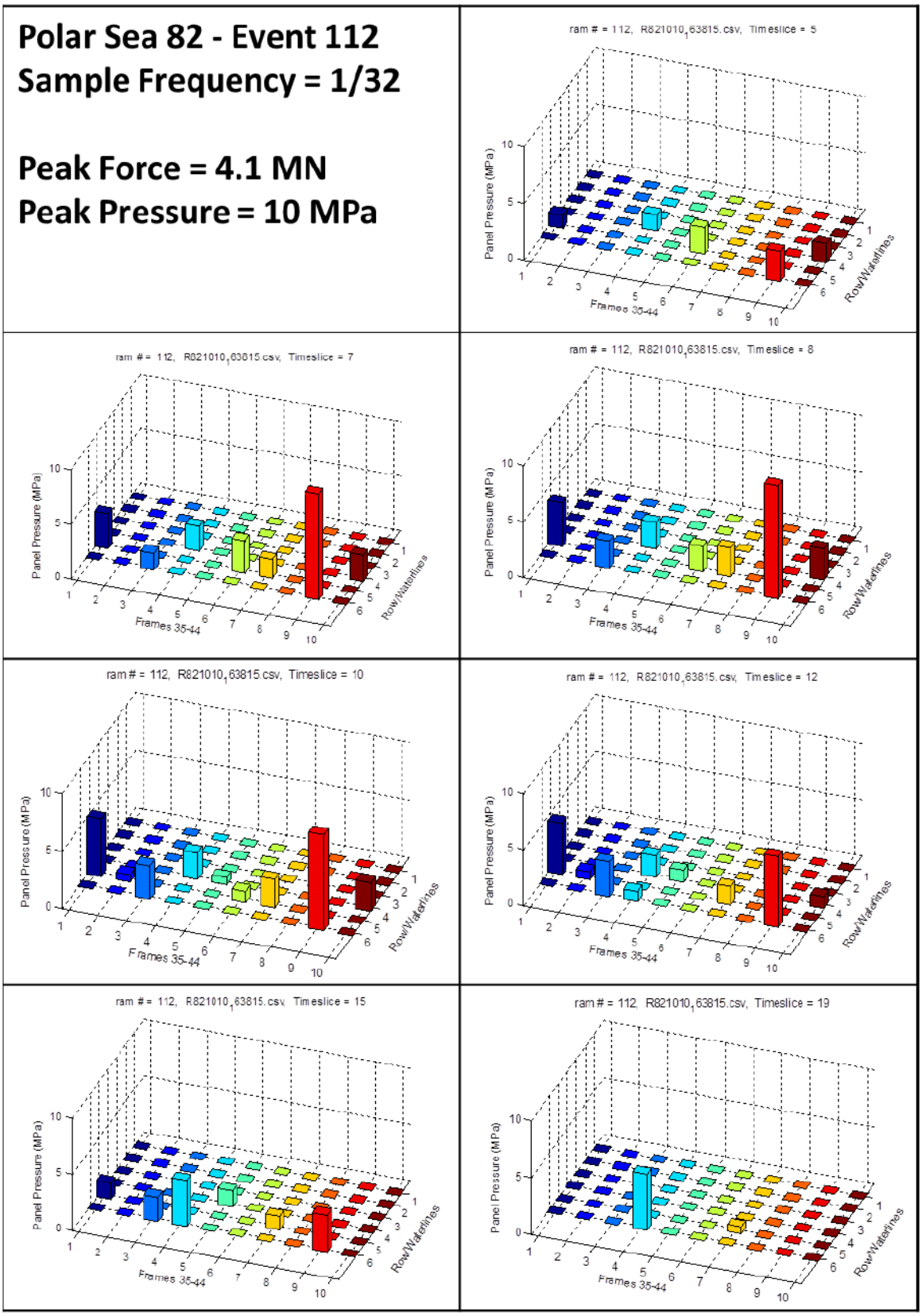

Figure 123 Illustration of distribution of panel pressures through a *Polar Sea* 1982 ram #112

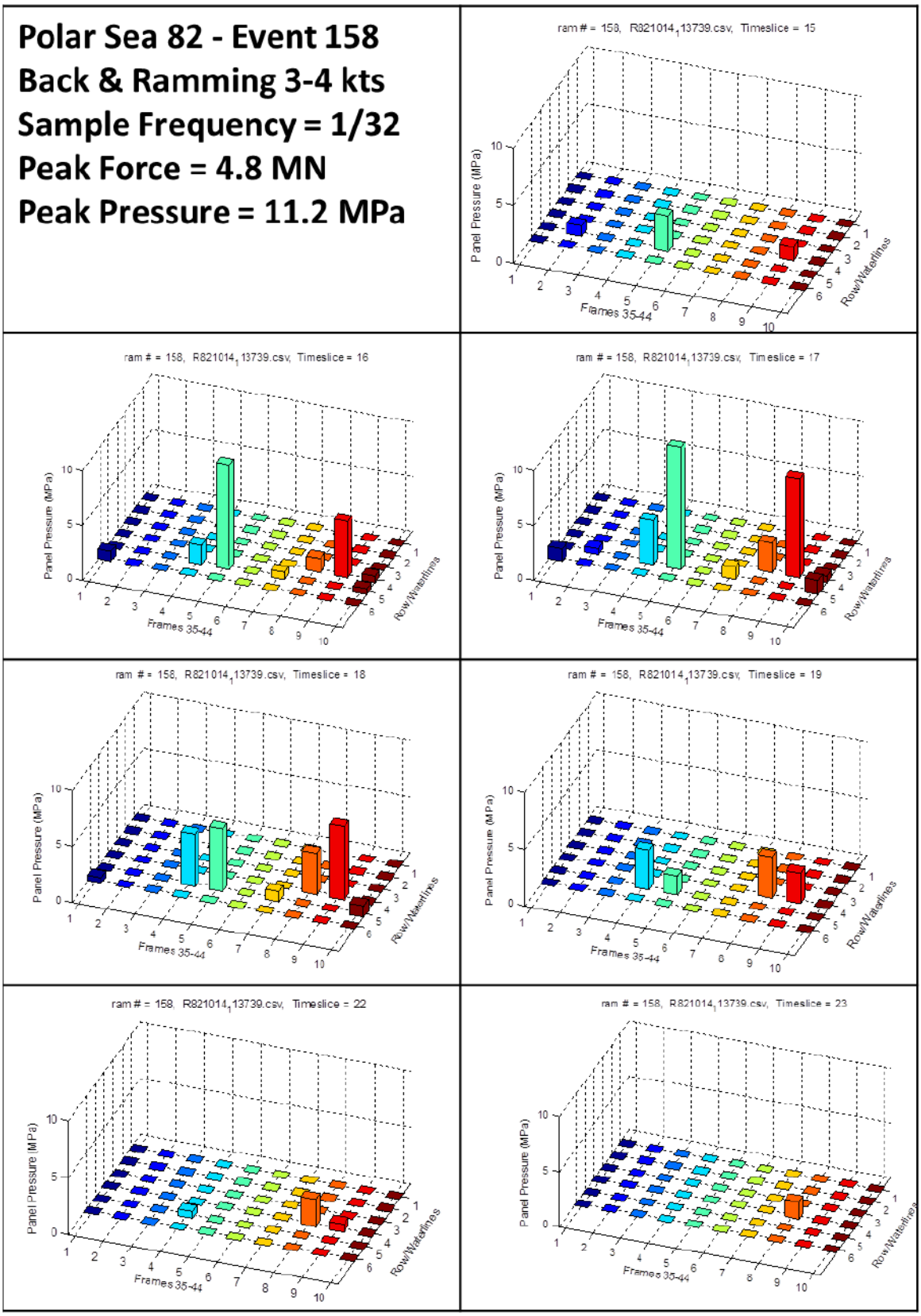

Figure 124 Illustration of distribution of panel pressures through a *Polar Sea* 1982 ram #158

4.4.2 Modeling HPZ Parameters Area, Force and Density

4.2.4.1 HPZ Area

Zou (1996) using *Louis S. St. Laurent* 1980 data first estimated a mean *HPZ* area to be 0.080 m^2 based on a sensor resolution of 0.0472 m^2. Figure 112 in Section 4.3.6 illustrates that higher *HPZ* areas up to 0.16 m^2 are possible if cutoff forces up to 2 MN are modeled.

Given that the sensor resolution from *Polar Sea* trials is 0.15 m^2, which is approximately three times the *Louis S. St. Laurent* sensor area and twice the mean estimated *HPZ* area, any further analysis using *Polar Sea* data will be biased toward a 0.15m^2 area. No further analysis of *HPZ* area was carried out for the *Polar Sea* trial data, assuming the mean *HPZ* area from the *Louis S. St. Laurent* data of 0.080m^2 to be reasonable. The response of any 0.15 m^2 subpanel is assumed to be an *HPZ*.

4.2.4.2 Consideration for Noise in the Measured Data

Before analyzing the *Polar Sea* data for *HPZ* force and density, the full range of gauge response was analyzed to understand the influence of noise in the system and low level sensor response suggesting low ice forces. Noise could result from thermal effects (i.e. based on temperature gradients from water to air both outside and inside the hull), hull vibration, wave effects, and interaction with thin ice before interacting with a MY floe. St. John *et al.*,(1984) comment that thermal response of the sensors made it extremely difficult to fully zero the system before any trials. They comment that the response is symmetrical meaning that a negative response in the sensor at some locations was balanced with a positive response elsewhere.

Histograms of pressures below 0.6 MPa (75 psi) on the system were plotted for each ram for each *Polar Sea* data set as illustrated in Figure 125. The average noise in the sensor for each ram was estimated as the mean of pressures less than 0, and mean of pressures greater than 0 but less than 75 psi (0.6 MPa). Figure 125 illustrates the symmetrical trend noted by St John *et al.* (1984).

While this noise signature has little effect on the analysis of peak local forces and pressures on subpanels, (St. John *et al*. (1984) suggest on the order of 10%), it is important for modeling *HPZ* density and force where application of cutoff force can bias results. As illustrated in Figure 125, considering pressures below 0.17 MPa (25 psi) for the Beaufort 1982, North Chukchi 1983 and South Chukchi 1983 will artificially increase *HPZ* density. Similarly, pressures below 0.10 MPa (15 psi) will increase density estimates from the Beaufort 1984 dataset and should be removed.

While the four datasets exhibit a near symmetrical trend in background noise as illustrated in Figure 125, the North Chukchi Sea dataset shows additional load response in the system at the 35 - 45 psi. It is likely that difficultly in zeroing the system may have resulted in this response introducing some error in the measured *HPZ* forces. As discussed in the next section, this noise too should be removed. Four approaches were considered:

- Raise cutoff pressure from 0.17 MPa to 0.5 MPa for North Chukchi Sea;
- Determine mean system noise for each **ram** based on pressure ranging from 0 to 75 psi (excluding zeros) and subtract this noise level from all measured pressures in each time frame through the ram duration;
- Determine mean noise for each time **frame** based on pressures ranging from 0 to75 psi and subtracting from panel pressures in each time frame.

As illustrated in the noise density histograms in Figure 126, each of the three methods remove the probability mass in the 35-45 psi range. The latter method seems more reasonable addressing only ramming events and time slices most influenced by this unique response.

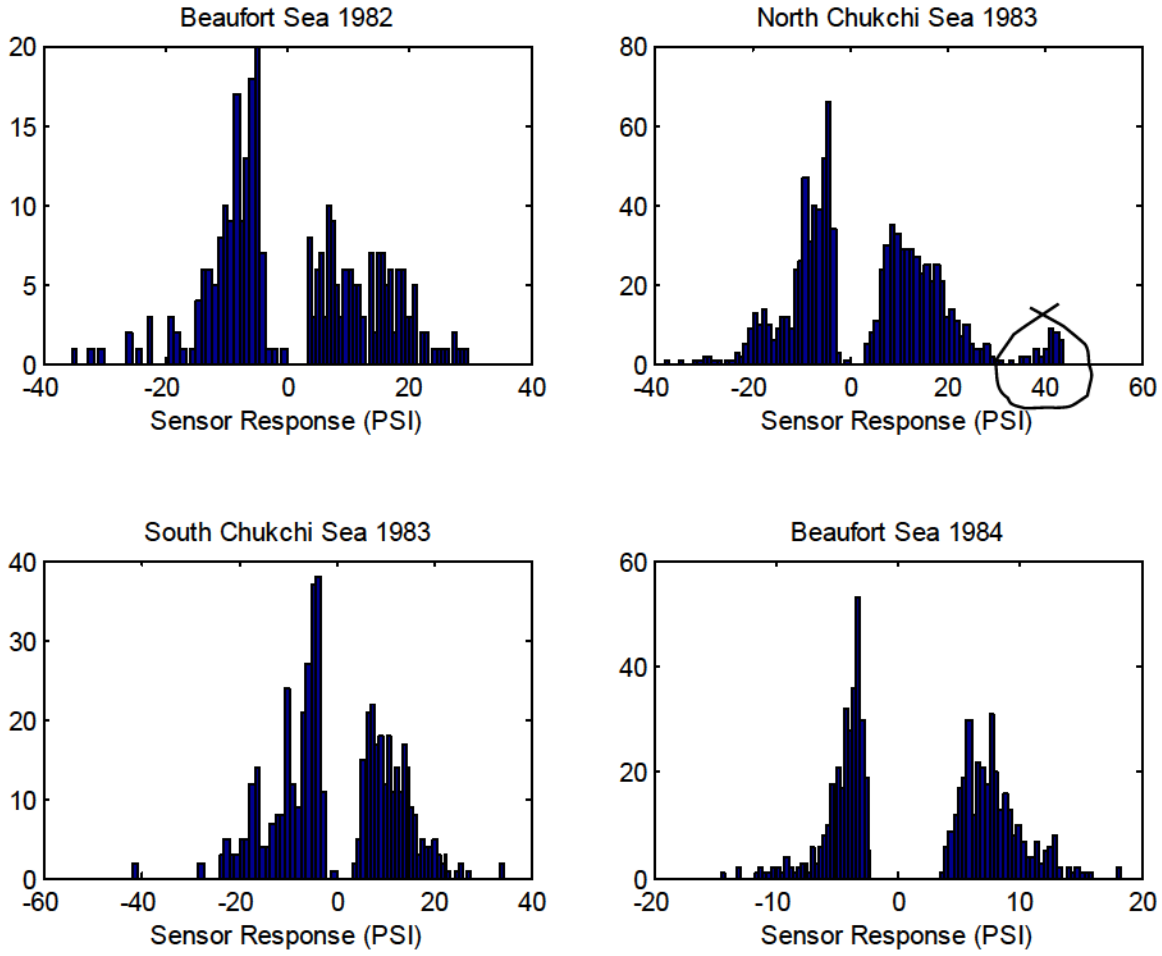

Figure 125 Sensor response during ramming events illustrating 1) the approximately symmetrical nature of background noise, and 2) the added response at the 35-45 psi level with the North Chukchi Sea data.

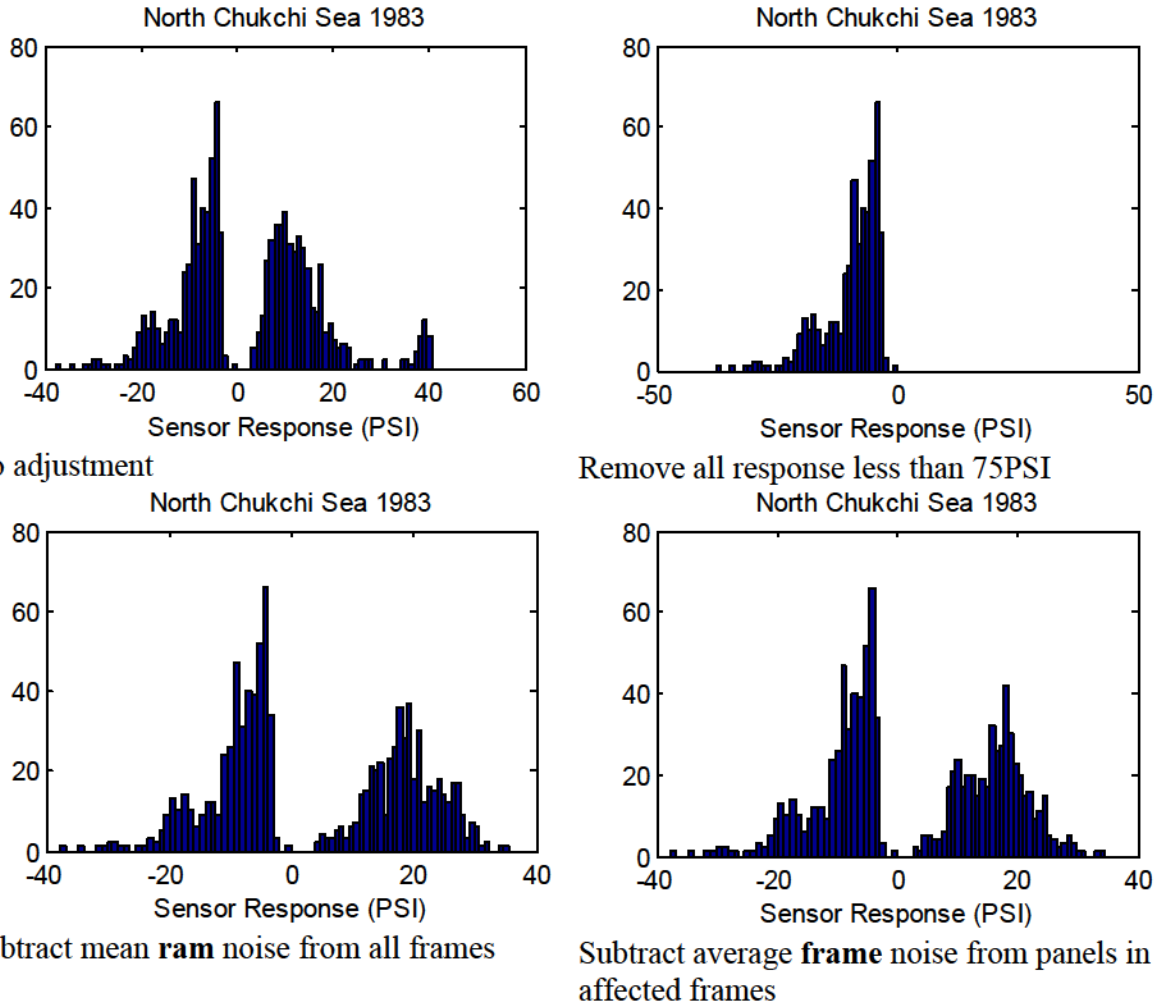

Figure 126 Histograms of system noise (psi) for North Chukchi Sea 1983 data illustrating different methods for noise reduction.

4.2.4.3 Sensor Resolution Scale Effects in Measured Data

Earlier it was rationalized that *HPZ* density based on single panel response from the *Polar Sea* data is reasonable. As a result of scale effects, pressures measured on the *Polar Sea* panel sensors having an area of 0.15 m^2 will be considerably lower than pressures measured on the *Louis S. St. Laurent* sensor having an area of 0.047 m^2; similarly for pressures corresponding to a mean *HPZ* area of 0.08m^2.

A scale effect correction was considered to adjust *Polar Sea* pressures to better reflect forces occurring on the average *HPZ* area of 0.08m^2. Since local pressures scale according to A$^{-0.7}$, a correction to *Polar Sea* measurements should consider the ratio

$$\frac{A_R^{-0.7}}{A_{PS}^{-0.7}} \qquad (46)$$

where A_R is reference area for pressure or force correction, and A_{PS} is *Polar Sea* sensor area of 0.15m^2. As noted above, A_R was taken as the mean *HPZ* area 0.08m^2. Resultant estimates of *HPZ* forces measured on the *Polar Sea* were factored by 1.55.

With respect to density estimates, the *Polar Sea* sensor resolution (i.e. one subpanel) at 0.15m^2 is on the order of three times the *Louis S. St. Laurent* 0.0472 m^2 pressure sensor and nearly twice the estimated mean *HPZ* area of 0.08m^2. Two observations are noted. Firstly, while unlikely, it is possible that two *HPZs* may occur within a single *Polar Sea* panel. Secondly, while it is possible that response on two (or three) adjacent *Polar Sea* panels represents the occurrence of a single, larger *HPZ* (i.e. area greater than 0.3 m^2 - 0.45m^2), given average *HPZ* area is half of the sensor area, these responses may indicate two adjacent *HPZs*. It is assumed that for density analysis that any active *Polar Sea* subpanel is a single *HPZ*, which may be conservative.

4.4.3 HPZ Force and Density based on Measured Peak Subpanel Pressures

HPZ force parameters γ and γ_0 were estimated for each *Polar Sea* dataset based on the 1/32nd time slice corresponding to the peak pressures on 0.15 m^2 subpanels through the ram duration. To consider noise in the system, pressures below a 0.172 MPa threshold were removed. *HPZ* forces were ranked and plotted against the Weibull plotting position and the parameters γ and γ_0 for an exponential fit determined. *HPZ* forces were factored by 1.55 to account for *HPZ* area scaling. *HPZ* density was estimated assuming each subpanel corresponds to one *HPZ*.

Illustrated in Figure 127 for the *Polar Sea* Beaufort 1982 dataset is:

- Histogram of *HPZ* forces corresponding to the peak pressure time slice for each ram;

- Distribution parameters γ an γ_0 corresponding to exponential fit to the tail of the *HPZ* force distribution;
- Histogram of number of *HPZs* corresponding the peak pressure time slice; and
- Sensitivity of *HPZ* density to *HPZ* threshold cutoff force using Equation (33), Section 4.4.6.

Results for the *Polar Sea* Beaufort 1982 data set using a threshold cutoff force of 0.2MN is illustrated in Figure 128. Consistency with the estimate of the *HPZ* force parameter γ is illustrated where the influence of very small *HPZ* forces not relevant for design is removed, as well as reduction in number of *HPZ*s and corresponding *HPZ* density with increasing force threshold.

Results for North and South Chukcki and Beaufort 1984 data sets including influence of 0.2 MN cutoff is illustrated in Figure 129 through Figure 134. For each *Polar Sea* dataset, a summary of exponential fit parameters γ and γ_0 to the tails of the *HPZ* force distribution as well as *HPZ* density corresponding to a range of *HPZ* force threshold ranging from 0 to 0.3 MN is illustrated in Table 12.

Table 12 Summary of exponential fit parameters for *HPZ* force and corresponding *HPZ* density for different *Polar Sea* trials.

Data Set	*HPZ* force parameters for time slice at peak pressure plus *HPZ* force scaling to *HPZ* area of 0.080m^2			Power Law Best Fit to local Pressure parameters **
	γ (MN)	γ_0 (MN)	ρ (*HPZ*/m^2)	$C \times A^{-ex}$
Beaufort 1982	0.59	0.00	0.93	$0.53A^{-0.77}$
		0.1	0.59	
		0.2	0.40	
		0.3	0.30	
North Chukchi 1983	0.41	0.0	0.81	$0.38A^{-0.79}$
		0.1	0.52	
		0.2	0.34	
		0.3	0.24	
South Chukchi 1983	0.28	0.0	1.1	$0.24A^{-0.68}$
		0.1	0.54	
		0.2	0.31	
		0.3	0.21	
Beaufort 1984	0.32	0.0	0.96	$0.28A^{-0.74}$
		0.1	0.49	
		0.2	0.29	
		0.3	0.21	

** see Figure 34

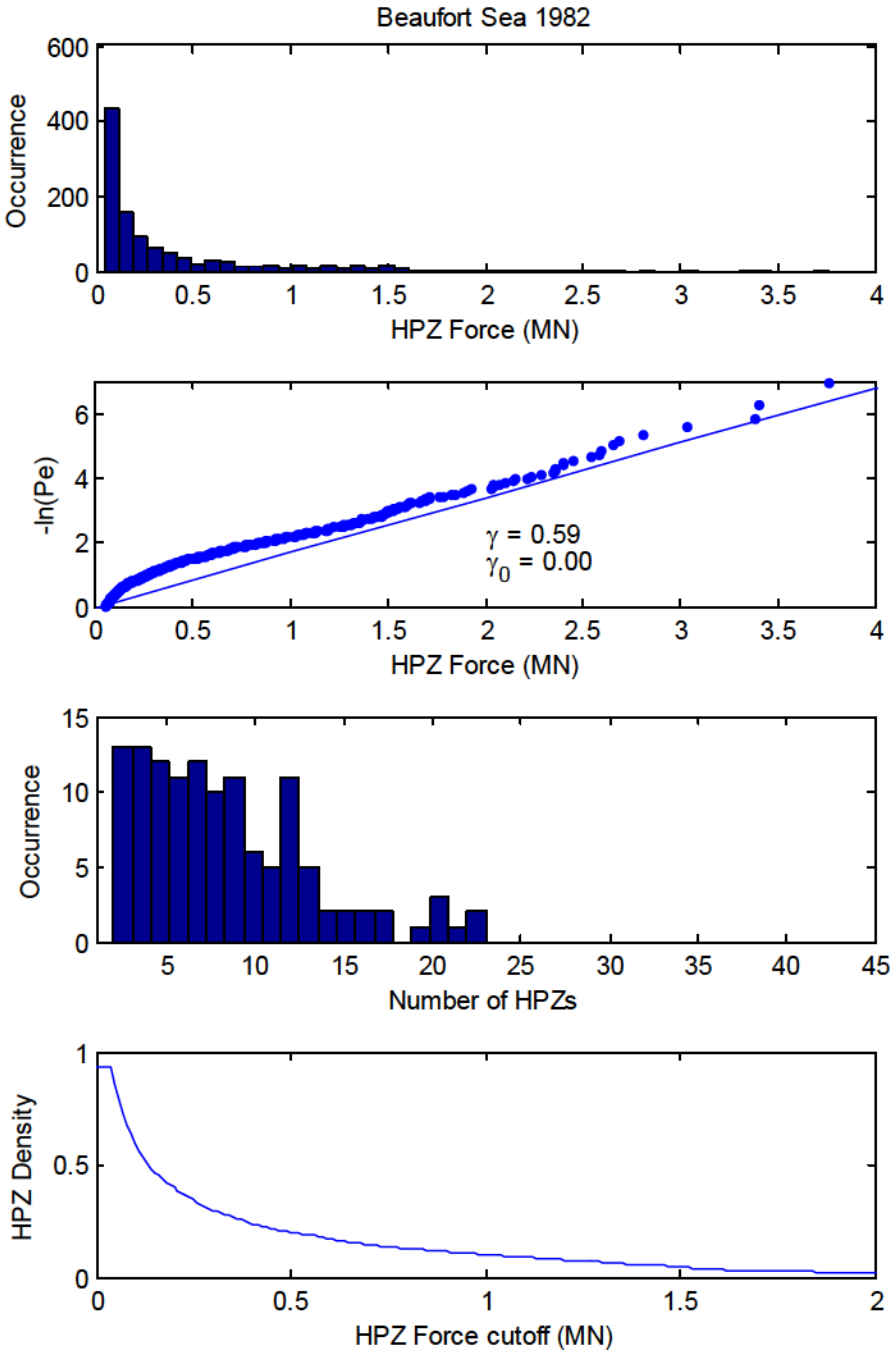

Figure 127 Distribution of *HPZ* force (i.e. individual panel), exponential force parameter γ and density vs. cutoff force for Beaufort Sea 1982 dataset. Threshold pressure of 0.17 MPa applied to remove sensor noise plus correction for area scale effects.

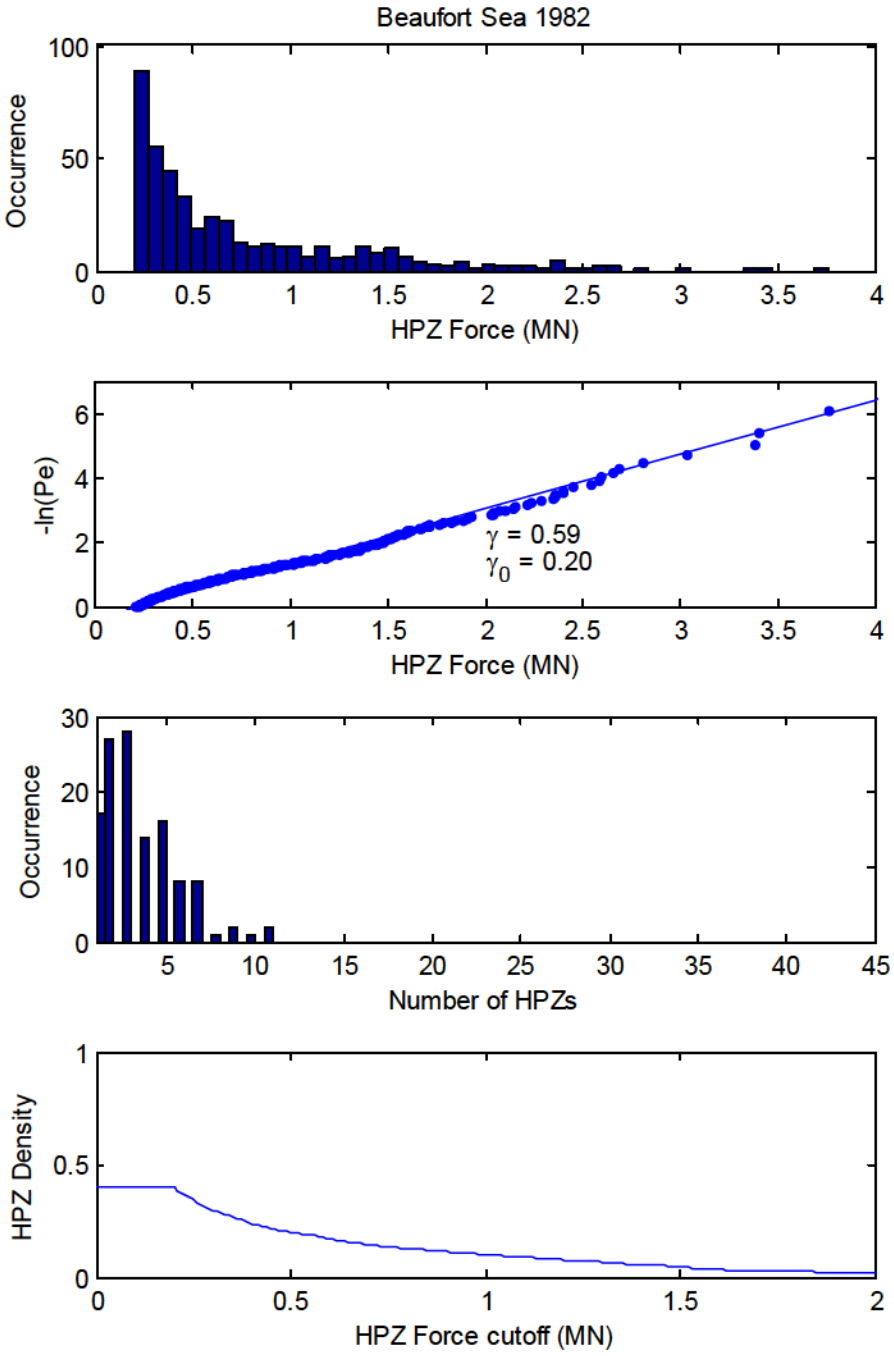

Figure 128 Distribution of *HPZ* force (i.e. individual panel), exponential force parameter γ and density vs. cutoff force for Beaufort Sea 1982 dataset with 0.2MN cutoff force applied

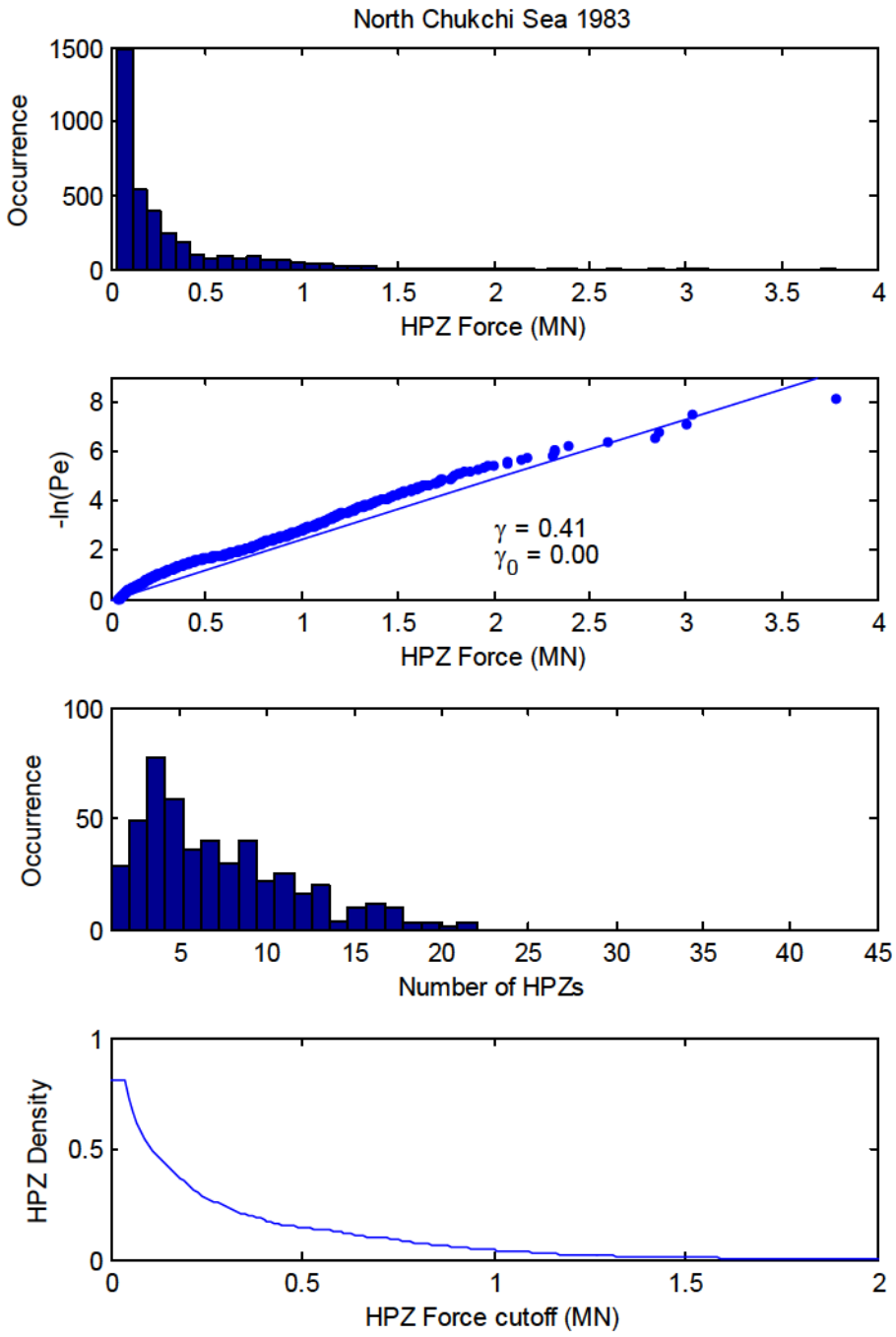

Figure 129 Distribution of *HPZ* force (i.e. individual panel), exponential force parameter γ and density vs. cutoff force for North Chukchi Sea 1983 dataset with 0 MN cutoff force applied

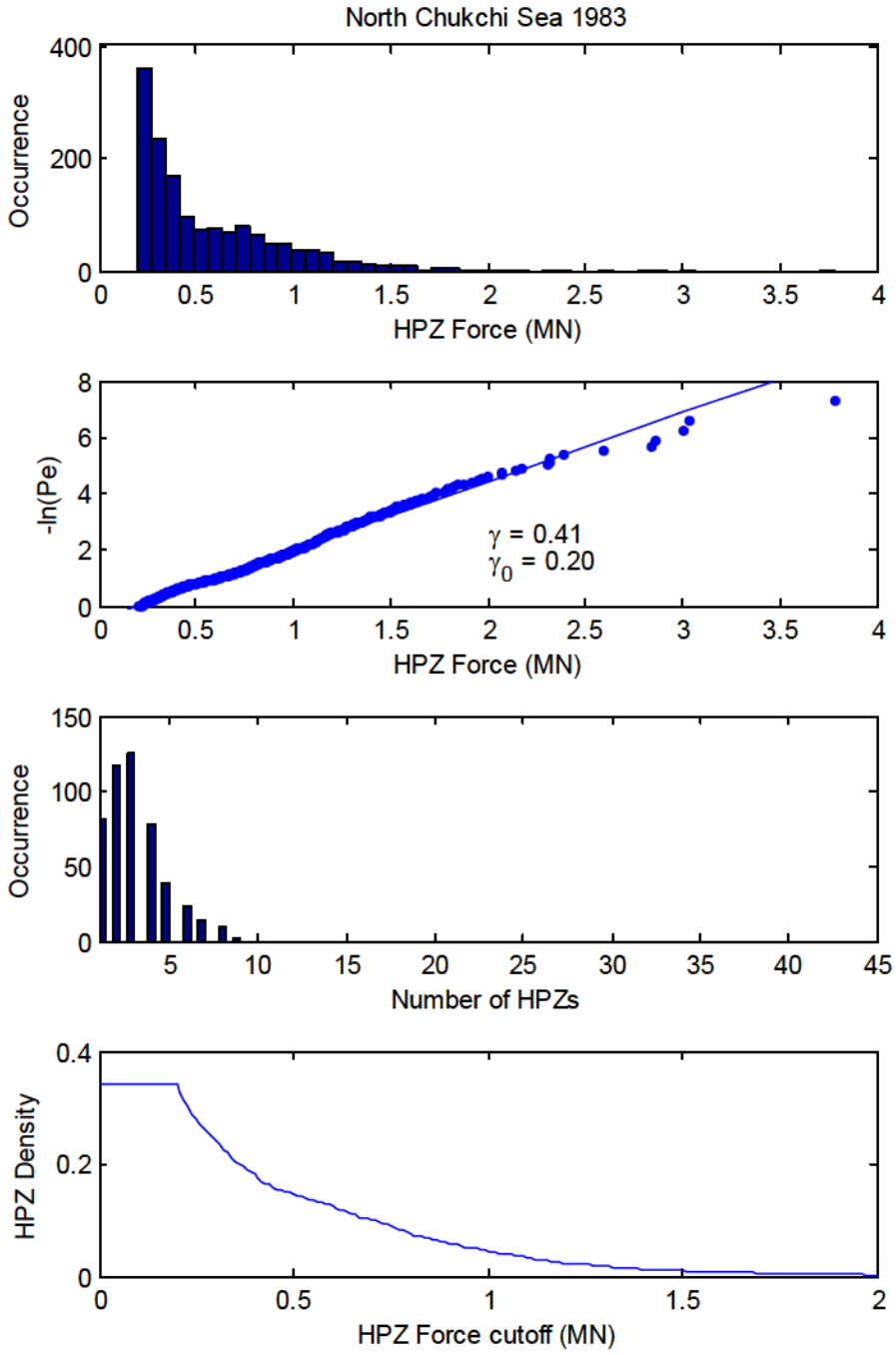

Figure 130 Distribution of *HPZ* force (i.e. individual panel), exponential force parameter γ and density vs. cutoff force for North Chukchi Sea 1983 dataset with 0.2MN cutoff force applied.

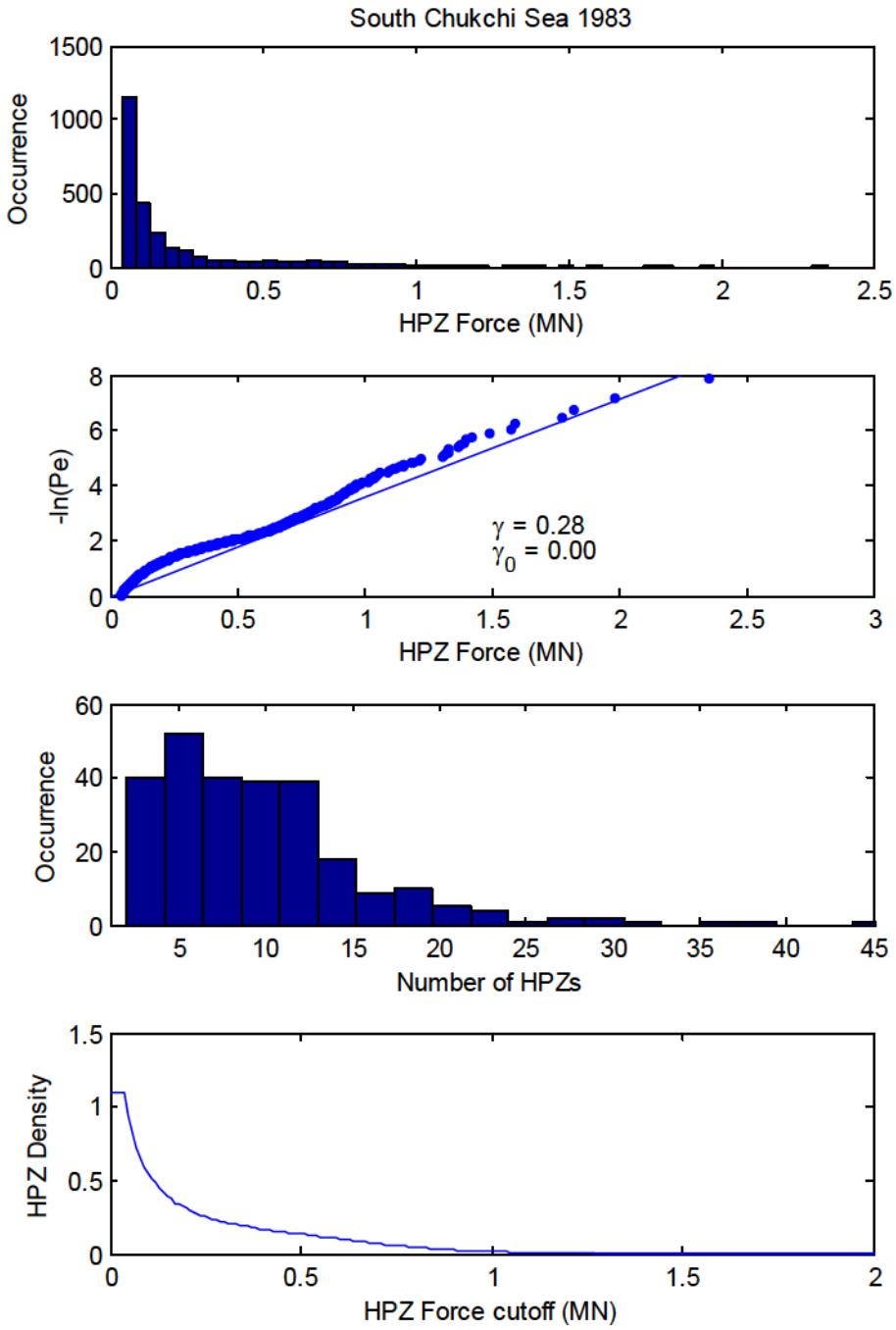

Figure 131 Distribution of *HPZ* force (i.e. individual panel), exponential force parameter γ and density vs. cutoff force for South Chukchi Sea 1983 dataset with 0 MN cutoff force applied

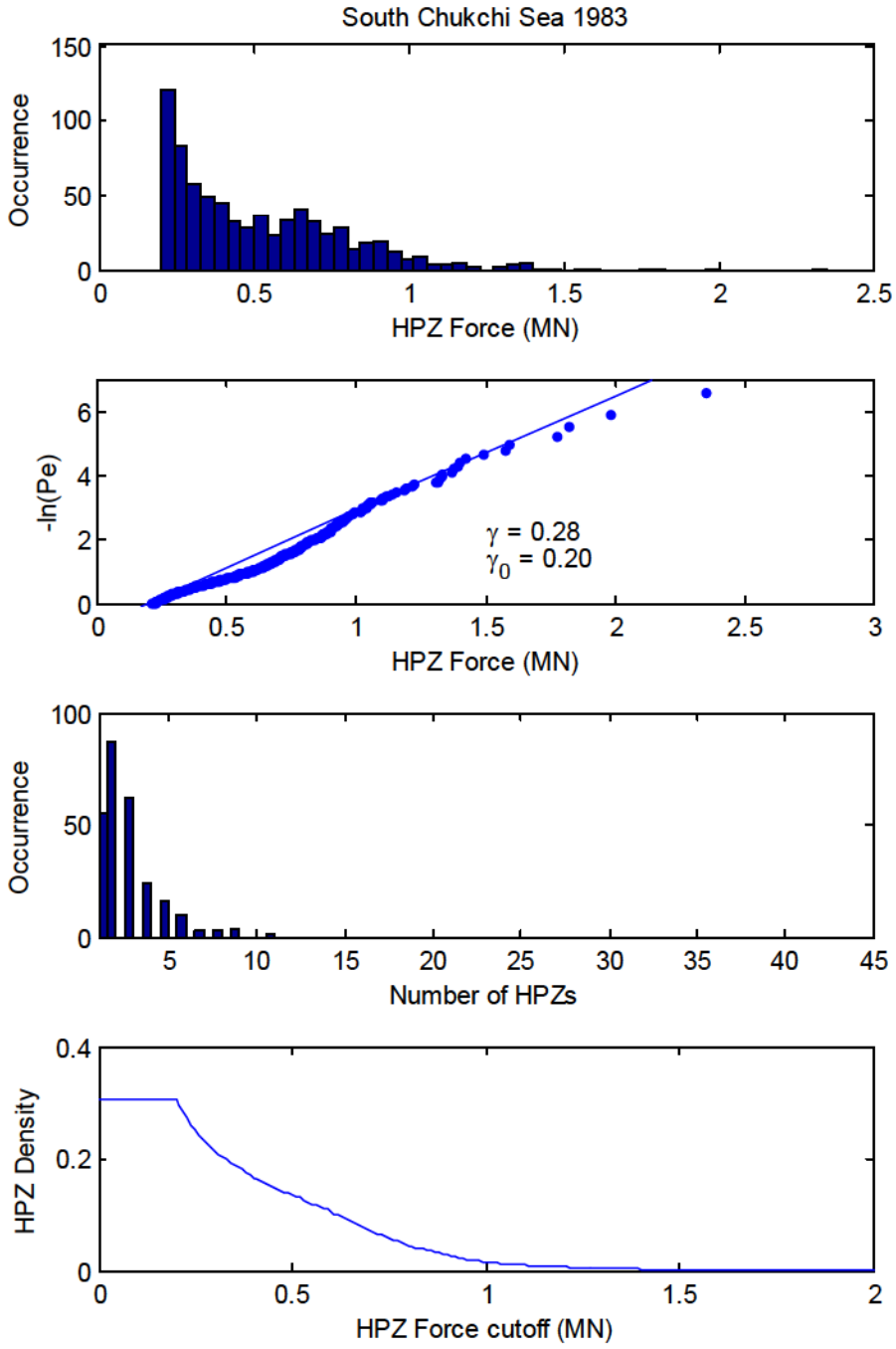

Figure 132 Distribution of *HPZ* force (i.e. individual panel), exponential force parameter γ and density vs. cutoff force for South Chukchi Sea 1983 dataset with 0.2MN cutoff force applied

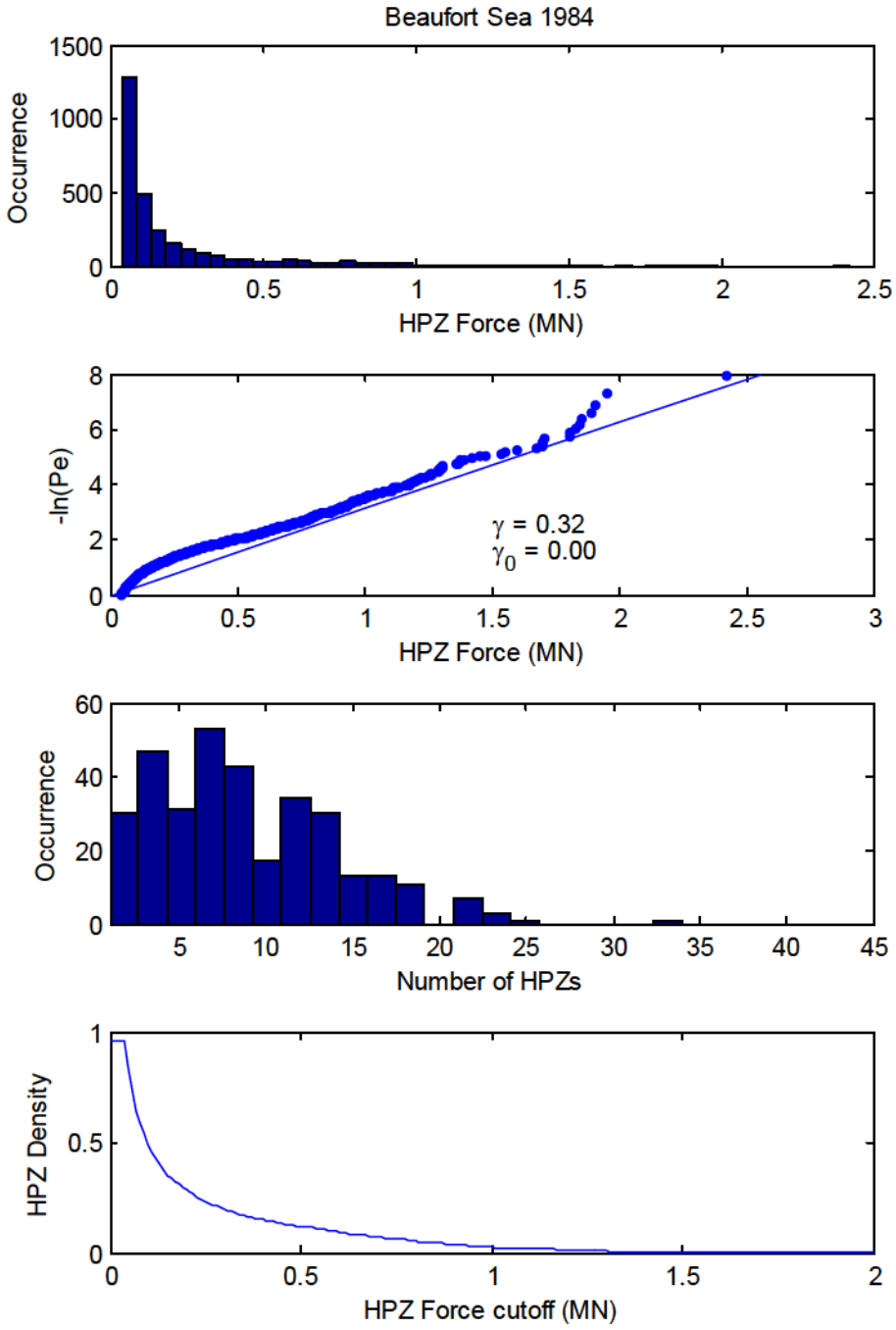

Figure 133 Distribution of *HPZ* force (i.e. individual panel), exponential force parameter γ and density vs. cutoff force for Beaufort Sea 1984 dataset with 0.0MN cutoff force applied

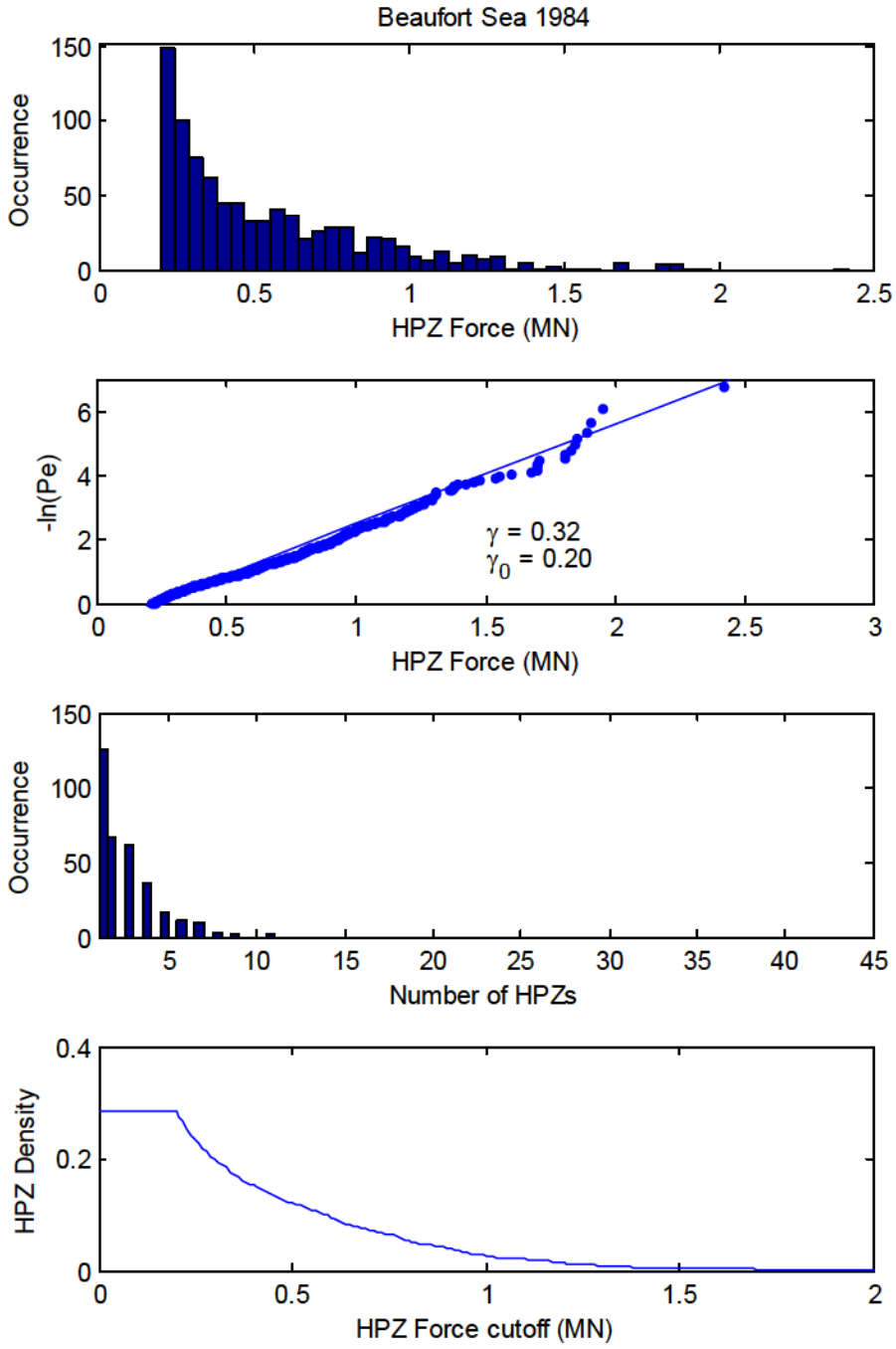

Figure 134 Distribution of *HPZ* force (i.e. individual panel), exponential force parameter γ and density vs. cutoff force for Beaufort Sea 1984 dataset with 0.2MN cutoff force applied

4.4.4 Simulation of Local Pressures from Polar Sea HPZ Forces

4.4.4.1 Correction for HPZs along Panel Edges

HPZ occurrence over specific panel areas is modeled as point forces. The *HPZ* area is assumed circular, and the centroid can be positioned anywhere within a panel area. As illustrated in Figure 135, an *HPZ* positioned with its centroid near the edge of the panel area will have a significant amount of area outside the panel area; up to 75% near the corners and 50% along the sides. As a result, the idealized point force model would, on average, over-predict panel forces (especially for the smallest panels) compared with actual measurements which reflect only measured forces within the panel area.

To address over-prediction of simulated *HPZ* forces on a panel area, a correction factor was estimated based on the proportion of *HPZ* area that could potentially be outside the panel boundary as illustrated in Figure 135. A simple simulation model was developed as illustrated in Figure 136. In these figures, the red square represents the panel area on the ship for example, and the black circle is the *HPZ* area. Using numerical simulation, the circular *HPZ* area was randomly populated with a large number of dots and then stepped incrementally across and down the whole panel area keeping the centroid of the *HPZ* within the square panel boundary (fewer dots are illustrated in the figures to illustrate the method). At each increment, the number of dots common between the panel area and *HPZ* area, relative to the total number of random dots within the whole *HPZ* area, were identified. Common dots are circled in red. The proportion of *HPZ* area within the panel area was estimated for the entire panel area. This process was repeated for different panel areas. Figure 136 and Figure 137 illustrate the relative geometry of select *HPZ* positions (with area A = 0.08 m^2) over a 0.15 m^2 panel and a 0.6 m^2 panel respectively. A select list of panel areas and corresponding proportions (also correction factors on simulated panel pressures) is given in Table 13 and Figure 138. For smaller panel areas on the order of the size of an *HPZ* (i.e. A_{HPZ} = 0.08 m^2), the extent at which forces are overestimated exceeds 20% on areas less than 0.6 m^2. For larger areas exceeding 5 m^2 the extent of over-estimated force is less than 6%.

Table 13 *HPZ* force correction factor applied to simulations for a range of panel areas

Panel Area (m^2)	0.15	0.60	1.5	3	6	9
Correction	0.671	0.825	0.883	0.915	0.937	0.946

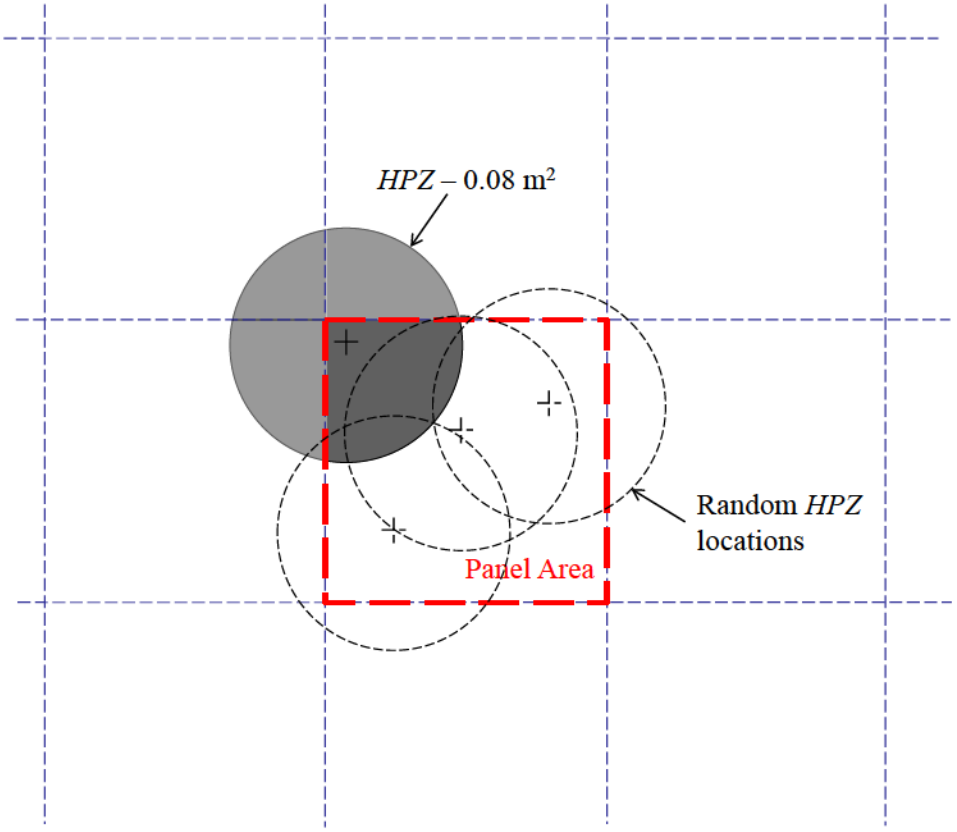

Figure 135 Illustration of proportion of *HPZ* (assumed circular) within a 0.15m^2 panel area

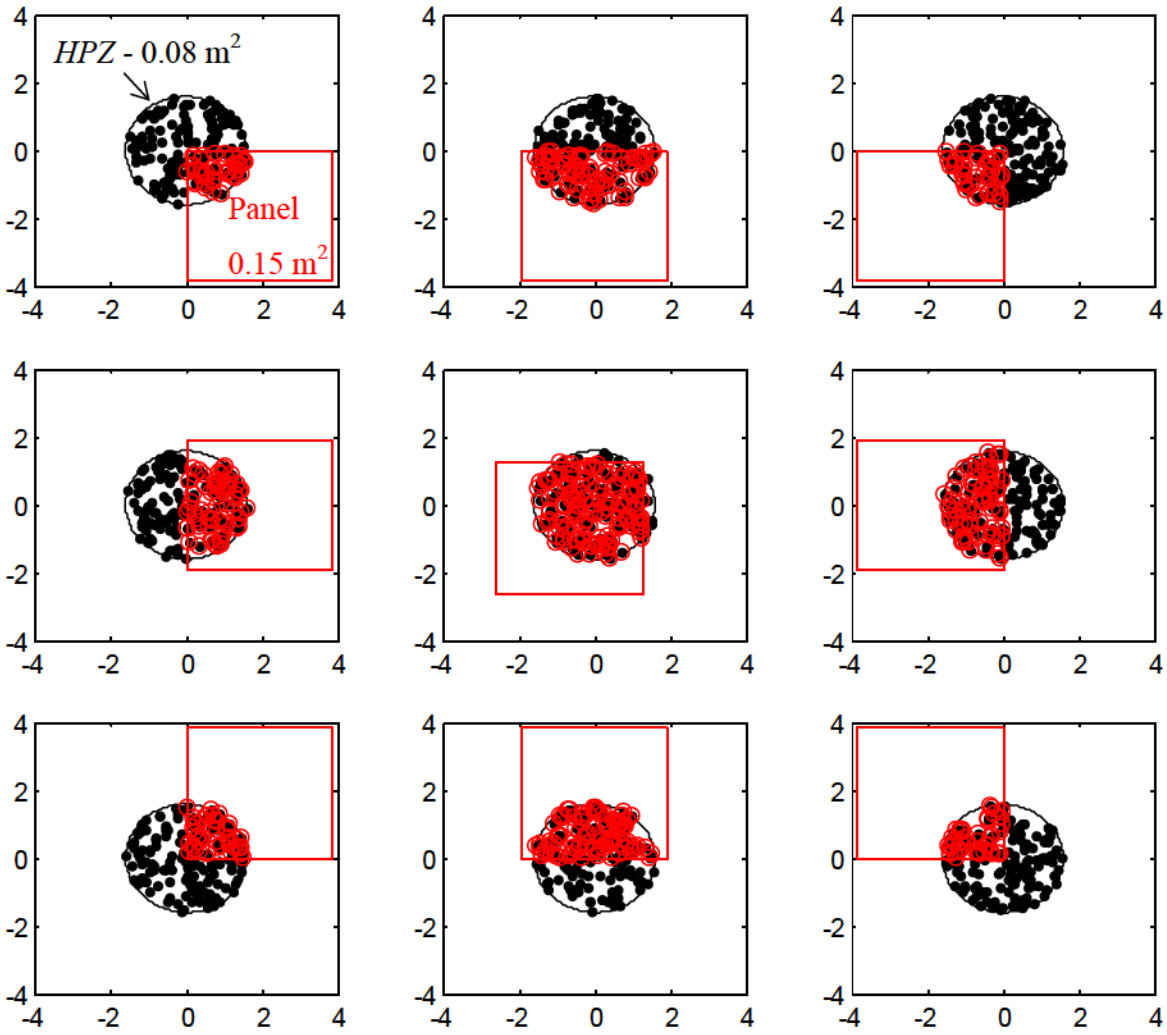

Figure 136 Illustration of numerical simulation process to estimate proportion of *HPZs* having area $A = 0.08$ m^2 within a 0.15m^2 panel area. Note: 1) Dots are used to fill the *HPZ* space and simply estimate overlap with panel area, and 2) in reality panel is stationary and *HPZ* moves.

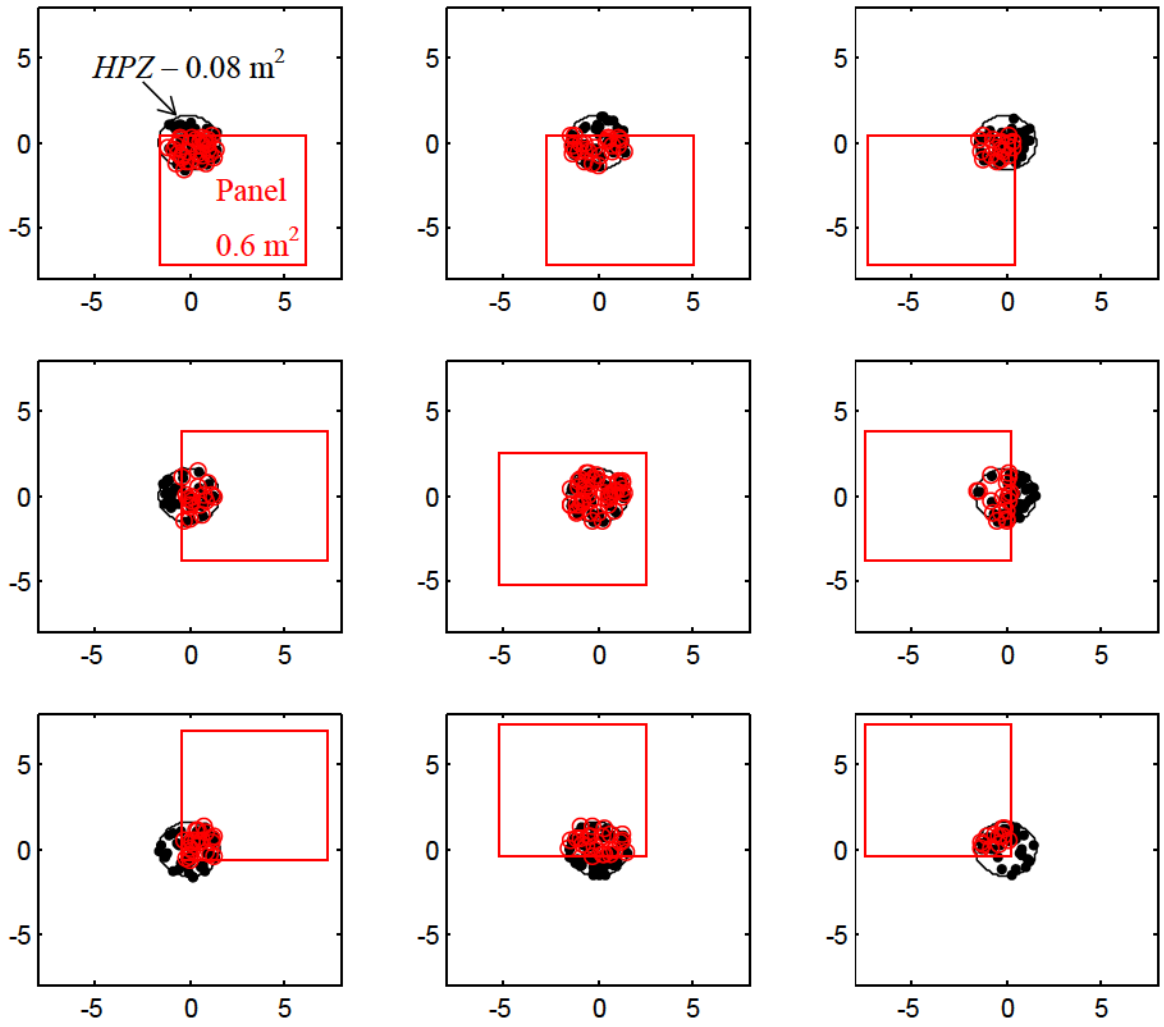

Figure 137 Illustration of numerical simulation process as in Figure 136 to estimate the proportion of *HPZ* of area $A = 0.08$ m^2 area within a 0.6m^2 panel area

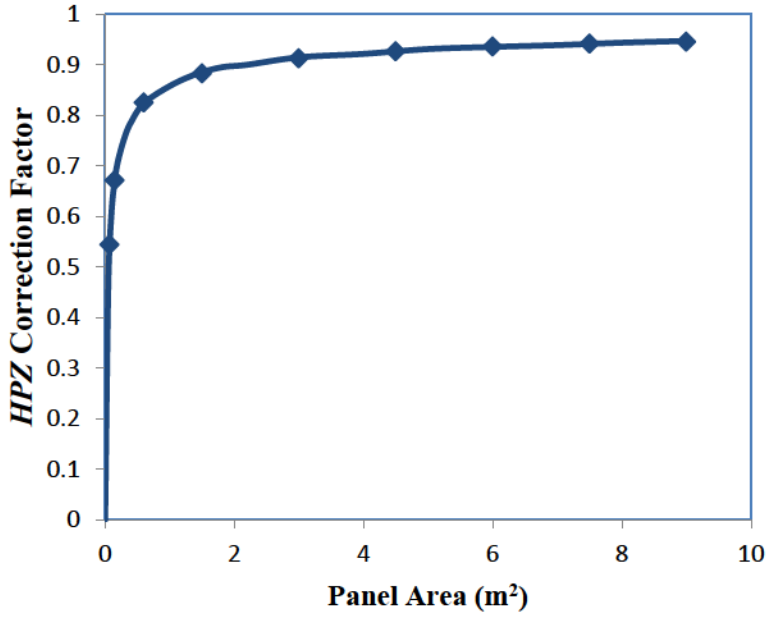

Figure 138 Proportion of *HPZ* area within panel areas and corresponding *HPZ* force and pressure correction factors from Table 13

4.4.4.2 Comparison of Simulated and Measured Local Pressures for Different Panel Areas

Using *HPZ* force parameters given in Table 12 as a guide, local pressure simulations were carried out for the various *Polar Sea* trials (Beaufort 1982, North Chukchi 1983, South Chukchi 1983, and Beaufort 1984) and comparison made between simulated and measured local pressures on a range of panel areas up to 9 m^2. Adjustment was made to the *HPZ* parameters as necessary to achieve better fits.

Simulation results consider the average pressure from *n* Poisson simulated *HPZs* each having a force sampled from an exponential force distribution. Measured results consider the average pressure over a specific panel area at a time slice corresponding to the peak panel pressure through the full ram duration. The plotting position of the pressures is then adjusted to ensure the distribution represents the expected pressures on any panel, and not a maximum of *n* panels. As noted earlier, in processing data, we are interested in a single panel 'parent' distribution.

Remarkable fits are achieved for each data set, as illustrated in Figure 139 through Figure 142. For these figures, density is modeled at 0.5 *HPZs*/m^2 with a cutoff of 0.0 MN. Results for density of 0.4 *HPZs*/m^2 for a cutoff force of 0.1 MN as well as 0.2 *HPZs*/m^2 with a cutoff of 0.3 MN are given in Appendix B. Density modeled at 0.5 *HPZs*/m^2 with zero cutoff, 0.4 *HPZs*/m^2 with 0.1 MN cutoff, or 0.2 *HPZs*/m^2 with 0.3MN cutoff seem reasonable.

The results for a density of 0.5 *HPZ*/m^2 were determined from iterations and best fit observations. While results are slightly conservative, it suggests that *HPZ* densities above 0.91 *HPZ*/m^2 shown earlier and also determined by Zou (1996) may be overly conservative and possibly biased toward very small pressure measurements that do not govern design. These could possibly be background low pressures resulting from extrusion of crushed ice as *HPZs* fail. Applying a cutoff pressure of 0.1 MN reduces the density within a range of 0.4 to 0.6 *HPZ*/m^2.

It was observed that *HPZ* parameters in Table 12 based on a peak pressure time slices were overly conservative. Alternatively, *HPZ* forces and density based on *HPZ* occurrence through a ram were determined as illustrated in Table 14. Refinement of parameters based on simulations resulted in a column of best fit *HPZ* force parameters that were subsequently used to simulate local design parameters as a function of panel area in the following sections. Building on this *HPZ* analysis, a new local pressure simulation model is developed in Section 4.5 that considers the rate of *HPZ* formation given impact conditions including speed and duration. This model estimates a 'parent' local pressure distribution given design area based on the maximum of *i HPZ* force slices through the ram duration. This approach to modeling exposure through a ram for a specific vessel design is an alternative to scaling local pressure exposure based on the ratio of duration from new vessel design to mean *Kigoriak* ram duration (see Section 2.3.3.3).

Table 14 Summary of exponential fit parameters for *HPZ* force and corresponding *HPZ* density for different *Polar Sea* trials.

Data Set	*HPZ* force parameters based on occurrence through the ram plus: i) scaling to *HPZ* area of $0.080m^2$, and ii) edge corrections			Best Fit from *HPZ* Simulation and comparison with data			Power Law Best Fit to local Pressure parameters **
	γ (MN)	γ_0 (MN)	ρ (*HPZ*/m^2)	γ (MN)	γ_0 (MN)	ρ (*HPZ*/m^2)	$C \times A^{-ex}$
Beaufort 1982	0.50	0.00 0.1 0.3	0.55 0.59 0.24	0.53	0 0.1 0.3	0.5 0.4 0.2	$0.53A^{-0.77}$
North Chukchi 1983	0.36	0.0 0.1 0.3	0.55 0.35 0.2	0.38	0 0.1 0.3	0.5 0.4 0.2	$0.38A^{-0.79}$
South Chukchi 1983	0.24	0.0 0.1 0.3	0.57 0.4 0.17	0.26	0 0.1 0.3	0.5 0.4 0.2	$0.24A^{-0.68}$
Beaufort 1984	0.30	0.0 0.1 0.2	0.96 0.32 0.2	0.32	0 0.1 0.2	0.5 0.4 0.2	$0.28A^{-0.74}$

** see Figure 34

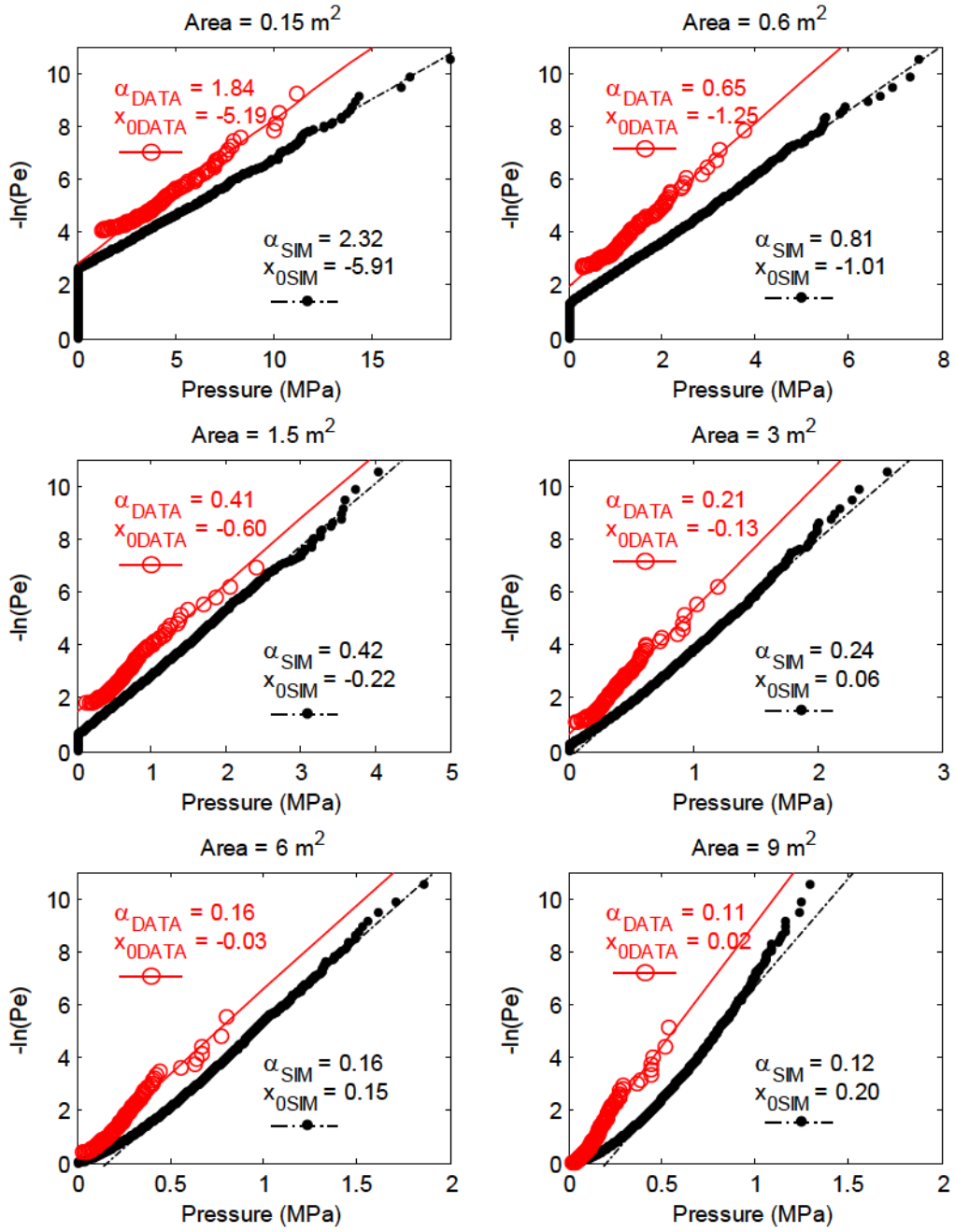

Figure 139 Comparison of simulated local pressure parameters with measured parameters based on *Polar Sea* Beaufort 1982 trials – $\gamma = 0.53$ MN; $\gamma_0 = 0.0$ MN; $\rho = 0.50$ *HPZ*s/m^2. Note that RED is measured data with solid line fit, and BLACK is simulated with dashed line fit.

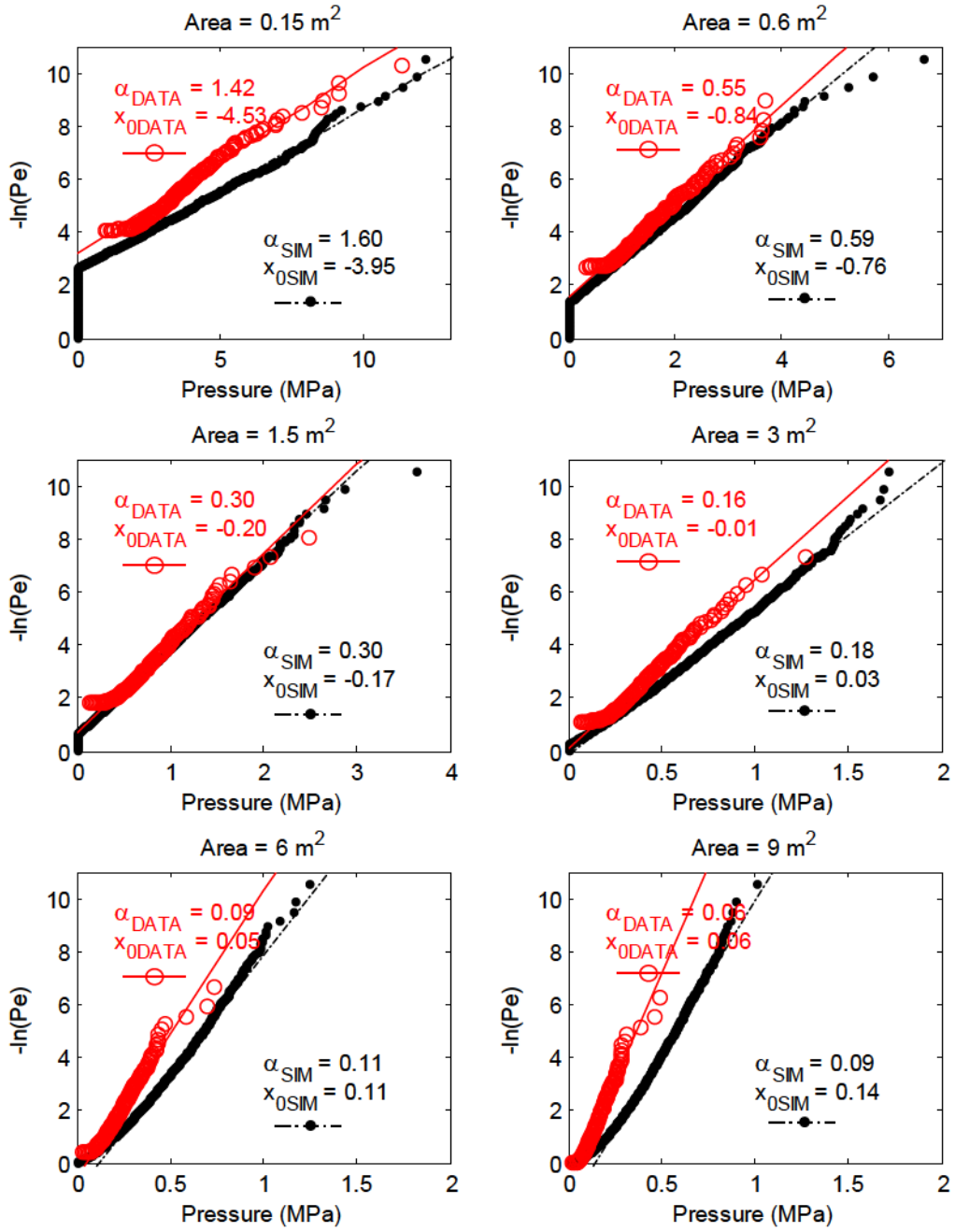

Figure 140 Comparison of simulated local pressure parameters with measured parameters based on North Chukchi 1983 trials – $\gamma = 0.38$ MN; $\gamma_0 = 0.0$ MN; $\rho = 0.50$ *HPZ*s/m^2.

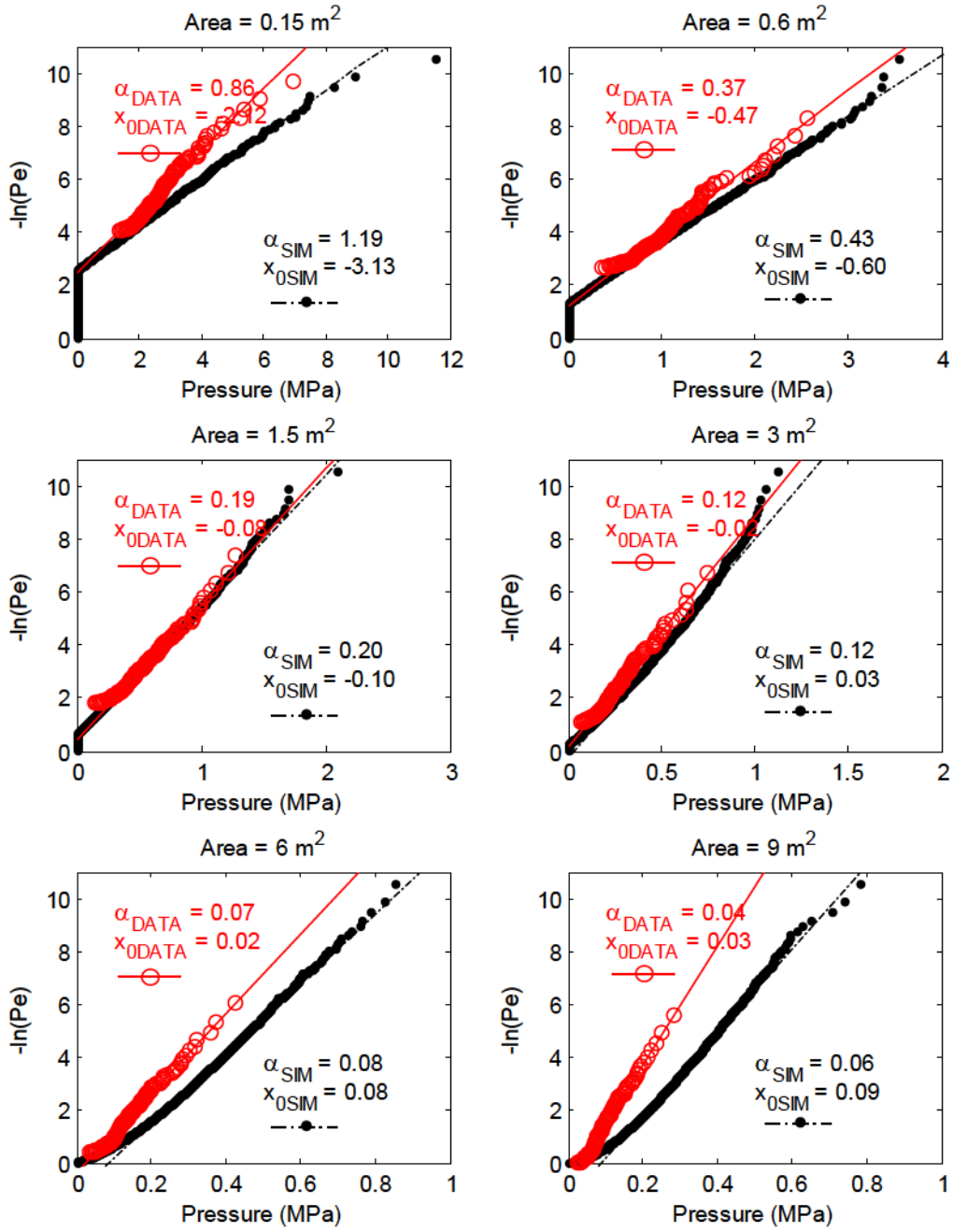

Figure 141 Comparison of simulated local pressure parameters with measured parameters based on South Chukchi 1983 trials – $\gamma = 0.26$ MN; $\gamma_0 = 0.0$ MN; $\rho = 0.50$ *HPZ*s/m^2.

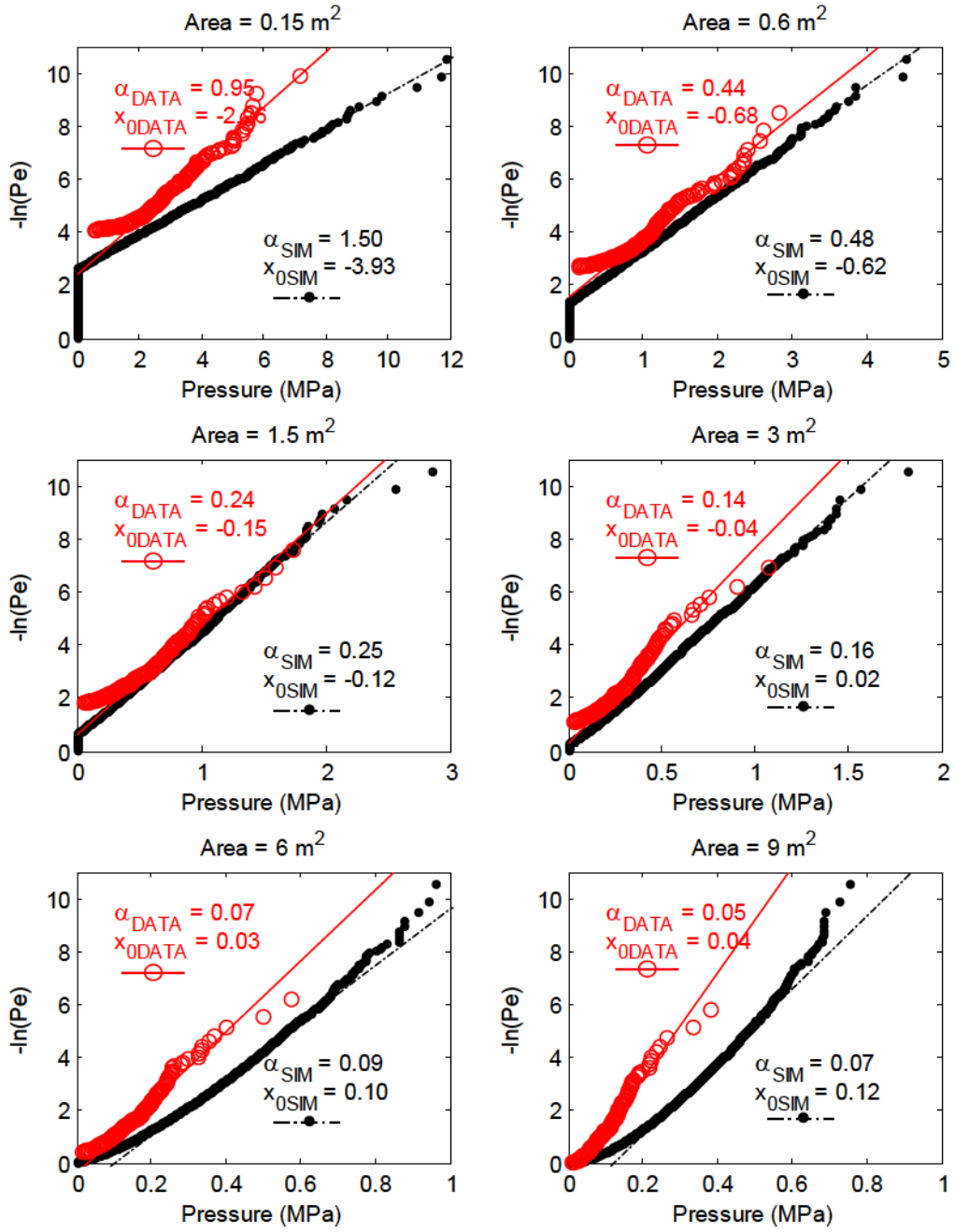

Figure 142 Comparison of simulated local pressure parameters with measured parameters based on Beaufort 1984 trials – $\gamma = 0.32$ MN; $\gamma_0 = 0.0$ MN; $\rho = 0.50$ *HPZ*s/m^2. .

4.4.5 Modeling Local Pressure Area Data – Simulated vs Measured

Figure 143 and Figure 144 illustrate the simulation of 'parent' local pressure design curves for α and corresponding x_0 comparing with measured Polar Sea data and the ISO 19906 local pressure design curve. Sensitivity to HPZ force parameter γ_0 and corresponding HPZ density values is also illustrated. As first introduced in Section 4.3.6, a direct correlation between force cutoff and density exists. The consistency in local pressure plots confirms the relationship between cutoff force and density illustrated in Figure 127– Beaufort Sea 1982, Figure 129– North Chukchi 1983, Figure 131 – South Chukchi 1983 - and Figure 133– Beaufort 1984. This relationship is important when analyzing data to establish *HPZ* force parameters. The choice of a density must include the correct cutoff force parameter γ_0. A system activation threshold, or threshold applied to data analysis may influence the density estimates and should be considered in simulation modeling.

Figure 145 and Figure 146 illustrate comparisons with other datasets including *Louis S. St. Laurent* 1994, *Terry Fox* 2001, *Oden* 2001, and *Kigoriak* 1981. Remarkable consistency is achieved. As noted earlier (referencing Table 14), it is interesting that the power law expression for α for each dataset reported in Jordaan *et al*. (2007), and the regression constant C from the expression $\alpha = C \cdot A^{-0.7}$ is similar with the *HPZ* force parameter γ. While not specificially derived for this thesis, given the strong correlation observed, the HPZ force parameter γ used in the above comparisons was assumed to be consistent with the C coefficient derived in Jordaan *et al*. (2007) local pressure analysis.

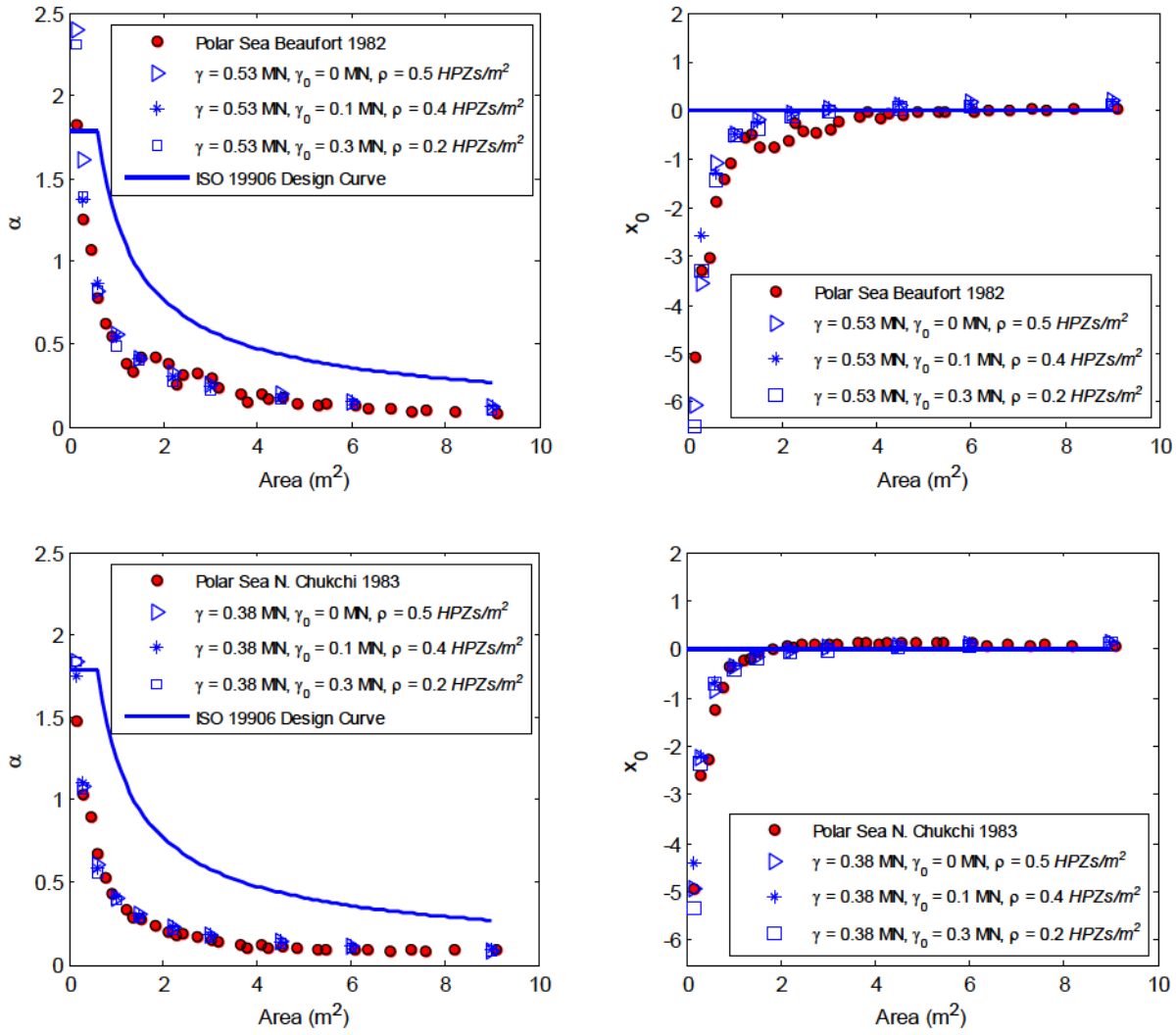

Figure 143 Comparison of simulated local pressure parameters α and x_0 vs. Area with measured parameters *Polar Sea* – measured data are illustrated with red dots.

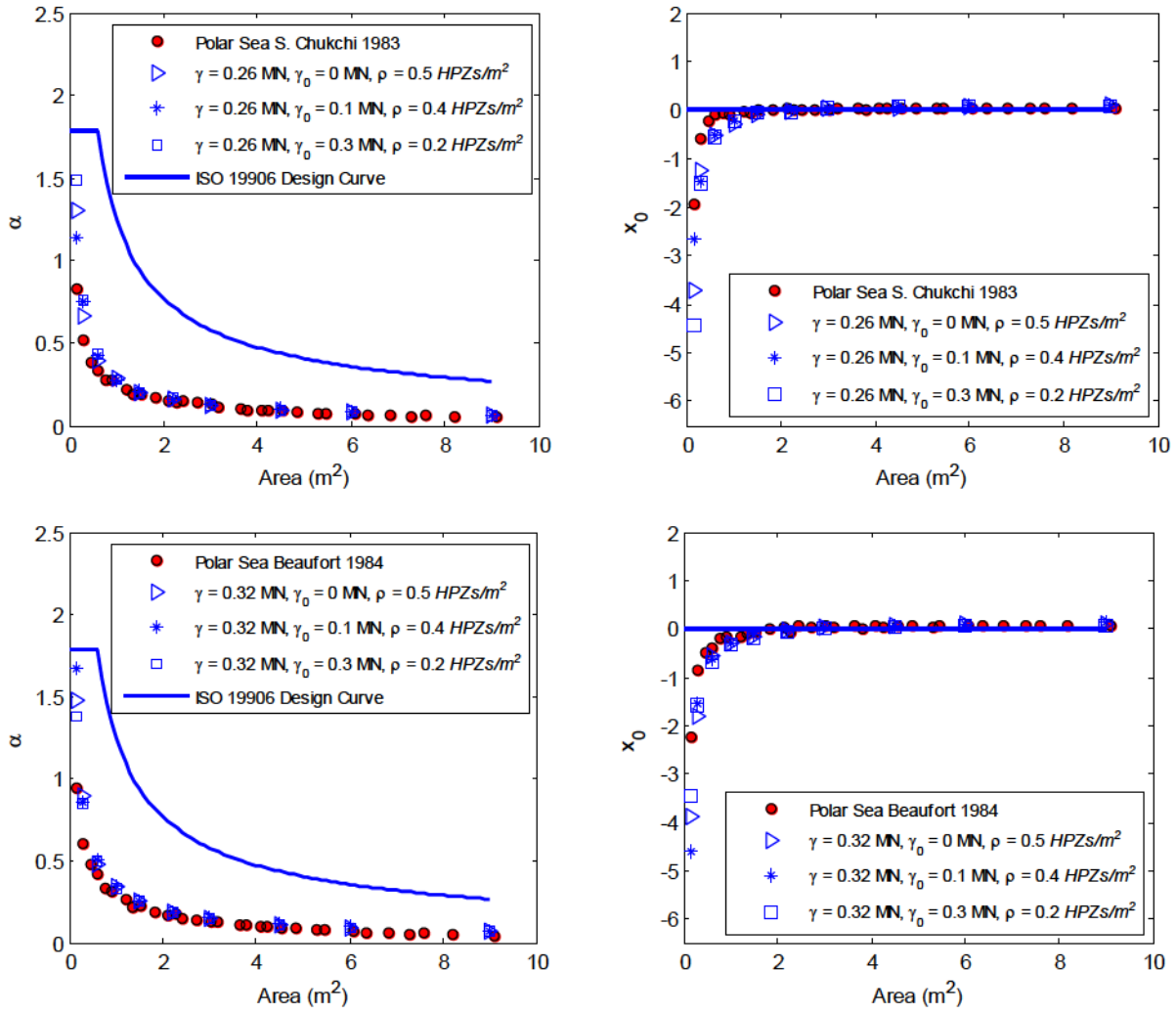

Figure 144 Comparison of simulated local pressure parameters α and x_0 vs. Area with measured parameters *Polar Sea* – measured data are illustrated with red dots.

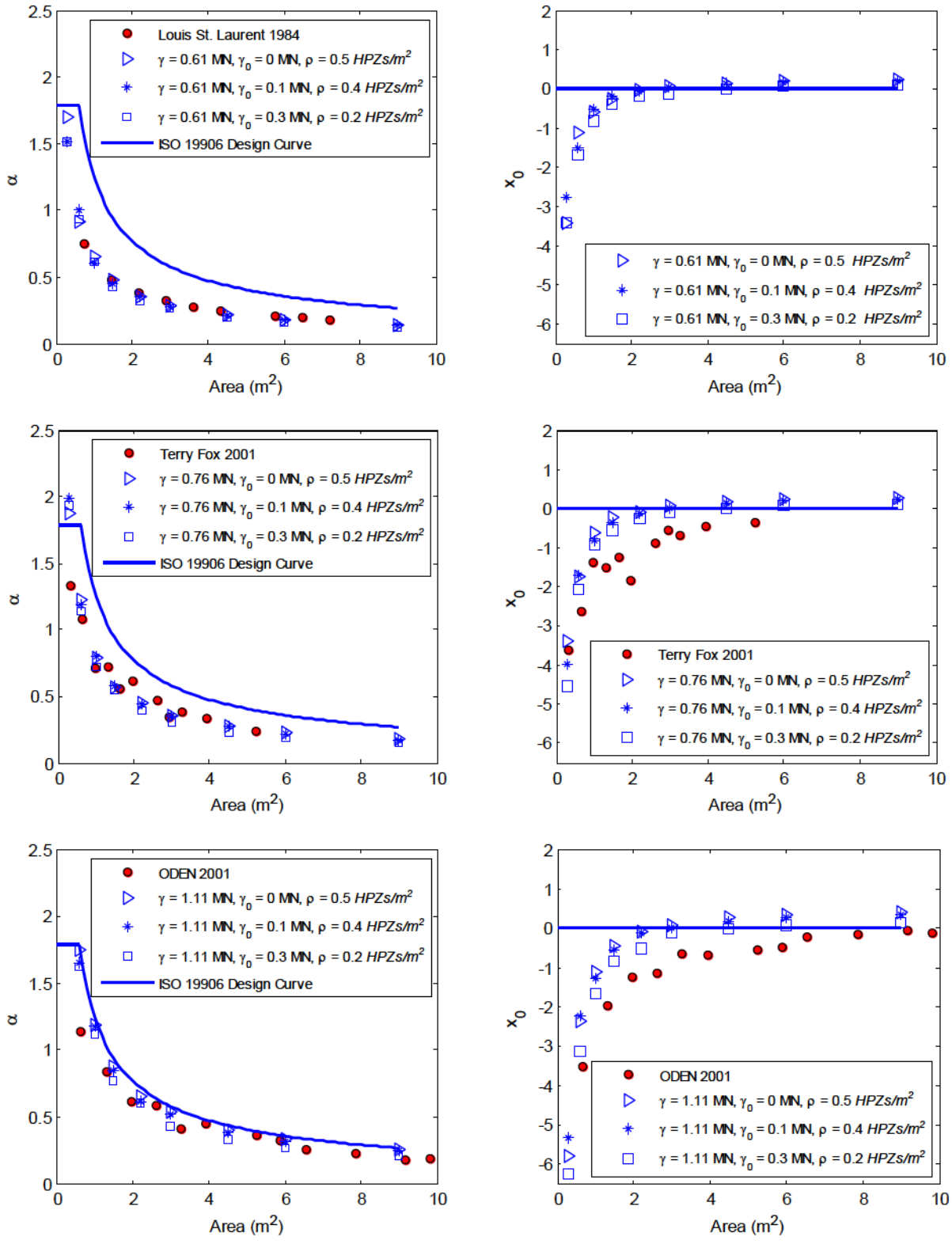

Figure 145 Comparison of simulated local pressure parameters α and x_0 vs. Area for other datasets – measured data are illustrated with red dots.

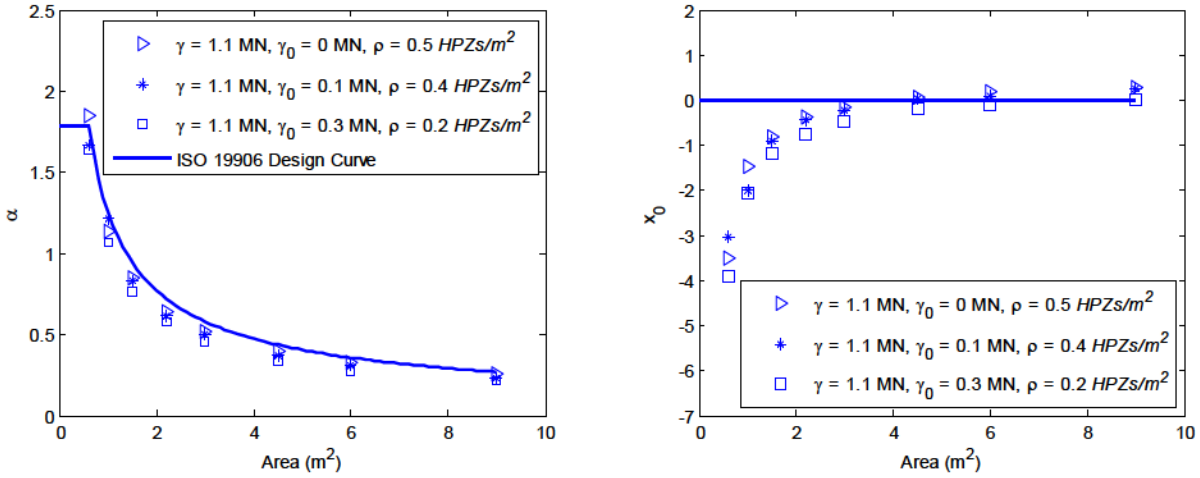

Figure 146 Comparison of simulated local pressure parameters α and x_0 vs. Area for *Kigoriak* Dataset – most aggressive ramming with strongest MY ice and used as base dataset for ISO 19906 design curve.

4.4.6 Modeling HPZ / Panel Hits or Misses

As discussed in Section 4.3.8, extremal analysis for ship design considers the maximum of n events within a time period, or spatially, the maximum action on one subpanel out of actions on n possible panels. A resultant design distribution can be modeled directly as $Fz(z) = Fx(x)^n$ where n is the number of events or actions and $Fx(x)$ is the base or 'parent' distribution. Similarly, an extremal distribution of $Fz(z)$ can be derived from Monte Carlo analysis by repeating many simulations of n events or actions from a 'parent' distribution, keeping only the maximum of n events and tossing the others.

Section 2.3.3.3, Section 4.3.8 and previous sections illustrate exposure for derivation of local pressure parameters from measured data and simulation (i.e. based on density). Of particular importance is having the correct 'parent' distribution for extremal analysis. To correctly model local pressures using an exponential 'parent' distribution and the parameter α, the distribution must be correctly positioned using the parameter x_0 which is proportional to exposure and as illustrated in Section 4.3.7, is proportional to the proportion of *HPZ* misses for any given panel area. A distribution of peak pressures among n possible panels is not a

'parent' distribution for 'any' panel but by nature of analysis is inherently extreme. Exposure adjustment is necessary.

For extremal analysis assuming exponential modeling of local design pressures, a designer has a couple of options for modeling a 'parent' distribution.

- model misses using a calibrated *HPZ* simulation model as discussed in previous sections – based on *HPZ* force and density – and directly estimating local pressure parameters α and x_0 based on Poisson simulated misses or zeros; or
- remove Poisson simulated zeros from simulated local pressure parameters, and then adjust for misses and exposure outside the simulations based on an independent analysis misses estimated from data to determine.

Regarding the last bullet item, an analysis of misses (or hits) was conducted using the *Polar Sea* Beaufort 1982 data and impacts with MY ice. As with local pressure analysis (see Section 2.3.3), measured pressures on all panel areas were scanned through the full ram duration to identify the peak pressure. The time location for peak pressure on a specific subpanel area may be different for each area (the birth and death of *HPZ*s is a random process). At this peak pressure time slice, all panels of a specific area having zero pressure (or near zero pressure) within the array of n possible panels within the full 9.1 m^2 senor area were identified and the proportion of misses estimated. Starting with the smallest subpanel area, incrementing panel areas were then analyzed (i.e. 1 subpanel – 0.15m^2, 2 subpanels – 0.30 m^2, 3 subpanels, 4 subpanels, etc). A minimal cutoff pressure of 0.172 MPa was modeled to remove system noise (See Section 4.4.1). No adjustment for forward movement of the vessel and sliding of contact from one panel to another was modeled. No adjustment for vessel side (i.e. panel located on only one side of vessel bow) was considered.

Figure 147 illustrates panel misses based on measured *Polar Sea* Beaufort 1982 trials and simulations based on *HPZ* density. Three measured curves include the influence of cutoff force – Fco = [0, 0.3, 0.5, 0.7] MN. Two simulation curves model the influence of density = [0.7, 0.5] zones/m^2. The measured curve with no cutoff force models considerably less misses being biased toward lower pressures that relative to peak design pressures are quite small. The curves with cutoff forces [0.3, 0.5, 0.7] MN respectively are quite similar

suggesting that cutoff force is needed to remove non design relevant *HPZ* pressures. The curves modeling cutoff force are consistent with simulated curved that modeled misses using an *HPZ* density of 0.7 *HPZ*/m^2. Modeling a density below 0.5 *HPZ*/m^2 without an appropriate cutoff force will model too few *HPZ*s. As noted earlier, the importance of modeling misses is to ensure that the 'parent' distribution used for extremal analysis has the correct plotting position and parameter x_0. As a result, while lower densities will increase the proportion of zeros or misses and reduce x_0, a correct cutoff force must be applied to simulations to shift x_0 upwards to the appropriate value.

If zeros are removed from the simulations and added independently based on measured misses, the curve corresponding to 0.3 MN cutoff force is a reasonable choice. If modeling simulated zeros, densities below 0.5 *HPZ*/m^2 should consider an appropriate cutoff force, otherwise the positional parameter x_0 could be too low.

For panel areas representative of design areas, example proportions of missed panels include ~64% for 0.6m^2 area, 38% for 1.26m^2 area and 20% for 2.24m^2 area. Panel areas greater than 3.5m^2 have less than 5% misses. While not particularly relevant for panel design (i.e., localized pressures are ultimately averaged over the full panel area), the proportion of misses for the smallest 0.15m^2 area are 58-59 of the 60 panels, or 98%. This is consistent with the exposure adjustment of 1/60 as discussed in Section 2.3.3.

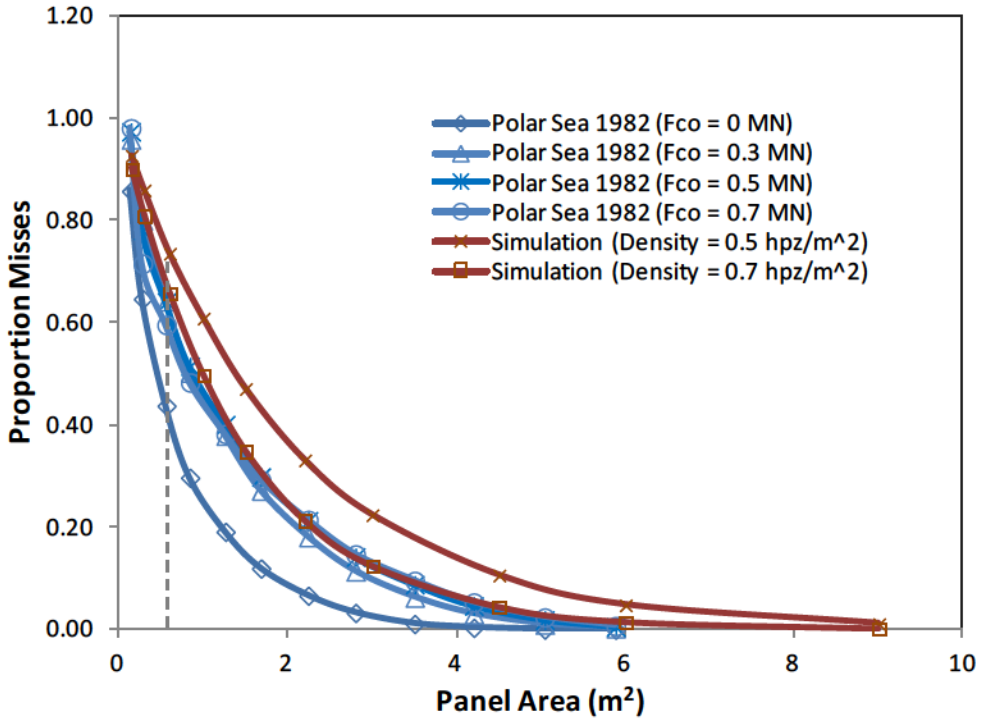

Figure 147 For full impact duration for *Polar Sea* Beaufort 1982 dataset, average number of misses for different panel areas

Other Operational Considerations

Consideration for 'misses' may also consider some special cases such as exposure for bergy bit impacts on the outer or shoulder bow where both bows side cannot simultaneously be impacted (See Figure 148). A Captain will likely exercise an avoidance maneuver and reduce exposure to any outer bow panel by 50% since contact on both sides is not possible. Choice of turn direction would be random. Reduction in stem contacts is also reduced as one side is more exposed.

With respect to floe interaction, the designer may consider the extent of penetration from global ram analysis and concentric head on impacts since there is some limiting penetration where panel contact on both sides of the bow is equally likely.

For codes development, it may be appropriate to consider exposure in two forms r and q.

1) Panel exposure q considering nature of ice failure and maximum pressure on any panel out of n exposed panels.
2) r depending on location along the bow as illustrated in Figure 149 – e.g. $r = 1$ for distance less than 5 m (TBD) from vessel stem or FP; $r = 0.5$ for distance aft of 5 m from FP.

Regarding r, for rational design, the designer could consider a comprehensive ram analysis based on vessel displacement and bow form, estimating the extent of penetration into a MY ice floe, directly quantifying the selection of exposure r (e.g. r = 1 for penetrations less that some design maximum; r = 0.5 for regions further along the vessel length).

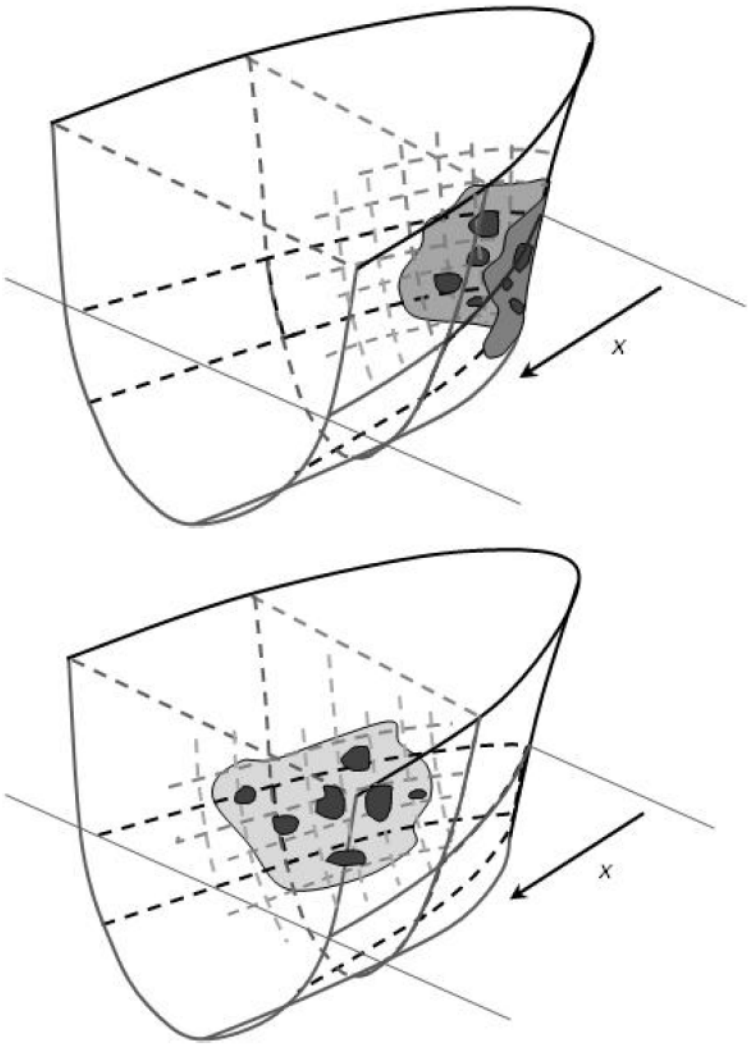

Figure 148 Illustration of nominal contact area and *HPZs* for both center bow and outer bow/shoulder impact

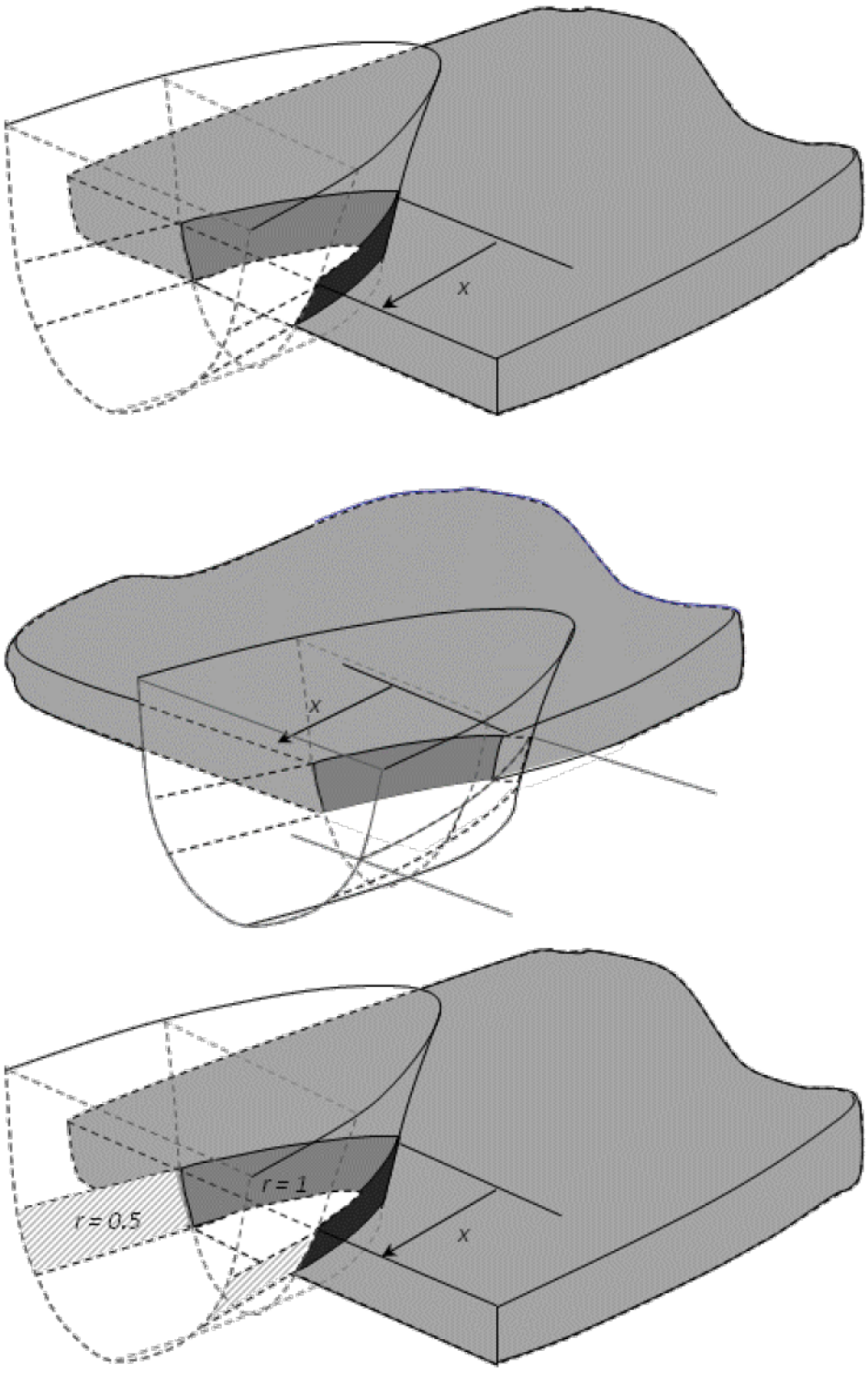

Figure 149 Illustration of bow imprint and regional exposure

4.4.7 Summary Discussion

Using *Polar Sea* datasets (i.e. Beaufort 1982, North Chukchi 1983, South Chukchi 1983, and Beaufort 1984), *HPZ* forces based on the smallest $0.15m^2$ single panels at a 1/32 time slice corresponding to peak pressure in each ram was determined. Each activated panel (pressures above a minimum threshold) was assumed to represent the occurrence of an *HPZ*. This is reasonable since on average, *HPZ* area according to Zou 1996 is estimated at $0.080m^2$ using a $0.048m^2$ resolution pressure. This area is approximately half the *Polar Sea* sensor resolution.

While it is unlikely that more than one *HPZ* be positioned within a single $0.15m^2$ panel, given the size of the *Polar Sea* panels relative to the smaller *HPA* areas, measured pressures may be somewhat low. A pressure-area scale effect correction was applied to the measured *HPZ* forces. For simulations consideration for edge effects was considered since an *HPZ* having an area of 0.08 m^2 could well be positioned across two adjacent 0.15 m^2 panels as discussed in Section 4.4.4.1. Comparison of both simulated and measured local pressure parameters α and x_0 is quite reasonable justifying that modeling local pressure on the basis of *HPZ* force and density is valid.

HPZ force and density parameters illustrated in Table 14 will be the basis for a new improved basis for *HPZ* occurrence modeling, the inclusion of *HPZ* formation rate, such that the number of significant *HPZs* through the ram duration can be simulated randomly such that the peak pressure can be determined. This model is discussed in the following section.

4.5 Modeling *HPZ* Rate

In the previous sections, *HPZ* force and density were determined from ship ram data to be used as inputs in simulations of local pressure design parameters α and x_0 vs. local design areas. The sensitivity of density to cutoff forces (and pressures) in both the measurement system as well as data analysis have been discussed - higher force cutoffs result in reduced apparent *HPZ* density. *HPZ* failure force varies depending on ice conditions. The data illustrate that more southerly regions, or conditions having warmer ice, tend to have lower pressures. While this may suggest that local pressures may be influenced by temperature and salinity, such analysis is outside the scope of this thesis.

Exposure is a key parameter in local pressure design. Exposure increases with increased number of impacts and longer durations, resulting in increased design pressures. For design we are concerned for the peak panel pressure over an exposed interaction area through the full interaction duration.

To date, local pressure models do not explicitly model the occurrence of *HPZs* through the ram duration. Such a model requires an *HPZ* formation rate (i.e. birth and death). The higher the rate and longer the duration, the greater the number of *HPZs* which subsequently leads to increased probability of a higher design force and design pressure.

4.5.1 Background

Earlier work by Jordaan (2001) and later Jordaan *et al*. (2007) modeled duration to enhance local pressure design by scaling exposure based on duration for a new design relative to *Kigoriak* measurements. *Kigoriak* trials and subsequent data were used to determine the α vs area design curve in ISO 19906. These trials are among the most aggressive MY ice ramming trials ever conducted. The mean duration of the *Kigoriak* rams was 0.7 seconds. This implies that longer durations provide more opportunity for higher pressures to occur. If designing for a larger ship for similar MY ice conditions, the local pressures can be enhanced by scaling the exposure parameter μ by the ratio of new estimated duration for a new vessel design to measured Kigorak duration (i.e. $\mu = t_{design}/t_{kig} = t_{design}/0.7$).

4.5.2 Modeling Local Pressures using HPZ Formation Rate

An improved approach to local pressure modeling is to explicitly model both rate of *HPZ* occurrence and ram duration in the development of a 'parent' local pressure distribution for extremal modeling. The expected number of *HPZs* through the ram can then be modeled as the product of formation rate and impact duration from which the maximum pressure out of *n HPZs* can be determined.

It is further hypothesized that *HPZ* formation rate is directly proportional to impact speed and impact duration a function of vessel displacement and impact speed (i.e. kinetic energy). The expected number of *HPZ* formations through the ram duration will be a function of *HPZ* rate and ram duration. Assumptions for this work are that the ice features are very large relative to vessel size and they are assumed fixed.

To determine *HPZ* rate, an iteration procedure is proposed. Firstly, for each set of *Polar Sea* trials, the average impact duration is determined from the measurements. Using average duration, *HPZ* rate is iterated until the product of rate and measured mean duration produces simulated local pressures on specific areas that are consistent with measured pressures.

It is reasonable to assume that such a process is random, and can be modeled using a discrete Poisson process. Since for design we are concerned for peak pressures on a panel, we are interested in the maximum of *n* expected *HPZ*s through the ram duration, consistent with the analysis approach by Jordaan *et al.*, (1993) and Jordaan, (2001). This model development including calibration with *Polar Sea* data is discussed in the following sections.

Once *HPZ* rates have been estimated, a relationship between *HPZ* rate and measured impact speeds can be determined. From a modeling perspective, *HPZ* rate is estimated as a function of impact speed, and duration is estimated using a global ship ram model (e.g. Fmax model discussed Section 4.2). The higher the impact speed and the longer the duration (larger ships moving faster), the greater the exposure and subsequent local pressure. A random process is modeled that also models correctly the material properties of a fracture material and corresponding scale effects.

4.5.3 Methodology for Estimating HPZ Rate

The following outlines the approach developed to determine *HPZ* rate including verification with *Polar Sea* trial data:

- for each set of ram trials estimate average ram duration;
- model new Poisson process that estimates number of *HPZ* occurrences (slices in time) through the ram duration based on product of an initial estimate of *HPZ* rate and mean duration;
- consistent with earlier simulations, for each *HPZ* occurrence, estimate using a second Poisson process, spatially the number *HPZ*s on the specific area based on *HPZ* density; for each *HPZ*, estimate a force based on the *HPZ* force distribution for the appropriate force parameter γ;
- for each occurrence in time, estimate pressure on each panel area based on the sum of *n HPZ* pressures over the panel area;
- determine the maximum pressure for the *n HPZ* occurrences (or slices) through ram duration;
- repeat for a large number of simulations and develop a distribution of peak pressures on panel areas;
- repeat for each panel area;
- compare simulated distribution of *HPZ* pressures as a function of local area with measured values; and
- iterate *HPZ* rate until simulated distribution matches the measured distribution.

Input parameters for each *Polar Sea* Data set - Beaufort 1982, North Chukchi 1983, South Chukchi 1983 and Beaufort 1984 - including mean durations, *HPZ* density, force parameters γ and γ_0 as well as vessel displacements and impact speeds where available are given in Table 15. Best estimates of *HPZ* rates range from 0.32 to 0.5 *HPZs*/s. As expected, higher rates correspond to higher impact speeds, and vise versa.

Figure 150 through Figure 154 illustrate the comparison of simulated local pressures with measured based on best estimate of *HPZ* rate for panel areas ranging from 0.6 m^2 through 9.0 m^2 for each *Polar Sea* dataset including. Subplots compare measured *HPZ* pressures on

specific areas (and corresponding α parameter fit to distribution tails) to simulated pressures. Histograms of pressures are illustrated in Figure 151. Interestingly, the distribution of pressures for increasing areas is approaching a normal distribution. This can be expected since the simulation process, and summation of forces from *n HPZs* over the panel area to estimate local pressures is consistent with the Central Limit Theorem - that distribution summations leads to normality in a resultant distribution. For illustration only, sensitivity to *HPZ* rate scaled by 100x and duration scaled by 10x for Beaufort 82 forces is illustrated in Figure 155 to Figure 158, including histograms.

The modeling of local pressures on different panel areas and comparison with measurements suggest that *HPZ* rate and density are not sensitive to panel area. Some deviation in simulation vs. measured exists (e.g. 1.5 m^2 area) but this is in part influenced by panel aspect ratio. Presently, simulations do not consider aspect ratio whereas measured pressures incorporate an aspect ratio effect. Pressure on a 10 subpanel area (1.5 m^2) based on a 5:2 aspect ratio will be higher than pressure on a 0.39 x 0.39 m area having an aspect ratio of one. Aspect ratio considered in analysis of measured local pressure data was limited to 3:1 (i.e. three columns one row of 0.15 m^2 panels).

4.5.4 Influence of Cutoff Force

Figure 159 through Figure 162 illustrate the simulation of local pressure parameters based on *HPZ* rate, duration and density based on cutoff force for each set of *Polar Sea* trials. Remarkable agreement is achieved, suggesting that the derivation of *HPZ* rate is reasonable. As illustrated earlier in this thesis, the correlation between *HPZ* density and threshold force is illustrated. Any density below 0.5 *HPZ*/m^2 will simulate too many zeros and hence must include the correct cutoff force. Interestingly, the density corresponding to zero cutoff force is consistent and reasonably modeled between 0.5 and 0.6 *HPZs*/m^2.

Modeling *HPZ* cutoff force with corresponding density must be exercised with caution. Cutoff force cannot be modeled as an absolute constant but scales depending on ice failure forces corresponding to a particular data set. The cutoff force parameters (and corresponding density) that properly scale density for Beaufort 84 data having γ = 0.32 is considerably

lower than cutoff force for Beaufort 82 data with γ given as 0.53 MN. Higher cutoff forces were modeled with the LSSL data given higher force parameters γ (See Section 4.3.6).

Table 15 Ship ram particulars including 0.1 MN pressure cutoff on data processing

	PS Beau82	PS N.Chuk83	PS S.Chuk83	PS Beau84
Vessel Displacement (kT)	13.1	13.1	13.1	13.1
HPZ Force Parameter γ (MN)	0.53	0.38	0.26	0.32
HPZ Force Parameter γ_0 (MN)	0.3	0.3	0.2	0.15
HPZ Density (*n HPZ*s/m^2)	0.2	0.2	0.2	0.2
Mean Ram Speed (m/s)	2.38	2.73	3.09	3 (estim)
Mean Ram Duration (s)	3.6	3.9	3.4	3.4
Initial estimated *HPZ* Rate (slice/s) *	0.3	0.4	0.55	0.50
Improved *HPZ* Rate (slice/s) **	**0.32**	**0.42**	**0.54**	**0.50**

* initial estimate based on iteration comparing simulated vs. measured local pressures

** improved estimate based on regressive modeling of rate vs. speed (see Section 4.5.5)

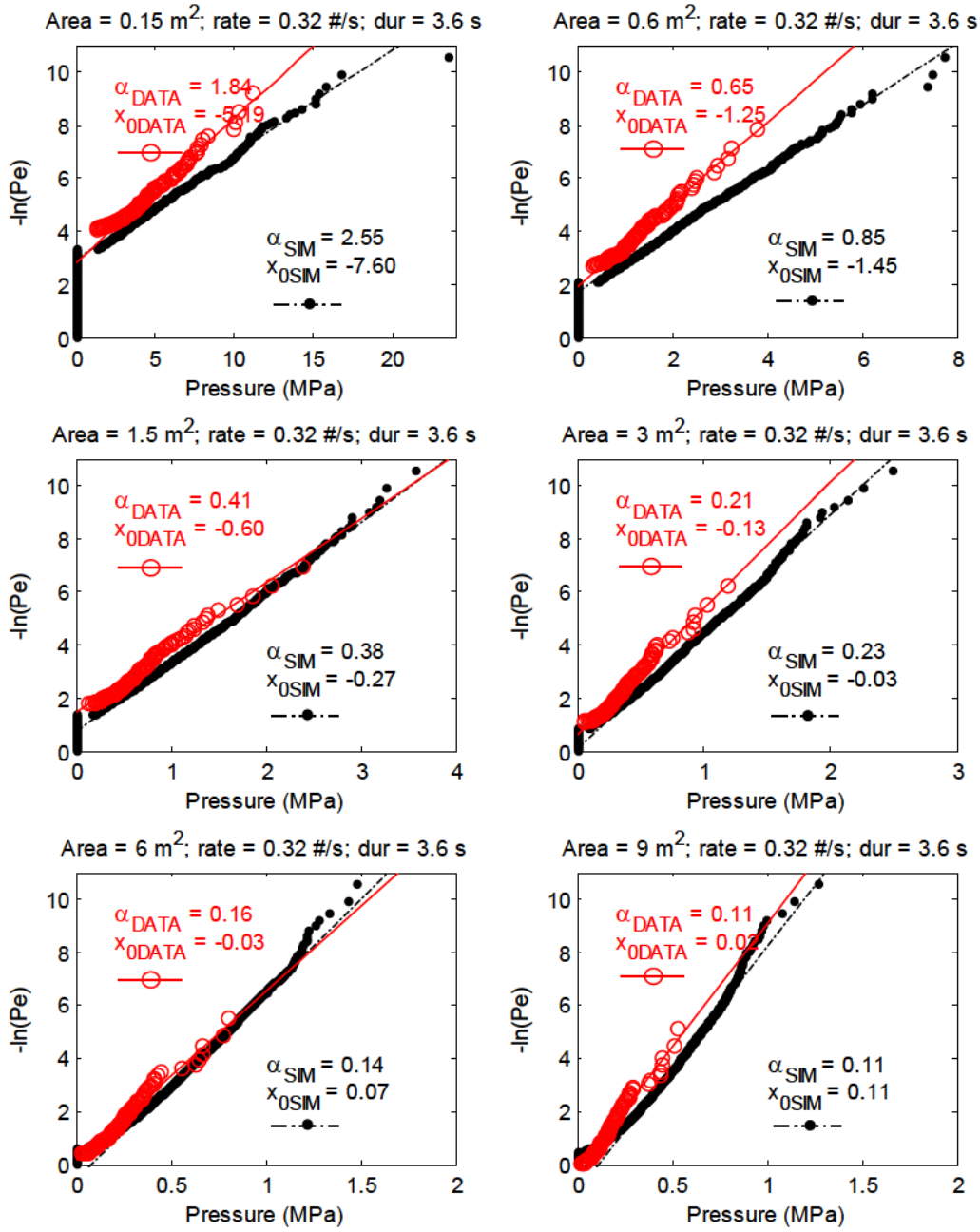

Figure 150 Comparison of measured and simulated local pressures based on *HPZ* rate for Beaufort 1982; $\gamma = 0.53$ MN, $\gamma_0 = 0.3$ MN, $\rho = 0.2$ *HPZ*s/m^2

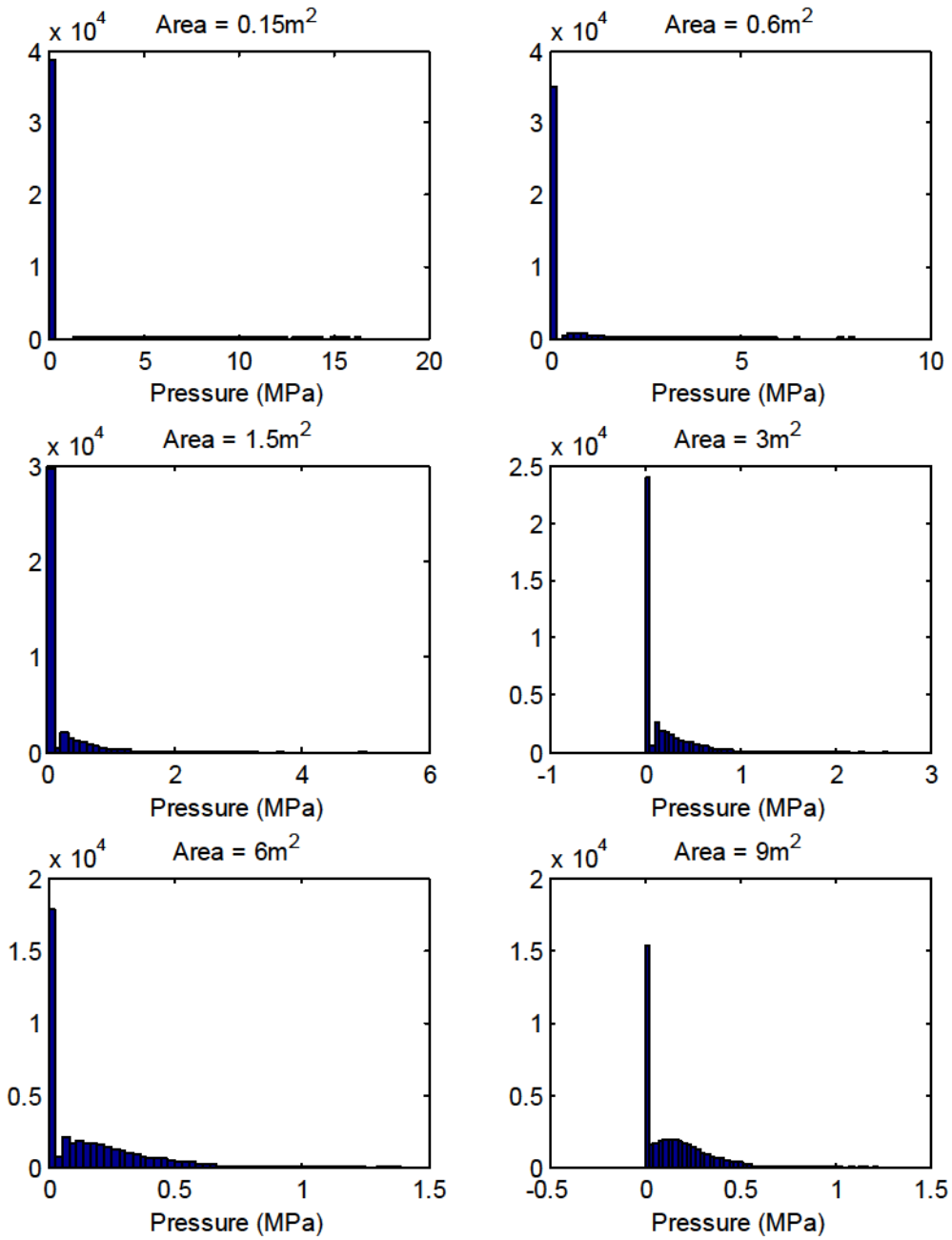

Figure 151 Histograms for local *HPZ* pressures for Beaufort 1982; $\gamma = 0.53$ MN, $\gamma_0 = 0.3$ MN, $\rho = 0.2$ *HPZs*/m^2

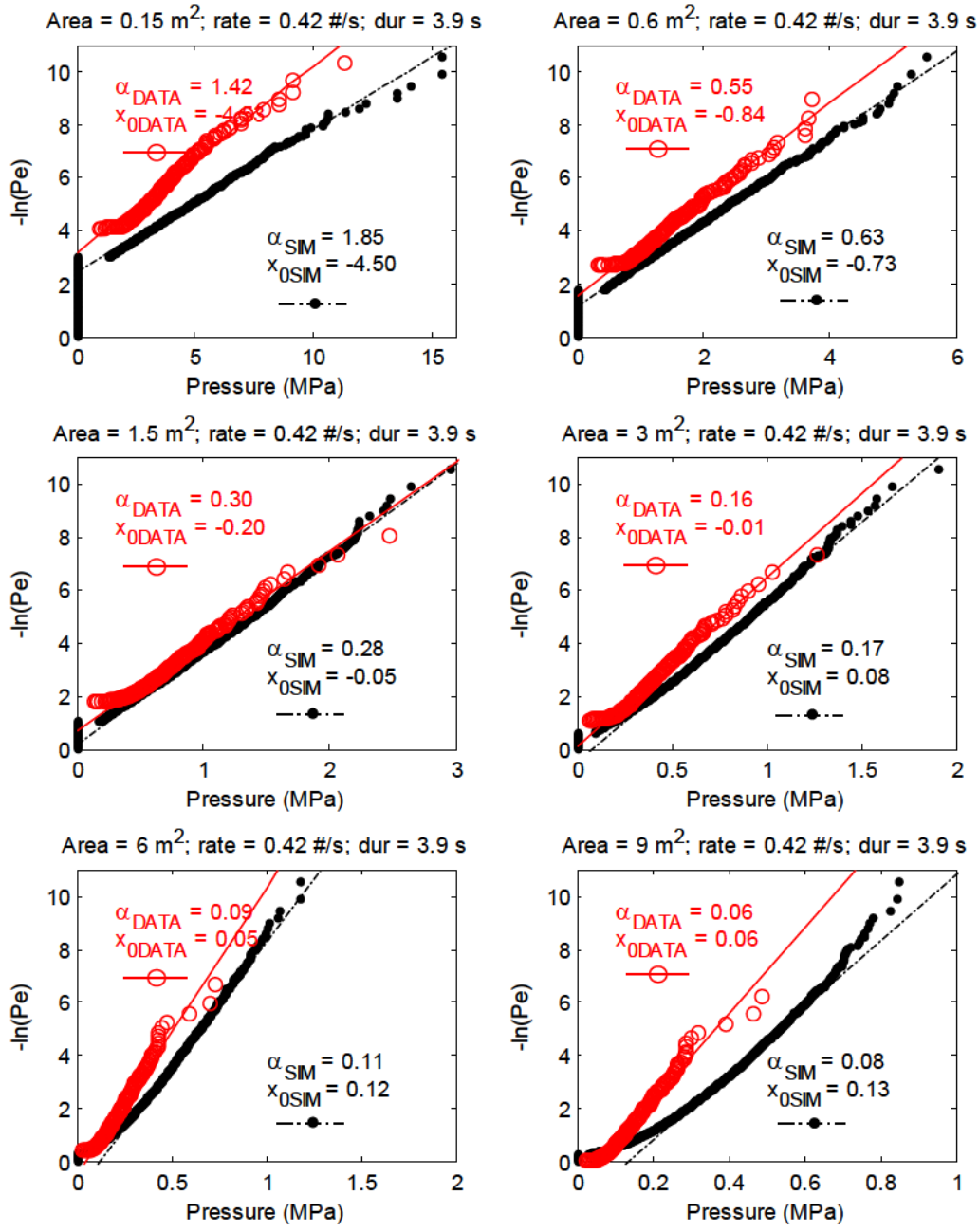

Figure 152 Comparison of measured and simulated local pressures based on *HPZ* rate for North Chukchi 1983; $\gamma = 0.38$ MN, $\gamma_0 = 0.3$ MN, $\rho = 0.2$ *HPZ*s/m^2

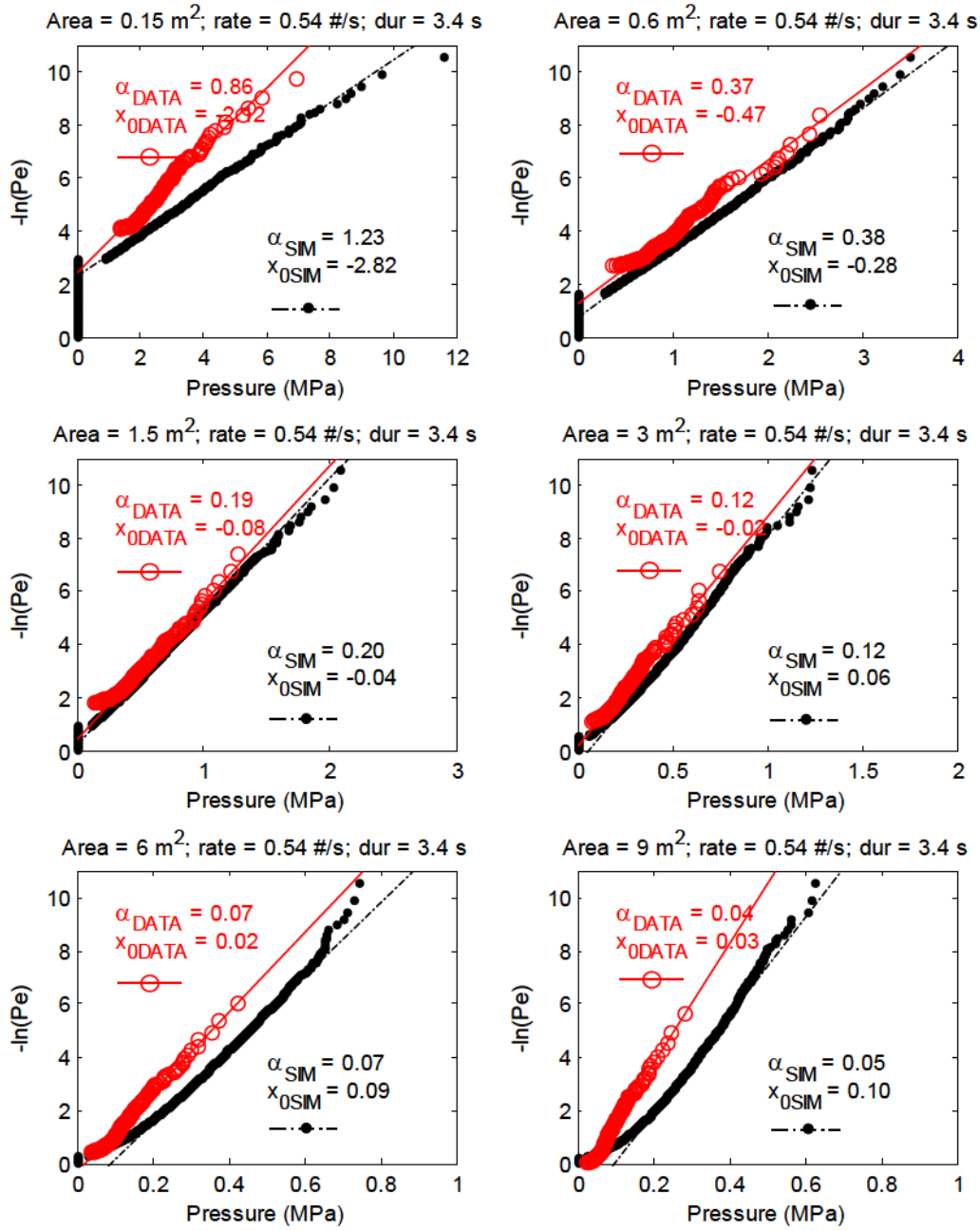

Figure 153 Comparison of measured and simulated local pressures based on *HPZ* rate for South Chukchi 1983; $\gamma = 0.26$ MN, $\gamma_0 = 0.2$ MN, $\rho = 0.2$ *HPZs*/m^2

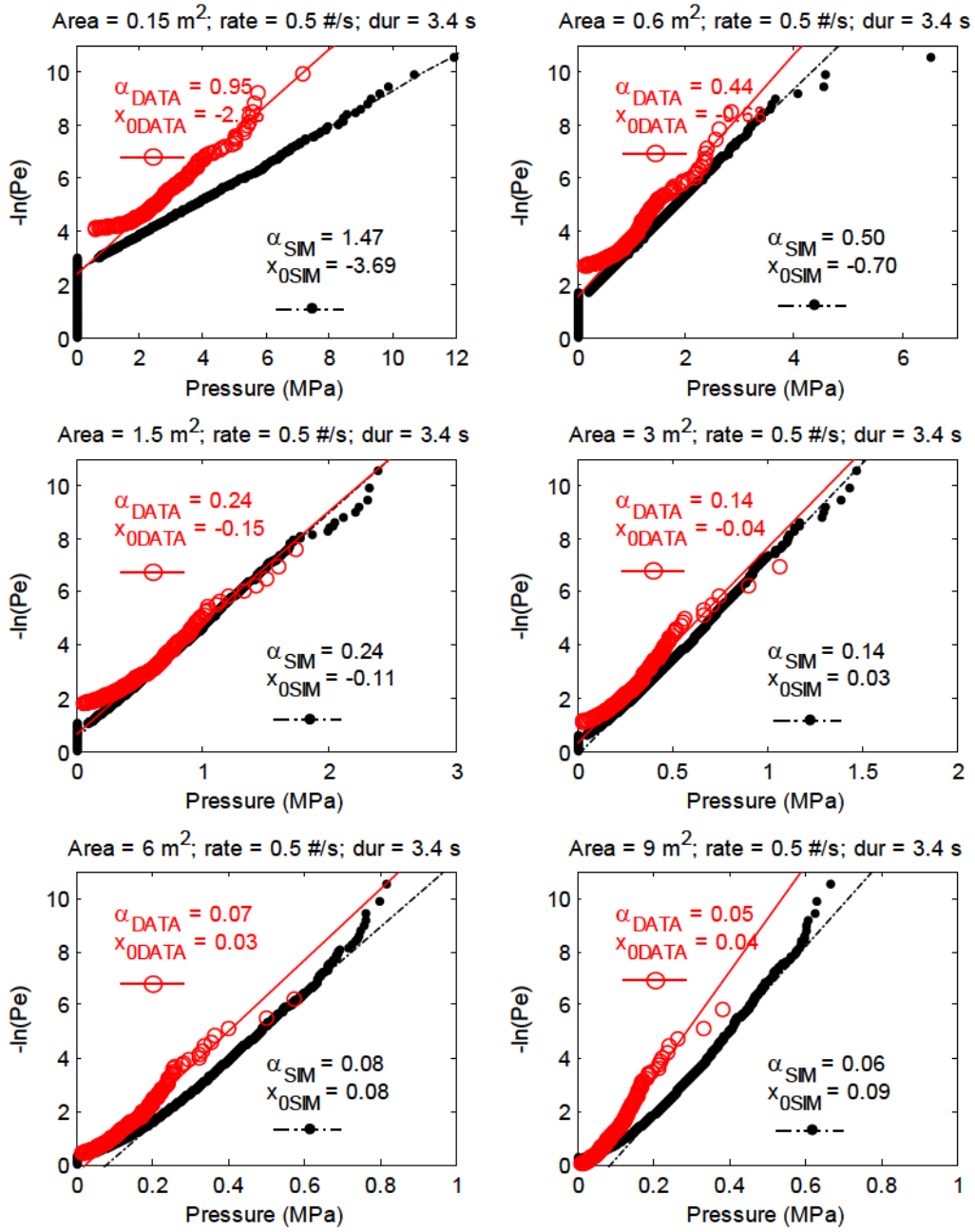

Figure 154 Comparison of measured and simulated local pressures based on *HPZ* rate for Beaufort 1984; $\gamma = 0.32$ MN, $\gamma_0 = 0.15$ MN, $\rho = 0.2$ *HPZ*s/m^2

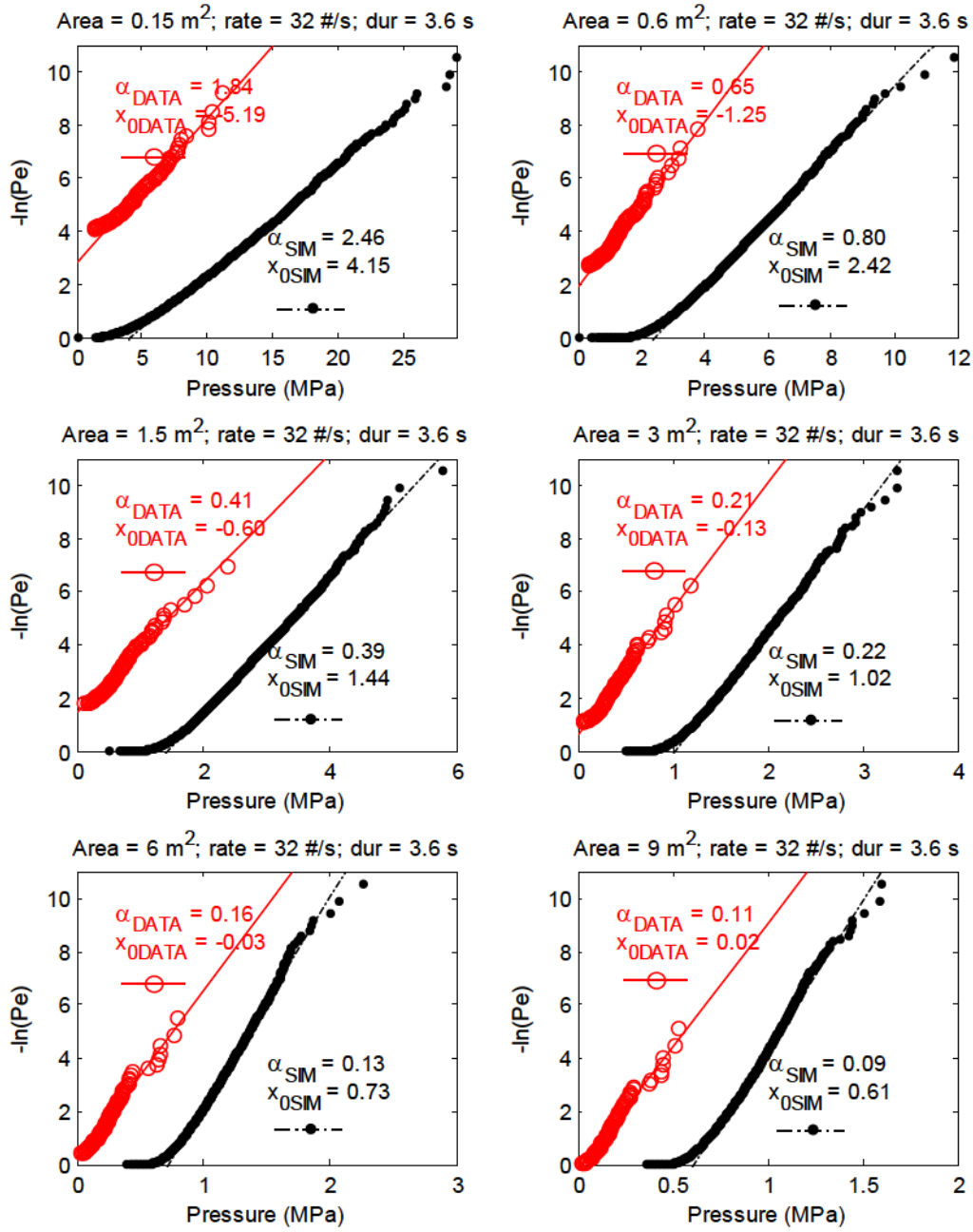

Figure 155 Local pressure simulation based on *HPZ* rate sensitivity (100x mean rate) for Beaufort 1982; $\gamma = 0.53$ MN, $\gamma_0 = 0.3$ MN, $\rho = 0.2$ *HPZ*s/m^2

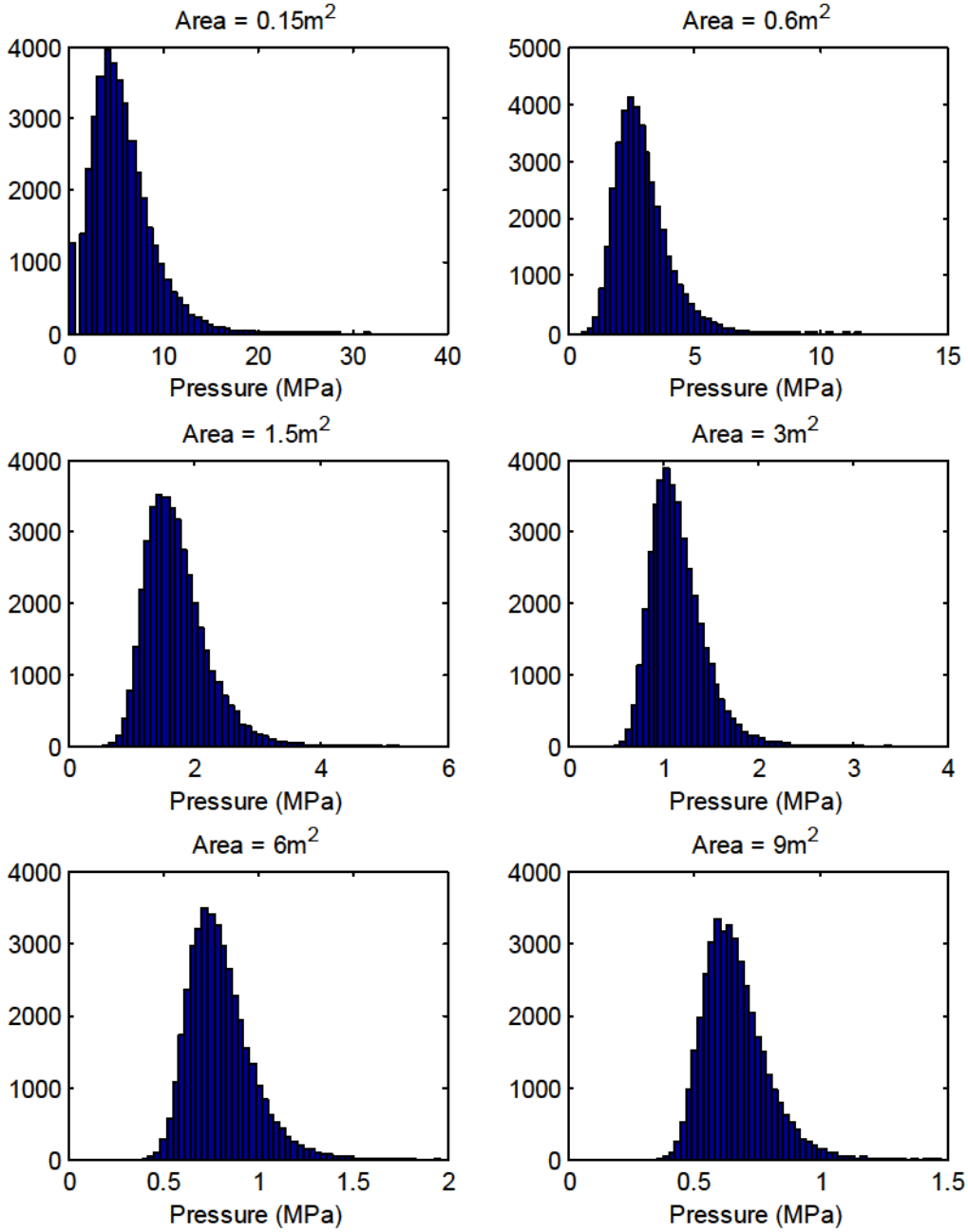

Figure 156 Histograms for local *HPZ* pressures with rate modeled as 100x mean rate for Beaufort 1982; $\gamma = 0.53$ MN, $\gamma_0 = 0.3$ MN, $\rho = 0.2$ *HPZ*s/m^2

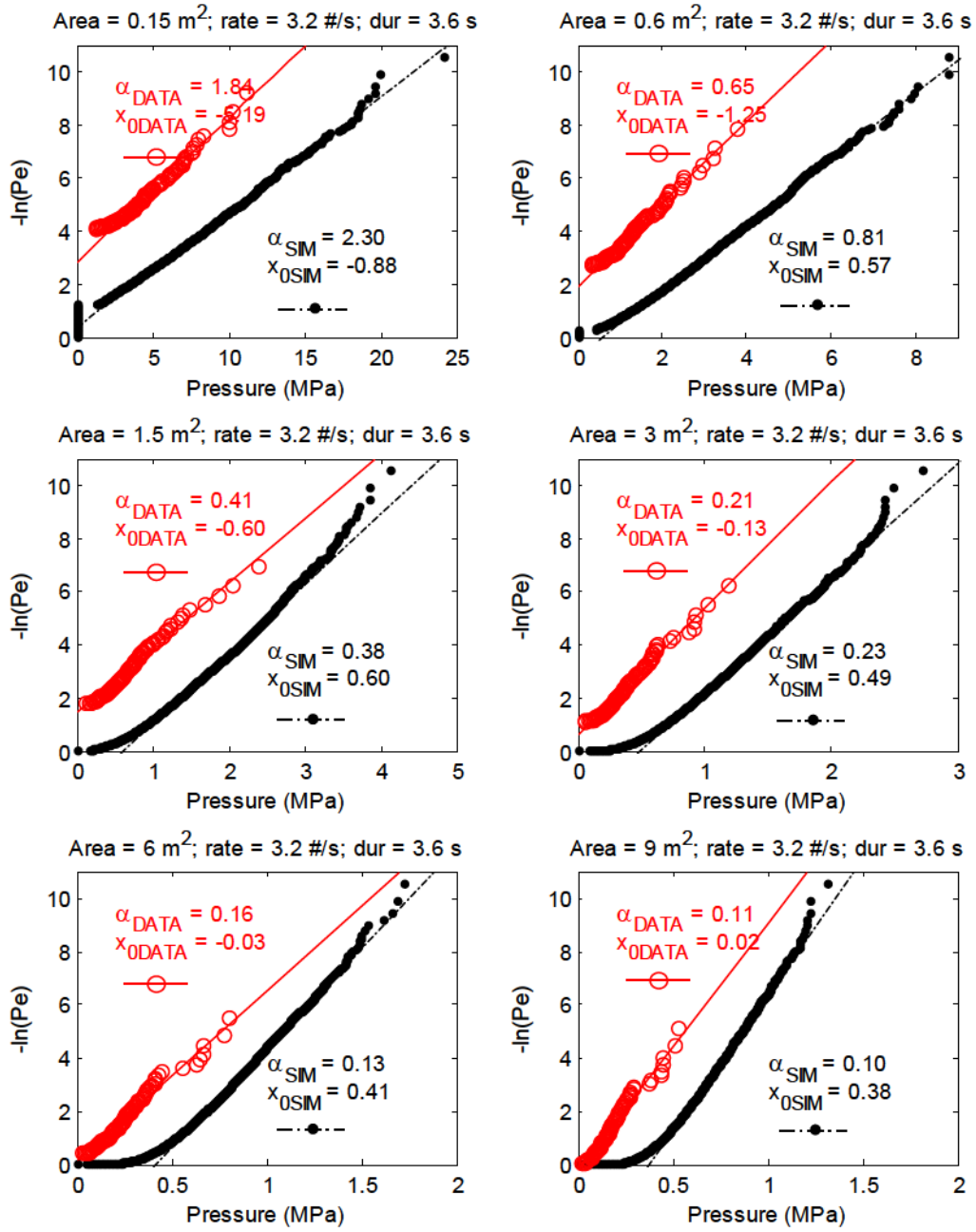

Figure 157 Local pressure simulation based on *HPZ* duration sensitivity (10x mean duration) for Beaufort 1982; $\gamma = 0.53$ MN, $\gamma_0 = 0.3$ MN, $\rho = 0.2$ *HPZ*s/m^2

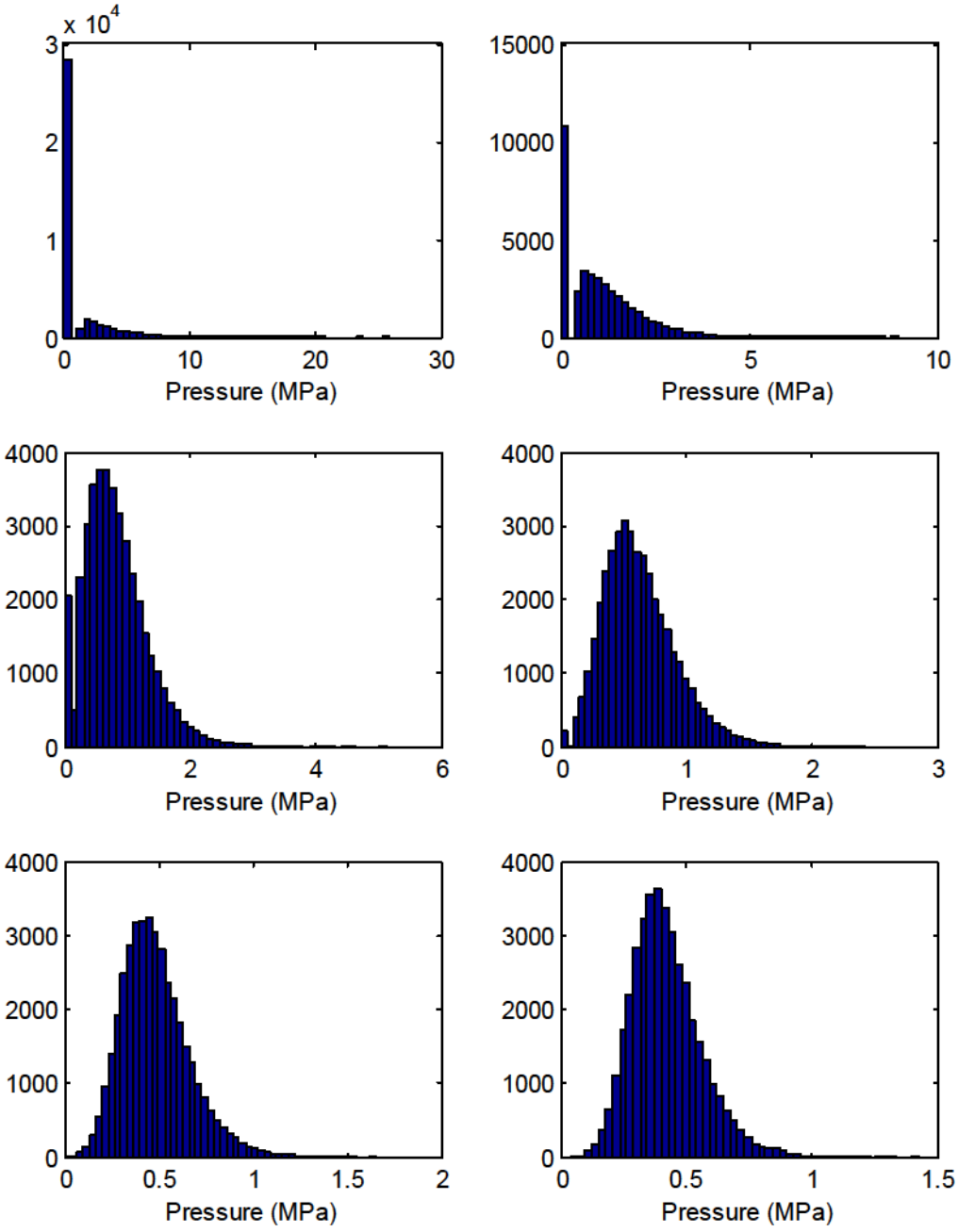

Figure 158 Histograms for local *HPZ* pressures with duration modeled as 10x mean duration for Beaufort 1982; $\gamma = 0.53$ MN, $\gamma_0 = 0.3$ MN, $\rho = 0.2$ *HPZ*s/m^2

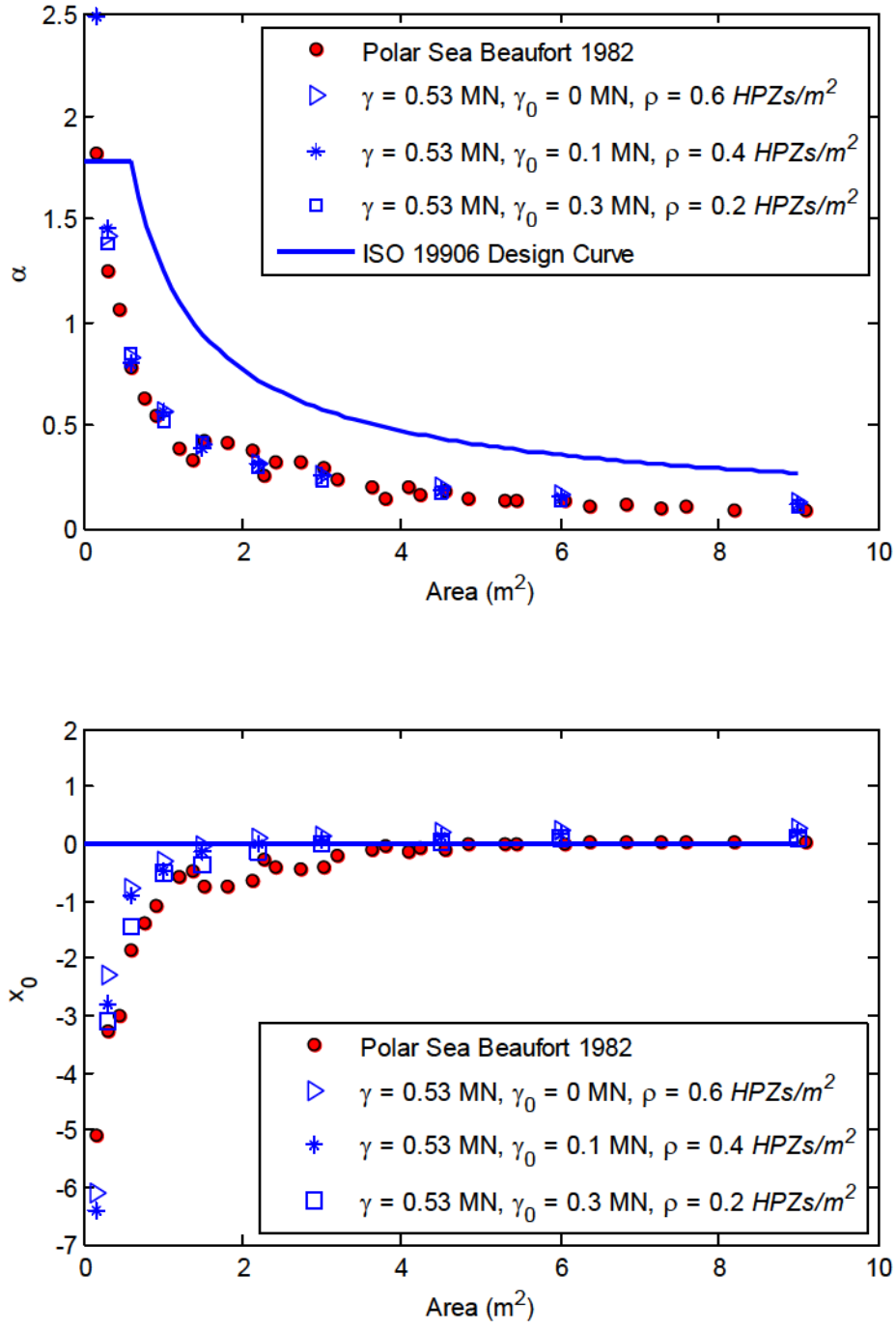

Figure 159 Simulated vs. measured local pressure parameters for *Polar Sea* Beaufort 1982; rate = 0.32 *HPZ*s/s, mean ram duration = 3.6 s

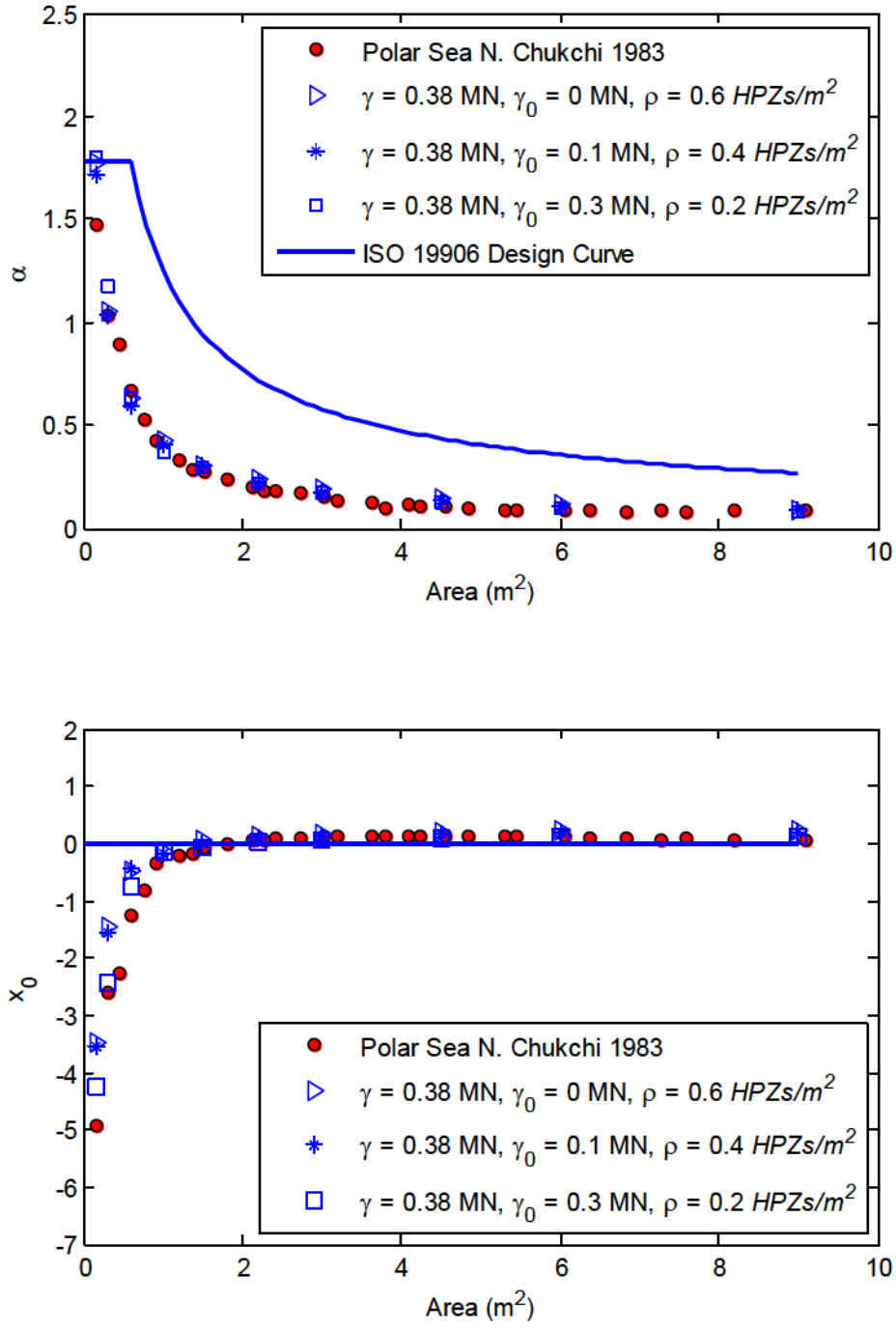

Figure 160 Simulated vs. measured local pressures parameters for *Polar Sea* North Chukchi 1983; rate = 0.42 *HPZ*s/s, mean ram duration = 3.9 s

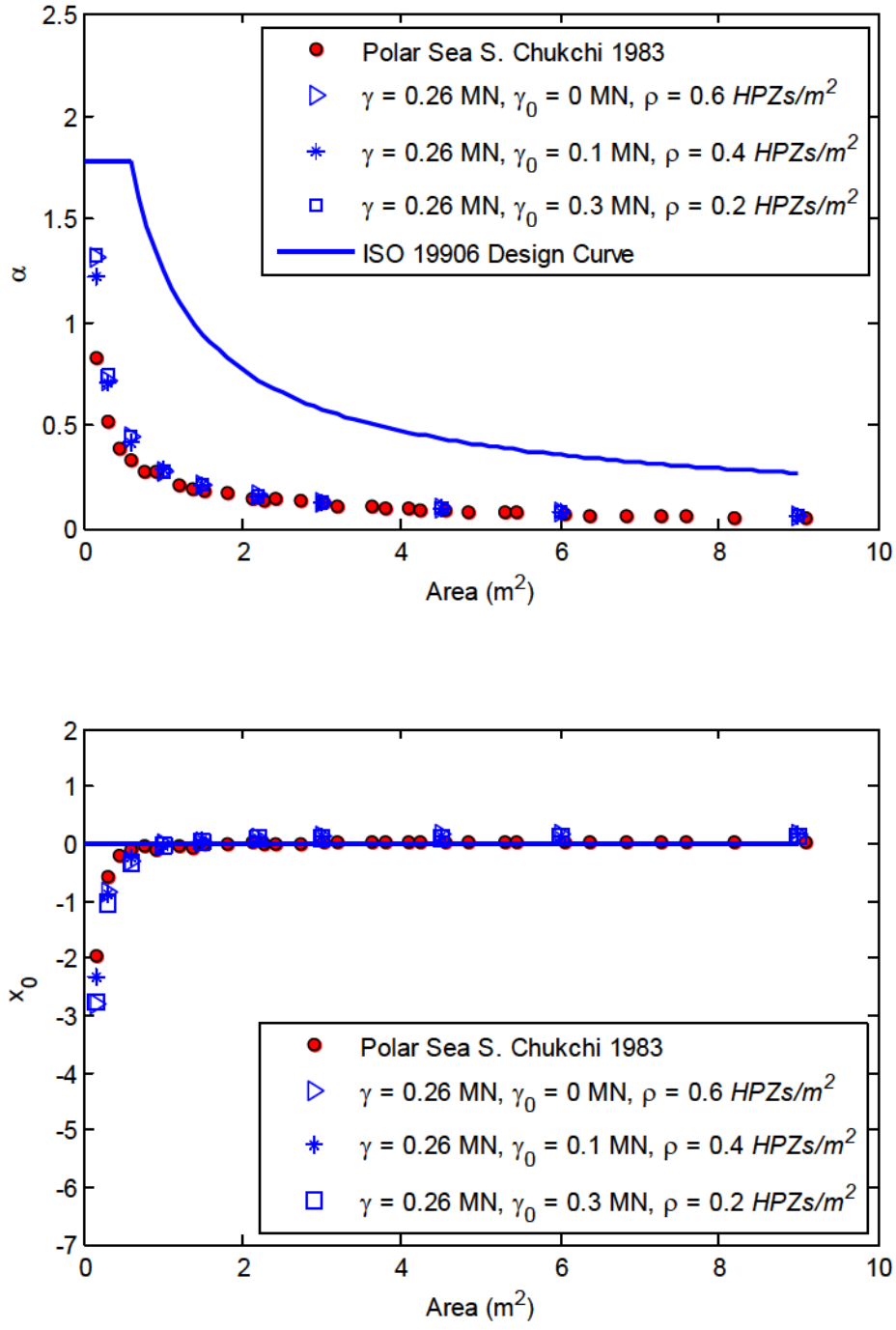

Figure 161 Simulated vs. measured local pressures parameters for *Polar Sea* South Chukchi 1983; rate = 0.54 *HPZ*s/s, mean ram duration = 3.4 s

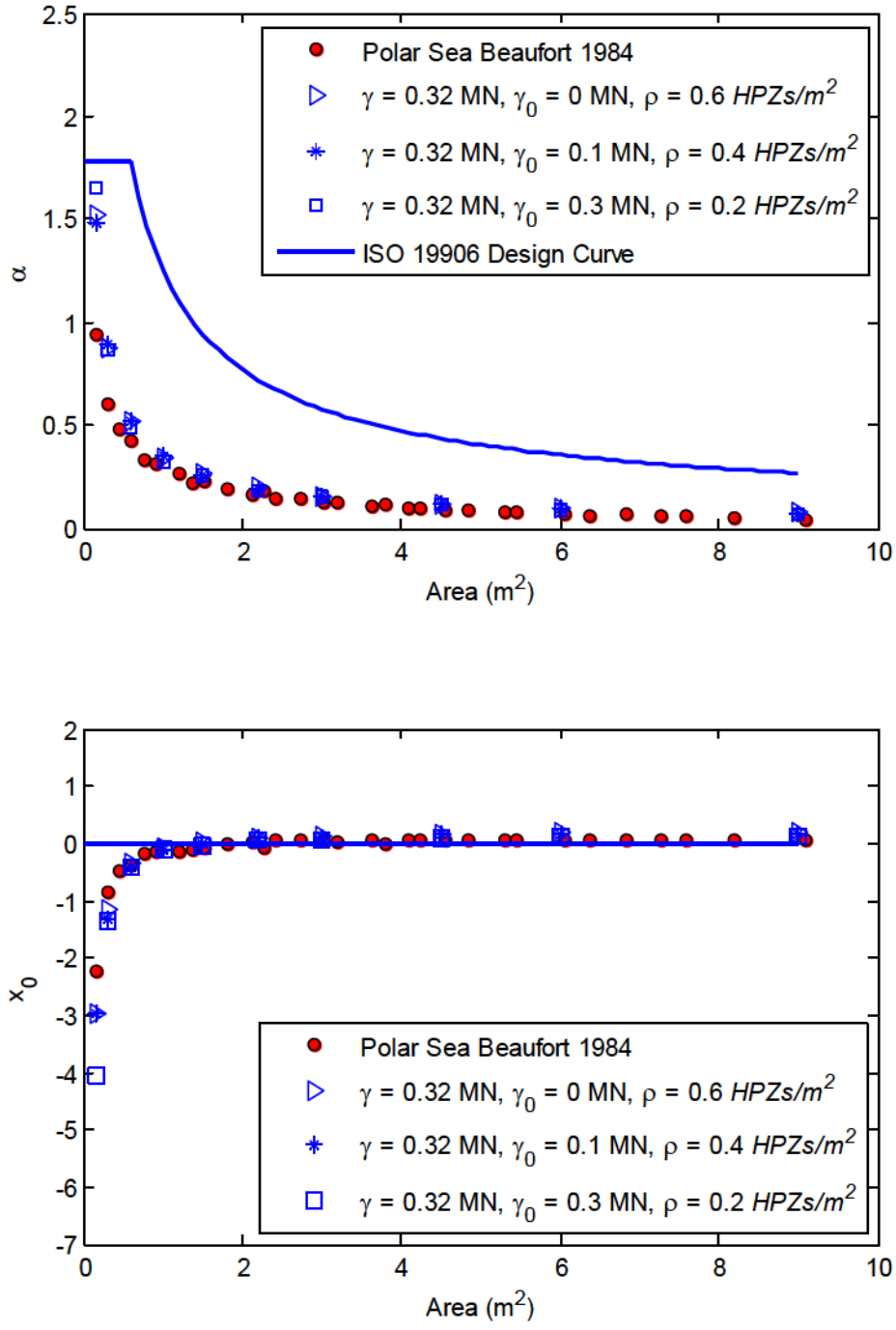

Figure 162 Simulated vs. measured local pressures parameters for *Polar Sea* Beaufort 1984; rate = 0.50 *HPZ*s/s, mean ram duration = 3.4 s

4.5.5 Relationship between HPZ rate and Ship Ram (or interaction) Speed

Initial *HPZ* rates were estimated in Section 4.5.3 (See Table 15). The process of modeling *HPZ* occurrence through the ram duration considers the mean occurrence based on *HPZ* rate and duration. Using measured durations from the *Polar Sea* data set and *Kigoriak* data, *HPZ* rates were iterated and input into the new Poisson process for *HPZ* formation in time, until simulated local pressure parameters reasonably match measured parameters. Using the initial estimates of *HPZ* rate, a simple regression of rate vs. impact speed was carried out as illustrated in Figure 163 (including regression of rate against speed squared).

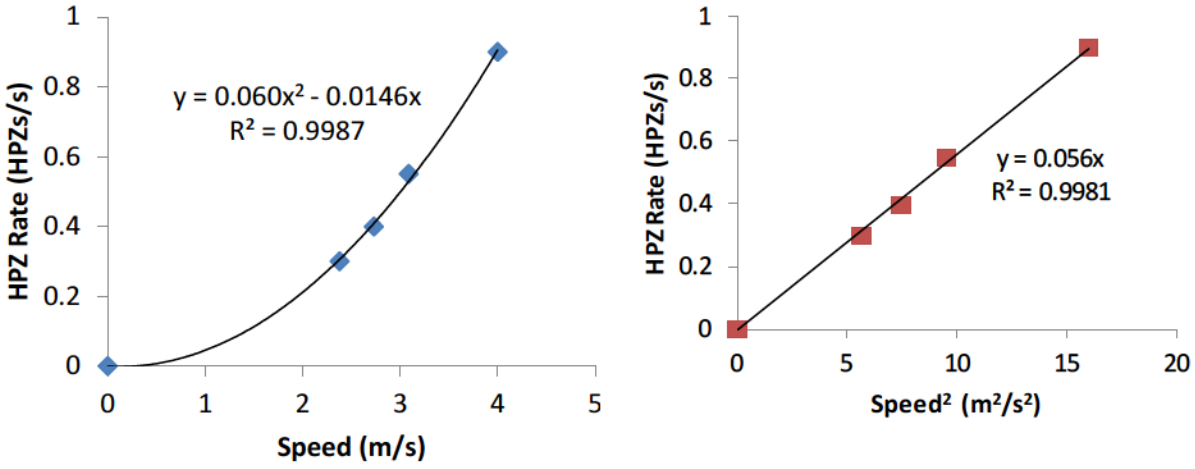

Figure 163 Regression results of *HPZ* rate against initial impact speed

A polynomial regression of *HPZ* rate against speed, as well as a linear regression of rate against speed squared was carried out. A rather simple expression is evaluated as

$$rate = \frac{1}{17.86} V^2 . \qquad (47)$$

Using this expression, the initial estimates of rate were updated as given in Table 15 and used in subsequent local pressure simulation modeling.

4.5.6 Example Verification

Local pressure simulations were carried out based on *Kigoriak* trials. *Kigoriak* trials were among the most extreme impact conditions ever carried out. As illustrated by Jordaan *et al*., 1991 and Jordaan, 2001, these measurements are the baseline for the local pressure design curve given in ISO 19906 (See Figure 33). Measured α values fall slightly below the ISO design curve. Simulations with the correct *HPZ* rate should produce local pressure parameters that closely match (slightly lower) the ISO curve.

Parameters most representative of *Kigoriak* impact conditions are given in Table 16. The mean impact speed and corresponding rate using Eq. (47) are 4.0 m/s and 0.9 *HPZ*s/s respectively. Corresponding local pressure parameters are illustrated in Figure 164. Given that the *Kigoriak HPZ* forces are considerably higher than *Polar Sea* estimates (1.1 MN vs. 0.52 MN for *Polar Sea* Beaufort 1982), sensitivity to increased cutoff force modeled while keeping the same density values was explored. The improved consistency among the local pressure parameter x_0 is illustrated in Figure 165. As noted in Section 4.5.4, this is a case where for higher *HPZ* forces require higher cutoff forces for corresponding density values to produce the correct local pressure results. Instead of an absolute cutoff force, a percentage of the *HPZ* force parameter seems appropriate (e.g. 0.5 to 1).

For comparison, a hypothetical test case was considered with a longer duration which would represent impacts aboard a much larger displacement vessel. Simulated local pressure parameters are illustrated in Figure 166. The parameter α is consistent as expected, and the plotting position x_0 for the 'parent' distribution will be shifted upwards as exposure is increased with longer duration.

Similarly, simulations were carried out for *Polar Sea* Beaufort 1982 type conditions as listed in Table 17. As with the *Kigoriak* case, impact trial conditions are compared with a hypothetical test case that represents a faster moving vessel having a larger displacement which leads to increased duration.

Simulated local pressure parameters are illustrated in Figure 167. Again, α is consistent and x_0 shifts in the positive direction based on increased exposure. These represent 'parent' distributions for extremal analysis that will consider the number of panels exposed given a global interaction area, and number of expected rams per annum.

Table 16 *Kigoriak* 1982 impact conditions and parameters

Ice Parameters	
Force parameter, γ (MN)	1.1
Force cutoff, γ_0 (MN)	0.1
Density, ρ (*HPZ*/m^2)	0.4
Trial based Impact Conditions	
Impact speed (m/s)	4.0
Impact rate (*HPZ*/s)	0.9
Impact duration (s)	0.7
Hypothetical Test Case	
Greater duration representing larger displacement vessel	
Impact speed (m/s)	4.0
Impact rate (*HPZ*/s)	0.9
Impact duration (s)	3.5

Table 17 *Polar Sea* Beaufort 1982 impact conditions and parameters

Ice Conditions	
Force parameter, γ (MN)	0.53
Force cutoff, γ_0 (MN)	0.1
Density, ρ (*HPZ*/m^2)	0.4
Trial based Impact Conditions	
Impact speed (m/s)	2.38
Impact rate (*HPZ*/s)	0.31
Impact duration (s)	3.6
Hypothetical Test Case	
Larger impact speed and greater duration representing larger displacement vessel	
Impact speed (m/s)	3.5
Impact rate (*HPZ*/s)	0.68
Impact duration (s)	7.60

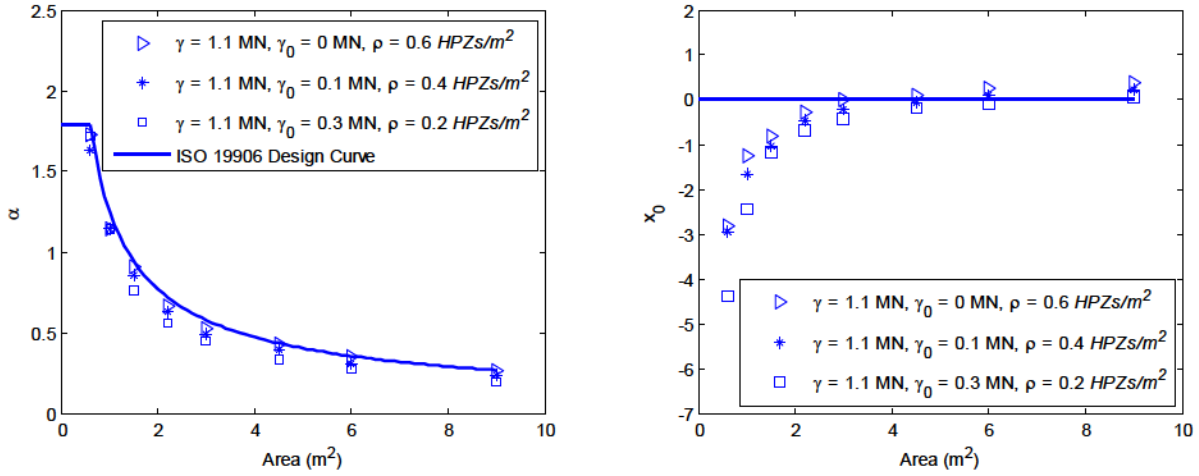

Figure 164 Simulated local pressure parameters α and x_0 for *Kigoriak* type interactions, v = 4 m/s, rate = 0.9 *HPZs*/s, duration = 0.7 s.

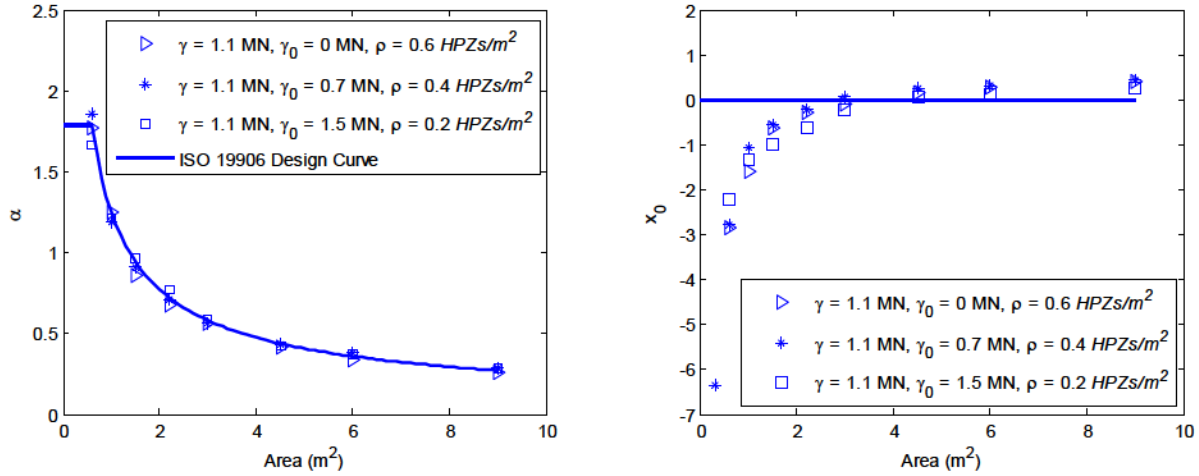

Figure 165 Simulated local pressure parameters α and x_0 for *Kigoriak* type interactions, v = 4 m/s, rate = 0.9 *HPZs*/s, duration = 0.7 s.

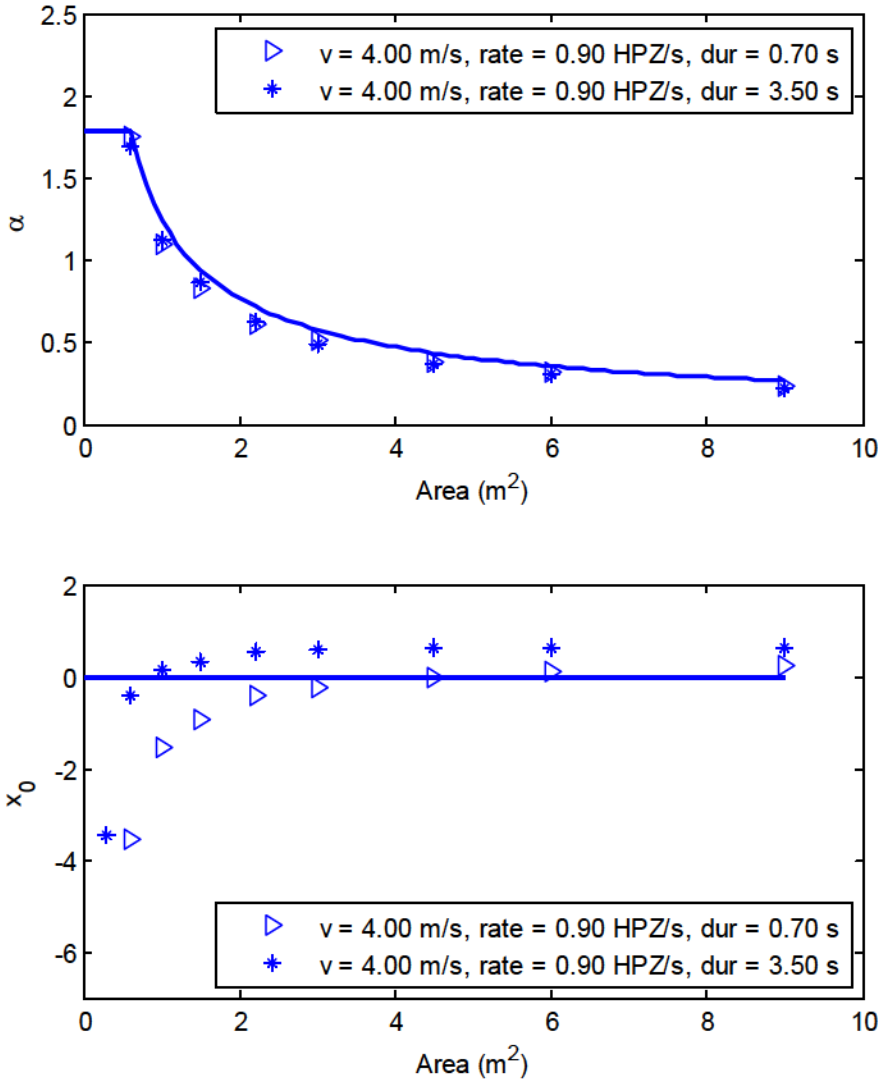

Figure 166 Simulated local pressure parameters α and x_0 for *Kigoriak* type interactions with *HPZ* parameters $\gamma = 1.1$ MN, $\gamma_0 = 0.1$ MN, $\rho = 0.4$ *HPZ*/m^2

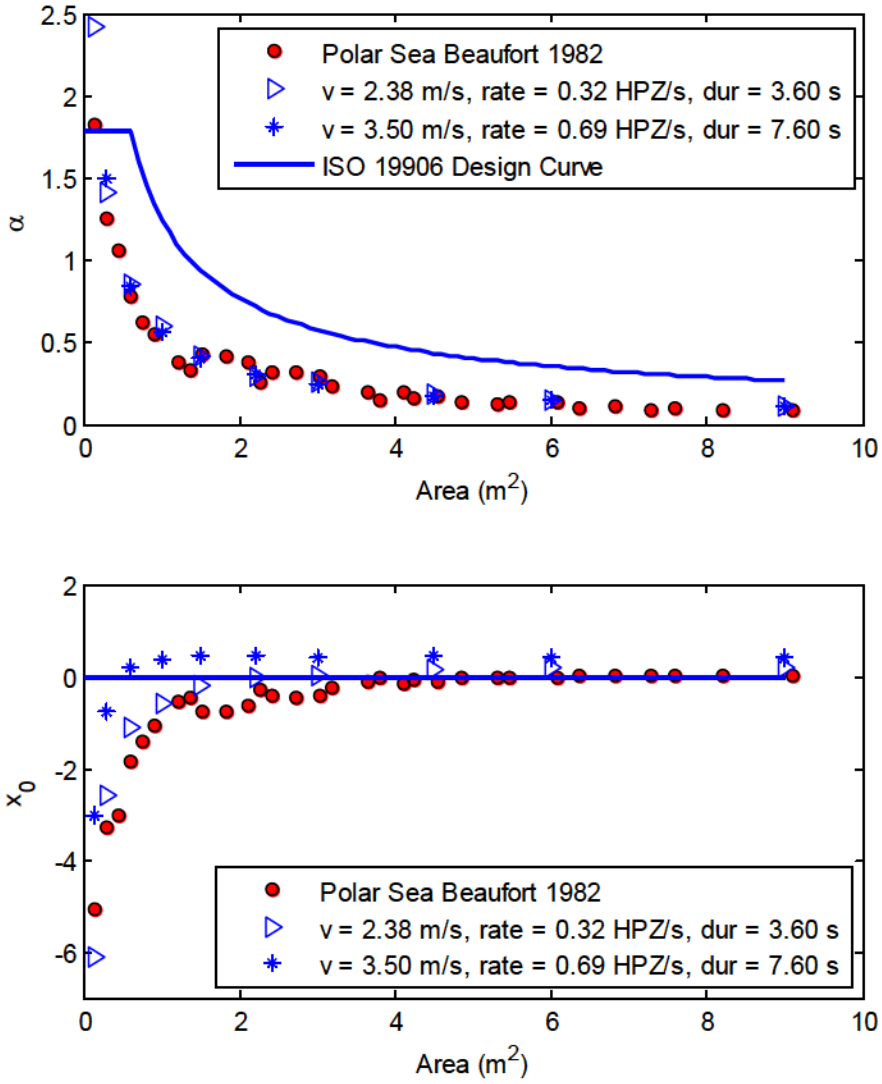

Figure 167 Simulated local pressure parameters α and x_0 for *Polar Sea* 1982 type interactions $\gamma = 0.53$ MN, $\gamma_0 = 0.1$ MN, $\rho = 0.4$ *HPZ*s/m^2

4.5.7 Sources of Error

With respect to sources of error in the work presented, the following comments are made:

- Estimation of ship ram speeds. For certain rams, direct speed measurements were not made and a range was reported in the data. (e.g., speed = 2 – 3 m/s). For such scenarios an average speed was estimated (e.g. 2.5 m/s).
- *HPZ* rates are estimated based on initial ship speed at start of interaction, but interaction speed will decrease from max to 0 over the ram duration. While in theory a mean speed Vmax/2 is more correct, the influence will only adjust the regression constant C by a factor of 2. The resultant rate will be the same. For simplicity and robustness, reference to Vmax is appropriate.
- Simulations have considered mean forward vessel speeds, and not a component of speed normal to the panel design area at a particular location. This effect, however, is covered in the regression coefficients relating rate to speed, but application of results may be limited to panel locations similar to *Polar Sea* panel location. Future analysis could consider the addition of an additional bow panel orientation parameter depending on the panel location.
- Simulations do not consider aspect ratio, whereas measurement areas with higher aspect ratio oriented along the waterline have higher pressures. This explains why simulated pressures on 1.5 m^2 area may occasionally be lower than measured. Measured pressures over 10 × 0.15m^2 subpanels are based on an aspect ratio of 5:2. In processing local pressures from data, the aspect ratio was limited to 3:1. This influence could be further assessed.
- Measurement of local pressures from the Polar Sea trials are based on hull strain gauge measurements. While uncertainty exists, our methodology of directly modeling distributions for pressure measurements (focusing on the distribution tails), inherently accounts for uncertainty directly in the analysis.

4.6 HPZ Modeling Summary

A comprehensive analysis of local pressure modeling has been carried out using *Polar Sea* data. Many *Polar Sea* trials with a 9.1 m^2 total area sensor having a 0.15 m^2 resolution have been carried out making available a very rich ship ice ram database for local pressure

analysis. Taylor *et al.*2010 provides strong evidence of local pressure area scale effect using *Polar Sea* data and follows a probabilistic approach to local design where increased exposure leads to increased pressures on any local area Jordaan (2001). Exposure increases with increased penetration and increased number of impacts. Daley (2004) using the same dataset suggests that some "pressure-area process" exists and attempts to demonstrate an inverse pressure area scale effect with pressures increasing with increasing area. An issue is that one is led to believe that the material properties of a fracture material changes and *HPZ*s don't fail. The truth is that increased global interaction area results from faster and larger displacement vessels penetrating further, the result being increased exposure on local panels within some global interaction area. There may be some confinement but with the geometry and interaction configurations of practical relevance, free surface effects allow large and small fractures to occur, thereby limiting the practical significance of scale effects. In the context of ship design, interactions with MY ice features do not last for minutes, hours or days, but rather seconds and fractions of seconds. Models with emphasis on confinement have limited practical significance for the problem at hand.

The results of the work presented in this chapter further demonstrate the reliability and strength of the probabilistic modeling approach adopted. Remarkable consistency with *Polar Sea* measurements is shown. It is noted that the key focus is MY ice interactions where ice crushing is the dominating failure model.

Following the work of Zou, 1996 using *Louis S. St. Laurent* data, *HPZ* forces and spatial density were derived from *Polar Sea* measurements. Using these inputs, local pressure parameters were simulated with consideration given to different sensor types and different area resolutions. Simulated local pressure results were remarkably consistent with *Polar Sea* measurements.

Building on this approach, a new model was developed that considered *HPZ* occurrence in time. This was further enhanced by identifying correlation between *HPZ* rate and ship impact speed. This model allows the designer to determine baseline 'parent' local pressure design parameters based on expected operational speed and vessel size. The faster a ship, the greater the *HPZ* rate. The larger and faster the ship, the longer the interaction duration

and subsequently the greater the exposure and demand for local pressures. A specific set of local pressure parameters can be derived for any ship and operations criteria. These can be further modeled using extremal analysis to develop actual local design pressures based on panel exposure and expected number of rams per year.

The model in time is an important new development. Interaction speed and duration can now be used to estimate the occurrence of *HPZs* in time as opposed to scaling time relative to *Kigoriak* estimates. This is important for modeling different vessels with different masses, and operational speeds. Rates will vary along the vessel being greater on the bow and least from midbody to stern. For fixed structures designed for iceberg impacts, rate and duration based on iceberg size and drift can be used to model exposure in time as opposed to scaling duration relative to *Kigoriak* impacts.

This analysis did not specifically address why ice strength varies from one region to another (i.e. that lower pressures occur in more southerly regions). This trend is captured in the α parameters derived for each data set (Jordaan *et al.*, 2007 and Taylor, 2010). The spirit of this work is to use direct measurements where possible. Opportunity exists to study ice properties in more detail to understand whether salinity and temperature can explain the variability in pressures on the same ship from region to region.

CHAPTER 5. Constructive Review of IACS Polar Class Rules

5.1 Polar Class Rules Development

5.1.1 Philosophy and Approach (IACS, 2006),

For ship design in arctic regions, the Polar Class Rules are developed on the hypothesis that impacting kinetic energy is transferred to crushing energy of the ice along with consideration for inertial effects (e.g. sway, and pitch of the vessel). Design loads and structural resistance are based on the expectation that a ship ice interaction event occurs on average once in a year (IACS, 2006).

While a mix of impact conditions may be expected during a vessels operational life, ice type and properties vary from region to region. Thickness may vary considerably whether first year or MY ice is present which has important implications when limit force modes (i.e. crushing or flexure failure) are modeled. Also, measurement of ice properties during transit is not practical.

The impact condition modeled in the current version of the code is a shoulder or glancing blow impact. While other conditions may be considered in the future, the maximum expected bow load based on this scenario is referenced as having a mature interaction model having sufficient accuracy for safe and robust design. Loads on other hull sections (e.g. side) are estimated as a percentage of the bow loads.

The approach to derivation of the Polar Class rules is outlined below:

- estimate the global interaction force using energy methods;
- estimate the average global contact area associated with the interaction and transform it to a rectangular area having deterministic aspect ratio influence by bow geometry;

- recognizing the actual contact area through which load is transferred into the hull is small relative to the nominal contact area (i.e. spalling events) and that local pressures are much higher, define a semi-local contact area by rescaling the global contact area dimensions but maintaining the aspect ratio; and
- recognizing that pressures are not uniform over the semi-local area, estimate peak pressures within the semi-local contact area (e.g. panel defined by transverse frame spacing and ice thickness) using peak pressure factors scaled according to frame spacing (i.e. the smaller the frame spacing, the smaller the effective panel loading area and the higher the local design plate pressure).

Plating thickness and scantling can be determined directly. All scantlings are based on plastic collapse limit state formulae including yield line theory for plating. Membrane effects are not included.

The purpose of this review is to demonstrate the importance of exposure in ship design, understand how pressure area scale effects are modeled, verify Polar Class coefficients and subsequent design pressures using an exposure based extremal analysis, and demonstrate how a full probabilistic methodology can be used to enhance design.

5.1.2 Initial Comments and Considerations

Consideration for ship ice interaction with glacial and MY ice is the main focus of this thesis. While different types of ice (e.g. first year and multi-year level ice and ridges) in varying concentrations may be present in certain arctic regions, besides glacial ice, the presence of multi-year ice, even in small concentrations, is the main hazard and will govern design. This was a conclusion out of the review of the ASPPR proposals (Carter *et al.*, 1996). Thick sea ice, having survived at least one summer and aging a second winter, will become largely brine free. With age, its material properties and strength approach that of glacial ice. Multi-year ice will typically encounter extreme environmental forces over its life (e.g. infield pressure) causing considerable deformation which results in very high variation in thickness. Having survived one year, progressive growth in subsequent seasons can result

in rather thick multi-year ice. The strength and geometry results in the highest ice structure interaction forces.

While the Polar Class rules are deterministic in nature, an element of exposure inherent in probabilistic methods is considered. A nominal ship ice interaction impact frequency of **once per year** is referenced. While no further discussion is provided, a more comprehensive modeling of exposure could be considered. Depending on the region and season of shipping activity (or operational demands of an icebreaker), the impact frequency with multi-year ice can be highly variable, from years between interactions to many interactions per year. Considering the number of interactions per year in the design methodology (i.e. the maximum of n expected events in a year) provides a much richer design solution, where performance of the vessel can be modeled and understood by the designer.

Before focusing on the specifics of the Polar Class rule development, it is useful to recap the mechanical properties of ice failure for the practical speeds associated with ship ice interactions. Recall from Section 3.1 that in addition to varying thickness, deformation as part of the aging process distorts the crystal orientation and unlike laboratory or ice growth in benign environments, the resultant crystal structure, including orientation, is highly random having many flaws. As noted earlier in this thesis, flaws, discontinuities and *HPZ*s lead to crack initiation, growth and fracture. Larger contact areas and increased number of *HPZ*s result in large stresses at flaws that lead to fracture and/or microstructural damage. Ice structure interaction events having free surface effects are even more fracture prone. Cracks migrate toward free surfaces, resulting in spalling events at both macro and micro levels. The actual contact area with the structure is much reduced from the nominal or projected contact area, which leads to a fundamental material property; fracturing materials have an inherent scale effect. With increasing contact area, average pressures progressively reduce, or alternatively, pressures increase with reducing contact area.

5.2 Energy Based Ship Ice Collision Modeling

A critical but constructive review of the technical background for modeling ice failure pressures in the IACS Polar Class rules has been carried out. Comparisons are made using

measured full scale ship ram data that are modeled based on exposure or annual number of equivalent rams. An energy based approach was used in the Polar Class rules to model interaction events. Initial kinetic energy (KE) of the ship is dissipated through work done in ice crushing (IE_C) and kinetic energy rotation (IE_R) of ship based on inertial response and hydrodynamics. The expression is

$$KE = IE_C + IE_R \tag{48}$$

$$\frac{1}{2}(M + M_a)V_n^{\,2} = \int_0^{\delta} Fn(\varsigma)d\varsigma + IE_{Ri}$$

where M is the mass displacement of the ship, M_a is the added mass, V_n is the velocity normal to the ice crushing, F_n is the crushing force per unit penetration ζ, IE_{Ri} represents the impact energy associated with the response of the vessel for each of the six degrees of freedom. With the exception of the crushing zone, the floe is assumed large and rigid.

The ship response upon impact (see Figure 168) is integrated into the energy formulation using the Popov *et al.*,(1967) approximation where the mass of the ship is adjusted using a correction factor Co to estimate an effective ship mass. The estimated effective mass considers both the inertial and hydrodynamic effects and is given as

$$M_{eff} = M/Co \tag{49}$$

The derivation of Popov mass adjustment coefficient Co is given in Appendix B.

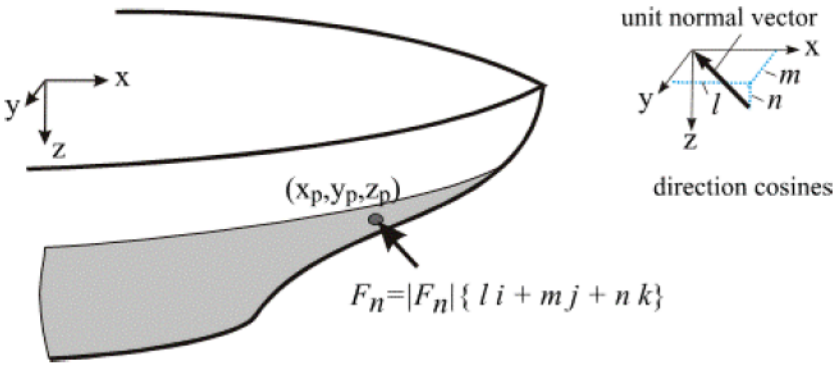

Figure 168 Illustration of impact geometry relative to vessel center of gravity and corresponding unit vectors and moment arms (Daley, 1999)

The simplified energy equation from which the maximum force can be determined at the point of maximum penetration is given as

$$\frac{1}{2}M_{eff}V_n^{\,2} = \int_0^{\delta} F_n(\zeta)d\zeta \qquad (50)$$

where ζ is the maximum penetration.

The extent of crushing will vary depending on vessel size. Figure 169 illustrates actual measured force vs. time for two vessels: 1) *Kigoriak*, a relatively small 7.5kT displacement vessel, and 2) MV *Arctic*, a 39kT medium displacement vessel (see also Figure 76 Figure 78). Smaller vessels may bounce multiple times before initial kinetic energy is dissipated, limiting crushing extent. Larger vessels will respond less and crush considerably more.

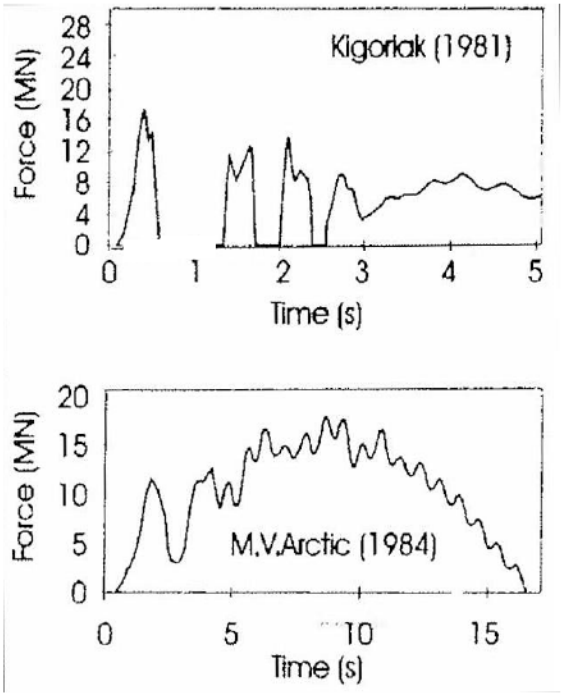

Figure 169 Measured vertical bow force through full ram duration for a relatively small 7.5 kT displacement *Kigoriak* and larger 39kT displacement MV *Arctic*.

5.2.1 Interaction Geometry

5.1.2.1 Glancing or Shoulder Impact

While a number of collision scenarios can be modeled (see Daley, 1999) the present version of the Polar Class rules only considers a shoulder or "glancing blow" impact scenario as illustrated in Figure 170. The nominal contact area normal to the shell plating develops as a function of penetration ζ and is given as

$$A_{NOM} = \frac{\zeta_n^{\,2} \tan(\phi/2)}{\cos^2(\beta')\sin(\beta')} \qquad (51)$$

where ϕ = edge opening angle and β' = normal frame angle. This assumes that all crushing energy is associated with one side of the vessel.

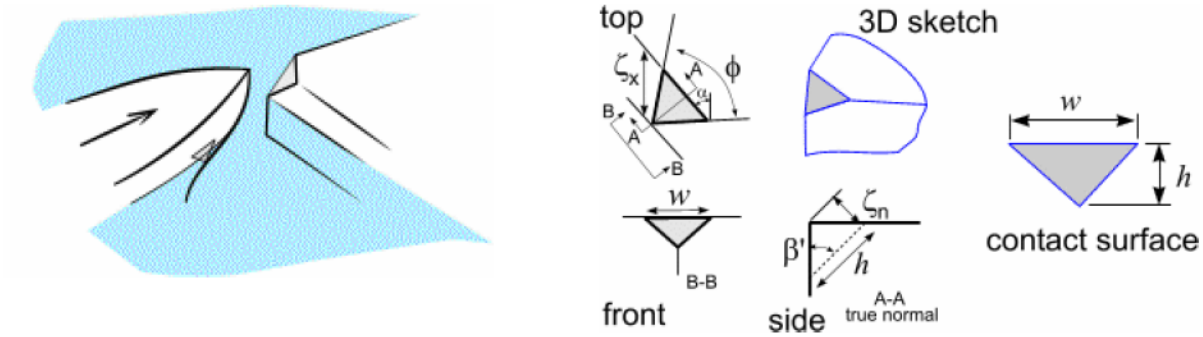

a) b)

Figure 170 Illustration of glancing impact on vessel bow (Daley, 1999)

5.1.2.2 Bow Impact

The interaction geometry for a concentric bow collision is illustrated in Figure 171 and Figure 172. The nominal contact area as a function of bow opening angle α, stem angle γ and penetration ζ is given as

$$A_{NOM} = \zeta_n^{\,2} \frac{\tan(\alpha)}{\cos(\gamma)\sin^2(\gamma)} \qquad (52)$$

The difference between a shoulder impact and concentric bow impact is the bow impact is driven by the geometry of the bow, the shoulder impact is driven by the geometry of the ice and angle ϕ in Eq. (51).

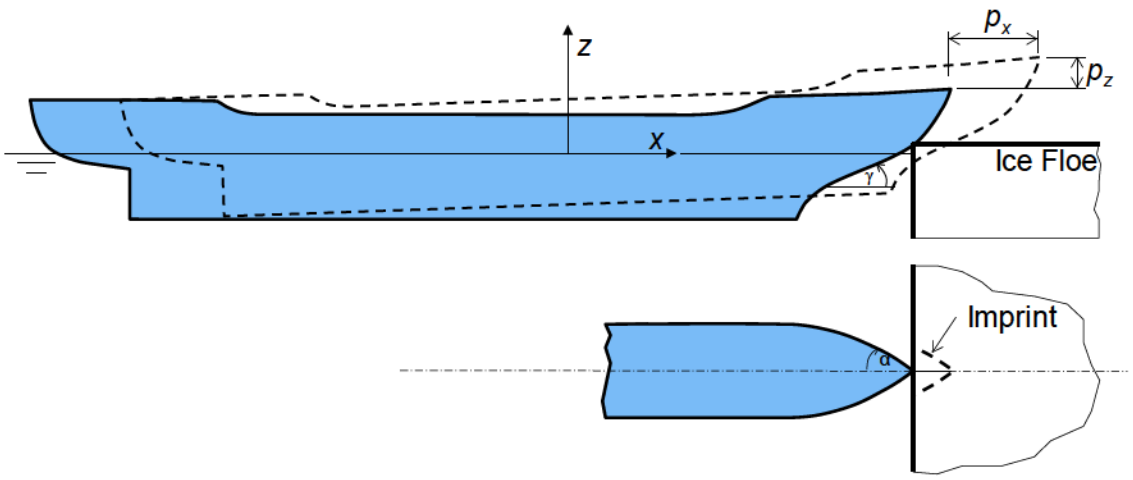

Figure 171 Ice ram interaction geometry and idealized bow geometry (after Riska, 1987)

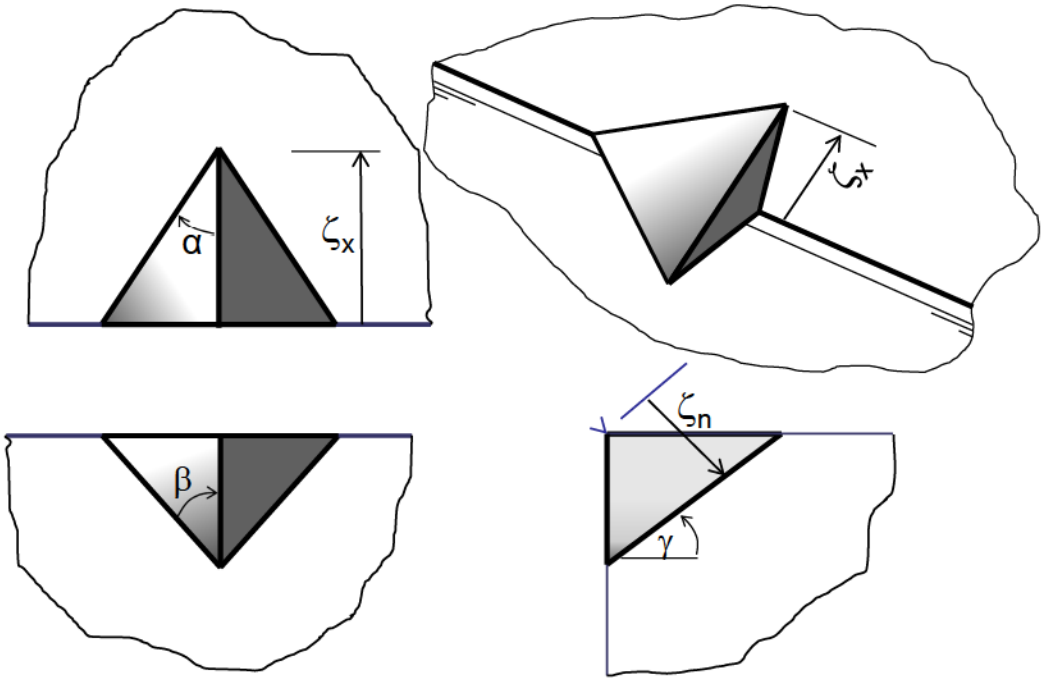

Figure 172 Illustration of concentric bow impact

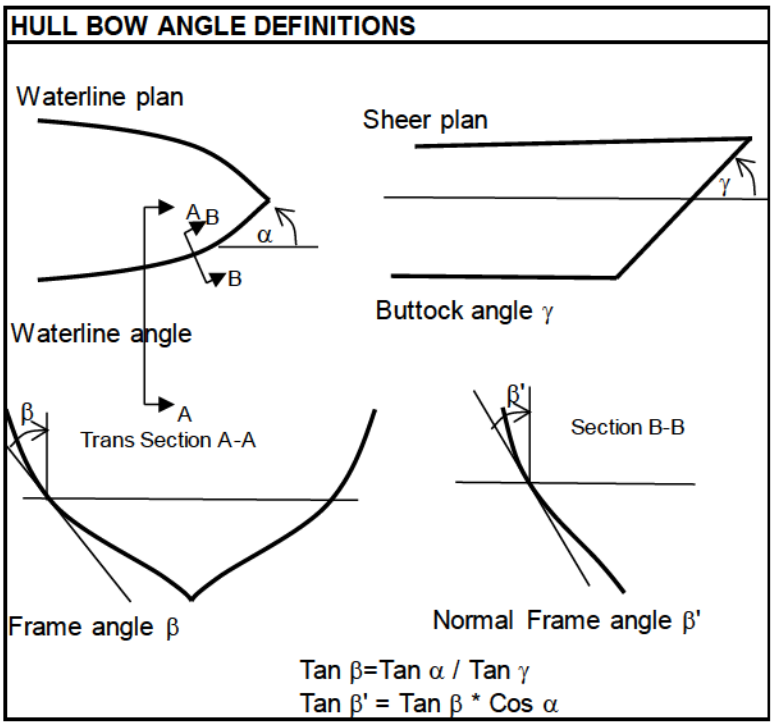

Figure 173 Ice ram interaction geometry and idealized bow geometry (after Riska, 1987)

5.2.2 Ice Crushing Forces

Ice crushing forces developed during a ship-ice collision are based on ice failure pressure and the development of contact area as the ship crushes into the ice feature. The maximum force typically corresponds to the average pressure on the maximum nominal contact area developed at the point of maximum penetration (see Section 4.2.1). Note that for fixed offshore structures, contact area develops as the ice penetrates onto the structure. The maximum force at maximum penetration is then

$$F_{MAX} = P_{avg} \cdot A_{nom} . \qquad (53)$$

The average global pressure over the nominal contact area A_{nom} is given as

$$P_{avg} = P_0 \cdot A_{nom}^{\,e_x} \qquad (54)$$

where P_0 is the reference pressure corresponding to pressure on 1 m^2 contact area and e_x models the pressure area scale effect.

The resultant maximum global force is then given as

$$F_{MAX} = P_0 \cdot A_{nom}^{1+e_x} \quad (55)$$

In the Polar Class rules, P_0 increases with increasing Polar Class (see Table 19). While ice may be stronger in the higher arctic regions, the range of P_0 values for Polar Classes 1 through 7 cannot be attributed solely to variability in the material properties of ice. It is rational, however, that P_0 should increase with increased exposure as introduced in Section 5.1. A Polar Class 1 ice management vessel would expect orders of magnitude more exposure (i.e. rams per year) than a PC 4 bulk carrier that may operate with detection avoidance strategies. Although not acknowledged in the technical background documentation for the Polar Code, the range for P_0 may be well explained with a probabilistic factor based on exposure and should be considered (see also Section 4.2.6).

The resultant normal force to the hull is

$$F_N = P_0 \cdot \left(\frac{\zeta_n^{\,2} \tan(\phi/2)}{\cos^2(\beta')\sin(\beta')} \right)^{1+e_x} \quad (56)$$

which can be written as

$$F_N = P_0 \cdot f_a^{\,1+e_x} \cdot \zeta_n^{\,2+2e_x} \quad (57)$$

where $f_a = \frac{\tan(\phi/2)}{\cos^2(\beta')\sin(\beta')}$, the interaction geometry coefficient for shoulder impacts. It is noted here that the shoulder impact is very sensitive to the angle ϕ defining the geometry of the ice. For comparison, the interaction coefficient for a concentric blow collision is

function of bow opening angle α, and stem angle γ, and given as $f_a = \frac{\tan(\alpha)}{\cos(\gamma)\sin^2(\gamma)}$ (See Daley, 1999).

Substitution of Eq. (56) into Eq. (50) gives

$$\tfrac{1}{2} M_{eff} V_n^{\,2} = P_0 \cdot f_a^{\,1+e_x} \cdot \int_0^{\zeta} \zeta_n^{\,2+2e_x} d\zeta$$

which can be solved for maximum penetration as

$$\zeta_{MAX} = \left[\frac{1}{2} \frac{M_{eff} \cdot V_n^{\,2} \cdot (3+2e_x)}{P_0 \cdot f_a^{\,1+e_x}} \right]^{\frac{1}{3+2e_x}} . \qquad (58)$$

Substituting ζ_{MAX} back into Eq. (56) gives the force at maximum penetration as a function of the ice failure scaling coefficient e_x as

$$F_{NMAX} = P_0^{\frac{1}{3+2e_x}} \cdot f_a^{\frac{1+e_x}{3+2e_x}} \cdot (3+2e_x)^{\frac{2+2e_x}{3+2e_x}} \cdot \left(\frac{1}{2} \frac{M}{C_0} \cdot V_n^{\,2} \right)^{\frac{2+2e_x}{3+2e_x}} \qquad (59)$$

which simplifies further to

$$F_{NMAX} = P_0^{\frac{1}{3+2e_x}} \cdot f_a^{\frac{1+e_x}{3+2e_x}} \left((3+2e_x) \frac{1}{2} \frac{M}{C_0} \cdot V_n^{\,2} \right)^{\frac{2+2e_x}{3+2e_x}}$$

Since the normal component of impact speed is a function of hull geometry, the geometric scaling factor (i.e. sin(α)cos(β) for shoulder hits and sin(γ) for concentric hits) can be separated out from *Vn* and Eq. (59) for shoulder hits can be written as

$$F_{NMAX} = P_0^{\frac{1}{3+2e_x}} \cdot \underbrace{\left(f_a^{\frac{1+e_x}{3+2e_x}} \cdot \left(\frac{1}{2} \sin^2(\alpha) \cos^2(\beta') \right)^{\frac{2+2e_x}{3+2e_x}} \right)}_{f_{ai}} \left((3+2e_x) \frac{M}{C_0} \cdot V^{\,2} \right)^{\frac{2+2e_x}{3+2e_x}} \qquad (60)$$

and for concentric hits

$$F_{NMAX} = P_0^{\frac{1}{3+2e_x}} \cdot \underbrace{\left(f_a^{\frac{1+e_x}{3+2e_x}} \cdot \left(\frac{1}{2}\sin^2(\gamma) \right)^{\frac{2+2e_x}{3+2e_x}} \right)}_{f_{ai}} \left((3+2e_x)\frac{M}{C_0} \cdot V^2 \right)^{\frac{2+2e_x}{3+2e_x}} \quad (61)$$

Further collection of terms leads to a final expression in terms of a pressure coefficient P_0, mass displacement M, and impact speed V given as

$$F_{NMAX} = P_0^{\frac{1}{3+2e_x}} \cdot \underbrace{\left(f_a^{\frac{1+e_x}{3+2e_x}} \cdot \left(\frac{1}{2}\frac{(3+2e_x)}{C_0}\cos^2(\beta') \right)^{\frac{2+2e_x}{3+2e_x}} \right)}_{f_{ai}} \left(M \cdot V^2 \right)^{\frac{2+2e_x}{3+2e_x}} \quad (62)$$

Despite the background derivation, an alternative f_{ai} term is prescribed in the Polar Code and given as

$$\min\left[\begin{array}{l} 0.60\ ;or \\ 0.097 - 0.68\left(\frac{x}{L} - 0.15 \right)^2 \frac{\alpha}{\sqrt{\beta'}} \end{array} \right] \quad (63)$$

where x is the distance from intersection of the stem with waterline (FP) and L is the vessel length between perpendiculars. This empirical expression models the changing bow geometry with distance aft of the vessel stem with a cutoff of 0.60.

If one models the assumption that e_x = -0.1 (AMARK and MUN, 1998) in Eq. (62), the resultant expressions for design force (as given in Polar Class rules) can be condensed to

$$F_{NMAX} = f_{ai} P_0^{0.357} V^{1.286} D^{0.643}), \quad (64)$$

where f_{ai} is the condensed interaction geometry coefficient based on hull form and position i from the intersection of the waterline and the stem in Eq. (63) and D is the vessel displacement in kT.

This expression is further simplified in the rules to

$$F_{NMAX} = f_{ai} \cdot CF_C \cdot D^{0.64}, \qquad (65)$$

where $CF_C = P_0^{0.36} V^{1.28}$ is defined as the Class Crushing Factor. The range of values for f_a and the term f_{ai} for several vessels having different bow geometries are given in Table 18 for both shoulder and head-on bow collisions. For code usage, the analytical expression for f_{ai} in Eq. (63) is easier to exercise and based on results in Table 18 gives values that are slightly more conservative. It also increases with increased distance from the vessel forward perpendicular (FP) to the contact location.

This now illustrates a primary goal of the Uniform Requirements (URs), to collapse class parameters into a single 'class factor' (AMARK and MUN, 1998). Following from Eq. (50) and Eq. (56) above, with the goal to use class factors to define loads, AMARK and MUN (1998) notes that two factors are required: one for crushing failure (*CFc*) being a function of P_0 and *Vs* and a second factor associated with loaded area or dimension (CF_D) defined as $P_0^{0.389}$ (See Eq. (74)).

Regarding the modeling of scale effect in the Polar Class Rules, the use of e_x = -0.1 is not consistent with other measures of scale effect associated with the failure of a fracturing material (See Section 2.3, Section 3.2 and Section 5.3.2). For global interactions, e_x has been shown to be appropriately modeled at -0.4. Modeling e_x = -0.1 means that for larger interaction areas, average pressures maybe be rather extreme, whereas for smaller local areas, pressures may be under conservative.

While exposure will be discussed further in Section 5.5.1, it is noted here that *CFc* may reflect varying levels of exposure, although no reference to a probabilistic calibration factor is provided.

Table 18 Range of f_a for icebreaking vessels for shoulder (glancing) and concentric hits

	MV Arctic	*Kigoriak*	Manhattan	*Polar Sea*
Stem angle γ °	30	24	17	14
Bow opening angle α °	33.5	61	30	29
Frame angle β °	48.9	76.1	62.1	65.8
Normal frame angle β′ °	43.7	63	58.6	62.8
Shoulder (ϕ = 150°)				
f_a	10.3	20.4	16.1	20.1
$f_{ai(theory)}$	0.42	0.51	0.28	0.24
$f_{ai\ (CODE)}$	min(0.47,0.6)	min(0.72,0.6)	min(0.37,0.6)	min(0.34,0.6)
Concentric bow collision				
f_a	3.1	11.9	7.1	9.8
$f_{ai(theory)}$	0.38	0.45	0.25	0.21

5.2.3 Limiting Flexure Force

In theory, ice force acting on a vessel cannot exceed the minimum of the crushing force exerted over the nominal contact area or the force needed to fail the ice sheet in flexure.

A limit flexure force is modeled in the Polar Code as

$$F_{f\,MAX} = \frac{1.2 \cdot CF_F}{Sin(\beta')}; \qquad (66)$$

where $CF_F = h_{ice}^{\ 2}\ \sigma_{flex}$ is a class factor for flexure failure (see Table 19), h_{ice} is the ice thickness, and σ_{flex} is the ice flexural strength. As noted in Table 19, h_{ice} is a class dependent parameter ranging from 7 m for Polar Class 1 to 2.5 m for Polar Class 7.

In certain regions where only low salinity first year ice forms, the use of this limit is reasonable. But for ships navigating polar waters, traversing different regions, particularly those with MY ice, thickness is highly variable, largely unknown and impractical to measure. If operational criteria are needed to regulate access of different classed vessels to particular

regions throughout the season, identifying and measuring MY ice thickness particularly in low concentrations is impossible. Hence, designers and ship owners should use caution when exercising this limit. It is recommended that this caution be noted in the Polar Class rules so designers can exercise judgment in their final design.

Flexure strength is also referenced as class dependent parameter having values ranging from 1.4 to 0.65 MPa for Polar Class 1 to 7 respectively. While outside the scope of this thesis, the dependency of these values on Class should too be substantiated. As with thickness, measurement of ice strength to guide operational restrictions is impractical.

5.2.4 Class Factors Described for Design

The full list of class factors is given in Table 19 below, of which we are primarily concerned with coefficients for crushing, flexure and dimensioning. In the present review, class based parameters speed, strength, ice thickness and flexure strength were back calculated from factors prescribed in the Polar Class rules (and table below) and shown to be consistent with values originally prescribed in AMARK and MUN (1998).

Table 19 Class factors in IACS rules and governing parameters.

Polar Class	Crushing Failure Class Factor	Load Patch Dimension Class Factor	Flex Failure Class Factor	Displ Class Factor	Long'l Strength Class Factor	Impact Speed (m/s)	Ice Strength (MPa)	Ice Thickness (m)	Flex Strength (MPa)
	CF_C	CF_D	CF_F	CF_{DIS}	CF_L	Vs	P_0	h_{ice}	σ_{flex}
1	17.69	2.01	68.6	250	7.46	5.68	6.02	7.000	1.400
2	9.89	1.75	46.8	210	5.46	3.99	4.21	6.000	1.300
3	6.06	1.53	21.17	180	4.17	3.00	2.99	4.200	1.200
4	4.5	1.42	13.48	130	3.15	2.51	2.47	3.500	1.100
5	3.1	1.31	9	70	2.5	1.99	2.00	3.000	1.000
6	2.4	1.17	5.49	40	2.37	1.77	1.50	2.800	0.700
7	1.8	1.11	4.06	22	1.81	1.50	1.25	2.500	0.650

5.2.5 Load Patch Definition (i.e. Ice Contact Area)

To determine the ice contact pressure, the contact area over which the force is applied to the hull is estimated. In the Polar Class rules, this contact area is referenced as the "load patch." The "glancing blow" or shoulder interaction scenario is used as the basis for determining load patch dimensions as illustrated in Figure 174. Other interaction scenarios are not considered although reference is made to Code enhancements at a later time. Several interaction scenarios are described by Daley (1999), and formulated for ease of insertion in the Polar Class rules at the appropriate time. As illustrated in Table 18, the use of the glancing blow scenario gives the largest values for the interaction geometry coefficient f_a, establishing an upper bound force for all interaction scenarios. Justification could be that captains exercising avoidance maneuvers (with an exception for icebreakers) will increase exposure to the outer bow (assuming the ice is detected). In some cases however, captains will repeatedly ram ice so as to avoid being stuck, thereby increasing center bow exposure. Additional documentation to justify this scenario and reference to verification could be documented in the Polar Class rules so that a designer can fully understand the basis for his design.

As part of this review, it is pointed out that the added exposure for dedicated ramming could well result in a higher center bow design load despite a lesser demanding bow geometry than for a reduced exposure (i.e. considering operational risk mitigation) but blunter shoulder geometry. Hence, consideration for exposure as well as the random location of ice contact across the bow is important.

Regarding load patch definition, the idealized ice edge geometry in Figure 174 is transformed into an idealized rectangular load patch having width W, height H and aspect ratio AR as illustrated in Figure 175. Aspect ratio, W/H is defined as

$$AR = 2 \cdot \tan(\phi / 2) \sin(\beta') \qquad (67)$$

where β' is the normal frame angle. Assuming $\phi = 150^{o}$, this becomes

$$AR = 7.46 \cdot \sin(\beta') > 1.3. \quad (68)$$

The more vertical the hull contact face, the lower the normal frame angle β', the shorter H, the greater the aspect ratio. Using this approach, aspect ratio relates to interaction geometry and used to define load patch dimensions (i.e. contact area). A minimum aspect ratio of 1.3 is modeled. The sensitivity of load patch aspect ratio to ice pressure is not modeled. While the prescription of the ice edge geometry using ϕ is rather influential in load estimates, no data are referenced to verify the selection of a value.

Nominal dimensions w_{nom} and h_{nom} are used to define the nominal contact area as a function of ice thickness and aspect ratio as

$$A_{nom} = w_{nom} \cdot h_{nom} = h_{nom}^{\ 2} AR \quad (69)$$

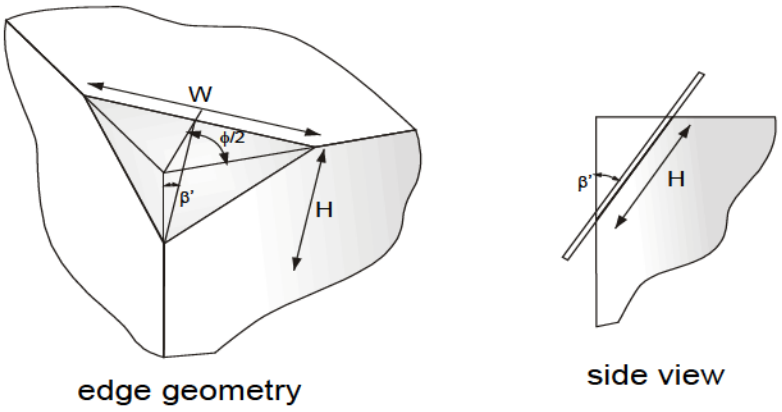

Figure 174 Characterization of idealized ice edge geometry (AMARK and MUN, 1998)

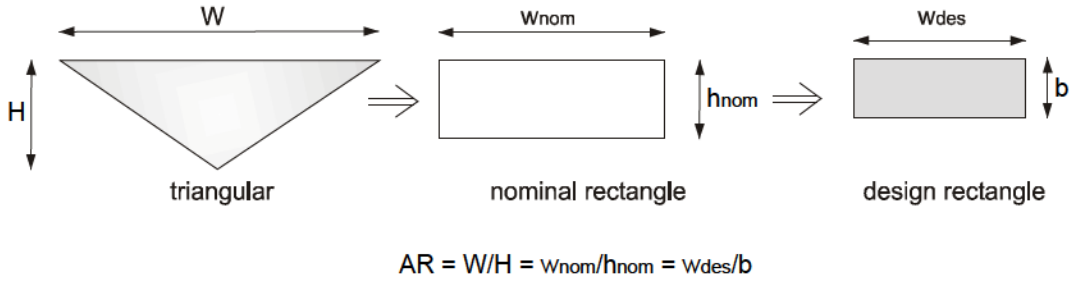

Figure 175 Load patch idealization (AMARK and MUN, 1998)

From Eq. (55), area can be defined as a function of force, F_N as

$$A_{nom} = \left[\frac{F_N}{P_0}\right]^{\frac{1}{1+e_x}}. \qquad (70)$$

From this load patch dimensions h_{nom} and w_{nom} can be defined as

$$h_{nom} = \frac{1}{AR^{1/2}}\left[\frac{F_N}{P_0}\right]^{\frac{1}{2+2e_x}} \qquad (71)$$
$$w_{nom} = h_{nom} \cdot AR$$

Again, substituting e_x = -0.1, h_{nom} and w_{nom} become

$$h_{nom} = \left[\frac{F_N}{P_0}\right]^{0.555} \cdot \frac{1}{AR^{0.5}} \qquad (72)$$
$$w_{nom} = \left[\frac{F_N}{P_0}\right]^{0.555} \cdot AR^{0.5}.$$

These define the nominal (or global) contact area. For local hull design (e.g. shell plate thickness) we need to estimate local pressures that result from the total impact force transferred into the structure through the much reduced local contact area resulting from fracture and edge spalling processes.

The approach used in the Polar Class rules is to adjust the nominal width using a power law expression with an exponent w_{ex} = 0.7, and the contact height adjusted to maintain aspect ratio. The corresponding rectangular local contact area dimensions are given as

$$w_{des} = w_{nom}{}^{w_{ex}} = w_{nom}{}^{0.7} \qquad (73)$$
$$b = h_{nom}{}^{w_{ex}} \cdot \frac{AR^{w_{ex}}}{AR} = h_{nom}{}^{0.7} \cdot AR^{-0.3}$$

Substituting w_{nom} and h_{nom} from Eq. (72) gives the load patch dimensions as a function of impact force, aspect ratio and class depend pressure coefficient P_0 as

$$w_{des} = \left[\frac{F_N}{P_0}\right]^{0.389} \cdot AR^{0.35} \qquad (74)$$

$$b = \left[\frac{F_N}{P_0}\right]^{0.389} \cdot \frac{1}{AR^{0.65}}$$

While possible reasons and models were explored to justify the adjustment of the nominal contact area to the local load patch dimensions (AMARK and MUN, 1998), the model used was based on a 2D brittle flaking model (See Figure 176 and Daley, 1991). This edge failure model modeled an indenter pushing against an idealized triangular ice edge and assumes that equally spaced flakes fail along a slip plane according to a Mohr Coulomb failure criterion. The model was considered to give good comparison with physical lab tests (Joensuu and Riska 1989). Jordaan (2001) discusses several challenges with this modeling: Mohr Coulomb models are valid for much lower confining stresses among granular materials; friction angle approaches zero for crushed ice under high pressure (Singh *et al.*, 1995); the failure of 3-5mm near parallel flakes across a complex stress region having low stress high shear on the outside, high stress high shear part way through, and high stress low shear near the center.

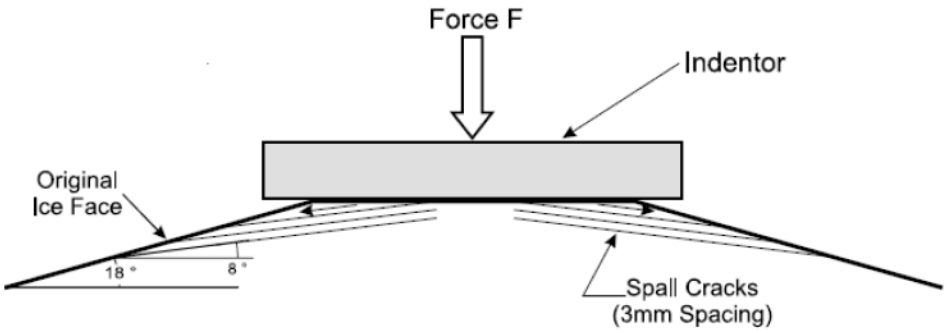

Figure 176 Approximation repetitive failure using Mohr Coulomb shear planes

The resultant use of the 0.7 scaling exponent is tested by exercising the Polar Class rules. A collision with an MV *Arctic* type ship was considered, a 40 kT vessel with a bow opening

angle α of 33.5° and stem angle γ of 30°. A corresponding impact force of 90 MN distributed over a nominal contact area of 20.14 m^2 with an aspect ratio of 5.12 is estimated. The corresponding dimensional parameters w_{nom} and h_{nom} defining the nominal contact area are 10.19 m and 1.98 m respectively. The dimensional parameters w_{des} and b defining the local contact area are estimated to be 5.08 m and 0.99 m respectively giving a local contact area of 5.0 m^2. The proportion of local contact area to nominal contact area is ~25%. Since local contact area scaling (e.g. $h_{nom}^{0.7}$) is not linear, the range of percent local contact area for vessel masses ranging from 10 kT to 100 kT having similar hull and bow forms is 33% to 23%.

Based on analysis of ship ram data, if the density of *HPZ*s as illustrated in Section 4.4 of this thesis is approximately 0.6/m^2, and *HPZ* contact area on average being 0.1 m^2, then within a nominal contact area of 20.14 m^2 (as estimated in the example above), the local contact area would be expected to be 1.2 m^2. The percentage of local contact area to nominal area in this case is 6%. For sensitivity, if the *HPZ* area was doubled to 0.2 m^2 (or density doubled) the local contact area would be ~12%. This is consistent with work by Korzhavin (1962), Johnston *et al.*, (1998) and Taylor (2010) who demonstrate that the actual contact area through which load is transferred into a structure is less than 10% of the nominal contact area. The percentage of local to global contact areas based on analysis of full scale data are approximately 1/5 to 1/2 of the values prescribed in the Polar Class rules, meaning that local design areas may be overly conservative. While design pressure being contact force over local contact area may now be considered conservative given larger local contact areas, the use of peak pressure factors in Section 5.2.8 may result in a correct pressure, but distributed over too large of a contact areas.

5.2.6 Line Load

For thinner level ice interactions, it is sometime useful to consider line load. Line load is an expression for linear-like distribution of local loading as a function of distance along the side of a ship's hull for a given ice thickness (See Section 3.2.2 and left-most graphic in Figure 61).

The line load Q is defined in the Polar Class rules, assuming ex = -0.1, as

$$Q = \frac{F_N}{w_{des}} = F_N^{0.61} \cdot P_0^{0.389} \cdot \frac{1}{AR^{0.35}} = F_N^{0.61} \cdot CF_D \cdot \frac{1}{AR^{0.35}}; \qquad CF_D = P_0^{0.389} \tag{75}$$

where

CF_D is the Class Factor for dimensions defined in the rules.

Different ice regimes will have different ice types and interaction scenarios. In the Canadian Arctic, the ice regime has considerable intrusions of multi-year ice, whereas the Russian Arctic is more typical of level ice and first year ridges with the occasional occurrence of second and MY ridges. Intuitively, as ice becomes thinner, the occurrence of *HPZs* is along a linear path. With thicker ice, *HPZ* occurrence will be spatially random in both the vertical and longitudinal extent of the interaction area, having more of an ellipsoidal shape depending on the interaction geometry and aspect ratio. Line loading has less importance for multi-year ice interactions.

5.2.7 Effective Design Area and Pressure

The effective local design area is then

$$A_{eff} = w_{des} \cdot b = \left[\frac{F_N}{P_0}\right]^{0.778} \cdot \frac{1}{AR^{0.3}}, \tag{76}$$

from which the effective design pressure given as

$$P_{av\_eff} = \frac{F_N}{A_{eff}} = \frac{Q}{b} = \frac{F_N^{0.61}}{AR^{0.35}} \cdot P_0^{0.389} \cdot \frac{P_0^{0.389}}{F_N^{0.389}} \cdot AR^{0.65} = F_N^{0.22} \cdot CF_D^{2} \cdot AR^{0.3} \tag{77}$$

Rewriting Eq. (76) for F_N and substituting into Eq.(77), the pressure area expression with consideration for aspect ratio and assuming e_x = -0.1 is

$$P_{av\_eff} = P_0^{0.22} \cdot \left[A_{eff} \cdot AR^{0.3}\right]^{\frac{0.22}{0.778}} \cdot P_0^{(0.389)2} \cdot AR^{0.3} = P_0 A_{eff}^{0.28} \cdot AR^{0.385} \quad (78)$$

The subsequent scale effect is modeled as $A^{+0.28}$; which models increasing local pressure with increasing contact area consistent with process pressure area scale effect discussed in Section 2.4.3.2. While one may perceive this as being rather conservative for larger contact area interactions, it also suggests that pressures reduce for smaller interaction areas, which is contrary to physical measurements at both local and global scales. As noted earlier, the correct theoretical description is that for increasing energy interactions (i.e. larger ships moving faster) penetrations will increase causing increasing contact areas and hence increasing pressures locally.

Later in this chapter, exposure will be explicitly addressed, which suggest that larger ships moving faster will penetrate further thereby increasing local design pressures. This same influence may be modeled in Eq. (78) but it must be understood that while this empirical equation may captures an exposure effect, it is not a material property of ice. This should be acknowledged.

5.2.8 Peak Local Design Pressures

Since ice pressures are not uniformly distributed across the rectangular load patch, local design pressures are scaled from average patch pressure in the horizontal dimension using localized peak pressure factors as illustrated in Table 20. Local peak pressure factors are suggested to range from 1.2 – 2.2 depending on the framing orientation and frame spacing (i.e. transverse or longitudinal). Figure 177 illustrates the nominal contact area based on ice sheet interaction, the reduced contact area from spalling at the surfaces, and a localized pressure patch based on ice thickness and transverse frame spacing.

For example, a load patch across a transversely framed structure may have a horizontal width of 4 m and height of 1.5 m spanning several main frames spaced at 0.4 m. For plating design the loaded area between the two main frames would be 1.5 × 0.4 m. The peak pressure factor applied to this localized area would be $1.8 - s = 1.8 - 0.4 = 1.4$. Other factors apply to different framing configurations.

Table 20 Peak Pressure Factors (PPF) for scaling local pressures for reduced contact areas.

Frame orientation	Expression for Peak Pressure Factor (PPF)	PPF range assuming 300 mm minimum frame spacing
Transverse no stringers	$1.8 - s > 1.2$	1.2 – 1.5
Transverse with stringers	$1.6 - s > 1.0$	1.0 – 1.3
Longitudinal	$2.2 - 1.2 \times s$	1.5 – 1.84

5.2.9 Hull Location Factors

Design pressures will vary over different parts of the hull from bow to midbody to stern, icebelt to bottom. Being most exposed, bow pressures will be highest in the bow, reducing moving aft as exposure reduces (with the exception of dual acting vessels that break ice in reverse with an icebreaking stern). Since the bow is most exposed and having the highest forces, hull area factors are applied to scale forces relative to the bow as illustrated in Figure 122 and Table 11. Factors range from 1 on the bow to 0.3 on the midbody bottom to a minimum of 0.15 on the stern bottom.

5.2.10 Shell Plating Thickness

Energy methods and the plastic yield line approach are used to design shell plating thickness as illustrated in Figure 178 (Hughes 1988 and Daley *et al.*, 2001). The assumption is that under uniform ice pressure (contact area bound by contact height and frame spacing for transverse framing), the plating is assumed to fold along yield lines forming perfect plastic hinges. Illustration of ice loading is illustrated in Figure 177. The energy balance is the external work done as the applied ice force moves through some displacement of the plating

δ, is equated to internal energy expended as perfect hinges form along the folding lines. The appropriate solution corresponds to the minimum work done for a set of hinges formed. The nominal plastic capacity is on the order of twice the traditional yield capacity.

Shell plating design depends on frame orientation (i.e. transverse or longitudinal) and angles relative to horizontal (See Figure 179). The equation for plating thickness for transversely framed structure having transverse frame angles greater than 70° is given as

$$t(mm) = \frac{500s\sqrt{\frac{(AF \cdot PPF \cdot P_{avg} \cdot)}{\sigma_y}}}{1+\frac{s}{2b}} \qquad (79)$$

where s is the transverse frame spacing, b is the height of the local ice contact area, σ_y is the yield strength of the steel, PPF is the peak pressure factor, AF is the hull area factor associated with contact locations.

The equation for plate thickness for a longitudinal framed vessel with longitudinal frame spacing $s < b$ the ice contact thickness and frame angles < 20°, the design ice contact area or patch is bounded by the longitudinal frame spacing s, and the large web frame spacing l, and the equation for thickness is given as

$$t(mm) = \frac{500s\sqrt{\frac{(AF \cdot PPF \cdot P_{avg} \cdot)}{\sigma_y}}}{1+\frac{s}{2l}}$$

assuming the longitudinal spacing is less that the load patch width w.

With regards to structural reliability, this model would represent a limit state characterized by limited plastic deformation. Comparison of different levels of structural capacity including elastic, hinge formation, and membrane capacity to the some nominal ultimate

limit state is illustrated in Figure 180. It can be seen that at a plastic hinge limit state, substantial membrane reserve capacity exists with little or no chance of rupture.

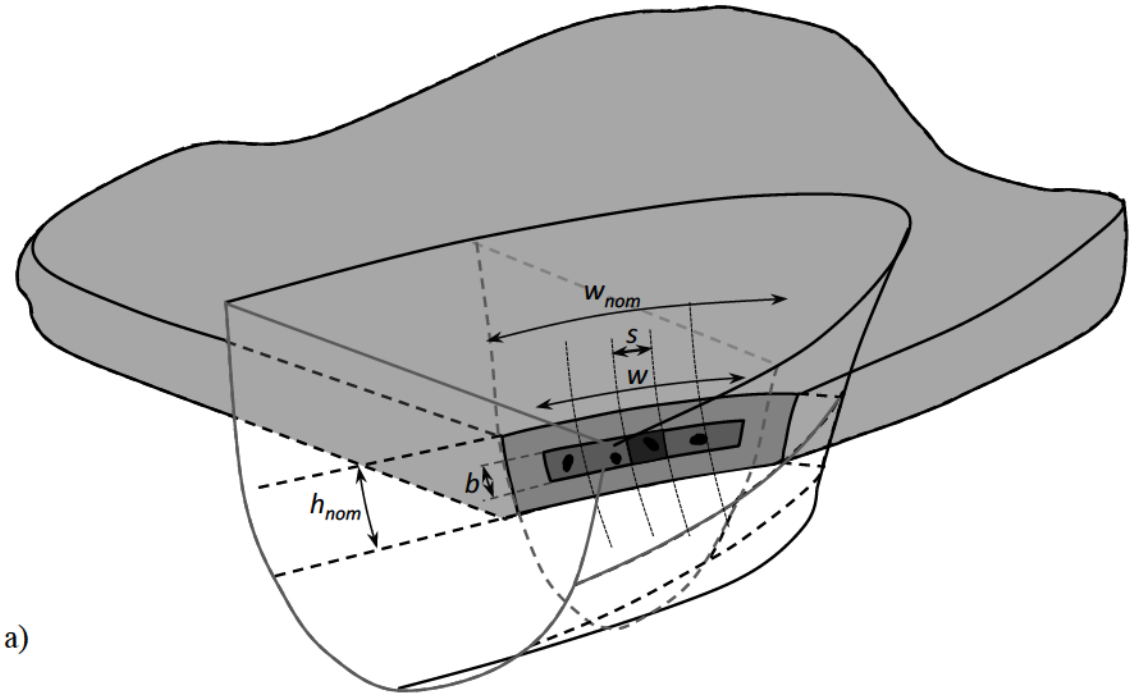

a)

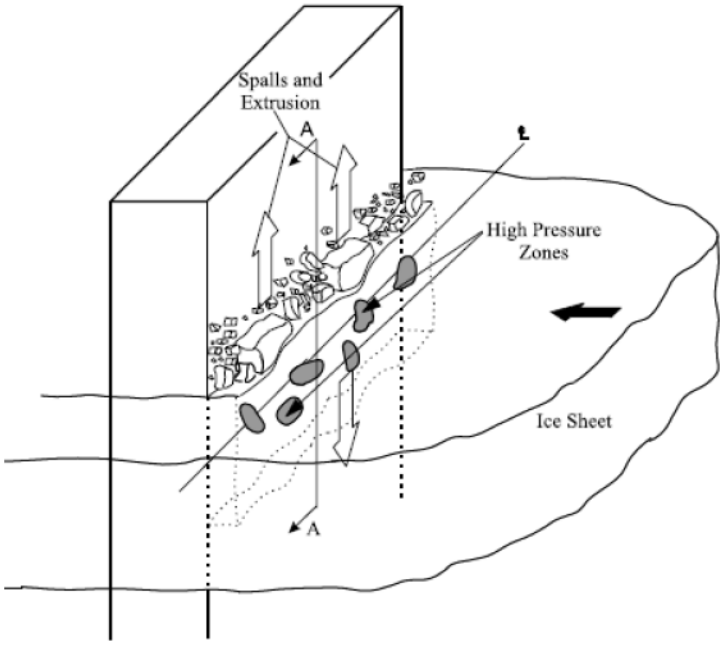

b)

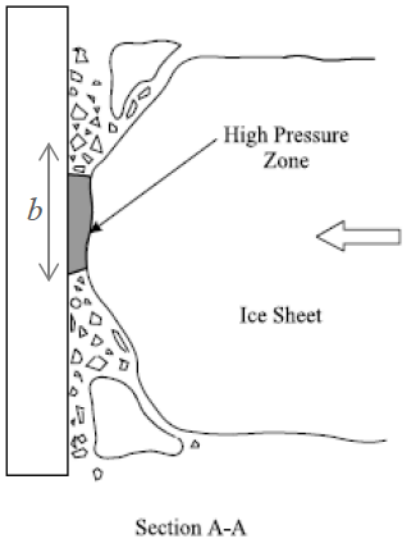

c)

Figure 177 Illustration of a) Polar Class rule definition of nominal, semi-local and local contact area dimensions for shoulder impact scenario b) localized contact given progressive fracture and spalling at surface edges and distribution of *HPZ*s c) localized contact area over an *HPZ*.

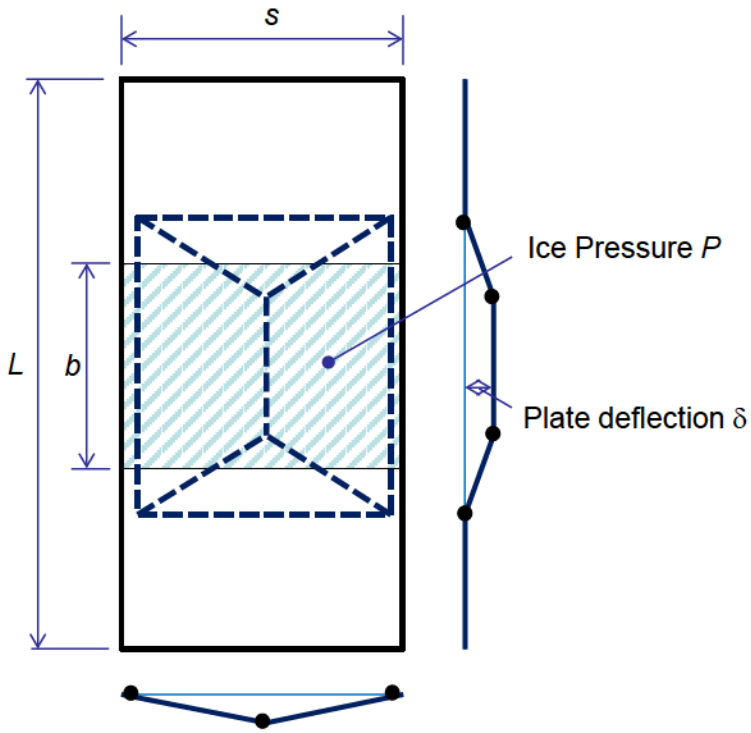

Figure 178 Illustration of yield line approach for shell plating design where s is main frame spacing L is the stringer spacing, and b is the height of the local ice contact area

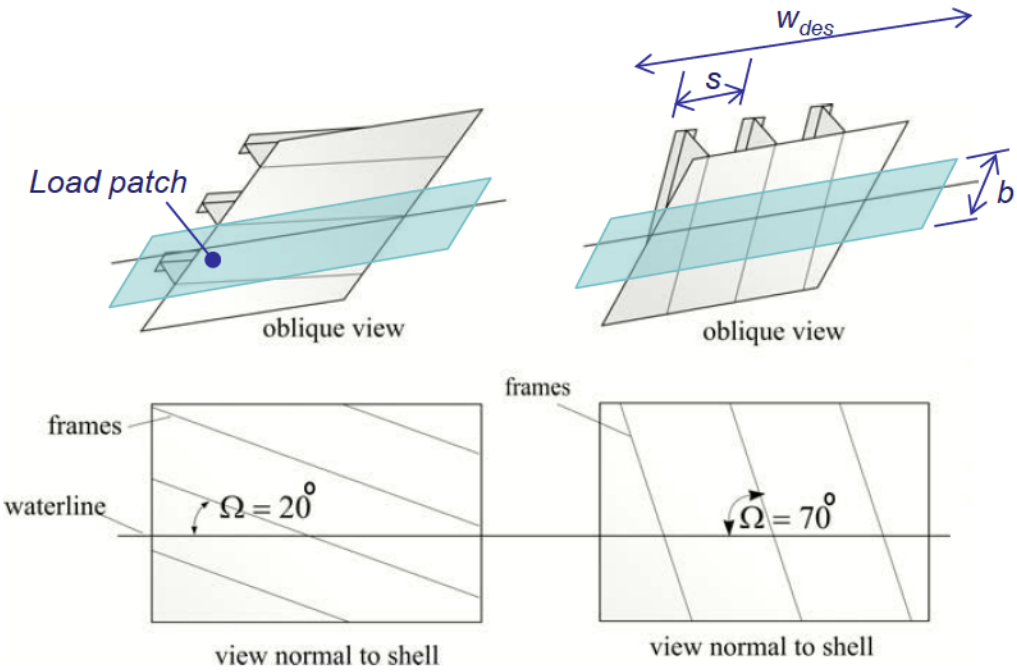

a) Longitudinal framing b) Transverse framing

Figure 179 Main frame angles that support shell plating relative to waterline (IACS, 2011),

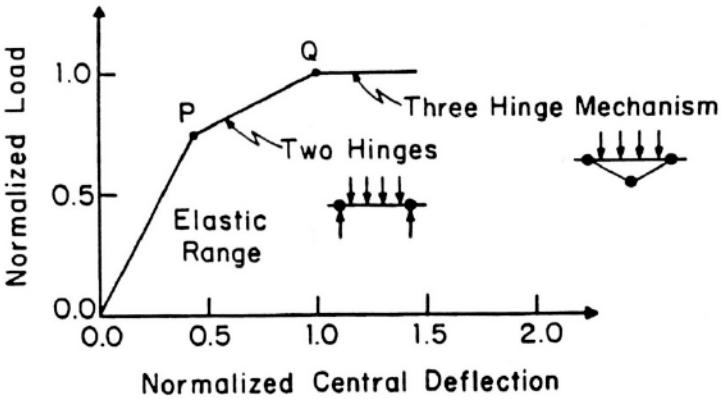

(a) Schematic Diagram Showing Development of Plastic Mechanism

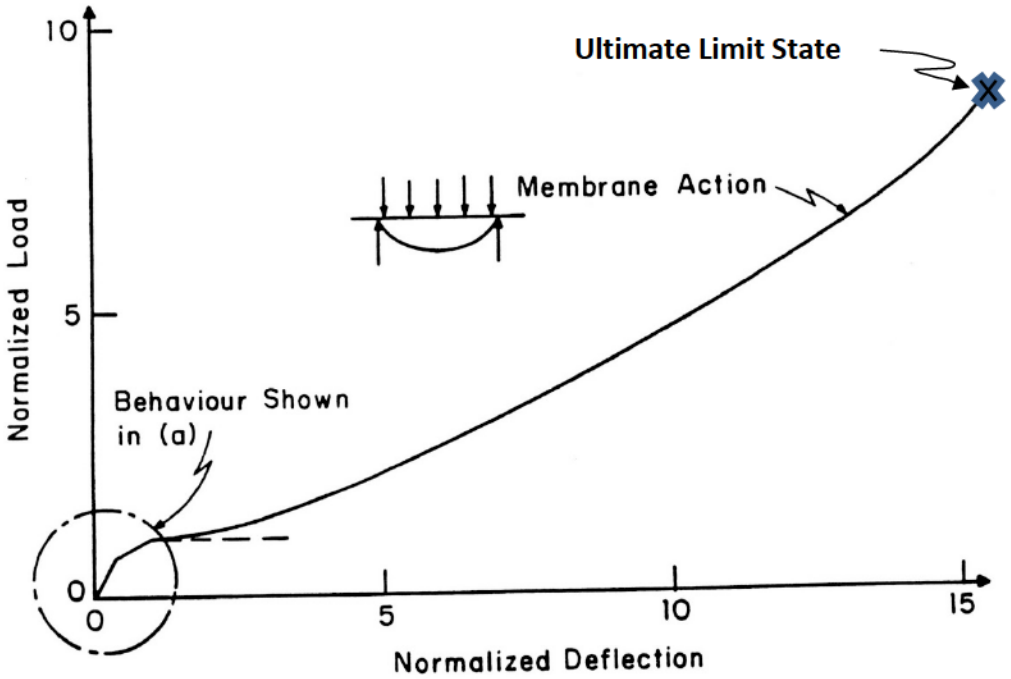

(b) Membrane Action

Schematic Diagram of Plate Failure Mechanisms.

Figure 180 Illustration of the plastic membrane capacity of steel plating comparing the relative difference between some ultimate limit state, elastic capacity and a plastic three hinge mechanism.

5.2.11 Polar Class Rule Design Illustration

To illustrate design pressures using the Polar Class rules, three Polar Class 1 vessel sizes were selected giving a range of impact energies and corresponding design forces and pressures. Vessel particulars are listed in Table 21. Global, semi-local and peak local pressures are estimated for the shoulder impact scenario illustrated in Figure 177a.

Table 21 Vessel Particulars

Polar Class	PC 1		
Displacement	10 kT;	**40 kT**;	100kT
Length	116 m;	**199 m**;	250 m
Breadth	17 m;	**23 m**;	36 m
Draft	7 m;	**11 m**;	14 m
Hull region	Bow; hull factor = 1		
Assumed contact location	0.08L from forward perpendicular (i.e. stem)		
Bow shape	$\gamma = 30^o$; $\alpha = 33.5^o$; $\beta = 48.9^o$; $\beta' = 43.7^o$		
Model Ice Parameters	$P_0 = 6.0$ MPa; $e_x = -0.1$; $V = 5.7$ m/s,		
Stringer Spacing	3200 mm		
Transverse frame spacing	500 mm		

Table 22 and Figure 181 illustrate the estimation of global and semi-local pressure area results. An MV *Arctic* type 40 kT vessel is used as a benchmark with comparison to both 10 and 100 kT vessels. The global contact force for a 40 kT vessel is 89.9 MN for the shoulder impact scenario at 16 m from the forward perpendicular. The Polar Class rules assume that impact forces increase from stem to outer bow and for the same 40 kT vessel assuming the bow geometry to be consistent, the impact force reduces to 83 MN if the contact location is 5 m from the forward perpendicular.

For the 40 kT vessel assuming outer bow 16 m contact location, the global contact area and corresponding global pressure for an aspect ratio of 5.12 is 20.1 m^2 and 4.5 MPa respectively. The semi-local contact area (i.e. based on reduced contact area dimensions w_{des} and b) and pressure are 5.0 m^2 and 18 MPa respectively. Pressures used for plate thickness

design are further scaled based on frame spacing and corresponding peak pressure factors given in Table 20 (i.e. pressures locally increase as frame spacing decreases and effective local panel area reduces – see also Figure 177a).

Table 22 Polar Class pressure-area results from illustrative examples

Item	Value		
Vessel Displacement	10 kT	40 kT	100 kT
Global Force	36.9 MN	89.9 MN	119 MN
Assumed Contact location (0.08 L)	9.3 m	15.9 m	20.1 m
Aspect Ratio (function of β')	5.12	5.12	5.12
Global Contact area	7.5 m^2	20.1 m^2	27.5 m^2
Global Pressure	4.9 MPa	4.5 MPa	4.3 MPa
Semi-local Contact area	2.5 m^2	5.0 m^2	6.2 m^2
Semi-local Pressure	14.7 MPa	18.0 MPa	19.1 MPa

Further observation from Figure 181 is that the semi local area and pressure for each displacement vessel is the intersection of:

- the process pressure area expression from Eq. (78); and
- the ratio of global impact force from Eq. (65) and arbitrary area (i.e. F_{GLOBAL}/A assuming no scale effect), where force is a function of class crushing factor, CF_C, which is a function of ice strength Po and impact speed V .

The pressure area expression from Eq. (78) essentially models increasing pressure with increasing vessel displacement. While no reference to exposure is given, it seems that the modeling of a process pressure-area scale effect using a power law exponent of +0.3 is used in this regard. Unfortunately, without acknowledging exposure, it suggests some alternative ice material property that is inconsistent with conventional theory and field data. Section 5.4 discusses an exposure based derivation using a conventional ice material property and scale effect that produces results consistent with the present code derivations assuming the resultant outcome (i.e. plate thickness and trends) is reasonable.

Further illustration of the Polar Class rules including semi local and peak local pressures based on frame spacing s is given in Figure 182. Peak local pressures are further factored from semi-local pressures using peak pressure factors from Table 20 based on the height b of the local ice contact area and the frame spacing s (i.e. local pressures are higher on smaller contact areas and are assumed to increase linearly with decreasing frame spacing s). For a 40 kT, a semi-local design pressure of 18 MPa is estimated on a semi-local design area of 5 m^2. A 100 kT vessel is predicted to have pressure of 19 MPa over an area of 6.2 m^2. Pressures locally are scaled depending on frame spacing and can range from a minimum of 1.2 to 1.8 for transverse framing having no stringer support (see Table 20). While local pressures on panel areas governed by frame spacing may be within reason, pressures on semi-local areas greater than 1 m^2, are excessive. Nowhere have such extreme pressures on these areas been measured. This is because pressure area scale effects are ignored (i.e. the area scaling exponent is modeled as -0.1). For illustration the global ice pressure area expression used in the Polar Class rules for PC1 design, $P = 6.02A^{-0.1}$ is plotted.

In the illustrative example, local pressures for the 100 kT vessel are governed by flexure failure of the ice using Eq. (66). Design pressures without the flexural strength limit are illustrated in Figure 183. The global force for the 150 kT vessel increases from 119 MN to 160 MN. Since the purpose of this work is to model scale effects and exposure, the influence of flexure strength is outside the scope and not included in subsequent analysis.

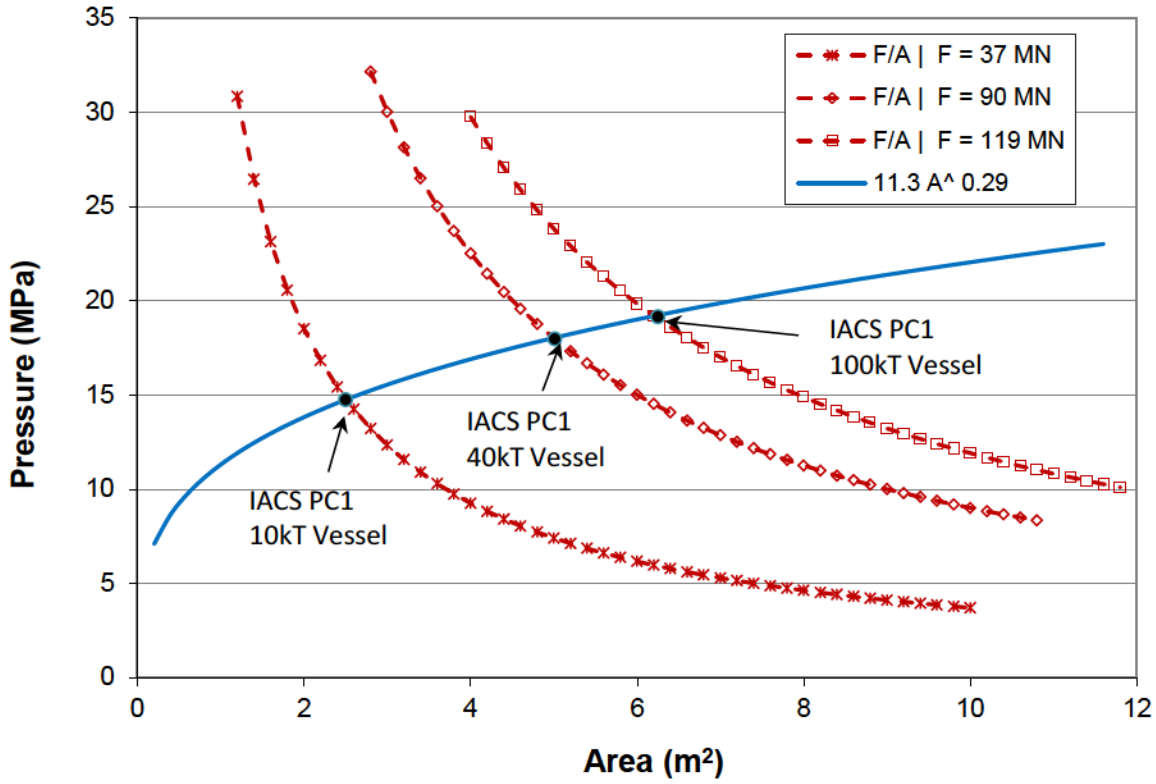

Figure 181 Illustration of IACS Polar Class 1 semi-local pressure area design points for 10, 40 and 100 kT vessels – intersection of global Force/Area curves for each vessel with process pressure-area curve from Eq. (78).

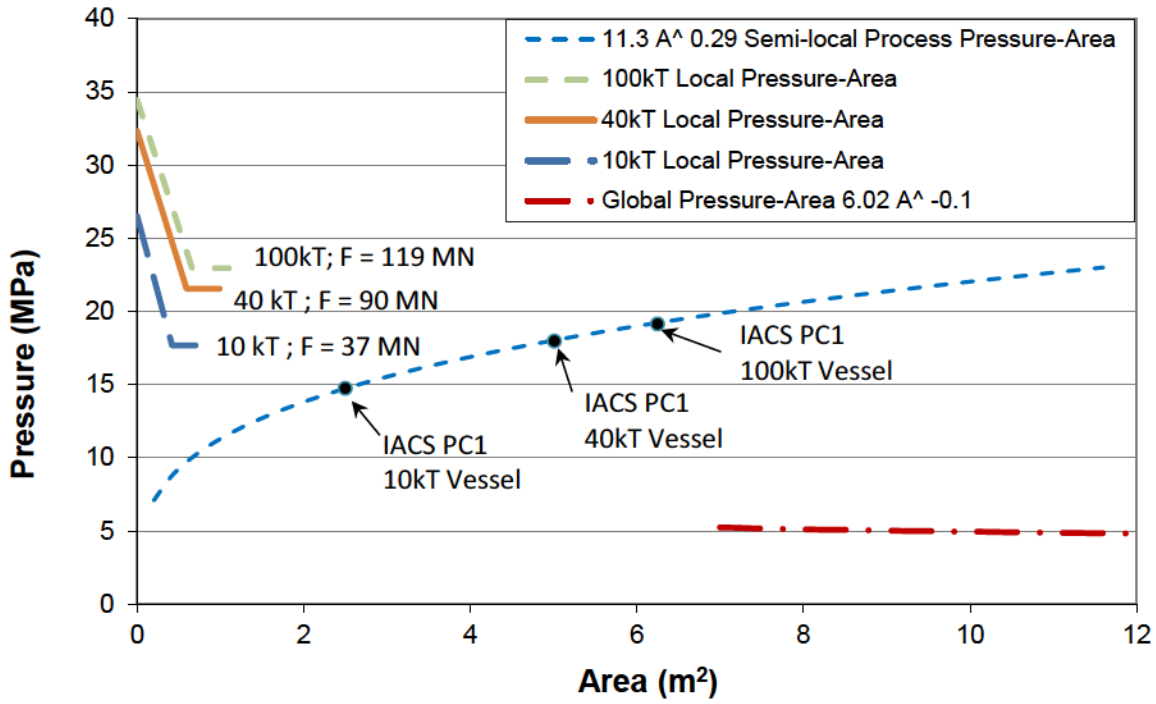

Figure 182 IACS Polar Class 1 Pressure area illustration for semi-local and local design areas (with flexure failure limit) – local pressures based on peak pressure factor from Table 20 that are scaled based on load patch height *b* and frame spacing *s*.

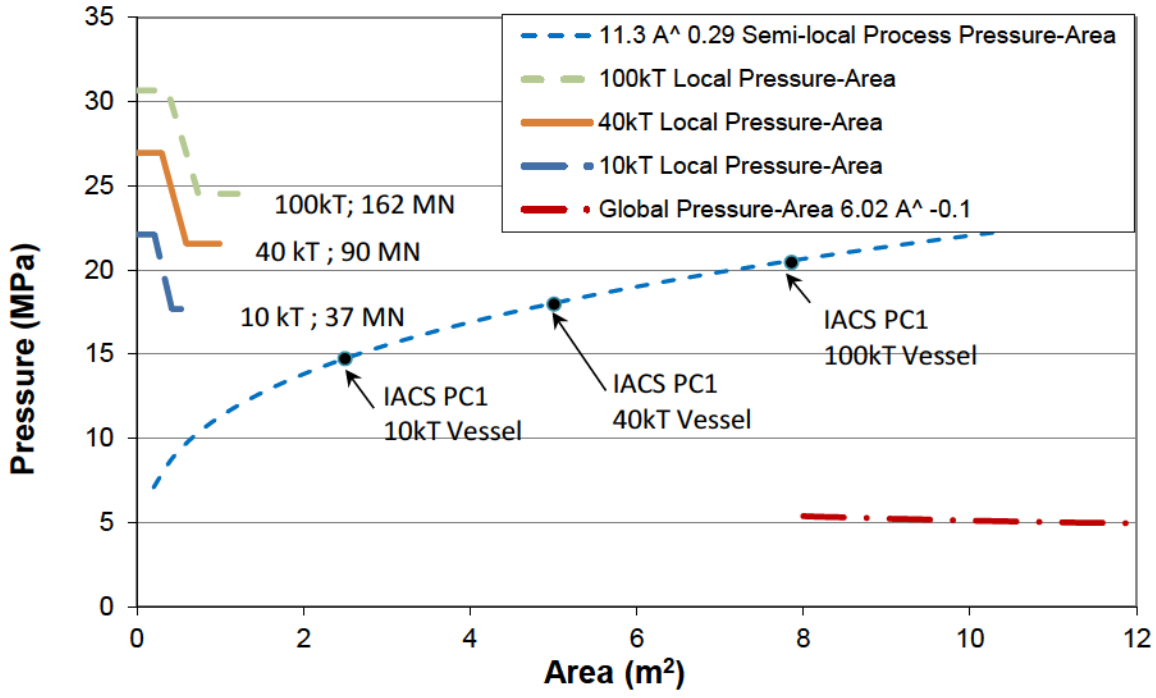

Figure 183 IACS Polar Class 1 illustration from Figure 182 with NO flexure failure limit.

5.2.12 Sensitivity of IACS Prediction to Inclusion of Pressure Area Scale Effects

The sensitivity of the Class Factor for Crushing (CFc) and the Class Factor for Load Patch Dimensions (CF_d) to the pressure area relationship $P_{AVG} = P_0 \cdot A^{ex}$ was assessed. Two coefficients for e_x were modeled: -0.1 as prescribed in the Polar Class rules, and -0.4 consistent with global pressure area scale effect derived from ship ram experiments and analysis. Plate thickness was estimated for a Polar Class 1 vessel having transverse framing. Vessel particulars given in Table 21 were used. It is noted that while e_x = -0.4 is used for illustration, the scale effect for local pressure based on full scale ship ram data is -0.7 as documented in Section 2.3.3.

The influence of exponent e_x on maximum force, contact area, pressure and plate thickness for a range of Polar Class 1 vessel displacements is illustrated in Table 23 and Table 24 as well as Figure 184. With e_x modeled as -0.1, estimated design ice pressures and plate thickness increases with increasing ship displacement. This is reasonable since larger vessels will penetrate further into the ice floe, having longer duration and increased exposure. Increased exposure results in increased local pressures (See Section 2.3.3). With e_x however modeled at -0.4, consistent with the global pressure area trend from experimental data at lab and field scales, for increasing vessel displacement and corresponding force, the plate pressure reduces and plate thickness remains approximately constant. An exponent less than -0.4 results in further decreasing pressure and decreasing plate thickness with increasing vessel displacement.

The intent of the Polar Class rules is to model increasing local pressure and plating thickness with increasing vessel displacement. As noted earlier, larger vessels moving faster and having increased kinetic energy will penetrate further, increasing global contact area and global impact force. With the increased penetration, contact duration and equivalent exposure, local pressures and corresponding plating thickness should increase. With the rule derivation however, when an improved ice load model is used however, the trend is the opposite. With the existing modeling and use of the pressure area exponent, e_x = -0.1, the approach should be acknowledged as empirical as opposed to suggesting that a new material property and/or process exists. Otherwise confidence in the Polar Class rules may be lost.

Table 23 Polar Class 1 maximum bow force, design pressure and plate thickness for different displacement vessels having main frame spacing of 0.5m modeled with pressure area exponent e_x = -0.1 and design area adjustment exponent given as w_{ex} = 0.7

Area Exponent	**e_x**	**-0.1**				
Displacement (kT)	D	10	25	39.9	100	150
Force Max (MN)	F	36.9	66.5	89.8	119.1	119.1*
Loaded Design Area (m^2)	A	2.5	4.0	5.0	6.2	6.2
Average Local Pressure (Mpa)	Pavg	14.7	16.8	18.0	19.1	19.1
Peak Local Pressure (Mpa)	Ppk	19.2	21.8	23.3	24.9	24.9
Plate thickness total (mm)	tpl	45.0	50.7	53.9	56.8	56.8

* same design results as for a 100kT vessel as a result of a flexure force limit.

Table 24 Polar Class 1 maximum bow force, design pressure and plate thickness for different displacement vessels having main frame spacing of 0.5m modeled with pressure area exponent e_x = -0.4 and design area adjustment exponent given as w_{ex} = 0.7

Area Exponent	**e_x**	**-0.4**				
Displacement (kT)	D	10	25	39.9	100	150
Force Max (MN)	F	25.0	41.3	53.3	87.9	109.7
Loaded Design Area (m^2)	A	3.2	5.8	7.8	14.0	18.1
Average Local Pressure (Mpa)	Pavg	7.8	7.1	6.8	6.3	6.1
Peak Local pressure	Ppk	10.1	9.3	8.9	8.2	7.9
Plate thickness total (mm)	tpl	33.7	34.4	34.6	34.7	34.6

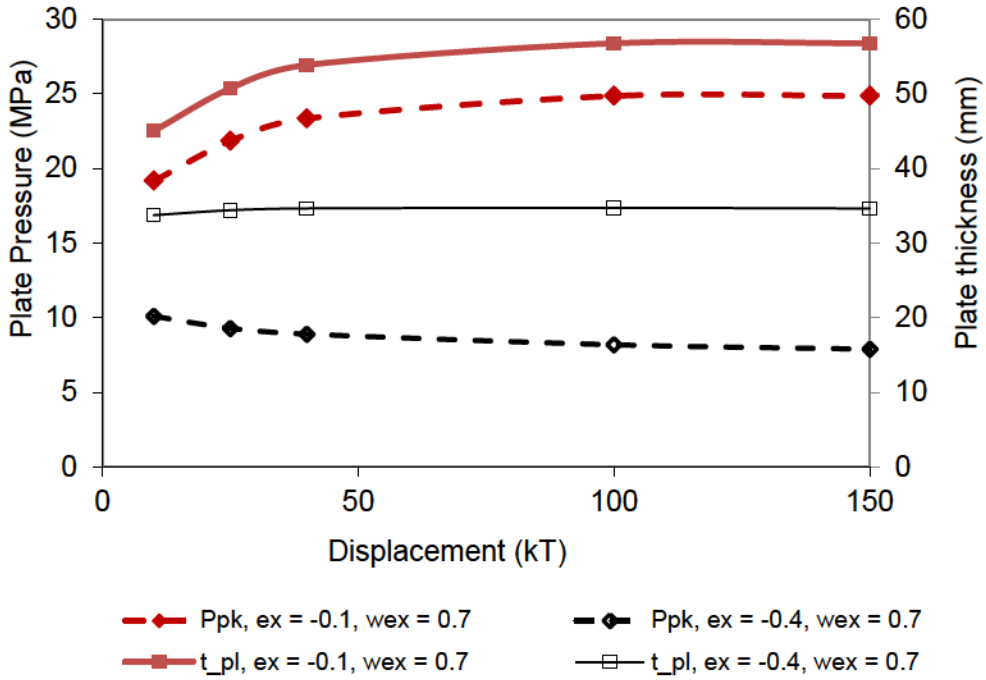

Figure 184 Influence of pressure-area exponent e_x on plate design pressure vs. ship displacement for Polar Class 1 vessel.

5.3 Discussion of Polar Class Rules

5.3.1 Exposure

Exposure is not explicitly modeled in the Polar Class rules. One reference to exposure as noted in Section 5.1.2, states that "while impacts are rare, it is assumed that the impact frequency [with severe ice] is once per year." This would be conservative in cases where multiple years occur between impacts but may be under conservative when multiple impacts occur each year.

In other civil engineering applications, exposure is estimated and incorporated in the design loads (e.g. extreme wind events on a tower; number of iceberg collisions with an offshore platform). This approach is more refined than suggesting a single a fixed number of impacts per year. Also, varying levels of operational performance can be modeled. While it may be assumed that a captain will always attempt to avoid ice impacts, multi-year ice detection and

avoidance cannot be assumed to be 100%, so reference to one impact per year may well be under conservative. The approach by Ralph and Jordaan (2013) estimates the number of expected interactions (i.e. collision probability) based on the occurrence of ice, the ice conditions (floe size and concentration) and the vessel transecting through an ice regime having an exposed width, vessel track and speed. Detection and avoidance performance (if known) can be modeled directly and the annual number of interactions per year explicitly estimated.

However, it cannot always be assumed that a captain will avoid ice. To avoid getting stuck or to prevent delay in a shipment of cargo, captains may well choose to ram a vessel into the ice and break through. Further, if the Polar Class rules are extended to consider icebreaker design, the annual number of interactions could well be 100s and 1000s. The Polar Class rules could be enhanced with exposure based methods particularly if icebreaker design is to be considered.

The reference to increasing ice crushing coefficient *Po* in Table 19 for increasing Polar Class cannot be justified without reference to exposure. Global pressures on average decrease with increasing contact area; area that may increase with increased ice thickness. Taylor (2010), using measured data and a probabilistic fracture mechanics model, illustrates that pressures decrease with increasing ice thickness. Hence, consideration for exposure is necessary and can be used to justify the trend in the crushing coefficient *Po* trend and extreme design parameters. Exposure can also be modeled directly in design calculations. Depending on the occurrence of extreme ice features along a route and with some measure of risk mitigation (detection and maneuvering), we can estimate the expected annual number of collisions accordingly (Ralph and Jordaan, 2013). Correlating these with Polar Class descriptions would add tremendous value to the Polar Class rules.

Finally, as discussed in the previous section, exposure can be used to justify the increase in pressures locally as larger energy interactions from larger, faster ships result in increased penetration, larger contact area and larger global forces. The mechanics of ice failure and pressure area scale effect need not be artificially specified to produce the correct design

trends. Section 5.4 illustrates this with an alternative formulation that explicitly models exposure.

5.3.2 Modeling Scale Effect

The derivation of class factors in the Polar Class rules assumes a global pressure area scale effect corresponding to e_x = -0.1. The background documentation to the Polar Code (AMARK and MUN, 1998) states that that e_x is always -0.1, despite evidence of stronger scale effect from various other experimental results (Sanderson, 1988, Riska 1987, Fuglem and Jordaan, 1999 to list a few). The AMARK authors suggest that there is confusion among researchers in the interpretation of scale effect, particularly the calibration of the coefficient e_x. Reference is only made to work by Frederking (1998) who first introduced the concept of process pressure area and compared with spatial pressure area (See section 2.3.4). In reference to the modeling by Frederking, the AMARK report author's interpretation of that data suggests that a process pressure area scale effect exists that models global pressures increasing with increasing area. Although in the end the use of Eq. (78) achieves this, justification for modeling the material property of ice using e_x = -0.1 could be clarified.

Riska (1987) describes this coefficient e_x from analysis of global ship ram measurements and other experiments to be -0.44. Sanderson (1988) compiles many data sets and illustrates a scale effect of -0.5. Fuglem and Jordaan (1999) derive this coefficient based on global pressure area analysis of ship rams as a normal distribution with a mean of -0.4 and standard deviation of 0.2. Reference to classical materials, dimensional analysis, geometric analysis, and Weibull theory as discussed in Section 3.2 support these findings. Although these reference global scale effects, for illustration, local design pressures from ship ram data follow a scale effect consistent with $A^{-0.7}$ as illustrated in Figure 33 and Figure 34 (Jordaan *et al.*, 2007, Taylor *et al.*, 2010).

Daley (2004) suggests that there is no a priori reason for pressures to decrease with increasing contact area and that confinement may raise effective pressures on local areas within a larger contact area. This suggests that increasing global contact area during progressive interactions will provide increasing local confinement that will suppress crack growth, limit fracture and increase local ice strength. This assumes that global fracture is

suppressed, which can only be true if *HPZ*s do not exist and a free surface does not exist. Otherwise, as experimental evidence verifies, for the practical applications for ship ramming and interaction geometry of interest, ice will fracture regardless of scale. The larger the contact area, the larger the number of exposed flaws. The distribution of increasing force across the entire contact area will introduce shear and tensile stresses across the entire interaction face and lead to progressive fracture events. Fracturing processes lead to scale effect.

The material properties of the ice will not change with increased global interaction forces such that it is no longer fracture prone. Temporary confinement may occur at specific instants during the interaction process (including some growth in contact area), which may suppress crack growth and fracture and allow local *HPZ* pressure to increase. Such durations are very short. Further, Jordaan (2001) experimentally verifies that suppression of crack damage is limited such that at some critical hydrostatic pressure, local damage is further enhanced as recrystallization processes weaken the ice structure (see Figure 55). Even if a fracture or a spall event does not destroy the *HPZ*, once the accumulation of microstructural damage at the center of the interaction area (and across the *HPZ* face) meets with the accumulation of damage from the free surface, all damaged material will rapidly extrude. This catastrophic failure including the *HPZ* will result in a sharp drop in contact force and pressure.

The underlying objective of the Polar Class rules is to model 'local pressures' on local panel areas as increasing with increasing energy interaction and global penetration and contact area; or in other words, exposure. While the end result may be reasonable, the methodology used to arrive at design pressures should be acknowledged as empirical or "best practice" and not justification for some alternative ice mechanical process or theory. Discussion of such practice would be helpful in understanding the Polar Class rules. Explicit modeling of exposure as discussed in Section 5.2.12 and further in Section 5.4 helps in this regard.

5.3.3 Class Dependency for Design Parameters

Design forces for crushing failure for different Polar Classes are a direct function of the Class Factor for Crushing (CF_C), which is a function of some ice crushing coefficient P_0, and impact speed V. A limit on crushing forces considers flexural failure, and hence inclusion of Class Factor for flexure, $CF_F = h^2\sigma_{flex}$ where σ_{flex} is the flexural strength and h the ice thickness. Each parameter is modeled as having class dependency.

5.3.3.1 Ice Strength

No reference to data or detailed discussion is provided to verify specific values for P_0 and V and particularly, dependency on Polar Class designation. The AMARK and MUN (1998) report suggests that the selection of parameters depends on "angle formulation", or iterated as required to "achieve a better fit between certain existing ship designs and particular classes."

The qualitative distinction of Polar Classes range from:

- unlimited year round operations in MY ice (i.e. PC1);
- year round operations in thick first year ice with old inclusions (i.e. PC 4); to
- summer/autumn operations in thin first year ice with old ice inclusions (i.e. PC 7).

While lower classes acknowledge the risk of interaction with old ice inclusions, it is important that the exposure be considered at all levels. Any Class, particularly Classes 1 through 5, should anticipate some MY ice interactions. A MY floe may block a route and ramming may be required. Some experiences regarding the need for ramming are given below:

> *Experience aboard the MV Arctic, a Canadian Arctic Class 4 vessel, involved repeated ramming of a multi-year ridge blocking access to a region, and successfully got through*. I. Jordaan

Ramming may be required for operational reasons: the season may be late, an onshore storm may be forecasted, fuel supplies may be on the other side of 3 miles of multiyear ice. Capt. P.C. Kimmerly (Carter *et al,* 1996)

While these may be considered extreme scenarios, it is realized that lower class vessels may encounter MY ice and some level of exposure should be considered. It is reasonable that the Class dependency for pressure coefficient P_0, be calibrated to varying levels of exposure based on number of annual rams with MY ice.

5.3.3.2 Ice Thickness and Flexural Strength

While a detailed study of flexural strength is outside the scope of this thesis, some general comments are provided. In the present Polar Class rules, ice thickness is a Class dependent parameter that defines a Class Factor for Flexure (CF_F) that models a flexural strength limit on design forces. While no specific data were referenced to verify the selection of flexural strength, σ_{flex} values, justification was that Polar Class 6 and 7 vessels are limited to vessel displacements between 30 – 40,000 kT, above which trends were aligned with the Baltic Rules. The flexural strength for different Polar Classes was scaled to achieve consistency.

It was noted earlier in Section 5.1 that when MY ice exists, it governs design loads. In the original ASPPR proposal review it was recommended that thickness, being a random quantity, should not be used as a defining parameter for limiting MY ice interactions and design loads among different vessel classes. Thickness is highly variable and operationally, captains have no practical means to measure thickness before entering any ice regime. While remote sensing technology is rapidly advancing, this capability does not yet exist.

Exposure is an alternative measure to distinguish ice Class, which considers the expected number of rams per year and ram duration. While technology to remotely measure thickness does not yet exist, detecting the occurrence of MY and glacial ice is possible. Based on concentration, exposure can be estimated based on a selected route and operational parameters (Ralph and Jordaan, 2013).

5.3.3.3 Summary

The Class Factor for Crushing is a function of the ice crushing coefficient P_0 and impact speed V. Estimating the Class Factor for Crushing by scaling P_0 according to exposure is reasonable and theoretically consistent. Modeling impact speed as a separate design parameter could be considered as opposed to a hidden factor within the Class Factor for Crushing. Modeling a limiting force for crushing based on a flexure model for MY ice should be revisited. Thickness, the key parameter in flexural strength, is not practically measureable during shipping operations.

The derivation of the Polar Class rules essentially ignores any global pressure area scale effect, modeling the area exponent e_x as -0.1 vs -0.4 as suggested in data. While resultant design trends maybe correct (i.e. increased local pressure with increased vessel displacement), it seems the pressure area exponent (e_x = -0.1) was arbitrarily assigned to achieve this trend. Acknowledgment of exposure can help in this regard.

5.4 Polar Code Comparison with Alternative Pressure Area Model

To extend the review of the Polar Code, an alternative approach was considered that is consistent with the mechanics of ice failure including:

- an improved global pressure-area model based on an area exponent -0.4 vs -0.1;
- estimation of local contact relative to global contact area based on *HPZ* density and *HPZ* area; and
- consideration for enhance peak pressures where exposure is a function of vessel displacement and impact speed (i.e. larger faster ships will penetrate further thereby increasing exposure and peak *HPZ* pressures).

5.4.1 Maximum Global Force

The original energy based maximum normal force equation given in Eq. (59) is used which models the transfer of initial kinetic energy into crushing and inertial (rotational) potential energy and given as

$$F_{NMAX} = P_0^{\frac{1}{3+2e_x}} \cdot f_a^{\frac{1+e_x}{3+2e_x}} \left((3+2e_x)\frac{1}{2}\frac{D}{C_0} \cdot V_n^{\,2} \right)^{\frac{2+2e_x}{3+2e_x}},$$

which can be further expressed in terms of vessel displacement D and horizontal impact speed V as

.

$$F_{NMAX} = P_0^{\frac{1}{3+2e_x}} \cdot \underbrace{\left(f_a^{\frac{1+e_x}{3+2e_x}} \cdot \left(\frac{1}{2}\frac{(3+2e_x)}{C_0}\cos^2(\beta') \right)^{\frac{2+2e_x}{3+2e_x}} \right)}_{f_{ai}} \left(D \cdot V^{\,2} \right)^{\frac{2+2e_x}{3+2e_x}}. \qquad (80)$$

The revised expressions were exercised for a range of Polar Classes (i.e. 1 through 5) and vessel displacements [10 25 40 100 and 150] kT.

5.4.2 Pressure Area Scale Effect

An improved pressure area model consistent with global measurements was used with the kinetic energy formulations. This modeled e_x as -0.4 and the average pressure given as

$$P = P_0 A^{-0.4}$$

where for Polar Class 1, P_0 is 6.02 MPa (see Table 19).

Exercising Eq. (80), Figure 185 illustrates the nominal pressure vs. nominal contact area for the varying vessel displacements. While the P_0 coefficient may be considered conservative, the global scale effect is reasonable.

5.4.3 Reduced Local Contact Area from Nominal Load Patch

As discussed in Section 5.2.5, the proportion of actual *HPZ* contact area through which loads are transmitted into the structure is less than 10% of the nominal contact area. If *HPZ* density is approximately 0.6 *HPZs*/m^2 and *HPZ* areas range from 0.1 to 0.2 m^2, within a nominal contact area of 10 m^2, 6 *HPZs* are expected covering an area ranging from 0.6 m^2 to 1.2 m^2. The proportion of load carrying area then ranges from 6% to 12%. For purposes here, a value of 10% is reasonable.

Maintaining consistency with the rule development, the nominal width and height of the global contact area are factored by 1/3. As the corresponding area scales as l^2 the local contact area is 10% of the nominal contact area. This can be refined with further study which is outside the present scope.

5.4.4 Increased Local Pressures with Increased Exposure - Vessel Displacement

While spalling and fracture will reduce the nominal contact area, exposure must also be considered. Longer penetration times and distances lead to the formation of more *HPZs* and hence increased probability of localize peak pressures. A factor based on vessel displacement and speed is determined to model that notion that larger ships moving faster would have greater exposure and higher likelihood of increased pressure on a local panel. It was assumed that this factor would be some function of $D^{\frac{2+2e_x}{3+2e_x}}$, consistent with the form of Eq. (59). A range of displacements from 10 to 150 kT were selected and original Polar

Class design pressures and plate thickness estimated. Assuming the trend in design pressures and plate thickness for varying vessel displacement to be reasonable - which is based on expert experience (albeit conservative for PC1) - an expression for localized pressure exposure factor was defined and given as,

$$PEF = \frac{D^{m_{ex}} v^{m_{ex}}}{9} \qquad (81)$$

where $m_{ex} = \frac{2+2e_x}{3+2e_x}$ consistent with the closed form kinetic energy expression from Eq. (59) with e_x = -0.4. It is noted here that the objective was to illustrate an alternative approach to design that is consistent with the fundamental mechanics of ice failure and also consistent with the design trends (i.e. plate thickness for increasing vessel size) based on expert judgment.

It is further noted that the peak pressure factor illustration above only considers exposure based on ship mass, impact speed and corresponding penetration, and does not model annual impact exposure. For a Polar Class 1, 40kT vessel, Figure 186 illustrates the peak pressure factor given in Eq.(81) and to model increased pressures locally for increasing vessel displacement and speed.

Exercising Eq.(81) for Polar Class 1 through 4 is illustrated in Figure 187. In this case, exposure is shown to reduce for lower Polar Classes because impact speed is lower for lower classes (See Table 19).

To verify whether the exposure based assumed in Eq. (81) is reasonable, the F_{MAX} software illustrated in Section 4.2 was exercised. Since exposure is some function of duration, durations were estimated for the crushing phase of a ram for a range of vessel displacements and vessel Classes (i.e. CAC 1 through 4). Mean vessel impact speeds were modeled as a beta distribution with parameters, mean and (standard deviation) given as 8 (2.5), 7 (2), 6 (1.5), and 5 (1) knots respectively. As shown Figure 187 the trend for duration vs. displacement follows well D^{mex} where m_{ex} = 0.545 consistent with Eq. (81).

While the dependence on displacement seems to be modeled reasonably, the simulated duration are considerably greater than predicted in Eq. (81). Closer examination identified that the smallest displacement vessel - consistent with the icebreaker *Kigoriak* at 6.4 kT – modeled a mean duration of approximately 1.1 - 1.2 seconds. The mean duration measured from *Kigoriak* trials was 0.7 seconds (see section 2.3.3.5). Normalizing the simulated results according to the ratio of measured to simulated (i.e. 0.7s/1.1s) produced the heavy line in Figure 187 where exposure as a function of vessel displacement is modeled as $0.32 \times D^{0.545}$.

While somewhat more conservative than the Polar Class estimated values, the adjusted curve is comparable, suggesting that Eq.(81) gives a reasonable base for modeling exposure. This curve is further suggested as a reasonable estimate for ship ram duration for local pressure modeling; to establish a 'parent' local pressure distribution for a given ship displacement, before annual exposure (i.e. number of rams per year) is modeled.

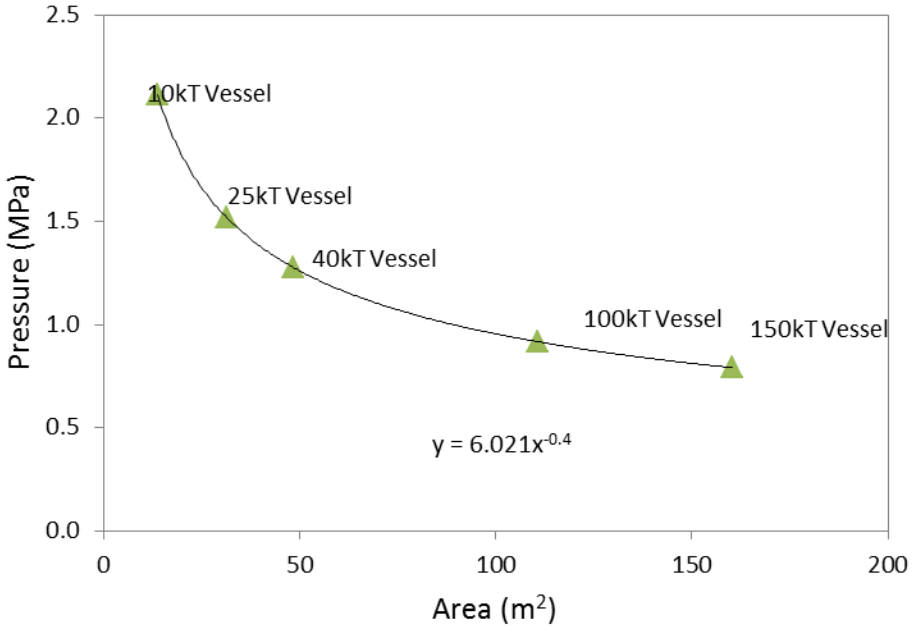

Figure 185 Illustration of global pressure area based on vessels having varying displacement from 10kt to 150kt.

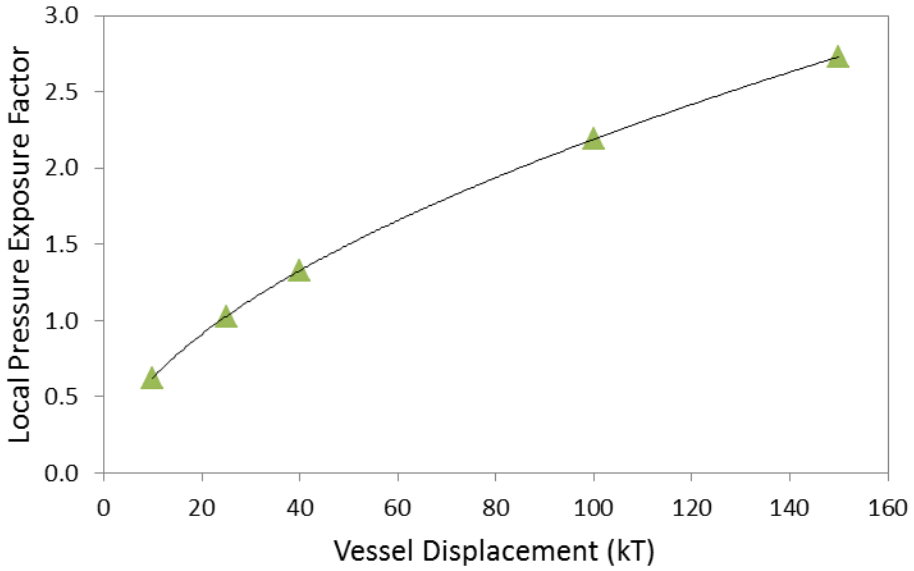

Figure 186 Illustration of local pressure exposure factor as a function of vessel displacement based on Eq. (81).

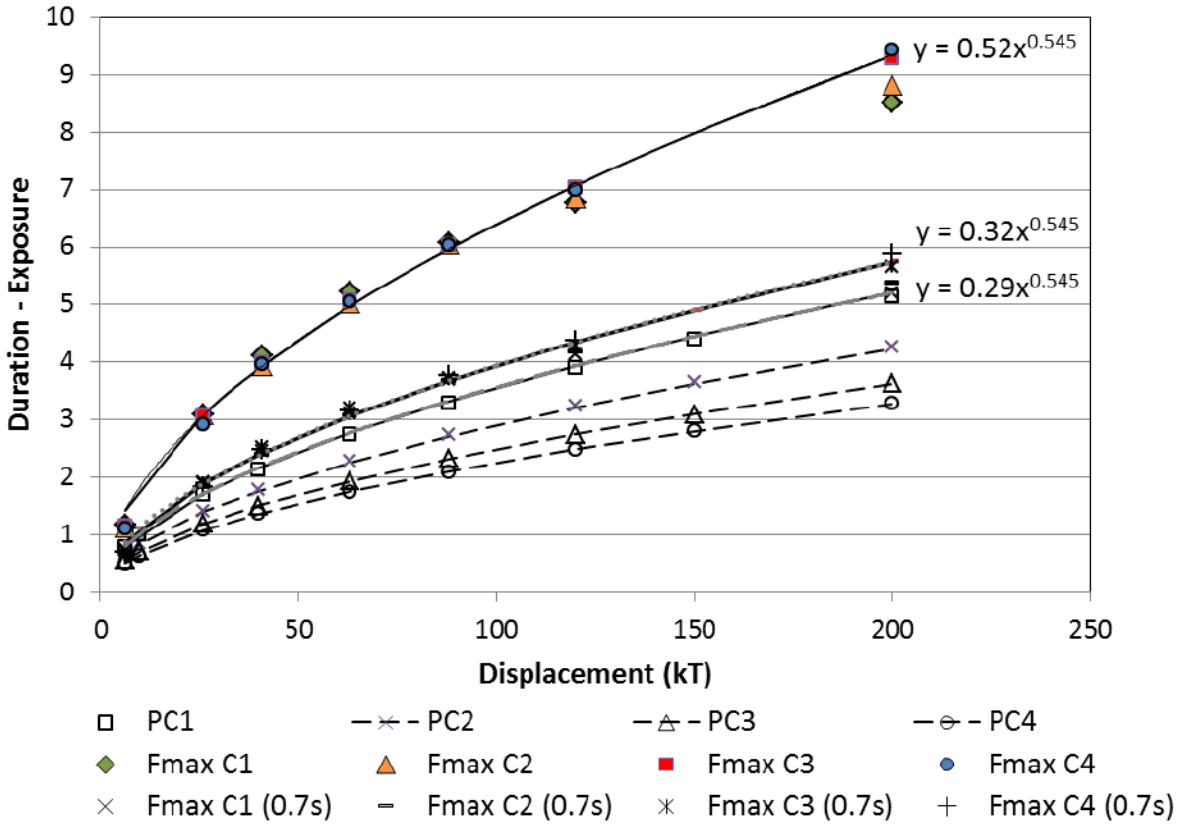

Figure 187 Illustration of ram duration and exposure as a function of vessel displacement.

5.4.5 Preliminary Results

Estimated vertical impact forces results and comparisons are given in Table 25 below. Using the Class coefficients as defined the Polar Class rules, estimated global impact forces modeling a pressure area scale effect $A^{-0.4}$ are significantly lower than forces estimated using $A^{-0.1}$. Parameters that influence force estimates include mass, impact speed, pressure coefficient *Po*, and the Popov *et al*. (1967) equivalent mass reduction coefficient (Co), which is a function of local contact location and geometry relative to vessel center of mass, and added mass. While uncertainty exists in each parameter, uncertainty with simple analytical expressions for both heave and pitch added mass (i.e. motions associated with bow collision), and rigid body inertial effects may be significant. While a detailed review of the Popov *et al*. (1967) model is outside the scope of this project, estimates of added mass were obtained for the MV *Arctic* using MAPS0 software (Qiu *et al*., 2015) as illustrated in Table 26. Heave and pitch estimates area considerably different. Subsequently revised estimates of the mass reduction coefficient for a shoulder impact is 2.15 for the new model compared with 2.55 in the original. Similarly for a bow collision, the new estimate is 1.7 vs 2.25. These revised added mass estimates are used in the alternative model.

Table 25 Comparison of influence of pressure area coefficient *ex* (i.e. A^{-ex}) on estimates of global vertical forces using Polar Class rules for MV *Arctic* type ship

Polar Class	Impact Speed Vs (m/s)	Ice Strength P_0 (MPa)	Polar Class Rules ex = -0.1	Estimated Forces e_x = -0.4 (MN)
1	5.675	6.021	72	42
2	3.986	4.217	40	24.5
3	2.997	2.985	25	15.4
4	2.508	2.464	18	11.6
5	1.988	2.002	12.6	8.1
6	1.766	1.497	9.7	6.3
7	1.466	1.308	7.3	4.9

Table 26 Comparison of Popov added mass coefficients with MAPS0 estimates.

Motion	Popov Added Mass Equations	Popov Added Mass Estimate for MV *Arctic*	MAPS0 Estimate
Surge (*Amx*)		0	0.04
Sway (*Amy*)	$2\times T/B$	1	1.1
Heave (*Amz*)	$2/3\times B\times Cwp^2/T/Cb/(1+Cwp)$	0.74	2.15
Roll (*Amroll*)		0.25	0.27
Pitch (*Ampit*)	$B/T/(3-2\times Cwp)/(3-Cwp)$	0.76	1.25
Yaw (*Amyaw*)	$0.3 + 0.05\times L/B$	0.73	0.82

It is also noted that the class coefficients are not derived specifically from data but rather iterated to give reasonable forces for known vessel classes (AMARK and MUN, 1998). Subsequent adjustment of the class coefficients for the alternative model and corresponding estimates of vertical bow forces is given in Table 27. Consistency between old and new model is achieved.

Table 27 Estimates of global vertical forces for MV *Arctic* type ship for alternative pressure area model (i.e. ex = -0.4) with adjusted Class coefficients.

Polar Class	Impact Speed Vs (m/s)	Ice Strength P_0 (MPa)	Estimated Forces, Revised Pressure Area e_x = -0.4 (MN)
1	6.0	6.5	54
2	5.5	5.0	39
3	3.8	4.0	26
4	3.0	3.0	18
5	2.5	2.25	12.8
6	2.0	1.75	8.9
7	1.75	1.5	7.2

Local Pressure and Plating Thickness

The resultant peak design pressures and corresponding plate thickness for a 3.2 m × 0.5 m panel including comparison with the existing Polar Class rule derivations are illustrated in Figure 188. Assuming the resultant trend in Polar Class panel pressures and plating thickness to be correct (i.e. the experience of senior expert ship operators and designers is reasonable), it is illustrated that the alternative approach based on conventional principles of ice mechanics and scale effect and exposure yield design results that are entirely consistent.

For the present illustration, incorporation of the local pressure scale effect, $A^{-0.7}$ has not been directly considered, but could be in future analysis. As shown in Section 4.5.6, however, the parameters for *HPZ* force and density correctly model the local pressure design parameters and scale effect consistent with $A^{-0.7}$.

5.4.6 Summary

Collision modeling using the revised pressure area exponent and consideration for duration based exposure produces results consistent with the Polar Code values. There is considerable uncertainty in the modeling of added mass and energy loss through inertial response, which should be addressed. The selection of a near constant pressure for design to cover off uncertainty in other parameters is reasonable.

What is shown is that the material properties of ice and scale effect for larger ship interactions need not change to get proper design trends. We only need to consider that larger vessels penetrate further and experience greater exposure. There is no fundamental error in the original work of Sanderson and others who suggested that a global scale effect exists. While the basis for exposure needs further calibration, a reasonable basis has been illustrated.

Section 5.7 discusses possible adjustment to the governing coefficients *Po* and *V* such that Polar Class rule estimates are more aligned with calibration estimates using extremal analysis on measured data. Global force measurements from the MV *Arctic* trials are used. Calibration considers the influence of annual number of rams and annual exposure on Class

factors, as well the influence of vessel displacement and corresponding duration based exposure on peak local pressure factors.

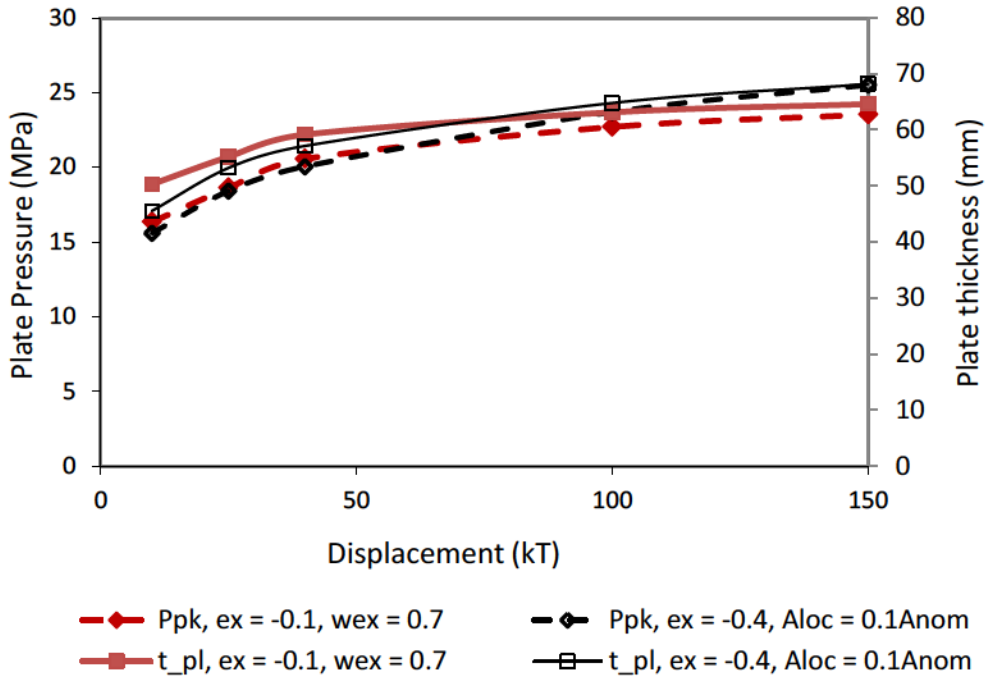

Figure 188 Illustration of peak pressures and shell plate thickness for a $3.2 \times 0.5\text{m}^2$ panel for varying vessel displacements including an additional local pressure factor that models increased exposure locally, based on increasing vessel displacement.

5.5 Extremal-Based Polar Code Design Comparison

5.5.1 Polar Class, Exposure and Class Equivalence

Key baseline parameters and class coefficients that govern the estimation of design forces using Polar Class rules are the listed in Table 19. As first introduced in Section 4.2, an estimate of the annual exposure and approximate number of rams with MY ice per year (10,000, 1000, 100, 10, 1, 1/10) MY ice) have been mapped to each of the seven (7) Polar Classes as outlined in Table 28.

The rationale for PC 1 is an extreme yet reasonable estimate of the number of impacts in one year. To illustrate, 10,000 rams with multi-year ice in a year equates to 50 rams per day for 200 days. Polar class 6-7 is shown to align with the highest Baltic classes 1A Super and 1A, a trend consistent in the development of the Polar Class rules (AMARK and MUN, 1998). Work by Zou (1996) illustrates that the highest Baltic Class design pressures were reasonably aligned with Grand Banks iceberg design conditions on stationary structures where impact occurrence is approximately 1/5 – 1/10 years. The distribution of annual hits among remaining classes seems reasonable and consistent with work by Carter *et al.* (1992), while reviewing the ASPPR proposals. Also, Carter *et al*. (1996) note that the MV *Arctic*, a CAC4 vessel, would be expect between 10 – 15 rams per year.

In addition to Polar Class designation and possible annual exposure, class equivalencies including Canadian ASPPR, Finish Baltic, Det Norsk Veritas, ABS and Russian rules are included.

Table 28 Class equivalencies and preliminary comparison to annual number of impacts.

IACS Polar Class	**MY Ice Exposure**	**Can. ASPPR**	**FIN**	**DnV**	**ABS**	**RUS**
PC1				Polar 30		LL1/L9
	10000	CAC1				
PC2	**1000**	CAC2		Polar 20	A5	
PC3	**100**	CAC3		Polar 10	A4	LL2/L8
PC4	**10**	CAC4		ICE 15	A3	LL3/L7/ ULA
	5			ICE 10		
PC5	**1**	**Type A**		**ICE 5**	**A2**	**LL4/L6**
PC6	**1/10**	Type A	**1A Super**	ICE 1A*/ 1A Super	A1	L5/UL
PC7	**1/20**	Type B	1A	DnV 1A	A0	L4/L1

5.5.2 Extremal Modeling of Global Impact Forces

The philosophy behind extremal modeling is that the vessel is designed for the maximum of n expected rams per year (i.e.. max $[X_1, X_2, X_3, \ldots, X_n]$), where Xi represents the distribution of forces for each year for n years.

The first step in extremal analysis is to determine a 'parent' distribution for loads, either computed using ship-ice interaction models or measured experimental data. For the Polar Class rule comparison, measured vertical global impact forces from MV *Arctic* ramming trials off Colberg Island are used. The global interaction geometry is illustrated in Figure 171. For the measured distribution of vertical forces illustrated in Figure 5 (see also Figure 189 below), a classical distribution such as a gamma distribution could be fitted (see Jordaan, 2005a), or alternatively, since concern is for extremes, an exponential distribution could be fitted to the tail of the 'parent' distribution as illustrated in Figure 190 using

$$F_X(x) = 1 - \exp[-\lambda(x - x_0)] \qquad (82)$$

where λ is the distribution parameter and x_0 the fitted exponential distribution plotting position.

The annual number of hits can be modeled in a Poisson process such that

$$F_Z(z) = \exp^{-\nu(1-F_X(z))} \quad (83)$$

where ν represents the average number of interaction per time period (i.e. one year). Combining Eq. (82) with Eq. (83), the maximum or design load W based on the expected number of encounters ν is given as

$$F_W(w) = e^{-\nu \exp[-\lambda(w-w_0)]} \quad (84)$$

where ν is the exposure parameter based on number of interactions in a year and λ is the exponential distribution parameter. Note that based on ship operability, the number of hits in a year can be based on the with of the ship, ship speed, density of ice, size of the ice floe as illustrated in Eq. (87)

The design load for 100 year return period (10^{-2} annual exceedence probability) is then given as

$$0.99 = e^{-\nu \exp[-\lambda(w_{100}-w_0)]} \quad (85)$$

from which

$$w_{100} = \frac{4.6 + \ln \nu}{\lambda} + w_0 \quad (86)$$

The design load can be determined for other return periods such as 1 in 10,000 years (i.e. 10^{-4} exceedence) where $F_W(w) = 0.9999$.

Depending on the requirements for the use of the vessel and expected number of interactions per annum, the appropriate design load distribution for maximum forces can be developed.

From Eq. (86), it is interesting to observe the logarithmic tendency of extremes based on the number of interactions; a linear trend.

5.5.3 Polar Code Deterministic Model

It is noted that measured data correspond to concentric bow impacts, whereas the Polar Class rules reference shoulder impacts. To ensure consistency between Polar Code estimates and extremal analysis, two model approaches are studied:

- shoulder model with impact point at 5 m from stem (as close as reasonable to the bow); and
- the bow geometry for concentric collisions is modeled (i.e. corresponding fa_i is determined) and vertical forces projected based on stem angle.

This is reasonable since the Class factors are not a function of bow geometry but rather ice strength and impact speed. The key goal is to verify the selection of Class factors for each Polar Class.

To fully understand the basis for the analytical formulation in the Polar Code, a detailed collision model was developed consistent with the energy based derivations given in Section 5.2. This also included the vessel mass correction approach developed by Popov *et al.* (1967) which accounts for vessel added mass for six degrees of motion as well as energy loss due to inertial motions given an eccentric collision event. The model is detailed in Appendix C.

5.5.4 Vessel Particulars

The vessel particulars used in the comparison are given as:

Polar Class	PC 1 - 4
Displacement	39 kTonnes
Length, Breadth, Draft	199 m, 23 m, 11 m
Hull region	Bow; hull factor = 1
Bow shape	$\gamma = 30^o$, $\alpha = 33.5^o$, $\beta = 48.9^o$, $\beta' = 43.7^o$
Contact location	$0.025 \times L = \sim 5$ m

5.5.5 Results

A comparison of vertical bow forces from the Polar Class rules with design forces estimated using the extremal rational approach and measured MV *Arctic* data is given in Table 29. Forces estimated using Polar Class shoulder impact scenario at 5 m from the forward perpendicular are entirely consistent with the theoretical based concentric bow estimates.

Extremal forces are presented in Table 29 for annual exceedence probabilities corresponding to both 10^{-2} (1/100 years) and 10^{-4} (1/10,000 years). As noted earlier, a 10^{-2} force and design strategy represents an Extreme Level Ice Event (ELIE) in ISO, and corresponds to elastic-plastic design where an occasional minor dent may be tolerable without loss of structural integrity. A 10^{-4} force and design strategy represents an Abnormal Level Ice Event (ALIE) in ISO corresponding to a fully plastic ultimate limit state (ULS) design. Consistent with ISO 19906 recommendations, 10^{-2} annual exceedance values have been illustrated with a factor 1.35 and show consistency with 10^{-4} exceedence values.

Observations from Table 29 with respect to alignment with exposure:

- PC1 force at approximately 70 MN is rather conservative, aligning with 10,000 annual rams and 10^{-4} annual exceedence condition. Alignment with the 10^{-2} condition is expected.
- A rather broad range of exposure exists between PC1 and PC2.
- With the exception of PC1, estimated PC vertical bow forces are rather low with PC2 aligning with 100 rams per year 10^{-2} exceedence condition; PC 3 aligning with 1 ram per year 10^{-2} exceedence.
- PC 4 was expected to align with 10 rams per year, PC5 1 ram per year, and PC6 and PC7 to be between 1/5 and 1/10 rams per year consistent with work by Zou (1996).

The PC1 force is consistent with a rational based load for 10,000 annual rams and a 10^{-4} exceedence level. Given that the structure model in the Polar Code for plating thickness is based on a yield line plastic collapse model, limit plastic deformation is allowed which is in line with the 10^{-2} annual exceedance condition. A different structural design strategy for a

10^{-4} load level compared with a 10^{-2} level, should be considered; one that considers ultimate collapse.

Adjustment may be considered to close the gap between PC1 and PC2. It is possible that an owner may wish to build a vessel that is more capable than ten (10) rams per year level but less than 10,000 ram per year level.

While these estimates are based on one vessel, it seems that optimization of the Po and V parameters, is warranted.

Table 29 Comparison of extremal based vertical global forces with Polar Class estimates

IACS Polar Class			Rational Design Approach using Exposure			
Polar Class	Vertical Force Shoulder* (MN)	Vertical Force Bow** (MN)	Number of Rams/yr	Fmax *** at 10^{-2} (MN) (× 1.35)	Fmax *** at 10^{-4} (MN)	Normalized 10^{-4} Fmax
PC1	72	72				
			10,000	*54 (73)*	70	*1.00*
			1,000	*46 (62)*	62	*0.90*
PC2	40	40	*100*	*39 (53)*	55	*0.81*
			10	*31 (42)*	46	*0.69*
PC3	25	25	*1*	*24 (32)*	40	*0.62*
PC4	18	18	1/5	20 (27)	35	0.5
PC5	12.6	12.6	1/10	16		

* area penetration for shoulder impact model using Polar Code; contact point 5 m from forward perpendicular

** area penetration based on concentric bow impact using theoretical collision mechanics model derivation; contact point assumed 5 m from Forward Perpendicular.

*** Estimated using measured 'parent' distribution from MV *Arctic* trials

5.5.6 Summary

While a comprehensive calibration is outside the scope of this work, Section 5.7 provides a first attempt at adjusting the underlying coefficients (i.e. Po and V) that govern the Class Crushing Coefficients and design forces such that better alignment is achieved with the suggested exposure. Ultimately, iteration of both exposure and class coefficients should occur until a final baseline is achieved.

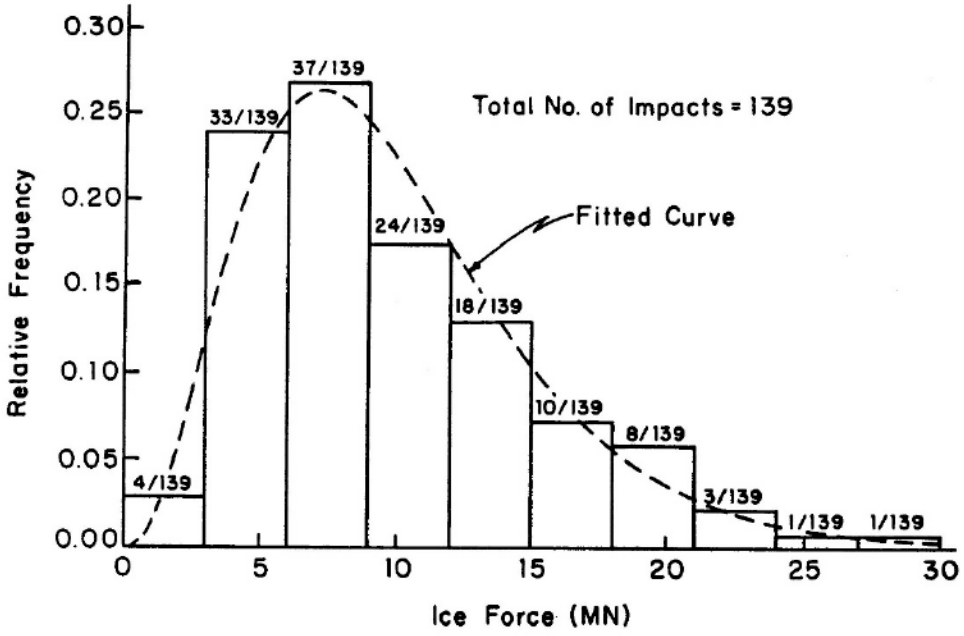

Figure 189 Histogram of measured MV *Arctic* ramming forces off Colburg Island in May 1984 (Carter *et al.*, 1992).

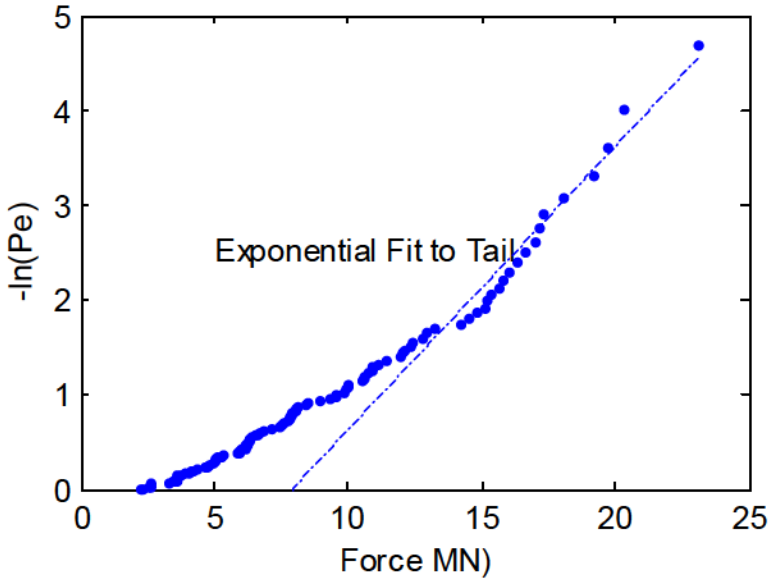

Figure 190 Modeling exponential fit to the tail of a '*Parent'* distribution of measured forces for *MV Arctic,* 1984.

5.6 Comparison of IACS Pressures with ISO Local Pressure Model

5.6.1 Design Parameters

Local design pressures for IACS Polar Class vessels were compared with design pressures derived using ISO19906 methodology and ASPPR proposals. Exposure was considered for both annual number of rams, and duration of a ram given a vessel's displacement and speed. For Polar Class comparisons, speed is a Class dependent parameter. A vessel having similar displacement to the MV *Arctic* (39kT) was modeled and further compared with a 10kT and 100kT vessels.

Vessel Particulars

Polar Class	PC 1 - 4
Displacement	40 kTonnes (with comparison to 10 and 100kT)
Hull region	Bow; hull factor = 1
Bow shape	$\gamma = 30^o$, $\alpha = 33.5^o$, $\beta = 48.9^o$
Location of impact	5 m from stem (i.e. ~ penetration distance) comparison to concentric bow impact.
Frame orientation	Transverse

Local Pressure Design

$\alpha = 1.25A^{-0.7}$

ν = number of rams per year 10,000, 1000, 100, 10, per year

Impact duration = 3.5s (predicted using global ship ram simulations)

r = 0.5; proportion of events on panel area (conservative; r = 0.5 for *Kigorak* rams)

$q_r = 1$ (hull region factor for bow impacts consistent with IACS)

To rationalize an upper bound extreme basis number of rams per year, an average of 28 rams per day for each day of the year would amount to 10,220 rams per year. Similarly, 10 rams per year would correspond to one occasional ram per week for a 10 week period.

5.6.2 Results

Comparison of local pressures based on Polar Code requirements for Polar Class 1 with ISO based 10^{-2} annual exceedence local pressure estimates for an annual exposure level of 10,000 rams is given in Figure 191. Comparison with 10 and 100kT vessel in addition to an MV *Arctic* type 40kT vessel is provided. Global forces corresponding to vessel mass represent normal component to the hull plating.

The collision model and fa_i coefficient was based on a distance x of 5 m from the stem consistent with code recommendations. Figure 192 illustrates the same design condition with contact at ~16m from the stem. Impact force and pressures increase with distance from the stem because the lever arm and subsequent pitch motion is reduced, reducing the pitch energy and increasing crushing energy.

ISO predictions based directly on measured local pressures and extrapolated according to extremal conditions are somewhat consistent with Polar Class estimates for local areas less than 1 m^2. The Polar Class estimates are based on peak pressures over panel areas consistent with a frame spacing s and estimated ice thickness b. Pressures, however, on contact areas greater than 1 m^2 are extremely conservative for a 10^{-2} exceedence probability design condition. A Polar Class pressure of 18 MPa on a 5 m^2 area is rather excessive, compared with an ISO extremal based pressure of 6 MPa.

One might suggest that the shoulder geometry with contact at the bow region (i.e. 5 m from stem) provides a reasonable comparison with ISO estimates. Earlier force estimates also confirm that the analytical basis is consistent with concentric impact geometry. It is noted that this load level is arbitrary and iterative since it is based on ice contact geometry with an assumed angle $\phi = 150^o$ (see Figure 170 and Figure 174). As Eq. (51) illustrates, a smaller angle will reduce loads; a larger angle will increase according to $\tan(\phi)$. Since this interaction model is the basis for Polar Class estimates, comparisons to other Polar Class levels for the same 40kt MV *Arctic* vessel will use this interaction geometry.

Figure 193 through Figure 196 illustrate similar results using the following comparisons:

- Polar class 2 and ISO estimate assuming 1000 rams;
- Polar class 3 and ISO estimate assuming 100 rams;
- Polar class 4 and ISO estimate assuming 10 rams; and
- Polar class 5 and ISO estimate assuming 1 rams.

5.6.3 Summary

While pressures on local contact areas greater than 1 m^2 are rather conservative, peak pressure on single panels (ice thickness b × frame span s) are comparable to ISO predictions. These suggest that while Polar Class 2 is reasonably aligned 1000 rams, Polar Class 3 and 4 may be under-conservative. The ISO based local pressure curve may be overly conservative particularly for lower Polar Classes. As noted in Figure 34 the local pressure parameter $\alpha = 1.25A^{-0.7}$ is an upper bound model. Depending on region of application or season, ice pressures may vary and an alternative parameter (e.g. $\alpha = 0.8A^{-0.7}$) may be considered. An observation from Figure 34 is that more southerly Arctic regions may have weaker ice resulting in reduced α values. This has not been studied specifically in this thesis but should be the focus of future work.

Recognizing that conservatism may exist in the ISO formulation, this preliminary analysis illustrates that plating design pressures in the Polar Class rules may be appropriate. Semi-local pressures on areas greater than 1 m^2 are rather conservative.

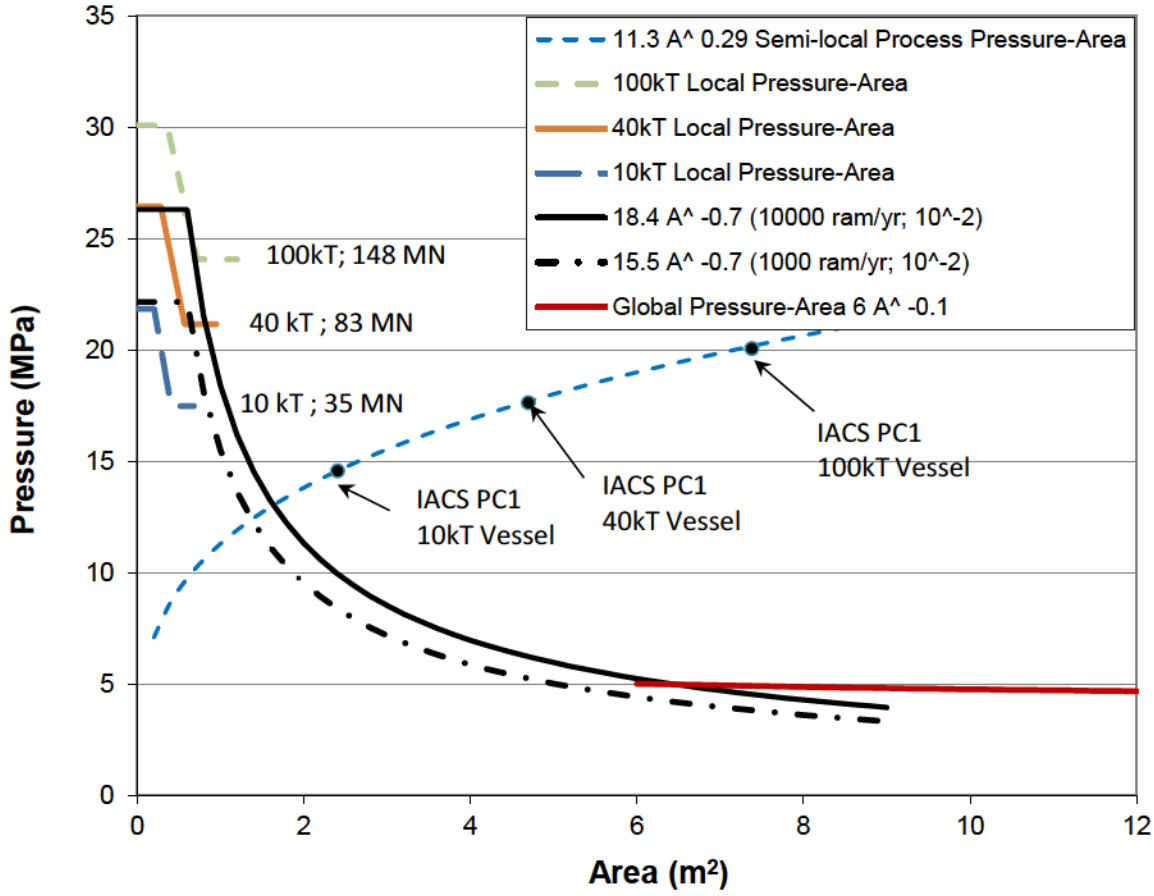

Figure 191 For shoulder impact model with contact 5 m from stem, comparison of ISO 10^{-2} exceedence, 10,000 ram local pressures on a 40 kTonne vessel with IACS Polar Class 1 local pressure-area predictions for 10, 40 and 100 kTonne vessels – note that IACS local pressure area effect is based on the height of the estimated load patch and frame spacing which, for a transverse framed structure is limited to a maximum span of 0.6m and for practical purposes greater than 0.3m.

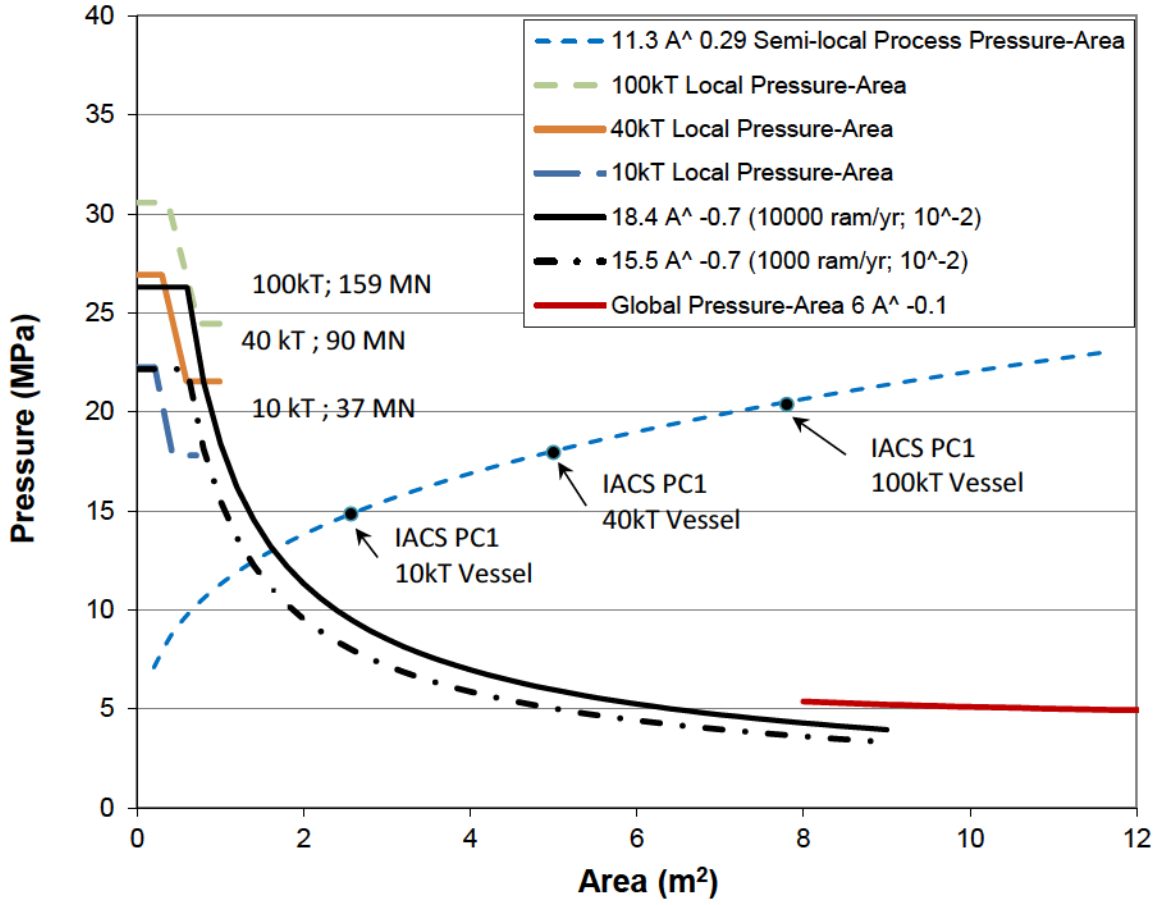

Figure 192 Pressure – area results for shoulder impact model with contact 15.9 m from stem, comparison of ISO 10^{-2} exceedence, 10,000 ram local pressures on a 40 kTonne vessel with IACS Polar Class 1 local pressure area predictions for 10, 40 and 100 kTonne vessels – note that IACS local pressure-area effect is based on the height of the estimated load patch and frame spacing which for a transverse framed structure, is limited to a maximum span of 0.6m and for practical purposes greater than 0.3m.

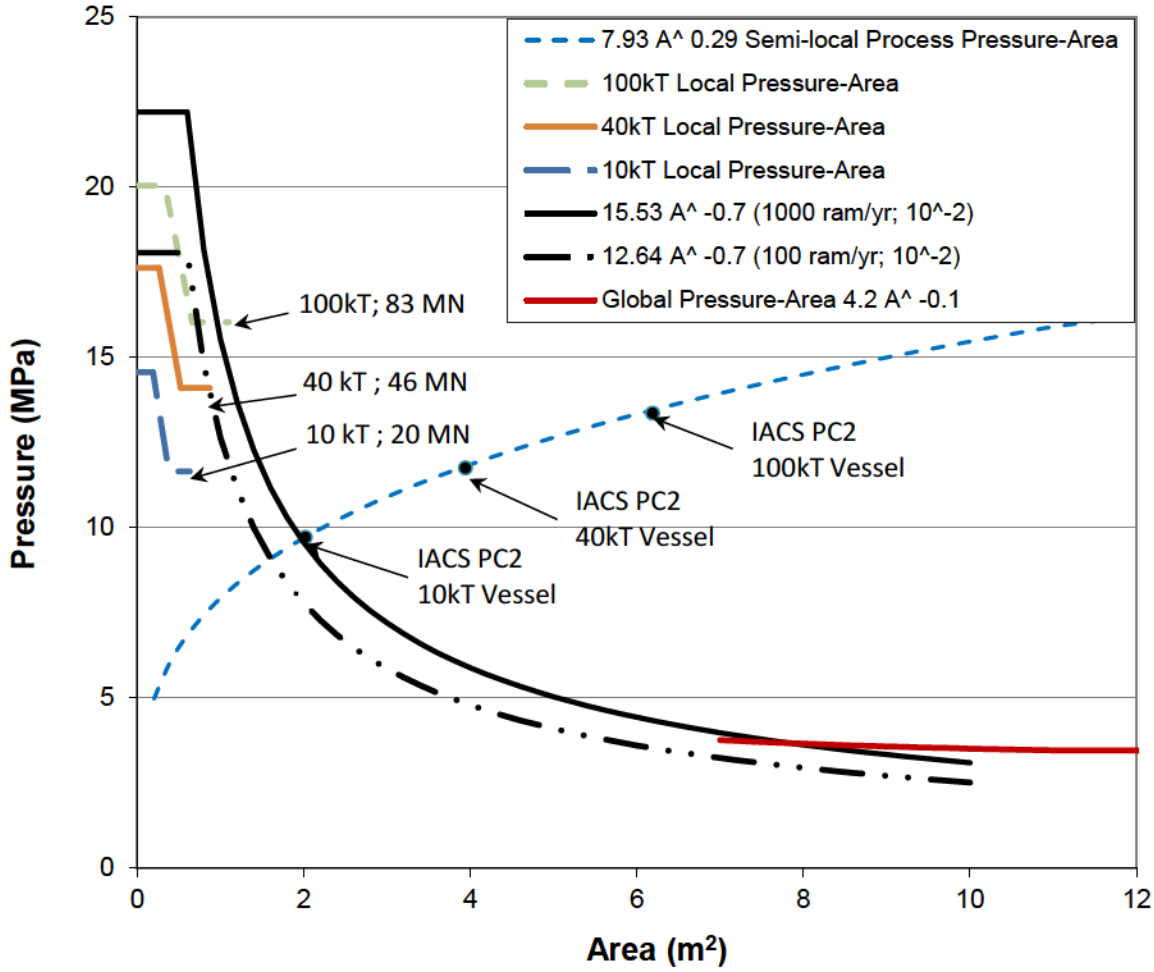

Figure 193 For shoulder geometry with contact reference 5 m from stem, comparison of ISO 10^{-2} exceedence, 1000 ram local 'bow' pressures on a 40 ktonne vessel with IACS Polar Class 2 local pressure-area predictions for 10, 40 and 100 kTonne vessels

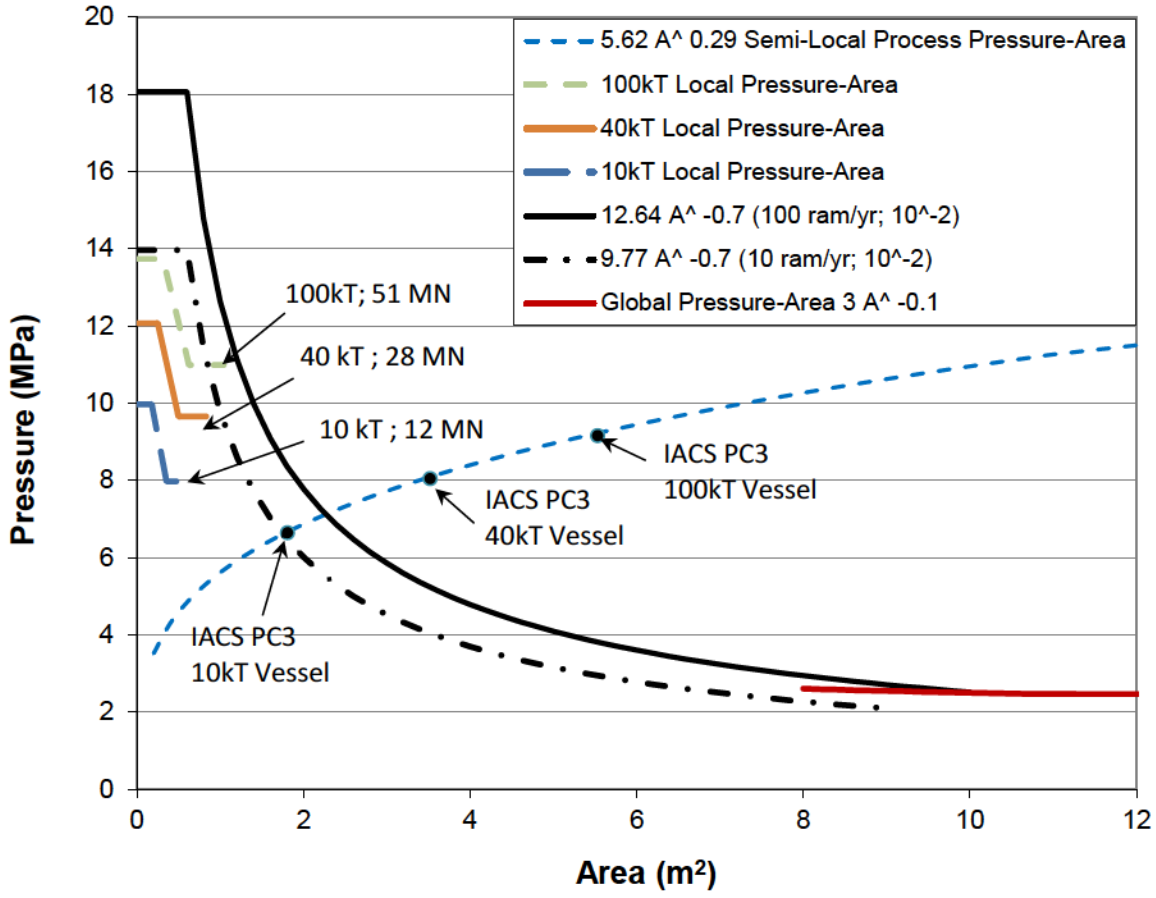

Figure 194 For shoulder geometry with contact reference 5 m from stem, comparison of ISO 10^{-2} exceedence, 100 ram local 'bow' pressures on a 40 ktonne vessel with IACS Polar Class 3 local pressure–area predictions for 10, 40 and 100 kTonne vessels

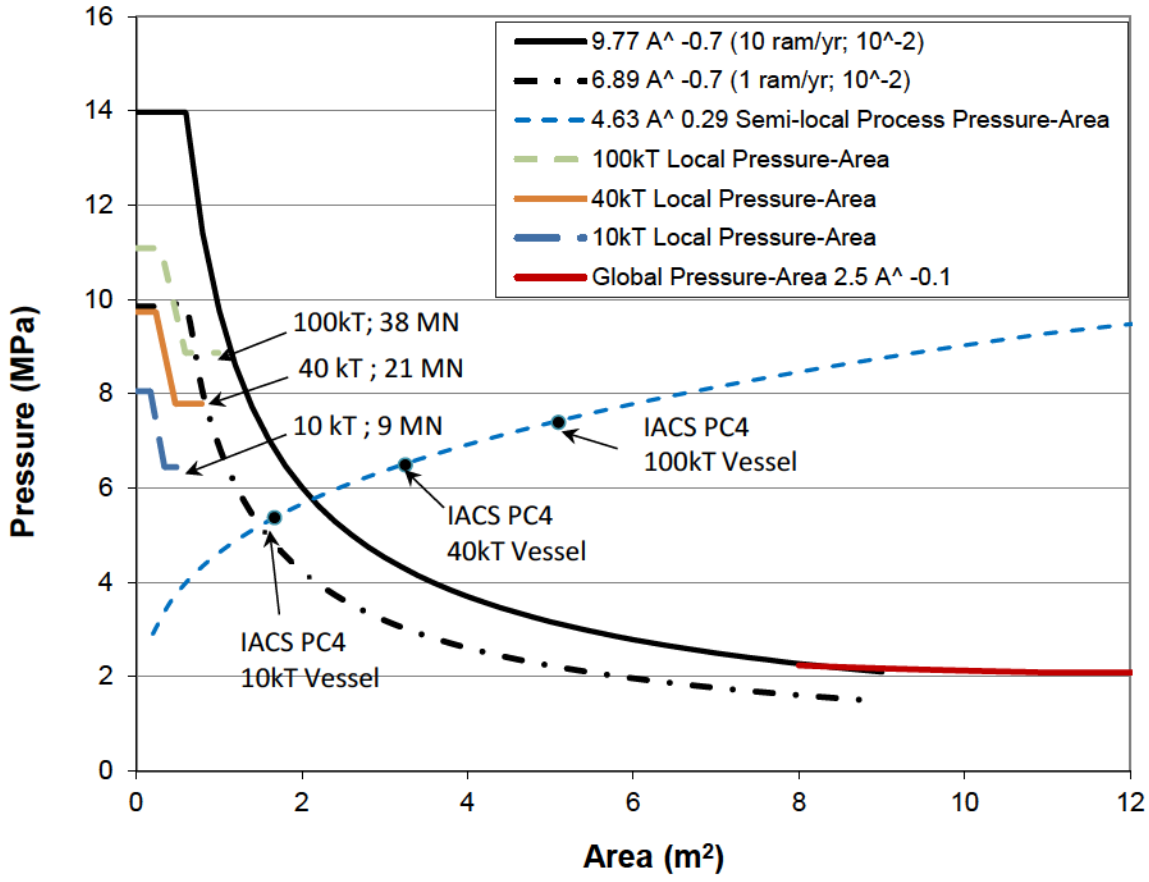

Figure 195 For shoulder geometry with contact reference 5 m from stem, comparison of ISO 10^{-2} exceedence, 10 ram local 'bow' pressures on a 40 kTonne vessel with IACS Polar Class 4 local pressure–area predictions for 10, 40 and 100 kTonne vessels

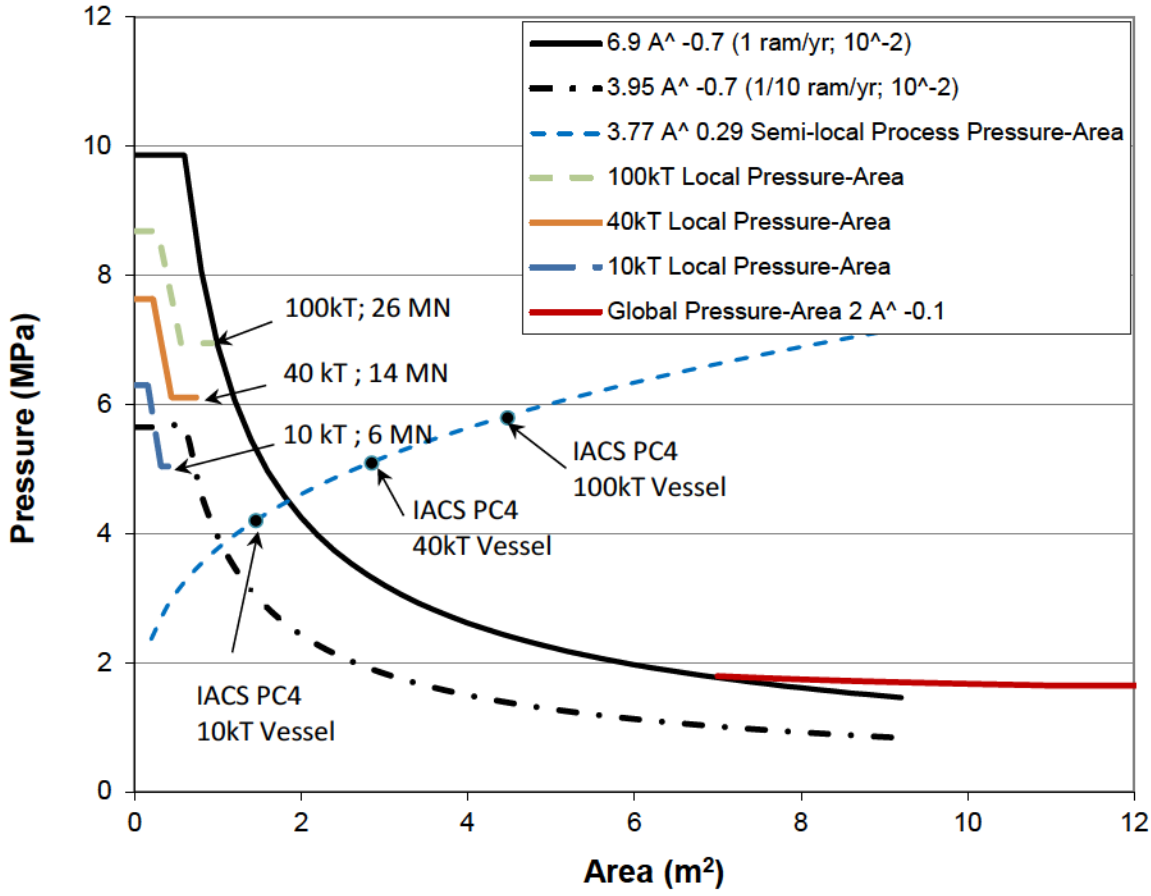

Figure 196 For shoulder geometry with contact reference 4 m from stem, comparison of ISO 10^{-2} exceedence, 10 ram local 'bow' pressures on a 40 kTonne vessel with IACS Polar Class 5 local pressure–area predictions for 10, 40 and 100 kTonne vessels

5.7 Preliminary Coefficient Verification Recommendations

5.7.1 Extremal Probabilistic Modeling

A reassessment of the Class coefficients that govern design forces and local pressures for plating design is discussed in this section. While global forces are ultimately governed by ice impact pressures, impact speed, vessel mass, added mass, and impact geometry, the verification approach is to adjust the key Class coefficients (*V*, *Po*) until global forces and local plating pressures are reasonably matched with extremal based estimates. Measured vertical bow forces as well as local design pressures are extrapolated from measured 'parent'

distributions using an extremal based methodology. Characteristic design values based on 10^{-2} annual exceedance probabilities are compared with corresponding polar class estimates.

As noted in Section 5.5.1, PC 1 was aligned with a rational estimate of an extreme number of loading events per year (i.e. 10,000), PC4 was aligned with 10 rams per year considering expert comments that the MV *Arctic*, a CAC4 vessel, would be expected to encounter on the order of 10-15 rams per year. PC6 was then aligned with the highest Baltic 1A Super Class which has been shown to be representative of a 1/10-1/5 year impact condition (Zou, 1996).

The approach is to ensure the IACS local pressure curve for a 40kT MV *Arctic* type vessel is between a range of ISO exposure ranges (e.g. For Polar Class 1, the IACS local pressures are between the 1000 and 10000 ram exposure based ISO curves; for Polar Class 2, IACS pressures are between the 1000 and 100 curves. Comparison is also made to 10kT and 100kT vessels having a similar bow geometry. For this exercise, the original Polar Class rule pressure area model is used.

5.7.2 Results

The results in Table 30 represent a first attempt to adjust of Polar Code coefficients *V* and *Po* to align estimated global vertical forces for the MV *Arctic* type vessel with extremal based estimates from measured MV *Arctic* impact trials.

Comparison of ISO based extremal local pressures with Polar Class local pressure estimates based on revised Class coefficients in Table 30 are illustrated in Figure 197 through Figure 202. Semi-local pressure are not illustrated here since they are not appropriate for shell plating design. Local pressure estimates are for a 40kT MV *Arctic* type vessel and corresponding impact duration and penetration. For comparison, Polar Class estimates of local pressure include comparison to 10 kT and 100kT vessels. While these figures represent local design pressures, for illustration, the global relationship associated with each Polar Class is plotted.

A remarkable alignment has been achieved between the modified Polar Class rule approach, the extremal ISO based local pressure model. Other global for data sets from different

vessels (varying mass, and bow geometry) including *Kigoriak*, *Manhattan*, and *Polar Sea* should be considered. It is noted that there has been no refinement to the ISO local pressure methodology to fine tune exposure. For instance, at some lower classes, it may be reasonable to incorporate some reduction in exposure based on detection and avoidance. Also, there is considerable uncertainty in parameters that ultimately govern the Polar Class estimates including: added mass, collision based inertial effects, opening angle of ice being contacted. But further research on these parameters is outside the thesis scope.

The power and attraction of the probabilistic based approach is that exposure and target reliability are specific criteria for characteristic design values. In the present illustrations, it is an annual 1/100 year return period (i.e. 10^{-2} annual exceedance probability). Depending on the limit state chosen for structural analysis (i.e. limited plasticity via yield line approach for plating in the Polar Class rules), the designer can now clearly understand the performance of his design. Two scenarios are particularly important: ELIE 10^{-2} design (limited plasticity in structure design); and ALIE 10^{-4} design loads (ultimate limit state).

Table 30 Revised Polar Class rule ice parameters and global force estimates

Polar Class	Number of impacts per year	Extremal Vertical Force (10^{-2})	Ice Strength P_0	Impact Speed Vs	Vertical Force from Revised Polar Class Rules
	N	(MN)	(MPa)	(m/s)	(MN)
1	10000	54	5.5	5.5	67
2	1000	46	4.5	4.75	49
3	100	39	4.0	4.0	40
4	10	31	3.25	3.25	28
5	1	24	2.5	2.5	18
6	1/5	16	1.75	2.0	11
7	1/10	11	1.5	1.5	8

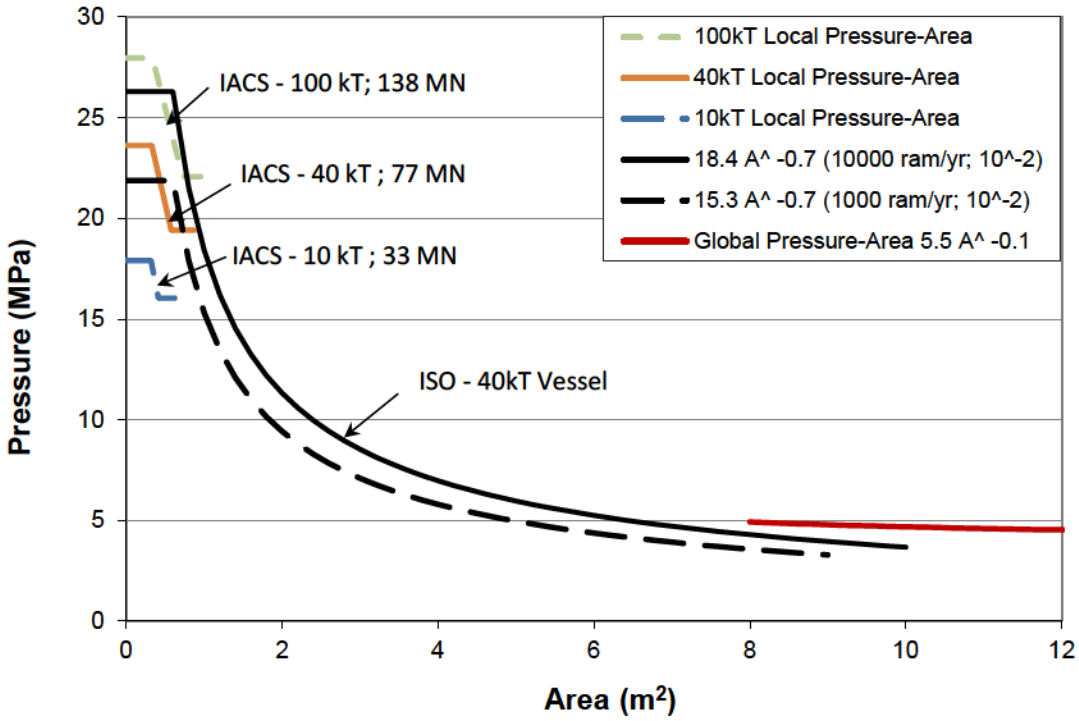

Figure 197 Local Pressures after *V* and *Po* adjustment for PC1 MV Arctic Type vessel

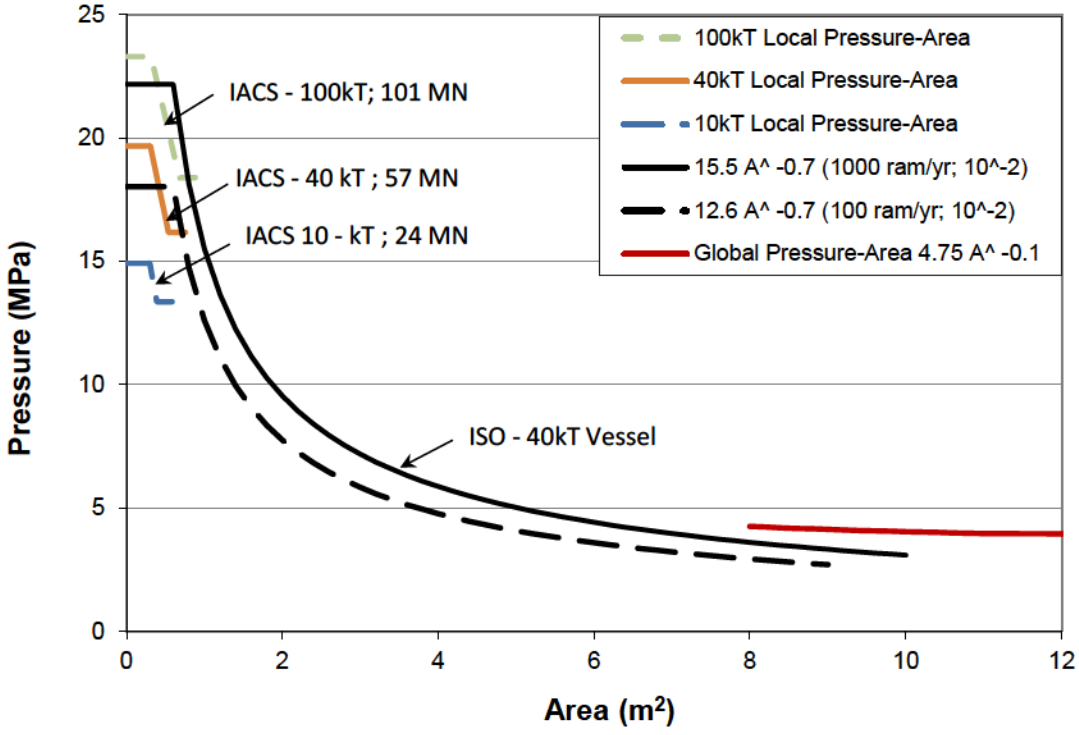

Figure 198 Local Pressures after *V* and *Po* adjustment for PC2 MV *Arctic* type vessel

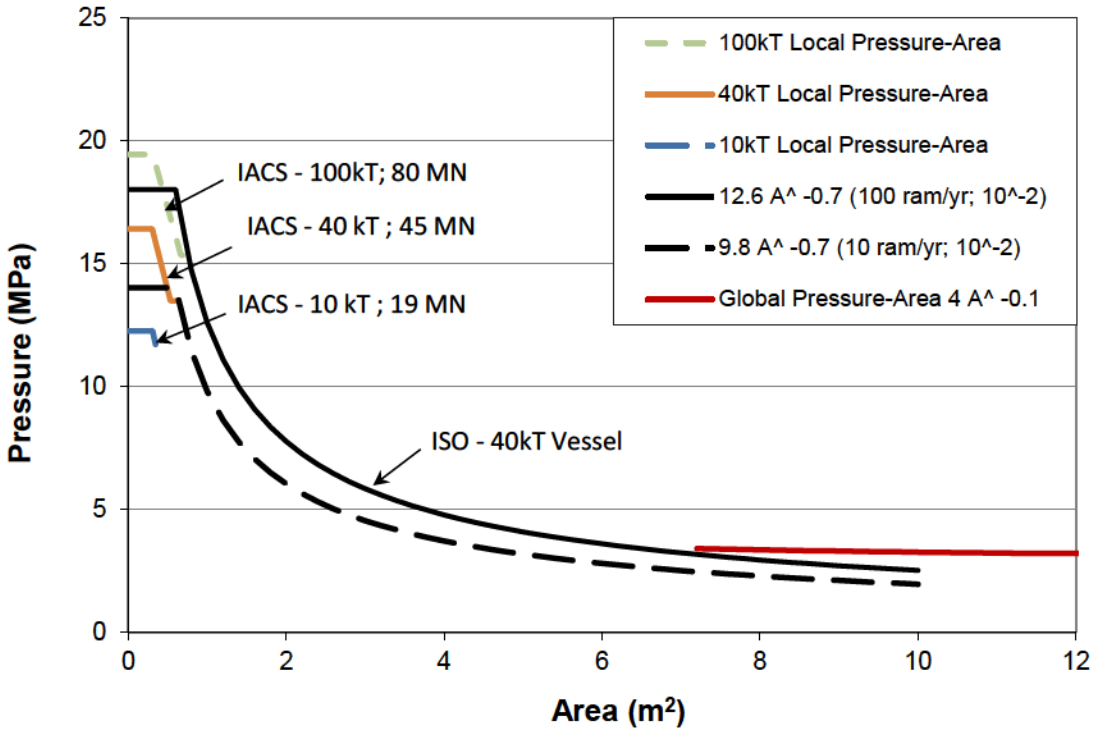

Figure 199 Local Pressures after *V* and *Po* adjustment for PC3 MV *Arctic* type vessel

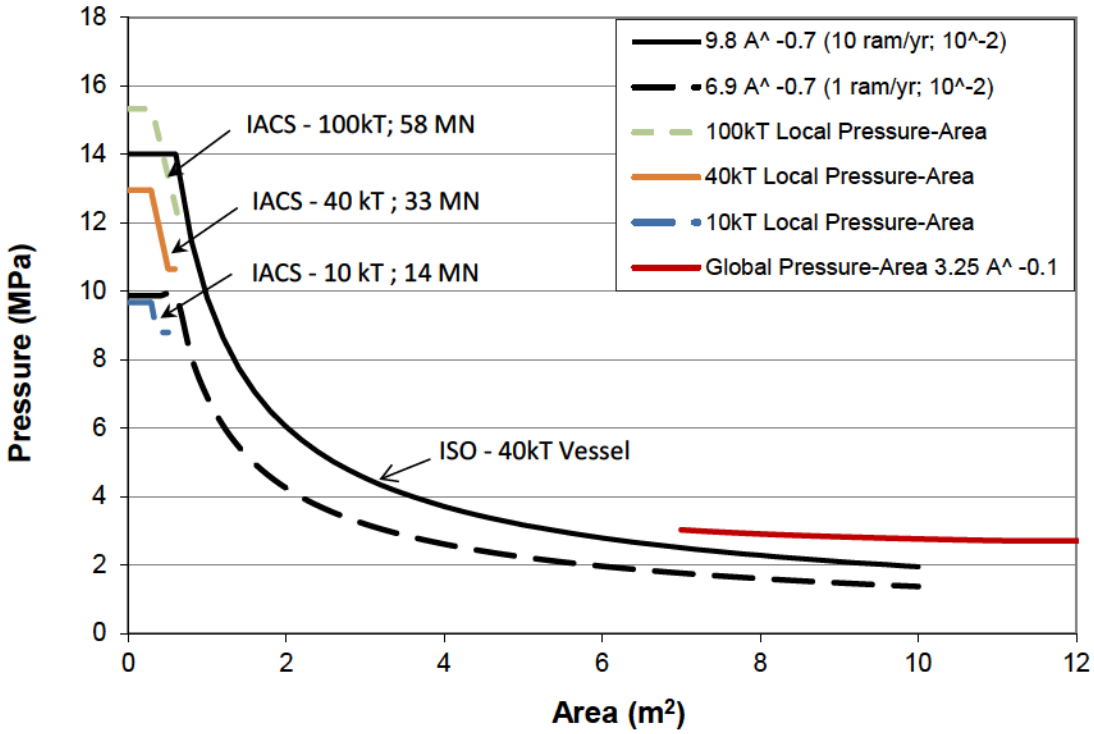

Figure 200 Local Pressures after *V* and *Po* adjustment for PC4 MV *Arctic* type vessel

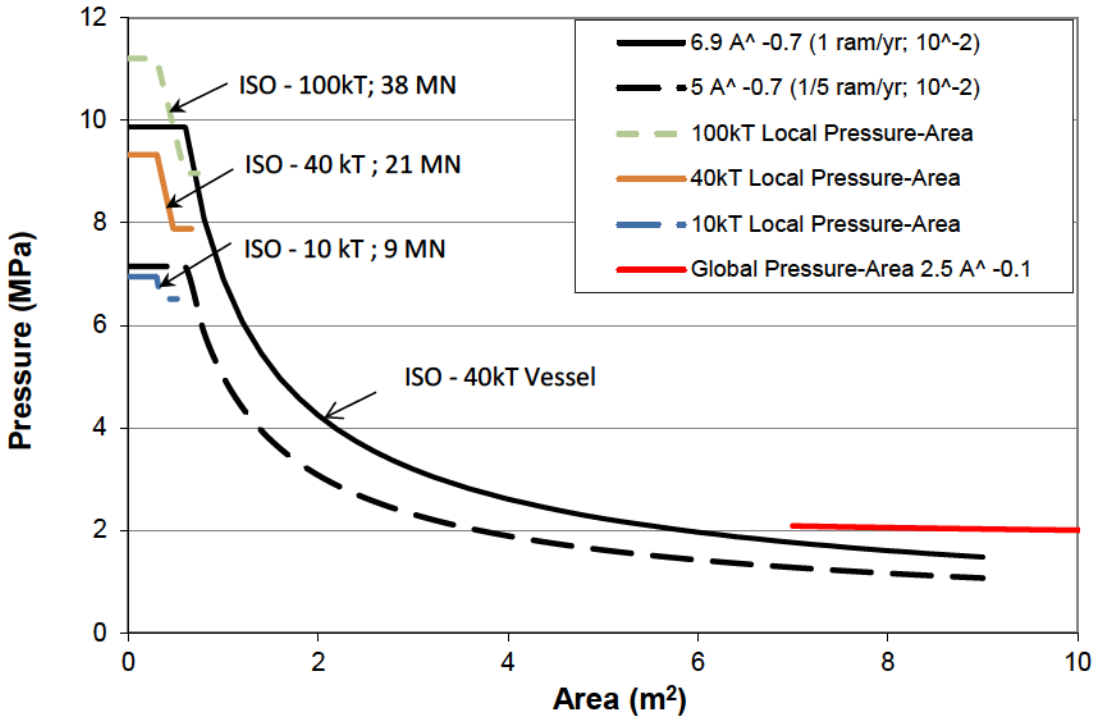

Figure 201 Local Pressures after *V* and *Po* adjustment for PC5 MV *Arctic* type vessel

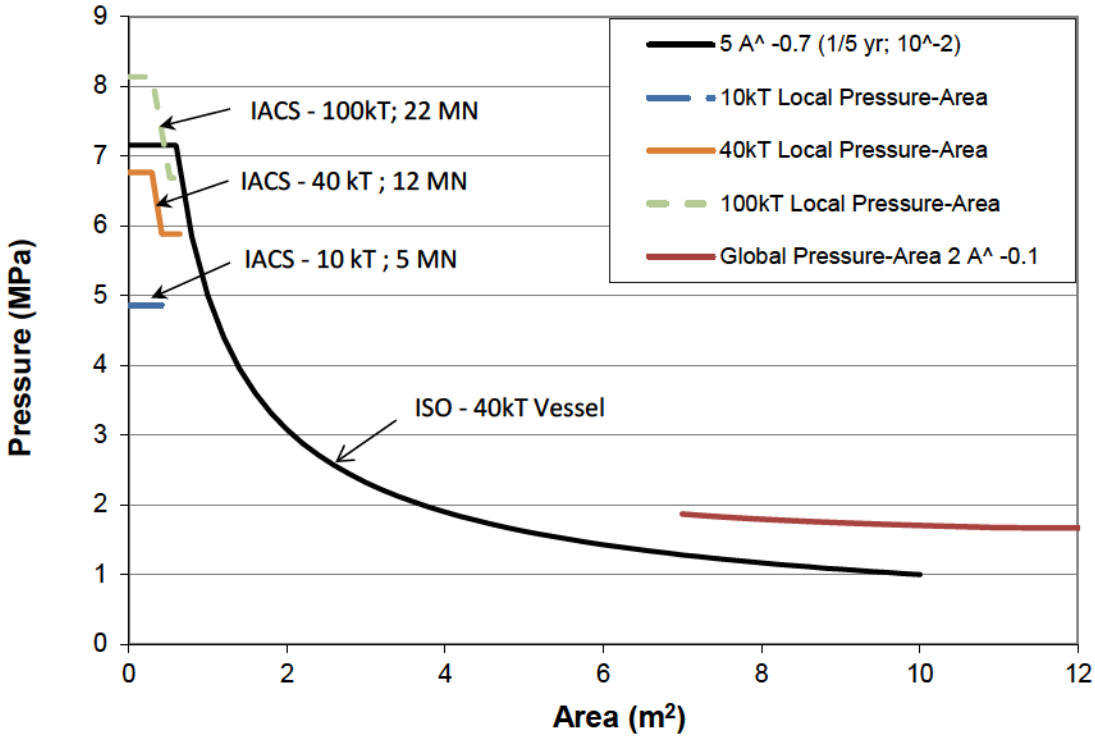

Figure 202 Local Pressures after *V* and *Po* adjustment for PC6 MV *Arctic* type vessel

5.8 Consideration for Icebreaker Design and Concentric Bow Impacts

Future versions of the Polar Code should consider icebreaker design. Changes required would be adjustment to the design approach that assumes captains will always avoid ice impact, as well as specific consideration for concentric bow geometry, as opposed to shoulder only impacts. Interaction geometry and models for different alternative scenarios are formulated in Daley (1999).

It is not entirely clear, however, that concentric bow impacts should be ignored even for conventional ship design. It has been illustrated previously that bow and shoulder impact loads are not dissimilar. While glancing impacts with blunt hull geometry may have steep force penetration curves, shoulder impacts have a reduced Popov equivalent mass that reduces impact force as eccentric impacts result in subsequent yaw motion. But the level of load resulting from shoulder impacts is based on an assumed ice angle of 150^{o} (see Figure 170). Loads are rather sensitive to this angle.

While the premise for this is that ship owners and captains will be motivated to avoid ice and any impacts will result from a maneuvering attempt, MY ice embedded in level ice is largely undetectable and impact can occur anywhere across the whole bow.
As a result, a designer would benefit from considering both.

It is also noted that ramming events should not be assumed to only occur with an icebreaker during ice management or escort operations. As referenced in Section 5.3.3.1 including experience on the MV *Arctic* and captain experience, there are times when delay in shipment of goods is not desirable, or risk of getting stuck exists and ramming may be required to transect ice. Enhancing the Code approach to allow a captain, with confidence in his vessel design, to ram through an ice ridge to ensure product delivery, or to ensure the safety of his vessel and crew, is very attractive.

CHAPTER 6. Illustrative Design Examples

6.1 Arctic Shipping Type Illustration

6.1.1 Overview

A hypothetical scenario is provided to illustrate the methodology (See Figure 203). Year-round shipping is required along a route that passes through a region frequented with MY ice floes. The average concentration of MY ice is assumed to be 0.02%. The mean floe diameter is assumed to be 0.25 km with an average area of 0.15 km^2 (note that these would be obtained from actual distributions). A 40,000 tonne displacement vessel is assumed to have a length of 200 m and a breath of 23 m.

6.1.2 Collision Frequency

For design, the number of expected collisions each year is needed. The length of Route A through the region is ~1500 km. The average annual density along the route is estimated at 0.02% / 0.15 = 1.33×10^{-3} per km^2. (or 13.3 per 100×100km) A 21 day turnaround is assumed for shipping requirements which results in approximately 16 round trips per season, or 32 transects each year.

The expected number of collisions within a given area (e.g. km^2) is illustrated in Figure 204 where

$$n = \rho \times \frac{d \times (Ws + L)}{A} \times p_{avoidance} \qquad (87)$$

where ρ is the floe density, d is the length of the route through a specific region, Ws is the ship breadth, L is the mean floe diameter, and A is the regional area (e.g. km^2). Here it is

assumed that ice movement relative to vessel speed is negligible. Sanderson (1988) provides a good summary for exercising this calculation.

Similarly, the density of iceberg fragments (i.e. bergy bits and growlers embedded in pack ice) within a particular region can be used to estimate the expected number of encounters. Note that reference is made to undetected small iceberg fragments only and not collisions with the full iceberg population. It is assumed the ship would have a strategy and systems for detection and avoidance of large ice masses.

Using Eq. (87) and Figure 204, the expected annual number of interactions is 21.8.

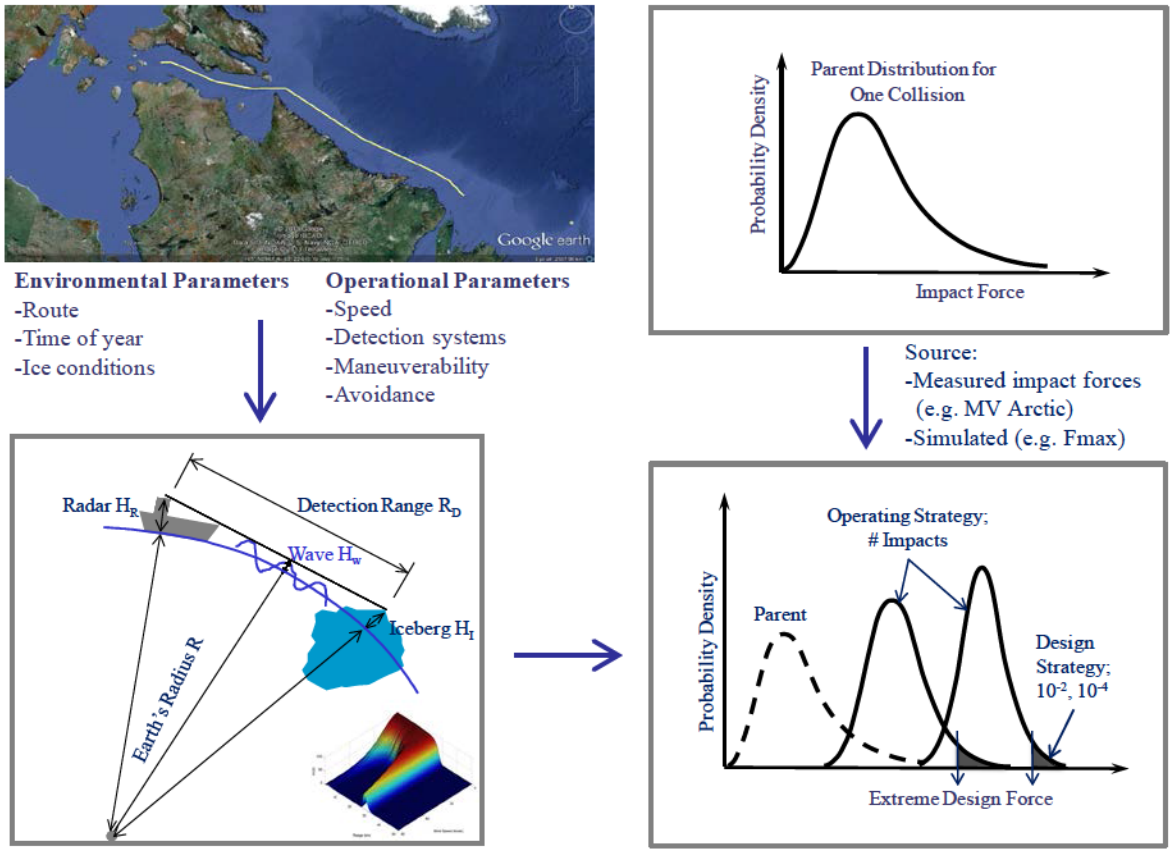

† bottom left block represents bergy bit iceberg detection and avoidance in open water; alternative systems would be utilized for multi-year ice features

Figure 203 Design strategy and application.

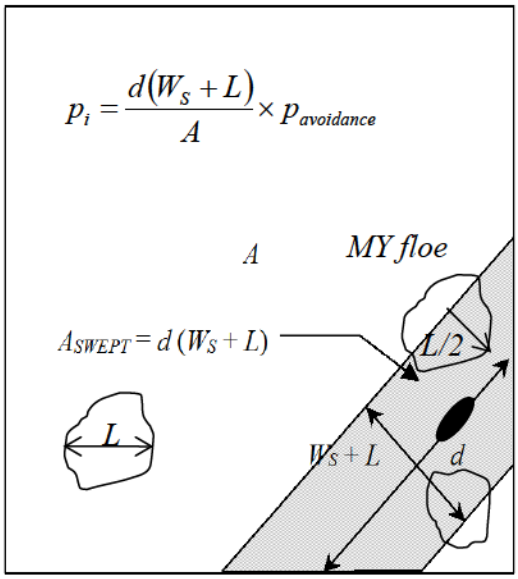

Figure 204 Illustration of ship ice floe encounter probability.

6.1.3 Global Force Estimation

For simplicity, extreme impact forces are estimated using the 'parent' distribution of MV *Arctic* measured forces. An exponential tail fit to the 'parent' data is illustrated in Figure 190. An alternative distribution could be provided using a ship-ice interaction model. The number of annual interactions can be modeled using a Poisson process for a mean of 21.8 impacts per year and design forces estimated using Eq. (86). The global design force corresponding to a 100 yr (or 10^{-2} annual exceedence probability) design strategy is 33.4 MN (see Figure 205). If an avoidance strategy could reduce impacts by 50%, the corresponding design force is 30.6 MN as shown Figure 206.

Mitigation strategies could be detection and avoidance, rerouting based on ice condition charts, or suspended shipping until exceedence conditions subside – the latter two resulting in increased route length and delay in delivery, or reduced number of shipments of cargo per year. The capital cost of increased steel for increased design load is weighed against the cost of delay in shipping, or reduced volume of cargo shipped.

6.1.4 Local Pressures

To estimate local pressures for plating design, impact penetration and duration is estimated from the global ram analysis based on vessel displacement, speed, bow shape and ice strength and thickness. For illustration here, the average impact duration based on average penetration, is t ~3 seconds. The proportion of true hits r on the design area is assumed to be 0.5. With 21.8 ram events per year along route A, the exposure is estimated as

$$\mu = 21.8 \cdot 0.5 \cdot \frac{3}{0.7} = 46.7$$

The corresponding design pressure for a 10^{-2} target exceedence probability, α, μ, and x_0 is given as

$$\begin{aligned} z_{0.01} &= x_0 + \alpha\left[-\ln\left(-\ln F_Z(z_e)\right) + \ln \mu\right] \\ &= x_0 + \alpha\left[4.6 + \ln 46.7\right] \\ &= x_0 + \alpha\left[8.4\right] \end{aligned}$$

Using $\alpha = 1.25A^{-0.7}$ and assuming $x_0 = 0$, the design pressure area design curve is $P = 10.5A^{-0.7}$ (see Figure 207). The pressure on a 2 m^2 panel is estimated to be 6.5MPa. The design pressure corresponding to a 50% reduction in number of impacts would be $P = 9.7A^{-0.7}$.

6.1.5 Classification

For this illustrative example, given the expected exposure corresponding to annual impacts with MY ice along the specified route, and the classification recommendations given in Section 5.7 and Table 30, this vessel would require at a minimum, a Polar Class 4 designation.

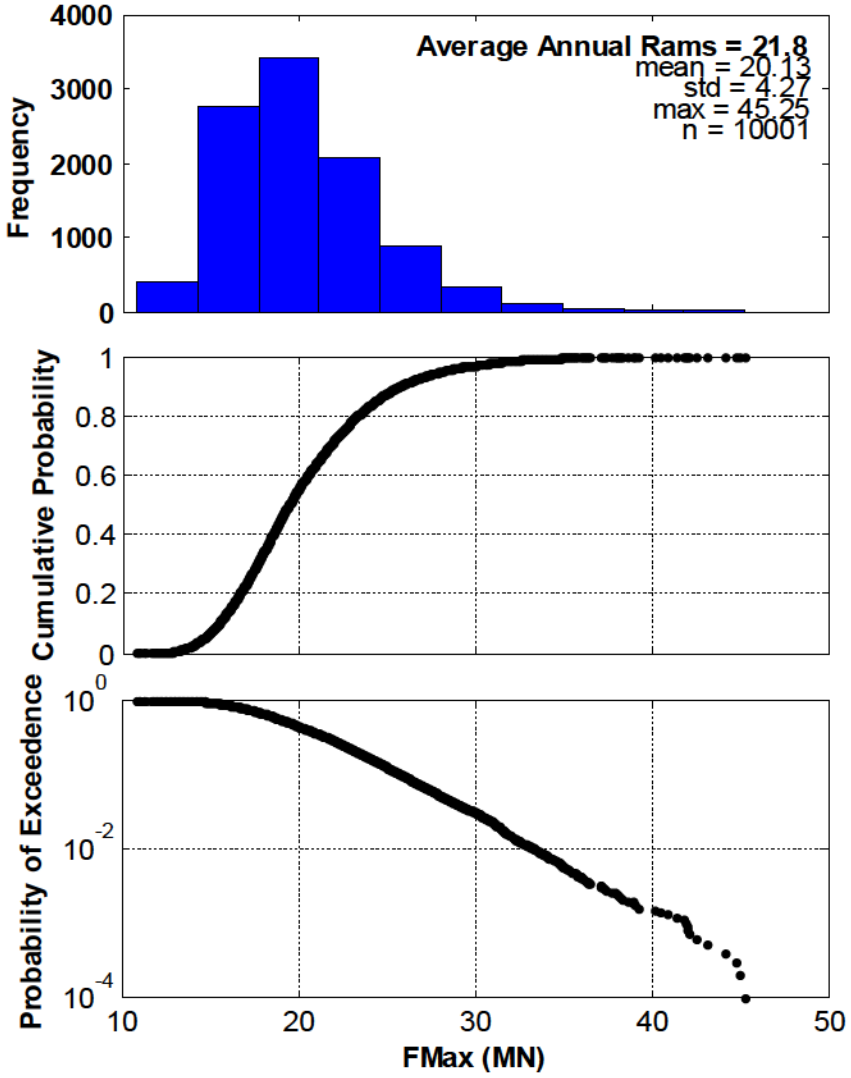

Figure 205 Simulated global impact forces along Route A based on 21.8 impacts per year using 'parent' distribution measured MV *Arctic* ram forces.

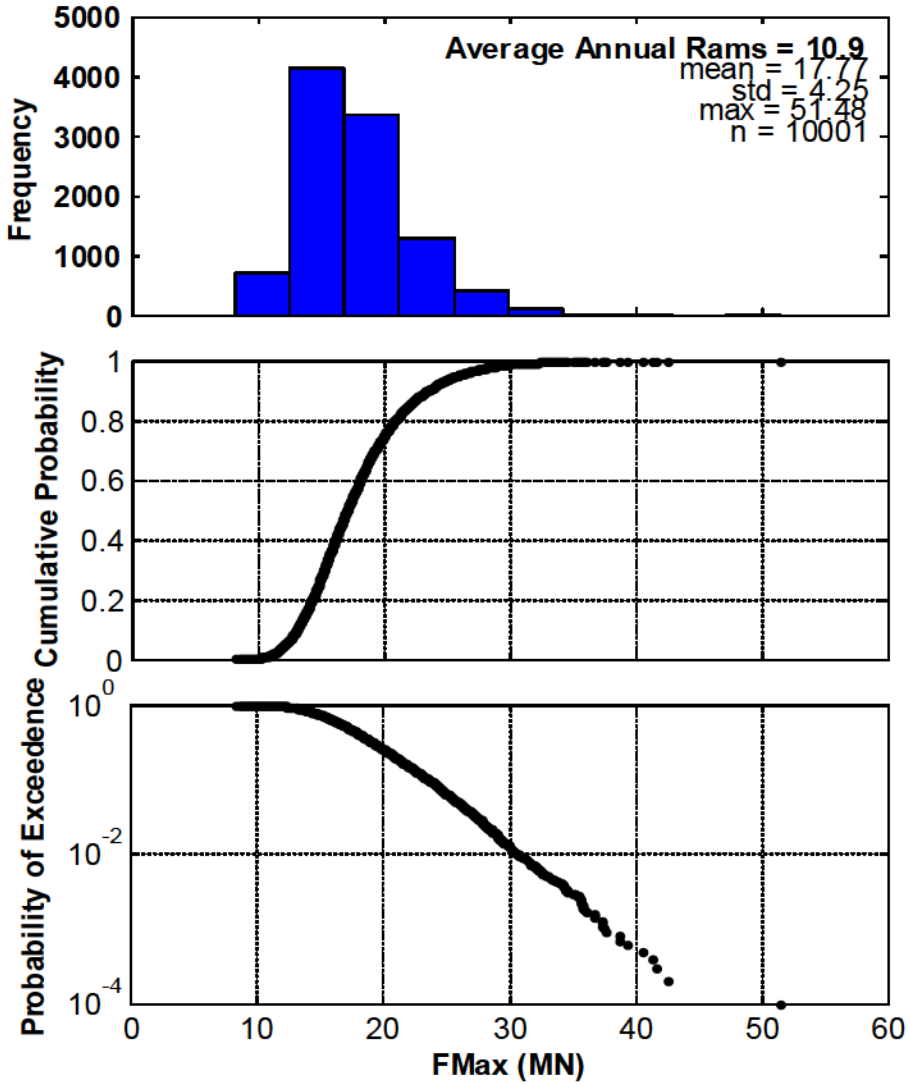

Figure 206 Simulated global impact forces along Route A corresponding to 50% collision avoidance.

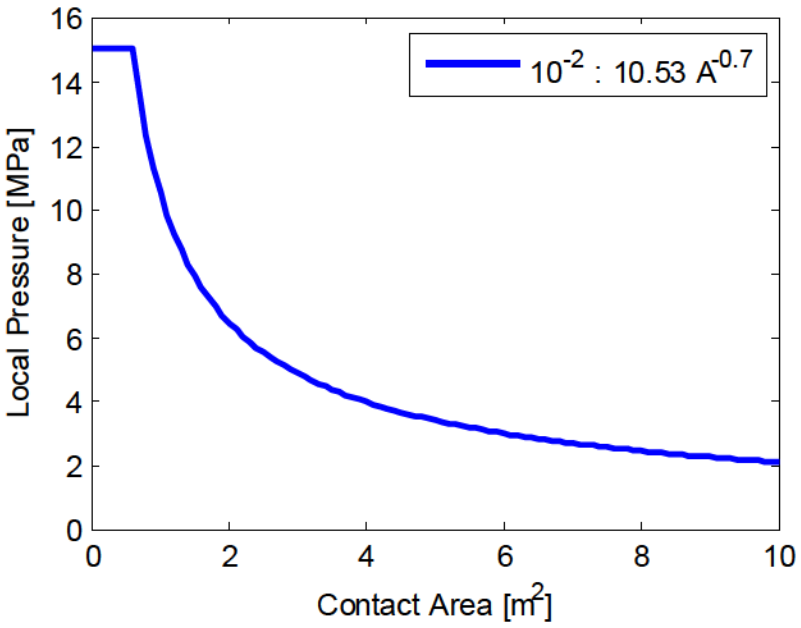

Figure 207 Local pressure design curve for route A.

CHAPTER 7. Thesis Summary

Ice is a complex material that exhibits different failure properties depending on the loading rate. As with other fracturing materials, scale effect is evident with strength decreasing with increased contact area. Further, the scale effect for local pressures within the global interaction area is different and considerably more demanding than the global relationship. Research to model and understand the relationship between local high pressure zone processes and global processes, and to demonstrate best practices for design, is the focus of this PhD thesis. Specifically, this thesis covers:

- an application of a probabilistic methodology showing the importance of exposure in modeling global design forces and local designs pressures;
- an understanding of local and global ice contact areas, corresponding pressures and their importance for design;
- a comprehensive review of the mechanics of ice structure interaction relevant to ship design, including experimental data and relationships that model ice pressures on respective contact areas and corresponding scale effects;
- a probabilistic methodology for modeling local design pressures based on maximum pressures on any subpanel area through the ram duration and the derivation of parameters α and x_0 representing an exponential distribution fit to the tails of measured local pressure distributions;
- an overview of probabilistic *HPZ* occurrence model that considers *HPZ* density and *HPZ* forces and extending the analysis to process *Polar Sea* data from Beaufort 1982, North Chukchi 1983, South Chukchi 1983, and Beaufort 1984 trials;
- the development of a new probabilistic *HPZ* model that considers the rate of *HPZ* occurrence through the ram duration in addition to density and force and correlates *HPZ* formation rate to vessel impact speed;

- a review of Polar Class rules for hull plating design with emphasis on the importance of exposure in design requirements including the illustration of an alternative approach that models exposure explicitly in rule derivations;
- an overview of extremal based probabilistic methodology for design including review of ASPPR proposals and consideration of annual exposure in design forces for different arctic Class vessels;
- a preliminary verification of Polar Class coefficients that govern design forces using the extremal based design methodology referenced in a review of the ASPPR proposals, modeling annual exposure (i.e. number of expected rams per year) with each Polar Class and estimating local design pressures; and
- the illustration of a probabilistic model for ship design, including global impact forces and local shell plating design pressures; model that considers the occurrence of extreme ice features, contact probability and influence of risk mitigation on design loads.

These are discussed in more detail below.

For design, global forces are governed by average pressures over a nominal contact area represented by the imprint of the hull into the ice sheet or iceberg, without correction for free surface spalling effects. The maximum global force will generally occur at the end of a ram or point corresponding to the maximum nominal contact area. The nominal contact area will grow monotonically, but due to the random occurrence of natural flaws in the ice, pressures will vary as fractures occur, continually changing the contact face. Scale effect exists such that pressures on larger contact areas, including zones of low and zero pressure average out to be smaller.

Local design pressures are associated with actual zones of contact with the structure, through which most of the force is transmitted into the structure. These *HPZ*s induce very high stresses in the ice that enhance fracture process at macro and micro levels. Fractures and spalls non-simultaneously reshape of the contact zone resulting in concentrated forces on reduced contact areas. A scale effect exists such that the smallest panel area will see the highest pressures but with increasing panel area the highest localized pressures are averaged with adjacent lower pressures such that pressure on the larger panel area is reduced.

Conversely, local pressures within the nominal contact area increases for reduced contact areas. This is expected since confinement will suppress damage and fracture effects. But a limit force exists such that confining stress will result in recrystalization of the ice and subsequent material damage softening. Unlike global pressures where the maximum force occurs at the end of a ram, maximum design local pressures may occur at any point through the ram duration. For design, we are interested in the maximum pressure on individual panels through the interaction duration.

A comprehensive review of ice mechanics was carried out to study the behavior of ice relatively fast loading conditions (i.e. ship rams) and to verify the pressure area scale effects at local and global levels. The review included: compilation of pressure-area data by Sanderson (1988) and Masterson *et al.*, (2007); experimental data sets from ship ram trials, and small scale experiments; geometric and similitude models following dimensional laws; statistical theories; and numerical models. Both experimental data and numerical models demonstrate clearly scale effect, although uncertainty exists. Under the fast loading rates of interest, ice behaves as a brittle fracturing material which theoretically models a scale effect. The scale effect on local pressures have been modeled to be as high as $P \propto A^{-0.8}$ with strong evidence that $P \propto A^{-0.7}$. For global processes that consider averaging of local pressure over some nominal contact area, the scale effect has been suggested to be as low as $P \propto A^{-0.25}$ but $P \propto A^{-0.4}$ and $A^{-0.5}$ seems most reasonable.

Extensive analysis of local pressure modeling has been carried out using several ship ram data sets. The approach is to model peak local pressures on subpanel areas through the entire ram duration. For design, we are interested in the maximum pressure on a single subpanel through a ram duration for the maximum ram event in a year. Results illustrate a local pressure area scale effect that is proportional to $A^{-0.7}$. A probabilistic approach to local design models the fitting of an exponential distribution to the tails of ranked measured pressures and averaged over different panel areas. Increased exposure (i.e. number of rams and duration) leads to increased pressures on any local area. This approach is directly consistent with fundamental mechanical properties of a fracturing material as well as the laws of probability. Exposure increases with increased penetration and increased number of impacts thereby increasing local design pressures.

An alternative process pressure area model developed using the *Polar Sea* data suggests an inverse pressure area scale effect with pressures increasing with increasing area. The intent is to model increasing pressures locally with increasing global interaction area. Unfortunately, justification for this model suggests that there is no basis for pressures to fall for increasing contact areas, referencing the influence of confinement and suppression of fracture events. This suggests that *HPZ*s do not fail if sufficient confinement exists. However, the high stress state associated with an *HPZ* enhances crack growth and fracture. Also, *HPZs* have a limiting force such that confining pressures will cause microstructural damage (i.e. recrystallization) which softens the ice. When exposure is considered, this modeling does not need to suggest that traditional scale effects are flawed and that the mechanics of a fracturing material are incorrectly modeled. Increased global interaction area results from faster and larger displacement vessels penetrating further, the result being increased exposure on local panels within some global interaction area. There may be some limited confinement during interactions, but with the geometry and interaction configurations of practical relevance, including the free surface effects, the ice will fail and scale effects exits.

An alternative local pressure methodology exists that was formulated using ship ram measurements from *Louis S. St. Laurent* trials. Local pressures are based on the density of *HPZs* corresponding *HPZ* forces within a local area. Similar to the local pressure methodology, *HPZ* forces are modeled using an exponential fit to the tail of a measured and ranked force distribution. The density is based on the number of *HPZ*s at a point of peak pressure through a ram within the instrumentation area. For simulation, a Monte Carlo process is used where the occurrence of *HPZ*s is assumed to follow a Poisson process. For design, local panel pressure is based on the sum of n simulated *HPZ* forces averaged over a design area. This methodology has been extended in this thesis to model *HPZ* parameters from the *Polar Sea* measurements (i.e. Beaufort 1982, North Chukchi 1983, South Chukchi 1983, and Beaufort 1984) and verified by comparing simulated local pressure parameters to measured parameters. Remarkable consistency is observed.

An new improved model for *HPZ* occurrence has been developed in this thesis that considers the *HPZ* formation rate through the ram duration. Rate has been correlated to impact speed

and with duration, *HPZ* occurrence through the ram duration can be modeled. This way, impacts with larger vessels and higher speeds have increased duration and will hence encounter an increased number of *HPZs* through a ram. The greater the number of *HPZs* formed, the greater the probability of a higher *HPZ* force and corresponding local panel pressure. This model was verified by comparing local pressure parameters α and x_0 derived for both simulated and measured data and rather reasonable consistency was observed. Based on *HPZ* density, *HPZ* force, vessel impact conditions (mass, impact speed, and corresponding duration) and ice strength, local pressure parameters α and x_0 for a 'parent' distribution of local pressures for a specific vessel can be estimated. The model in time is an important new development. Interaction speed and duration can now be used to estimate the occurrence of *HPZ*s in time as opposed to scaling exposure proportional to *Kigoriak* mean duration (current ISO approach). This is important for modeling different vessels with different masses, and operational speeds. Rates will also vary along the vessel being greater on the bow, least from mid-body to stern. For fixed structure design against iceberg impacts, rate and duration based on iceberg size, shape and drift speed can be used to model exposure in time. Extending this model to include spalling effects will allow the simulation of time varying global forces through ice structure interaction events. This is a big step forward for modeling floaters in ice including compliance effects, global mooring forces and subsequent local pressures for hull plating design.

This analysis did not specifically address why ice strength varies from one region to another (i.e. that lower pressures occur in more southerly regions). This trend is captured in the α parameters derived for each data set. Opportunity exists to study ice properties in more detail to understand whether salinity and temperature can explain the variability in pressures on the same ship from region to region.

A preliminary review of the IACS Polar Class rules has highlighted significant differences in design pressures compared with CSA, ISO and API codes. The approach to design in the Polar Class rules is to first estimate the global contact force and corresponding nominal contact area, and then estimate a semi-local contact area based on area losses due to fracture and spalling. A two dimensional (2D) brittle flaking model was used to estimate the proportion of local area to global - which on average is estimated to be on the order of 25-

30%. Forces through this reduced semi-local area result in higher pressures that are very high compared with other codes. Further localization is considered recognizing that pressures on smaller areas can significantly increase. Local pressures on plating between main frames are scaled higher using peak pressure factors. The final local pressure and contact area used for plating design is based on some reduced height of the contact ice feature, and frame span. To initially estimate the global contact area, a global pressure area model consistent with $P = Cp\ A^{-Dp}$ is used except that unlike conventional models that capture scale effect with Dp = -0.4, the Polar Class rules only model a minimal scale effect with Dp = -0.1. The final design equation for semi local contact area models a pressure area effect with pressure increasing with increasing contact area and a scale effect proportional to $A^{+0.3}$. The intent of this empirical equation is to model the effect that with higher energy collisions from larger ships moving faster, pressures locally will increase. In probabilistic extremal analysis, this trend is entirely consistent with exposure modeling. The resultant trend in design is reasonable - increased pressures for larger vessels moving faster.

A challenge with the existing formulations is that if one was to introduce the conventional global pressure area scale effect, the exposure based trend is lost. Modeling Dp = -0.4 in the rule formulations results in a decreasing in local pressure with increasing ship displacement. Exposure needs to be considered. As a comparison, the rule formulation was remodeled considering conventional pressure area scale effect. Also, the reduction in contact area from nominal to local was modeled using the *HPZ* model developed in this thesis. Local pressures are less than 10% of the nominal contact area. Using the F_{MAX} software (a dynamic time-step ship ice structure interaction software developed during the review of the ASPPR proposals), a model for exposure based on impact duration was developed as a function of vessel size and impact speed and correlated to a peak pressure factor. The results were entirely consistent with the design trend in the original formulation of the rules, with local design pressures increasing with increasing vessel displacement.

A preliminary verification of Polar Class coefficients that govern design forces was carried out. The probabilistic extremal based design methodology originally developed for the review of the ASPPR proposal revisions was adopted. Annual exposure, the number of expected rams per year, was mapped with each Polar Class and local design pressures for

shell plating design estimated and compared with rule recommendations. The assignment of annual rams corresponded to 10,000, 1000, 100, etc., for Polar Classes 1 through 7 respectively. Polar Class rule requirements for local plating based on design pressures for different size vessels of different classes compare reasonably well to the ISO local pressure requirements. Recommendations on adjustment to certain class coefficients are suggested where Polar Class 1 requirements may be reduced and lower Polar Classes increased. This assumes that the vessel will encounter MY or glacial ice during its life. While the current version of the Polar Code models large forces particularly for the higher classes, it does consider some structural plasticity, modeling hinge formation in plating collapse. For ultimate limit state conditions, this limited plasticity will be conservative and opportunity to consider membrane effects exists. While local peak design pressures for shell plating design may be reasonable, semi-local pressures are excessive.

A probabilistic methodology for design should be considered in the rules, not to replace but to enhance the current formulations. An example illustration of a design based on an arctic shipping route, ice conditions, design strategy, risk mitigation via detection and avoidance and resultant local pressures for structural design (i.e. plating) is provided. Reliability targets are used to estimate design loads that coincide with a particular structural design limit state. For example, high frequency low level events corresponding to on the order of 1/10 year exceedance would correspond to elastic design. Extreme Level Ice Events (ELIE) corresponding to a 1/100, 10^{-2} annual exceedence probability would correspond to some ultimate limit state (ULS) where limited plasticity would be considered in the design (e.g. hinge formation or some allowable permanent set). Abnormal-Level Ice Events (ALIE) corresponding to 1/10,000 year, 10^{-4} annual exceedence probability would consider an Abnormal Limit State (ALS) modeling substantial plastic deformation without catastrophic loss. To illustrate, the exceedance probability for a PC1 vessel designed for 10,000 maximum events in a year would be 10^{-8}. While rather rare, the design is reasonable given that the corresponding structural limit state would be ALS with membrane effects modeled. A probabilistic methodology for design of ships based on the principles of safety and consequences is important and necessary both for design and safety validation. Such approaches for the shipping industry are appropriate and should be considered.

CHAPTER 8. Recommendations for Future Work

A new *HPZ* rate model, similating *HPZ* occurrence spatially and in time, is developed for modeling local pressures including a correlation between rate and initial impact speed. This model can now be used to model pressures on different parts of the structure since interaction rate will vary from bow to stern. For floaters in ice, change in drift direction can be also studied. Further, the influence of random occurrence of localized *HPZ*s across a structure and the potential for localized stress concentrations can be studied.

While the *HPZ* rate model development to date is most applicable for local pressure design, given that global force is the sum *n HPZ* forces at any instant in time, the *HPZ* rate model can be extended to model a time history of global forces. Consideration would be given next to spalling processes and loss of contact area towards the outer perimeter of the nominal contact area to refine *HPZ* density estimates across the full global face. This global *HPZ* model would be rather useful in modeling the dynamics associated with compliant systems such as drillships or moored floaters giving a better estimate of global mooring forces and hull pressures for plating design. The influence on subsequent vessel classification requirements will add tremendous value as industry endeavers to be more efficient with arctic exploration and development.

It has been shown that the *HPZ* force parameter is highly correlated to the constant in the alpha (α) vs area relationship defined for local pressure modelling in the Jordaan *et al.*, (2007) and Taylor *et al.*, (2009) work. A relationship was not developed for this thesis but should be studied. Estimating the *HPZ* force based on this local pressure analysis methodology is considerably more effieicent and should be explored. Further, understanding how salinity and temperature influence the variability in pressures from region to region should be explored.

While it has been shown that larger impacts have the greatest exposure, contact area and subseqently highest pressures locally, collection of full scale data, with instrumentation to measure local pressures across the full global contact area would add great value. While it is intuitive that global pressure is the sum of *n HPZ* forces aeveraged over the nominal contact, the *HPZ* density relative to the nominal contact area may be different than the density specific to local regions. Experimentally this could be verified using a large scale ice impact experiment measuring local pressures at 0.1-0.2 m^2 level and global contact areas up to 75-150 m^2. This could be achieved using a vessel, or a purpose build floating structure to ram large ice features, or by directing icebergs or MY ice into a fixed structure. A further extension of this work would be model the same processes using compliant structures (i.e. floaters in ice) to measured global mooring (or dynamic positioning) forces, and local hull pressures.

In the literature, the random global pressure area relationship, $P = CpA^{-Dp}$ models the coefficients *Cp* and *Dp* as a lognormal and normal distributions respectively. As noted in this thesis, a lognormal distribution for *Cp* is intuitively conservative for numbers of events where design is based on the maximum of *n* events in a time period. Since there is no theoretical basis to select a lognormal distribution, consideration for an alternative Weibull distribution is suggested. The modeling of a normal distribution for *Dp* raised to a power translates into a second equivalent lognormal distribution. The effect is that the variance on pressures increases with increasing contact area. Since there is no theoretical or experimental justification for this trend, research to identify an alternative model is needed.

The review of the Polar Class rules and preliminary results of extremal analysis to verify polar class crushing coefficients used to calculate design forces should be extended to include: additional vessels having range of displacements; refinement of the probabilistic local pressure model and exposure inputs, as first analysis in the review in the thesis was conservative. Illustration of the influence of Polar class assignement to varying ice strength in different ice regions should also be carried out.

CHAPTER 9. References

AMARK and MUN (1998). Unified Requirements Load Model – Synthesized Approach. Report for IACS Polar Harmonization Semi-Permanent Working Group on behalf of Canada/Russia Bilateral Project Steering Committee: Institute for Marine Dynamics, Transport Canada, and Russian Maritime Register.

Ashby, M.F., Palmer, A.C., Thouless, M., Goodman, D.J., Howard, M.W., Hallam, S.D., Murrell, S.A.F., Jones, N., Sanderson, T.J.O., Ponter, A.R.S., 1986. Non-simultaneous failure and ice loads on arctic structures. Offshore Technology Conference 1986. Houston. Paper No. OTC 5127, pp. 399-404.

ASPPR, 1995. Canadian Arctic Shipping Pollution Prevention Regulations, Equivalent Standards for Construction of Arctic Class Ships, Transport Canada Ship Safety, Report TP 12260.

Bazant Z.P., 1999. Size effect on structural strength: a review. Archive of Applied Mechanics 69 703-725 Ó Springer-Verlag 1999.

Bhat, U.S., 1990. Modelling of size effect in ice mechanics using fractal concepts. J. Offshore Mech. Arct. Eng. 112, 370.

Blanchet, D. 1990. Thirteenth Canadian Geotechnical Colloquium: Ice Design Criteria for Wide Arctic Structures. Canadian Geotechnical Journal. Vol. 27, No. 6, pp. 701-725.

Cammaert, A.B., Crocker, G.B., 1991. Fractal characteristics of ice. Proc. 11th Conf. on Port Ocean Eng. Under Artic Cond., POAC vol. 91, 1, pp. 13.

Carter, J.E., Frederking, R., Jordaan,I.J., Milne,W.J., and Muggeridge, D.B., 1991. Review and Verification of Proposals for the Revision of the Arctic Shipping Pollution Prevention Regulations, Report on Phase I – Concept Review. Report for Canadian Coast Guard Northern, by Memorial University of Newfoundland Ocean Engineering Research Center. Report TP11472E.

Carter, J.E., Frederking, R., Jordaan,I.J., Milne,W.J., Nessim, M.A., and Brown, P.W., 1992. Review and Verification of Proposals for the Revision of the Arctic Shipping Pollution Prevention Regulations. Report for Canadian Coast Guard Northern, by by Memorial University of Newfoundland Ocean Engineering Research Center. Report TP11366E.

Carter, J.E., Daley, C., Fuglem, M., Jordaan, I.J. Keinonen, A., Revill, C., Butler, T., Muggeridge, K., Zou, B., 1996. Maximum Bow Force for Arctic Shipping Pollution

Prevention Regulations Phase II. Report for Transport Canada Ship Safety, Northern Region by Memorial University of Newfoundland Ocean Engineering Research Center. Report TP12652.

Chai, H., Lawn, B.R., 2006. A universal relation for edge chipping from sharp contacts in brittle materials. Acta Materialia 55, 2555–2561.

Conrad, N., 1976. On microcrack growth and arrest in simulated fibrous composites. Mechanics and Materials Research Center, Texas A&M University, College Station, Report MM 3168-76-10. Cormeau, A., Jordaan, I.

Cotterell, B. and Rice, J., 1980. Slightly curved or kinked cracks. International Journal of Fracture 16, 155–169.

Croasdale, K., 1975. Ice forces on marine structures. Proceedings, 3rd International Symposium on Ice Problems. IAHR Hanover, NH. pp. 315 – 337.

Croasdale, K.R., 1980. Ice Forces on Fixed Rigid Structures. In IAHR Working Group on Ice Forces on Strutures, a State-of-the-Art report ed. T. Carstens. CRREL Special Report No. 80-26, pp. 34-106.

Croasdale, K., 2001. Local Ice Load Data Relevant to Grand Banks Structures Report for: National Research Council of Canada, Contract Number: 40731, PERD/CHC Report 20-61, 01680, March 2001.

Crocker, G.B., 1993. Size distributions of bergy bits and growlers calved from deteriorating icebergs. Cold Reg. Sci. Technol. 22, 113.

Crocker, G., Croasdale, K., McKenna, R., English, G., Guzzwell, J., and Bruneau, S., C-CORE Iceberg Impact Experiment – Phase 2 Final Report, Contract Report for Petro-Canada Resources Limited, Mobil Research and Development Corporation, Chevron Petroleum Technology Company, Husky Oil, and the National Energy Board of Canada, C-CORE Publication 96-C16, 1997.

Daley. C., 1994. Compilation of Medium Scale Ice Indentation Test Results and Comparison to ASPPR. National Research Council of Canada, PERD.

Daley. C., 1992. Ice edge contact and failure. Cold Regions Science and Technology 21 (1992). 1–23.

Daley. C., Tuhkuri, J., and Riska, K., 1998. The role of discrete failures in local ice loads. Cold Regions Science and Technology 27 (1998). 197–211.

Daley, C. 1999. ENERGY BASED ICE COLLISION FORCES, Proc. of the 15th International Conference on Port and Ocean Engineering under Arctic Conditions, Helsinki University of Technology in Espoo,Finland on August 23-27, 1999

Daley, C., Kendrick, A., and Appolonov, E., 2001. Plating and framing design in the unified requirements for Polar Class ships. Proceeding of the 26th international conference of Port and Ocean Engineering under Arctic Conditions. POAC'01. August 12-17, 2001.

Daley, C., 2004. A Study of the Process-Spatial Link in Ice Pressure-Area Relationships. Prepared for National Research Council as part of its Program on Energy Research and Development. PERD/CHC Report 7-108.

Dome, 1982. Measurement of ice pressures and forces on the Canmar *Kigoriak* during repeated trials in 1981. Dome Petroleum ltd.

Dowdeswell, J.A., Forsberg, C.F., 1992. The size and frequency of icebergs and bergy bits derived from tidewater glaciers in Kongsfjorden, northwest Spitsbergen. Polar Res. 11, 81.

Dunwoody, A.B., 1991. Non-simultaneous ice failure. A report to Amoco Production, Tulsa, OK.

Ebeling, C. 1997. Introduction to Reliability and Maintainability Engineering, McGraw Hill publication, Boston, ISBN: 0-07-018852-1.

Eranti, E., 1992. Dynamic ice structure interaction — Theory and applications. Ph.D.Thesis, Technical Research Centre of Finland, Espoo, Finland.

Evans, A.G., 1978. Fracture toughness: the role of indentation techniques. Fracture Mechanics Applied to Brittle Materials: Proceedings of the 11th National Symposium on Fracture Mechanics, Part II, 112–135. American Society for Testing and Materials.

Fischer, R. A.; Tippett, L. H. C., 1928. Limiting forms of the frequency distribution of the largest and smallest member of a sample. Proc., Cambridge Philosophical Society 24 (1928) pp. 180-190

Fransson, L., Olofsson, T., Sandkvist, J., 1991. Observations of the failure process in ice blocks crushed by a flat indentor. Proceedings of POAC '91, St. John's, Canada.

Frèchet, M., 1927. Sur la loi de probabilitè de l' ècart maximum. Ann. Soc. Polon. Math. 6 (1927) 93

Frederking, R.M.W., Jordaan, I.J., McCallum, J.S., 1990. Field tests of ice indentation of medium scale Hobson's Choice Ice Island, 1989. In: Proceedings, 10th IAHR Symposium on Ice, Espoo, Finland, Vol. 2, pp. 931–944.

Frederking, R., 1998. The pressure-area relation in the definition of ice forces, 8th Int. Offshore and Polar Engineering Conference, May 24-29, 1998, Montreal, Vol. II, pp. 431-437.

Frederking, R., 1999. The Local Pressure-Area Relation in Ship Impact with Ice. Proceedings 15th International Conference on Port and Ocean Engineering under Arctic Conditions, POAC'99, Vol.2, pp 687-696, Helsinki, Finland, August 23-27, 1999.

Frederking, R., 2000. Local Ice Pressures from the Louis S. St. Laurent 1994 North Pole Transit, National Research Council Canadian Hydraulics Centre Technical Report HYD-TR-054, Ottawa, May 2000.

Frederking, R., 2005. LOCAL ICE PRESSURES ON THE ODEN 1991 POLAR VOYAGE. Proceedings 18th International Conference on Port and Ocean Engineering under Arctic Conditions, POAC'05 Vol.1, pp 353-363, Potsdam, NY, USA, 2005.

Frederking, R. and Ritch, R., 2009. The Nature of the Process Pressure-Area Relation from CCGS Terry Fox Bergy Bit Impacts. Proceedings of the Nineteenth (2009) International Offshore and Polar Engineering Conference. Osaka, Japan, June 21-26, 2009.

Frederking, R., Hewitt, K., Jordaan, I.J., Sudom, D., Bruce, J., Fuglem, M., and Taylor, R., 2011. Overview of Molikpaq Multi-year Ice Load Analysis, 2007 JIP. Proceedings of the 21st International Conference on Port and Ocean Engineering under Arctic Conditions July 10-14, 2011. Montréal, Canada

Fuglem, M., and Jordaan, I., 1999. Estimate Max Bow Force Arctic Vessels 14th Ice Symposium 1999 Balkema, Rotterdam, ISBN 90 5410 971 8.

Fuglem, M., Parr, G. and Jordaan, I.J., 2013. Plotting positions for fitting distributions and extreme value analysis. Canadian Journal of Civil Engineering, 2013, 40(2)

Galileo, G.L., 1638. Discorsi i Demostrazioni Matematiche intorno aÁ due Nuove Scienze, Elsevirii, Leiden 1638. pp. 178±181 (English transl. by T. Weston, London 1730)

Glen, J.W., 1955. The creep of polycrystalline ice. Proceedings of the Royal Society London. Series A 228 1175., 519–538.

Glen, I.F. and Blount, H., 1984, Measurement of Ice Impact Pressures and Loads Onboard CCGS Louis S. St. Laurent, Offshore Mechanics and Arctic Engineering Symposium, New Orleans, Vol. III, pp. 246-252.

Gordon, J.E. 1968. The New Science of Strong Materials or Why You Don't Fall Through the Floor. 2nd edition. Princeton University Press. Reprinted, 2006.

Griffith, A. A., 1921. The phenomena of rupture and flow in solids. Phil. Trans. 221A (1921) 179-180

Hallam, S.D., 1986. The role of fracture in limiting ice forces. In IAHR 86. Vol. 2, pp. 287-319

Haung, Y., 2010. Model test study of the nonsimultaneous failure of ice before wide conical structures, Cold Regions Science and Technology. 63 (2010) 87-96

Hutchinson, J.W. and Suo, Z., 1992. Mixed mode cracking in layered materials. Advances in Applied Mechanics. Academic Press, Vol. 29, pp. 63-191.

ISO, 2010. Petroleum and natural gas industries — Arctic offshore structures, International Standard by The Organization for Standardization (ISO). Reference number ISO/FDIS 19906:2010(E).

IACS, 2006. Structural Requirements for Polar Class Ships – Technical Background, IACS UR I2, AHG/PSR, August 2006.

IACS, 2011. Requirements Concerning Polar Class, International Association of Classification Societies, IACS Req. 2011.

Jefferies, M.G., 1988. Draft Report on Dynamic Ice Structure Interaction with the Molikpaq at Amauligak I-65, Main Report, Vol. I of II, Internal Report Gulf Canada Resources.

Joensuu, A., Riska, K., 1989. Contact between ice and structure in Finnish. Laboratory of Naval Architecture and Marine Engineering, Helsinki University of Technology, Espoo, Finland, Report M-88.

Johnson, M., 1993. Variation of Local Pressures during Ice–Structure Interaction, M. Eng. Thesis, Faculty of Engineering and Applied Science, Memorial University of Newfoundland.

Johnston, M.E., Croasdale, K.R. and Jordaan, I.J., 1998. Localized pressures during ice–structure interaction: relevance to design criteria. Cold Regions Science and Technology 27 (1998). 105–117

Jordaan. I.J., Nessim, M.A., Ghoneim, G.A. and Murray, A.M., 1987. A Rational Approach to the Development of Probabilistic Design Criteria for Arctic Shipping, Proceedings 6th Offshore Mechanics and Arctic Engineering Symposium, Houston, Vol. IV, pp. 401-406.

Jordaan, I.J., McKenna, R.F., 1991. Processes of deformation and fracture of ice in compression. In: Jones, S.J. *et al.*, Eds.., Ice–structure Interaction, IUTAM-IAHR Symposium, St. John's, Newfoundland, Canada. Springer-Verlag.

Jordaan, I.J., and McKenna, R.F., 1991. "Processes of Deformation and Fracture of Ice in Compression", in Ice-Structure Interaction, Jones S.J., et.al. (Eds), IUTAM-IAHR Symposium St. John's, Newfoundland, Canada, Pub. by Springer Verlag, 1991.

Jordaan, I.J., Maes, M.A., Brown, P.W., and Hermans, I.P., 1993. Probabilistic analysis of local ice pressures. Proceedings, 11th International Conference on Offshore Mechanics and Arctic Engineering, Calgary, AB, Vol. II, pp. 7-13.

Jordaan, I.J., Fuglem M. and Matskevitch, D.G., 1996. Pressure-area relationship and the calculation of global forces. *Proceedings of 13th International Symposium on ice*, Volume I, Bejing, China.

Jordaan, I., Matskevitch, D. and Meglis, I., 1997. Disintegration of ice under fast compressive loading. *Proceedings of the Symposium on Inelasticity and Damage in Solids Subject to microstructural Change*, pp. 211-231.

Jordaan, I. and Xiao, J. 1999. Compressive Ice Failure. Ice in Surface Waters, Shen (ed.) © 1999 Balkema, Rotterdam, ISBN 90 5410 9718.

Jordaan, I., 2001. Mechanics of ice-structure interaction. Engeering Fracture Mechanics, Vol. 68, pp. 1923-1968.

Jordaan, I., 2005a. Decisions under Uncertainty: Probabilistic Analysis for Engineering Decisions. Cambridge University Press.

Jordaan, I., Sudom, D., Li, C., Stuckey, P., Ralph, F., 2005b. Principles for local and Global Design using Pressure-area relationships. POAC'05 Conference, New York, June 2005.

Jordaan, I. J., Frederking, R., and Li, C., 2006. Mechanics of ice compressive failure, failure, probabilistic averaging and design load estimation. Proceedings 18th International Symposium on Ice, IAHR'06 Vol. 1, pp 223-230, Sapporo, Japan, 2006.

Jordaan, I. J., Li, C., Mackey, T., Stuckey, P., Sudom, D., and Taylor, R., 2007. "Ice Data Analysis and Mechanics for Design Load Estimation, Final Report", prepared for NSERC, C-CORE, Chevron Canada Resources, National Research Council of Canada, Petro-Canada and Husky Energy.

Jordaan, I. J., Taylor, R., and Wells, J., 2009. Ice Crushing, Damage Layers, and Pressure-Area Relationships, *Proceedings of 18th International Conference on Port and Ocean Engineering under Arctic Conditions*, June 9-12, 2009, Lulea, Sweden

Jordaan, I. J., Bruce, J., Masterson, D., and Frederking, R., 2010. Local ice pressures for multiyear ice accounting for exposure, Cold Regions Science and Technology, Vol. 61, pp 97–106.

Kamesaki, K. 1997. Experimental Studies on Nonsimultaneous Failure Characteristics of Vertical Sided Indentors. Proceedings of the Seventh (1997) International Offshore and Polar Engineering Conference. Honolulu, USA, May 25-30,1997.

Kamio, Z., Takawaki, T., Matsushita, H., et al., 2000. Medium scale field indentation tests: physical characteristics of first-year sea ice at Notoro Lagoon, Hokkaido. Proceedings of the Tenth International Offshore and Polar Engineering Conference. p. 562.

Kärnä, T., Muhonen, A., 1990. Preliminary results from ice indentation tests using flexible and rigid indenters. Proceedings 10th IAHR Symposium on Ice, Espoo, Finland, Vol. 3, pp. 261-275.

Kärnä, T., Qu, Y., and Yue, Q., 2006. Baltic model of global ice forces on vertical structures. Proceedings, 18th IAHR Symposium on Ice, Sapporo 2006.

Kendall, K., 1978. Complexities of compression failure. Proc. R. Soc., London A361, 245–263.

Kergomard, C., 1989. Analyse morphometrique de la zone marginale de la banquise polaire au nord-ouest du Spitsberg a partir de l'imagerie SPOT panchromatique. Bull.-SFPT 115, 17.

Kheisin, D.E. and Cherepanov, N.W. 1970 Change of ice structure in the zone of impact of a solid body against the ice cover surface. Problems of the Arctic and Antarctic, 1970, Issues 33-35 (A.F. Treshnikov), Israel Program for Scientific Translations (1973) 239-245. 19

Korzhavin, K., 1962. Action of ice on engineering structures. Cold Regions Research and Engineering Laboratory (CRREL). Draft Translation, Hanover, NH, No. 260.

Kry, P.R., 1978. A Statistical Prediction of Effective Ice Crushing Stresses on Wide Structures. Imperial Oil Limited, Production Research Division, Calgary, Alberta, Canada.

Kuehn, G.A., Schulson, E.M., Jones, D.E., and Zhang, J. 1993. The compressive strength of ice cubes of different sizes. 11th International Symposium and Exhibit on offshore Mechanics and Arctic Engineering. Calgary, Alberta, Canada: Transactions of the ASME, 1999, pp. 142-148.

Kujula, P., 1994. On the Statistics of Ice Loads on Ship Hull in the Baltic. ACTA POLYTECHNICA SCANDINAVICA. Mechanical Engineering Series No. 116. Helsinki University of Technology. 1994.

Kujula, P., 1994. Modelling of Nonsimultaneous Ice Crushing as a Poisson Random Process. International Journal of Offshore and Polar Engineering. Vol. 6, No.2, June 1996 (ISSN 1053-5381).

Kujula, P., and Arughadhoss, S.(2012) Statistical Analysis of Ice Crushing Pressures on a Ship's Hull During Hull–ice Interaction. Cold Regions Science and Technology. 70 (2012) 1-11.

Kurdyumov, V.A. and Kheisin, D.E. 1976. Hydrodynamic model of the impact of a solid on ice. Translated from Prikladnaya Mekhanika, 1976;12(10):103-109.

Lensu, M., 1990. The fractality of sea ice cover. Proc. IAHR Ice Symp. Espoo, Finland, pp. 300–313.

Li, C., Jordaan, I., and Barrette, P., 2005. Strain localization and fracture cylindrical ice specimens under confining pressure. *Proceedings of 18th International Conference on Port and Ocean Engineering under Arctic Conditions*, Vol. 1, pp. 213-224.

Løset, S. and Carstens, T., 1996. Sea ice and iceberg observations in the western Barents Sea in 1987. Cold Reg. Sci. Technol. 24, 323.

Maes et al. 1992. Probabilistic behavior of a Poisson field of flaws in ice subjected to indentation. IAHR Ice Symposium 1992 Banff, Alberta.

Mariotte, E., 1740. TraiteÂ du movement des eaux. Posthumously edited by M. de la Hire. Engl. transl. by J. T. Desvaguliers, London 1718. p. 249, also Mariotte's collected works, 2nd edn. The Hague 1740

Masterson, D. M., Nevel, D.E., Johnson, R.C. Kenny, J.J., and Spencer, P.S., 1992. The medium scale Iceberg Impact Test Program, IAHR Ice Symposium, Banff, Alberta, Proceeding s of the 11th International Symposium on Ice, Volume 2, pp. 930-966.

Masterson, D.M. and Frederking, R., 1993. Local contact pressures in ship/ice and structure/ice interactions, Cold Regions Science and Technology, Vol. 21, pp. 169-185.

Masterson, D.M., Frederking, R.M.W.,Wright, B., Kärnä, T., Maddock,W.P., 2007. A revised ice pressure-area curve. Proceedings, Nineteenth International Conf. on Port and Ocean Engineering under Arctic Conditions, Dalian, vol. 1. Dalian University of Technology Press, pp. 305–314

Masterson, D.M., Spencer, P.A., Nevel, D.E., and Nordgren, R.P., 1999. Velocity effects from multi-year ice tests. Proceedings of 18th Conference on Offshore Mechanics and Arctic Engineering, St. John`s, Newfoundland, pp. 1-27.

Masterson, D.M., and Kiring, J., 2008. Polar Class Ship Regulations and Ice Loads – A Comparison with CSA and API. Paper No. ICETECH08-164-R0.

Masterson, D.M., and Frederking, R. 2010. Personal (email) communication regarding design, setup and operation of the medium scale tests.

Matlock, H., Dawkins, W.P., Panak, J.J., 1969. A Model for the Prediction of Ice–Structure Interaction. Annual Offshore Technology Conference, Dallas, USA. pp. 687–694.

Matsushita, H., Takawaki, T., Hirayama, K.I., 1997. Medium scale field indentation tests - physical properties and strength of the ice sheet. Proceedings of the 7th International Offshore and Polar Engineering Conference. Vol. 2. p. 368.

Melanson, P.M., Meglis, I.L., Jordaan, I.J., and Stone, B.M., 1999. Microstructural change in ice: I. Creep behavior under triaxial stress conditions. Journal of Glaciology, Vol. 45, No. 151, 1999.

Meglis, I.L., Melanson, P.M., and Jordaan, I.J., 1999. Microstructural change in ice: II. Creep behavior under triaxial stress conditions. Journal of Glaciology, Vol. 45, No. 151, 1999.

Muhonen, A., 1991. Medium scale indentation tests—PVDF pressure measurements, ice face measurements and interpretation of crushing video. Client Report by Helsinki University of Technology, Ship Laboratory, Feb. 20, 1991.

Palaniswamy, K. and Knaus, W. 1978. On the problem of crack extension in brittle solids under general loading. Mechanics of Today, Vol. 4.

Palmer, A.C., and Sanderson, T.J., 1991. Fractal Crushing of ice and Brittle solids. Proc. R. Soc. Lond. A 1991 **433**, 469-477

Palmer, A.C., Dempsey, J.P., 2002. Models of large-scale crushing and spalling related to high-pressure zones. Proceedings, IAHR Conference, Dunedin, NZ.

Palmer, A.C., Dempsey, J.P., 2007. Understand the size effect. Recent Development of Offshore Engineering in Cold Regions. Yue (ed.). POAC-07, Dalian, China, June 27-30, 2007.

Palmer, A.C., Dempsey, J.P., and Masterson, D.M., 2009. A revised ice pressure-area curve and a fracture mechanics explanation. Cold Regions Science and Technology 56 (2009) 73–76.

Palmer, A. and Croasdale, K. 2013. Arctic Offshore Engineering. World Scientific Publishing Co. Pte. Ltd. Toh Tuck Link, Singapore 5962224.

Paik, J., L., 2012. Lessons Learned; what maritime accidents can teach us about human error and structural design and engineering. Marine Technology, April 2012

Parsons, B.L., 1991a. A normalized group model for the fragmentation if ice. Cold Reg. Sci. Technol. 20, 99.

Parsons, B.L., 1991b. The size effect of nominal ice failure pressure, fractals, self-similarity, and non-stationary. Proc. 11th Conf. on Port Ocean Eng. Under Artic Cond., St John's. Canada, pp. 24–28.

Peirce, F. T.: J., 1926. Textile Inst. 17, 355

Popov, Yu., Faddeyev, O., Kheisin, D., and Yalovlev, A., (1967) "Strength of Ships Sailing in Ice", Sudostroenie Publishing House, Leningrad, 223 p., Technical Translation , U.S. Army Foreign Science and technology Center, FSTC-HT-23-96-68.

Ralph, F., and Jordaan, I. 2013. Probabilistic Methodology for Design of Arctic Ships. Proceedings of the 32nd International Conference on Ocean, Offshore and Arctic Engineering. June 9-14, 2013, Nantes, France

Ralph, F., McKenna, R., Crocker, G. and Croasdale, K. (2004). "Pressure/Area Measurements from the Grappling Island Iceberg Impact Experiment". 17th **IAHR Symposium on Ice**, St. Petersberg, Russia.

Riska, K. and Varsta, P. 1977. Failure Process of Ice Edge Caused by Impact with Ships Side. Symposium in connection with 100 Years Celebration of Finnish Winter

Navigation, Oulu, Finland, December 16–17, 1977. Publ. Board of Navigation, Helsinki 1979, pp. 235–262.

Riska, K., 1987. On the mechanics of the ramming interaction between a ship and a massive ice floe, Thesis for degree of Doctor of Technology, Technical Research Centre of Finland, Publication 43, Espoo, Finland.

Riska, K., Rantala, H., Joensuu, A., 1990. Full scale observations of ship-ice impact. Helsinki University of Technology, Report M-97, 1990

Riska, K., 1991. Observations of the line-like nature of ship-ice contact. In: Proceedings, 11th International Conference on Port and Ocean Engineering Under Arctic Conditions, St. John's, Newfoundland, Canada, Vol. II, pp. 785–811.

Ritch, R., Frederking, R., Johnston, M., Browne, R. and Ralph, F., 2008. Local ice pressures measured on a strain gauge panel during the CCGS Terry Fox bergy bit impact study, Cold Regions Science and Technology, Vol. 52, pp 29–49.

Rothrock D. A., and Thorndike, D.S., 1984. Measuring the sea ice floe size distribution, J. Geophys Res. 89, 6477-6486.

Sammonds, P.R., and Rist, M.A., 2000. Sea ice fracture and friction. IUTAM Symposium on Scaling Laws in Ice Mechanics and Ice Dynamics.

Sanderson, T.J.O., 1988. Ice Mechanics - Risks to Offshore Structures. Graham and Trotman, London, 253 pp.

Sandwell, 1990. 1990 ice indentator tests—field test report and executive summary. Report of Project 112390 by Sandwell, Calgary, Alberta, Vols. I and II, November 1990.

Sandwell, 1992. Reduction and analysis of 1990 and 1989 Hobson's choice ice indentation tests data. Final Report, Project 112588 by Sandwell, Calgary, Alberta to Conoco Exxon Prod. Res., Mobil R&D, and National Research Council of Canada, August 1992.

Sandwell, 1993. Medium scale uniform pressure tests on first-year sea ice at Resolute Bay, N.W.T. 1993. Draft Final Report, Project 113077 by Sandwell, Calgary, Alberta to National Research Council, Institute for Mechanical Engineering, Ottawa, Vols. I and II, August 1992

Savage, S.B., Crocker, G.B., Sayed, M., Carrieres, T., 2000. Size distributions of small ice pieces calved from icebergs. Cold Reg. Sci. Technol. 31, 163.

Sih, G., 1973. Some basic problems in fracture mechanics and new concepts. Engineering Fracture Mechanics, Vol. 5, pp. 365-377.

Sih, G.C., and Tzou, D.Y., 1983. Mechanics of nonlinear crack growth: effect of specimen size and loading steps. Proceedings of conference on modeling problems in crack tip mechanics.

Singh, S., 1993. Mechanical behavour of viscoelastic material with changing microstructure. Ph. D. Thesis, Memorial University of Newfoundland.

Singh, S. K., Jordaan, I. J., Xiao, J., and Spencer, P. A., 1995. The flow properties of crushed ice. Transaction of the Amercian Society of Mechanical Engineering (ASME), 1995. 117:276-82.

Sodhi, D.S., 1992. Ice-structure interaction with segmented indentors. In: Proceedings, 11th IAHR Symposium on Ice 1992, Banff, Alberta, Canada, Vol. 2, pp. 909–929.

Sodhi, D.S., 1998. Non-simultaneous crushing during edge indentation of freshwater ice sheets. Cold Regions Science and Technology 27, 179–195.

Sodhi, D., Takeuchi, T., Nakazawa, N., Akagawa, S., and Saeki, H., 1998. Medium-scale indentation tests on sea ice at various speeds. Cold Regions Science and Technology 28 1998. 161–182.

Sodhi, D.S., Takeuchi, T., Kawamura, M., Nakazawa, N., Akagawa, S., 2001. Measurement of ice forces and interfacial pressures during medium-scale indentation tests in Japan. POAC '01. p. 617.

Spencer, P., and Morrison, T., 2012. High Pressure Zones, Statistics and Pressure-Area Effects. ICETECH 2012. Banff, Alberta. Paper No. ICETECH12-148-RF.

St. John, J. and Daley, C., 1984. Shipboard Measurement of Ice Pressures in the Bering, Chukchi, and Beaufort Seas. Third International Offshore Mechanics and Arctic Engineering Symposium, Volume III, ASME, New Orleans, LA.

St. John, J., Daley, C., Blount, H. and Glen, I., 1984. Ice loads and ship response to ice USCG *Polar Sea* deployment. Technical report prepared for the Transport Canada. TP 6093E.

Tuhkuri, J., 1993. Laboratory investigations of ice-structure contact. In: Proc. 12th Conf. Port and Ocean Engineering under Arctic Conditions, Vol. 2. The Hamburg Ship Model Basin, Hamburg, pp. 617-626.

Tuhkuri J., 1995. Experimental observations of the brittle failure process of iceand ice-structure contact. Cold Regions Science and Technology 23 (1995) 265-278.

Takeuchi, T., Akagawa, S., Kawamura, M., et al., 2000. Examination of factors affecting total ice load using medium field indentation test data. Proceedings of 10th International Offshore and Polar Engineering Conference. p. 607.

Takeuchi, T., Masaki, T., Akagawa, S., et al., 1997. Medium-scale indentation tests (MSFIT) ice failure characteristics in Ice/Structure interactions. Proceedings of 7th International Offshore and Polar Engineering Conference. Vol. 2. p. 376.

Taylor, R.S., Fuglem, M., Jordaan, I.J., Frederking, R.M.W, 2007. Analysis of JOIA data: probabilistic averaging for global load estimation. Technical Report - Ian Jordaan and Associates.

Taylor, R.S., Frederking, R, and Jordaan, I. J. 2008. The nature of high pressure zones in compressive ice failure. Proceedings 19th IAHR Symposium on Ice, Vancouver, British Columbia, Canada.

Taylor, R., Jordaan, I., Li, C., and Sudom, D., 2009. Local Design Pressures for Structures in Ice: Analysis of Full-Scale Data. Journal of Offshore Mechanics and Arctic Engineering AUGUST 2010, Vol. 132 / 031502-1.

Taylor, R., 2010. Analysis of Scale Effect in Compressive Ice Failure and Implications for Design. A Thesis Submitted to the School of Graduate Studies for the Degree of Doctor of Philosophy, Faculty of Engineering and Applied Science, Memorial University of Newfoundland. March 2010.

Taylor R and Jordaan, I (2011) The Effects of Non-simultaneous Failure, Pressure Correlation, and Probabilistic Averaging on Global Ice Load Estimates, ISOPE, 2011

Thouless, M., Evans, A., Ashby, M. and Hutchinson J., 1987. The edge cracking and spalling of brittle plates. Acta Metall, Vol. 35, pp. 1333-1341.

Tippett, L. H. C., 1925. On the extreme individuals and the range of samples. Biometrika 17 (1925) 364

Timco, G.W., 1986. Indentation and Penetration of Edge-loaded freshwater ice sheets in the brittle range. Prodceeding s of the 5th International Symposium on Offshore eMechanics and Arctic Enginneering (OMAE). Toyko, 13-18 April 1986, Vol. 4, pp. 444-452

Timco, G.W., Jordaan, I.J., 1987. Times series variations in ice crushing. Proc. 9th Conf. on Port Ocean Eng. Under Arctic Conditions, pp. 13– 20.

Tuhkuri, J., 1994. Analysis of ice fragmentation process from measured particle size distribution of crushed ice. Cold Regions Science and Technology. 23 (1994), 69.

Tuhkuri, J., 1995. Experimental observations of the brittle failure process of ice and ice-structure contact. Cold Regions Science and Technology. 23, (1995), pp. 265-278.

Turcotte, D.L., 1986. Fractals and fragmentation. J. Geophys. Res. 91, 1921–1926.

Varsta, P., 1983. On the mechanics of ice loads on ships in level ice in the Baltic Sea. Technical Research Centre of Finland, Publication 11, Espoo, Finland.

von Mises, R., 1936. La distribution de la plus grande de n valeurs. Rev. Math. Union Interbalcanique 1 (1936) 1.

Weibull, W., 1939. The phenomenon of rupture in solids. Proc. Royal Swedish Inst. Eng. Res. (Ingenioersvetenskaps Akad. Handl.) 153 (1939) 1 – 55.

Weibull, W., 1951. A statistical distribution function of wide applicability. J. Appl. Mech. ASME 18.

Weiss, J., 2001. Fractal and fragmentation of ice: a fractal analysis of scale invariance. Eng. Fract. Mech. 68, 1975.

Weiss, J., Gay, M., 1998. Fracturing of ice under compression creep as revealed by a multifractal analysis. J. Geophys. Res. 103, 24005

Withalm, M. and Hoffmann, N.P., 2010. Simulation of full-scale ice–structure-interaction by an extended Matlock-model. Cold Regions Science and Technology 60 (2010) 130–136.

Xiao, J., 1997. Damage and fracture of brittle viscoelastic solids with application to ice load models. Ph.D Thesis, Memorial University of Newfoundland.

Xu, Y., Xu, J., and Wang, J., 2004. Fractal model for size effect on ice failure strength. Cold Regions Science and Technology. 40 (2004) 135– 144

Zou, B., 1996. Ships in Design: The Interaction Process, and Principles for Design. A Thesis, Faculty of Engineering and Applied Science, Memorial University.

Zou, B., Xiao, J. and Jordaan, I., 1996. Ice fracture and spalling in ice-structure interaction. Cold Regions Science and Technology, Vol. 24, pp. 213-220.

CHAPTER 10. Bibliography

Addison, R., Dower, J., Hall, J., and Jordaan, I. 2004. Report of the Expert Panel on Science Issues Related to Oil and Gas Activities, Offshore British Columbia. A Report for Natural Resources Canada, for the Royal Society of Canada.

Bazant, Z. P., 1993. Scaling laws in mechanics of failure. J. Eng. Mech. ASCE 119(9) (1993) 1828-1844

Bennett, J.G., 1936. Broken coal, J. Inst. Fuel. **10**. 22-29

Bhat, S. U., 1988. ANALYSIS FOR SPLITTING OF ICE FLOES DURING SUMMER IMPACT, Cold Regions Science and Technology, 15 (1988) 53-63

Cullen, W.D., 1990. The Department of Energy, (UK). The Public Inquiry into the Piper Alpha Disaster, by the Non. Lord Cullen.

Daley, C., St. John, J.W., Seibold, F, and Bayly, I., 1985. Analysis of extreme ice loads and pressures on USCGC *Polar Sea*, SNAME Annual Meeting, November 1984, Paper No. 8.

Daley, C., (2003). IACS Unified Requirements for Polar Ships – Background to Design Ice Loads. Prepared for IACS Ad-Hoc Group for Polar Ship Rules and Transport Canada.

Daley, C., (2003). IACS Unified Requirements for Polar Ships – Background to Framing Requirements. Prepared for IACS Ad-Hoc Group for Polar Ship Rules and Transport Canada.

Daley, C., (2003). IACS Unified Requirements for Polar Ships – Background to Longitudinal Strength Requirements. Prepared for IACS Ad-Hoc Group for Polar Ship Rules and Transport Canada.

Dempsey, J.P, Palmer, A.C., Sodhi, D.S., 2001. High pressure zone formation during compressive ice failure. Engineering Fracture Mechanics, 68: 1961-1974.

Fujiwara, A., Kamimoto, G. and Tsukamoto, A., 1977. Destruction of basaltic bodies by high velocity impacts. Icarus **31**, 277-288.

Gagnon, R.E., Sinha, N.K., 1991. Energy dissipation through melting in large-scale indentation pressure experiments on multi-year ice. In: Proceedings, 10th International Conference on Offshore Mechanics and Arctic Engineering OMAE., Stavangar, Norway, Vol. IV, pp. 157–161.

Harding L.E. and Englar, J.R., 1988. The Nestucca Oil Spill: Fate and Effects to May 31, 1989. Environment Canada, Regional Program Report 98-01.

Iyer, S.H., 1983. Size effects in ice and their influence on the design of offshore structures. Proceedings of POAC '83, 7th Int. Conf. on Port and Ocean Engineering under Arctic Conditions, April 5-9, 1983, Helsinki, VTT Symposium 37 vol. 3, pp.414-432.

Johnston, M.E., 2006. Evolution of an inertial measurement system called MOTAN: summary of installations on five ice-strengthened ships. Proceedings of ICETECH 2006. Banff, Canada. CD-Rom.

Jordaan, I., C. Li, Mackey, T. and Nobahar, A., 2005c. Design ice pressure-area relationships: Molikpag data. Technical report prepared for the National Research Council of Canada, PERD/CHC 14-121.

Kendrick, A., Daley, C., 1998. Unified Requirements Load Model -'Synthesized Approach. Prepared for IACS Unified Polar Rules Harmonization Semi-Permanent Working Group Prepared by AMARK Inc, Montreal and Memorial University, St. John's on behalf of, Institute for Marine Dynamics, Transport Canada, Russian Maritime Register, Sept. 1998.

Lawn, B., 1993. Fracture of brittle solids. Cambridge University Press.

Li, C., 2007. Probability and Fracture Mechanics Applied to Ice Load Estimation and Associated Mechanics. Doctoral Thesis. Memorial University, April 2007.

McDowell, G.R., Bolton, M.D., Robertson, D., 1996. The fractal crushing of granular materials. J. Mech. Phys. Solids 44, 2079.

Meany, R., Kenny, S., Sinha, N.K., 1991. Medium-scale ice-structure interaction: Failure zone characterization. In: Proceedings, 11th International Conference on Port and Ocean Engineering Under Arctic Conditions, St. John's, Newfoundland, Canada, Vol. I, pp. 126–140.

Melchers, R., 1998. Structural reliability analysis and prediction. John Wiley and Sons Ltd.

Miller, K., 1980. The application of fracture mechanics to ice problems. Physics and Mechanics of ice, *the Proceeding of the 1st IUTAM Symposium on Ice*, pp. 265-277.

Nessim, M., Jordaan, I.J., Lantos, S., and Cormeau, A., 1986. Probability-based design criteria for ice loads on fixed structures in Beaufort Sea. Final report, Volume I, *Det Norske Veritas (Canada) Ltd.*

Palmer, A., Goodman, D., Ashby, M., Evans, A., Hutchinson, J. and Ponter, A. 1982. Fracture and ice forces on offshore structures. *Proceedings of Symposium on Applied Glaciology.*

Ralph, F., Jordaan, I., Clark, P., and Stuckey, P. (2006) Estimating Probabilistic Iceberg Design Loads on Ships Navigating in Ice Covered Waters. Paper No. ICETECH06-05-006, Banff.

Rawson K.J., and Tupper, E.C., 1983. Basic Ship Theory, Volume 1. Longman Group Limited. New York.

Ritch, R. and St. John, J., 1994. Hull/ice interaction load measurements on board the Louis S. St-Laurent during the 1994 Arctic voyage – trip report and data summary, December, 1994, Report on contract no. T8080-4-6051 for Transport Canada

Ritch, R., St. John, J., Browne, R., and Sheinberg, R., 1999. Ice load impact measurements on the CCGS Louis S. St. Laurent during the 1994 Arctic Ocean crossing, Proceedings of the 18th International Conference on Offshore Mechanics and Arctic Engineering, July 11-16, 1999, St. John's Newfoundland, paper OMAE99/P&A-1141.

Royal Commission on the Ocean Ranger Marine Disaster, (1984). The loss of the semisubmersible drill rig Ocean Ranger and its crew. Publisher: [St. John's, Nfld.]: Royal Commission on the Ocean Ranger Marine Disaster, 1984-1985. Microform. ISBN: 0660118289, ISBN13: 9780660118284, Edition: (v. 4)

Riska, K. 1994. The determination of bow force of ship ramming a massive ice floe. Technical report prepared for *Canadian Coast Guard Northern*.

Saeki, H. Hirayama, K.-I., Kawasaki, T., Akagawa, S., Kato, K., Kamesaki, K., Saka, K., Kurokawa, A., 1996. JOIA project of study of ice load. Proceedings, 13th International Symposium on Ice, Beijing, China, Vol. 1, pp. 17–27.

Schulson, E.M., 1990. The brittle compressive fracture of ice. Acta Metall. Mater. 38, 1963.

Schulson, E.M. and Duval, P., 2009. Creep and Fracture of Ice. Cambridge University Press. New York. 2009.

Schoutens, J.E., 1979. Empirical analysis of Nuclear and high explosive catering and ejecta. Nuclear Geophysics sourcebook. Vol.55, part 2 section 4, Defence Nuclear Agency Report DNA 65 01H-4-2.

Selvadurai, A., 2000. Fracture evolution during indentation of a brittle elastic solid. Mechanics of cohesive-frictional materials, pp. 325-339.

Sodhi, D., 2000. Absense of size effect in brittle crushing and breaking through loads of ice sheets. *Proceedings of IUTAM Symposium on Scaling Laws in Ice Mechanics and Ice Dynamics*. Pp. 55-66.

St. John, J. and Minnick, P., 1993. Swedish icebreaker Oden ice impact load measurements during International Arctic Ocean Expedition 1991; Instrumentation and measurement

summary, STC Technical Report 2682 to U.S Coast Guard Headquarters under contract DTCG23-91_D-ENM026, Delivery Order 92-0007, May 1993.

Webber, L. and Nixxon W., 1991. Crack opening and propagation in S2 freshwater ice. *Proceedings of the 10th International OMAE Conference*, Vol. 4, pp. 245-252.

Wells, J., Jordaan, I.J., Derradji, A. and Bugden, A., 2006. Laboratory investigation of the fracture behaviour of polycrystalline ice with embedded monocrystals. Technical report prepared for Institute for Ocean Technology, National Research Council (IOT/NRC), in process.

Wierzbicki, T., 1985. Spalling and buckling of ice sheets. *Civil Engineering in the Arctic Offshore*, pp. 953-961.

WOCOEEAP, 1986. Report and Recommendations of the West Coast Offshore Exploration Environmental Assessment Panel. Submitted to the Governments of BC and Canada, April 1986. Minister of Supply and Services Canada. ISBN0-662-54428-5. At: <http://www.offshoreoilandgas.gov.bc.ca/reports/environmental-assessment/default.htm>

APPENDIX A

Ship Ice Interaction Model
For Simulating Maximum Bow Force

A.1. Equations for Vessel Motion and Stiffness

As illustrated in Figure A1, during a collision with ice, the vertical force on the bow will cause pitch and heave motions of the vessel. The acceleration at the bow is the combination of acceleration at the center of mass of the vessel and rotation due to pitch given as

$$\ddot{x}_b = \ddot{x}_c + \frac{L_{BP}}{2}\ddot{\theta} \tag{A1}$$

The acceleration at the bow can also be written in terms of vertical force F_v and Moment M at the bow given as

$$\ddot{x}_b = \frac{F_V}{(1+\delta_Z)m} + \frac{M}{I}\frac{L_{BP}}{2} \tag{A2}$$

where m is the mass, δ_Z is the added mass factor for heave an I is the moment of inertia. The moment at the bow can be written in terms of vertical bow force F_v as

$$M = F_v \frac{L_{BP}}{2} \tag{A3}$$

And the moment of inertia as

$$I = m(1+\delta_\theta)R_\theta^2 \tag{A4}$$

where δ_θ is the added mass for pitch, R_θ is the radius of gyration of the ship in pitch which can be approximated as

$$R_\theta = r_\theta^2 \frac{L_{BP}}{12} \tag{A5}$$

Substitution back into Equation (A2) gives

$$\ddot{x}_b = \frac{F_V}{(1+\delta_Z)m} + \frac{\left(F_V \frac{L_{BP}}{2}\right)\frac{L_{BP}}{2}}{m(1+\delta_\theta)R_\theta^2 \frac{L_{BP}^2}{12}}$$
$$= \frac{F_V}{m}\left(\frac{1}{(1+\delta_Z)} + \frac{3}{(1+\delta_\theta)r_\theta^2}\right) \qquad (A6)$$

Heave and pitch added mass factors δ_z and δ_θ respectively, can be determined based on vessel beam B, and draft T, from Rawson and Tupper (1983) as

$$\delta_Z = \delta_\theta = \left(0.2 + \frac{B}{3T}\right) \qquad (A7)$$

The resistance of the vessel, or its stiffness to both heave and pitch can represented as

$$k_H = \rho g B L_{BP} C_{WP} \qquad (A8)$$
$$k_P = \rho g I_{WP}$$

Where C_{WP} is the waterplane coefficient and I_{WP} is the waterplane inertial calculated as

$$C_{WP} = \frac{A_{WP}}{L_{BP}B} \qquad (A9)$$
$$I_{WP} = \frac{nBL_{BP}^3}{12}$$

Here A_{WP} is the waterplane area and n is based on the bow shape and can be approximated as $n = 1.29 \cdot C_{WP} - 0.49$.

To allow combination of k_H and k_P, the pitch stiffness can be re-written as

$$k_B = \frac{k_P}{(L_{BP}/2)^2} \quad (A1088)$$

from which the equivalent vertical stiffness at the bow can be written as

$$k_\gamma = \frac{1}{\left(\frac{1}{k_H} + \frac{1}{k_B}\right)} \quad (A11)$$

A.2. Interaction Geometry and Global Force

The geometry of the interaction is illustrated in Figure A1. The bow shape has been approximated by a V shape. Penetration and volume of ice crushed is approximated by the idealized wedge formed defined by bow opening angle α and stem angle γ. The extent of penetration depends on vessel surge (p_x) and bow rise (p_y).

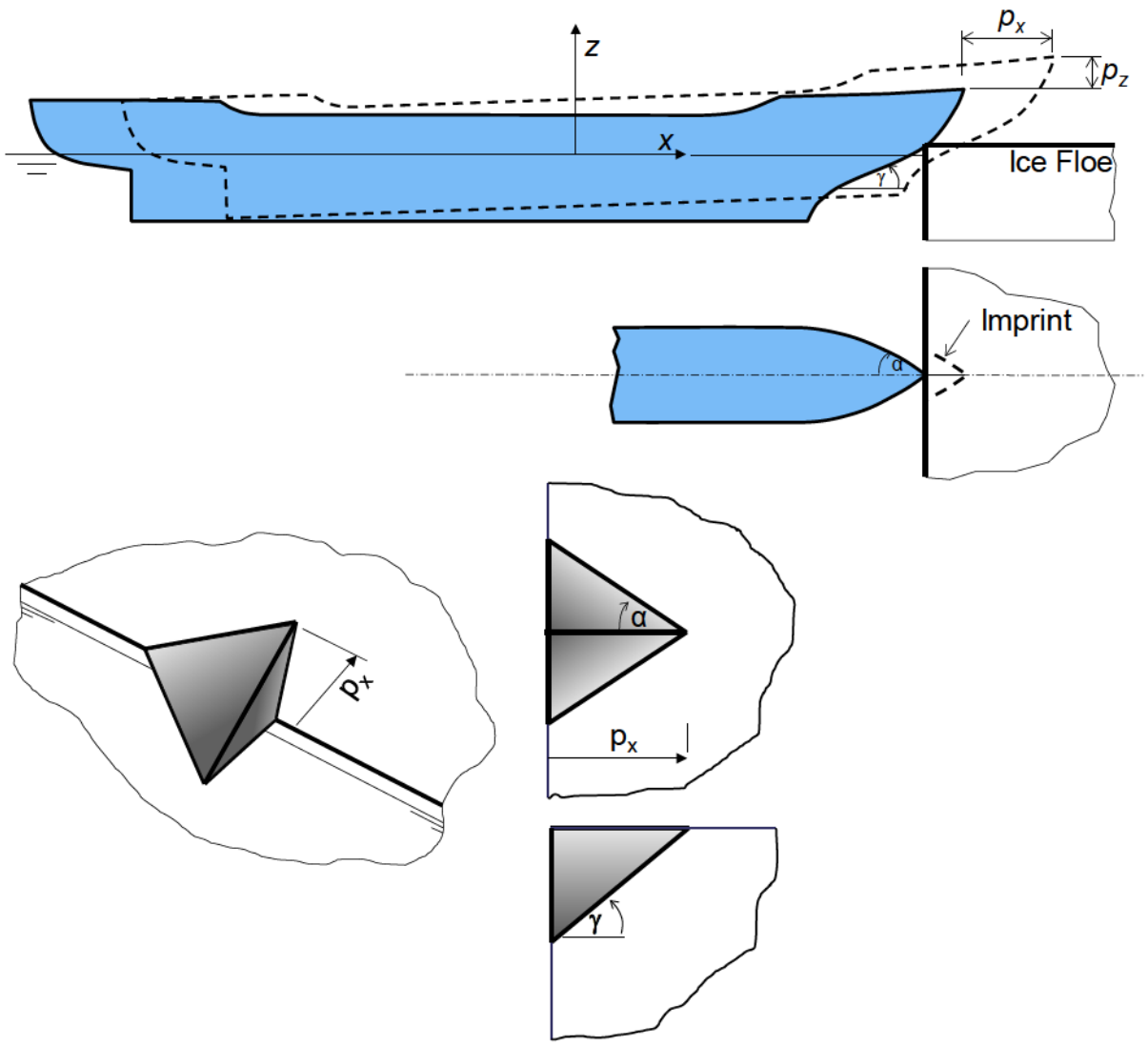

Figure A1 Ice ram interaction geometry and idealized bow geometry (after Riska, 1984)

Based on the interaction geometry as illustrated in Figure A1 and Figure A2, the vertical projected area Av of the wedge is given by

$$A_V = p_x^2 \tan\alpha \qquad (A12)$$

Limitations to this are discussed in Section A.4.

Corresponding vertical force F_V and horizontal force F_H as a function of project vertical area, nominal ice crushing strength (or nominal pressure) P and stem angle γ is given as

$$F_V = A_V P \qquad \text{(A13)}$$
$$F_H = F_V \tan\gamma$$

The nominal area associated with nominal pressure P can be given as

$$A_P = \frac{A_V}{\cos\gamma} \qquad \text{(A14)}$$

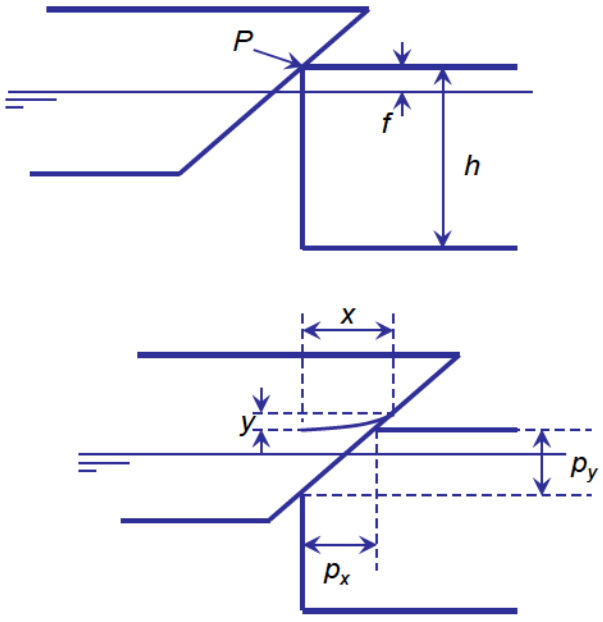

Figure A2 Geometry and parameters for determining contact area

A.3 Frictional Forces

The friction force will act tangential to the vessel plating and is defined in terms of the global normal force on the bow and corresponding normal force to the shell plating. The relationship of global normal force F_N to the normal force to the shell plating F'_N is

$$F_N = F'_N \sin\alpha \tag{A15}$$

$$F'_N = \frac{F_N}{\sin\alpha} = \frac{F_V}{\cos\gamma \sin\alpha} \tag{A16}$$

The corresponding tangential force relative to the shell plate is given as

$$F'_T = C_F F_N \tag{A17}$$

where C_F is the friction coefficient.

The components frictional force F'_T in of heave and surge plane is given as

$$\begin{aligned} F_{TH} &= F_T \sin\gamma = F'_T \sin\gamma\cos\alpha \\ F_{TS} &= F_T \cos\gamma = F'_T \cos\gamma\sin\alpha \end{aligned} \tag{A18}$$

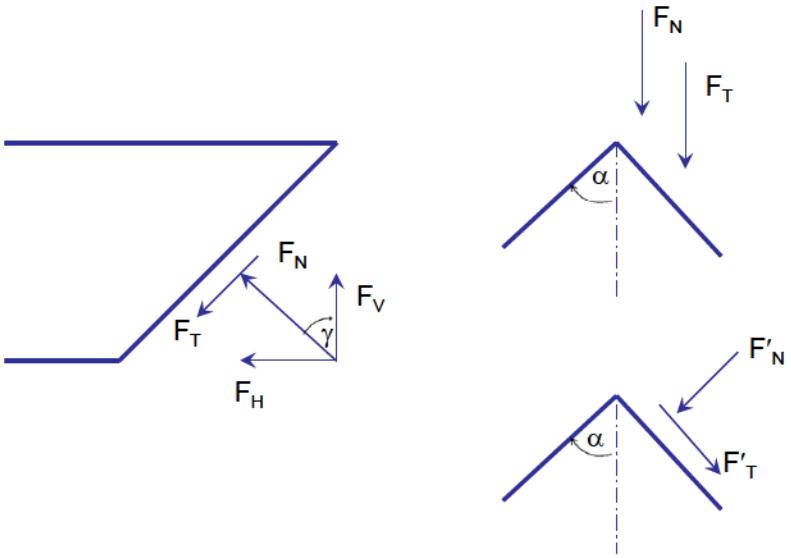

Figure A3 Definition of friction force and components relative to global force

A.4 Contact Area Limitations

The volume of ice crushed and the associated contact area can be limited by ice thickness, vessel draft, and vessel width. As before, the vertical projected area is estimated, followed

by the nominal interaction area, and finally the components of force acting on the hull including friction.

If penetration includes the skeg, the corresponding contact area of the skeg is not added directly to the full bow contact area. It is assumed that the unique shape of the skeg and geometry relative to the penetrated bow and associated pressure area effects are independent. The developing skeg area will have no confining effect on the main bow area and vis versa. Hence, the skeg area and corresponding force is added separately to the bow force.

A.4.1 Limited Ice Thickness

For this scenario, the vertical contact area A_V is calculated for the infinitely thick ice sheet from which the area A_{V2} below the limited ice sheet thickness is subtracted off. A_{V2} is calculated as.

$$A_{V2} = p_{x2}^2 \tan\alpha$$
$$p_{X2} = \frac{p_{Y2}}{\tan\gamma}$$
$$p_{Y2} = p_Y - h \qquad \text{(A19)}$$

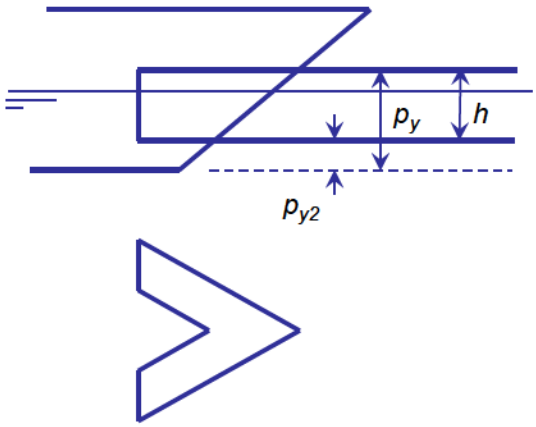

Figure A4 Geometry and parameters for contact area that is limited by ice thickness

A.4.2 Limited Vessel Draft

When area crushed is limited by vessel draft, a similar approach to limited thickness is used except that P_{Y2} is adjusted to account for vessel draft, ice freeboard, and slide-up.

$$p_{Y2} = D - d$$
$$D = p_Y - f + y \qquad \text{(A20)}$$

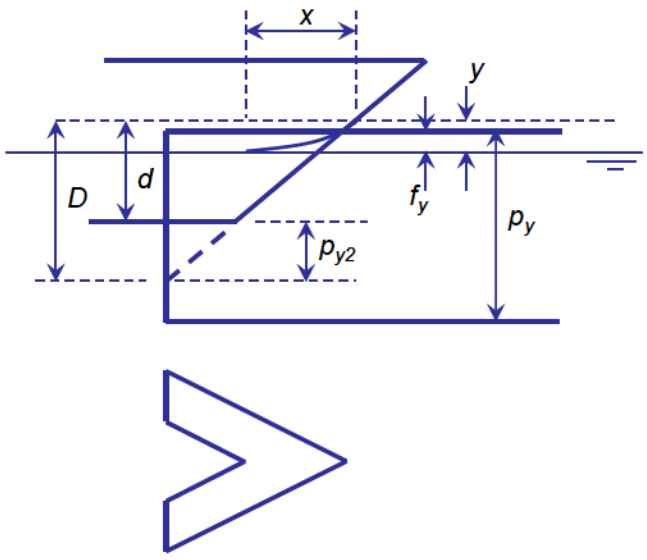

Figure A5 Geometry and parameters for contact area that is limited by vessel draft

A.4.3 Limited Vessel Width

For the limiting vessel width scenario it is necessary to subtract off the area A_1 from both sides of the vessel.

$$A_{VL} = A_V - 2A_1 \qquad \text{(A21)}$$

$$A_V = p_X^2 \tan\alpha$$

$$A_1 = \frac{1}{2}\left(\frac{w-b}{2}\right)\left(\frac{w-b}{2}\right)\frac{1}{\tan\alpha}$$

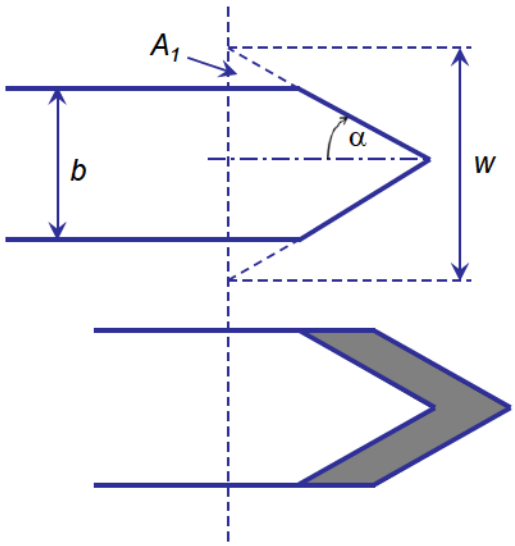

Figure A6 Geometry and parameters for contact area that is limited by vessel breadth

A.4.4 Spoon-Shaped Bow

Modeling a spoon shaped bow is more complex incorporating a second bow opening angle α_2. Three separated vertical areas are developed and summed to obtain a more accurate estimate of the interaction area.

$$A_{VS} = 2A_1 + 2A_2 + A_3 \qquad \text{(A22)}$$

$$A_1 = \frac{1}{2}x_\alpha \tan\alpha$$

$$A_2 = \frac{1}{2}(p_x - x_\alpha)(p_x - x_\alpha)\tan\alpha_2$$

$$A_3 = 2(p_x - x_\alpha)x_\alpha \tan\alpha_2$$

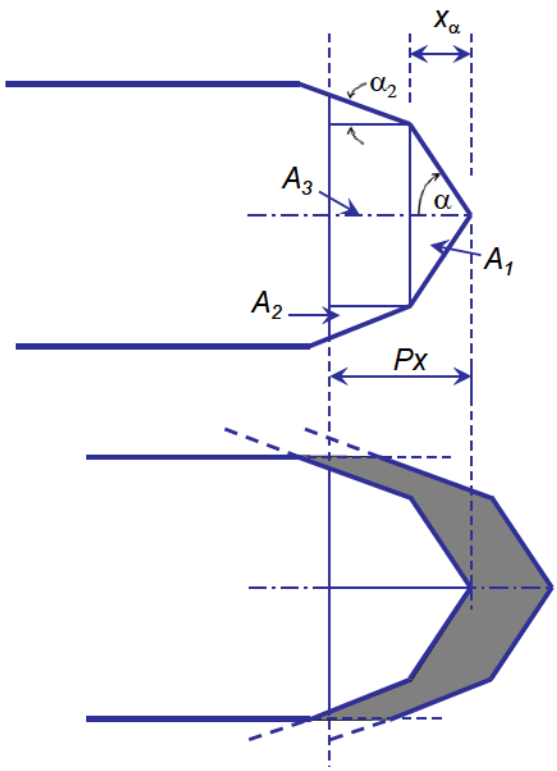

Figure A7 Geometry and parameters for determining contact area for spoon shaped bow

A.5 Flexure Failure

Depending on geometry of the bow and the thickness of the ice sheet, crushing may be minimal, and the actual bow force may be limited due to flexure failure of the ice. For such cases, limiting flexure failure was incorporated into the model.

$$F = c_f \sigma_f h^3 \qquad \text{(A23)}$$

where c_f is a constant, σ_f is the flexural strength of the ice sheet and h is the ice thickness. It is noted that for first year ice, this limiting condition is valid where ice thickness is somewhat consistent. For deformed MY ice, the thickness is very difficult to measure and will have considerable variability. Hence, because of uncertainty in thickness measurements,

incorporating limiting flexure forces will also be uncertain and possibly under conservative. Caution must be exercised.

A.6 Hull Natural Vibration and Equivalent Stiffness

In addition to crushing and vertical motions of the bow, the resultant maximum force acting on the bow will be influenced by the natural vibration of the hull. In the simulation, only the first natural vibration model was modeled using the addition simple spring at the point of contact having a mass m_F, added mass δ_F and spring constant K_F given as

$$K_F = (1+\delta_f) m_F (2\pi N_{V2})^2 \qquad (A24)$$

where

$$N_{V2} = 150K^{0.64} \quad [Hz] \text{ and} \qquad (A25)$$

$$K = \left(\frac{BD_E^3}{\left(1.2 + \frac{B}{3T}\right) L^3 D} \right)^{\frac{1}{2}} \qquad (A26)$$

Here, D_E is the equivalent depth of the vessel dependent on the height and extent of the superstructure, and L, B, T, and D are parameters for vessel length, beam, draft, and displacement. The parameter K is Todd's formula (Rawson and Tupper, 1983). As a first approximation, D_E is assumed to be 1.9.

A.7 Resultant Equations of Motion

The final equations of motion for both surge and heave/pitch motion for individual rams is

$$\ddot{x} = \frac{\left(-k_x x - c_x x'\right) - F_H}{M_x}$$
$$\ddot{y} = \frac{\left(-k_y y - c_y y'\right) - F_V}{M_y} \quad \text{(A27)}$$

where F_H and F_V are the horizontal and vertical component of ice crushing force, k_x and k_y are the horizontal and vertical spring constants, and c_x and c_y are the horizontal and vertical damping coefficients. Time is set as zero at first contact. As the interaction progresses, the bow accelerates upward due to heave and pitch, while the horizontal motion decelerates as crushing and inertial forces erode the initial kinetic energy slowing the vessel to a stop at some point t in time.

As the vertical velocity increases, the rate of penetration decreases. When the direction of motion approaches the stem angle, penetration approaches zero and the force approaches the static beach load.

As an approximation, surge stiffness and horizontal damping is set to zero. Vertical damping is estimated as

$$c_y = 0.1\sqrt{k_y M_y} \quad \text{(A28)}$$

As noted earlier, the numerical solution uses a Runge-Kutta procedure.

One difficulty with the numerical solution was that after initial impact, there was some resonance during the beaching phase of the interaction. With the vessel and ice modeled as rigid bodies, there was repeated loss of contact as the interaction progressed. In reality, there will be some flexure of the vessel and ice such that the vessel remains in contact. To account for this, a soft elastic layer was integrated between the vessel and the ice such that the force can fluctuate linearly from *Fx* to zero as contact is lost.

APPENDIX B

Local Pressure Simulation

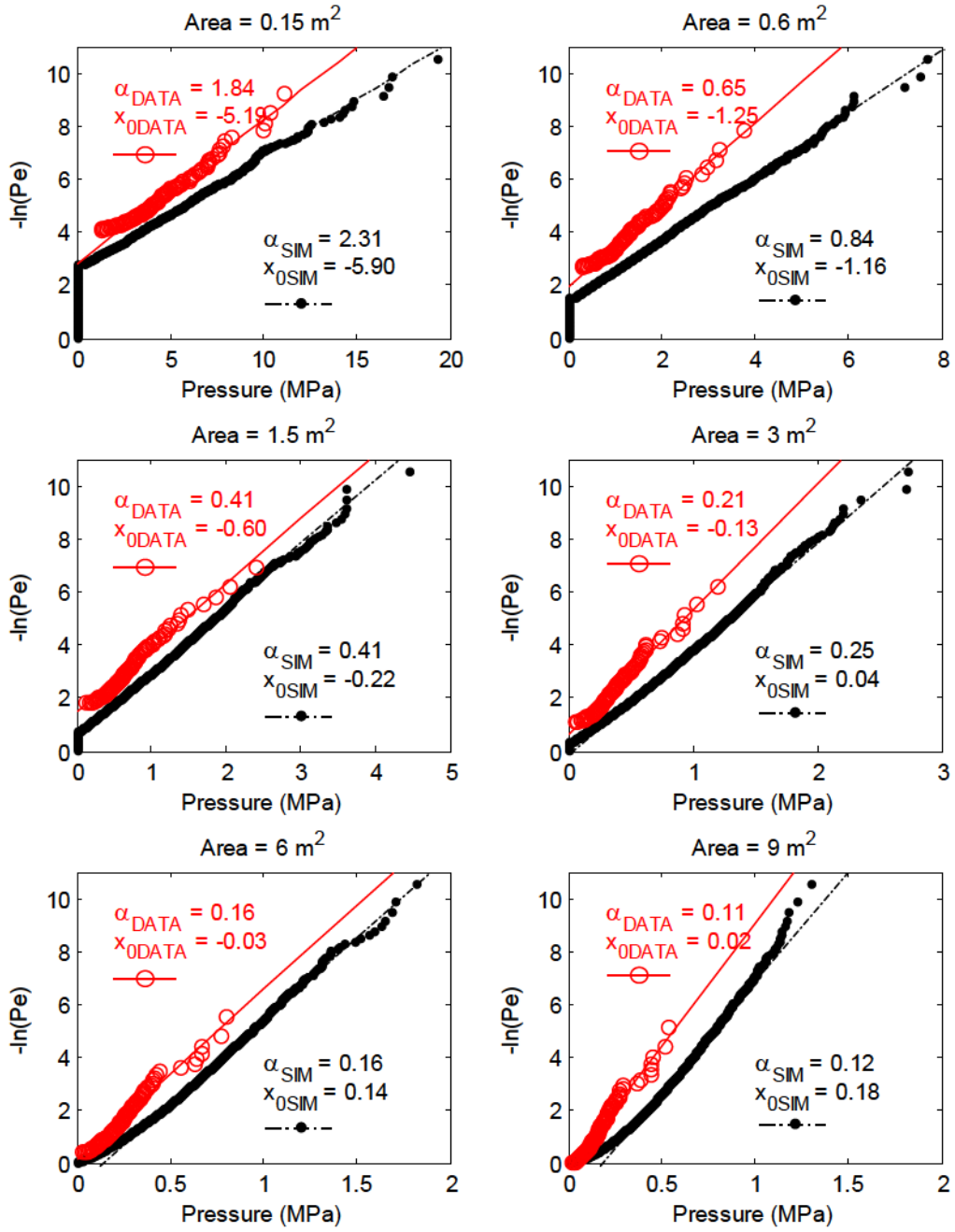

Figure B1 Comparison of simulated local pressure parameters with measured parameters based on *Polar Sea* Beaufort 1982 trials – $\gamma = 0.53$ MN; $\gamma_0 = 0.10$ MN; $\rho = 0.40$ *HPZ*s/m^2 (note that for this dataset, the x0 seems overly conservative at 0.1)

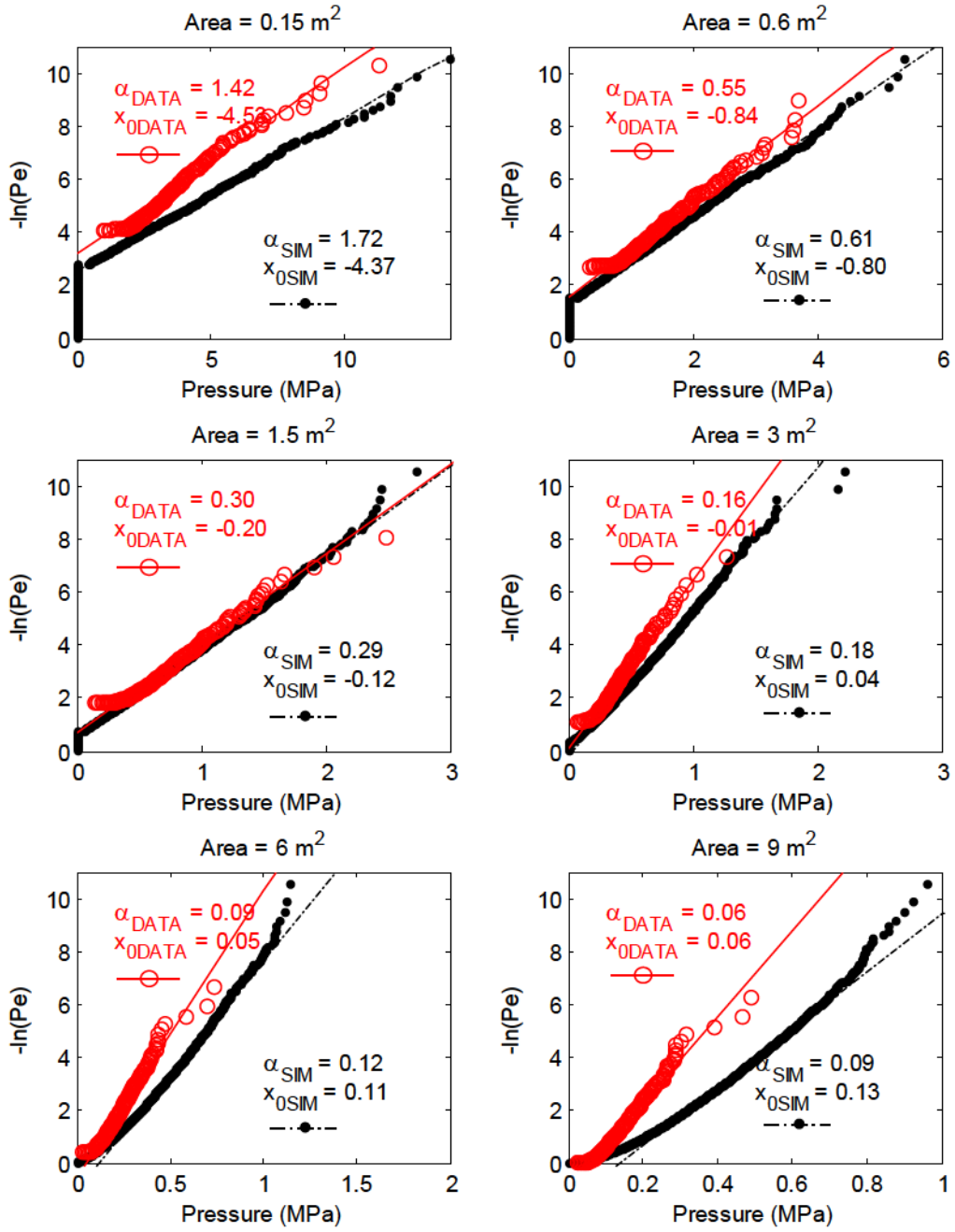

Figure B2 Comparison of simulated local pressure parameters with measured parameters based on North Chukchi 1983 trials – $\gamma = 0.38$ MN; $\gamma_0 = 0.10$ MN; $\rho = 0.40$ *HPZ*s/m^2

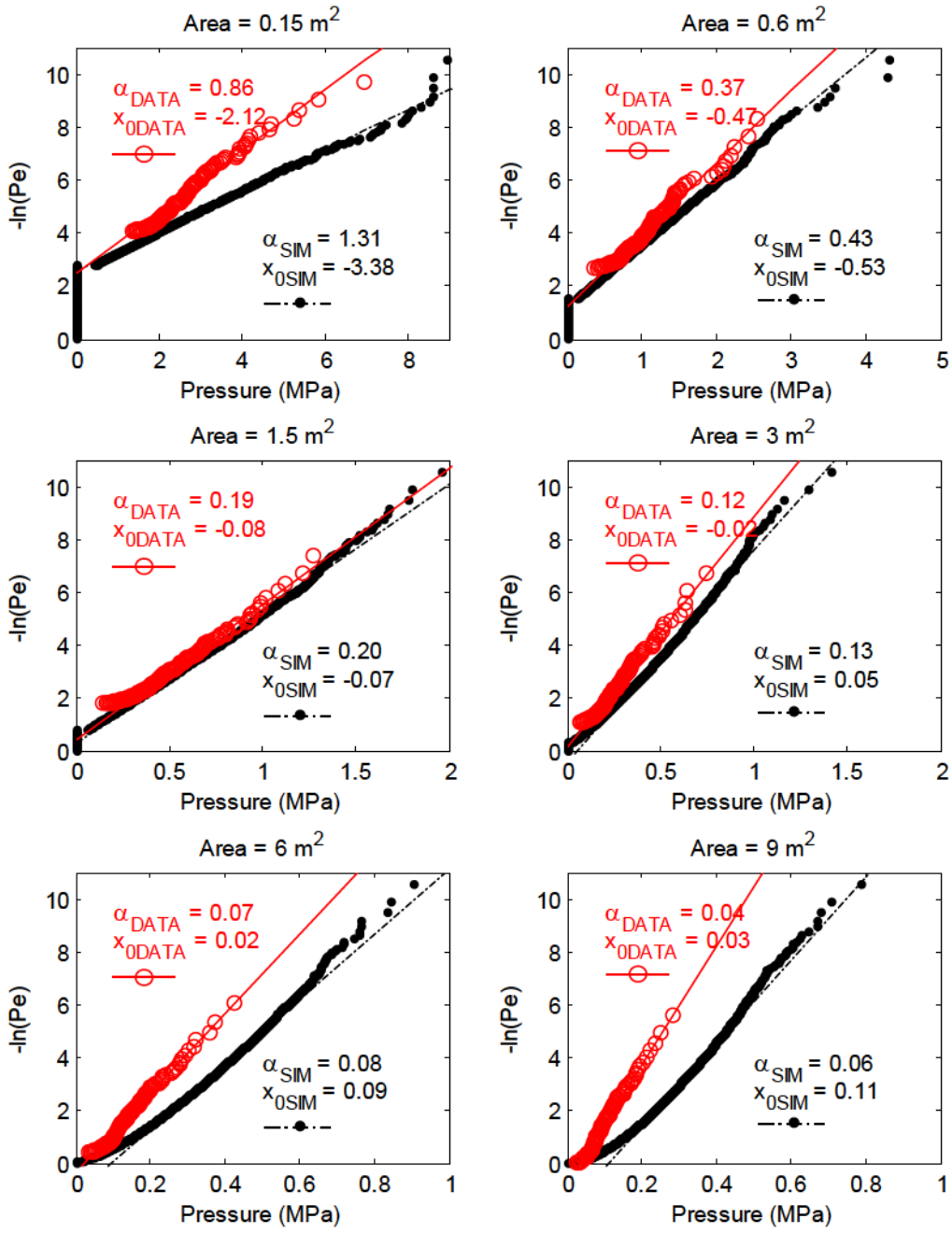

Figure B3 Comparison of simulated local pressure parameters with measured parameters based on South Chukchi 1983 trials – $\gamma = 0.26$ MN; $\gamma_0 = 0.10$ MN; $\rho = 0.40$ *HPZ*s/m^2.

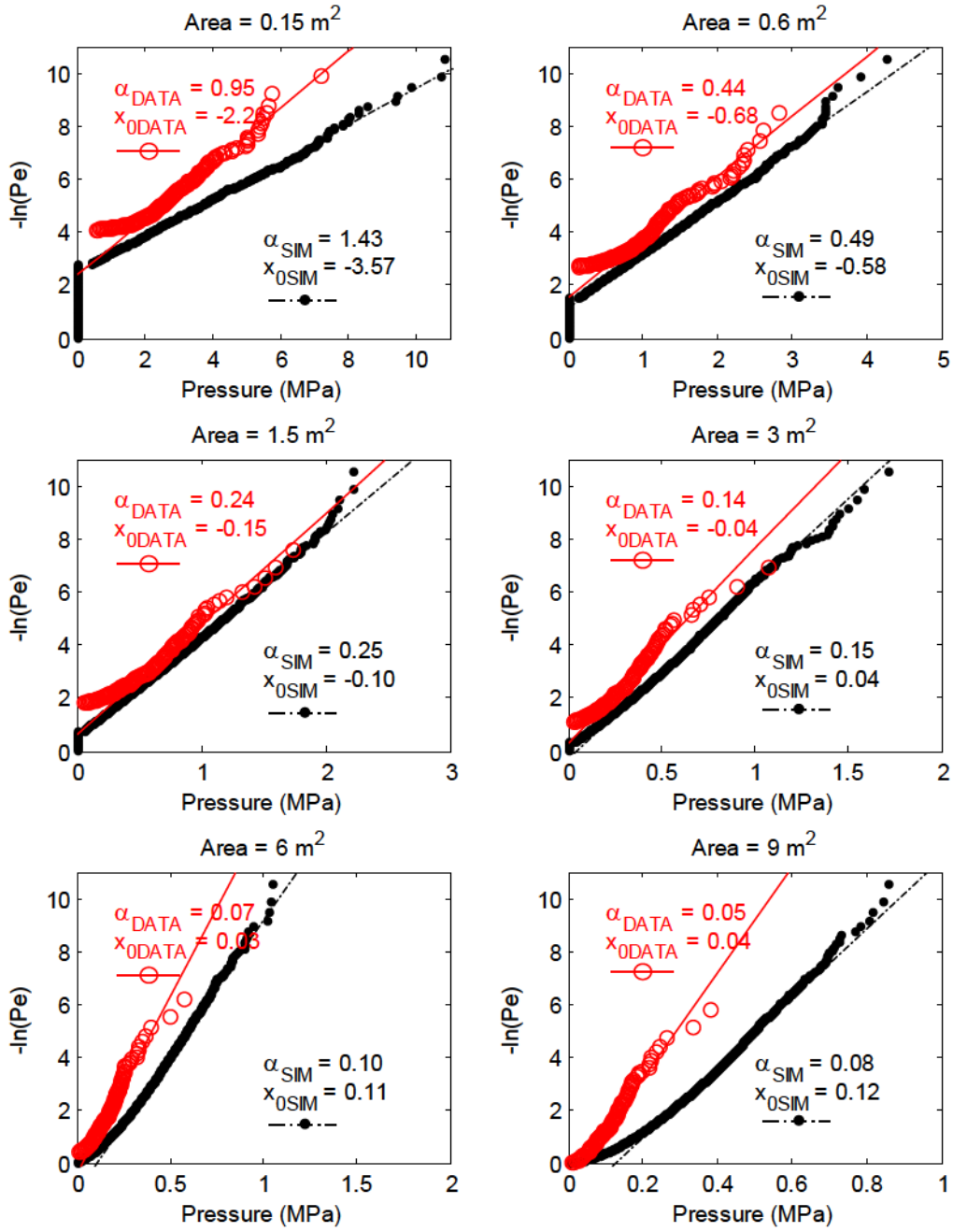

Figure B4 Comparison of simulated local pressure parameters with measured parameters based on Beaufort 1984 trials – $\gamma = 0.32$ MN; $\gamma_0 = 0.10$ MN; $\rho = 0.40$ *HPZ*s/m^2

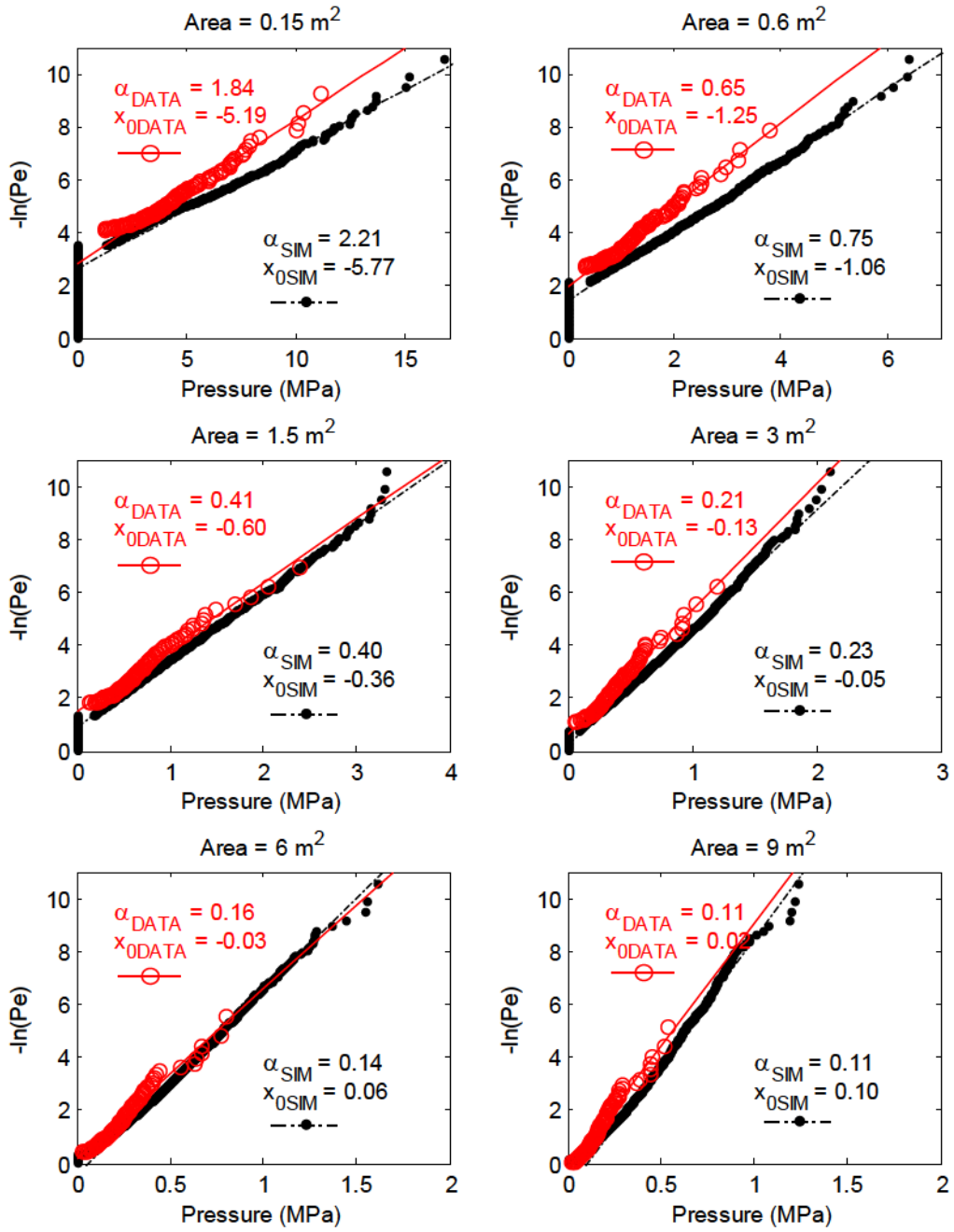

Figure B5 Comparison of simulated local pressure parameters with measured parameters based on *Polar Sea* Beaufort 1982 trials – $\gamma = 0.53$ MN; $\gamma_0 = 0.3$ MN; $\rho = 0.20$ *HPZ*s/m^2

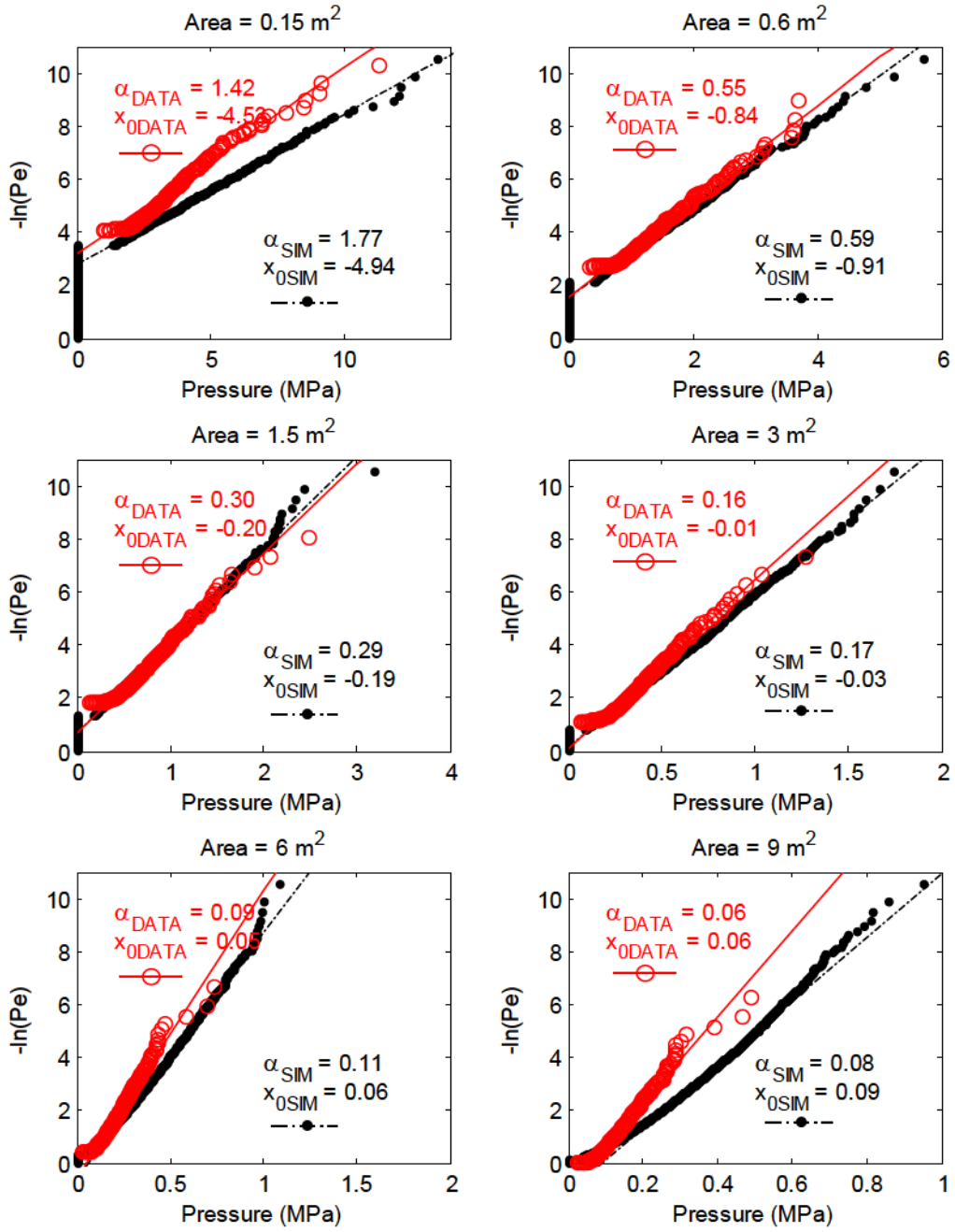

Figure B6 Comparison of simulated local pressure parameters with measured parameters based on North Chukchi 1983 trials – $\gamma = 0.38$ MN; $\gamma_0 = 0.30$ MN; $\rho = 0.20$ *HPZ*s/m^2

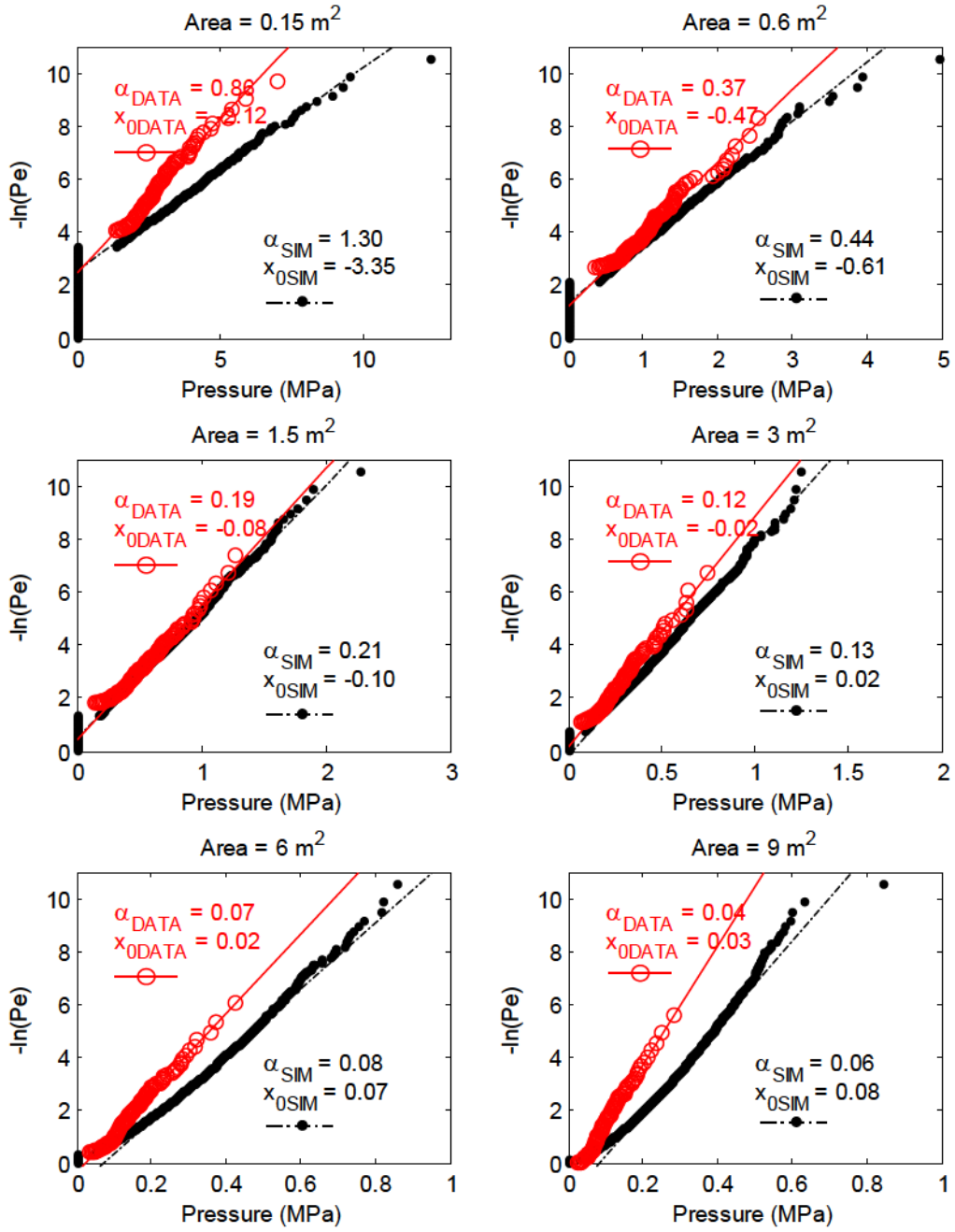

Figure B7 Comparison of simulated local pressure parameters with measured parameters based on South Chukchi 1983 trials – $\gamma = 0.26$ MN; $\gamma_0 = 0.30$ MN; $\rho = 0.20$ *HPZ*s/m^2.

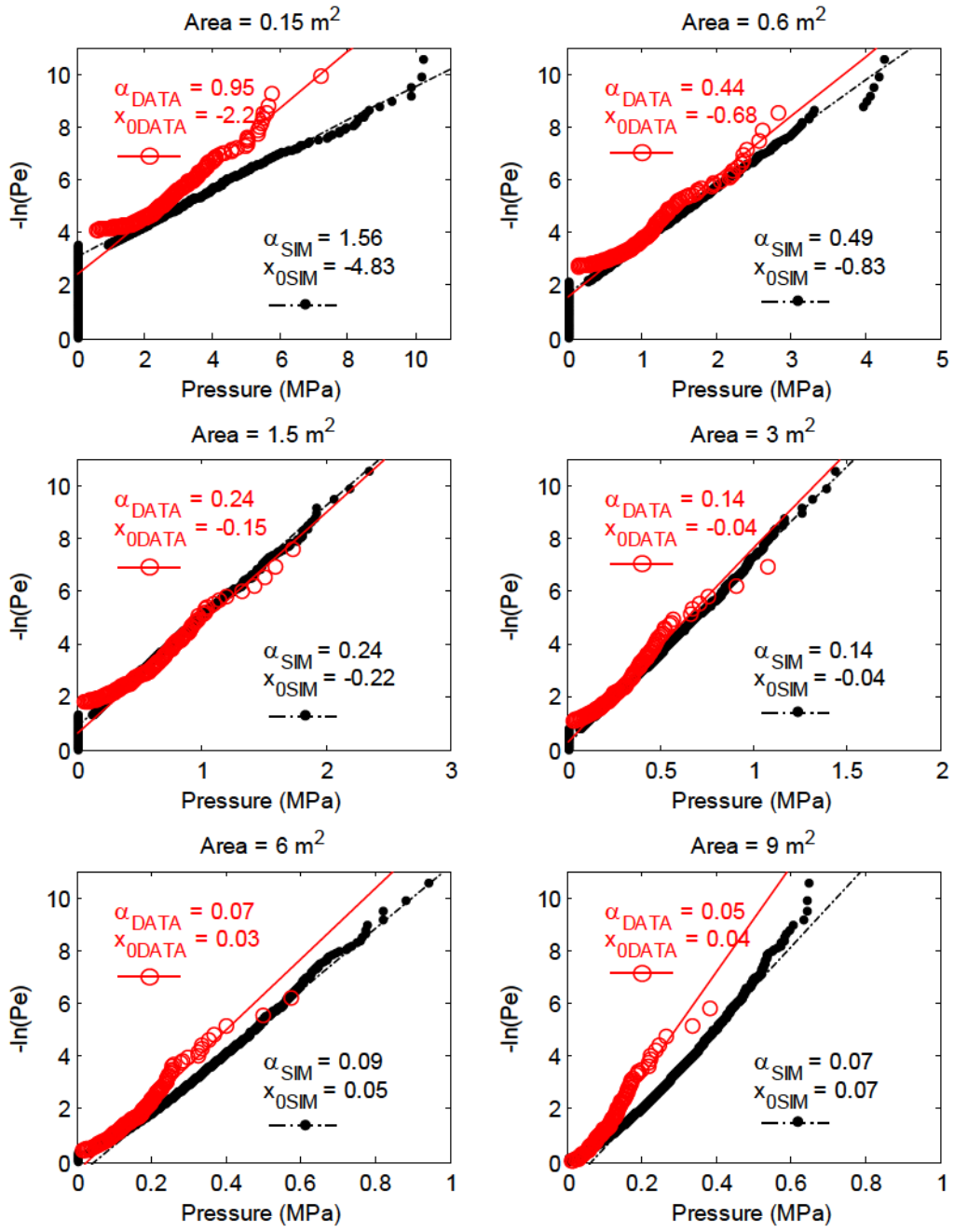

Figure B8 Comparison of simulated local pressure parameters with measured parameters based on Beaufort 1984 trials – $\gamma = 0.32$ MN; $\gamma_0 = 0.20$ MN; $\rho = 0.20$ *HPZ*s/m^2

APPENDIX C

Derivation / Example Illustration of

Closed form Kinetic Energy Ship ram Model Including Popov Model for

MV Arctic type vessel

1. Original Model
2. Revised Model

Original MODEL

Hull Particulars

D	39.9 tonnes			
Len	199.0 m	=B*LtoB	LtoB	7
B	23.0 m	=(1000*D/(1.025*Cb*(LtoB/BtoT)))^(1/3)		
T	11.5 m	=B*BtoT	BtoT	2.5
H	22.0 m	=B/BtoT		
Cwp	0.88			
Cm	0.9			
Cb	0.74			
v	5.68 m/s			

HULL BOW ANGLE DEFINITIONS

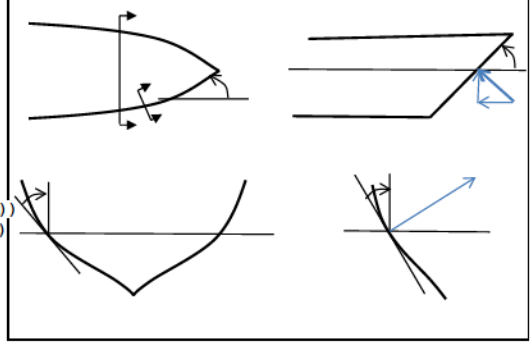

HULL ANGLES

sym	yes/no	y
alpha	α	33.5
gamma	γ	30
beta	β	48.9
bbeta	β'	43.71

Tan β = Tan α / Tan γ
Tan β' = Tan β * Cos α

BETA = ATAN(TAN(alpha) / TAN(gamma))
BBETA = ATAN(TAN(beta)* COS(alpha))

deg-rad
deg 0.017453

Directional cosines

l	0.50
m	0.00
n	0.87

Collision Point

xp	94.525	4.975 from FP
yp	0.00	
zp	0	

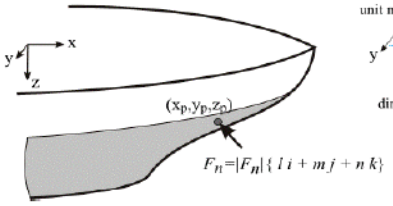

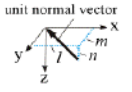

direction cosines

Moment arms

ll1	0.00	= n*yp - m*zp	0.00 ll1^2
mm1	-81.86	= l*zp - n*xp	6701.23 mm1^2
nn1	0.00	= m*xp - l*yp	0.00 nn1^2

Added Mass Terms

Amx	0		Surge
Amy	1.0	= 2*T/B	Sway
Amz	0.74	= +2/3*B*Cwp^2/T/Cb/(1+Cwp)	Heave
Amrol	0.25		roll
Ampit	0.76	= 1+B/T/(3-2*Cwp)/(3-Cwp)	pitch
Amyaw	0.73	=0.3+0.05*Len/B	yaw

Mass radii of gyration (squared)

rx2	85.71	=Cwp*B^2/(11.4*Cm)+H^2/12
ry2	2439.42	=0.07*Cwp*Len^2
rz2	2475.06	= Len^2/16

Polar Class Coefficients

PC	Vs	Po
1	5.675	6.021
2	3.986	4.217
3	2.997	2.985
4	2.508	2.464
5	1.988	2.002
6	1.766	1.497
7	1.466	1.308

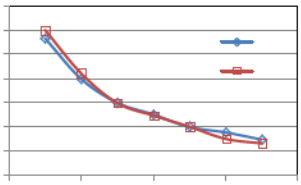

Collision Terms

		2.24
Mass reduction coeff	Co	2.24 = I^2/(1+Amx) + m^2/(1+Amy) + n^2/(1+Amz) + ll1^2/(rx2*(1+Amrol)) + mm1^2/(ry2*(1+Ampit)) + nn1^2/(rz2*(1+Amyaw
Effective Mass	Me	17807659 kg
Normal Velocity	Ve	2.84 m/s
Kinetic Energy	KE	71688349

Ice Terms

Bow collision geometry		y
Polar Class	PC	1
Pressure constant	Po	6.02
PA Scale coefficient	ex	-0.1
ice shape angle	ϕ	150
Shape factor	fa	3.06
(3+2*ex) =	fx	2.8
shape coeff	fai	0.38

Bow Penetration $F_n = \left[3+2\cdot ex\right]^{\frac{2+2ex}{3+2ex}} \cdot Po^{\frac{1}{3+2ex}} \cdot \left[\frac{\tan(\phi)}{\cos(\beta)\cdot\sin^2(\gamma)}\right]^{\frac{1+ex}{3+2ex}} \cdot \left[\frac{1}{2}\frac{\Delta_n}{C_o}V_n^2\right]^{\frac{2+2ex}{3+2ex}}$

fa = 3.06 =(TAN(alpha*deg)/COS(gamma*deg)/(SIN(gamma*deg)

Glancing Blow $F_n = \left[3+2\cdot ex\right]^{\frac{2+2ex}{3+2ex}} \cdot Po^{\frac{1}{3+2ex}} \cdot \left[\frac{\tan(\phi/2)}{\sin(\beta')\cdot\cos^2(\beta')}\right]^{\frac{1+ex}{3+2ex}} \cdot \left[\frac{1}{2}\frac{\Delta_n}{C_o}V_n^2\right]^{\frac{2+2ex}{3+2ex}}$

fa = 10.34 =(TAN(phi*deg/2+8*deg)/SIN(bbeta*deg)/(COS(bbeta*de

Results

Penetration	2.44 m
Duration	1.25 s
Normal Force	82.17 MN
Vertical Force	71.16 MN

82.17 =(fx)^((2+2*ex) / fx)*(Po*1000000)^(1/fx)*fa^((1+ex)/fx)*KE^((2+2*ex) /fx) /1000000

82.17 =(Po*1000000)^(1/(3+2*ex))*fai*(fx*D*1000000/Co*v^2)^((2+2*ex) /(3+2*ex)) /1000000

Note fai =fa^((1+ex)/fx)*0.5^((2+2*ex)/fx) *I^(2*(2+2*ex)/(3+2*ex))
where I above is the unit normal

Revised MODEL

Hull Particulars

D	39.9 tonnes			
Len	199.0 m	=B*LtoB	LtoB	7
B	23.0 m	=(1000*D/(1.025*Cb*(LtoB/BtoT)))^(1/3)		
T	11.5 m	=B*BtoT	BtoT	2.5
H	22.0 m	=B/BtoT		
Cwp	0.88			
Cm	0.9			
Cb	0.74			
v	5.00 m/s			

HULL BOW ANGLE DEFINITIONS

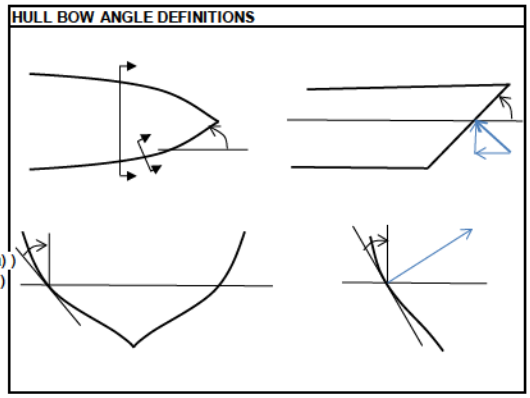

HULL ANGLES

sym	yes/no	y
alpha	α	33.5
gamma	γ	30
beta	β	48.9
bbeta	β'	43.71

Tan β = Tan α / Tan γ
Tan β' = Tan β * Cos α

BETA = ATAN(TAN(alpha) / TAN(gamma))
BBETA = ATAN(TAN(beta)* COS(alpha))

deg-rad
deg 0.017453

Directional cosines

l	0.50
m	0.00
n	0.87

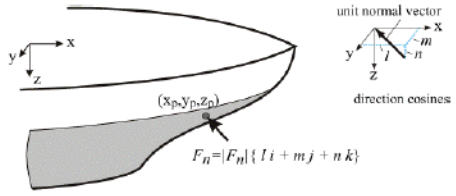

Collision Point

xp	94.525	4.975
yp	0.00	
zp	0	

Moment arms

ll1	0.00	= n*yp - m*zp	0.00 ll1^2
mm1	-81.86	= l*zp - n*xp	6701.23 mm1^2
nn1	0.00	= m*xp - l*yp	0.00 nn1^2

Added Mass Terms

Amx	0.04		Surge
Amy	1.1		Sway
Amz	2.15	MAPS results	Heave
Amrol	0.27	Wei 2014	roll
Ampit	1.25		pitch
Amyaw	0.82		yaw

Mass radii of gyration (squared)

rx2	85.71	=Cwp*B^2/(11.4*Cm)+H^2/12
ry2	2439.42	=0.07*Cwp*Len^2
rz2	2475.06	= Len^2/16

Polar Class Coefficients

PC	Vs	Po
1	6.000	6.500
2	5.000	5.000
3	3.800	4.000
4	3.000	3.000
5	2.500	2.250
6	2.000	1.750
7	1.750	1.500

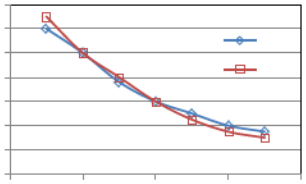

Collision Terms

		1.70
Mass reduction coeff	Co	1.70 = l^2/(1+Amx) + m^2/(1+Amy) + n^2/(1+Amz) + ll1^2/(rx2*(1+Amrol)) + mm1^2/(ry2*(1+Ampit)) + nn1^2/(rz2*(1+Amyaw
Effective Mass	Me	23478953 kg
Normal Velocity	Ve	2.50 m/s
Kinetic Energy	KE	73371728

Ice Terms

Bow collision geometry		y
Polar Class	PC	2
Pressure constant	Po	5.00
PA Scale coefficient	ex	-0.4
ice shape angle	ϕ	150
Shape factor	fa	3.06
(3+2*ex) =	fx	2.2
shape coeff	fai	0.44

Bow Penetration $F_n = [3+2\cdot ex]^{\frac{2+2ex}{3+2ex}} \cdot Po^{\frac{1}{3+2ex}} \cdot \left[\frac{\tan(\phi)}{\cos(\beta)\cdot\sin^2(\gamma)}\right]^{\frac{1+ex}{3+2ex}} \cdot \left[\frac{1}{2}\frac{\Delta_n}{C_o}V_n^2\right]^{\frac{2+2ex}{3+2ex}}$

fa = 3.06 =(TAN(alpha*deg)/COS(gamma*deg)/(SIN(gamma*deg)

Glancing Blow $F_n = [3+2\cdot ex]^{\frac{2+2ex}{3+2ex}} \cdot Po^{\frac{1}{3+2ex}} \cdot \left[\frac{\tan(\phi/2)}{\sin(\beta')\cdot\cos^2(\beta')}\right]^{\frac{1+ex}{3+2ex}} \cdot \left[\frac{1}{2}\frac{\Delta_n}{C_o}V_n^2\right]^{\frac{2+2ex}{3+2ex}}$

fa = 10.34 =(TAN(phi*deg/2+8*deg)/SIN(bbeta*deg)/(COS(bbeta*de

Results

Penetration	3.58 m
Duration	2.17 s
Normal Force	45.12 MN
Vertical Force	39.08 MN

45.12 =(fx)^((2+2*ex) / fx)*(Po*1000000)^(1/fx)*fa^((1+ex)/fx)*KE^((2+2*ex) /fx) /1000000
45.12 =(Po*1000000)^(1/(3+2*ex))*fai*(fx*D*1000000/Co*v^2)^((2+2*ex) /(3+2*ex)) /1000000
Note fai =fa^((1+ex)/fx)*0.5^((2+2*ex)/fx) *l^(2*(2+2*ex)/(3+2*ex))
where l above is the unit normal